

Improving BEM-based Aerodynamic Models in Wind Turbine Design Codes

The wind energy industry is experiencing remarkable growths annually. Despite the great progress made, further cost reductions in turbine technology are necessary for wind energy to reach its full potential in terms of the large-scale supply of electricity. Improving the reliability of aerodynamic models embedded in the design software currently used in industry is indispensable to guarantee reductions in the cost of wind energy.

Due to its relatively high computational efficiency compared to free-wake vortex methods and CFD, the Blade-Element-Momentum theory still forms the basis for many aerodynamic models. Yet various experimental campaigns have demonstrated that BEM-based design codes are not always sufficiently reliable for predicting the aerodynamic load distributions on the wind turbine blades.

In this Doctoral thesis, a detailed investigation of the aerodynamics of wind turbines is described with the aim of providing a better understanding of the limitations of the BEM theory. This work identifies the importance to pursue turbine aerodynamics and modelling with an integrated approach, emphasising on the need to understand the local blade aerodynamics, inflow distribution as well as the geometry and vorticity distribution of the wake. To enable this approach, new analytical methodologies were developed which compensate for the limitations in experimental data. Guidelines are presented for developing improved models for BEM-based aerodynamics codes for wind turbines.

ISBN: 978-99932-0-483-1

Delft University Wind Energy Research Institute
DUWIND

Department of Mechanical Engineering
Faculty of Engineering
University of Malta

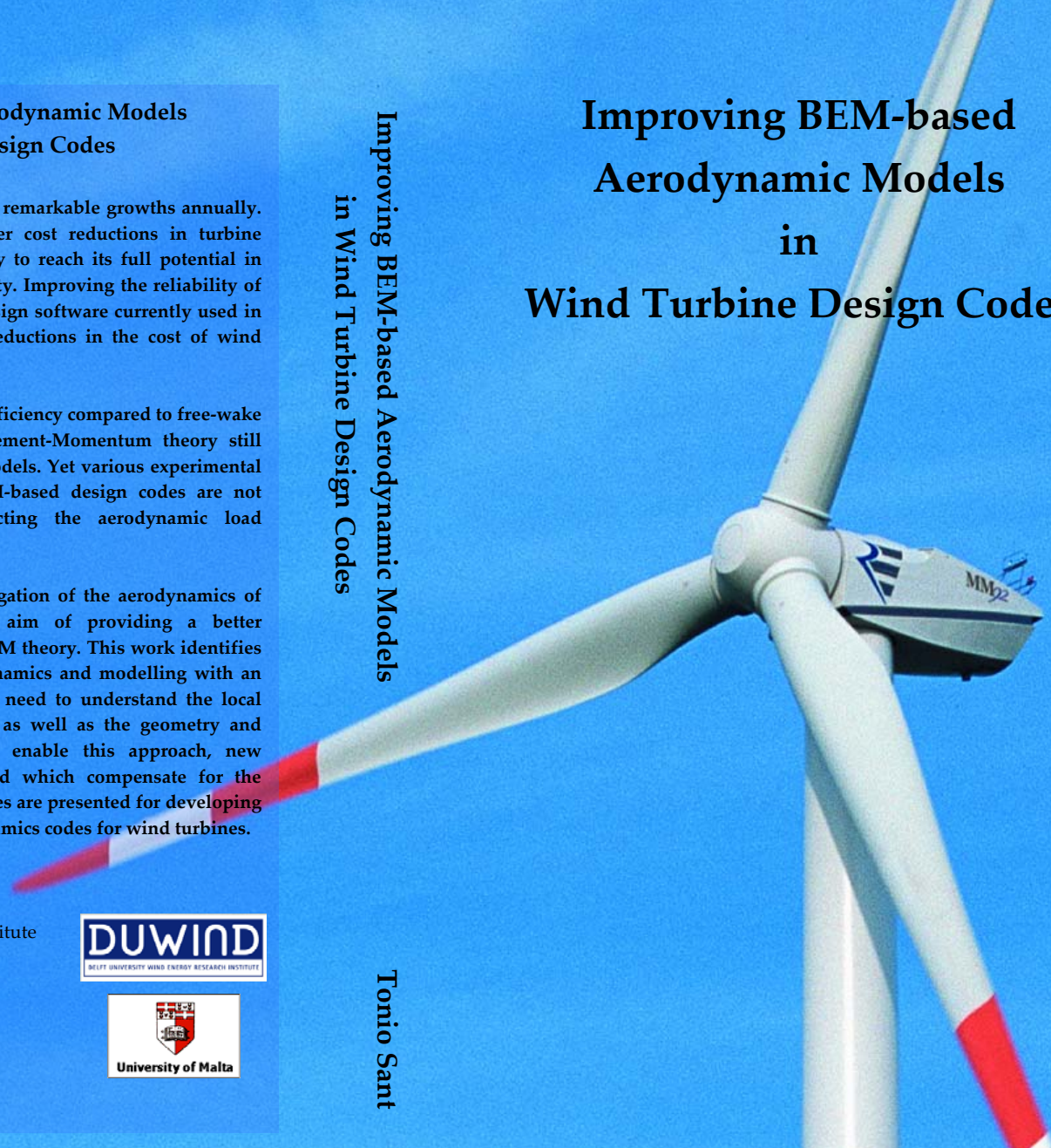
January 2007



Improving BEM-based Aerodynamic Models
in Wind Turbine Design Codes

Tonio Sant

Improving BEM-based Aerodynamic Models in Wind Turbine Design Codes



Tonio Sant

Improving BEM-based Aerodynamic Models in Wind Turbine Design Codes

Proefschrift

ter verkrijging van de graad van doctor
aan de Technische Universiteit Delft,
op gezag van de Rector Magnificus prof. dr. ir. J.T. Fokkema,
voorzitter van het College voor Promoties,
in het openbaar te verdedigen
op maandag 22 januari 2007 om 15:00 uur
door

Tonio SANT
Bachelor of Engineering, University of Malta
geboren te Malta

Dit proefschrift is goedgekeurd door de promotor:
Prof. dr. ir. G.A.M. van Kuik

Toegevoegd promotor:
Dr. ir. G.J.W. van Bussel

Samenstelling promotiecommissie:

Rector Magnificus, voorzitter
Prof. dr. ir. G.A.M. van Kuik, Technische Universiteit Delft, promotor
Dr. G.J.W. van Bussel, Technische Universiteit Delft, toegevoegd promotor
Prof. dr. ir. drs. H. Bijl, Technische Universiteit Delft
Prof. dr. ir. H.W.M. Hoeijmakers, University of Twente
Prof. ing. P.P. Farrugia, University of Malta
Ir. H. Snel, Energy Research Centre of the Netherlands
Dr. S.J. Schreck, National Renewable Energy Laboratory, USA

Key words: wind turbine, aerodynamics, blade-element momentum theory, vortex theory, angle of attack, aerofoil data

This PhD thesis was supported by the University of Malta and Delft University of Technology.

Published and distributed by author in cooperation with:

DUWIND
Delft University Wind Energy Institute
Kluyverweg 1
2629 HS Delft
+31 15 278 5170
www.duwind.tudelft.nl

Department of Mechanical Engineering
Faculty of Engineering
University of Malta
Msida, Malta
+356 2340 2360
www.eng.um.edu.mt

ISBN: 978-99932-0-483-1

Copyright © 2007 Tonio Sant

All rights reserved. Any use or application of data, methods or results from this thesis will be at the user's own risk. The author accepts no liability for damage suffered from use or application. No part of this book may be reproduced in any form, by print, copy or in any other way without prior permission from the author.

Cover picture: Courtesy of REpower Systems AG

Printed in Malta by Print Right Ltd, Marsa.

To my wife Maris and family

Summary

Due to its relatively high computational efficiency compared to free-wake vortex methods and CFD, the Blade-Element-Momentum theory still forms the basis for many aerodynamic models integrated in design software for horizontal-axis wind turbines. Yet various experimental campaigns have demonstrated that BEM-based design codes are not always sufficiently reliable for predicting the aerodynamic load distributions on the wind turbine blades. This is particularly true for stalled and yawed rotor conditions. Thus, it is presently necessary to try to improve BEM methods in order to provide more cost-effective wind turbine designs and hence reduce the cost of wind energy.

In this thesis, a detailed investigation of the aerodynamics of wind turbines in both axial and yawed conditions is carried out based on wind tunnel measurements with the aim of providing a better understanding of the limitations of the BEM theory. This work identifies the need to pursue turbine aerodynamics and modelling in an integrated approach, emphasising on the need to understand the local blade aerodynamics, inflow distribution as well as the geometry and vorticity distribution of the wake. To enable this approach, new methodologies and analytical models are developed which compensate for the limitations in experimental data. Among these models is a free wake vortex code, which is based on a prescribed bound circulation distribution over the rotor blades. This free-wake vortex model *HAWT-FWC* is developed and validated using the hot-film and the tip vortex smoke visualisation data from the TUDelft rotor experiments and will be used to generate induced velocity distributions for the measured aerodynamic load distributions at the NREL Phase IV wind turbine.

In this research project, the aerodynamics of two different wind turbine rotors is investigated:

- (1) The TUDelft model rotor which is tested in the open-jet wind tunnel facility at Delft University of Technology. Detailed hot-film measurements are performed in the near wake of the model rotor when operating in attached flow conditions over the blades (low angles of attack). The measurements are taken at different planes parallel to the rotorplane, both upstream and downstream. Smoke visualisation experiments are also carried out to trace the trajectories of tip vortex cores in the rotor wake in attached and stalled flow conditions. These experiments are carried out in close collaboration with Wouter Haans, a Phd colleague at TUDelft. However, due to limited dimensions of the blades it is not possible to measure the aerodynamic blade load distributions directly. By applying blade-element theory a methodology is developed to estimate the time-dependent aerodynamic load distributions at the rotor blades from the hot-film measurements:

- (i) initially, inflow velocities at the blades are estimated from the hot-film measurements taken at the different planes parallel to the rotorplane.
- (ii) the results from step (i) are used to derive the steady/unsteady angle of attack and the relative velocity distributions at the blades.
- (iii) the results from step (ii) are used in an advanced unsteady aerofoil model to yield the distributions for bound circulation and aerodynamic loading at the blades. A new and efficient numerical method for implementing this aerofoil model in rotor aerodynamics codes is developed.

Both the inflow measurements and the derived aerodynamic loads on the TUDelft rotor are used to carry out a detailed investigation of the BEM theory when modelling both axial and yawed conditions. Two different approaches are applied: the first approach in which the inflow measurements and aerodynamic loads are used to compute separately the momentum and blade-element theory parts of the BEM equation for axial thrust. The discrepancy between the two parts is a measure of the incapability of the BEM theory to model axial or yawed conditions. In the second approach, a typical BEM code is employed to model the TUDelft rotor and the results are compared with those obtained from the hot-film measurements. Despite the fact that only attached flow conditions are being studied and also the fact that the results derived from the inflow measurements have a rather high level of uncertainty in general, this comparison results in a better understanding of the limitations of BEM-based design codes and further insight is obtained of how these can be improved.

- (2) The NREL Phase VI wind turbine which was extensively tested in the NASA Ames wind tunnel in 2000. The experimental data required for the study are obtained from the NREL. This data consists of time-accurate blade pressure measurements for the rotor operating in both axial and yawed conditions together with measurements of the local flow angles measured at different radial locations in front of the blades using five-hole probes. The experimental data also consists of strain gauge measurements for the output torque and the root flap/edge moments. However detailed inflow measurements at the rotor are not performed. In this thesis, a novel and comprehensive methodology is presented for using the blade pressure measurements in conjunction with the free-wake vortex model *HAWT-FWC* to estimate the angle of attack distributions at the blades more accurately, together with the induced velocity distributions at the rotorplane and wake geometry. This methodology consists of the following sequence of steps: Initially, a spanwise distribution for the angle for attack is assumed at the blades. This is then used together with the values of C_n and C_l obtained from the blade pressure measurements to estimate the lift coefficients at the blades. Using the Kutta-Joukowski law, the bound circulation distribution at the blades is then determined and prescribed to *HAWT-FWC* to generate the free vortical wake. The induced velocity at the blades is estimated and used to calculate a new angle of attack distribution. The process is repeated until convergence in the angle of attack is

achieved. One advantage for applying this methodology is that the solution is in itself unsteady and could be readily applied to study yawed conditions, under which complex aerodynamic phenomena are known to occur (e.g. dynamic stall and unsteady induction). A second advantage concerns the fact that the wake geometry is inherently part of the solution. Thus it is possible to derive the pitch and expansion of the helical wake from the measured C_n and C_t , which otherwise can be obtained using time-consuming smoke visualisation experiments. The three-dimensional vorticity circulation distribution in the wake can also be investigated under different operating conditions.

Using the above methodology, new 3D lift and drag aerofoil data are derived from the NREL rotor blade pressure measurements. This new data is considerably different from the corresponding 2D wind tunnel aerofoil data due to the presence of blade tip/root loss effects, stall-delay or else unsteady conditions resulting from rotor yaw (mainly dynamic stall). The new 3D lift and drag aerofoil data is then used to improve BEM load predictions in axial and yawed conditions. It is found that with this new data, the BEM predictions improved considerably even when dealing with highly stalled and yawed conditions. For yawed conditions, new inflow corrections to account for skewed wake effects in BEM codes are also derived.

From this research, it is possible to draw guidelines on how BEM-based models can be improved. These guidelines can be summarised in two:

- (1) *Improvement of aerofoil data:* It is clear from this study that BEM predictions improve substantially when more accurate 3D aerofoil data is used. In this thesis, a new engineering model for 3D lift and drag coefficients in axial conditions is developed based on the measurements on the NREL rotor. A similar model for unsteady conditions is not developed since the amount of derived unsteady aerofoil data was to a certain extent limited. Yet this data is very useful for other researchers to develop such improved models.
- (2) *Improvement of engineering models for skewed wake effects in yaw:* The BEM theory is incapable with modelling the effects of a skewed wake on the induction at the blades that result in yawed rotors. Various engineering models to correct for this incapability are developed in the past years and are used in state-of-the-art design codes. Yet this study has demonstrated that such models are limited for two reasons and better models are required:
 - (a) first of all, the unsteady and periodic induction distribution at the blades resulting from rotor yaw may have a higher harmonic content than that catered for by these presently available engineering models. Also the unsteady distributions are dependent not only on the yaw angle but also on the operating tip speed ratio and

rotor geometry. This study has shown that because the aerodynamics of yawed rotors is complicated, it is vital to introduce more theoretically comprehensive models. An approach is proposed for interfacing BEM-codes to prescribed-wake vortex models when treating yawed conditions;

(b) secondly, the currently available models only correct the local axial induction at the blades to the corresponding annular-averaged value. This study shows that, due to the deficiency of the axial momentum equation in yaw, the annular-averaged axial induction computed by BEM may also need to be corrected. It is found from the analysis on both the TUDelft and NREL rotors that this correction not only depends on the rotor yaw angle but also on the operating axial thrust coefficient. An engineering model to model this correction is required if BEM predictions in yawed rotors are to be improved.

Samenvatting

Vanwege relatief lange rekentijden van vrije-zog wervel methoden en numerieke stromings dynamica (Computational Fluid Dynamics of CFD in het Engels) vormt de Blad Element Impuls (Blade Element Momentum of BEM in het Engels) theorie nog steeds de basis van ontwerp programmatuur voor horizontale-as windturbines. Verscheidene meetcampagnes hebben echter aangetoond dat BEM ontwerp codes niet altijd voldoen om de aerodynamische belastingsverdelingen op windturbinebladen nauwkeurig te voorspellen. Dit geldt in het bijzonder voor rotoren in overtrek en in scheefstand. Daarom is het belangrijk de BEM methoden te verbeteren, om zo rendabeler windturbineontwerpen te maken en daarmee de kosten van windenergie te reduceren.

In deze dissertatie is een uitgebreid onderzoek uitgevoerd naar de aerodynamica van windturbines in zowel rechte aanstroming als scheefstand, gebaseerd op windtunnelmetingen, met het doel een beter begrip van de beperkingen van de BEM theorie te krijgen. Deze studie maakt de noodzaak duidelijk om een integrale aanpak te volgen in turbine aerodynamica en modellering, met nadruk op de lokale bladaerodynamica, de verdeling van de aanstroomsnelheden en de positie en sterkte van de wervelsterkte in het zog. Om deze aanpak mogelijk te maken, zijn nieuwe methoden en analytische modellen ontwikkeld welke de beperkingen van experimentele data compenseren. Een van deze modellen is een vrij wervelzog model dat is gebaseerd op een voorgeschreven circulatieverdeling over de rotorbladen. Dit vrije wervelzog model *HAWT-FWC*, is ontwikkeld en gevalideerd met de hittefilm en de tipwervel rookvisualisatie data uit de TUDelft rotor experimenten, en zal worden gebruikt om de geïnduceerde snelheidsverdelingen bij de gemeten aerodynamische belastingsverdelingen te bepalen.

In dit onderzoeksproject is de aerodynamica van twee verschillende windturbinerotoren onderzocht:

- (1) De TUDelft modelrotor die getest is in de open-straal windtunnel van de Technische Universiteit Delft. Gedetailleerde hittefilm metingen zijn uitgevoerd in het nabije zog van de modelrotor bij aanliggende stromingscondities over het blad (kleine invalshoeken). De metingen zijn uitgevoerd in verschillende vlakken parallel aan het rotorvlak, zowel stroomopwaarts als stroomafwaarts. Rook visualisatie experimenten zijn ook uitgevoerd om de banen van de tipwervelkernen in het rotor zog te bepalen bij zowel aanliggende als overtrokken stroming. Deze experimenten zijn uitgevoerd in nauwe samenwerking met Wouter Haans, een collega-promovendus aan de TUDelft in hetzelfde vakgebied. Vanwege de beperkte afmetingen van het rotorblad is het niet mogelijk de aerodynamische belastingsverdelingen op het blad te meten. Om de verdeling van de tijdsafhankelijke aerodynamische belastingen op de rotorbladen te schatten uit de hittefilm metingen is op de volgende wijze gebruik gemaakt van de bladelement theorie:

- (i) eerst zijn de instroomsnelheden ter plekke van de bladen geschat uit hittefilm metingen in de verschillende vlakken parallel aan het rotorvlak.
- (ii) de resultaten uit stap (i) zijn gebruikt om de stationaire/instationaire invalshoek en de verdeling van de relatieve snelheden ter plekke van de bladen af te leiden.
- (iii) de resultaten uit stap (ii) zijn gebruikt in een geavanceerd instationair model voor profielaerodynamica, om de verdelingen van de gebonden wervelsterkte en de aerodynamische belastingen op de bladen te bepalen. Voor het implementeren van dit instationaire profielmodel in rotoraerodynamica codes is een nieuwe efficiënte methode ontwikkeld.

Zowel de instroommetingen als de berekende aerodynamische belastingen op de TUDelft rotor zijn gebruikt om een gedetailleerd onderzoek uit te voeren naar de BEM-theorie voor het modelleren van een rechte en scheve aanstroming. Twee verschillende methoden zijn gevolgd: de eerste methode waarbij de instroommetingen en de aerodynamische belasting gebruikt worden om afzonderlijk de impuls en de bladelement theorie waarden voor de axiaalkracht in de BEM vergelijking te berekenen. De discrepantie tussen deze twee waarden is een maat voor de toepasbaarheid van de BEM-theorie voor axiale of scheve aanstromingscondities. In de tweede methode is een echte BEM-code gebruikt om de TUDelft rotor te modelleren en zijn de resultaten vergeleken met die uit de hittefilm metingen. Ondanks het feit dat enkel aanliggende stromingscondities bestudeerd zijn en het feit dat de resultaten, die bepaald zijn uit de instroommetingen, in het algemeen tamelijk onnauwkeurig zijn, leidde dit tot een beter begrip van de beperkingen van op BEM gebaseerde ontwerpcodes en tot een verder inzicht in hoe deze te kunnen verbeteren.

- (2) De NREL Fase VI windturbine die uitvoerig getest werd in de de NASA Ames windtunnel in 2000. De experimentele data, die benodigd zijn voor het onderzoek, werden verkregen van het NREL. Deze data bestaan uit tijdsafhankelijke drukmetingen op het roterende blad in zowel rechte aanstroming als scheefstand, gecombineerd met metingen van de locale stromingshoek, gemeten op verschillende radiale posities voor de bladen met vijf-gats-drukmeters. Tijdens de experimenten zijn ook rekstrookmetingen van het koppel en de klap- en zwaaimomenten aan de bladwortel verricht. Gedetailleerde instroommetingen aan de rotor zijn echter niet uitgevoerd. In deze dissertatie is een nieuwe en uitgebreide methode toegepast om de invalshoekverdelingen op de bladen, de verdelingen van de geïnduceerde snelheid in het rotorvlak en de zoggeometrie nauwkeuriger te bepalen door gebruik te maken van de drukmetingen op het blad in combinatie met het vrije-wervel zogmodel *HAWT-FWC*. Deze methode bestaat uit de volgende reeks stappen: eerst wordt een verdeling in spanwijdterichting van de invalshoek ter plaatse van de bladen aangenomen. Deze wordt dan gebruikt om, samen met de C_n - en C_t -waarden verkregen uit de drukmetingen op de bladen, de liftcoëfficiënten op de bladen te schatten.

Gebruikmakend van de wet van Kutta-Joukowski wordt dan de verdeling van de gebonden wervelsterkte op de bladen bepaald en opgelegd aan *HAWT-FWC* om het vrije wervelzog te generen. De geïnduceerde snelheid ter plaatse van de bladen wordt geschat en gebruikt om een nieuwe invalshoekverdeling te berekenen. Dit proces wordt herhaald totdat convergentie van de invalshoek bereikt is. Een voordeel van het toepassen van deze methode is dat de oplossing inherent instationair is en rechtstreeks toegepast zou kunnen worden voor het bestuderen van scheefstand, waarvan het bekend is dat complexe aerodynamische processen optreden (bijvoorbeeld dynamische overtrek en instationaire inductie). Een tweede voordeel betreft het feit dat de zoggeometrie een inherent deel van de oplossing is. Het is dus mogelijk uit de gemeten C_n en C_t de onderlinge afstand en de expansie van het spiraalvormige zog af te leiden, welke anders verkregen kan worden uit tijdrovende rookvisualisatie experimenten. Ook voor andere operationele condities kan op deze wijze het driedimensionale wervelzog worden bepaald en onderzocht.

Met behulp van deze methode zijn nieuwe driedimensionale lift- en weerstand-profieldata bepaald uit de drukmetingen op de NREL rotorbladen. Deze nieuwe data verschillen aanzienlijk van de tweedimensionale windtunnel profieldata vanwege blad tip- en wortel-verlies effecten, uitstel van overtrek of ook instationaire effecten die het gevolg zijn van scheefstand.(voornamelijk dynamische overtrek). De nieuwe driedimensionale lift- en weerstandswaarden voor het profiel zijn vervolgens gebruikt om verbeteringen in BEM berekeningen voor rechte aanstroming en scheefstand aan te brengen. De BEM resultaten zijn aanzienlijk beter met deze nieuwe data, zelfs wanneer het condities betreft met sterke overtrek en scheefstand. Voor scheefstandcondities zijn ook nieuwe instroomcorrecties afgeleid om BEM codes corrigeren voor scheefstandeffecten.

Uit dit onderzoek volgen richtlijnen voor de wijze waarop op BEM gebaseerde modellen verbeterd zouden kunnen worden. Deze richtlijnen kunnen als volgt worden samengevat:

- (1) *Verbetering van profieldata*: het blijkt duidelijk uit deze studie dat BEM voorspellingen aanzienlijk verbeteren wanneer nauwkeuriger driedimensionale profieldata gebruikt worden. In deze dissertatie is een nieuw engineering model voor driedimensionale lift- en weerstandscoefficienten in rechte aanstroming ontwikkeld gebaseerd op de metingen aan de NREL rotor. Een vergelijkbaar model voor instationaire omstandigheden is niet ontwikkeld omdat er onvoldoende instationaire profiel gegevens afgeleid konden worden. Desalniettemin zijn deze data erg bruikbaar voor andere onderzoekers om verbeterde modellen op te stellen.
- (2) *Verbetering van engineering modellen voor de effecten van het zog in scheefstandcondities*: de BEM theorie is niet in staat de effecten van een scheef zog op de inductie ter plaatse van de bladen te modelleren. Verscheidene engineering modellen ter correctie hiervan

zijn de laatste jaren ontwikkeld en toegepast in moderne ontwerpcodes. Deze studie heeft echter aangetoond dat dergelijke modellen om twee redenen een beperkte geldigheid hebben en dat betere modellen vereist zijn:

- (a) allereerst heeft de instationaire en periodieke verdeling van de inductiesnelheden ter plaatse van de bladen in scheefstand waarschijnlijk een hogere harmonische dan die in de huidige engineering modellen wordt meegenomen. Bovendien zijn de instationaire verdelingen niet alleen afhankelijk van de scheefstandhoek, maar ook van de gehanteerde tipsnelheden en de rotorgeometrie. Deze studie heeft laten zien dat, vanwege de complexiteit van de aerodynamica van rotoren in scheefstand, het essentieel is om meer theoretisch onderbouwde modellen te introduceren. Voorgesteld wordt om een aanpak te kiezen waarbij voor het berekenen van scheefstandcondities een BEM code wordt gekoppeld aan een eenvoudig-wervelzogmodel.

- (b) ten tweede wordt in de huidige modellen alleen de lokale axiale inductiesnelheid ter plaatse van de bladen gecorrigeerd met de gemiddelde waarde over de annulus. Deze studie laat zien dat, ten gevolge van een fout in de axiale impulsvergelijking in scheefstand, de gemiddelde axiale inductie over de annulus berekend door BEM ook gecorrigeerd moet worden. Uit de analyse van zowel de TUDelft als de NREL rotor blijkt dat de correctie niet slechts afhangt van de scheefstandhoek van de rotor maar ook van de axiaalkrachtscoëfficiënt. Een gecorrigeerd engineering model is nodig om BEM voorspellingen bij scheefstaande rotoren te verbeteren.

Table of Contents

Acknowledgements	i
Abbreviations	ii
Nomenclature	iii
List of Developed Software Codes	xi
Chapter 1 Introduction	1
1.1 The Role of Aerodynamics in Wind Turbine Design	2
1.2 Principles of HAWT Aerodynamics	5
1.3 Current Status of Aerodynamic Design Models for Horizontal -Axis Wind Turbines	8
Chapter 2 Aim of Thesis and Approach.....	11
2.1 Problem Statement.....	11
2.2 Aim of Thesis	14
2.3 Approach	15
2.3.1 <i>Research work on the TUDelft wind tunnel turbine</i>	15
2.3.2 <i>Research work on the NREL Phase VI wind tunnel turbine</i>	15
2.3.3 <i>Development of Free-wake Vortex Model</i>	17
2.4 Organization of Work	18
2.5 Co-ordinate Systems Analysis	20
Chapter 3 The Blade-Element-Momentum Theory	23
3.1 The Simple Linear Momentum Theory for a Yawed Actuator Disc	23
3.2 The Momentum Equations	25

3.3	The Blade-Element Theory	26
3.3.1	<i>The Blade-Element Velocity</i>	26
3.3.2	<i>The Induced Velocity at Each Blade Element</i>	26
3.3.3	<i>Flow Velocity Relative to a Moving Blade Element</i>	27
3.3.4	<i>Aerodynamic Loads</i>	28
3.3.5	<i>The Blade-Element Equations for Thrust and Torque</i>	29
3.4	The Blade-Element-Momentum Equations	30
3.5	Corrections to the Blade-Element-Momentum Theory	31
3.6	Description of Program <i>HAWT_BEM</i>	40
3.6.1	<i>Time-based Numerical Solution for the BEM Equation</i>	40
3.6.2	<i>Program Structure</i>	43
Chapter 4	Aerodynamic Analysis of the Delft Model Turbine	45
4.1	Introduction	45
4.2	Wind tunnel Measurements	48
4.2.1	<i>Wind Tunnel</i>	48
4.2.2	<i>Part I: Inflow Measurements</i>	49
4.2.3	<i>Part II: Smoke Visualization Measurements</i>	76
4.3	Estimating the Aerodynamic Loads at the Blades from the Wind Tunnel Inflow Measurements.....	87
4.3.1	<i>Methodology</i>	87
4.3.2	<i>A Theoretical Method for Finding the Unsteady Lift Coefficient in Attached Flow for a Rotating Blade in Yaw</i>	90
4.3.3	<i>Developed Software Tools</i>	98
4.3.4	<i>Assessment of Wind Tunnel Blockage Effects</i>	110
4.3.5	<i>Quantification of Errors in Deriving Blade Loading due to Errors in Inflow Measurements</i>	121
4.3.6	<i>Results and Discussion</i>	128
4.4	Investigating the Limitations of the BEM Theory for Axial/Yawed Wind Turbines.....	182
4.4.1	<i>Results from Approach A</i>	183
4.4.2	<i>Results from Approach B</i>	188
4.5	Conclusions.....	207

Chapter 5	Development of a Free-Wake Vortex Model	211
	5.1 Introduction	211
	5.2 Free-wake Vortex Numerical Model	212
	5.2.1 <i>Blade Model</i>	212
	5.2.2 <i>Near Wake Model</i>	213
	5.2.3 <i>Far Wake Model</i>	221
	5.2.4 <i>Numerical Solution</i>	222
	5.2.5 <i>Program Structure</i>	226
	5.3 Verification and Validation of Free-Wake Vortex Model	228
	5.3.1 <i>Verification and Validation Methodology</i>	228
	5.3.2 <i>Results and Discussion</i>	234
	5.4 Conclusions.....	274
Chapter 6	Aerodynamics Analysis of the NREL Phase VI Wind Turbine	277
	6.1 Introduction	277
	6.2 NASA/Ames UAE Wind Tunnel Data Used	279
	6.3 Estimating the Angle of Attack from Blade Pressure Measurements using the Free-Wake Vortex Model	283
	6.3.1 <i>Methodology</i>	283
	6.3.2 <i>Axial Conditions</i>	285
	6.3.3 <i>Yawed Conditions</i>	320
	6.4 BEM Predictions for the NREL Phase VI Rotor with New Aerofoil Data and Inflow Corrections	362
	6.4.1 <i>Axial Conditions</i>	363
	6.4.2 <i>Yawed Conditions</i>	373
	6.5 Conclusions.....	393
Chapter 7	Guidelines for Improving the Reliability of BEM-based Design Codes	397
	7.1 Modelling of Aerofoil Data.....	397
	7.2 Correcting for skewed wake effects in yaw.....	403
	7.2.1 <i>Development of engineering model using a heuristic</i>	

	<i>approach based on Fourier series</i>	404
	7.2.2 <i>Alternative approach using prescribed-wake vortex model</i>	405
	7.2.3 <i>Correction to the axial momentum equation for yawed rotors</i>	411
Chapter 8	Project Outcome, Conclusions and Recommendations	413
	8.1 Project Outcome	413
	8.2 Conclusions	416
	8.3 Recommendations	417
References	419
Appendices		
	Appendix A Maximum Power Coefficient for a Yawed Actuator Disc	429
	Appendix B Calculation of Aerodynamic Loads Induced at the Yaw Bearing	432
	Appendix C Calculation of the Induced Velocity from a Vortex Filament using the Biot-Savart Law	436
	Appendix D Linear and Spline Numerical Interpolation.....	441
	Appendix E Vortex Filament Stretching	446
Curriculum Vitae	449
Author Publications	450

Acknowledgements

This Phd thesis would have not been possible without the support and help of many people.

First of all I am thankful to God for granting me the health and energy, especially in the most difficult moments. I would like to express my heartfelt thanks to my supervisor prof. dr. ir. Gijs van Kuik and co-supervisor dr. Gerard van Bussel for their guidance and the invaluable advices they gave me during my research. I am greatly indebted to prof. ing. Peter Paul Farrugia for giving me the opportunity to carry out this work and for relieving me from my duties at the University of Malta to be able to finish my studies on time. Many thanks also go to the University of Malta and Delft University of Technology for the financing of the project.

I am very grateful to Wouter Haans for his cooperation in the experimental work on the TUDelft wind tunnel turbine and for the many discussions we had throughout the course of this work. Many thanks also go Simon Toet for his technical assistance in using the wind tunnel equipment. I would like to extend my gratitude to my other colleagues at the wind energy research group at Delft University of Technology for their hospitality, sharing their knowledge and for offering fruitful suggestions: Ruud van Rooij, Nando Timmer, Carlos Ferreira, Toni Subroto, Wim Bierbooms, Michiel Zaaijer, Dick Veldkamp, Eric van der Pol and former colleagues Nord Jan Vermeer, Sander Mertens and Albert Bruining. Our secretary, Sylvia Willems is thanked for her practical assistance, which saved me lots of time and allowed me to concentrate on my work during my short stays in Delft. My colleague at the University of Malta, dr.ing. Martin Muscat, is acknowledged for his support in facilitating my access to the Mechanical Engineering Computer Lab required for the extensive computations.

Dr. Scott Schreck and his colleagues at the National Renewable Energy Laboratory are acknowledged for providing the data of the NASA Ames wind tunnel experiments. This data was very stimulating for the intended research work. Herman Snel and Gerard Schepers from the Energy Research Centre of the Netherlands as well as Jeppe Johansen from the Risø Laboratory of Denmark are also thanked for their interest and valuable discussions.

The members of the Doctoral Examination Committee are also thanked for their attention to this thesis.

Most of all, I would like to express to gratitude to my wife Maris and family for their support and prayers. Without their patience and encouragement, completion would have never been reached.

Tonio Sant
Delft, September 2006

Abbreviations

AEP – Annual Energy Yield

ATC – Annual Total Cost

BEM – Blade Element Momentum Theory

BET – Blade Element Theory

COE – Cost of Energy

CFD – Computational Fluid Dynamics

DTU – Denmark Technical University

ECN – Energy Research Centre of the Netherlands

EAWE – European Academy of Wind Energy

EWEA – European Wind Energy Association

HAWT – Horizontal-axis wind turbine

IEA – International Energy Agency

NASA – National Aeronautics and Space Administration, USA

NLR – National Aerospace Laboratory, the Netherlands

NREL – National Renewable Energy Laboratory, USA

PIV – Particle Imaging Velocimetry

TU Delft – Delft University of Technology, The Netherlands

UAE – Unsteady Aerodynamics Experiment

WECS – Wind energy conversion system

Nomenclature

a	- index to represent vortex age of trailing or shed vortex filament <u>or</u> parameter used in engineering model for stall-delay or wake skew angle <u>or</u> parameter equal to $\frac{1}{2}$ in unsteady aerofoil theory for attached flow
a_1	- disk averaged <u>or</u> azimuthally (annular) averaged axial induction factor ($= u_a/U$)
$a_{1,m}$	- optimum disk averaged axial induction factor for a given yaw angle
$a_{1,c}$	- axial induction factor at blade lifting line ($= u_{a,c}/U$)
a_2	- azimuthally (annular) averaged tangential induction factor ($= u_t/R\Omega$)
$a_{2,c}$	- tangential induction factor at blade lifting line ($= u_{t,c}/R\Omega$)
a_3	- azimuthally (annular) averaged radial induction factor ($= u_r/U$)
$a_{3,c}$	- radial induction factor at blade lifting line ($= u_{r,c}/U$)
b	- index to represent blade number <u>or</u> parameter used in engineering model for stall-delay <u>or</u> parameter equal to half chord length in unsteady aerofoil theory for attached flow (m)
b_1	- constant in exponential decay function approximating Wagner's function
b_2	- constant in exponential decay function approximating Wagner's function
b_s	- mid-span of elliptical wing (m)
c	- local blade chord (m)
c_o	- maximum chord length of elliptical wing (m)
d	- rotor diameter (m) <u>or</u> parameter used in engineering model for stall-delay <u>or</u> distance measured from smoke visualisation photo, corrected for parallax effects (m)
d_a	- distance between rotor hub centre and yaw bearing centre (m)
dA_η	- tangential (chordwise) component of aerodynamic loading at a blade element (N/m)
dA_ζ	- normal component of aerodynamic loading at a blade element (N/m)
dT	- axial thrust loading at a blade element (N/m)
dT_{2D}	- axial thrust loading at a blade element computed from 2D lift and drag coefficients (N/m)
dT_{3D}	- axial thrust loading at a blade element computed from 3D lift and drag coefficients (N/m)
dQ	- torque loading at a blade element (Nm/m)
dQ_{2D}	- torque loading at a blade element computed from 2D lift and drag coefficients (Nm/m)
dQ_{3D}	- torque loading at a blade element computed from 3D lift and drag coefficients (Nm/m)
f	- Prandtl tip and root loss factor
f_d	- parameter used to correct 2D drag coefficient for 3D effects

f_l	- parameter used to correct 2D lift coefficient for 3D effects
f_r	- Prandtl root loss factor
f_t	- Prandtl tip loss factor
f_L	- aerodynamic blade lift loading (N/m)
f_Q	- aerodynamic blade torque loading (Nm/m)
f_T	- aerodynamic blade thrust loading (N/m)
h	- perpendicular distance of vortex filament from a given point (m) <u>or</u> parameter used for engineering model for stall-delay <u>or</u> angular calibration constant for hot-film probe <u>or</u> vertical distance between smoke visualisation plane and measuring grid (m)
i	- blade station number or trailing vortex number <u>or</u> index to denote radial location of hot-film probe in measuring plane
ip	- index to denote radial location of point at which the induced velocity is computed by prescribed-wake or free-wake vortex model
j	- index to denote angular position of hot-film probe in measuring plane
jp	- index to denote azimuthal location of point at which the induced velocity is computed by prescribed-wake or free-wake vortex model
k	- angular calibration constant for hot-film probe <u>or</u> index to number of vortex filament along a given helix in prescribed-wake vortex model <u>or</u> reduced frequency
k_a	- parameter to correct axial momentum equation for yawed conditions
k_c	- ratio of the exit jet velocity to the true free-stream velocity
k_e	- ratio of the axial induced velocity at the tunnel exit computed by the prescribed-wake vortex code to the tunnel exit jet velocity
l	- length of vortex filament (m)
m	- index to represent rotor time step
n	- total number of blade stations and trailing vortices per blade <u>or</u> constant for speed calibration of hot-film
$nRev$	- number of rotor revolutions to generate free-wake
$nfwRev$	- number of helical revolutions in far wake model of free-wake code
$nwRev$	- number of helical revolutions in wake of prescribed-wake vortex model
p	- tip vortex pitch measured along a direction parallel to the free-wind speed (m)
p_w	- tip vortex pitch taken along a direction parallel to the rotor axis (m)
pfw	- tip vortex pitch in far wake model of free-wake code (m)
r	- position vector <u>or</u> radial location along blade (m)
r_c	- viscous core radius of vortex filament (m)
r_{ceff}	- viscous core radius of vortex filament, corrected for filament strain effects (m)
r_w	- radial location of vortex node on a given helix in prescribed-wake vortex model (m)
s	- reduced time
t	- time (sec)

u_a	- disk-averaged <u>or</u> azimuthally (annular) averaged axial induced velocity (m/s)
$u_{a,c}$	- axial induced velocity at blade lifting line. Can be directly on lifting line or at a given axial distance from it (m/s)
$u_{a,exit}$	- axial induced velocity at tunnel exit jet as computed by prescribed-wake vortex model (m/s)
u_t	- azimuthally (annular) averaged tangential induced velocity (m/s)
$u_{t,c}$	- tangential induced velocity at blade lifting line (m/s)
u_r	- azimuthally (annular) averaged radial induced velocity (m/s)
$u_{r,c}$	- radial induced velocity at blade lifting line (m/s)
u_x	- tangential induced velocity (m/s)
u_y	- axial induced velocity (m/s)
u_z	- radial induced velocity (m/s)
u_x	- induced velocity at near wake node along the X axis (m/s)
u_y	- induced velocity at near wake node along the Y axis (m/s)
u_z	- induced velocity at near wake node along the Z axis (m/s)
\hat{u}	- 3D induced velocity vector at blade element (m/s)
\hat{u}_c	- 3D induced velocity vector at blade element in BEM, corrected for skewed wake effects (m/s)
v	- local blade deflection (m)
w_a	- axial flow velocity in rotor wake (along the y or Y_a axis) (m/s)
$w_{a,aver}$	- azimuthally (annular) averaged axial flow velocity in rotor wake (along the y axis) (m/s)
$w_{a,c}$	- axial flow velocity at blade lifting line (along the y axis). Maybe directly on lifting line or at a given axial distance from it (m/s)
w_b	- velocity of fluid bypassing rotor wake (m/s)
w_h	- horizontal flow velocity in rotor wake (along the X_a axis) (m/s)
w_r	- radial flow velocity in rotor wake (along the z axis) (m/s)
w_t	- tangential flow velocity in rotor wake (along the x axis) (m/s)
w_v	- vertical flow velocity in rotor wake (along the Z_a axis) (m/s)
z	- parameter for viscous modelling of vortex core
A	- rotor cross-sectional area (m^2) <u>or</u> constant for speed calibration of hot-film ($V^2/^\circ C$)
A_0, A_1, \dots, A_3	- amplitudes in Fourier series-based engineering model for skewed wake effects
A_1	- constant in exponential decay function approximating Wagner's function
A_2	- constant in exponential decay function approximating Wagner's function
A_η	- tangential (chordwise) aerodynamic load at blade element acting along the η axis (N)
A_ζ	- normal aerodynamic load at blade element acting along the ζ axis (N)
B	- total number of blades in rotor <u>or</u> constant for speed calibration of hot-film
B_F	- blockage factor for rotor in wind tunnel
C_d	- drag coefficient

$C_{d,2D}$	- drag coefficient for 2D flow
$C_{d,2D-MIN}$	- minimum drag coefficient for 2D flow
$C_{d,3D}$	- drag coefficient corrected for 3D effects (tip/root loss and/or stall delay)
$C_{d,s}$	- drag coefficient at stall
$C_{d,max}$	- maximum drag coefficient
C_{dp}	- pressure drag coefficient
C_n	- normal coefficient
C_m	- moment coefficient
C_l	- lift coefficient
$C_{l,2D}$	- lift coefficient for 2D flow
$C_{l,3D}$	- lift coefficient corrected for 3D effects (tip/root loss and/or stall delay)
$C_{l,lin}$	- lift coefficient that would be obtained if the 2D lift slope is extended linearly beyond stall
$C_{l,s}$	- lift coefficient at stall
C_l^c	- circulatory lift coefficient
C_l^{nc}	- non-circulatory lift coefficient
C_t	- tangential coefficient
C_T	- rotor axial thrust coefficient
C_Q	- rotor torque coefficient
C_P	- rotor power coefficient
$C_{P,Max}$	- optimum rotor power coefficient for a given yaw angle
D_j	- diameter of open-jet wind tunnel tube (m)
D_j'	- diameter of tunnel jet at a given downstream distance from rotorplane (m)
D'	- diameter of rotor wake at a given downstream distance from rotorplane (m)
E	- hot-film voltage (V)
F	- location of rotor hub centre
F_{sa}	- correction factor used in BEM model to correct for skewed wake effects in yaw
F_{A1}	- right-hand side of BEM equation for axial flow (blade-element theory part) (m^2/s^2)
F_{A2}	- left-hand side of BEM equation for axial flow (momentum part) (m^2/s^2)
GXB	- geometric influence coefficient for X-component of induced velocity from bound vortex in wake of prescribed-wake vortex model (m^{-1})
GYB	- geometric influence coefficient for Y-component of induced velocity from bound vortex in wake of prescribed-wake vortex model (m^{-1})
GZB	- geometric influence coefficient for Z-component of induced velocity from bound vortex in wake of prescribed-wake vortex model (m^{-1})
GXT	- geometric influence coefficient for X-component of induced velocity from trailing vortex in wake of prescribed-wake vortex model (m^{-1})
GYT	- geometric influence coefficient for Y-component of induced velocity from trailing vortex in wake of prescribed-wake vortex model (m^{-1})
GZT	- geometric influence coefficient for Z-component of induced velocity from

	trailing vortex in wake of prescribed-wake vortex model (m^{-1})
<i>H</i>	- tower height <u>or</u> vertical distance between smoke visualisation camera and measuring grid (m)
<i>IBX</i>	- geometric influence coefficient for <i>X</i> -component of induced velocity from bound vortex in near wake of free-wake vortex model (m^{-1})
<i>IBY</i>	- geometric influence coefficient for <i>Y</i> -component of induced velocity from bound vortex in near wake of free-wake vortex model (m^{-1})
<i>IBZ</i>	- geometric influence coefficient for <i>Z</i> -component of induced velocity from bound vortex in near wake of free-wake vortex model (m^{-1})
<i>ISX</i>	- geometric influence coefficient for <i>X</i> -component of induced velocity from shed vortex in near wake of free-wake vortex model (m^{-1})
<i>ISY</i>	- geometric influence coefficient for <i>Y</i> -component of induced velocity from shed vortex in near wake of free-wake vortex model (m^{-1})
<i>ISZ</i>	- geometric influence coefficient for <i>Z</i> -component of induced velocity from shed vortex in near wake of free-wake vortex model (m^{-1})
<i>ITX</i>	- geometric influence coefficient for <i>X</i> -component of induced velocity from trailing vortex in near wake of free-wake vortex model (m^{-1})
<i>ITY</i>	- geometric influence coefficient for <i>Y</i> -component of induced velocity from trailing vortex in near wake of free-wake vortex model (m^{-1})
<i>ITZ</i>	- geometric influence coefficient for <i>Z</i> -component of induced velocity from trailing vortex in near wake of free-wake vortex model (m^{-1})
<i>K</i>	- parameter used in BEM model to correct for skewed wake effects using the Glauert model <u>or</u> function used to smoothen experimental data using the Gaussian kernel.
<i>K_v</i>	- correction factor applied to Biot-Savart equation to correct for viscous core effects
<i>L</i>	- distance taken from smoke visualisation photo, uncorrected for parallax errors (m)
<i>LFA</i>	- local flow angle (deg)
<i>LSSTQ</i>	- low-speed shaft torque (Nm)
<i>M_{tot}</i>	- total number of time-marching steps in free-wake code
<i>O</i>	- location of rotor yaw bearing centre
<i>P</i>	- rotor power developed (W)
<i>Q</i>	- rotor output torque (Nm)
<i>Q_{NORM}</i>	- dynamic pressure (N/m^2)
<i>R</i>	- rotor tip radius (same as <i>R_t</i>) (m)
<i>R_r</i>	- rotor hub radius (m)
<i>R_t</i>	- rotor tip radius (same as <i>R</i>) (m)
<i>R_{r,w}</i>	- inner wake boundary radius for prescribed-wake vortex model (m)
<i>R_{t,w}</i>	- outer wake boundary radius for prescribed-wake vortex model (m)
<i>R_{t,w1}</i>	- outer wake boundary radius for prescribed-wake vortex model at the first tip vortex core location (m)

$R_{t,io2}$	- outer wake boundary radius for prescribed-wake vortex model at the second tip vortex core location (m)
Re	- Reynolds number at blade section
$ReleaseRoot$	- radial location at which inboard edge of vortex sheet is shed from blade in prescribed-wake vortex model (expressed as fraction of R)
$ReleaseTip$	- radial location at which outboard edge of vortex sheet is shed from blade in prescribed-wake vortex model (expressed as fraction of R)
$RCTF$	- relative computational time factor for free-wake solution
REM	- blade root edge bending moment (Nm)
RFM	- blade root flap bending moment (Nm)
S_c	- viscous core growth constant (sec)
T	- tower base location <u>or</u> rotor axial thrust (N)
T_a	- measured flow temperature ($^{\circ}C$)
T_f	- preset flow temperature ($^{\circ}C$)
U	- free windspeed or wind tunnel speed (m/s)
U_{jet}	- open-jet tunnel exit velocity (m/s)
U_p	- flow velocity component measured along x_p axis of hot-film (m/s)
U_x	- free windspeed component parallel to rotor disk (m/s)
U_y	- free windspeed component normal to rotor disk (m/s)
U'	- resultant flow velocity at yawed actuator disc in accordance with simple momentum theory (m/s)
V	- flow velocity relative to aerofoil (m/s)
V_{eff}	- measured effective flow velocity by hot-film (m/s)
$V_{eff,Xa}$	- measured effective flow velocity with hot-film aligned along the X_a axis (m/s)
$V_{eff,Ya}$	- measured effective flow velocity with hot-film aligned along the Y_a axis (m/s)
$V_{eff,Za}$	- measured effective flow velocity with hot-film aligned along the Z_a axis (m/s)
V_p	- flow velocity component measured along y_p -axis of hot-film (m/s)
V_n	- normal component of flow velocity relative to blade section (m/s)
V_r	- 2D resultant flow velocity relative to blade section acting in η - ζ plane (m/s)
V_{rel}	- 3D resultant flow velocity relative to blade section (m/s)
V_t	- tangential component of flow velocity relative to blade section (m/s)
V_{η}	- tangential component of flow velocity relative to blade section (same as V_t) (m/s)
V_{ζ}	- normal component of flow velocity relative to blade section (same as V_n) (m/s)
V_{ξ}	- radial component of flow velocity relative to blade section (m/s)
$V_{A,\eta}$	- absolute velocity component of blade element along the η axis (m/s)
$V_{A,\zeta}$	- absolute velocity component of blade element along the ζ axis (m/s)
$V_{A,\xi}$	- absolute velocity component of blade element along the ξ axis (m/s)
W_p	- flow velocity component measured along z_p axis of hot-film (m/s)
W_X	- velocity of near wake node along the X axis in free-wake vortex code (m/s)
W_Y	- velocity of near wake node along the Y axis in free-wake vortex code (m/s)
W_Z	- velocity of near wake node along the Z axis in free-wake vortex code (m/s)

Y_{ap} - axial distance of plane parallel to rotorplane at which induced velocity distribution is computed using prescribed-wake or free-wake vortex model (m)

Greek Nomenclature

α - angle of attack (deg) or viscous core growth constant

α_o - zero lift angle of attack (deg)

α_e - equivalent angle of attack, accounting for unsteady effects (deg)

α_{sweep} - sweep angle of attack (deg)

α_s - stalling angle of attack (deg)

$\dot{\alpha}$ - rate of change of angle of attack with time (deg/s)

β - blade coning angle (deg)

χ - rotor axis tilt angle (deg)

χ^s - wake skew angle (deg)

δ - cut-off distance (m)

δ_v - viscous core diffusivity coefficient

ε - vortex filament strain

ε_a - relative error in $u_{a,c}$ between that predicted by prescribed-wake vortex code and that obtained from hot-film measurements by assuming that the free-stream velocity is equal to the tunnel exit jet velocity (%)

ε_{kc} - error in the calculated axial induced velocity due to discrepancy between tunnel-exit velocity and true free-wind speed (%)

ε_Q - error in the derived blade torque loading due to errors in the inflow measurements (%)

ε_T - error in the derived blade axial thrust loading due to errors in the inflow measurements (%)

$\varepsilon_{va,c}$ - error in the flow velocity at the lifting line obtained from the inflow measurements (%)

ϕ - rotor or blade azimuth angle (deg) or indicial response function derived by Wagner for unsteady aerofoils

ϕ_p - angular position of hot-film probe (deg)

ϕ_w - angular position of wake vortex filament node in prescribed wake vortex model (deg)

γ - parameter used in the cosine segmentation of radial segments of lifting lines (deg)

λ - rotor operating tip speed ratio

μ - blade aspect ratio

μ_a - air dynamic viscosity (Ns/m^2)

φ - local inflow angle (deg)

$\varphi_0, \varphi_1, \dots, \varphi_B$ - phase angles in Fourier series-based engineering model for skewed wake

	effects (<i>deg</i>)
ω	- bandwidth used in smoothing method using the Gaussian kernel
θ	- local blade pitch angle (<i>deg</i>)
θ_{tip}	- pitch angle at blade tip (<i>deg</i>)
ρ	- density of air (kg/m^3)
τ	- index to denote time step
n_{tot}	- total number of equally-spaced time steps in one whole rotor revolution
ηp	- index to denote azimuthal location of point at which the induced velocity is computed by prescribed-wake or free-wake vortex model
ν	- kinematic viscosity of air (m^2/s)
ξ_n	- relative error when varying n (%)
ξ_{fw}	- relative error due to far wake (%)
ξ_{wp}	- relative error for wake periodicity (%)
$\xi_{\Delta\phi}$	- relative error when varying $\Delta\phi$ (%)
ζ	- vorticity (s^{-1})
Δ	- phase shift angle used in the Boeing-Vertol model for dynamic stall (<i>deg</i>)
$\Delta\phi$	- azimuthal step for one rotor revolution (<i>deg</i>)
$\Delta\tau$	- incremental time step (<i>sec</i>)
Ω	- rotor angular speed (<i>rad/s</i>)
Θ	- collective pitch angle of blade (<i>deg</i>)
Ψ	- yaw angle (<i>deg</i>)
Γ	- circulation (m^2/s)
Γ_B	- bound circulation (m^2/s)
$\Gamma_{B,MAX}$	- maximum bound circulation along elliptical wing (m^2/s)
$\Gamma_{B,2D}$	- bound circulation based on 2D lift coefficient (m^2/s)
$\Gamma_{B,3D}$	- bound circulation based on 3D lift coefficient (m^2/s)
Γ_T	- trailing circulation (m^2/s)
Γ_S	- shed circulation (m^2/s)

List of Developed Software Codes

HAWT_BEM – Blade-element momentum model

HAWT_LFIM – Model to derive aerodynamic loads from wake inflow measurements

HAWT_PVC – Prescribed-wake vortex model

HAWT_FWC – Free-wake vortex model

1. Introduction

Energy is fundamental to economic and social development. On the dawn of the 21st century we are being faced with one of the toughest challenges ever – that of securing energy supply. We are still heavily dependent on oil resources which will eventually become depleted within a few decades. Energy consumption is also expected to increase up to about 40% by the year 2010. An increasing world population, an enlarged global economy and an improved standard of living all contribute to greater demands for energy. At the same time, we are facing the greatest threat to our survival on planet earth: global climate change. Climate change is not just an environmental threat but also an economic threat. Rising sea levels, more severe droughts and health issues will increase insurance costs radically in the future.

Wind energy is one of the most effective power technologies that is ready today to be deployed globally on a scale that can aid in tackling this problem. Wind energy is a significant and powerful resource and is safe, clean and abundant. It is being very successful in penetrating the energy market, especially in Europe which has a share of 70% of the global wind energy industry. Backed by effective policies, the wind energy industry is experiencing a remarkable growth of 20-25% per annum (EWEA, [23]). This is considered to be very high for an industry manufacturing heavy equipment. In the past 20 years, the size of wind turbines increased rapidly from about 15m diameter having a capacity of 50kW to about 120m having a capacity of 5MW. The initial capital cost of the turbines also decreased from 3500Euros/KW to about 1000Euros/KW. A number of assessments confirm that the world's wind resources are enormous and well distributed. The total available resource that is technically recoverable is estimated to be 53,000 Terawatt hours (TWh)/year, which is over twice as large as the projection for the world's entire electricity demand in 2020 (EWEA, Greenpeace, [24]). Lack of resource is therefore unlikely to be a barrier to a penetration of wind energy in the energy market. A major barrier is cost since wind energy has to face fierce competition from conventional sources of energy based on fossil-fuels and nuclear energy. Despite the great progress made, wind energy still has a long way to go before it reaches its full potential in terms of the large-scale supply of electricity. While it can already be cost competitive with newly built conventional plants at sites with good wind speeds, significant further cost reductions are necessary. In the IEA report "Long-Term Research and Development Needs for Wind Energy for the Time Frame 2000 to 2020" [94], it has been estimated that if wind energy is going to supply 10% of the world's electricity needs by 2020, cost reductions in the technology of 30 to 50% are still necessary. Research and development work could contribute up to 40% of those reductions. The

challenge faced by the wind energy community is to produce more cost-competitive wind turbines through highly optimized designs.

1.1 The Role of Aerodynamics in Wind Turbine Design

A wind turbine is a complex system working in a complex environment. It is composed of subsystems working together in a tightly coupled manner. Furthermore, wind turbines must be adapted to specific meteorological and topographical characteristics of each particular site. This makes the design of a Horizontal-Axis Wind Turbine (HAWT) a complex process that is characterized by several trade-off decisions aimed at finding the optimum overall performance and economy. The design approach is multi-disciplinary and integrates several branches of engineering including aerodynamics, mechanical, materials, electrical, control and manufacturing engineering. The design objectives are to maximize energy yield, reduce overall costs and maximize the lifetime of the system (see Fig. 1.1). These objectives will determine the minimum cost of energy (COE).

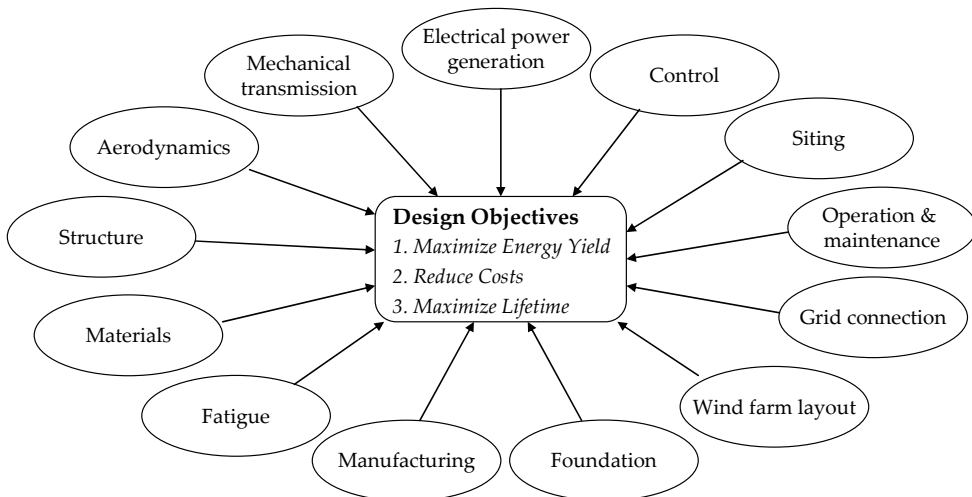


Figure 1.1 – Design considerations for a Wind Energy Conversion System.

A typical design process starts off with the identification of sub-systems and components making up the whole wind energy conversion system (WECS) (see Fig. 1.2). Basically three types of models are integrated in the design process: (1) an aerodynamics model that estimates the aerodynamic performance, loads and annual energy yield (AEP) for a given rotor geometry and operating site; (2) a structures model that will calculate the total loads and induced stresses on the load bearing components resulting from the aerodynamic loads (computed by the aerodynamics model) and due to gravity and dynamics. This model will

also estimate the fatigue lifetime of each component; and (3) a cost model that computes the expenses required to manufacture the WECS components, together with other costs required to install and operate the system at the installation site. The cost model calculates the equivalent annual total cost (ATC) taking into account all costs incurred over the expected lifetime of the system. Finally, the annual cost of energy (COE) is determined (equal to the ratio AEP/ATC) (see Fig. 1.2). Throughout the design optimization, the different variables of the aerodynamic, structure and cost models are altered systematically to yield the minimum COE. For offshore wind turbines, the design process becomes more complicated since it should cater for more costly foundations and for a tougher environment. For description of integrated design approaches for offshore wind turbines refer to work of Kuhn [43]), Hendriks *et al.* [38] and van der Tempel [92].

As illustrated in Fig. 1.2, aerodynamics plays a vital role in the design process as it will determine the AEP and the aerodynamic loads which in turn influence the costs of the different WECS components. The aerodynamic design of a HAWT rotor has the objective of providing the optimized geometry (diameter, number of blades, blade shape) that will yield the lowest COE possible. It is subject to three constraints that may be conflicting: (1) Maximization of power coefficient; (2) Maximization of energy yield; and (3) Reduction of blade loads (see Fig. 1.3).

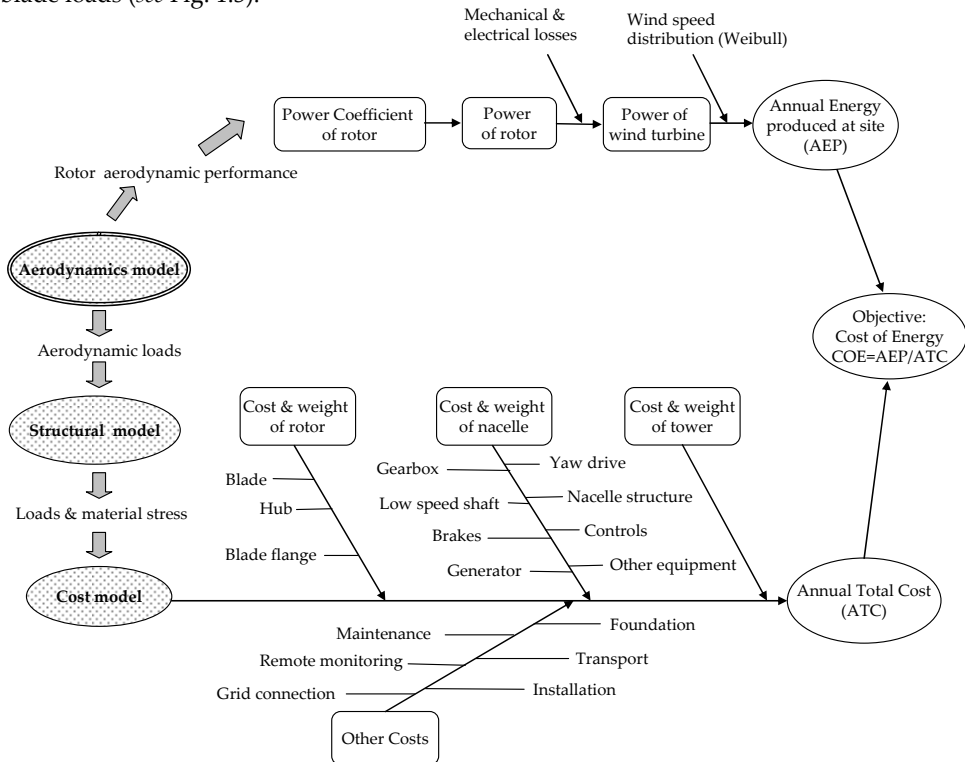


Figure 1.2 – Typical scheme of models for design optimization.

Maximizing the power coefficient will increase the energy yield. However to maximize the energy yield, the power coefficient should be maximized over a wide range of windspeeds. In the earlier days, aerodynamic design focused only on maximizing the power coefficient C_P . But it was discovered that the maximum C_P was only achieved at a small range of wind speeds, especially in stall-regulated turbines with the detriment of reducing the annual energy yield (Snel, [81]). Increasing the chord and twist of the blades will help in increasing the energy yield at low windspeeds. This is helpful for sites where the mean annual windspeed tends to be on the low side. Yet doing so may increase the blade weight and thus the gravitational loads of the supporting structure.

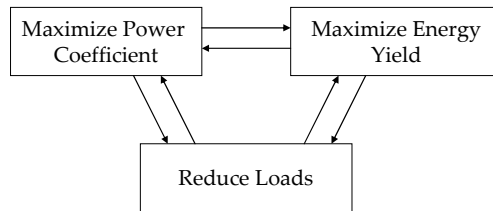


Figure 1.3 – Constraints for aerodynamic design.

Wind turbine operation is limited by a cut-out windspeed beyond which the rotor has to be brought to a standstill due to high windspeeds. A higher cut-out wind speed will contribute to a larger energy yield since benefit will be taken from the high windspeeds (which have larger energy intensities). On the other hand, this will push to greater structural demands resulting from higher loads.

It should be clear that although profound knowledge of aerodynamics is an indispensable requirement, it alone is not sufficient to determine the loads and stresses on the WECS components. These depend on the deformation (which may be unsteady) of the system components in response to the external loads. The aerodynamic loads on the blades act as external loads. The interaction between these aerodynamic loads and the dynamic behavior of the system components is known as aeroelasticity. A prerequisite is to ensure that the wind turbine is aeroelastically stable during the operations. In a complex operating environment, the unsteady aerodynamic loads may cause the WECS to become aeroelastically unstable which causes the large vibrations that reduce the fatigue lifetime of the system. Aeroelastic analysis demands that aerodynamic models inherently form part of structural dynamics models. This adds to the computational power required by design software tools.

1.2 Principles of HAWT Aerodynamics

In simple words, a Horizontal-Axis Wind Turbine (HAWT) is a propeller-type rotor that extracts energy from the wind. Since the turbine extracts kinetic energy from the fluid stream, the air flowing through the rotor experiences a decrease in the velocity. The momentum change of the air will exert an axial thrust on the rotor. The rotor also imparts a swirl velocity component to the air in a direction opposite to that of the shaft.

Each rotor blade may be considered as a rotating wing. The air flowing around the blades causes the latter to experience lift (resulting from bound circulation around the blades) and drag forces. The combined action of these forces yields an output torque at the rotor shaft, thereby producing power. Due to the fact that the blades rotate instead of moving linearly as in a normal wing, the local aerofoil lift and drag coefficients may be different from those obtained in 2D wind tunnel data. This is especially noted at high angles of attack when the phenomenon of stall-delay is known to take place, resulting in significantly larger aerofoil coefficients. Stall delay will be described in Chapter 3.

The wake from the rotating blade comprises a vortical shear layer or vortex sheet, as shown in Fig. 1.4, which is a schematic reconstruction of the wake formed by a rotating blade as observed in flow visualization and field measurements.

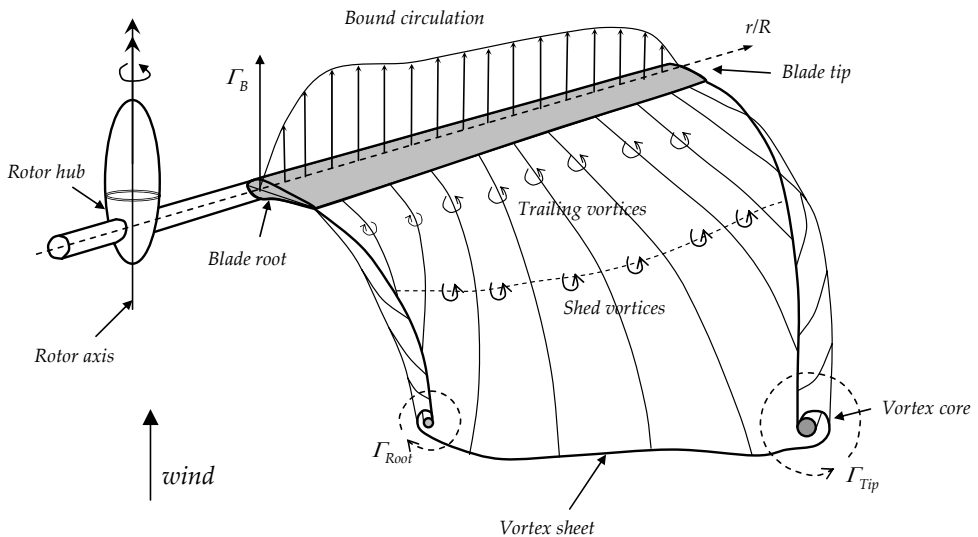


Figure 1.4 – Schematic diagram showing wake developed by a rotating blade of a wind turbine.

The circulation distribution in the vortex sheet originates from the bound circulation (Γ_B) developed at the blades. The former circulation is composed of two vector components: *trailing circulation* (Γ_T) that is released from the blades in a direction perpendicular to the blade's trailing edge and is related to the spanwise variation of the bound circulation ($\partial\Gamma_B/\partial r$); *shed circulation* (Γ_s) that is released from the blades in a direction parallel to the blade's trailing edge and is related to variation of bound circulation with time ($\partial\Gamma_B/\partial t$). The geometry of the vortex sheet emerging from the blades will change such that the edges will roll-up (similar to that observed on a wing in linear flight) to form a tip and root vortex as shown in Fig. 1.4.

A HAWT rotor is normally oriented with the wind such that the axis of rotation is parallel to the incoming wind velocity vector (often referred to as the axial condition). The wake formed behind a HAWT consists of vortex sheets, one per blade (as described in Fig. 1.4), that trace a helical path as a result of rotor rotation. The vortex sheets will roll-up to form a tip and root vortex, as illustrated in Fig. 1.5. The root vortex is usually distorted by the presence of the turbine nacelle and consequently it is very difficult to observe it in experiments. The wake (slipstream) boundary which is usually defined by the radial location of the tip vortices, expands downstream as a consequence of the retardation of the flow. The wake vorticity is responsible for slowing down of the air as it flows through the rotor. It will also alter the local angle of attack at the blades, thereby influencing the aerodynamic forces. When the wind speed and rotor speed are constant with time, there is no shed circulation in the wake.

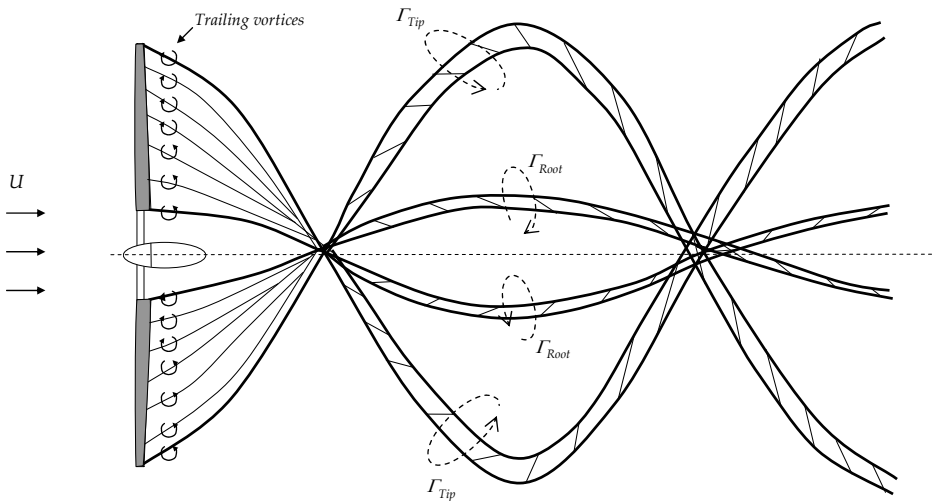


Figure 1.5 – Schematic diagram showing helical wake developed by a wind turbine in axial conditions.

1.3 Current Status of Aerodynamic Design Models for Horizontal-Axis Wind Turbines

A yawed rotor is one which is operating with its axis of rotation not parallel to the incoming wind velocity vector. In the real operating environment of a HAWT, the direction of the wind changes frequently with respect to the rotor axis. As a result, the turbine may operate in yaw for considerable amounts of time. This yawed condition introduces a cyclic angle of attack at the blades and causes the helical wake to become skewed as shown in Fig. 1.6, yielding an unsteady and complex induction distribution at the rotorplane. In fact the wake is quite similar to that of a helicopter rotor in forward flight with the main difference being that it expands instead of it contracts. The time-dependent aerodynamic loads at the blades will cause shed circulation in the wake. When the angle of attack at a blade section exceeds the aerofoil's stalling angle, dynamic stall takes place causing the maximum aerodynamic loads to be much higher than those predicted by 2D static aerofoil data. The hysteresis effects introduced by dynamic stall may have a negative effect on the aeroelastic damping behaviour of wind turbine blades. They reduce the fatigue lifetime leaving an adverse impact on the economics of the system. The phenomenon of dynamic stall will be described in Chapter 3.

The flow field across a wind turbine may be separated intuitively into two regions: the *global flow field* which extends far upstream of the turbine to far downstream and a *local (rotor/blade) flow field* which is the flow around the individual blades. Physically these two parts are inherently tied together, but for both the understanding of the physics and also for

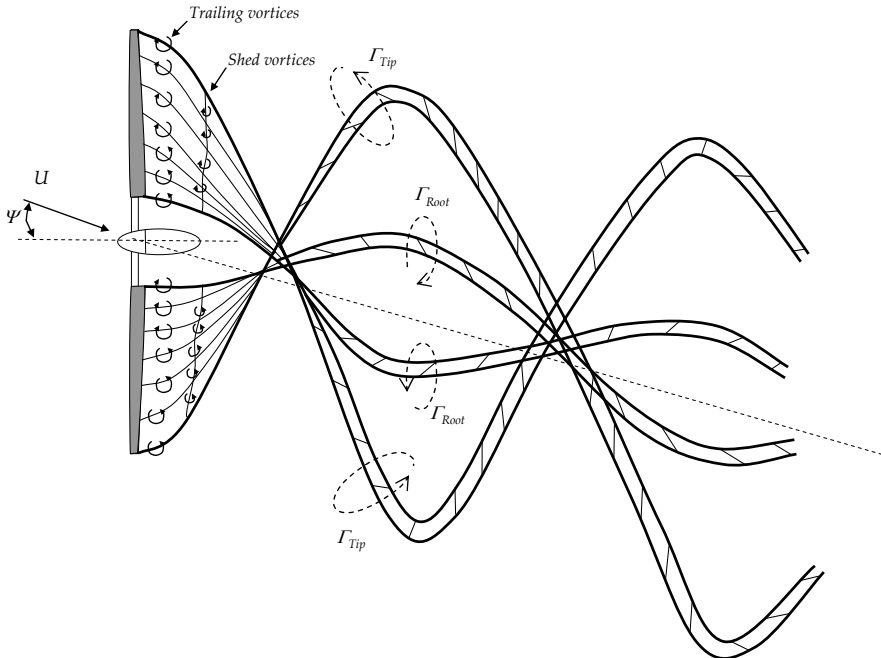


Figure 1.6 – Schematic diagram showing helical wake developed by a wind turbine in yawed conditions.

1.3 Current Status of Aerodynamic Design Models for Horizontal-Axis Wind Turbines

modelling, it may be convenient to treat them separately. The interaction between the two regions is strong: the flow in the global region determines the inflow condition at the rotor blade and the forces on the blades (which can be seen as a localized pressure change) influences the flow in the global region.

1.3 Current Status of Aerodynamic Design Models for Horizontal-Axis Wind Turbines

Since aerodynamic modelling should ultimately serve as a design tool, fast and robust codes are required. Throughout the design process, different wind turbines should be modelled over wide range of operating conditions (including yaw, extreme gusts, start/stop sequences and standstill conditions).

Various mathematical models exist to model the aerodynamic loads on rotors: Blade-Element-Momentum methods, Prescribed or Free-wake Vortex methods, Acceleration Potential methods and CFD techniques. An overview of these methods may be found in the following references: (Snel, [80]; Leishman, [50]; Conlisk, [18]; van Bussel [15] and Vermeer *et al.*, [99]). These were initially developed to treat propeller and helicopter aerodynamics, but could then be easily adapted to model HAWTs. Due to its relatively high computational efficiency, many aeroelastic design codes still rely on the Blade-Element-Momentum (BEM) theory for predicting the aerodynamic loads. However, this theory is simple and lacks the physics to model the complex flow fields around a rotor and consequently its accuracy may be unsatisfactory. Its limitations are mostly observed when treating stalled flows and unsteady conditions such as in rotor yaw. Other methods are much more comprehensive, especially free-wake vortex methods and CFD. Yet unfortunately, with present computer capacity, they are still too computationally expensive to be fully integrated into wind turbine design codes. The complexity of wind turbine design is prohibiting the use of these more elaborate methods that are systematically used today in other aerodynamic applications.

In the past years, several corrections were added to BEM codes to improve their accuracy. These mainly took the form of engineering models that mainly fall under two classifications: (1) *aerofoil data models* that correct 2D static aerofoil for 3D effects (blade tip/root loss, stall delay and dynamic stall) and (2) *inflow models* that correct for the uneven induced velocity distribution at the rotorplane due to skewed wake effects in yaw as well as for conditions of heavy and/or unsteady loading on the rotor. A brief overview of some of these models will be presented in Chapter 3. The engineering models were developed using experimental data or using the more advanced models, including CFD.

It is often thought that in the future, the increased computer power that will become available to the wind turbine designer will make it possible to integrate the more advanced

models in aeroelastic design codes and thus replacing BEM-based models completely. This would make research in the field of BEM improvements futile. However, considering the present situation, there are still various reasons why effort should still be devoted to improving BEM codes:

- First of all, one should keep in mind the fact that the increased computer power that will be available in the future for more sophisticated aerodynamic modelling will be partly limited by the structural dynamicists' request to employ more accurate (thus more computational demanding) structural analysis codes. A typical example would be the inclusion of complex wave and foundation design models for offshore systems.
- Secondly, the BEM method is considerably accurate when treating attached flow conditions (low angles of attack) in axial flow. In the recent years, it was shown that this method is also sufficiently accurate for stalled conditions provided that reliable aerofoil data is used. Accordingly, more effort should be made to obtain more reliable aerofoil data from wind tunnel rotor experiments and CFD. Also, it is still unclear to what extent is BEM accurate in yaw when reliable aerofoil data is used. Further research is required to investigate this.
- Thirdly, even though the more elaborate methods are comprehensive, they do not necessarily always yield better results than BEM. This has been realized in a recent European project (Schepers *et al.*, [70]).

2. Aim of Thesis and Approach

2.1 Problem Statement

In the past years, BEM codes were extensively tested against experimental measurements. In many situations, the reliability of such codes was found to be unacceptable, in particular when the angle of attack at the blades was large and in yawed conditions. For instance this was observed a few years ago, in year 2000, in a blind comparison study organized by the NREL. In this study, a two-bladed wind turbine was extensively tested in the NASA Ames wind tunnel for a wide range of operating conditions (Schreck, [73]). When comparing the predicted results by different aerodynamics/aeroelastic codes from various universities/institutions with the measured data considerable inconsistencies were found (Simms *et al.*, [78]). In some cases, deviations of the BEM predictions from the measurements exceeded 200%, even though the simplest operating conditions of a wind turbine were being considered (i.e. uniform windspeed and constant rotor speed, blade pitch and yaw angle). This has shown that the aerodynamic interaction between the rotor blades and the wake is non-linear and more three-dimensional in nature than for fixed wings in linear flight. Certain aerodynamic phenomena associated with wind turbine blades are still poorly known and are therefore challenging to predict accurately, as in the case of stalled blades and the unsteady effects experienced in yawed conditions. For a given aerofoil geometry, the steady and unsteady aerofoil data of a wind turbine blade may differ considerably from that normally obtained in 2D static wind tunnel experiments. To-date, fundamental limits exist in the validity of models used for wind turbine design and certification. As explained by Leishman [50], a major challenge for researchers is to better understand the aerodynamic issues associated with wind turbines to develop more rigorous models suitable for a wider range of applications and to better integrate and validate these models with reference to good quality experimental measurements. These models should also be computationally efficient if they are to be used in design codes.

Wind tunnel tests on model turbines are indispensable to have a better understanding of the underlying physics and to improve engineering models for design codes. The controlled environment offered by a wind tunnel provides a set of measurements that is free from the uncertainties caused by the different atmospheric effects that are always present in open field tests of turbines. To improve the predictions of BEM-based design codes, more reliable aerofoil data models and inflow correction models are required. However, using the experimental data to improve these models is not an easy task. Two major problems are encountered:

- *Problem I: Wind tunnel experimental data is usually rare and limited.* This is because turbine testing is very expensive. Also certain parameters may be very difficult to measure accurately. To be able carry out a detailed experimental investigation of a turbine's aerodynamic behaviour, the following set of measurement data would be ideally required:
 - (1) Surface pressure measurements using pressure tappings at different radial locations on the blades. By integrating these pressures normal and along the local chordline, the normal and chordwise aerodynamic loads may be derived.
 - (2) Measurements of the 3D inflow distribution in the near wake and at the rotorplane using different anemometry techniques such as hot-film anemometry, PIV and laser-doppler techniques.
 - (3) Measurements of the wake geometry to establish the expansion of the wake, location of the tip vortices and the wake skew angle in the case of yawed conditions. This is usually accomplished using smoke visualization techniques (Vermeer *et al.*, [99]).

Despite the fact that over the past years various databases of wind tunnel data have been produced, a complete set of data comprising the above three measurement data sets for a wind turbine operating over a wide range of operating states in both axial and yawed conditions is still presently unavailable in the wind energy community.

- *Problem II: There is a difficulty in determining accurately the angle of attack.* To be able to derive the local aerofoil lift and drag coefficients C_l and C_d from the measured C_n and C_t obtained from blade pressure measurements knowledge of the angle of attack is required as illustrated in Figure 2.1.

The angle of attack may be estimated directly from detailed inflow measurements but these are not always available. Alternatively flow direction probes may be installed at different radial locations of one blade, just in front of the leading edge to measure the local inflow angle (*LFA*) as shown in Fig. 2.2. Though, due to the influence of the bound circulation at the blades and the wake vorticity, the inflow angle may differ significantly from the angle of attack. A correction has to be then applied to estimate the angle of attack from the inflow angle, as discussed by Rooij *et. al.* [66]. Because of the flow field across the rotor is complex, the correction that is usually obtained from simple 2D wind tunnel calibration procedures is unreliable. Also, the probes may distort the flow over the blades and this may cause errors in blade surface measurements. When dealing with yawed conditions, the influences of the unsteady shed vorticity and the effects resulting from the skewed wake will make the required correction very difficult to establish.

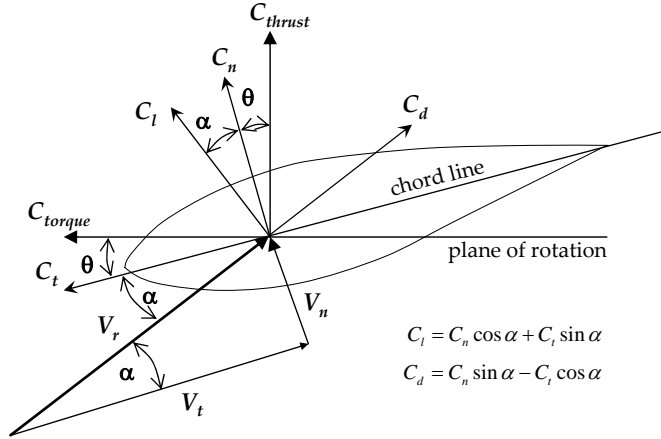


Figure 2.1– Blade section aerodynamic load coefficients and relative velocity flow components.

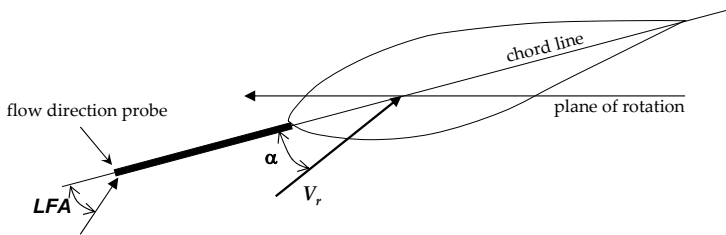


Figure 2.2 – Measuring the local flow angle using a flow direction probe.

Another method to determine the angle of attack is the so-called inverse BEM method which makes use of the Blade-Element-Momentum equations to estimate the axial and rotation induction factors from the known blade loading, thereby finding the angle of attack. This method has been applied by Snel *et al.* [82], Bruining *et al.* [13] and later by Laino *et al.* [44]. The accuracy of this method is limited by the capability of the BEM theory in predicting accurately the induction factors at the rotorplane. This method would not always be reliable, especially in high loading and yawed conditions.

Research showed that when the new aerofoil data, derived from blade pressure measurements in conjunction with any of the above methods for finding the angle of attack, was used in BEM codes, correlation with the experimental load measurements generally improved. Yet the problem of accurately deriving the angle of attack for the measurements remained a major source of uncertainty. Different researchers used different methods for estimating the angle of attack and consequently discrepancies resulted in the derived lift and drag data, even though the same blade pressure measurements were being used. As a

result, it may be argued that the uncertainty in deriving the angle of attack is a major stumbling block to carry out a clear quantitative assessment of the trustworthiness of BEM-based codes.

2.2 Aim of Thesis

In this thesis, a detailed investigation of the aerodynamics of wind turbines in both axial and yawed conditions was carried out based on wind tunnel measurements with the aim of providing a better understanding of the limitations of the BEM theory.

As already mentioned in section 2.1 above, to be able to accomplish a detailed experimental investigation of wind turbine aerodynamics, it is very helpful that the experimental data consists of the following data sets: blade pressure measurements (to derive the aerodynamic loading), inflow measurements in the near wake and the rotorplane as well as measurements concerning the wake geometry. It goes without saying that, when any of these three data sets is unavailable, it will impose restrictions to which detail the aerodynamic analysis can be performed. This study focused on developing new methodologies that make use of limited experimental data in conjunction with advanced aerodynamic models to derive the additionally required aerodynamic performance data for both axial and yawed rotors. In this way, a deeper aerodynamic study could be performed. The methodologies were developed for two particular cases:

- (i) *Case A*: The wind turbine experimental data only consists of detailed inflow measurements in the near wake and wake geometry data
- (ii) *Case B*: The wind turbine experimental data only consists of blade pressure measurements.

Each methodology is described in detail and its limitations examined.

The experimental data and the new aerodynamic data derived using the respective methodology were used to carry out a thorough assessment of a BEM code. The major scope of this assessment was to provide guidelines that would be useful in developing new engineering models.

2.3 Approach

In the research work, the experimental data of two different wind turbines were considered: (1) The Delft University of Technology (TUDelft) wind tunnel model turbine and (2) the NREL Phase VI wind turbine.

2.3.1 Research work on the TUDelft wind tunnel turbine

The first part of the project dealt with the TUDelft model turbine. A series of experiments were conducted on this rotor for both axial and yawed conditions in the open-jet wind tunnel facility of Delft University of Technology with the close collaboration of another Ph.D researcher Wouter Haans. The experiments consisted of the following:

- a. Detailed hot-film measurements in the near wake along planes parallel to the rotorplane (both upstream and downstream of the rotorplane)
- b. Smoke visualization experiments to trace the tip vortex paths of the turbine wake and thus obtain detailed regarding the wake geometry.

Unfortunately, the apparatus was incapable of measuring the pressure distributions over the blades. The situation was therefore identical to *Case A* described in section 2.2 above. A methodology was developed to derive the time-dependent aerodynamic load distributions at the rotor blades from the hot-film measurements in conjunction with an advanced unsteady aerofoil model. The application of this methodology was limited to attached flow conditions (low angles of attack) only for which unsteady aerofoil models are known to be reliable. Very briefly, the sequence of steps in applying this method are as follows: the angle of attack and flow relative velocities at the blades are first estimated directly from the hot-film inflow measurements. The advanced unsteady aerofoil model is used to derive the lift coefficient distributions at the blades. The drag coefficients are estimated from 2D wind tunnel static aerofoil data. This is acceptable since small angles of attack were being considered (attached flow conditions). Finally the aerodynamic loads at the blades are computed using the blade-element theory equations. The results from this method were then compared with those predicted by a BEM code.

2.3.2 Research work on the NREL Phase VI wind tunnel turbine

The second part of the project dealt with the NREL Phase VI wind turbine. This turbine was tested in the NASA Ames 80ft X 120ft wind tunnel way back in the year 2000. The data collected from these experiments [73], usually referred to as the NASA Ames Unsteady Aerodynamics Experiments (UAE), is very extensive and is currently being analyzed by several institutions through the IEA Annex XX. It is being used as a benchmark by the wind turbine aerodynamics community in assessing the validity of improved aerodynamics codes based on BEM, CFD or Vortex Methods [19, 44, 45, 72, 87, 90, 95]. In these

experiments, time-accurate blade pressure measurements were taken with the rotor operating in both axial and yawed conditions together with strain gauge measurements for the output torque and the root flap/lead moments. However, detailed inflow measurements at the rotorplane were not carried out. The situation is therefore identical to *Case B* described in section 2.2 above. In this project a novel and comprehensive methodology is being proposed for using the blade pressure measurements inconjunction with a free-wake vortex model to estimate the angle of attack distributions at the blades more accurately, together with the inflow distributions at the rotorplane and wake geometry. The new 3D lift and drag data together with the derived inflow distributions at the rotorplane are then used to assess the improvement in BEM load predictions in axial and yawed conditions. Emphasis here is made in determining the accuracy to which the BEM theory is capable to model aerodynamic loads in highly stalled and yawed conditions if reliable 3D aerofoil data are used.

The proposed methodology for coupling the blade pressure measurements with a free-wake vortex model is based on the principle that, in a wind turbine wake, it may be assumed that vorticity is conserved. Thus the circulation in the wake corresponds to that around the blades. From the blade pressure measurements, it is possible to estimate the bound circulation at the blades which may then be used to generate the free-wake. The sequence of steps in applying this method are as follows: Initially, a spanwise distribution for the angle for attack is assumed at the blades. This is then used together with the values of C_n and C_t obtained from the blade pressure measurements to estimate the lift coefficients at the blades. Using the Kutta-Joukowski law, the bound circulation distribution at the blades is then determined and prescribed to the free-wake vortex model to generate the free vortical wake. The induced velocity at the blades is estimated and used to calculate a new angle of attack. The process is repeated until convergence in the angle of attack is achieved. Originally, this method was applied by Tangler *et al.* [90, 91] but using a prescribed vortex model and treating axial conditions only. However a free-wake vortex model is a more realistic representation because the wake geometry is allowed to develop freely depending on the circulation that is shed from the blades into the global flow field. This is even more important for yawed conditions since the resulting complex skewed wake geometry is more difficult to prescribe. Another advantage of using a free-wake vortex method concerns the fact that the wake geometry is inherently part of the solution. Thus it is possible to derive the pitch and expansion of the helical wake, which otherwise could be obtained using time-consuming smoke-visualization experiments.

Fig. 2.3 summarises the main problems and possible solution methodologies proposed in this project for using limited experimental data to investigate in detail the aerodynamics of wind turbines and perform a thorough assessment of BEM-based design codes.

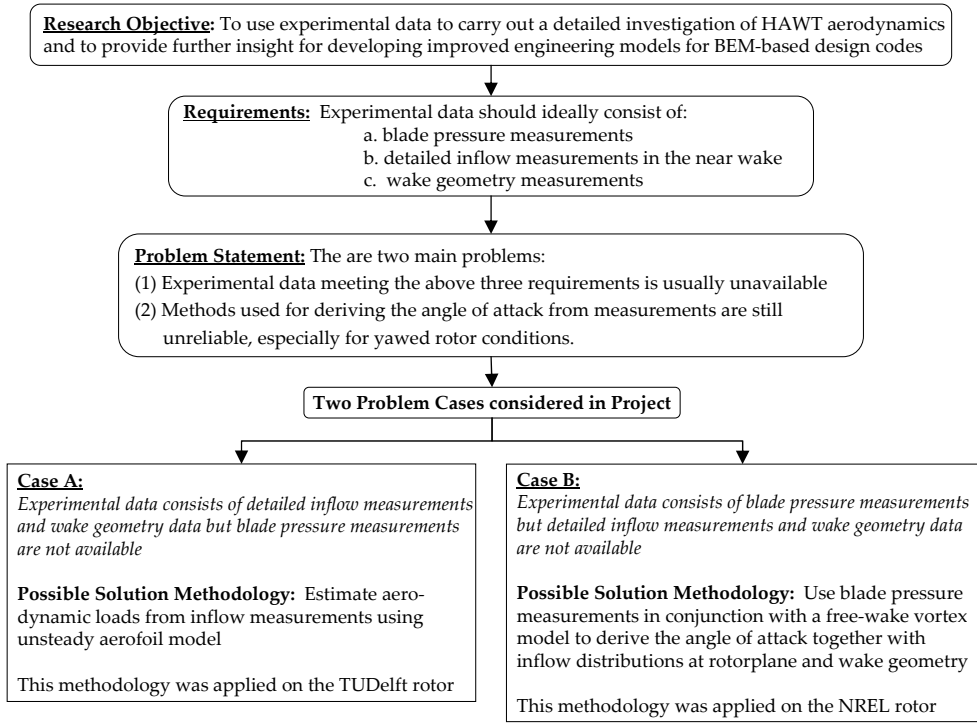


Figure 2.3 - The main problems and possible solution methodologies proposed in this project for using limited experimental data to investigate in detail the aerodynamics of wind turbines and perform a thorough assessment of BEM-based design codes.

2.3.3 Development of Free-wake Vortex Model

The free-wake vortex model used to analyse the NREL rotor (see section 2.3.2 above) was developed during this project. This model is somewhat different than other free-wake vortex methods that rely on aerofoil data to iteratively determine the blade loading. It was specifically designed to be used in the proposed method for finding the angle of attack. The input to this code is a prescribed spanwise distribution of bound circulation that may be time-dependent. From this prescription, the code will generate a wake and then calculates the 3D induced velocities at different points in the flow field of the rotor.

The project also focused on the verification and validation of this new free-wake vortex model. The hot-film near wake inflow measurements carried out on the Delft wind turbine (refer to section 2.3.1) were used as a bases for the validation. These inflow measurements were used together with the unsteady aerofoil theory and the Kutta- Joukowski theorem to determine the bound circulation distributions at the blades. These distributions were then

prescribed to the vortex model. The latter then computed the wake induced velocities and these were compared with the induced velocities obtained from the hot-film measurements. The procedure for validating the vortex model is illustrated in Fig. 2.4. A limitation of this approach is the uncertainty due to the employed unsteady aerofoil theory. However the measurements are limited to attached flow conditions only, for which the unsteady aerofoil model is considerably accurate. Apart from inflow measurements, smoke visualization experiments were also carried out on the Delft rotor to measure the location of the tip vortex paths. These measurements were also used to validate the free-wake vortex model (see Fig. 2.4).

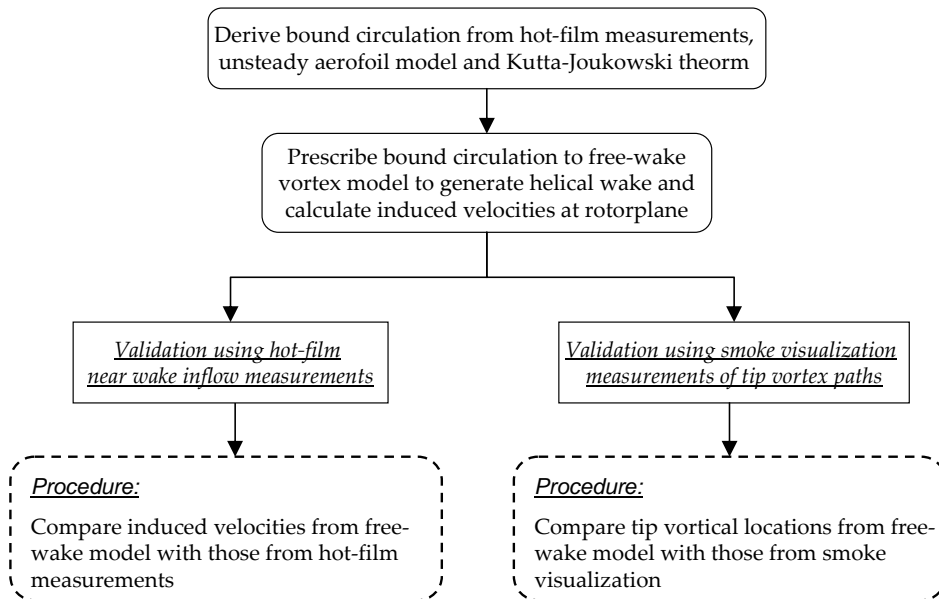


Figure 2.4 - Validation procedure of developed free-wake vortex model using measurement data from the TUDelft wind tunnel rotor.

2.4 Organization of Work

The research work was organized into different project phases. Fig. 2.5 lists these phases in a chronological order. This dissertation documents the work carried out as follows: In Chapter 3, a review of the BEM theory for a yawed HAWT is presented. A brief literature survey of various engineering models developed in the past years for BEM is also presented. Chapter 4 describes in detail the wind tunnel experiments and the aerodynamic analysis carried out on the TUDelft turbine during *Phases I, II and III* of the project. Chapter 5 presents the details of the free-wake model developed in *Phase IV* together with its verification and validation undertaken in *Phase V*. Chapter 6 describes the analysis

accomplished using the NREL experimental data in *Phases VI and VII*. From this study further insight on the limitations of BEM codes was obtained and a number of guidelines on how the reliability of such codes can be improved are presented and discussed. These guidelines are given in Chapter 7.

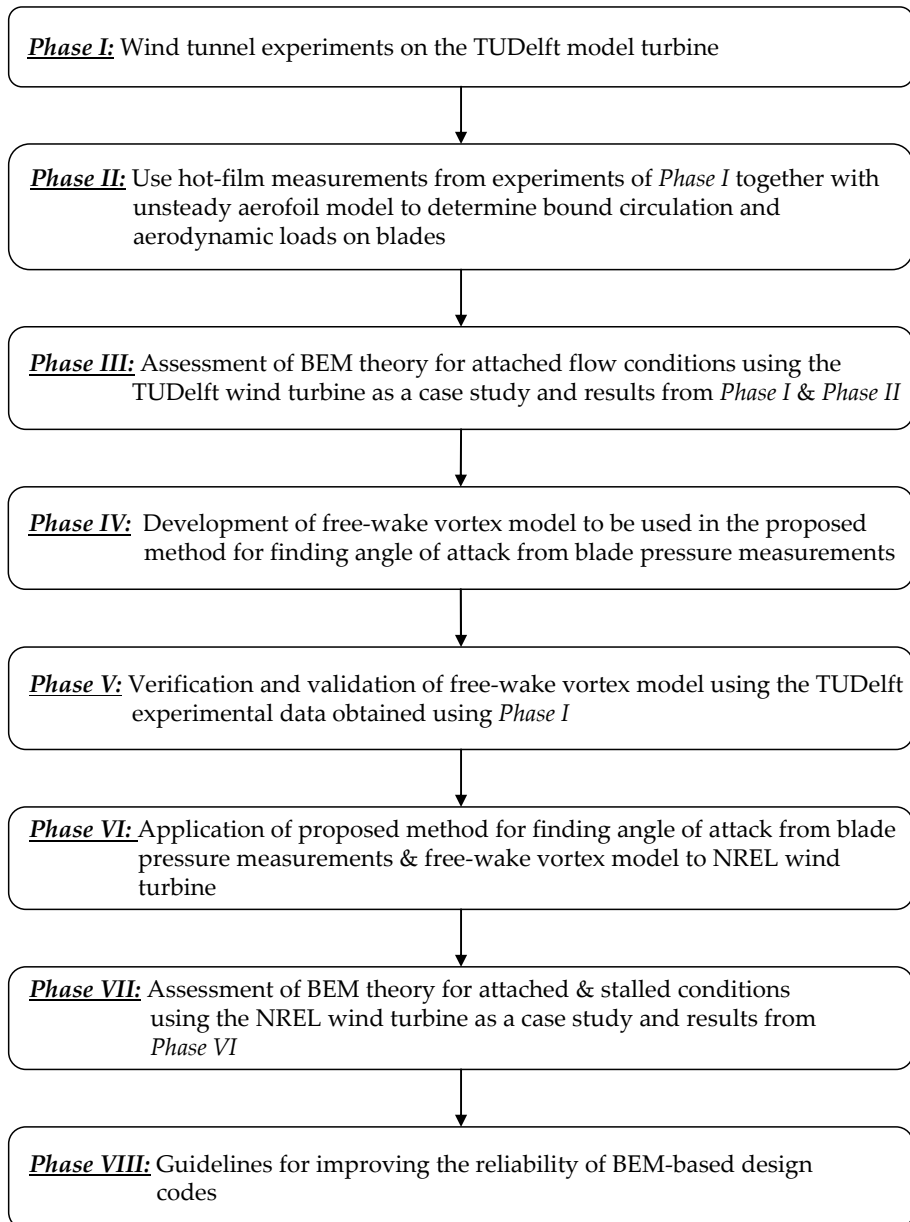


Figure 2.5 – Project Phases.

2.5 Co-Ordinate System Analysis

A pre-requisite in the aerodynamic modelling of horizontal-axis wind turbines in axial and yawed conditions is to have a suitable set of co-ordinate systems to be able to define accurately the position and velocity vectors of each blade element together with velocity vectors of the flow field in three-dimensional space. The required co-ordinate systems, which have been adapted from Spera [88] are displayed in Fig. 2.6.

In Fig. 2.6, the X - Y - Z axes are the fixed reference system whose origin is at the pivot centre at O . The Z axis is vertical and aligned with the tower. It co-incides with the yaw axis. The rotor axis may be tilted in the vertical plane by a fixed angle χ . Ψ is the yaw angle. The hub centre is at F and is at a distance d_a from O along the rotor axis. Each blade may also have a coning angle β as shown in the diagram. ϕ is the azimuth angle of the first blade and is equal to zero when the blade is vertical and pointing upwards. The tower base is located at T . T lies on the ground and vertically below O such that distance H is equal to the tower height. The X_t - Y_t - Z_t axes are identical to the X - Y - Z axes with the only difference that their origin is at T .

The coordinate systems whose origin is at F include the:

- x_r - y_r - z_r axes - these are rotating axes with the y_r axis aligned with the rotor axis. The angle between the z_r axis and the z axis is equal to β .
- X_a - Y_a - Z_a axes - these are non-rotating axes with the Y_a axis aligned with the rotor axis. The Z_a axis coincides with the z_r axis at ϕ equal to zero.

The coordinate systems that are located locally at all the elements of each rotor blade are the:

- x - y - z axes - these are located in the surface of revolution that a rigid blade would trace in space, with the axis normal to this surface. When β is equal to zero, the y axis becomes parallel to the Y_a axis.
- x_p - y_p - z_p axes - these are the principal bending co-ordinates, where the z_p axis coincides with the blade's elastic axis.
- η - ζ - ξ axes - these are the principal co-ordinates of the deformed blade along each point on the elastic axis. For a rigid rotor these axes coincide with the x_p - y_p - z_p axes.

The blade is considered to deflect in the flapwise direction, i.e. about the y_p axis. For the sake of simplicity, edgewise (lead-lag) deflections are neglected. θ is equal to the angle between the x and η axis at a given blade element and is equal to the local pitch angle. The X_n - Y_n - Z_n co-ordinate system shown in Fig. 2.6 is similar to the X_a - Y_a - Z_a but has its origin at O . In the \underline{X} - \underline{Y} - \underline{Z} system, the \underline{Z} axis coincides with the Z axis and the angle between the \underline{Y} and Y axes is equal to Ψ .

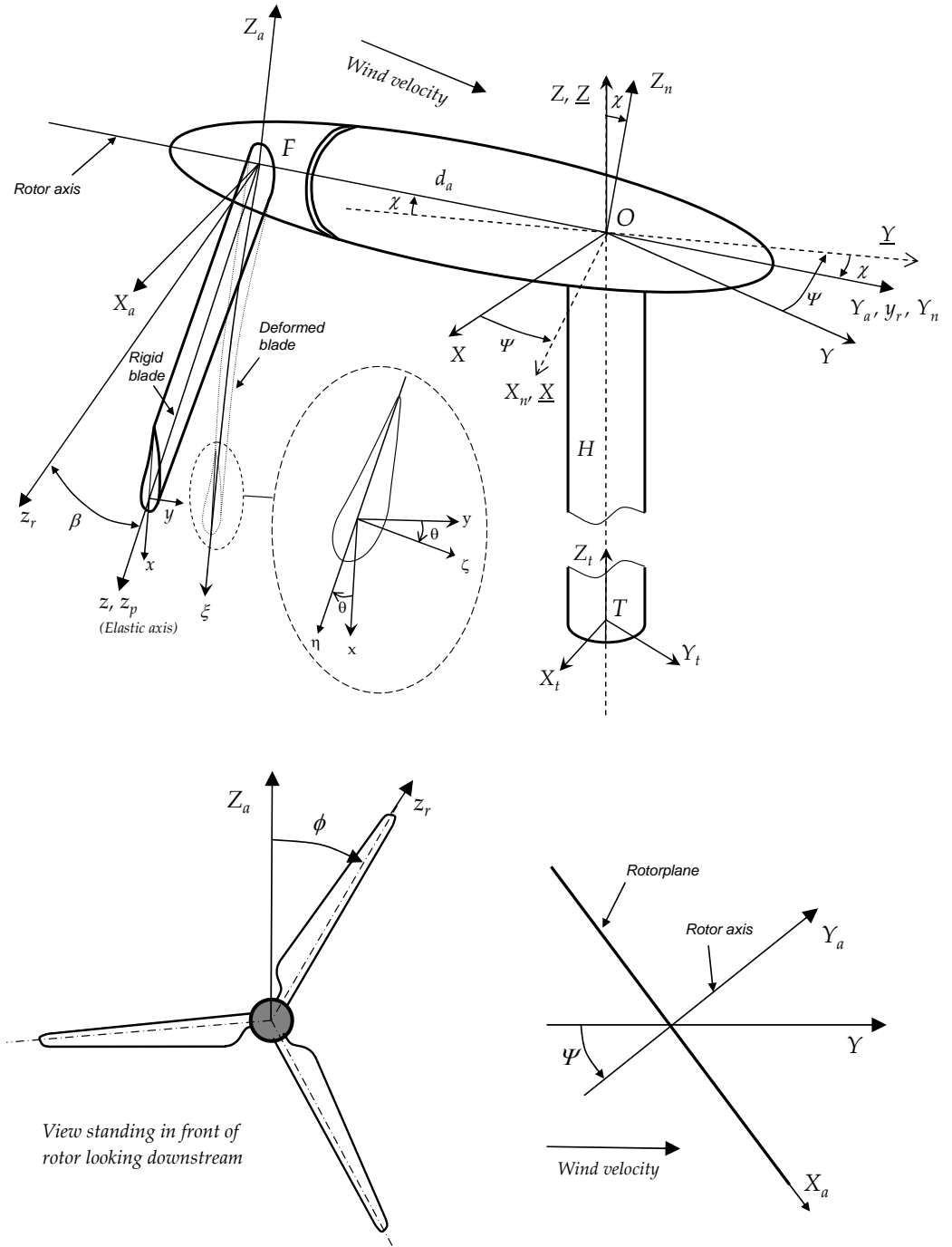


Figure 2.6 - Co-ordinate systems used for modelling the wind turbines.

Transformation Matrices

A vector \vec{G} in the X-Y-Z reference may be transformed into an equivalent vector \vec{E} in the moving η - ζ - ξ reference frame by means of transformation matrix S where

$$\vec{E}_{\eta-\zeta-\xi} = S * \vec{G}_{X-Y-Z}$$

where

$$S = A_6 * A_5 * A_4 * A_3 * A_2 * A_1$$

$A_1 \dots A_6$ are orthogonal matrices that transform from one co-ordinate system to another where

$$A_1 = \begin{bmatrix} \cos\Psi & \sin\Psi & 0 \\ -\sin\Psi & \cos\Psi & 0 \\ 0 & 0 & 1 \end{bmatrix}$$

$$A_2 = \begin{bmatrix} 1 & 0 & 0 \\ 0 & 1 & -\chi \\ 0 & \chi & 1 \end{bmatrix}$$

$$A_3 = \begin{bmatrix} \cos\phi & 0 & -\sin\phi \\ 0 & 1 & 0 \\ \sin\phi & 0 & \cos\phi \end{bmatrix}$$

$$A_4 = \begin{bmatrix} 1 & 0 & 0 \\ 0 & 1 & -\beta \\ 0 & \beta & 1 \end{bmatrix}$$

$$A_5 = \begin{bmatrix} \cos\theta & -\sin\theta & 0 \\ \sin\theta & \cos\theta & 0 \\ 0 & 0 & 1 \end{bmatrix}$$

$$A_6 = \begin{bmatrix} 1 & 0 & 0 \\ 0 & 1 & -v' \\ 0 & v' & 1 \end{bmatrix}$$

It is assumed that both χ and β are small ($<5^\circ$). v' is the local blade slope due to flexure. In this thesis, the two wind turbines considered were investigated for conditions of no coning ($\beta=0^\circ$) and no rotor axis tilt ($\chi=0^\circ$). Also the blades were very rigid and thus v' was also taken as zero. However these parameters were still included in the mathematical modelling and the newly developed computer software. This will make it much easier to upgrade the computer codes in the future to cater for aeroelastic effects.

3. The Blade-Element-Momentum Theory

This chapter presents a review of the Blade-Element-Momentum (BEM) theory for yawed HAWTs. It is mainly a reformulation of the theory to be found in many textbooks [53, 77, 88]. The limitations of this theory are discussed and a brief overview of various BEM engineering correction models developed over the past years is also presented.

3.1 The Simple Linear Momentum Theory for a Yawed Actuator Disc

Under the linear momentum theory, the fluid is considered to be inviscid, incompressible and with no swirl. The turbine is modelled as an actuator disc (representing a turbine with an infinite number of blades) which reduces the velocity component normal to it. In Fig. 3.1, the windspeed is U and the yaw angle is Ψ . The flow velocities are resolved in the plane of the rotor disc (U_x) and perpendicular to it (U_y). It is assumed that only U_y is affected by the presence of the rotor plane. At the rotor, U_y changes by a value u_a and the flow velocities here become

$$U_x = U \sin(\Psi) \quad U_y + u_a = U \cos(\Psi) + u_a$$

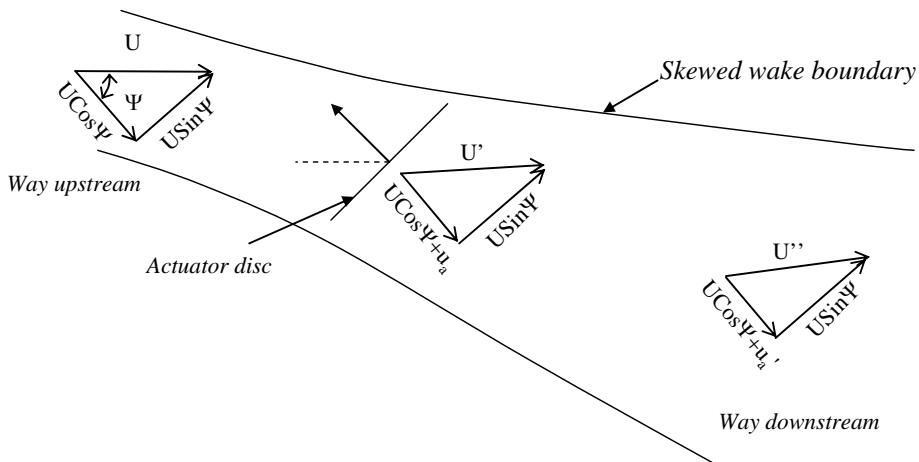


Fig. 3.1 -Yawed actuator disc in skewed flow.

These yield a resultant flow velocity at the disc equal to

$$U' = \sqrt{U^2 \sin^2 \Psi + (U \cos \Psi + u_a)^2} \quad (3.1)$$

Far downstream the velocity perpendicular to the rotorplane is equal to $U_y + u_a'$. Using the Bernoulli energy equation together with the linear momentum equation, it can also be proved that u_a' is twice u_a . Since a wind turbine in its normal operating condition extracts energy from the fluid stream, then the flow velocity decreases across the rotor and therefore u_a is negative. For a yawed rotor, Glauert [30] expresses the momentum equation for the axial thrust T as

$$T = 2\rho u_a U' A \quad (3.2)$$

Define the axial thrust co-efficient by

$$C_T = \frac{T}{\frac{1}{2}\rho A U^2} \quad (3.3)$$

A is the cross-sectional area of the rotor disc. By substituting Eqts. 3.1 and 3.2 in Eq. 3.3 and putting $u_a = a_1 U$ the following expression for C_T results in

$$C_T(a_1, \Psi) = 4a_1 \sqrt{\sin^2 \Psi + (\cos^2 \Psi + a_1)^2} \quad (3.4a)$$

Eq. 3.4a is invalid for high loading conditions in which for C_T approaches and exceeds unity. Anderson *et al.* [3] have obtained the following empirical equation for values of $(-a_1)$ larger than about 0.38 and at zero yaw angle:

$$C_T(\Psi) = 0.5776 - 0.96 * a_1 \quad (3.4b)$$

To the authors' knowledge there is yet no empirical equation available similar to Eq. 3.4b that accounts for yawed flow in HAWTs.

Using the above simple theory, it can be shown that the maximum power coefficient that can be achieved by a yawed turbine disk is given by

$$C_{P,Max}(a_{1,m}, \Psi) = \frac{4(-a_{1,m})^{\frac{3}{2}} [\cos(\Psi) + a_{1,m}]^2}{[\cos(\Psi) + 2a_{1,m}]^{\frac{1}{2}}} \quad (3.5)$$

where $a_{1,m}$ is the axial induction factor that yields the maximum power coefficient $C_{P,Max}$ at a given yaw angle. The mathematical solution for Eq. 3.5 is presented in Appendix A.

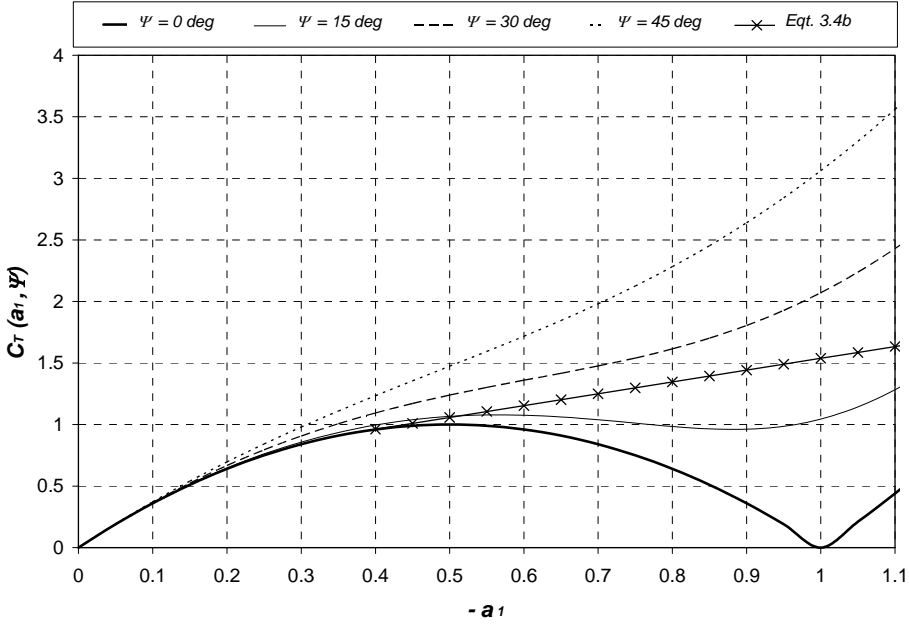


Figure 3.2 – Variation of the axial thrust coefficient with the axial induction factor for different yaw angles as predicted by Eqs. 3.4a and b.

3.2 The Momentum Equations

In deriving the linear and angular momentum equations, the fluid flow stream at the disc is divided into independent annuli or streamtubes. The elemental axial thrust δT resulting from a change in linear velocity in each streamtube is given by substituting Eq. 3.1 in Eq. 3.2 and replacing A by the cross-sectional area of an annular element. This results in

$$\delta T = 4\pi\rho(u_a)r\sqrt{(U\cos\Psi + u_a)^2 + U^2\sin^2\Psi}\delta r \quad (3.6a)$$

u_a is the azimuthal averaged axial induced velocity for the given annulus. For $(-u_a) > 0.38U$ Eq. 3.6a is invalid and the following equation is used instead

$$\delta T = C_T\rho\pi rU^2\delta r \quad (3.6b)$$

where C_T is an empirical equation similar to Eq. 3.4b. To find the elemental torque δQ at a given annulus, it is assumed that the swirl velocities at a given annulus far upstream and far downstream of the rotor act in imaginary planes parallel to the rotor plane of rotation. The elemental torque is given by the rate of change of moment of momentum due to the swirl in the stream tube. Using this principle in conjunction with Eq. 3.1 results in

$$\delta Q = 4\pi\rho(u_t)r^2\sqrt{(UCos\Psi + u_a)^2 + U^2Sin^2\Psi}\delta r \quad (3.7)$$

u_t is the azimuthal average tangential induced velocity at the given annulus.

3.3 The Blade-Element Theory

The blade element theory (BET) is used to calculate the aerodynamic forces (and moments) on the blade due to its motion through the air (combination of wind velocity, induced velocity and rotational velocity) to determine the performance and loads on the entire rotor. It is assumed that each blade behaves like a two-dimensional aerofoil to produce aerodynamic forces (lift and drag) and moments (pitching moments), with the influence of the wake and the rest of the rotor contained entirely in an induced velocity at the blade element.

3.3.1 The Blade Element Velocity

The velocity of a point A at a given point at radius along the ξ axis of a rigid blade in the η - ζ - ξ reference frame is expressed by the following three equations of motion given in Spera, [88]:

$$\begin{aligned} V_{A,\eta} &= r\Omega\text{Cos}\theta - \dot{\Psi}\left[(d_a + \beta r)\text{Cos}\theta + v\right]\text{Cos}\phi - \dot{\Psi}r\text{Sin}\theta\text{Sin}\phi \\ V_{A,\zeta} &= r\Omega\text{Sin}\theta + v - \dot{\Psi}(d_a + \beta r)\text{Sin}\theta\text{Cos}\phi + \dot{\Psi}r\text{Cos}\theta\text{Sin}\phi \\ V_{A,\xi} &= (v'r - v)\Omega\text{Sin}\theta - \dot{\Psi}\left[d_a + (v - v'r)\text{cos}\theta\right]\text{Sin}\phi \end{aligned} \quad (3.8)$$

3.3.2 The Induced Velocity at Each Blade Element

In yawed rotors, the blade-to-blade aerodynamic interference and the skewed wake induce a three-dimensional induced velocity at each blade element which may be represented by the following vector in the x_r - y_r - z_r reference frame

$$\hat{u} = \begin{bmatrix} u_t/f \\ u_a/f \\ u_r \end{bmatrix} \quad (3.9)$$

u_a and u_t are the average axial and tangential induced velocities respectively at a given annulus. u_r is the radial component of induced velocity. The BEM theory is incapable of

calculating the radial component of induced velocity and this is taken as zero. f is the Prandtl tip/root loss factor that accounts for the fact that the rotor has a non-infinite number of blades and for the reduced loading at the tip/root of the blades. At a given blade radial position, this factor is given by

$$f = f_t * f_r \quad (3.10a)$$

where

$$f_t = \frac{2}{\pi} \text{Cos}^{-1} \left[\exp \left(- \left\{ \frac{B/2 [1 - r/R_t]}{r/R_t \text{Sin} \varphi} \right\} \right) \right] \quad (3.10b)$$

$$f_r = \frac{2}{\pi} \text{Cos}^{-1} \left[\exp \left(- \left\{ \frac{B/2 [r/R_t - R_t/R_t]}{R_t/R_t \text{Sin} \varphi} \right\} \right) \right] \quad (3.10c)$$

φ is the inflow angle which is described in section 3.3.4. For the derivation of the Prandtl tip/root loss factor refer to [77].

3.3.3 Flow Velocity Relative to a Moving Blade Element

The flow velocity relative to a moving blade element can be computed by transforming the wind velocity vector from the X-Y-Z reference frame to the η - ζ - ξ reference frame, adding the induced velocity vector and subtracting the blade element velocity. The matrix S (refer to Chapter 2, page 22) is used to transform U from the X-Y-Z frame to the η - ζ - ξ frame. The matrix $A_6 A_5 A_4$ transforms the induced velocity vector \hat{u} from the x_r - y_r - z_r frame into the η - ζ - ξ frame. The flow relative velocity at each blade element becomes

$$V_{(\eta-\zeta-\xi)} = S \bar{U}_{(X-Y-Z)} + A_6 A_5 A_4 \hat{u}_{(x_r-y_r-z_r)} - V_{A(\eta-\zeta-\xi)} \quad (3.11)$$

The magnitude of the resultant flow relative velocity in the η - ζ plane is given by

$$V_r = \sqrt{V_\eta^2 + V_\zeta^2} \quad (3.12)$$

The magnitude of the resultant flow relative velocity is then given by

$$V_{rel} = \sqrt{V_\eta^2 + V_\zeta^2 + V_\xi^2} \quad (3.13)$$

3.3.4 Aerodynamic Loads

The aerodynamic loads on each blade element are assumed to act on the ξ axis which is located at $c/4$ away from the blade's leading edge. Fig. 3.3 shows the velocity triangles on a blade element at a given radius. The aerodynamic loads are also shown.

In Fig. 3.3, the reference chordline and the η axis are considered to coincide with one another. Since the flow relative velocity has three components, there are two velocity diagrams: one in the η - ζ plane (Fig. a) and the other in the η - ξ plane (Fig. b). The two corresponding angles of attack are:

1. normal angle of attack:

$$\alpha = \tan^{-1} \left(\frac{V_\zeta}{V_\eta} \right) \quad (3.14)$$

2. lateral angle of attack (usually defined as the sweep angle):

$$\alpha_{sweep} = \tan^{-1} \left(\frac{V_\xi}{V_\zeta} \right) \quad (3.15)$$

α_{sweep} indicates the presence of spanwise flow and its direction. It contributes to delay the onset of stall. The inflow angle φ is equal to the sum of the local values of α and θ .

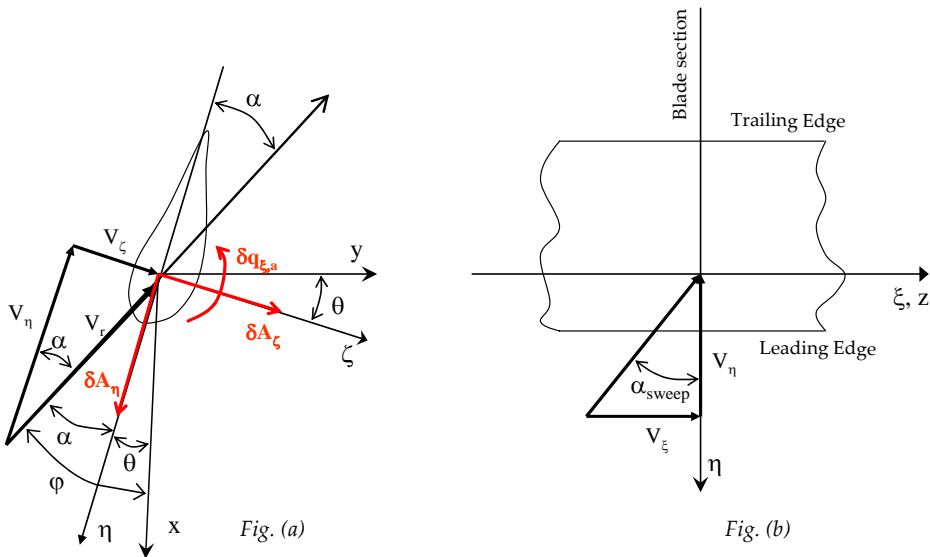


Figure 3.3 – Velocity triangles and aerodynamic loads at a given blade element.

The expressions for the aerodynamic loads on the element of chord c and finite width δr are

$$\begin{aligned}\delta A_\eta &= \frac{1}{2} \rho c V_r \left[C_l(\alpha, \text{Re}) V_\zeta - C_d(\alpha, \text{Re}) V_\eta \right] \delta r \\ \delta A_\zeta &= \frac{1}{2} \rho c V_r \left[C_l(\alpha, \text{Re}) V_\eta + C_d(\alpha, \text{Re}) V_\zeta \right] \delta r\end{aligned}\quad (3.16)$$

The aerodynamic force in the spanwise direction has been neglected. The Reynolds number at the element is taken as

$$\text{Re} = \frac{\rho V_r c}{\mu_a} \quad (3.17)$$

The blade element also experiences a pitching moment given by

$$\delta q_{\xi,a} = \frac{1}{2} \rho c^2 V_r^2 C_m \delta r - e_{e,a} c \delta A_\zeta \quad (3.18)$$

$$e_{e,a} = \frac{x_{a,c} - x_{e,a}}{c} \quad (3.19)$$

where

$\delta q_{\xi,a}$ – increment of aerodynamic pitch moment loading (Nm)

C_m – aerodynamic pitching moment coefficient about the aerodynamic centre of the aerofoil

$e_{e,a}$ – relative eccentricity of the elastic centre of aerofoil

$x_{a,c}$ – distance from leading edge to aerodynamic centre (usually $c/4$) (m)

$x_{e,a}$ – distance from leading edge to elastic centre (m)

3.3.5 The Blade-Element Equations for Thrust and Torque

Referring to Fig. 3.3 and neglecting the effect of small blade deflections, the rotor axial thrust and torque due to a blade element are given by

$$\delta T = \delta A_\zeta \text{Cos}\theta - \delta A_\eta \text{Sin}\theta \quad (3.20a)$$

$$\delta Q = r \text{Cos}\beta \left(\delta A_\eta \text{Cos}\theta + \delta A_\zeta \text{Sin}\theta \right) \quad (3.20b)$$

3.4 The Blade-Element-Momentum Equations

The Blade-Element-Momentum (BEM) Theory combines the momentum theory with the blade element theory (BET) to determine the axial and tangential induced velocities. The basic assumption is that the force of a blade element is solely responsible for the change of momentum of the air which pass through the annulus swept by the element. It is therefore assumed that there is no radial interaction between the elements. The BEM equation for axial thrust is obtained by equating Eqs. 3.6 to Eq. 3.20a and simplifying. This yields the following equation that is used to determine u_a .

$$\begin{aligned}
 & -4(u_a)\sqrt{(UCos\Psi + u_a)^2 + U^2 Sin^2\Psi} \\
 & = \frac{c}{2\pi r} \left\{ \sum_{b=0}^{B-1} V_r C_l(\alpha, Re) [V_\eta Cos\theta - V_\zeta Sin\theta] + \sum_{b=0}^{B-1} V_r C_d(\alpha, Re) [V_\zeta Cos\theta + V_\eta Sin\theta] \right\} \quad (3.21)
 \end{aligned}$$

For $(-u_a) > 0.38U$, the left hand side of the above equation is replaced by $C_T U^2$, where C_T is an empirical expression such as Eq. 3.4b.

The BEM equation for angular torque is obtained by equating Eq. 3.7 to Eq. 3.20b. After simplifying, this yields an equation that is used to find u_t .

$$\begin{aligned}
 & 4(u_t)\sqrt{(UCos\Psi + u_a)^2 + U^2 Sin^2\Psi} \\
 & = \frac{c}{2\pi r} \left\{ \sum_{b=0}^{B-1} V_r C_l(\alpha, Re) [V_\zeta Cos\theta + V_\eta Sin\theta] + \sum_{b=0}^{B-1} V_r C_d(\alpha, Re) [V_\zeta Sin\theta - V_\eta Cos\theta] \right\} \quad (3.22)
 \end{aligned}$$

In the BEM theory, Eqs. 3.21 and 3.22 are solved iteratively to find the axial and tangential induced velocities. These are then used in the BET theory to find the required spanwise aerodynamic load distributions. These loads are then integrated along each blade span to yield the global rotor loads. The solution procedure is described in section 3.6.

3.5 Corrections to the Blade-Element-Momentum Theory

Previous validation efforts have revealed that the BEM theory may be considerably accurate when modelling axial conditions (no rotor yaw) where the local angles of attack at the blades are small. However for conditions of high angles of attack and/or yawed flow, the theory fails to predict accurately the blade load distributions that are required for aeroelastic tailoring of the blades. Basically, the main sources for inaccuracies in the BEM theory are two:

- (1) the limitations of momentum equations: Eqts. 3.6 and 3.7 are based on the assumption that each individual streamtube (or strip) can be analyzed independently of the rest of the flow. Such an assumption works well for non-yawed conditions and when the circulation at the blades is relatively uniform so that most of the circulation is shed at the blade root and tip. However when the turbine is yawed, a time-dependent circulation that varies radially along the blades is formed. This creates a radial interaction and exchange between flows through adjacent stream tubes and thus invalidates this assumption. As already described in section 1.2, as the wind flows through the yawed turbine, a vortical wake is created downstream of the rotor similar to that created by a helicopter rotor in forward flight, the major difference being that the wake expands rather than it contracts. The BEM theory lacks the physics to mathematically model how the wake characteristics affect the distribution of induced velocity at the rotor disk. When a rotor is yawed, the wake becomes skewed. In a yawed rotor, the trailing and shed vorticity shed from the blades into the wake is on average closer to the downwind side of the rotor plane resulting in higher induced velocities in this region. The upwind side will experience a lower induced velocity. Consequently, the local induced velocities at the blades will vary considerably from the azimuthally (annular) averaged values. However the BEM equations 3.21 and 3.22 are only capable of calculating an axial and tangential induced velocity at each streamtube that are azimuthally averaged (u_a and u_t).
- (2) the inaccuracies in the aerofoil data: In the early days, 2D static wind tunnel aerofoil data (C_l and C_d) were used to compute the aerodynamic loads on wind turbine blades with BEM theory. Due to the complex 3D nature of the flow over rotating wind turbine blades, the aerofoil characteristics will vary considerably from the 2D static aerofoil characteristics, especially at the inboard sections and at the tip/root regions of the blades. As a result, the use of 2D static aerofoil data did not yield a good correlation of the calculated aerodynamic loads with those observed in experiments. In a wind turbine two aerodynamic phenomena take place: (a) *Stall-delay* phenomena and (b) *Unsteady flow* phenomena.
 - (a) *Stall-delay*: Since the 1940's, Himmelskamp [39] investigated the aerodynamic behaviour of propellers and noted that the lift forces on a rotating blade are larger than those on a non-rotating one. The same phenomenon was observed on wind turbine

blades in the past years [13, 62, 74, 75, 82, 87, 103]. Evidence shows that for attached flow conditions, below what would otherwise be the stall angle of attack of a non-rotating aerofoil, there is little difference between the 2D flow conditions and the rotating conditions. However, when stall occurs, the air in the separated region, which is moving very slowly with respect to the blade surface, is rotating with the blade and therefore it experiences a centrifugal force causing it to flow radially outwards. The flow towards the tip on the suction side experiences a Coriolis force in the main flow direction, acting as a favourable pressure gradient. This reduces the displacement thickness of the boundary layer, delaying the onset of stall and resulting in higher lift coefficients. This phenomenon is often known as *stall-delay* and is most predominant in the inboard sections. The effect of stall-delay on the lift characteristics of a rotating wing is illustrated in Fig. 3.4.

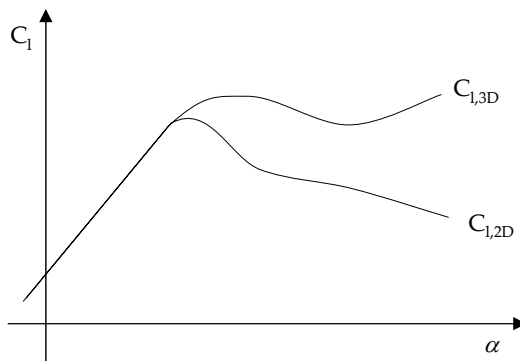


Figure 3.4 – Comparison of the lift characteristics of a rotating wing ($C_{l,3D}$) with those of a static non-rotating wing in 2D flow ($C_{l,2D}$).

(b) *Unsteady flow*: In certain operating conditions of a wind turbine such as rotor yaw, each blade element aerofoil is subjected to an unsteady angle of attack and flow velocity. This causes the lift and drag coefficients to be different from the corresponding 2D static values at the same angle of attack. When the time-dependent variation of the angle of attack is below the stall angle (α_s) for static conditions, the flow over the blades remains attached and the variation of lift will be similar to that shown in Fig. 3.5. When the angle of attack at a blade section exceeds the aerofoil's static stalling angle, dynamic stall occurs. In a 2D non-rotating environment, the phenomenon of dynamic stall is characterized by a delay in the onset of flow separation to a higher angle of attack than would occur statically. This results in higher lift. When flow separation does occur, a shedding of a concentrated vortical disturbance is formed at the leading edge. As long as this vortex remains on the upper aerofoil surface, it produces enhanced lift. However the flow causes the vortex to be swept over the chord towards the trailing edge. This produces a state of full separation resulting in a rapid aft movement of the centre of pressure and an increase in the pitching moment, together with a drop in lift. If the angle

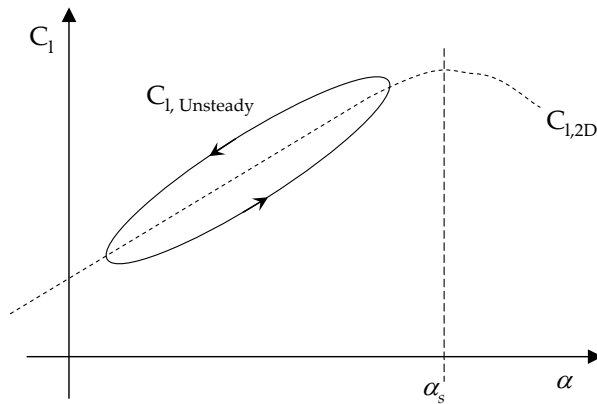
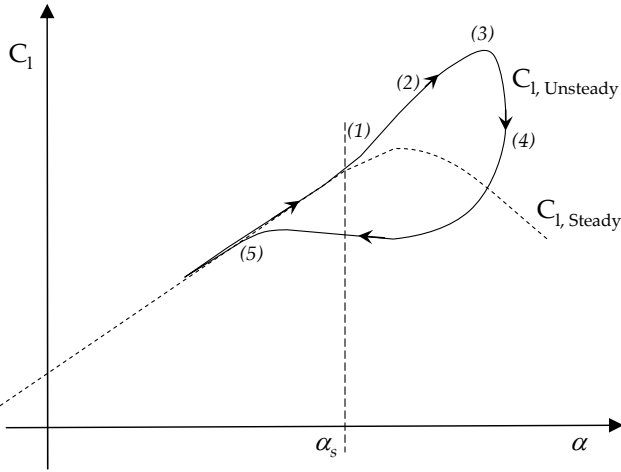


Figure 3.5 – Typical variation of the unsteady lift coefficient for small angles of attack ($\alpha < \alpha_s$).

of attack is reduced well below the static stall angle, flow re-attachment may take place. Yet flow re-attachment can only take place if the angle of attack becomes small enough again. There is generally a significant lag in this process until the fully separated flow reorganizes itself until it is ready for re-attachment. Fig. 3.6 shows a typical variation of the lift coefficient with angle of attack together with a schematic explaining the flow topologies observed in dynamic stall.

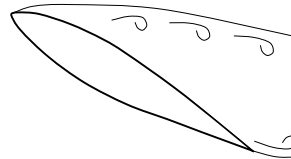
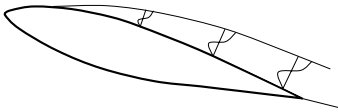
The delay in flow separation and the lag in the flow reattachment process results in a hysteresis variation. These hysteresis effects introduced by dynamic stall may have a negative effect on the aeroelastic damping behaviour of wind turbine blades. This in turn reduces the fatigue lifetime leaving an adverse impact on the economics of the system.

The phenomenon of dynamic stall is not fully understood and is still undergoing much research. Much of what is known about dynamic stall has been obtained from 2D wind tunnel experiments on non-rotating wings. Dynamic stall also occurs in a rotor environment where it has a much more three-dimensional character and depends on both the radial and azimuth positions on the blades.



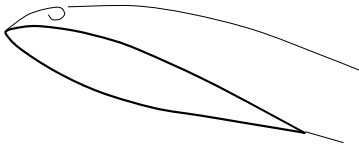
Stage 1: Aerofoil exceeds α_s and flow reversal occurs in upper boundary layer

Stage 3-4: Lift stall occurs. After vortex reaches trailing edge, full separation occurs.



Stage 2: Formation of vortex at leading edge

Stage 5: When angle of attack decreases again, boundary layer reattaches front to rear



Stage 2 - 3: Vortex convects towards trailing edge, causing extra lift

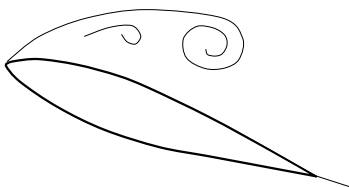


Figure 3.6 – Schematic showing the unsteady lift coefficient and the basic flow topologies during dynamic stall. Adapted from Leishman [49].

To reduce the uncertainties in the BEM theory due to the limitations of the momentum equations and due to inaccuracies in the aerofoil data, various corrections were included in the past years. This has resulted in the so-called ‘extended BEM’ theory. These corrections took the form of basic ‘engineering models’ that were derived from experimental data or data from more advanced codes (based on vortex theory or CFD). A short review of some of these models is now presented. These models fall under two different classifications:

- Type I models: those that correct the axial induction factor computed by the BEM theory for the non-uniform induction distribution at the rotorplane resulting from the skewed wake of a yawed rotor. An early model for skewed wake effects has been proposed by Glauert [30]. It estimates the axial induced velocity at the blades using the equation

$$u_{a,c} = u_a \left(1 + K * \frac{r}{R} * \text{Sin}\phi \right) \tag{3.23}$$

where K depends on the yaw angle. Eq. 3.23 was derived from the smoke visualization of the fully roll-up strong tip vortices formed on helicopter rotors in forward flight. Various formulas for K were proposed [49] which are given in Table 3.1. χ_s is the wake skew angle which is calculated from

$$\tan \chi_s = \frac{U \text{Sin}\Psi}{U \text{Cos}\Psi + u_a} \tag{3.24}$$

Since in the equation above u_a will vary radially, then χ_s will also vary radially. However χ_s is usually taken to be equal to that between 70-80% R .

Table 3.1 - Various models for parameter K (Eq. 3.23)

Author(s)	K
Coleman et al.(1945)	$\tan(\chi/2)$
White&Blake (1979)	$2^{1/2} \text{Sin}\chi$
Pitt&Peters (1981)	$(15\pi/32)\tan(\chi/2)$
Howlett (1981)	$\sin^2\chi$

Other models were developed in the past years, some of which were examined against measurements in the JOULE Dynamic Inflow projects [83, 84]. These models have been implemented in various BEM-based aeroelastic models. One such model is that developed by the DTU [60] that is similar to Glauert’s model but introduces a radial variation for the induction. The model was derived with a curve fitting procedure from

an actuator disk vortex ring model. The local induced velocity was found to depend on the radial location, azimuth angle and the wake skew angle according to:

$$u_{a,c} = u_a \left(1 + f_{2,mdk} \left(\frac{r}{R} \right) \tan \left(\frac{\chi_s}{2} \right) \sin(\phi) \right) \quad (3.25a)$$

where

$$f_{2,mdk} \left(\frac{r}{R} \right) = \frac{r}{R} + 0.4 \left(\frac{r}{R} \right)^3 + 0.4 \left(\frac{r}{R} \right)^5 \quad (3.25b)$$

Other engineering models for yaw were developed in the JOULE I and II projects. Further details may be found in references [83] and [84].

A major shortcoming of Eq. 3.23 is that it considers only the induced velocity due to the tip vorticity alone. It is shown that vorticity originating from the blade root as well as shed vorticity will cause the induction distribution at the rotor disk to have a higher harmonic content than that modelled by Eq. 3.23. This was revealed in past inflow measurements taken on the Delft wind tunnel model [69, 96]. ECN [69] has developed a new engineering model that accounts for such effects. This consists of a second order Fourier series having the form:

$$u_{a,c} = u_a \left[1 - A_1 \cos(\phi - \varphi_1) - A_2 \cos(2\phi - \varphi_2) \right] \quad (3.26)$$

where amplitudes A_1 and A_2 and phases φ_1 and φ_2 have been modelled as a function of radial position and yaw angle.

In the BEM model described in sections 3.3 and 3.4, skewed wake effects are accounted for by modifying Eq. 3.9 and introducing a correction factor F_{sa} as follows:

$$\hat{u}_c = \begin{bmatrix} \left(\frac{u_t}{f} \right) \\ \left(\frac{u_a}{f} \right) F_{sa} \\ 0 \end{bmatrix} = \begin{bmatrix} u_{t,c} \\ u_{a,c} \\ u_{r,c} \end{bmatrix} \quad (3.27)$$

where F_{sa} determines the ratio of the local axial induced velocity at the blades to the azimuthally averaged value as modelled by anyone of the engineering models described above. For instance for $f=1$, if Glauert's engineering model is to be used, then F_{sa} would be equal to

$$F_{sa} = \left(1 + K * \frac{r}{R} * \text{Sin}\phi \right) \quad (3.28)$$

As it can be noted from Eq. 3.27, the correction for skewed wake effects is only being applied to the axial component of the induction. No correction is done for the tangential and radial components since these are usually very small in magnitude and thus their influence on aerodynamic loading is insignificant.

- Type II models: those that correct static 2D aerofoil data for 3D rotating effects (stall-delay) and unsteady aerodynamic effects (unsteady aerofoil models for both attached flow and dynamic stall).

Engineering Models for Stall-Delay

An early empirical model for modifying 2D static aerofoil data to represented more accurately the power augmentation at high angles of attack resulting from stall-delay has been developed by Viterna and Corrigan [100] in 1981. This model was used extensively in the past years for wind turbine modelling in stalled flow conditions. The equations for this model are as follows:

For $\alpha \geq \alpha_s$:

$$C_l = \frac{C_{d,\max}}{2} \sin 2\alpha + K_l \frac{\cos^2 \alpha}{\sin \alpha} \quad (3.29a)$$

$$C_d = C_{d,\max} \sin^2 \alpha + K_d \cos \alpha \quad (3.29b)$$

$$K_l = \left(C_{l,s} - C_{d,\max} \sin \alpha_s \cos \alpha_s \right) \frac{\sin \alpha_s}{\cos^2 \alpha_s} \quad (3.29c)$$

$$K_d = \frac{C_{d,s} - C_{d,\max} \sin^2 \alpha_s}{\cos \alpha_s} \quad (3.29d)$$

$$\mu \leq 50: \quad C_{d,\max} = 1.11 + 0.018\mu \quad (3.29e)$$

$$\mu > 50: \quad C_{d,\max} = 2.01$$

where $C_{d,\max}$ is the maximum drag coefficient and μ is the blade aspect ratio.

In year 1993, Snel *et al.* [82] presented a method to evaluate the first order effects of the blade rotation on stall characteristics through a simplified solution of the 3D boundary layers equations. An order of magnitude analysis of the different boundary layer equations was carried out to enable the identification of the most important

parameters. It was shown that the local blade solidity (c/r) is the most influential parameter affecting stall-delay. In this work, a simple empirical model to correct 2D lift coefficient data for stall-delay was developed with observation of wind tunnel data (Ronsten, [62]) and results from a CFD model *ULTRAN_V* developed at NLR. The model is given by

$$C_{l,3D} = C_{l,2D} + a \left(\frac{c}{r} \right)^b \Delta C_l \quad (3.30a)$$

where

$$\Delta C_l = C_{l,lin} - C_{l,2D} \quad (3.30b)$$

a and b are empirical constants. $C_{l,lin}$ is the lift coefficient that would be obtained if the linear part of the static 2D C_l - α curve is extended beyond stall. Although this model improved agreement for power prediction when compared with experimental data, it is limited due to the fact that the drag coefficient remains uncorrected. It is a well known fact that 3D rotating effects may alter the 2D C_d values significantly, especially at the inboard regions.

A third model was developed by Du and Selig [22]. This traces its roots in the work of Snel *et al.* [82] as it also originates from the 3D incompressible boundary layer equations for a rotating system. A rigorous analysis of the integral boundary layer equations is applied. The model corrects both the lift and drag coefficients as follows:

$$C_{l,3D} = C_{l,2D} + f_l (C_{l,lin} - C_{l,2D}) \quad (3.31a)$$

$$C_{d,3D} = C_{d,2D} - f_d (C_{d,2D} - C_{d,0}) \quad (3.31b)$$

$$C_{l,lin} = 2\pi(\alpha - \alpha_0), \quad C_{d,0} = C_{d,2D} \text{ for } \alpha = 0 \quad (3.31c)$$

f_l and f_d are factors that depend on the separation point of the flow on the aerofoil's upper chamber as predicted by the boundary layer theoretical analysis. These factors are related to the local solidity, c/r , (which accounts for rotor geometry) and the modified tip speed ratio, Λ (which accounts for the effects of rotation). Λ is given by

$\Omega R / \sqrt{U^2 + (\Omega R)^2}$. f_l and f_d are given by

$$f_l = \frac{1}{2\pi} \left[\frac{1.6(c/r) a - (c/r)^{\frac{d}{\Lambda} \frac{R}{r}}}{0.1267 b + (c/r)^{\frac{d}{\Lambda} \frac{R}{r}}} - 1 \right] \quad (3.32a)$$

$$f_d = \frac{1}{2\pi} \left[\frac{1.6(c/r) a - (c/r)^{\frac{d}{2\Lambda} \frac{R}{r}}}{0.1267 b + (c/r)^{\frac{d}{2\Lambda} \frac{R}{r}}} - 1 \right] \quad (3.32b)$$

In the above equations, terms a , b and d are empirical correction factors. Another engineering model was developed by Chaviaropoulos *et al.* [17] using CFD and corrects all aerofoil coefficients (C_l , C_d and C_m) for 3D rotating effects. The model was derived based on results obtained from a 3D incompressible flow Navier-Stokes solver. It also accounts for the effects of blade twist since this was found to play an important role in massively separated flow. The model equations are

$$C_{X,3D} = C_{X,2D} + a \left(\frac{c}{r} \right)^h \cos^n(\text{twist}) \Delta C_X \quad \text{where } X = l, d, m \quad (3.33a)$$

where

$$\Delta C_l = C_{l,lin} - C_{l,2D} \quad (3.33b)$$

$$\Delta C_d = C_{d,2D} - C_{d,2D-MIN} \quad (3.33c)$$

$$\Delta C_m = C_{m,2D} - C_{m,lin} \quad (3.33d)$$

where a , h and n are empirical constants. However validations studies [45, 65, 73] on different rotors suggest these models may not always be sufficiently accurate.

Engineering Models for Unsteady Flow Effects

Examples for unsteady aerofoil models used in attached flow conditions are Theordorsen's model [93] and Leishman's indicial response method using Duhamel's superimposition [49, pp 336-340]. The latter model is described in detail in chapter 4, section 4.3.2. Examples of dynamic stall models include the Boeing-Vertol model, the ONERA model [11], and the Beddoes-Leishman model [47]. The most-straight forward model is the Boeing-Vertol model which is based on correcting the static 2D lift coefficient in accordance with the following equations

$$C_l(\alpha, \dot{\alpha}) = \frac{\alpha - \alpha_0}{\alpha - \alpha_0 - \Delta} C_{l,2D}(\alpha - \Delta) \quad (3.34a)$$

Δ is the shift in the angle of attack given by

$$\Delta = \gamma \left(\frac{c|\dot{\alpha}|}{2V_r} \right)^{1/2} \text{sign}(\dot{\alpha}) \quad (3.34b)$$

where γ is an empirical constant. A brief description of the different dynamic stall models is presented by Leishman [49, 50]. Snel [79] developed a heuristic model for dynamic stall based on the observation of experimental data.

Most unsteady aerofoil models for attached flow conditions have been derived based on 2D non-rotating wings and therefore there may be inaccurate when applied for 3D conditions on a rotating wind turbine blade. Several dynamic stall models are semi-empirical and were also derived from non-rotating 2D wing experiments. Consequently they are also inaccurate when treating 3D dynamic stall on a rotating blade. Due to the blade advancing-and-retreating effect resulting from yaw, each rotating blade is subjected to unsteady radial flow components that may be much larger in magnitude than in a non-yawed rotor. Such radial flows influence the dynamic stall behavior significantly, as described in reference [48]. Although it is a well known fact that radial flow over the blades helps in preventing flow separation over the blades at high angles of attack and thus contributes to stall delay, it is still unclear how 3D effects influence stall in an unsteady environment.

Although the inclusion of both *Type I* and *Type II* engineering models improved BEM aerodynamic load predictions, better models are still required. This was noted during the “blind comparison” investigation organized by National Renewable Energy Laboratory (NREL) way back in the year 2000 [73, 78]. Considerable discrepancies between predicted and experimental results were observed even at low windspeeds at which the angle of attack is small.

3.6 Description of Program *HAWT_BEM*

HAWT_BEM is a BEM code developed in this project using MathCad© version 11 and is applicable to both axial and yawed rotors. This code was used for all computations required with the BEM theory throughout this project.

3.6.1 Time-based Numerical Solution for the BEM Equations

This section describes the numerical solution of the BEM theory equations described above as implemented in *HAWT_BEM*. Since in a yawed turbine the flow at the blades becomes unsteady, then the solution has to be solved as a function of time (or rotor azimuth angle ϕ). Consider the situation in which the rotor is rotating at constant angular speed Ω in a uniform wind front equal to U . One whole rotor revolution is divided into a fixed number of azimuth steps (n_{tot}), as shown in Fig. 3.7. An index τ is used to denote the azimuth angle of the first blade. $\tau=0$ denotes when the first blade is at an azimuth angle equal to zero (vertical pointing upwards). The azimuthal step, $\Delta\phi$, is equal $2\pi/n_{tot}$ while the incremental time step, $\Delta\tau$, is equal to $\Delta\phi/\Omega$.

Each turbine blade is discretized into a fixed number of equally spaced sections as shown in Fig. 3.8. The total number of blade sections is equal to n . The cross-sectional area of the

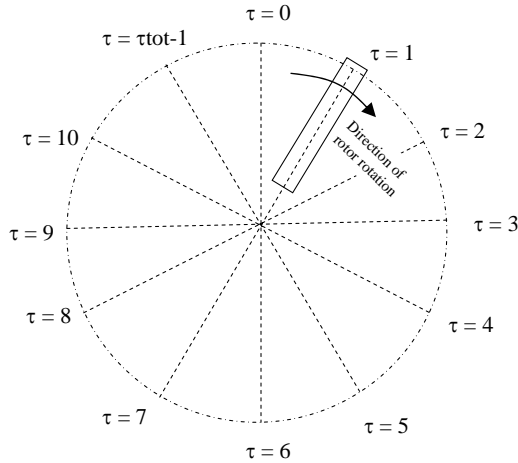


Figure 3.7 - Division of one whole rotor revolution into a fixed amount of azimuthal steps.

rotorplane swept by the blades (from $r=R_r$ to $r=R_t$) is divided into n annular elements (as illustrated by the shaded area in Fig. 3.9). An index notation is used to represent each parameter at each rotor time step (τ), blade (b), and radial location (i). The parameters local to the blade (equal angle of attack, Reynolds number, flow relative velocity and aerodynamic loading) are denoted by the three-letter index notation $(\alpha)_{\tau,b,i}$. The parameters that are only a function of the radial location and rotor azimuth angle are only denoted by a two-letter suffix notation (τ, i) . Thus the azimuthally averaged axial and tangential induced velocities at each annulus are denoted by $(u_a)_{\tau,i}$ and $(u_t)_{\tau,i}$, respectively. The total number of blades is equal to B and $b=0$ denotes the first blade. Given that $(\phi)_{\tau}$ is the rotor azimuth angle at time step τ , then the azimuth angle of each blade is given by

$$(\phi)_{\tau,b} = (\phi)_{\tau} + \frac{2\pi b}{B}$$

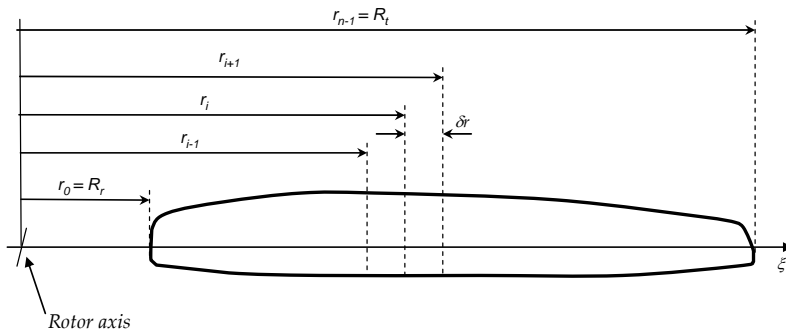


Figure 3.8 – Discretization of blade into a fixed number of equally spaced blade sections.

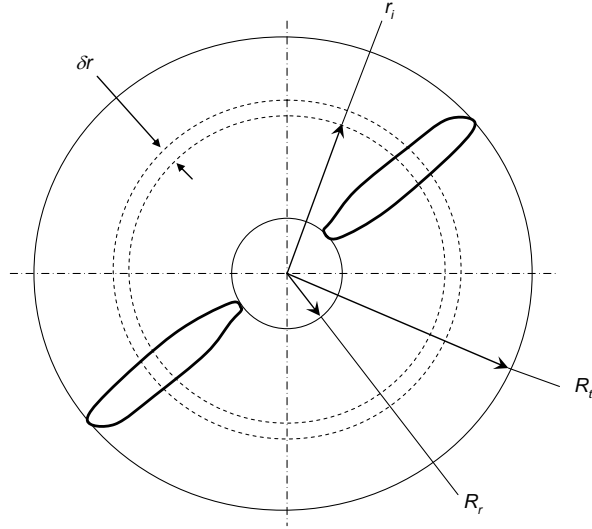


Figure 3.9 – Division of swept area by blades into a fixed number of annuli.

The solution starts by assuming initial values for the azimuthally averaged axial and tangential induced velocities for each time step and radial location ($(u_a)_{\tau,i}$ and $(u_t)_{\tau,i}$). The solution is started with an impulsive start of the rotor. Initially, the rotor is at an azimuth angle of zero ($\tau=0$) and the following sequence of steps is applied to each blade element for all the time steps (z_{tot}) in one whole rotor revolution:

Step 1: The absolute velocities, $(V_{A,\eta})_{\tau,b,i}$, $(V_{A,\zeta})_{\tau,b,i}$ and $(V_{A,\xi})_{\tau,b,i}$ are found using Eqts. 3.8.

Step 2: The correction factor for skewed wake effects, $(F_{sa})_{\tau,b,i}$ is determined using a *Type I* engineering model (refer to section 3.5)

Step 3: The Prandtl tip/root loss factor, $(f)_{\tau,b,i}$ is then calculated in accordance with Eq. 3.10.

Step 4: The local induced velocities at each blade element, $(\hat{u}_c)_{\tau,b,i}$ are found from Eq. 3.27

Step 5: The flow relative velocity components, $(V_\eta)_{\tau,b,i}$, $(V_\zeta)_{\tau,b,i}$ and $(V_\xi)_{\tau,b,i}$ are found using Eqts. 3.11.

Step 6: The resultant flow relative velocities, $(V_r)_{\tau,b,i}$ and $(V_{rel})_{\tau,b,i}$ are found using Eqts. 3.12 and 3.13.

Step 7: The angle of attack, sweep angle and Reynolds number, $(\alpha)_{\tau,b,i}$, $(\alpha_{sweep})_{\tau,b,i}$ and $(Re)_{\tau,b,i}$ are found from Eqts. 3.14, 3.15 and 3.17.

Step 8: The lift and drag coefficients, $(C_l)_{\tau,b,i}$ and $(C_d)_{\tau,b,i}$ together with the pitching moment coefficient $(C_m)_{\tau,b,i}$ are found from 2D wind tunnel data which may be corrected for stall-delay, or unsteady flow (e.g. dynamic stall) using a *Type II* engineering model (refer to section 3.5.)

Step 9: Eqts. 3.21 and 3.22 are then solved to yield new values for $(u_a)_{\tau,i}$ and $(u_i)_{\tau,i}$.

The new values for $(u_a)_{\tau,i}$ and $(u_i)_{\tau,i}$ obtained in *Step 9* are used in *Step 1* and the whole sequence of steps is repeated until convergence in these parameters is achieved at all blade elements and rotor azimuth positions. The aerodynamic loading components $(\delta A_\eta)_{\tau,b,i}$, $(\delta A_\zeta)_{\tau,b,i}$ and $(\delta q_{\xi,a})_{\tau,b,i}$ are evaluated using Eqts. 3.16 and 3.18. These are then integrated numerically to find the resulting 3D aerodynamic forces and moments at the yaw bearing in accordance with the method described in Appendix B.

3.6.2 Program Structure

Fig. 3.10 describes the structure of code *HAWT_BEM*. This code is organized into three separate modules: the *Data Input Module* in which the parameters describing the rotor geometry and operating condition are inputted, together with the required aerofoil data. The *Data Processing Module* implements the numerical solution of the BEM equations described above in section 3.6.1 to determine the spanwise distributions of the various aerodynamic parameters at different blade azimuth positions. The 3D aerodynamic loads induced by the rotor blades at the yaw bearing and the rotor output power are calculated using the solution described in Appendix B. The *Data Output Module* outputs the local blade and rotor global results as a function of blade/rotor azimuth angle.

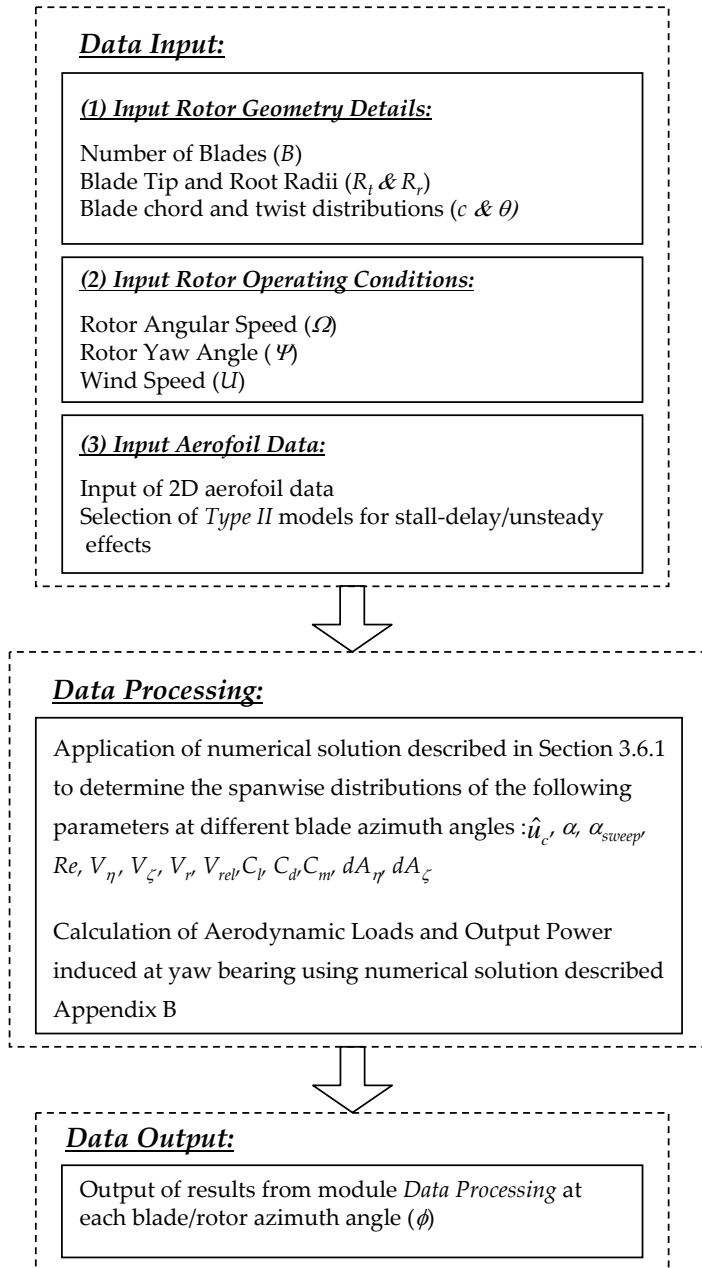


Figure 3.10 – Structure of code HAWT_BEM.

4. Aerodynamic Analysis of the TUDelft Model Turbine

4.1 Introduction

This chapter describes the aerodynamic analysis carried out on the TUDelft model wind turbine. A series of experiments were carried in the Delft University of Technology open tunnel jet facility. The experiments consisted of detailed hot-film inflow measurements in the near wake of the turbine and smoke visualization experiments to trace the tip vortex paths in the turbine wake. The experiments were carried out in both axial and yawed conditions. The inflow measurements were limited to one rotor tip speed ratio and blade pitch setting only that yielded attached flow conditions over the blades. The smoke visualization experiments were carried out at different tip speed ratios and blade pitch settings that resulted in both attached and stalled flow at the blades. The measurements were mainly required for three reasons: (1) to obtain a better understanding of the aerodynamics of wind turbines in yaw; (2) to assess the limitations of BEM models in yaw for attached flow conditions where the uncertainty in the aerofoil data is not the issue that limits BEM models from predicting loads accurately. This assessment was a first step before carrying out a more extensive assessment on the NREL rotor in both attached and stalled conditions (refer to Chapter 6); (3) to use the experimental data to validate the newly developed free-wake vortex model in both axial and yawed conditions (refer to Chapter 5).

As already outlined in Chapter 2, to be able to provide an in-depth investigation of the limitations of the BEM theory it is vital to have the unsteady aerodynamic loading distributions along the blades. Since the experimental set-up used in this study on the TUDelft rotor was incapable of acquiring such distributions through blade pressure measurements, unsteady aerofoil theory had to be employed in order to derive the aerodynamic loads from the inflow measurements. The unsteady lift coefficient could be predicted with reasonable accuracy since the inflow measurements were carried out in attached flow conditions only.

This chapter is organized in three separate sections:

A. Section 4.2 will describe the experiments in detail together with the data reduction procedures that were required to obtain the required experimental data. The main experimental results are also presented.

B. Section 4.3 implements a method for deriving the steady/unsteady bound circulation and aerodynamic load distributions at the blades by coupling the inflow measurements with an

unsteady aerofoil model. In this procedure, the angle of attack values at the blades are estimated from the hot-film measurements and used in the unsteady aerofoil model to be able to determine the lift coefficients. The latter are then used to estimate the distributions for the bound circulation and aerodynamic loads at the blades using the blade-element theory. To be able to carry out these computations in an efficient and organized manner, a dedicated computer program, *HAWT_LFIM*, was developed.

C. Section 4.4 deals with the assessment of a typical BEM code (*HAWT_BEM*, see section 3.6) using both the experimental inflow measurements and the aerodynamic load results from sections 4.2 and 4.3.

Rotor Details

The wind tunnel model rotor was a horizontal-axis wind turbine with the specifications listed in table 4.1 below.

Table 4.1 – Wind turbine geometric specifications

Number of blades	2
Airfoil section	NACA0012
Rotor radius R	0.6 m
Blade root radius	30% of tip radius
Chord c	0.08 m (constant)
Blade length	0.42 m
Blade twist	$\theta(r/R)=(6+\theta_{tip}) - 6.67(r/R), 0.3 \leq r/R \leq 0.9$
	$\theta(r/R)=\theta_{tip}, 0.9 < r/R \leq 1$

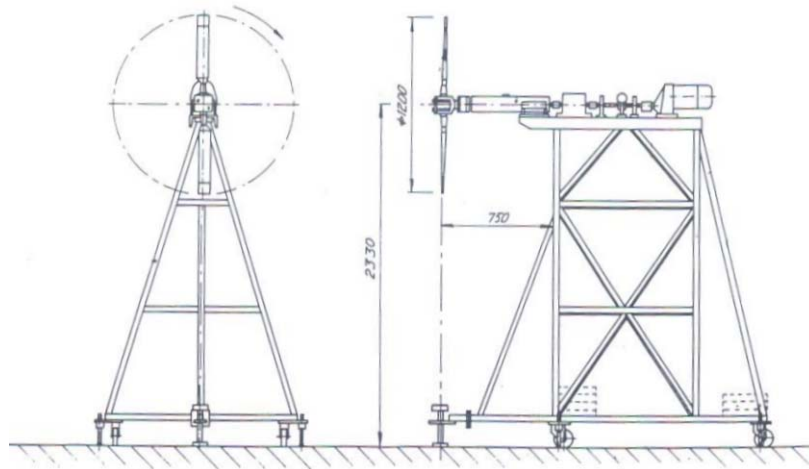


Figure 4.1 – Wind turbine model at Delft University of Technology.

The rotor shaft and its bearings are placed on an extended support leaving 0.75 m free space behind the rotorplane to minimize the interaction of the developed wake with the support structure within a distance of about one rotor radius from the rotorplane. The rotor hub height is 2.33m above the ground. A variable pitch mechanism is installed in the rotor hub, capable of adjusting the blade pitch with accuracies of $\pm 0.1^\circ$. The rotor is linked to a constant speed drive unit consisting of a 1.5kW motor/generator, with the rotational speed that is adjustable from 0 to 16Hz. Strain gauges are installed on the rotor shaft and one of the blades to be able to measure the rotor axial thrust and blade root edgewise and flapping bending moments. The aerodynamic behavior characteristics of the model turbine when operating in axial conditions are shown in Figs. 4.2 and 4.3.

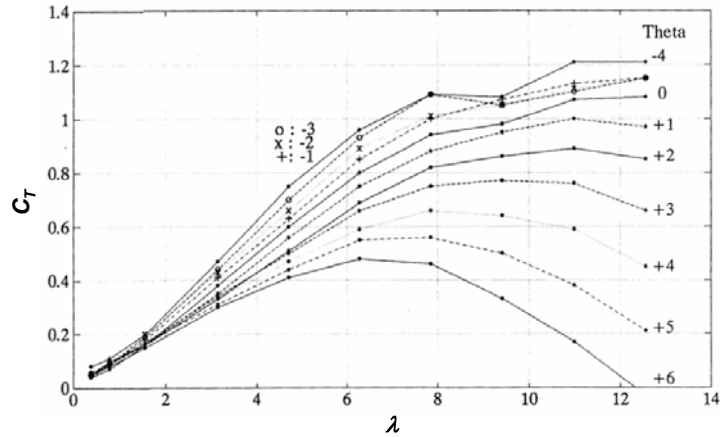


Figure 4.2 - Variation of axial thrust coefficient with tip speed ratio and blade tip pitch angle Θ_{ip} (deg) (Source: Vermeer [97]).

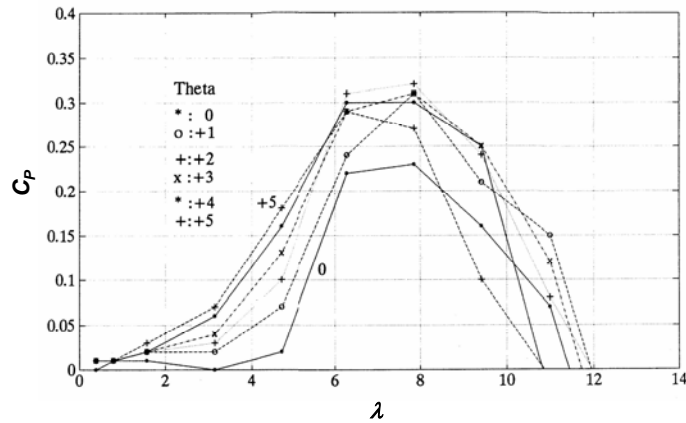


Figure 4.3 - Variation of power coefficient with tip speed ratio and blade tip pitch angle Θ_{ip} (deg) (Source: Vermeer [97]).

4.2 Wind Tunnel Measurements

The wind tunnel measurements on the model turbine were performed in the open jet wind tunnel of Delft University of Technology. Both the wake inflow and smoke visualization experiments were carried out in close collaboration with Phd colleague Wouter Haans.

4.2.1 Wind Tunnel

The open jet wind tunnel consisted of a flow channel with a circular cross-section, a large inlet fan, flow straighteners and gauzes. Fig. 4.4 is a schematic diagram of the tunnel. The flow straightener was a hexagonal shaped honeycomb structure made out of thin aluminum sheets. There were three identical gauzes: one just behind the flow straightener and two spaced by 0.2m at 2m upstream of the tunnel jet exit. The tunnel had an exit jet diameter of 2.24m and its central axis was 2.33m above the ground. The fan was driven by a 45kW dc motor in a Ward-Leonard circuit. The exit jet wind velocity could be adjusted by controlling the rotational speed of the fan. The tunnel maximum windspeed was equal to 14.5m/s. The turbulence level was equal to $1.2 \pm 0.2\%$ at $U_{jet} = 5.5\text{m/s}$, the speed at which measurements were taken. The exit jet velocity profile was not uniform throughout, as may be noted in Fig. 4.5. A velocity dip was observed at the centre of the exit and this is mainly due to the centre body containing the motor-fan drive mechanism.

The tunnel was situated in a hall (length 35m, width 20m, height 5.5m) and the tunnel exit was approximately 11m from the back wall.

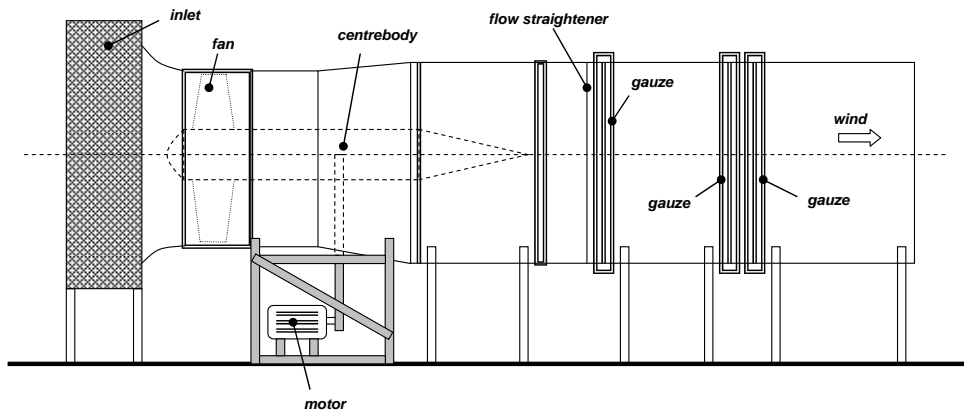


Figure 4.4 – Open jet wind tunnel at Delft University of Technology.

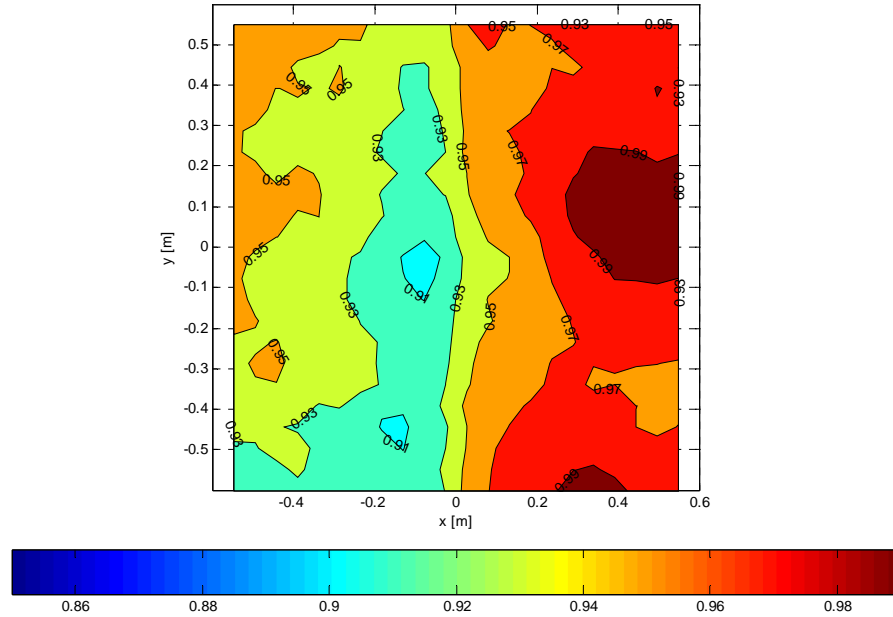


Figure 4.5 – Velocity distribution measured in the empty tunnel at 1 m downstream from the tunnel jet exit with the pitot readings set to 5.5m/s. The velocities are non-dimensionalized with respect to the maximum velocity recorded. $(x,y) = (0,0)$ coincides with the central axis of the tunnel.

4.2.2 Part I: Inflow Measurements

Experimental Set-up

The rotor was placed in front of the wind tunnel exit with the hub centre located in the jet centre and 1 m downstream from the jet exit plane. Fig. 4.6 is a schematic overview of the rotor and its position relative to the wind tunnel. The conventions for the yaw angle and azimuth angle are also shown. Seen from above, a positive yaw angle implies that the rotor is rotated counter-clockwise. Standing in between the tunnel exit and rotor while looking downwind, the rotor azimuth angle increases as the rotor rotates in the clockwise direction. The azimuth angle is zero when the first blade is vertical and pointing upwards. The axial distance is defined with respect to the rotor axis. The tunnel wind velocity was measured at the jet exit plane using three inter-connected pitot-static tubes that were connected to an electronic pressure sensor, together with ambient pressure and temperature readings. The near wake velocities of the rotor model were measured using constant temperature hot-film anemometry. This technique makes use of hot-wires or hot-films that act as sensors and are very useful in obtaining the fast response velocity measurements. Using different probe

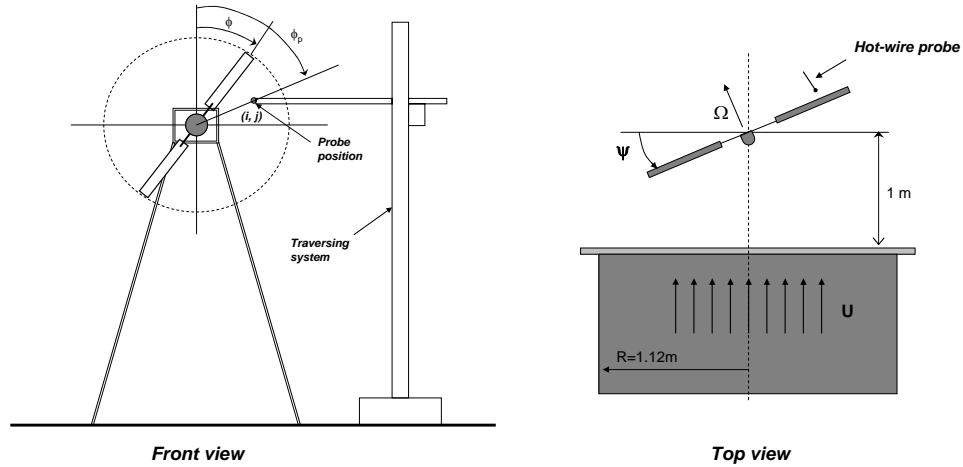


Figure 4.6 – Schematic overview of test set-up with frame of reference.



Figure 4.7 – The model wind turbine and open jet wind tunnel used.

orientations or multi-sensor probes, it is possible to obtain three-dimensional components of complex flows. The sensor consists of a very fine wire or film that is attached between two supporting needles. The wire or film is usually made out of a quartz fiber and coated with platinum. Current passed through the sensor raises its temperature above the adiabatic recovery temperature of the gas. The hot-wire or film then responds to changes in total temperature and mass flux. In subsonic applications where the fluid temperature is low and constant, the problem of heat transfer through the support needle (end losses) and radiation effects can be ignored and the sensor's response can be taken to be as a function of

the flow velocity only. In a constant temperature system, the hot-wire or film is maintained at constant temperature. Electronic circuits used in a constant temperature anemometer include a bridge circuit with a feedback system to maintain the wire or film at constant resistance. The bridge voltage is a measure of the cooling of the wire and therefore a measure of velocity.

In these wind tunnel inflow measurements, two different types of single hot-film probes were used: one with the film normal to the probe (TSI 1201-20) and one with the film parallel to the probe (TSI 1211-20), (refer to Fig. 4.8). In each of the two probes, the hot-film consists of a platinum film on a fused quartz substrate. The two probes are very similar, with the exception for the hot-film orientation.

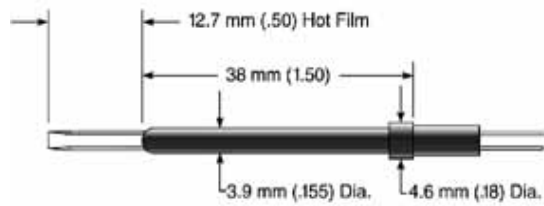


Fig (a): Normal probe (TSI 1201-20)

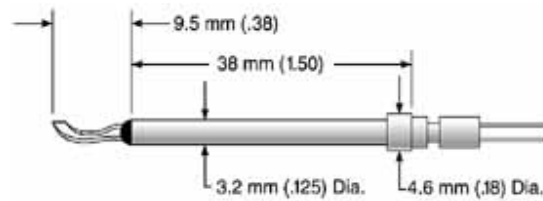


Fig (b): Parallel probe (TSI 1210-20)

Figure 4.8 - The normal and parallel types of single hot-film probes used. (Courtesy: TSI Instruments).

Experimental Procedure

The experiments were carried out at a rotor speed and tunnel velocity of 11.65Hz and 5.5m/s, yielding a tip speed ratio of 8. This yielded a Reynolds number equal to about 150,000 at the blades. The blade tip pitch angle was set to 2°. This was very close to the conditions for peak power (see Fig. 4.3). The experiments were carried out at different yaw angles of the rotor (0°, 30° and 45°). A major disadvantage of using hot-films in rotor experiments is that it is physically impossible to measure the inflow directly in the

rotorplane. An estimate had to be made by taking wake measurements at different planes parallel to the rotor plane both upstream and downstream as shown in Fig. 4.9. Interpolation was then applied to derive the wake velocities in the rotorplane. The hot-film measurements were taken at the following planes: 3.5cm, 6.0cm and 9.0cm downstream of rotorplane and 6.0cm upstream of rotorplane. In dimensionless form, these distances are equivalent to Y_a/R equal to 0.058, 0.1 and 0.15 downstream and 0.1 upstream of the rotorplane. For each plane, the measuring points were located at radial positions 40, 50, 60, 70, 80, 90 and 100% R and at azimuth increments of 15° . These yielded traces of velocity against ϕ over a whole rotor revolution (i.e. 0° to 360°). Terms i and j in Fig. 4.6 are integers that denote the radial and azimuth positions respectively of each measurement point within the measurement plane. τ is an integer representing the azimuth position of the rotor. Note that the probe azimuth angle (ϕ) is different from the azimuth angle of the rotor (ϕ). Whilst the rotor was rotating, the probe was positioned at different i and j positions in each measuring plane. For each measurement point, the hot-film readings were taken every 2° increments of rotor azimuth angle. At each point, 54 velocity traces were taken corresponding to 54 consecutive rotor revolutions and the mean velocity trace was determined. Since it was necessary to measure the three different components of the wake velocities, the readings had to be repeated for different orientations of the hot-film probes. Six different hot-film orientations were required to be able to derive the flow velocity components using a new method developed by Haans [37].

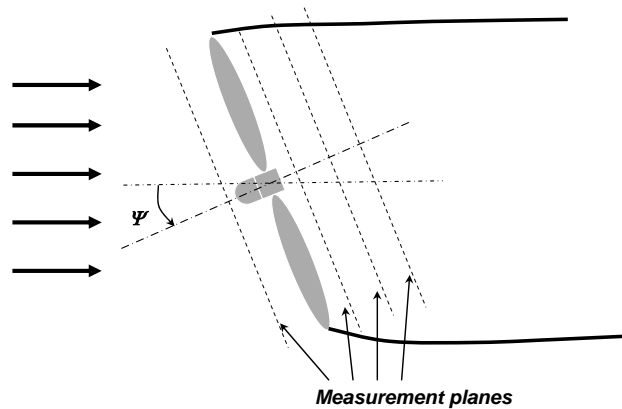


Figure 4.9 - Hot-film measurements at different planes parallel to the rotorplane.

Data Reduction

This section describes the procedures adopted to calibrate the hot-films and deduce the 3D components of the measured velocities in the near wake of the rotor.

Hot-film Co-ordinate System Definitions

In order to be able to measure 3D flow components using hot-films, a suitable system of co-ordinates should be defined. Fig. 4.10 shows the local co-ordinate systems (x_p - y_p - z_p) used for the normal and parallel probes. In both cases, the co-ordinate axes are attached to the hot-film and not to the probe. The y_p -axis is always aligned with the hot-film.

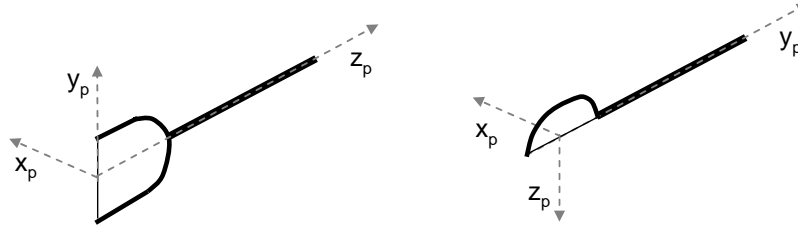


Fig. (a): Normal probe

Fig. (b): Parallel probe

Figure 4.10 - Local Cartesian system of co-ordinates for the normal and parallel probe calibration.

The calibration procedure of each hot-film consisted of two steps: (a) a speed calibration and (b) an angular calibration.

(a) *Speed Calibration* - the hot-film voltage, E , was correlated with a known windspeed of the tunnel jet (U_{jet}) with the hot-film in a normal position to the flow (with the y_p - z_p plane aligned with the flow). For the correlation, the temperature corrected, averaged King's law was used [14] given by:

$$\overline{E^2} = (\overline{T_f} - \overline{T_a}) \left(A + B \overline{U_{jet}}^n \right) \quad (4.1)$$

where T_f and T_a are the preset hot-film and measured flow temperature respectively. A , B and n are calibration constants with A set equal to $\left[\overline{E^2} / (\overline{T_f} - \overline{T_a}) \right]_{U_{jet}=0}$. B and n were derived from measuring E at different wind tunnel speeds and then applying a curve fitting procedure using the method of least-squares. For this speed calibration, U_{jet} was determined using a single pitot-static tube located in the vicinity of the hot-film.

(b) *Angular Calibration* – this calibration procedure was required to derive the characteristics of the hot-films at different flow directions. The basis for this procedure is based on the fact that given that V_{eff} is the velocity measured when correlating with the hot-film voltage E when the latter is normal to the flow as for the speed calibration (Eq. 4.1), V_{eff} is correlated to the 3D velocity components in accordance with [14]:

$$V_{eff}^2 = h^2 U_p^2 + k^2 V_p^2 + W_p^2 \quad (4.2)$$

U_p , V_p and W_p are the 3D flow velocity components in the direction of the hot-film axis of Fig. 4.10 (x_p , y_p , z_p), respectively while h and k are the angular calibration constants for the particular hot-film. To determine the values for h and k , each hot-film was subjected to a constant axial velocity whilst being rotated in a vertical plane parallel to the axial direction. In doing so, the hot-film was oriented in different orientations such that U_p , V_p or W_p was zero. Two orientations were used both for the normal and parallel probes. These orientations are shown in Fig. 4.11. Eq. 4.2 was applied to each different orientation to yield the equations given in Fig. 4.11. During the angular calibration, V_{eff} was recorded for the range $-90^\circ < \theta < 90^\circ$, with increments of 10° . For each θ , 10,000 sample readings were taken and the averaged values were found. The corresponding standard deviations were found to be very small (on the order of 0.001% of the averaged values) and therefore their influence could be neglected. To determine h or k for each probe orientation, a trial-and-error algorithm was used. The method was based on using the experimental values for V and assuming different values of h (or k) to estimate V_{eff} in accordance with the corresponding equation from Fig. 4.11. For each θ , the error between the estimated value of V_{eff} and the experimental value was found. The assumed value of h (or k) that yielded the minimum error was taken to be the correct required value. This minimum error was found to be less than 5%. The angular calibration process was repeated frequently in order to minimise the uncertainty due to hot-film ageing. The values of h and k were found to be on the order of 1.1 and 0.25 respectively for both probes. It was found that the variation of these angular calibration constants only varied minimally with the tunnel wind speed. This simplified considerably the data reduction process. Fig. 4.12 illustrates typical characteristic curves derived for the hot-films using the experimental measurements taken during the angular calibration procedures. The curves for the estimated values for V_{eff} using the derived values of h and k are also shown. Note that for orientation 1 of the parallel probe, the characteristic curve is asymmetric since for negative θ the prong of the probe will disturb the flow approaching the hot-film. Consequently for negative θ , Eq. (3) of Fig. 4.11 is invalid for $\theta < 0^\circ$.

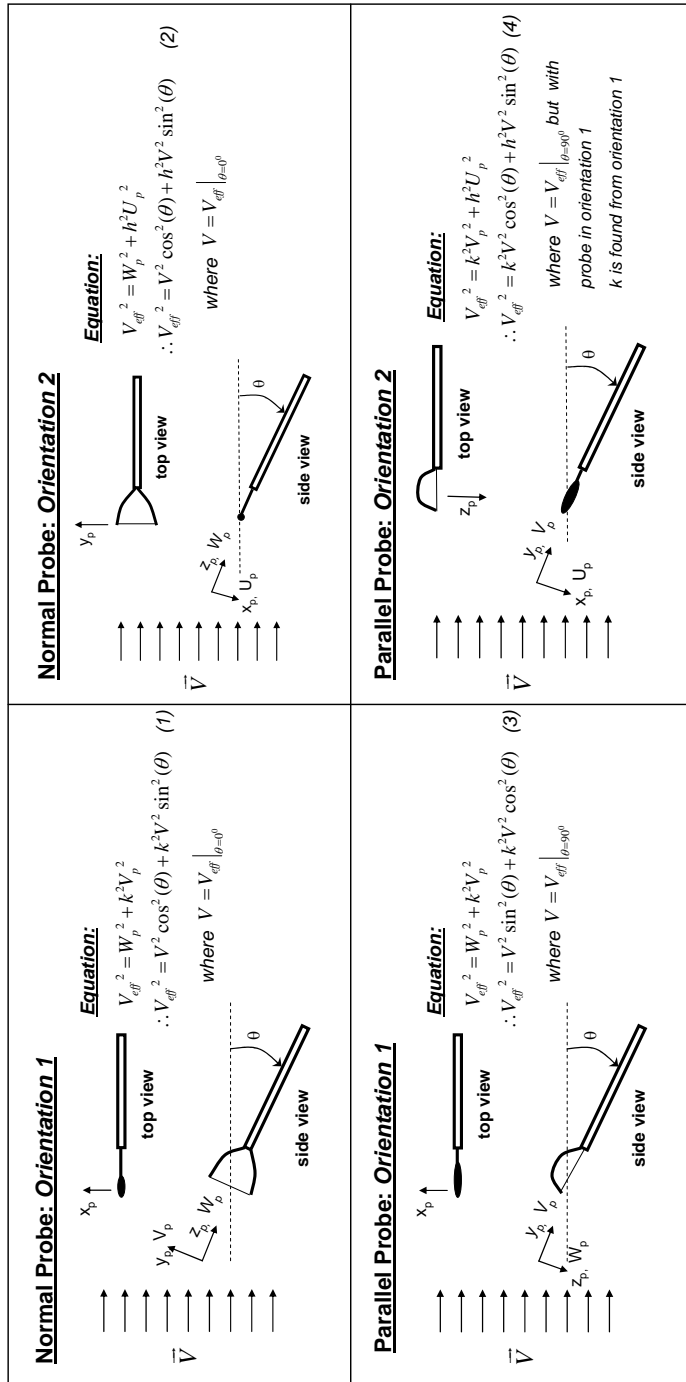


Fig. 4.11 – Different orientations and corresponding equations used for the angular calibration of the hot-film probes

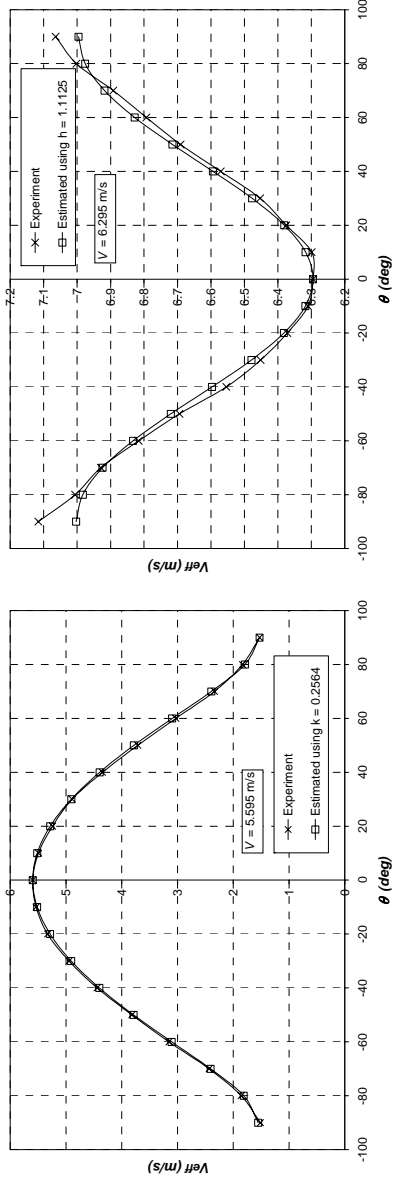


Fig. (a): Normal probe, Orientation 1

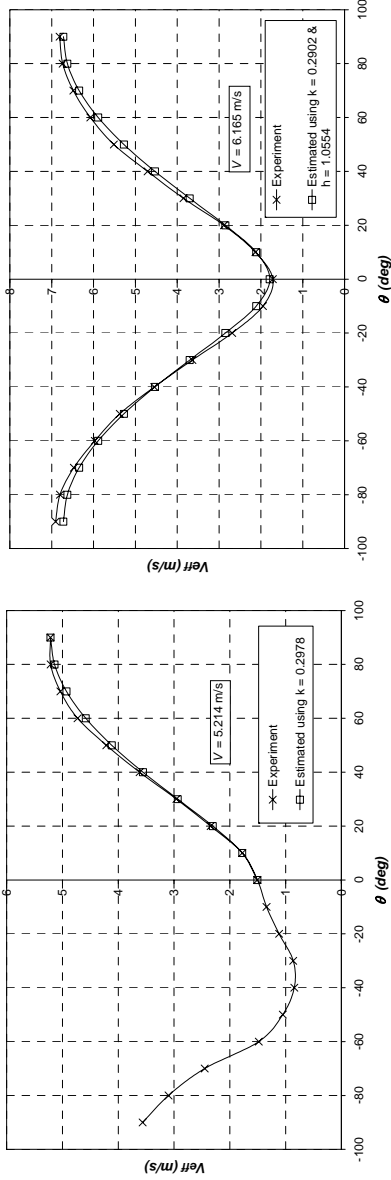


Fig. (c) Parallel probe, Orientation 1

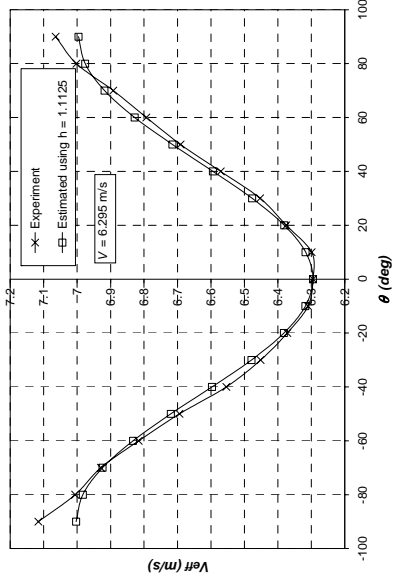


Fig. (b): Normal probe, Orientation 2

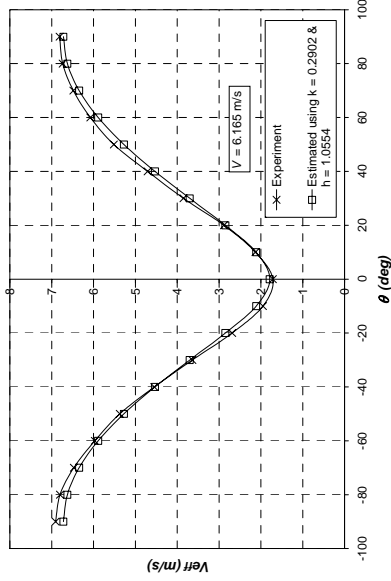


Fig. (d) Parallel probe, Orientation 2

Fig. 4.12 – Typical characteristic curves for the hot-film probes as derived from the angular calibration procedures

Derivation of 3D near wake velocities from hot-film measurements

This section describes the technique adopted to derive the 3D near wake velocity components from the hot-film effective velocities (V_{eff}) measured with different hot-film orientations at the different points in the rotor near wake as discussed in section 4.2.2.

The required 3D wake velocity components at a given point were the axial, horizontal and vertical components denoted by w_h , w_a and w_v , such that they were aligned with the global co-ordinate axes X_a - Y_a - Z_a , respectively. Two different methods were adopted to deduce these components: a traditional method and a new method being proposed by Wouter Haans [37].

(a) *Traditional Method:* With this method, three hot-film orientations were required. Two were taken with the normal probe, while the third was taken with the parallel probe. In one of the normal probe orientations, the hot-film was aligned with the X_a axis of the rotor while in the second normal probe orientation, the hot-film was aligned with the Z_a . In the parallel probe orientation, the hot-film was oriented with the Y_a axis. Eq. 4.2 was applied for each orientation to yield the following three equations:

$$\begin{aligned} V_{eff, X_a}^2 &= k^2 w_h^2 + h^2 w_v^2 + w_a^2 \\ V_{eff, Y_a}^2 &= h^2 w_h^2 + w_v^2 + k^2 w_a^2 \\ V_{eff, Z_a}^2 &= h^2 w_h^2 + k^2 w_v^2 + w_a^2 \end{aligned} \quad (4.3)$$

In the equations above, V_{eff, X_a} , V_{eff, Y_a} , V_{eff, Z_a} are the averaged hot-film effective velocities measured during the experimental procedure. It should be emphasised that Eq. 4.2 only holds for an instantaneous point in time. Since it was impossible to measure the three different effective velocities simultaneously, the above system of equations could strictly speaking be only applied on the assumption that the wake velocities for a given point and rotor azimuth angle are constant and do not vary with time. This assumption is only valid when turbulence levels in the wake was small. Since the rotor was operating such that the flow was attached, turbulence levels were small, even behind the rotorplane. The required 3D velocity components were solved by reorganizing the above equations in matrix form and applying matrix inversion as follows:

$$\begin{bmatrix} w_h^2 \\ w_v^2 \\ w_a^2 \end{bmatrix} = \begin{bmatrix} k^2 & h^2 & 1 \\ h^2 & 1 & k^2 \\ h^2 & k^2 & 1 \end{bmatrix}^{-1} \begin{bmatrix} V_{eff, X_a}^2 \\ V_{eff, Y_a}^2 \\ V_{eff, Z_a}^2 \end{bmatrix} \quad (4.4)$$

A main disadvantage of this method regards the fact that the directions of the flow velocities remain unknown. Component w_a was found to be significantly larger than the other components, and it could be easily assumed that it acts in the downstream direction.

(b) *New Method*: Wouter Haans developed a more advanced approach that is capable of finding the directions of the w_h and w_v . The method makes use of six different probe orientations of the asymmetric response of the parallel probe to the flow angle due to the obstruction of the flow resulting from the probe's prongs (see Fig. 4.12(c)). In this method, the traditional approach was still used to find the axial flow component w_a . Details of the method are given in [37].

The final step in data-reduction process was to obtain the flow components in local rotor coordinates (x - y - z reference frame) by using the following matrix transformation:

$$\begin{bmatrix} w_r \\ w_t \\ w_a \end{bmatrix} = \begin{bmatrix} \sin(\phi) & \cos(\phi) & 0 \\ \cos(\phi) & -\sin(\phi) & 0 \\ 0 & 0 & 1 \end{bmatrix} \begin{bmatrix} w_h \\ w_v \\ w_a \end{bmatrix} \quad (4.5)$$

The local inflow measured velocity at any point in a particular measuring plane depends on the geometrical location of the point and the rotor azimuth angle. The axial, tangential and radial velocities can thus be written as $w_a(\phi, r/R, \phi_p)$, $w_t(\phi, r/R, \phi_p)$ and $w_r(\phi, r/R, \phi_p)$.

For the sake of the data-processing and calculation using the developed software codes, a three-letter index notation was used to denote a velocity component at each point. For instance the axial flow velocity was represented by $(w_a)_{\tau,i,j}$ where τ, i and j are indices denoting the rotor azimuth angle (ϕ), the radial location (r/R) and the azimuth angle of the measuring location (ϕ_p).

Inflow Results

Derived Wake Velocities

Since the measurements were carried out at different yaw angles and different measurement planes, the resulting database was quite an extensive one containing at least 24MB of data. Figs. 4.13, 4.14 and 4.15 plot typical measured signals for the flow velocity components (w_a , w_t and w_r) at $\psi=0^\circ$ obtained at various points (r/R , ϕ) as a function of rotor azimuth angle (ϕ).

To be able to interpret the velocity signals, it is helpful to understand the distinct axial and tangential velocity patterns measured when each blade passes by the hot-film probe. Such patterns are illustrated in Fig. 4.16 and are mainly induced by the bound circulation of the blades. The axial velocity pattern (seen in Fig. 4.16(a)) is characterized by an increase in the flow velocity followed by a rapid decrease. The peak to peak velocity difference ($w_{a,max} - w_{a,min}$) will decrease as the distance of the probe from the rotorplane (i.e. Y_a) is increased. This may be observed in Figs. 4.13(a), 4.14(a) and 4.15(a). Since the rotor has two blades, then two blade passage signals can be recognized over one whole rotor revolution. The tangential velocity pattern is characterized by 'U-shaped' pattern (seen in Fig. 4.16(b)). The tangential velocity is normally negative i.e. opposite to the direction of the rotating blade. This agrees well with the law of conservation of momentum. The negative peak tangential velocity decreases as the probe is moved away from the rotorplane, as noted in Figs. 4.13 (b), 4.14(b) and 4.15(b).

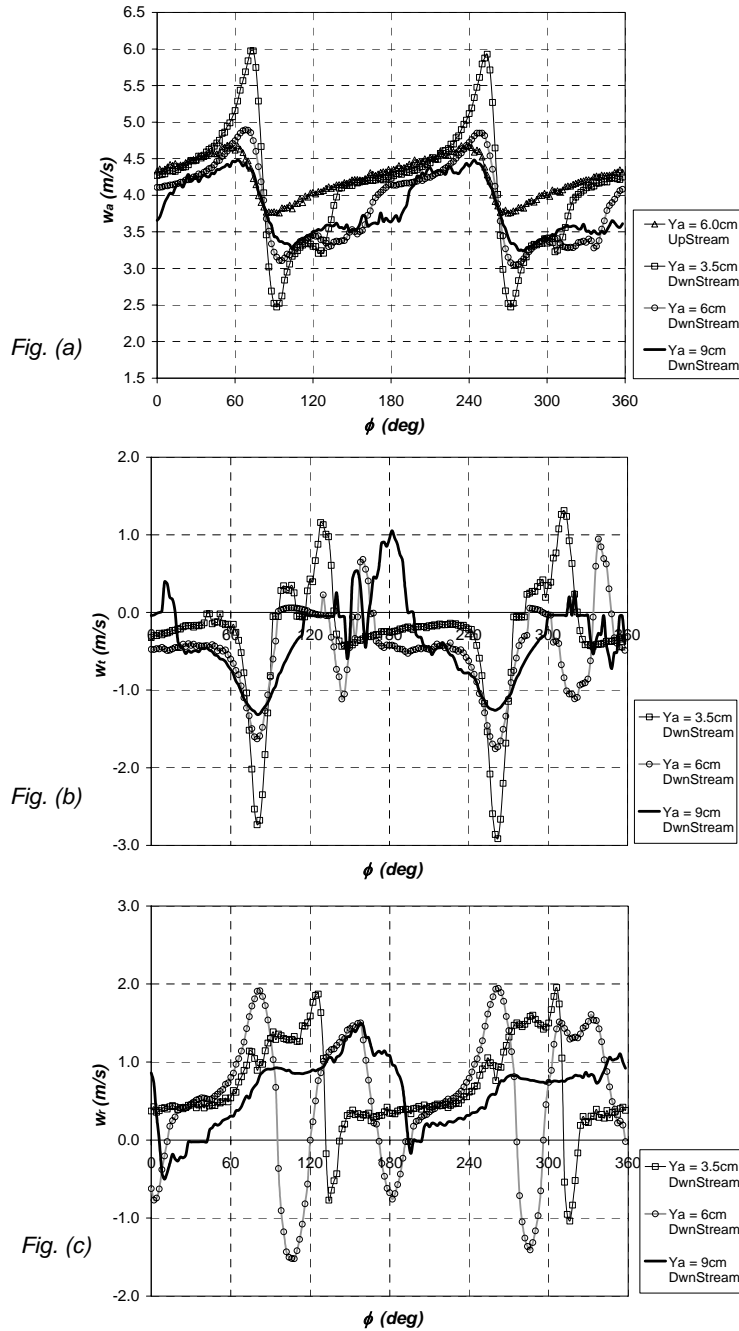


Figure 4.13 - Axial, tangential and radial velocities derived from the hot-film measurements for $\Psi=0^\circ$. The probe is located at $(r/R, \phi_p) = (0.4, 75^\circ)$. Blade passage is observed at $\phi = 75^\circ$ and 255° .

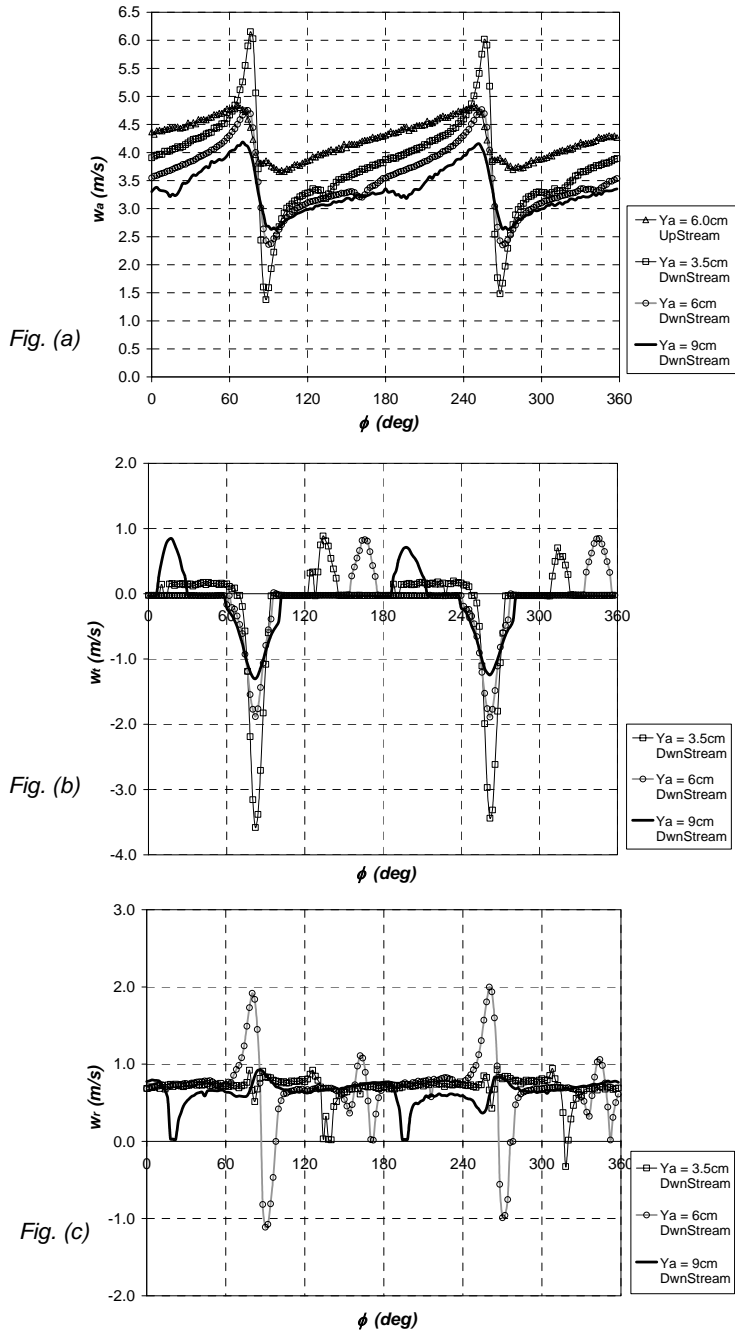


Figure 4.14 - Axial, tangential and radial velocities derived from the hot-film measurements for $\psi=0^\circ$. The probe is located at $(r/R, \phi_p) = (0.7, 75^\circ)$. Blade passage is observed at $\phi = 75^\circ$ and 255° .

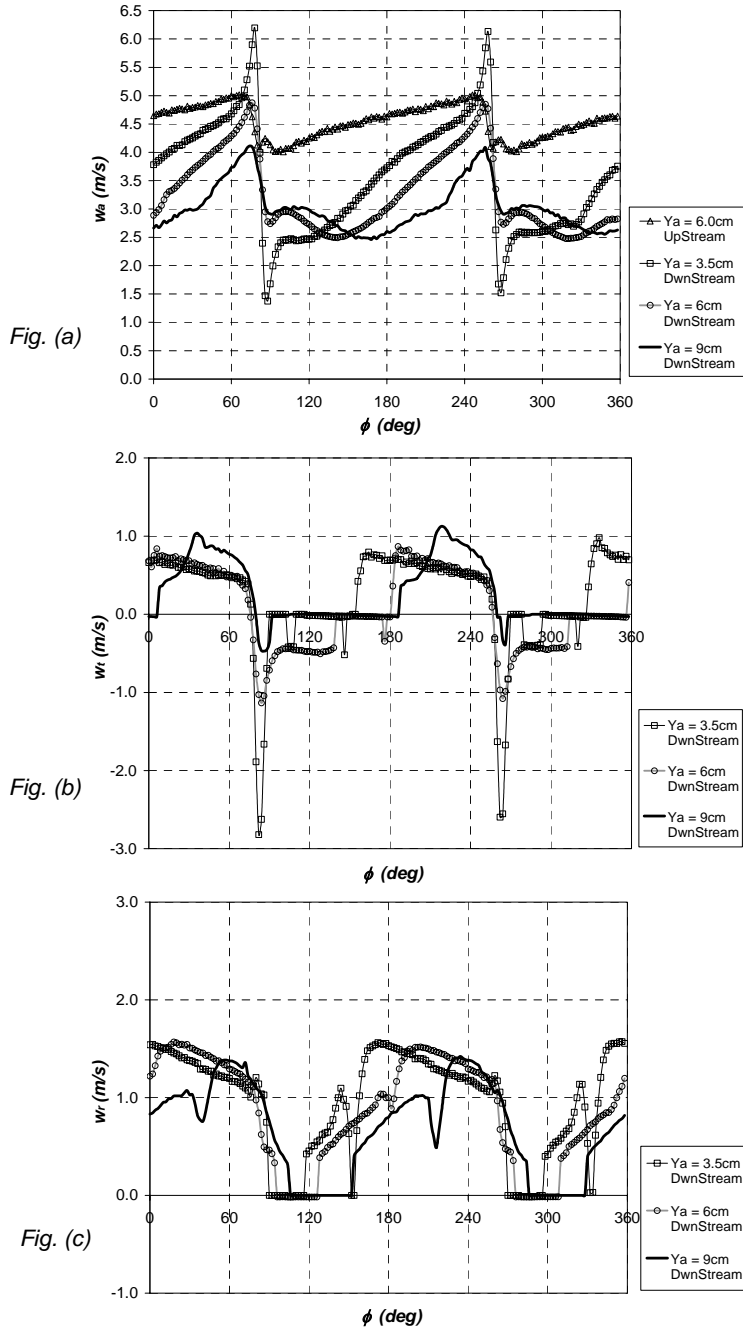


Figure 4.15 - Axial, tangential and radial velocities derived from the hot-film measurements for $\Psi=0^\circ$. The probe is located at $(r/R, \phi_p) = (0.9, 75^\circ)$. Blade passage is observed at $\phi = 75^\circ$ and 255° .

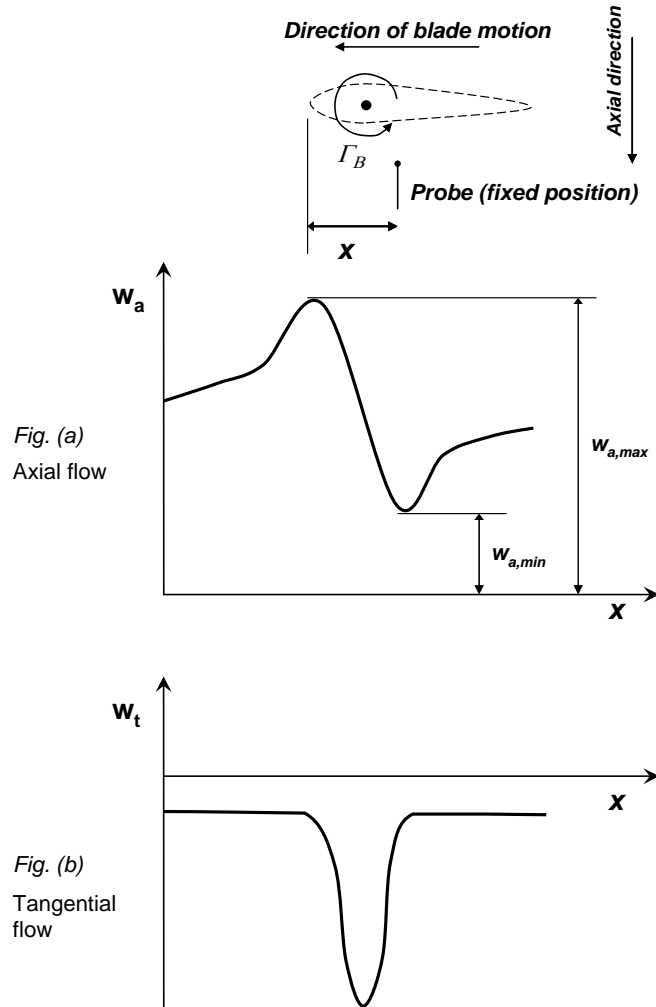


Figure 4.16 – Distinct axial and tangential flow velocity patterns induced by blade passage.

In the w_t -signals, some turbulence may also be observed at ϕ positions other than those at the blade passage positions. This turbulence may also be observed in the w_a signals and results from the effect of the wake vortex sheet passing by the hot-film probe.

Fig. 4.17 shows typical axial velocity signals at different yaw angles for a given probe location. It is noted that the flow velocity at this location decreases as the yaw angle is increased. For a more detailed physical explanation of these inflow measurements refer to the work of Haans [37], Vermeer [98, 99] and Mast [55].

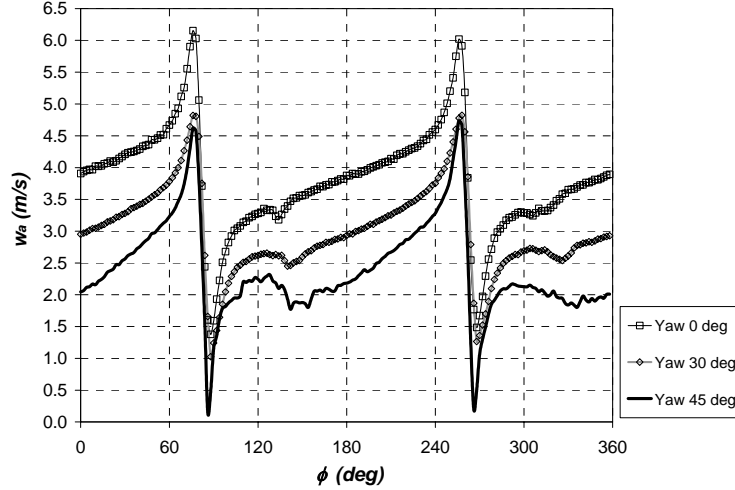


Figure 4.17 - Axial velocity variation derived from the hot-film measurements for $\Psi=0^\circ, 30^\circ$ and 45° at 3.5cm ($Y_a/R=0.058$) downstream from the rotorplane. The probe is located at $(r/R, \phi_p) = (0.7, 75^\circ)$. Blade passage is observed at $\phi = 75^\circ$ and 255° .

Determination of axial flow velocity at the blade passage location ($w_{a,c}$)

From the experimental axial flow velocity signals as shown in Figs. 4.13(a), 4.14(a) and 4.15(a), it was possible to estimate the axial flow velocities at the blade passage locations for each of the probe measuring locations (i.e. at $r = 40, 50, 60, 70, 80, 90\%R$ at azimuthal increments of 15°). These were obtained for each of the four measuring planes (i.e. at $Y_a = 6\text{cm}$ upstream and 3.5cm, 6cm and 9cm downstream) and were required to be able to estimate the flow velocities at the blades from which the angle of attack could then be found. The axial flow velocity at the blade passage location (denoted by $w_{a,c}$) was estimated by taking it to be equal to the average of the maximum and minimum velocities. Referring to Fig. 4.16(a), this is equal to

$$w_{a,c} = \frac{w_{a,\max} + w_{a,\min}}{2} \quad (4.6)$$

In the index representation, the value of $w_{a,c}$ at a given location $(r/R, \phi_p)$ at a particular measurement plane is denoted as $(w_{a,c})_{i,j}$. Recall that index i denotes the radial location (40, 50, 60, 70, 80, 90 or 100%R) of the hot-film measurement point. Index j denotes the azimuthal location of this point ($0^\circ, 15^\circ, 30^\circ, \dots, 345^\circ$).

The results obtained for $w_{a,c}$ at $\Psi=0^\circ$ are given in Fig. 4.18(a). The mean values of $w_{a,c}$ obtained from the different probe positions (at azimuthal increments of 15°) at each radius are shown in this plot. The corresponding standard deviations are also presented. For axial

conditions ($\psi=0^\circ$), $w_{a,c}$ should ideally be constant with ϕ . But this was not the case due to various sources of error which will be discussed later. For instance Fig. 4.18(b) plots the variation of $w_{a,c}$ with the blade azimuth angle over one whole rotor revolution for $\psi=0^\circ$. It is noted that the variation is not constant with ϕ . A major contribution for this non-ideal trend is the non-uniformity in the tunnel exit jet, as depicted earlier in Fig. 4.5. There is a velocity dip for positions near $\phi=0^\circ$ which in fact results in a discontinuous behaviour in the velocity variation between 330° - 360° and 0° - 30° . This discontinuity may be easily observed in Fig. 4.18(b).

Linear interpolation was employed to estimate the spanwise variations of $w_{a,c}$ at the rotorplane ($Y_a = 0\text{cm}$) using the mean values for the 6cm upstream and 3.5cm downstream planes:

$$\left(w_{a,c}\right)_{Y_a=0\text{cm}} = \left(w_{a,c}\right)_{Y_a=-6\text{cm}} + \frac{\left(w_{a,c}\right)_{Y_a=3.5\text{cm}} - \left(w_{a,c}\right)_{Y_a=-6\text{cm}}}{3.5 - (-6)} \cdot (0 - (-6)) \quad (4.7)$$

These interpolated values are included in Fig. 4.18(a). These values are an estimate for the axial flow velocities at the blade lifting lines and they were used to estimate the angle of attack from the measurements, as will be described later on in section 4.3.

Figs. 4.19 and 4.20 present the values of $w_{a,c}$ obtained in yawed conditions ($\psi=30^\circ$ and 45°). Since in yawed conditions, the flow velocities at the blades are unsteady, the results are plotted as a function of the blade azimuth angle (ϕ). For yawed conditions only, the variations of $w_{a,c}$ versus ϕ were also smoothed to damp out the 'jerky' variations introduced due to uncertainties in the measurements. The smoothed variations are included in Figs. 4.19 and 4.20. In the data smoothing, a technique that implements a Gaussian kernel was used to compute local weighted averages of the input vector $w_{a,c}$. In the index representation using (i,j) , the smoothed value of $w_{a,c}$ at a given point (i,j) was found from

$$\left(w_{a,c}\right)_{i,j}^{(smoothed)} = \frac{\sum_{k=1}^{j_{tot}} K\left(\frac{(\phi_p)_j - (\phi_p)_k}{\omega}\right) \left(w_{a,c}\right)_{i,k}}{\sum_{j=1}^{j_{tot}} K\left(\frac{(\phi_p)_j - (\phi_p)_k}{\omega}\right)} \quad (4.8)$$

$$K(x) = \frac{1}{\sqrt{2\pi} \cdot 0.37} \cdot e^{-\left(\frac{x^2}{2 \cdot (0.37)^2}\right)}$$

ω is the bandwidth that should be prescribed. In this analysis, ω was set equal to 0.8. This was found to be reasonable. This smoothing method was useful since the data lies along a band of constant width (equal to 15°).

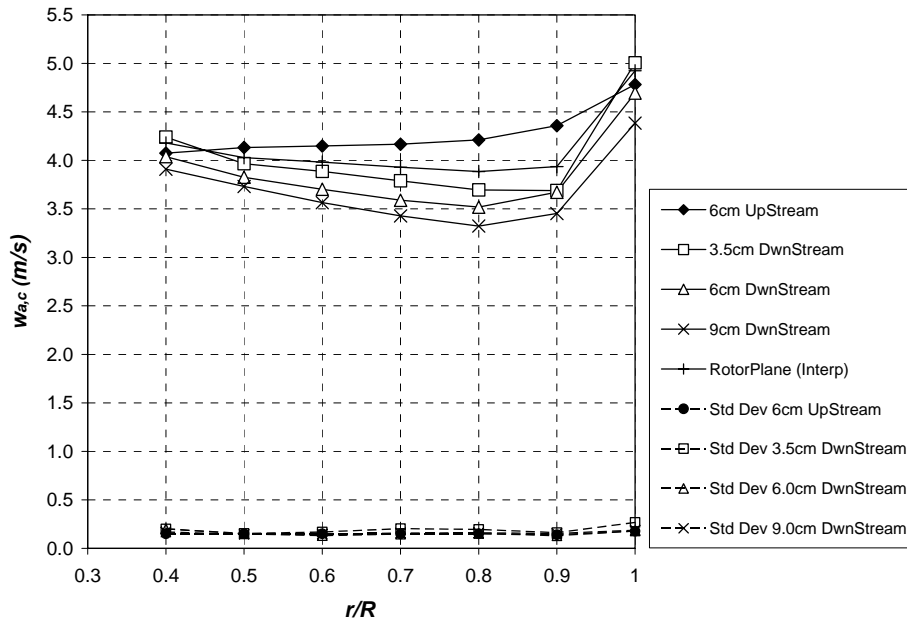


Figure 4.18(a) – Axial flow velocity distribution at blades derived from the hot-film measurements using Eq. 4.6 for $\Psi=0^\circ$.

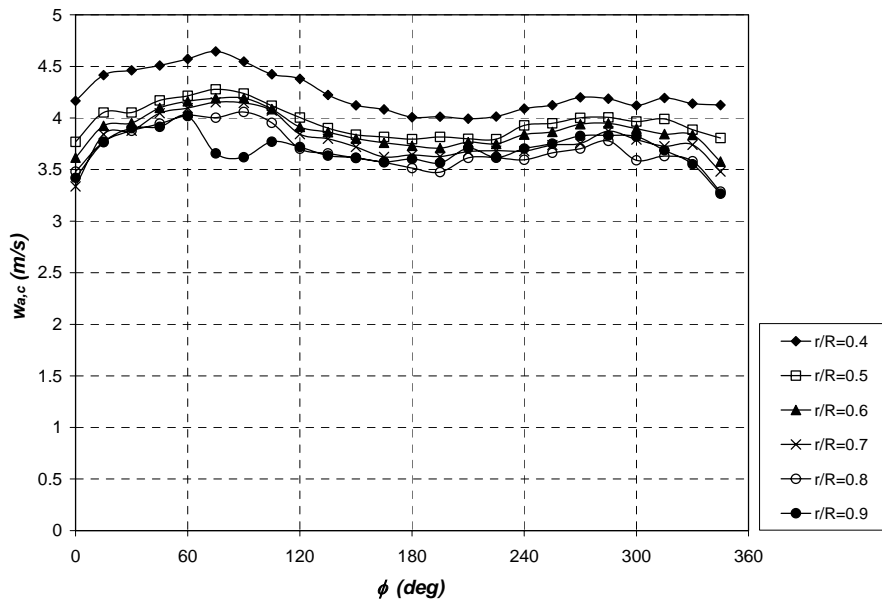


Figure 4.18(b) – Variation of the axial flow velocity at the blades with azimuth angle for $\Psi=0^\circ$ at 3.5cm downstream of the rotorplane.

Using these smoothed distributions, linear interpolation was used to estimate the variations of $w_{a,c}$ with ϕ at the rotorplane for different radial locations using Eq. 4.7. The interpolated values were an estimate for the unsteady axial flow velocities at the lifting line of the blades in yawed conditions. The interpolated values are included in Figs. 4.19 and 4.20. In these figures, the discontinuous behavior in the velocity variation between 330° - 360° and 0° - 30° is observed, as was already noted at $\psi=0^{\circ}$ (see Fig. 4.18(b)). This discontinuity is mainly due to the non-uniformity in the tunnel exit jet, (see Fig. 4.5). Yet it is not excluded that the wake circulation from the skewed wake (tip and in particular root circulation) resulting from rotor yaw as well as the influences of the centrebody structure of the test-rig could have yielded abrupt changes of $w_{a,c}$ with ϕ . These abrupt changes could also contribute to the discontinuous behavior in the velocity variation between 330° - 360° and 0° - 30° .

Sources of error

The main sources of error in the inflow measurements are the following:

- (1) The non-uniformity in tunnel exit jet: as already explained earlier in section 4.2.1, Fig. 4.5, it was found that the tunnel exit velocity varies from 5.2 to 5.8m/s when the pitot readings are set to 5.5m/s. Thus it is reasonable to assume that the uncertainty interval introduced by the non-uniformity in the tunnel exit jet is 5.5 ± 0.3 m/s.
- (2) The hot-film probes in measuring the effective velocities (V_{eff}) mainly due to errors in the speed calibration constants.
- (3) Errors in the data reduction technique described earlier (see page 54) mainly due to errors in the angular calibration constants. Also, the data reduction technique assumes that for a given rotor azimuth position, the velocity at any point does not change with time and thus the different hot-film measurements using different probe orientations need not be carried out simultaneously. The presence of some fluctuations (such as due to turbulence) invalidates this assumption.
- (4) The traversing system experienced some inaccuracies in positioning the hot-film probe at the required locations. The positioning accuracy was estimated to be around ± 1 cm.

The rotor angular speed and the pitot readings at the tunnel exit could be adjusted very accurately at the required setting (720 rpm and 5.5m/s respectively). Therefore the errors in the experimental data due to possible fluctuations in these parameters were negligible. Haans [37] has carried out an in-depth uncertainty analysis for these measurements at $\psi=0^{\circ}$ estimating the uncertainty to due to individual sources of error. In this analysis, it was

concluded that the overall uncertainty in w_a at the vicinity of blade passage is on the order of 10%.

Alternatively, it was possible to use a simple method to derive an estimate for this uncertainty by considering the results of $w_{a,c}$ obtained at $\Psi=0^\circ$. As already described in the previous section, in the ideal situation, $w_{a,c}$ should be independent of ϕ at $\Psi=0^\circ$. For each radial location and measurement plane, $w_{a,c}$ was obtained at azimuth increments of 15° yielding a sample size of 24 readings. The mean and standard deviations were computed and the results were plotted earlier in Fig. 4.18(a). Assuming the velocity distribution of each sample follows a normal distribution, the uncertainty interval at 95.45% confidence could be taken as $\pm 2\sigma$ where σ is the standard deviation. This uncertainty interval was computed over radial locations 40, 50, 60, 70, 80 and 90% R and the four measurement planes and it was found to be in the range of 6 – 10% of the mean values of $w_{a,c}$. This is of the same order as that obtained by Haans [37].

The above simple method for estimating the uncertainty in the hot-film measurements could not be applied for yawed conditions for the simple reason that $w_{a,c}$ is no longer independent on ϕ . However, it was justified to assume the same uncertainty level of 6-10% for $\Psi=30^\circ$ and 45° as well. This is because of the fact that the same apparatus and rotor speed and blade pitch settings were used and also because the hot-film speed and angular calibration constants were very close to those for axial conditions. An important point to note regards the fact that the uncertainty in U due to the non-uniformity in the tunnel exit jet ($\pm 0.3\text{m/s}$) is considerably high (on the order of $\pm 5\%$ of 5.5m/s) and should contribute a considerable proportion of the 6 – 10% uncertainty in $w_{a,c}$. Yet, when the rotor is yawed, the magnitude of the axial flow velocity component at the measurements planes is less dependent on the windspeed U than at no rotor yaw. It also follows that in yaw, the uncertainty contribution due to the tunnel exit-jet non-uniformity should be less. It is possible that this could result in a lower overall uncertainty level in yaw than for no yaw. But a more elaborate uncertainty analysis would be necessary to confirm this.

Comparison with previous data by Vermeer

In year 1998, Vermeer [96] carried out similar inflow measurements using the same wind tunnel and rotor with hot-wire probes (*see also Schepers [69]*). The measurements were performed for the same wind speed and tip speed ratio and at $\Psi = 0^\circ, 30^\circ, 45^\circ$ and 60° . The measurements were carried out at radial locations 50, 60, 70 and 80% R and were limited to one measurement plane only (at 6cm downstream of the rotorplane). Using this data, the distributions of $w_{a,c}$ could be obtained for this plane using the procedure described on page 64. These distributions were compared with those from the new measurements. The comparison at $\Psi=30^\circ$ is shown in Fig. 4.21. The agreement is reasonably good and this adds to confidence in the measurements. The maximum discrepancy is seen at blade azimuth angles $0^\circ < \phi < 90^\circ$. The same level of agreement was also obtained for $\Psi = 0^\circ$ and 45° .

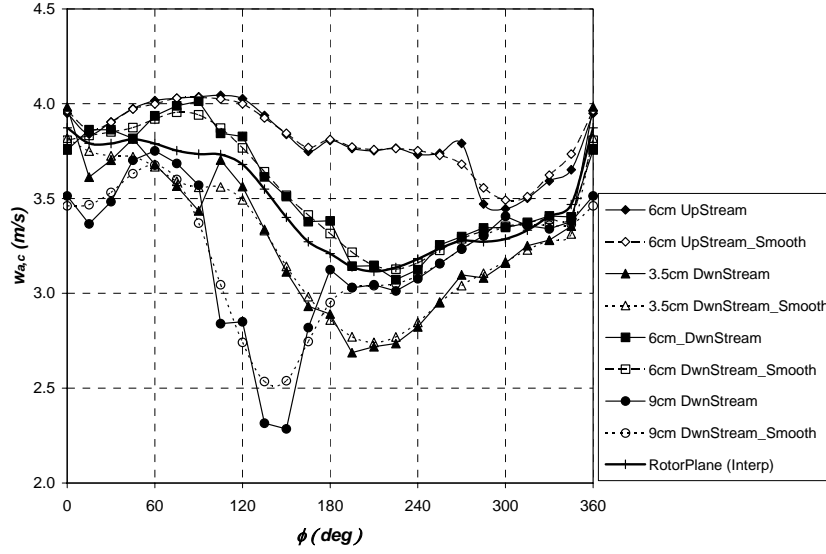


Fig. (a) $r/R = 0.4$

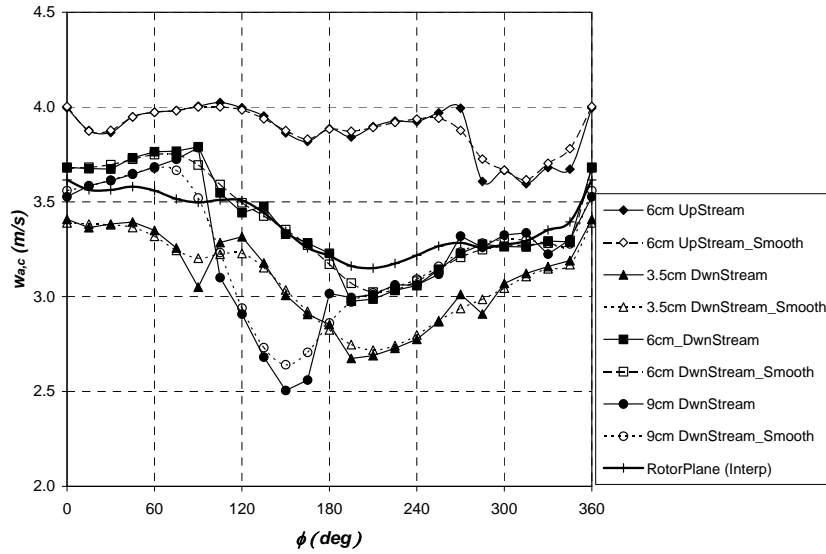


Fig. (b) $r/R = 0.5$

Fig. 4.19 – Variation of axial flow velocity at blades with blade azimuth angle at different radial locations at $\Psi=30^\circ$.

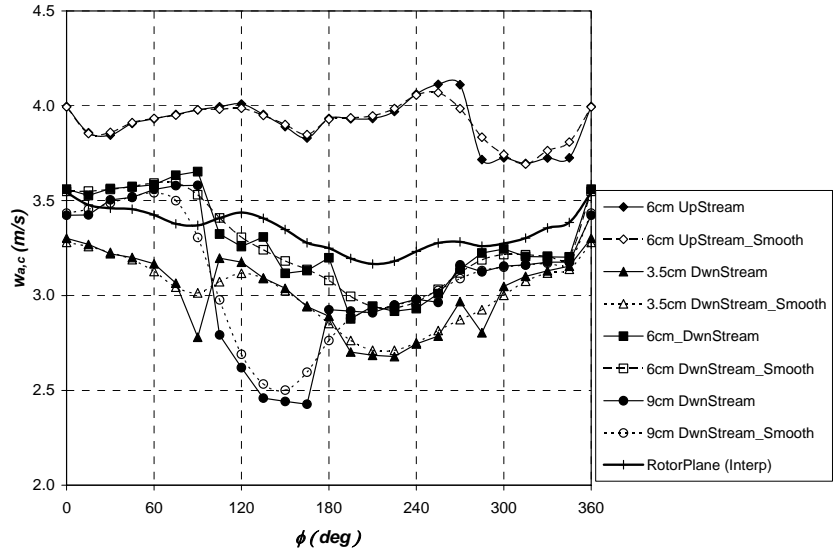


Fig. (c) $r/R = 0.6$

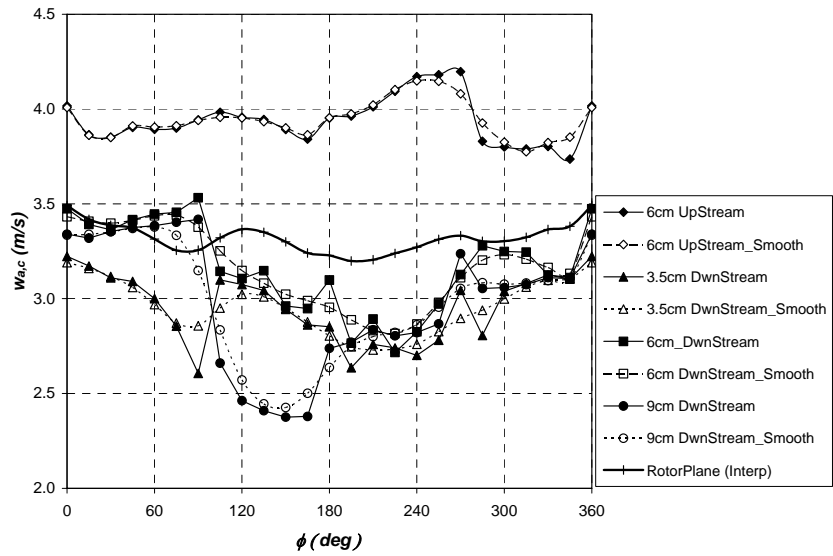


Fig. (d) $r/R = 0.7$

Fig. 4.19 – contd. from previous page ($\Psi=30^\circ$).

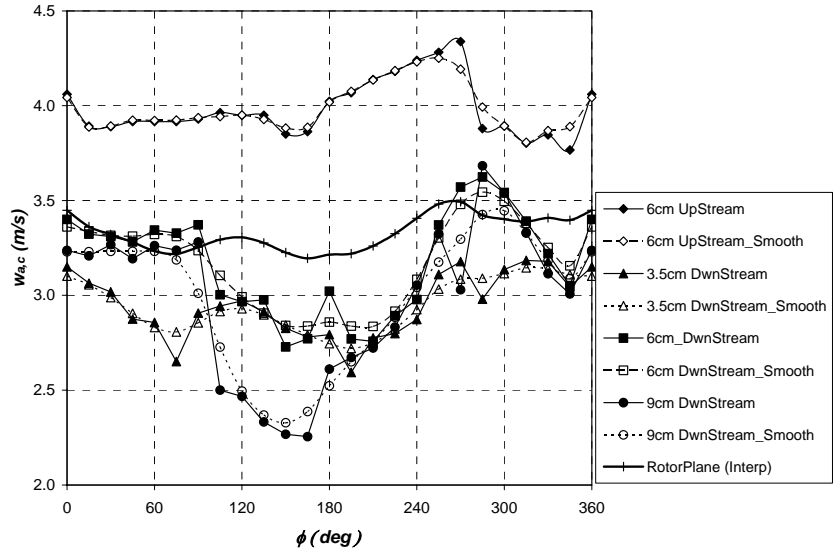


Fig. (e) $r/R = 0.8$

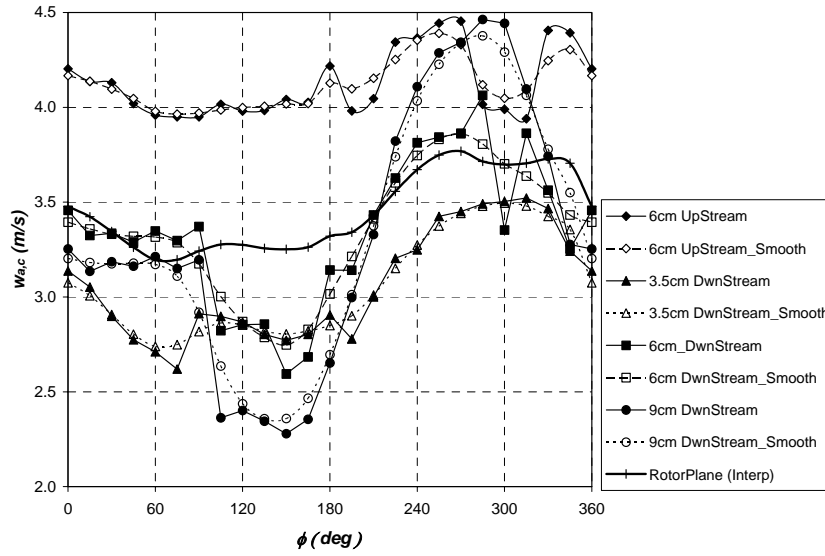


Fig. (f) $r/R = 0.9$

Fig. 4.19 – contd. from previous page ($\Psi=30^\circ$).

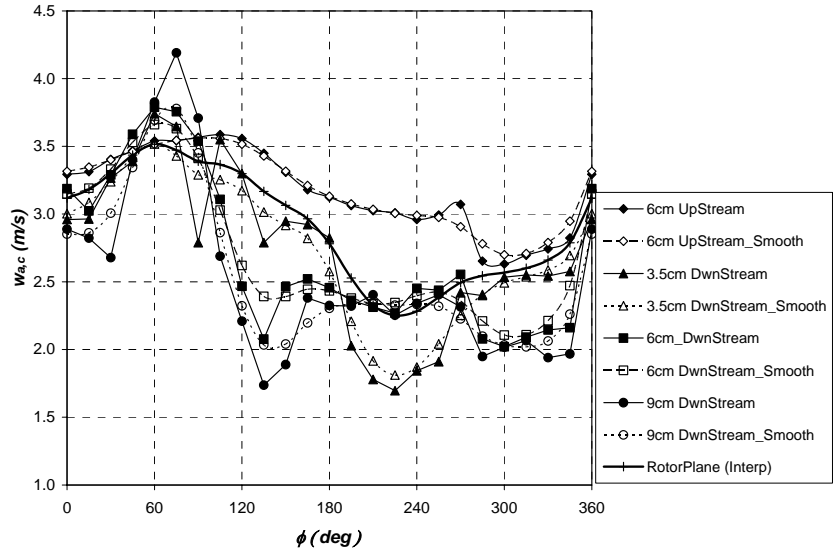


Fig. (a) $r/R = 0.4$

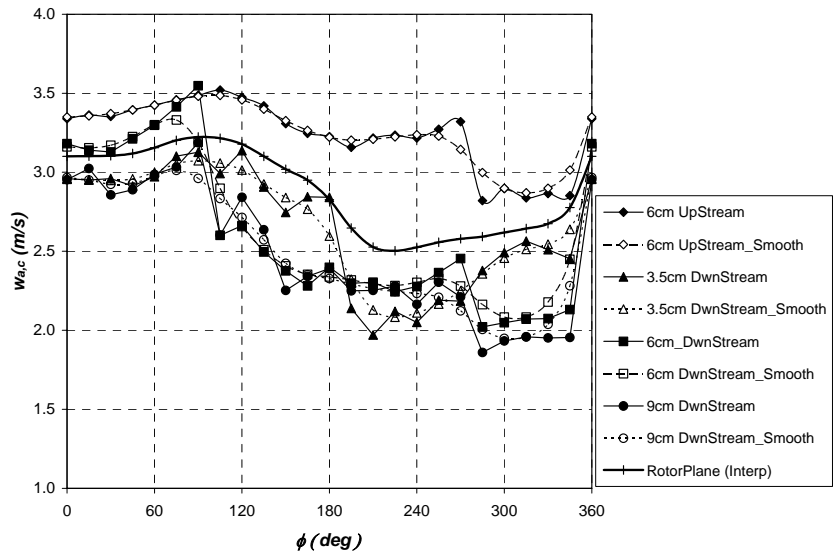


Fig. (b) $r/R = 0.5$

Fig. 4.20 – Variation of axial flow velocity at blades with blade azimuth angle at different radial locations at $\Psi=45^\circ$.

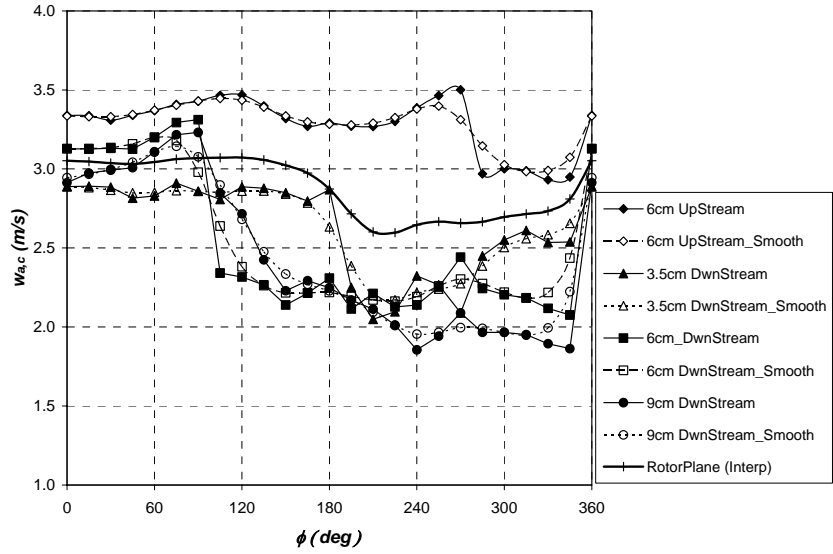


Fig. (c) $r/R = 0.6$

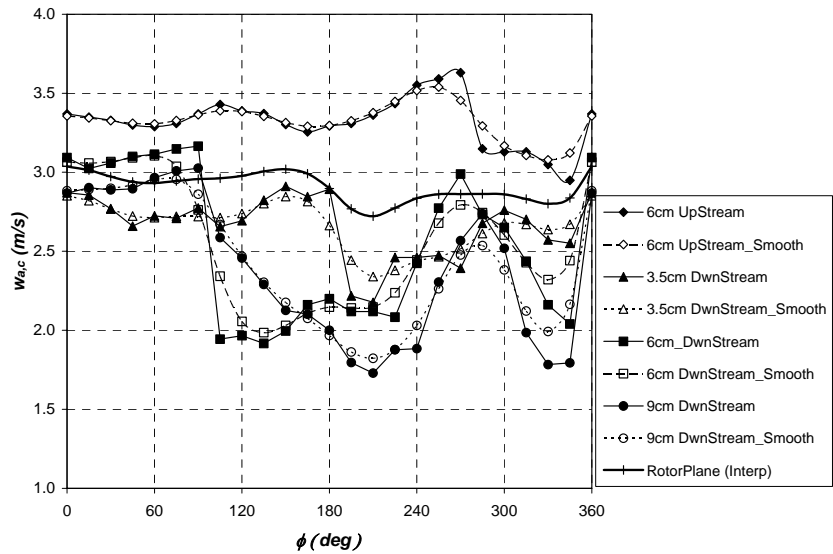


Fig. (d) $r/R = 0.7$

Fig. 4.20 – contd. from previous page ($\Psi=45^\circ$).

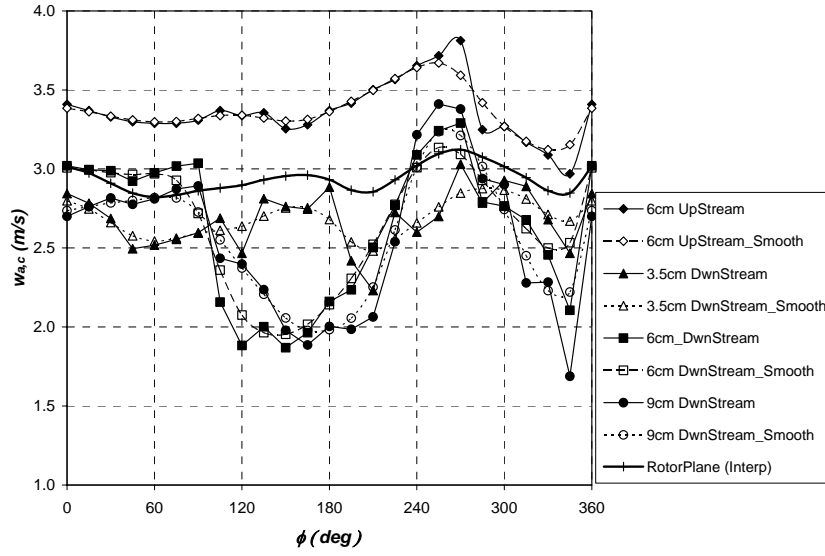


Fig. (e) $r/R = 0.8$

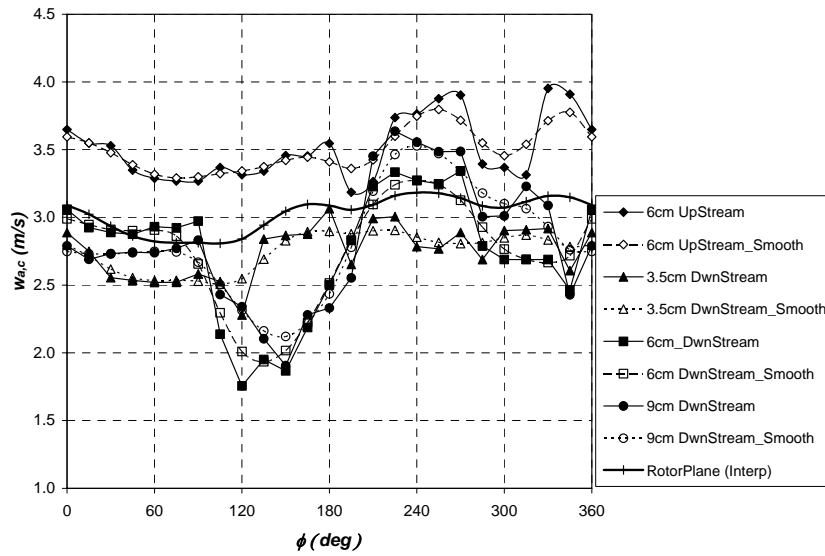


Fig. (f) $r/R = 0.9$

Fig. 4.20 – contd. from previous page ($\Psi=45^\circ$).

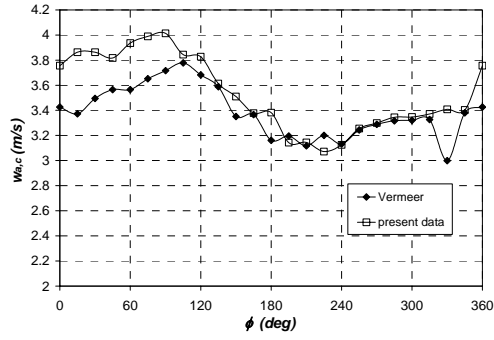


Fig. (a) $r/R = 0.5$

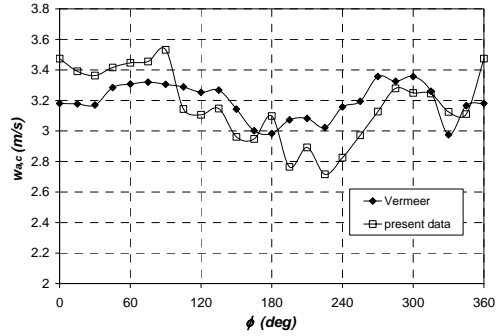


Fig. (c) $r/R = 0.7$

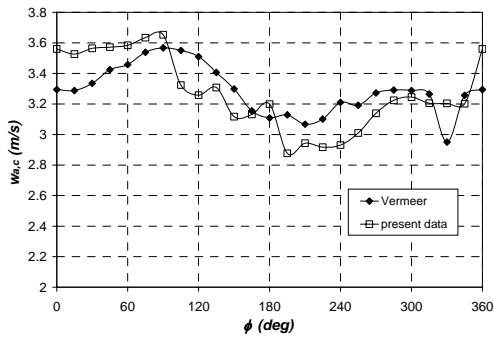


Fig. (b) $r/R = 0.6$

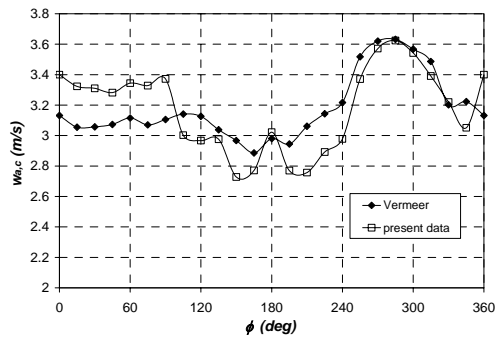


Fig. (d) $r/R = 0.8$

Figure 4.21 – Comparison of distributions of $w_{a,c}$ with ϕ with those from Vermeer [96] at $\Psi=30^\circ$ and 6cm downstream of the rotorplane ($Y_a/R=0.1$), see also Schepers [69].

4.2.3 Part II: Smoke Visualization Measurements

The following sections describe the wind tunnel smoke visualization experiments to track the tip vortex paths of the wake in axial and yawed conditions.

Experimental Set-up

Fig. 4.22 illustrates the schematic diagram of the apparatus used in the smoke visualization experiments. The rotor position with respect to the tunnel exit was kept the same as for the wake inflow measurements (i.e. with the rotor hub 1 m downstream from the tunnel exit). A smoke jet was created using a generator that uses oil to produce smoke. The jet was injected into the tunnel jet stream through a nozzle that was located well upstream from the rotor. The nozzle position with respect to the blade tip (at 90° or 270° azimuth positions) had to be adjusted at different yaw angles of the rotor for optimal visualization of the tip vortex. During the experiments the wind tunnel hall lights were switched off to create a complete dark environment. A stroboscope was synchronized with the rotor to flash when the azimuth angle of the first blade was 90° . In this way it was possible to capture the smoke flow patterns in a horizontal plane passing through the rotor hub and observe the position of the wake tip vortices relative to the blade tip. A digital camera, with its lens focused on this plane, was used to record multiple images of these smoke flow patterns. A reference grid consisting of equally-spaced wires was constructed. This was installed in a horizontal plane on top of the rotor such that the wires were parallel and perpendicular to the wind tunnel axis (refer to Fig. 4.22).

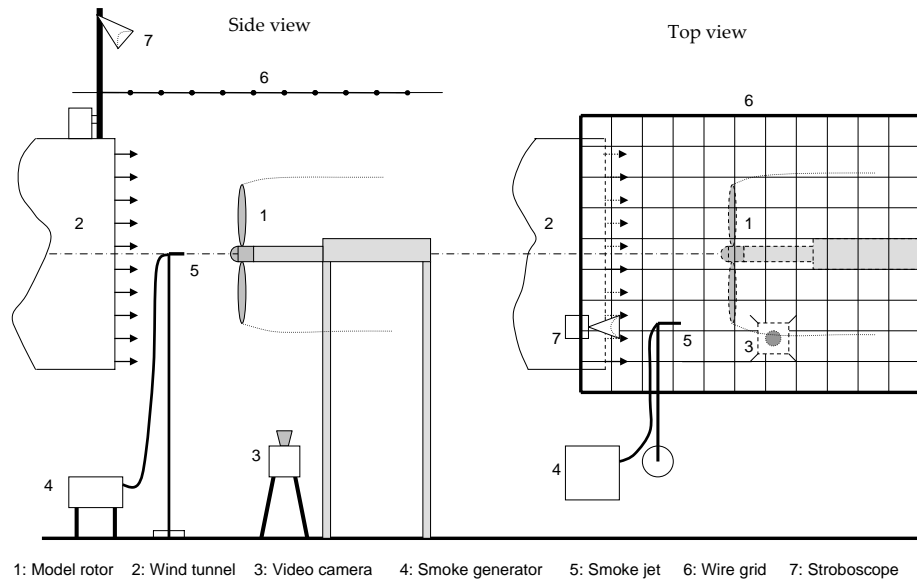


Figure 4.22 – Schematic diagram of experimental set-up used for smoke visualization.

Experimental procedure

Throughout the experiments, the wind tunnel exit jet velocity U_{jet} was maintained constant at 5.5m/s. The smoke visualizations were performed at different yaw angles, tip speed ratios and blade tip pitch angles: Five different rotor yaw angles: 0° , -15° , -30° , -45° and $+45^\circ$. For each of these yaw angles, the tip vortex core positions were recorded at nine combinations of the following tip speed ratios and tip pitch angles: $\lambda = 6, 8$ and 10 and $\theta_{tip} = 0^\circ, 2^\circ$ and 4° . These settings were selected so that the rotor would operate in both attached and stalled flow conditions over the blades. The smoke was injected on both sides, at azimuth angles equal to 90° and 270° (refer to Fig. 4.23). The vertical distances between the camera, rotor and grid were measured for each rotor setting. These distances were required for the parallax correction which will be described later on.

The measurement campaign employed ensured repeatability and randomization of data. For each rotor setting, two smoke injections were carried out on every side, each yielding at least 75 photos. The tip vortex measurements for $\lambda = 8, \theta_{tip} = 0^\circ$ and $\lambda = 6, \theta_{tip} = 2^\circ$ were repeated. Furthermore, two symmetry checks were accomplished:

- (1) at $\Psi = 0^\circ$, were the tip vortex core locations at 90° and 270° were compared;
- (2) at $\Psi = -45^\circ$ and $+45^\circ$, were the tip vortex core locations at 90° and 270° were compared for the corresponding upwind and downwind sides.

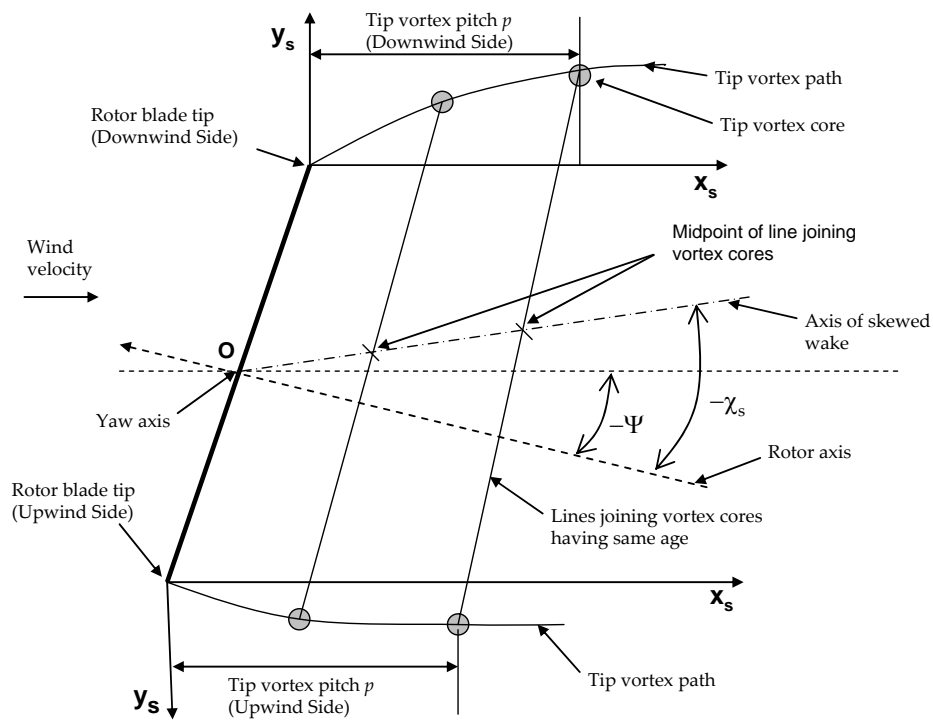


Figure 4.23 – Definitions used in the wake geometry.

In a separate measurement campaign, the axial thrust force on the rotor was measured for yaw angles going from change this $\Psi = -45^\circ$ and $+45^\circ$ with steps of 15° . For each yaw angle, the axial thrust was measured at each of the nine combinations of λ and θ_{ip} . These measurements are described in further detail in reference [36].

Data Processing

The Photos

Figure 4.24 displays typical photos derived from the visualisations. Due to the stroboscopic light source and the camera orientation, the photos appear to be instantaneous pictures of the unsteady helical tip vortex structure in a horizontal plane that cross-sections the rotor hub. The tip vortices are clearly identifiable by the swirling smoke pattern, with the centre of the vortex indicated by the centre of the smoke-free area. The blade tip can be identified on the photos, together with the grid in the background.

The presence of wake expansion is evident from the photos. For yawed conditions, wake expansion is larger on the downwind side than on the upwind side and this leads to wake skew. Using photo editing software, the distances of each vortex core relative to the blade tips were measured against the length of grid's squares. Knowing the size of these squares, 0.1 m x 0.1 m, the positions of the tip vortex cores could be established after application of camera parallax correction to the photo measurements. Figure 4.25 is a schematic used for parallax correction. Here, h and H are the perpendicular distances between grid and smoke visualisation plane and between grid and camera, respectively. L is the measurement taken from the photo while d is the corrected (actual) distance. Applying similar triangles, distance d is given by

$$d = \frac{H - h}{H} \cdot L \quad (4.9)$$

Other factors were thought to influence parallax effects, such as lens and camera sensor misalignment. However these were considered to be negligible since the values of h and H were large (about 1.28 m and 2.80 m, respectively) and therefore their effect was ignored.

Using the above method, the location of each vortex centre relative to the blade tips could be found. The position of each vortex core was expressed using local coordinates (x_s, y_s) . These coordinates are attached to the blade tip and lie in the horizontal plane passing through the rotor hub centre (see Fig. 4.23). The x_s -axis lies along the undisturbed flow direction, while the y_s -axis is perpendicular to the undisturbed flow.

Wake expansion, tip vortex pitch and wake skew angle were derived from the known tip vortex positions. Fig. 4.23 illustrates how these parameters have been found. Wake expansion could be determined from the path followed by the tip vortices.

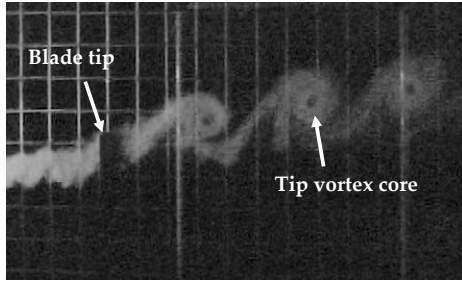


Fig.(a): $\Psi = 0^\circ$, $\lambda = 8$ $\theta_{tip} = 2^\circ$

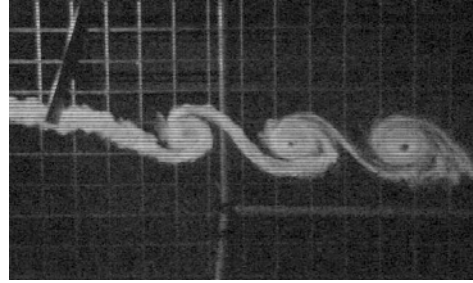


Fig.(b): $\Psi = -15^\circ$, $\lambda = 8$ $\theta_{tip} = 2^\circ$; Upwind side

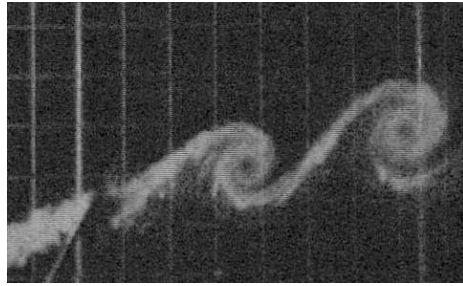


Fig.(c): $\Psi = -30^\circ$, $\lambda = 8$ $\theta_{tip} = 2^\circ$; Downwind side

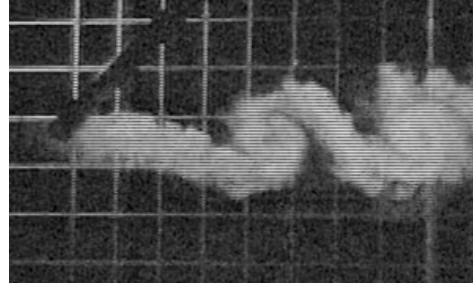


Fig.(d): $\Psi = -45^\circ$, $\lambda = 8$ $\theta_{tip} = 2^\circ$; Upwind side

Figure 4.24 – Typical smoke visualisation photos showing tip vortex cores and the blade. Note that the flow is from left to right.

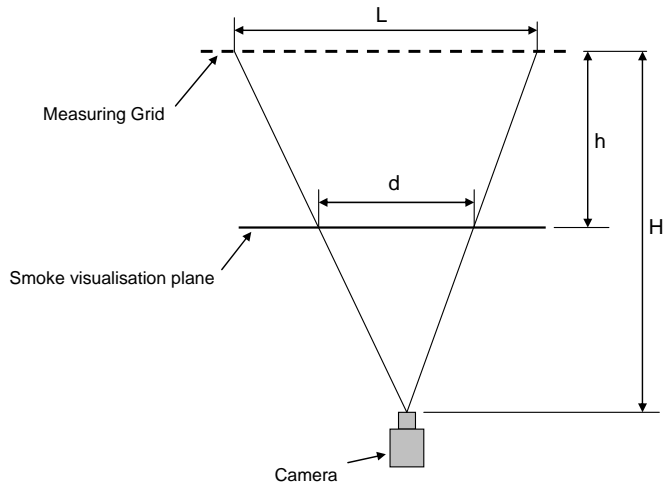


Figure 4.25 – Schematic diagram used for parallax correction.

The tip vortex pitch p was determined by measuring the distance along the x_s -axis between two successive vortex cores originating from the same blade. An upwind and downwind p has been defined, for the tip vortices shed on the upwind and downwind side of the rotor plane, respectively. Since in this study, the flow visualisation was limited to a small distance downstream of the rotor plane (less than $2R$), only the first pitch is quoted.

The wake skew angle χ_s was found as follows: a straight line was drawn joining the vortex cores on the upwind side to the ones having the same age on the downwind side. This could be done, since a two-bladed model has been used. The midpoint of each line was then found. The axis of the skewed wake was determined by constructing a best-fit straight line originating at the yaw axis and passing through these midpoints (see Fig. 4.23). The wake skew angle could then be taken as the angle between the rotor axis and the axis of the skewed wake.

An analysis into the uncertainties of the estimated vortex centre locations has been performed. As stated, the contribution of parallax bias uncertainties to the total uncertainty has been ignored. It is estimated namely, that its effect on the error in the vortex centre location is substantially smaller than 1.5 cm. Averaging of the measured vortex centre locations is the main contributor to the random uncertainty. Enclosed within the contribution from averaging is the effect of the vertical drift of the smoke, out of the measurement plane. For each visualisation measurement, six photos have been used for averaging. The maximum interval of random uncertainty in the average tip vortex location has been estimated at ± 1.5 cm and ± 0.5 cm in the x_s - and y_s -direction, respectively. It is estimated that the random uncertainty in average tip vortex location translates in an uncertainty interval of $\pm 1.5^\circ$ in χ_s .

Axial Force

A measurement campaign solely dedicated to the measurement of axial thrust (T) on the rotor at all different settings was carried out. The thrust measurements had to be corrected due to considerable structural interference. Details of this correction are explained in reference [36]. The corrected values for the thrust were azimuthally averaged and non-dimensionalized using the standard equation:

$$C_T = \frac{T}{\frac{1}{2}\rho AU^2} \quad (4.10)$$

where A is the rotor swept area equal to πR^2 .

For each measurement of both the tip vortex locations and C_T , λ was taken to be equal to the average over 36 rotor revolutions. The maximum standard deviation over the 9 different settings of (λ, θ_{ip}) was equal to 0.12. C_T was also taken to be equal to the average over 36

rotor revolutions. The maximum standard deviation over the 9 different settings of (λ, θ_{tip}) was equal to 0.018.

Results and Discussion

Axial thrust coefficients

As already earlier, C_T was measured over the range of yaw angles -45° to 45° at increments of 15° . The C_T values (averaged over one whole revolution) are shown in Fig. 4.26. Ideally, at a given (λ, θ_{tip}) , the variation of C_T with Ψ should be symmetrical about $\Psi=0^\circ$. However, it can be observed that there is a consistent lack of symmetry with the C_T values for negative yaw being slightly lower than the corresponding values at positive yaw. Probably, the reason for the asymmetry is the non-uniformity in velocity distribution of the tunnel exit jet. Referring to Fig. 4.5, the velocity dip region is not located centrally at the tunnel axis, but is shifted slightly to the right. The differences in C_T are largest for $\Psi = \pm 15^\circ$. At $\Psi = \pm 30^\circ$ and $\Psi = \pm 45^\circ$, the symmetry is better. The maximum difference is 0.076 at $\Psi = 15^\circ$ and $(\lambda, \theta_{tip}) = (10, 2^\circ)$.

Tip vortex locations

Fig. 4.27 illustrates the tip vortex locations obtained from the smoke visualization photos at $\Psi=0^\circ$. The tip vortex trajectory determines the wake boundary and hence the wake expansion. Recall that y_s and x_s are the distances relative to the blade tip in a direction perpendicular and parallel to the undisturbed windspeed (see Fig 4.23). For this axial flow condition, only the trajectory on one side is plotted since the wake expansion appeared to be symmetrical. It may be noted that the wake expansion is highly sensitive to both λ and θ_{tip} . Figs. 4.28(a) and (b) displays the tip vortex locations at $\Psi = -30^\circ$ at both the upwind and downwind side. Fig. (a) shows the effect of changing θ_{tip} , while maintaining λ constant at 8. Fig. (b) shows the effect of changing λ , while maintaining θ_{tip} constant at 2° . In both cases, the wake expansion on the downwind side is significantly larger than that on the upwind side. This is due to the fact that in a yawed rotor, there is a component of the free stream velocity (equal to $U \sin(\Psi)$) that acts in a direction parallel to the rotorplane (refer to Fig. 3.1, Chapter 3).

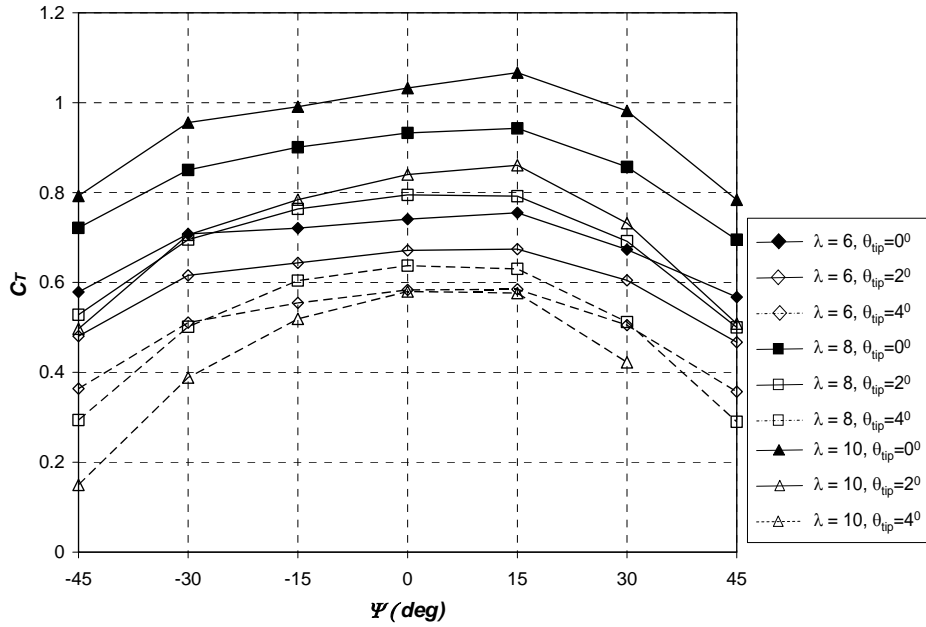


Figure 4.26 – Variation of axial thrust coefficient with yaw angle at all combinations of λ and θ_{tip} .

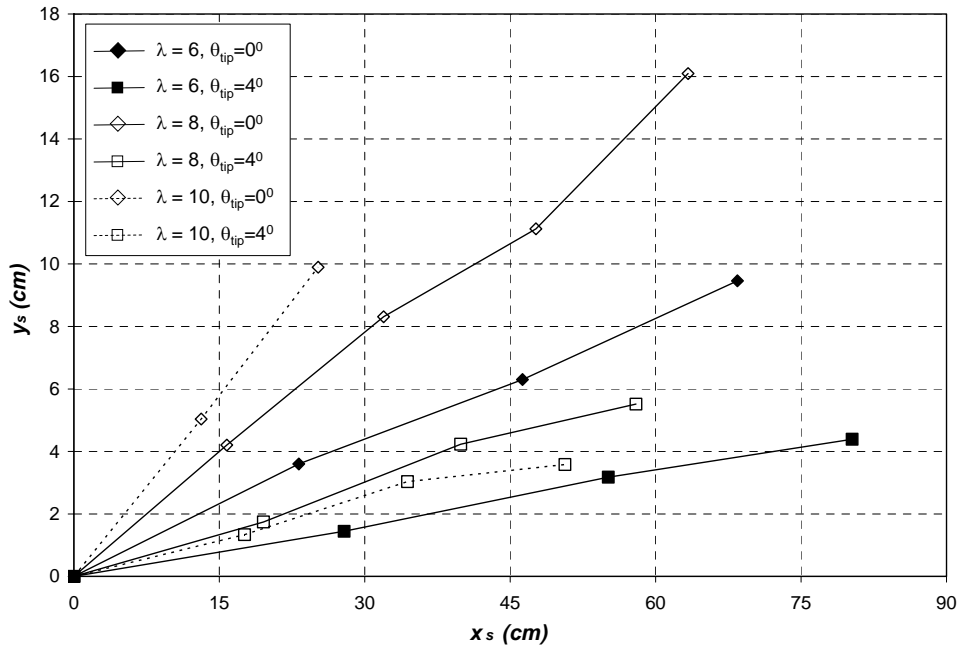


Figure 4.27 – Tip vortex locations at $\Psi = 0^\circ$ at different combinations of λ and θ_{tip} .

Tip vortex pitch

From the tip vortex locations as shown in Figs. 4.27 and 4.28, it was possible to extract the tip vortex pitch (p) at different (λ, θ_{ip}) . As shown in Fig. 4.23, p is the pitch along the x_s -axis. The results for $\Psi=0^\circ$ are given in Fig. 4.29. In this plot the pitches on both the right and left hand side are included. Note that the differences in p between the left and right hand sides are small. Higher λ 's yield higher values for p , but it may be observed that θ_{ip} also has a considerable influence over p . From knowledge of the rotational speed and p , it is possible to obtain an estimate the transport velocity of the vortex cores. It was observed that this velocity is generally not much smaller than the free-stream velocity (on the order of 70-95% of U).

Fig. 4.30 shows the tip vortex pitch variations at $\Psi=30^\circ$ for both the upwind and downwind sides. p is larger on the upwind side than on the downwind side. Consequently, the tip vortex core velocities on the upwind and downwind side are different and this reflects the asymmetry of the wake as a result of rotor yaw.

Wake skew angle

A parameter often used in modelling the skewed wakes of yaw rotors is the wake skew angle χ_s . It is used in several engineering models of BEM codes as already outlined in chapter 3 (section 3.5). In Fig. 4.31, the variation of χ_s with Ψ is plotted for the different rotor settings. χ_s was derived from the tip vortex locations using the procedure described earlier in page 80. It is observed that $|\chi_s| > |\Psi|$ at all tip speed ratios and blade pitch settings. This is due to the fact that the wake expansion is larger on the downwind side than that on the upwind side. For the subject rotor, χ_s may be as much as 8° larger than Ψ .

To investigate the influence of the rotor axial thrust on the wake skew angle, $|\chi_s|$ was plotted against C_T for the different yaw angles, see Fig. 4.32. It is noted that for each yaw angle, the relation of $|\chi_s|$ with C_T is quite linear. Higher thrust values result in larger wake skew angles.

In BEM engineering models for yaw, the wake skew angle is usually modelled to be a function of the axial induction factor (or velocity) (for example see Eq. 3.24, Chapter 3). The linearity found in Fig. 4.32 and also the fact that generally smoke visualization measurements are much cheaper to perform than inflow measurements suggest that it could be simpler to develop engineering models that relate $|\chi_s|$ with C_T than $|\chi_s|$ with a_1 .

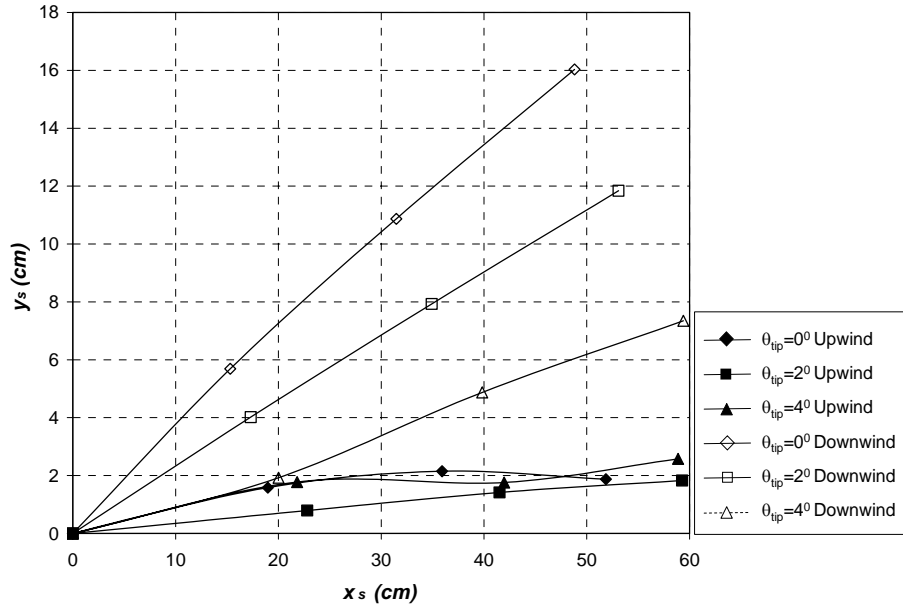


Figure (a) – Effect of changing θ_{tip} while maintaining λ constant at 8.

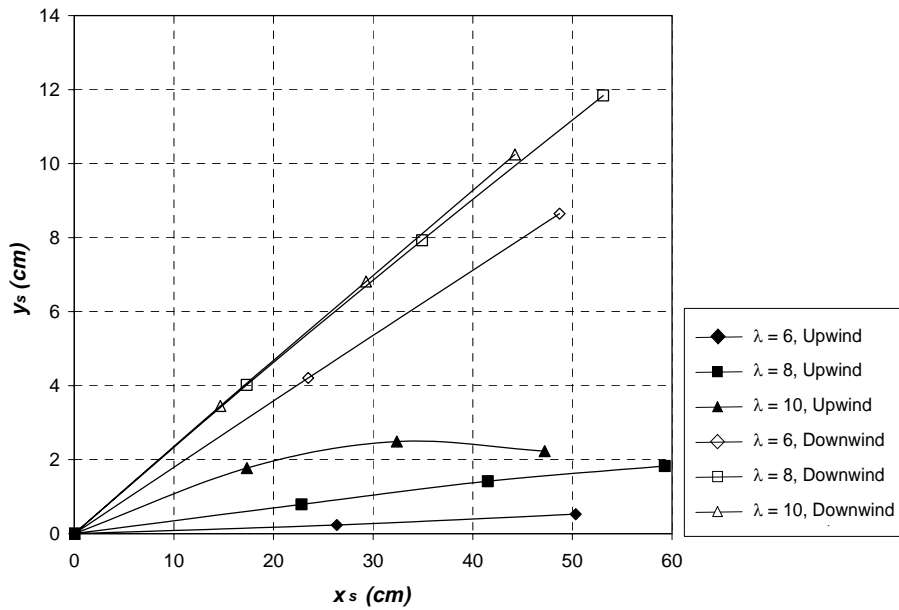


Figure (b) – Effect of changing λ while maintaining θ_{tip} constant at 2° .

Figure 4.28 – Tip vortex locations at $\Psi = -30^\circ$ at upwind and downwind side for different combinations of λ and θ_{tip} .

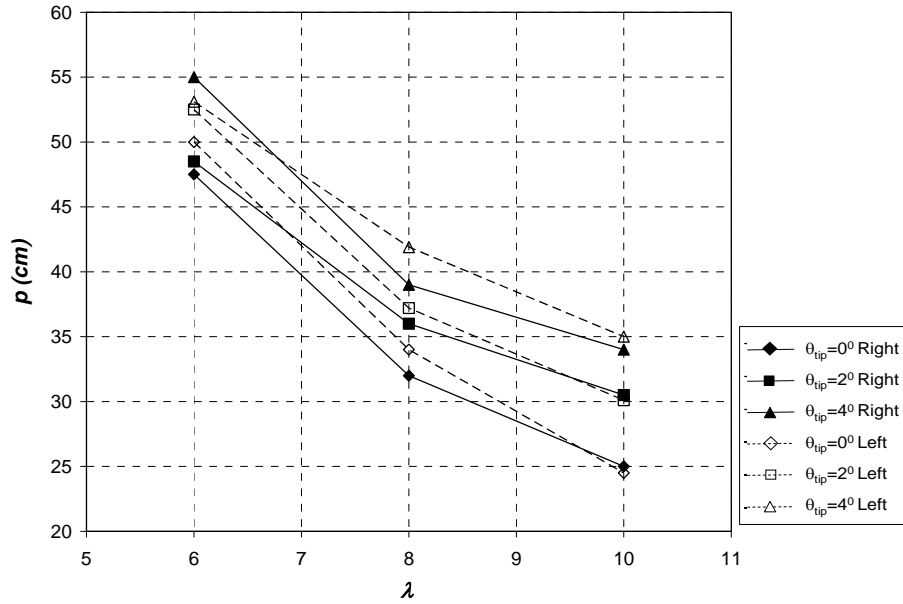


Figure 4.29 – Variation of tip vortex pitch with tip speed ratio at $\Psi = 0^\circ$ at right & left side for different θ_{ip} .

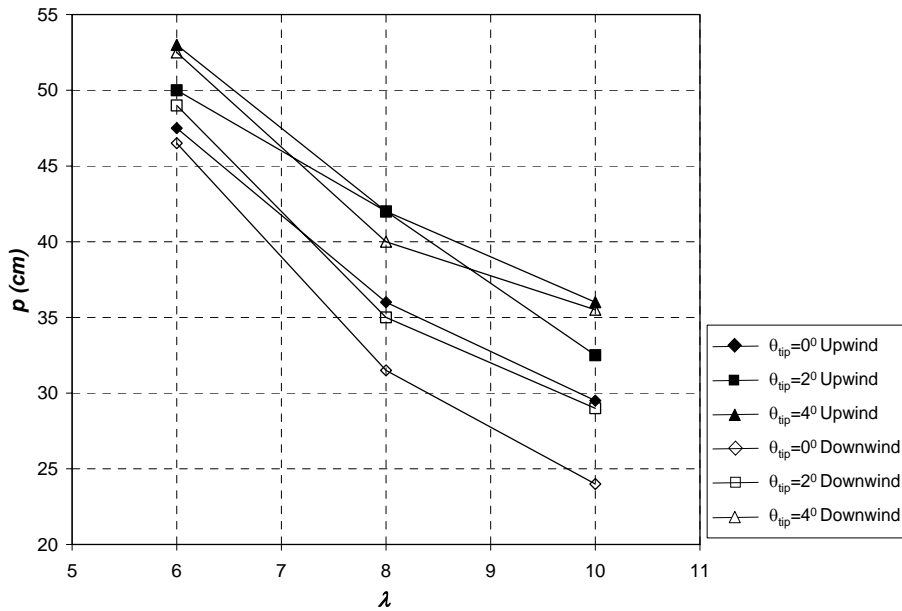


Figure 4.30 – Variation of tip vortex pitch with tip speed ratio at $\Psi = -30^\circ$ at upwind & downwind side for different θ_{ip} .

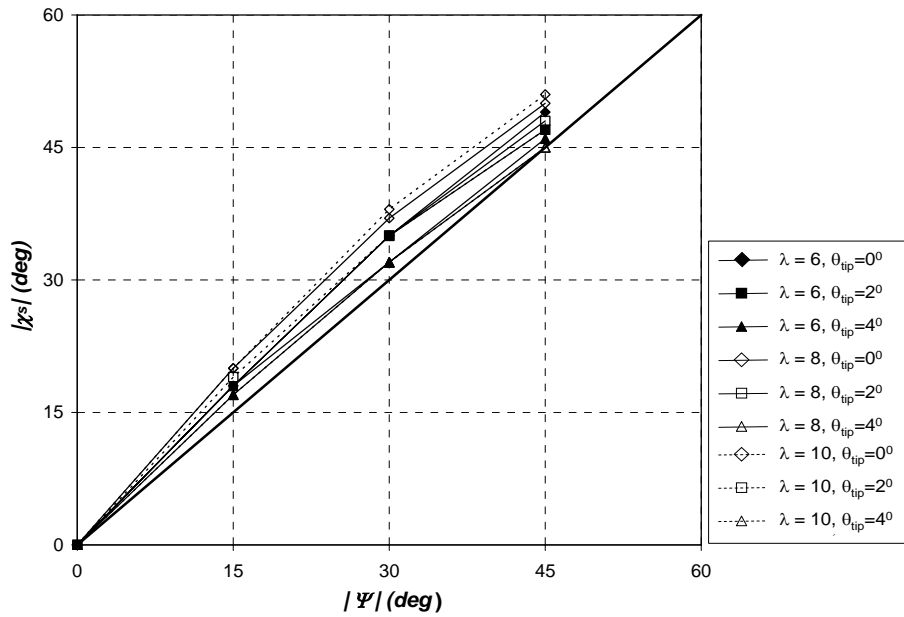


Figure 4.31 – Variation of wake skew angle with rotor yaw angle for different combinations of λ and θ_{tip} .

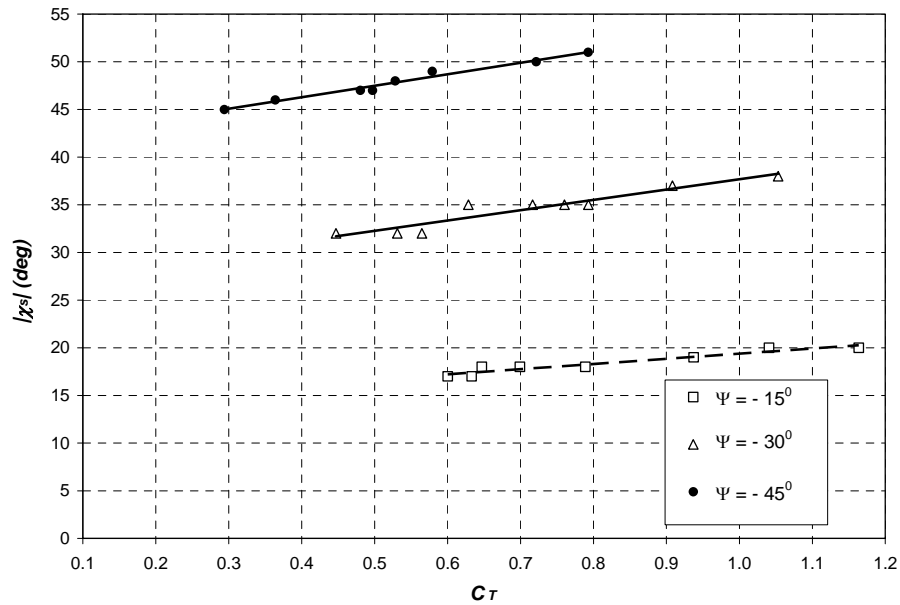


Figure 4.32 – Variation of wake skew angle with rotor axial thrust coefficient for the different yaw angles.

4.3 Estimating the Aerodynamic Loads at the Blades from Wind Tunnel Inflow Measurements

4.3.1 Methodology

As already outlined earlier in section 4.1, one of the objectives of the experiments on the TUDelft wind turbine was to provide experimental data to be able to carry out an in-depth investigation of the limitations of the BEM theory for yawed conditions. A second objective was to use the experimental data to validate a newly developed free-wake vortex code (see Chapter 5). In order to reach these objectives, it was vital to have the unsteady aerodynamic loading distributions along the blades apart from the near wake inflow measurements. Since the experimental set-up used in this study was incapable of measuring such distributions, unsteady aerofoil theory that accounts for shed vorticity effects in the wake had to be employed in order to derive the aerodynamic loads from the inflow measurements. The unsteady lift coefficient could be predicted with reasonable accuracy since the inflow experimental data available was for turbine operating conditions at which the flow behaviour over the blades remained attached, even at a yaw angle of 45°.

Fig. 4.33 illustrates the sequence of steps used in deriving the aerodynamic loads distributions on the blades from the inflow measurements taken in the wind tunnel experiments for operating conditions with $\lambda=8$, $\theta_{tip}=2^\circ$ and yaw angles 0°, 30° and 45°. In section 4.2.2, it was explained how the axial flow velocities ($w_{a,c}$) at the blade lifting lines were estimated by interpolating linearly the measured values at the 3.5cm downstream and 6cm upstream planes (refer to Figs. 4.18(a), 4.19 and 4.20). The former were then used to find the local angle of attack and relative flow velocity at radial locations 40, 50, 60, 70, 80, 90% R using the following blade-element-theory equations:

$$\alpha = \tan^{-1} \left(\frac{w_{a,c}}{r\Omega} \right) - \theta \quad (4.11)$$

$$V_r = \sqrt{(w_{a,c})^2 + (r\Omega)^2} \quad (4.12)$$

The above equations were applied for the different azimuth angles along the whole blade revolution. Tangential flow velocities were ignored since these were found to be very small compared to absolute velocities of the blades. The 2D unsteady lift coefficient ($C_{l,2D}$) was calculated using the unsteady aerofoil model described later on section 4.3.2. This was used to determine the bound circulation at the blades with the Kutta-Joukowski theorem in accordance with:

$$\Gamma_{B,2D} = \frac{1}{2} c V_r C_{l,2D} \quad (4.13)$$

It was found that at the 40% R and 90% R locations, the bound circulation was unrealistically high, even though the angle of attack was determined directly from the measurements. This

was because a 2D unsteady aerofoil model was being used to determine the lift coefficients. Thus a tip/root loss correction had to be employed to $\Gamma_{B,2D}$ such that the bound circulation decreases gradually to zero at the blade tip and root. The corrected bound circulation distribution is being denoted by $\Gamma_{B,3D}$. For each blade azimuth angle, the blade-element theory equations 3.16 were applied to determine the chordwise and normal aerodynamic load distributions along the blades between 40% R and 90% R . For these calculations, a lift coefficient corrected for tip/root loss was used. This was derived using the corrected bound circulation together with the Kutta-Joukowski theorem:

$$C_{l,3D} = \frac{2\Gamma_{B,3D}}{cV_r} \quad (4.14)$$

The drag coefficient was obtained from 2D wind tunnel static data for the NACA0012 aerofoil at low Reynolds number. No correction was applied to the static drag coefficient for unsteady effects in the aerodynamic loads. This is acceptable since for attached flow conditions the influence of drag on the vortex wake structure is minimal. No tip/root loss correction was applied to the drag coefficient. This was justified since the angles of attack were very small and thus the drag was very small compared with the lift.

The global aerodynamic loads and the output power of the turbine were computed by numerically integrating the loading distributions at each time step in accordance with the numerical method described in Appendix B. To check the validity of these calculations, the axial thrust derived from the inflow measurements were checked against their corresponding measured values. Finally, the inflow measurements were assessed for possible uncertainties due to tunnel blockage. This assessment was carried out using a newly developed prescribed wake vortex code (named *HAWT_PVC*).

This Chapter is organized into five separate sections as follows:

- A. Section 4.3.2 describes the unsteady aerofoil model.
- B. Section 4.3.3 describes the software tools developed for this work. These include: (1) *HAWT_LFIM* which is basically a blade-element-theory code implementing the sequence of steps in Fig. 4.33 and (2) *HAWT_PVC* which is the prescribed wake vortex model used to assess tunnel blockage effects. This code was also found very useful in deriving a tip/root loss correction for $\psi \neq 0^\circ$.
- C. Section 4.3.4 presents the methods used to assess whether the hot-film measurements were influenced by tunnel blockage effects.
- D. Section 4.3.5 presents a simplified analytical approach for quantifying errors in the derived blade loading resulting from errors in the inflow measurements.

- E. Section 4.3.6 presents the results including the distributions for the angle of attack (α), flow velocities relative to the blades (V_r) and aerodynamic loading (dT , dQ).

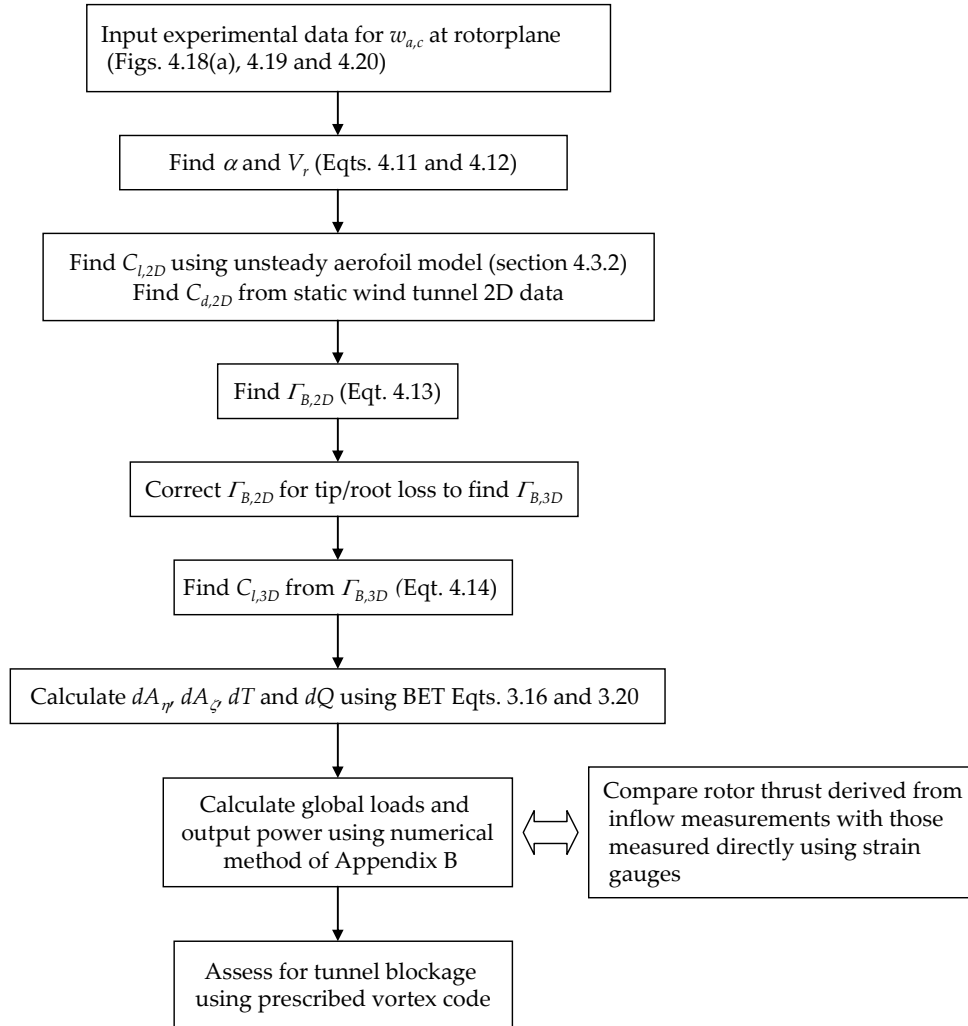


Figure 4.33 – Sequence of steps used in deriving the rotor aerodynamic loads from the inflow measurements.

4.3.2 A Theoretical Method for Finding the Unsteady Lift Coefficient in Attached Flow for a Rotating Blade in Yaw

This section describes a theoretical approach for deriving the unsteady lift coefficients at the blades of a yawed rotor from the inflow measurements. The method is only applicable for attached flow conditions, at which the angles of attack are small. The method was adapted from Leishman [49, pgs 333-340] to evaluate the unsteady lift coefficient as a function of time. In this approach, the instantaneous lift coefficient is considered to be the sum of two components, the non-circulatory and circulatory lift. The former is the lift that arises from the acceleration effects of the flow while the latter is due to the circulation about the aerofoil.

A. Non-Circulatory Lift Coefficient

For an almost rigid blade (experiencing minimal flapping), the non-circulatory lift coefficient is found from [49]:

$$C_l^{nc}(t) = \frac{\pi b}{V^2} \left(V \dot{\alpha} - ab \ddot{\alpha} \right) \quad (4.15)$$

where a is equal to $-1/2$ for a pitch axis at the quarter chord location. b is equal to half the chord length.

B. Circulatory Lift Coefficient

An indicial response method may be used to evaluate the circulatory lift coefficient. If the indicial response function is known, then the unsteady loads due to arbitrary changes in angle of attack can be obtained through the superimposition of the indicial aerodynamic responses by applying Duhamel's integral. Consider a general system in response to a time-dependent forcing function $F(t, t > 0)$. Given that the indicial response function F of the system is known, then the system response $u(t)$ to the forcing can be mathematically expressed in terms of Duhamel's integral as

$$u(t) = F(0)\phi(t) + \int_0^t \frac{dF}{dt} \phi(t - \sigma) d\sigma \quad (4.16)$$

By analogy with the equation above, the circulatory lift coefficient, C_l^c , in response to an unsteady angle of attack can be expressed as

$$C_l^c(t) = 2\pi \left(\alpha(0)\phi(s) + \int_0^s \frac{d\alpha(\sigma)}{dt} \phi(s - \sigma) d\sigma \right) \quad (4.17)$$

where ϕ is the indicial response function derived by Wagner [102] for the lift on a thin aerofoil undergoing a step change in angle of attack in incompressible flow. s is the reduced time given by

$$s = \frac{2}{c} \int_0^t V dt \quad (4.18)$$

which represents the relative distance travelled by the aerofoil through the flow in terms of aerofoil semi-chords during time interval t .

A major difficulty in solving Duhamel's intergral in Eq. 4.17 deals with the Wagner function ϕ . Although the Wagner function is known exactly, its evaluation is not in a convenient analytic form. Therefore, the function is usually approximated by a simply exponential or algebraic approximation. One approximation to the Wagner function, attributed to R.T. Jones is written in the form of an exponential decay function as follows:

$$\phi(s) = 1 - A_1 e^{-b_1 s} - A_2 e^{-b_2 s} \quad (4.19)$$

where A_1 , A_2 , b_1 and b_2 are taken as 0.165, 0.335, 0.0455 and 0.3 respectively. Eq. 4.17 includes the time-history effects of the shed wake on the lift.

C. Time-Varying Incident Velocity

Eqts. 4.15 and 4.17 only consider the situation in which the local free-stream velocity relative to the aerofoil, V , is constant. In yawed flow, the blade element of the wind turbine blades will encounter a time-varying incident velocity. Consequently, the shed wake vorticity leaves the aerofoil at a non-uniform velocity. A pictorial representation of this phenomenon is given in Fig. 4.34.

Leishman [49] modifies Eqts. 4.15 and 4.17 to account for the time variation in incident velocity as follows:

$$C_l^{nc}(t) = \frac{\pi b}{V^2} \left(\frac{d(V\alpha)}{dt} - ab \ddot{\alpha} \right) \quad (4.20)$$

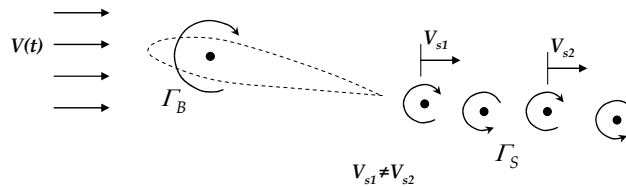


Figure 4.34 - time-dependent free-stream velocity causes shed vorticity to be convected at a non-uniform speed (V_s).

$$C_l^c(s) = \frac{C_{l_\alpha}}{V(s)} \left[V(s_0)\alpha(s_0)\phi(s) + \int_{s_0}^s \frac{d(V\alpha)}{ds}(\sigma)\phi(s-\sigma)d\sigma \right] \quad (4.21)$$

$$= C_{l_\alpha} \alpha_e(s)$$

C_{l_α} is the lift-curve slope equal to 2π /radian for incompressible flow. $\alpha_e(s)$ can be viewed as an effective angle of attack in that it contains all the time-history information related to the unsteady condition.

D. Recursive Solution for the Circulatory Lift using the Duhamel's Integral

Leishman [49, pg 337] presents a solution for solving Eq. 4.17 recursively. This section presents this solution however modified to solve Eq. 4.21 to be able to cater for an unsteady flow velocity.

From Eq. 4.21, the effective angle of attack may be expressed as

$$\alpha_e(s) = \frac{1}{V(s)} \left[V(s_0)\alpha(s_0)\phi(s) + \int_{s_0}^s \frac{d(V\alpha)}{ds}(\sigma)\phi(s-\sigma)d\sigma \right] \quad (4.22)$$

Substituting Eq. 4.19 in 4.22,

$$\alpha_e(s) = \frac{1}{V(s)} \left[V(s_0)\alpha(s_0)(1 - A_1 e^{-b_1 s} - A_2 e^{-b_2 s}) + \int_{s_0}^s \frac{d(V\alpha)}{ds}(\sigma)(1 - A_1 e^{-b_1(s-\sigma)} - A_2 e^{-b_2(s-\sigma)})d\sigma \right]$$

$$= \frac{V(s_0)\alpha(s_0)}{V(s)} - \frac{V(s_0)\alpha(s_0)A_1 e^{-b_1 s}}{V(s)} - \frac{V(s_0)\alpha(s_0)A_2 e^{-b_2 s}}{V(s)}$$

$$+ \frac{1}{V(s)} \int_{s_0}^s \frac{d(V\alpha)}{ds}(\sigma)d\sigma - \frac{A_1}{V(s)} \int_{s_0}^s \frac{d(V\alpha)}{ds}(\sigma)e^{-b_1(s-\sigma)}d\sigma - \frac{A_2}{V(s)} \int_{s_0}^s \frac{d(V\alpha)}{ds}(\sigma)e^{-b_2(s-\sigma)}d\sigma$$

Terms $V(s_0)\alpha(s_0)A_1 e^{-b_1 s} / V(s)$ and $V(s_0)\alpha(s_0)A_2 e^{-b_2 s} / V(s)$ containing the initial values of V and α are short term transients and can be neglected. Consequently, the Duhamel integral may be expressed as

$$\alpha_e(s) = \frac{1}{V(s)} [V(s)\alpha(s) - X(s) - Y(s)] \quad (4.23)$$

where $X(s)$ and $Y(s)$ are equal to

$$X(s) = A_1 \int_{s_0}^s \frac{d(V\alpha)}{ds}(\sigma) e^{-b_1(s-\sigma)} d\sigma \quad (4.24a)$$

$$Y(s) = A_2 \int_{s_0}^s \frac{d(V\alpha)}{ds}(\sigma) e^{-b_2(s-\sigma)} d\sigma \quad (4.24b)$$

Assume a continuous system with time step Δs which may not be constant and that $s_0 = 0$. For the next time step $s + \Delta s$,

$$\begin{aligned} X(s + \Delta s) &= A_1 \int_0^{s+\Delta s} \frac{d(V\alpha)}{ds}(\sigma) e^{-b_1(s+\Delta s-\sigma)} d\sigma \\ &= A_1 e^{-b_1(\Delta s)} \int_0^s \frac{d(V\alpha)}{ds}(\sigma) e^{-b_1(s-\sigma)} d\sigma + A_1 \int_s^{s+\Delta s} \frac{d(V\alpha)}{ds}(\sigma) e^{-b_1(s+\Delta s-\sigma)} d\sigma \\ X(s + \Delta s) &= X(s) e^{-b_1\Delta s} + A_1 e^{-b_1(s+\Delta s)} \int_s^{s+\Delta s} \frac{d(V\alpha)}{ds}(\sigma) e^{b_1\sigma} d\sigma \\ &= X(s) e^{-b_1\Delta s} + I \end{aligned} \quad (4.25)$$

where

$$I = A_1 e^{-b_1(s+\Delta s)} \int_s^{s+\Delta s} \frac{d(V\alpha)}{ds}(\sigma) e^{b_1\sigma} d\sigma$$

To evaluate I , a simplified estimate for $d(V\alpha)/ds$ is used by applying a backward difference approximation at time $s + \Delta s$:

$$\frac{d(V\alpha)}{ds} = \frac{V(s + \Delta s)\alpha(s + \Delta s) - V(s)\alpha(s)}{\Delta s}$$

Thus

$$\begin{aligned} I &= A_1 e^{-b_1(s+\Delta s)} \left[\frac{V(s + \Delta s)\alpha(s + \Delta s) - V(s)\alpha(s)}{\Delta s} \right] \int_s^{s+\Delta s} e^{b_1\sigma} d\sigma \\ &= A_1 \left[\frac{V(s + \Delta s)\alpha(s + \Delta s) - V(s)\alpha(s)}{\Delta s} \right] \left[\frac{1 - e^{-b_1\Delta s}}{b_1} \right] \end{aligned} \quad (4.26)$$

Expand term e^{-b_1s} in the form of a power series

$$e^{-b_1 s} = 1 - b_1 \Delta s + \frac{b_1^2 \Delta s^2}{2!} + \frac{b_1^3 \Delta s^3}{3!} + \dots \quad (4.27)$$

Substituting the above equation in Eq. 4.26 and neglecting terms $b_1^2 \Delta s^2$ and higher since $b_1 \Delta s$ is very small, we will end up with the following simple relation for integral I

$$I = A_1 [V(s + \Delta s)\alpha(s + \Delta s) - V(s)\alpha(s)] \quad (4.28)$$

Putting Eq. 4.28 in Eq. 4.25, we end up with a recursive equation given by

$$X(s + \Delta s) = X(s) e^{-b_1 \Delta s} + A_1 [V(s + \Delta s)\alpha(s + \Delta s) - V(s)\alpha(s)]$$

or

$$X(s) = X(s - \Delta s) e^{-b_1 \Delta s} + A_1 [V(s)\alpha(s) - V(s - \Delta s)\alpha(s - \Delta s)] \quad (4.29)$$

A recursive solution may be derived for $Y(s)$ in Eq. 4.24b using a similar method.

In summary, the recursive solution for the indicial Eq. 4.22 consists of the following three one-step formulas:

$$\alpha_c(s) = \frac{1}{V(s)} [V(s)\alpha(s) - X(s) - Y(s)] \quad (4.30a)$$

$$X(s) = X(s - \Delta s) e^{-b_1 \Delta s} + A_1 [V(s)\alpha(s) - V(s - \Delta s)\alpha(s - \Delta s)] \quad (4.30b)$$

$$Y(s) = Y(s - \Delta s) e^{-b_2 \Delta s} + A_2 [V(s)\alpha(s) - V(s - \Delta s)\alpha(s - \Delta s)] \quad (4.30c)$$

E. Numerical Solutions Algorithms for Conditions of Steady Yaw

In this work, a new approach is presented for solving the non-circulatory and circulatory lift coefficients (Eqts. 4.20 and 4.21, respectively) as a function of time for a rotor in steady yawed conditions. The main advantage of this approach is that the solution is based on matrix inversion and thus is computationally efficient.

We now consider a wind turbine in a fixed yaw angle, rotating at constant angular speed Ω in a steady and uniform wind flow field. Under such operating conditions, the unsteady wake may be assumed to be periodic. Consider one whole revolution of the rotor blade that is divided into a given number of equally-spaced azimuthal positions, as shown in Fig. 3.7 (section 3.6). The number of azimuthal positions is equal to τ_{tot} . τ denotes the number of the time step. The time elapse during one time step is given by

$$\Delta \tau = \frac{2\pi}{\Omega * \tau_{tot}} \quad (4.31)$$

Numerical Solution for the Non-Circulatory Lift Coefficient

Given that V and α are known at each blade azimuth angle, (i.e. at each rotor time step), Eq. 4.20 may be solved as follows:

It is first necessary to establish a method for evaluating $d\alpha/dt$, $d(V\alpha)/dt$ and $d^2\alpha/dt^2$ at each blade azimuth angle. A simple way of doing so is to apply a forward difference approximation at each time step. For $d\alpha/dt$, this would be

$$\left. \frac{d\alpha}{dt} \right|_{\tau} = \frac{\alpha_{\tau+1} - \alpha_{\tau}}{\Delta\tau} \quad (4.32)$$

The global error in this method is only in the order $O(\tau^2)$. In this work, a more accurate method was used based on the Adam-Bashforth multi-step numerical integration technique. This technique makes use of data at previous time steps in order to predict a solution at the next. In the case of a fourth-order Adam-Bashforth method, four previous data points are required and the equation takes the form of

$$\alpha_{\tau} = \alpha_{\tau-1} + \frac{\Delta\tau}{24} [55\dot{\alpha}_{\tau-1} - 59\dot{\alpha}_{\tau-2} + 37\dot{\alpha}_{\tau-3} - 9\dot{\alpha}_{\tau-4}] \quad (4.33)$$

Since we have a periodic wake then $\alpha_{\tau_{tot}} = \alpha_0$ and the above equation may be written at each blade time step to form a system of τ_{tot} equations which may be written in matrix form as

$$\begin{bmatrix} \Delta\alpha_0 \\ \Delta\alpha_1 \\ \Delta\alpha_2 \\ \Delta\alpha_3 \\ \circ \\ \Delta\alpha_{\tau} \\ \circ \\ \Delta\alpha_{\tau_{tot}-1} \end{bmatrix} = \begin{bmatrix} 55 & 0 & 0 & 0 & 0 & -9 & 37 & -59 \\ -59 & 55 & 0 & 0 & 0 & 0 & -9 & 37 \\ 37 & -59 & 55 & 0 & 0 & 0 & 0 & -9 \\ -9 & 37 & -59 & 55 & 0 & 0 & 0 & 0 \\ \circ & \circ & \circ & \circ & \circ & \circ & \circ & \circ \\ 0 & 0 & -9 & 37 & -59 & 55 & 0 & 0 \\ \circ & \circ & \circ & \circ & \circ & \circ & \circ & \circ \\ 0 & 0 & 0 & 0 & -9 & 37 & -59 & 55 \end{bmatrix} * \begin{bmatrix} \dot{\alpha}_0 \\ \dot{\alpha}_1 \\ \dot{\alpha}_2 \\ \dot{\alpha}_3 \\ \circ \\ \dot{\alpha}_{\tau} \\ \circ \\ \dot{\alpha}_{\tau_{tot}-1} \end{bmatrix} \quad (4.34a)$$

or
$$[\Delta\alpha] = A * [\dot{\alpha}] \quad (4.34b)$$

where
$$\Delta\alpha_{\tau} = \frac{24}{\Delta\tau} (\alpha_{\tau} - \alpha_{\tau-1}) \quad (4.34c)$$

The vector $[\Delta\alpha]$, $[\Delta\alpha_0 \ \Delta\alpha_\tau \ \Delta\alpha_{\tau+1} \ \dots \ \Delta\alpha_{\tau_{tot}-1}]^T$, can be easily evaluated from knowledge of α at each blade time step. The rate of change of α with time is then found by find the inverse of matrix A and using

$$[\dot{\alpha}] = A^{-1} * [\Delta\alpha] \quad (4.34d)$$

The global error in this method is only in the order $O(\tau^5)$. An identical approach is adopted to find $d(V\alpha)/dt$ and $d^2\alpha/dt^2$ using the same matrix A . After these time derivatives are evaluated at each time step, they are substituted in Eq. 4.20 to yield the non-circulatory lift coefficient at all blade time steps.

Numerical Solution for the Circulatory Lift Coefficient

Given that V and α are known at each blade azimuth angle, (i.e. at each rotor time step), Eqs. 4.21 may be solved recursively as follows:

Applying Eqs. 4.30a,b,c for each time step τ ,

$$\alpha_{e\tau} = \frac{1}{V_\tau} [V_\tau \alpha_\tau - X_\tau - Y_\tau] \quad (4.35)$$

$$X_\tau - p_\tau X_{\tau-1} = P_\tau \quad (4.36a)$$

$$Y_\tau - q_\tau Y_{\tau-1} = Q_\tau \quad (4.36b)$$

where

$$p_\tau = e^{-b_1 \Delta s_\tau} \quad q_\tau = e^{-b_2 \Delta s_\tau} \quad (4.37)$$

$$P_\tau = A_1 (V_\tau \alpha_\tau - V_{\tau-1} \alpha_{\tau-1}) \quad (4.38a)$$

$$Q_\tau = A_2 (V_\tau \alpha_\tau - V_{\tau-1} \alpha_{\tau-1}) \quad (4.38b)$$

Using Eq. 4.18, the values for a small incremental change in s becomes

$$\Delta s_\tau = \frac{\Delta \tau}{c} [V_\tau + V_{\tau-1}] \quad (4.39)$$

The value of X at each time step τ is solved as follows: Eq. 4.36(a) is applied for each time step in order to give τ_{tot} equations which can be written in matrix form as

$$\begin{bmatrix} 1 & 0 & 0 & 0 & 0 & 0 & 0 & -p_0 \\ -p_1 & 1 & 0 & 0 & 0 & 0 & 0 & 0 \\ 0 & -p_2 & 1 & 0 & 0 & 0 & 0 & 0 \\ 0 & 0 & -p_{\tau-1} & \cdot & 0 & 0 & 0 & 0 \\ 0 & 0 & 0 & -p_{\tau} & \cdot & 0 & 0 & 0 \\ 0 & 0 & 0 & 0 & \cdot & 1 & 0 & 0 \\ 0 & 0 & 0 & 0 & 0 & \cdot & 1 & 0 \\ 0 & 0 & 0 & 0 & 0 & 0 & -p_{\tau\text{tot}-1} & 1 \end{bmatrix} * \begin{bmatrix} X_0 \\ X_1 \\ X_2 \\ \cdot \\ X_{\tau-1} \\ X_{\tau} \\ \cdot \\ X_{\tau\text{tot}-1} \end{bmatrix} = \begin{bmatrix} P_0 \\ P_1 \\ P_2 \\ \cdot \\ P_{\tau-1} \\ P_{\tau} \\ \cdot \\ P_{\tau\text{tot}-1} \end{bmatrix}$$

or

$$G * [\bar{X}] = [\bar{P}] \quad (4.40)$$

The values of \bar{X} , $[X_0 \ X_{\tau-1} \ X_{\tau} \dots X_{\tau\text{tot}-1}]^T$, at each time step are then evaluated using matrix inversion such that

$$[\bar{X}] = G^{-1} * [\bar{P}] \quad (4.41)$$

The values of \bar{Y} are calculated in a similar fashion however replacing p and P with q and Q respectively. Once the values of X and Y at each time step are obtained, Eq. 4.35 is employed to obtain the equivalent circulatory angle of attack to be used to find the circulatory lift coefficient.

Summary of Numerical Solution to Estimate the Unsteady Lift Coefficient from the Inflow Measurements

From inflow measurements, the values of α and V_r at each time step may be evaluated (Parameter V_r in a rotating blade is equal to V). These can then be used to find p , P , q and Q using Eqts. 4.37, 4.38 and 4.39, and thus find the circulatory lift coefficient. The latter is then added to the non-circulatory lift coefficient (computed using Eq. 4.20) to give the total lift coefficient as a function of time.

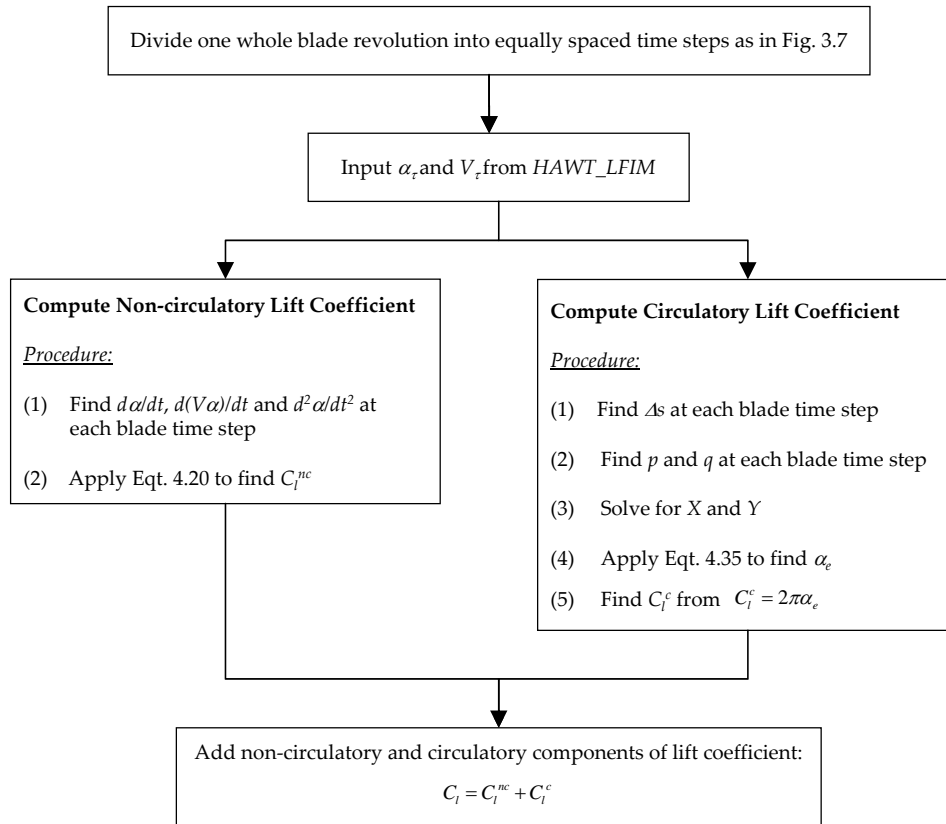


Figure 4.35 – Summary of method used to determine the unsteady lift coefficient.

4.3.3 Developed Software Tools

A. Description of Program HAWT_LFIM

Program HAWT_LFIM (LFIM meaning *Loads from Inflow Measurements*) was specifically developed to derive the aerodynamic loads at the rotor blades from the inflow measurements using the procedure of Fig. 4.33. This code was written using MathCad© version 11 and is applicable for both non-yawed and yawed conditions. Fig. 4.36 describes the structure of this code. This code is organized into three separate modules: in the *Data Input Module* in which the experimental parameters describing the rotor geometry and operating condition are inputted, together with the axial flow velocities ($w_{a,c}$) of Figs. 4.18(a), 4.19 and 4.20. The *Data Processing Module* implements the various blade-element theory equations and the unsteady aerofoil theory to be able to estimate the aerodynamic loading

distributions at the blades. The latter are integrated numerically to be able to find the rotor global aerodynamic loads and output power. The *Data Output Module* outputs the results as a function of rotor azimuth angle.

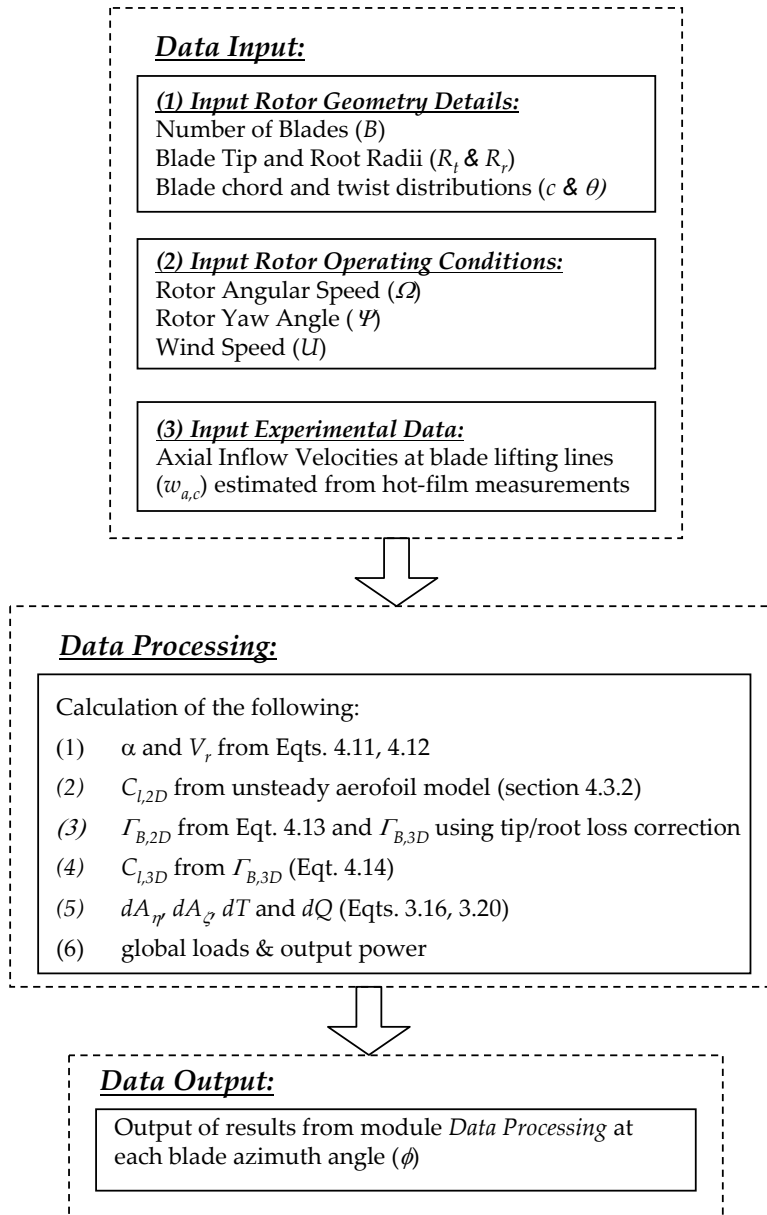


Figure 4.36 – Structure of code HAWT_LFIM.

B. Description of Program HAWT_PVC

As already described earlier in section 4.3.1, the prescribed wake vortex model was mainly developed to be able to estimate quantitatively the influence of wind tunnel blockage. This code was also helpful in applying a tip/root loss correction at $\Psi \neq 0^\circ$. The main function of the code is to estimate the induced velocities in the rotor wake using a known bound circulation distribution. The code, named HAWT_PVC (PVC meaning *Prescribed Vortex Code*) is also written using MathCad© version 11 and is applicable for both non-yawed and yawed conditions. Fig. 4.37 describes the structure of this vortex model. The inputs to the model are the blade geometry and the rotor operating parameters together with the known bound circulation distributions at the blades.

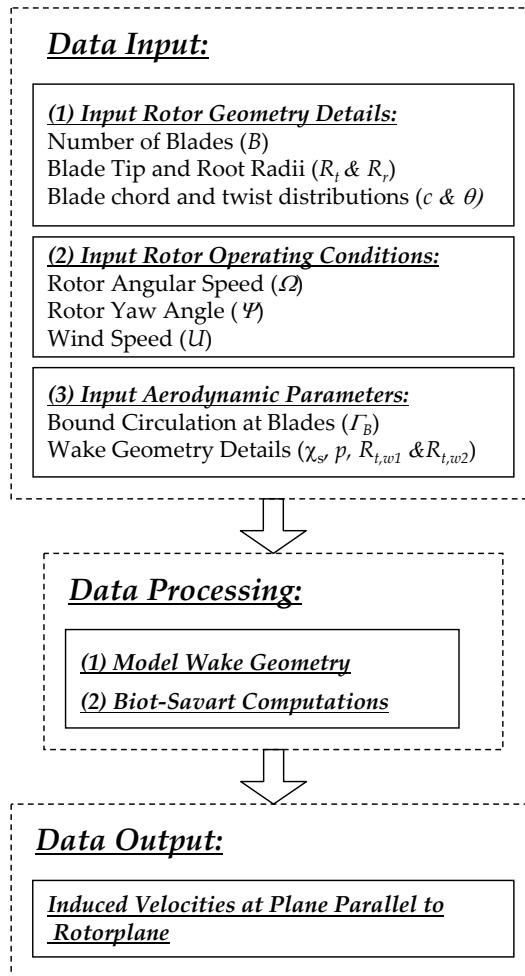


Figure 4.37: Structure of computer code HAWT_PVC.

Since in a yawed rotor the bound circulation at the blades becomes time-dependent, then this circulation is prescribed to the code as a function of blade azimuth angle. The wake parameters derived from the smoke visualization experiments (refer to section 4.2.3) are also inputted and used by the code to model the prescribed wake geometry. From the known bound circulation distributions, the trailing circulation distribution is derived and used in conjunction with the Biot-Savart law (refer to Appendix C) to calculate the 3D induced velocity distributions at any required plane parallel to the rotorplane.

Blade and Wake Model

Fig. 4.38 gives details for the adopted model for the rotor blades and wake. Each blade is modelled using a lifting-line with a single lumped vortex located along the quarter-chord point of the blade sections. The lifting line consists of a fixed number (n) of piecewise constant spanwise segments, each of equal length.

The wake consists of helical vortex sheets, one per blade. Each vortex sheet consists of helices located at different radial locations. Each helix is segmented into straight-line vortex filaments to represent trailing circulation in the wake (refer to Fig. 4.38). For yawed conditions, the helices are skewed, depending on the inputted value of χ . The modelling of shed circulation was not included, since for the operating conditions of the TUDelft rotor being considered in this study, this circulation component was found to be very small.

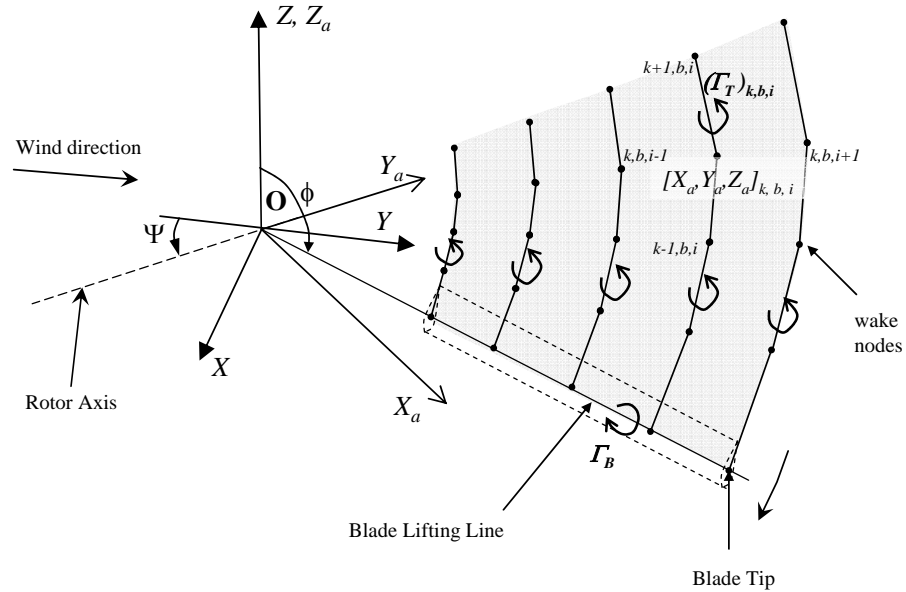


Figure 4.38: Modelling of blades and wake in prescribed-wake vortex model.

The trailing filament nodes are interconnected by nodes. To determine the 3D Cartesian coordinates of each wake node, the following mathematical model is used:

Each rotor revolution is divided into a fixed number (n_{tot}) of equally-spaced azimuth steps as in Fig. 3.7. The azimuthal step of the wake helices is maintained equal to that of the rotor (i.e. $2\pi/n_{tot}$). Thus the number of filaments used for each revolution in each helix is also equal to n_{tot} . The wake extends downstream depending on the prescribed number of revolutions (n_{wRev}) and the value of the pitch p . Since in the smoke visualization experiments, a slight variation was observed between the tip vortex pitch values on the upwind and downwind sides (some results are plotted in Figs. 4.29 and 4.30), the average value of the two values for p is used in the model. It is assumed that the vortex sheet pitch is equal to that of the tip vortex at all radial locations in the wake. As shown in Fig. 4.23 pitch p is taken along an axis parallel to the free wind direction. In the wake model, a pitch p_w acting along the Y_a axis is used and this is given by

$$p_w = p \cos(\Psi) \quad (4.42)$$

Wake Geometry

Each wake node is denoted by indices k, b, i (see Fig. 4.38), where b and i denote the blade number and the radial location from which the helix is originating. i is equal to 0 for all wake nodes that lie on the helix that is originating from the blade root. i is equal to $n-1$ for the wake nodes that lie on the helix originating from the blade tip. $b=0$ denotes the first blade. k denotes the node number on the helix, where $k=0$ is for the starting node that lies on the respective blade lifting line. The total number of vortex filaments used to represent a single helix is denoted by k_{tot} and this is equal to $n_{wRev} * n_{tot}$.

Figs. 4.39(a), (b) and (c) describe the geometry used to define the wake outer (tip) and inner (root) boundaries. For yawed conditions, both of these are skewed with respect to the rotor axis and their central axis is the wake skew axis. Thus the helical trailing vortices have the wake skew axis as their central axis and not the Y_a axis. The outer wake boundary is defined using the prescribed terms $R_{t,w1}$ and $R_{t,w2}$ that are derived from the smoke visualization of tip vortex cores (refer to section 4.2.3). These define the expansion of the wake in the near field of the rotor. It is assumed that the cross-section of the wake in a plane parallel to the rotorplane is annular, as shown in Fig. 4.39(c). At any distance Y_a from the rotorplane, the radii of the outer and inner wake boundaries are denoted by $R_{t,w}$ and $R_{r,w}$ respectively.

For the outer wake boundary, a quadratic fit is applied for the variation of $R_{t,w}$ with Y_a for $Y_a < p_w$ such that

$$R_{t,w}(Y_a) = a_0 Y_a^2 + a_1 Y_a + a_2 \quad (4.43)$$

where constants a_0, a_1 and a_2 are determined by applying the following three boundary conditions: (i) at $Y_a=0$ (i.e. at the rotorplane), $R_{t,w}=0.99R_t$; (ii) at $Y_a = p_w/2$, $R_{t,w}=R_{t,w1}$ and (iii) at

$Y_a = p_w$, $R_{t,w} = R_{t,w2}$ (refer to Fig. 4.39(a)). In boundary condition (i), it is being assumed that the outboard edge vortex sheet is released from the blade at $0.99R_t$.

Applying the above three boundary conditions to Eq. 4.43 leads to three equations that may be written in matrix form as

$$\begin{bmatrix} 0 & 0 & 1 \\ \left(\frac{p_w}{2}\right)^2 & \left(\frac{p_w}{2}\right) & 1 \\ p_w^2 & p_w & 1 \end{bmatrix} * \begin{bmatrix} a_0 \\ a_1 \\ a_2 \end{bmatrix} = \begin{bmatrix} 0.99R_t \\ R_{t,w1} \\ R_{t,w2} \end{bmatrix} \quad (4.44)$$

Using matrix inversion, constants a_0 , a_1 and a_2 may be evaluated, as follows:

$$\begin{bmatrix} a_0 \\ a_1 \\ a_2 \end{bmatrix} = \begin{bmatrix} 0 & 0 & 1 \\ \left(\frac{p_w}{2}\right)^2 & \left(\frac{p_w}{2}\right) & 1 \\ p_w^2 & p_w & 1 \end{bmatrix}^{-1} * \begin{bmatrix} 0.99R_t \\ R_{t,w1} \\ R_{t,w2} \end{bmatrix} \quad (4.45)$$

For $Y_a > p_w$, $R_{t,w}$ is set constant and equal to $R_{t,w2}$. For the inner wake boundary no wake expansion is taken into consideration. This boundary takes the form of a skewed cylinder having a constant radius equal to the rotor blade root radius R_r .

To summarize, the wake boundaries are defined by the following equations:

$$\begin{aligned} R_{t,w}(Y_a) &= a_0 Y_a^2 + a_1 Y_a + a_2 \quad \text{if } Y_a \leq p_w \\ &= R_{t,w2} \quad \text{if } Y_a > p_w \\ R_{r,w}(Y_a) &= R_r \quad \forall Y_a \end{aligned} \quad (4.46)$$

The co-ordinates of each wake node in polar co-ordinates is denoted by $[(r_w)_{k,b,i}, (\phi_w)_{k,b}, (Y_s)_k]$ where the central axis is aligned with the wake skew axis Y_s (refer to Fig. 4.39(a)). r_w denotes the radial distance and is equal to $R_{t,w}$ for the wake nodes lying on the outer edge of the vortex sheets ($i=n-1$), i.e. the wake nodes that lie on the helix originating from the blade tip (at $r=0.99R_t$). r_w is equal to $R_{r,w}$ for the wake nodes lying on the inner edge of the vortex sheets ($i=0$), i.e. the wake nodes that lie on the helix originating from the blade root (at $r=R_r$). For $Y_a \leq p_w$, the outermost helix (from the blade, $i=n-1$) will experience an expansion in accordance with Eq. 4.46 while the innermost helix (from the blade root, $i=0$) does not expand.

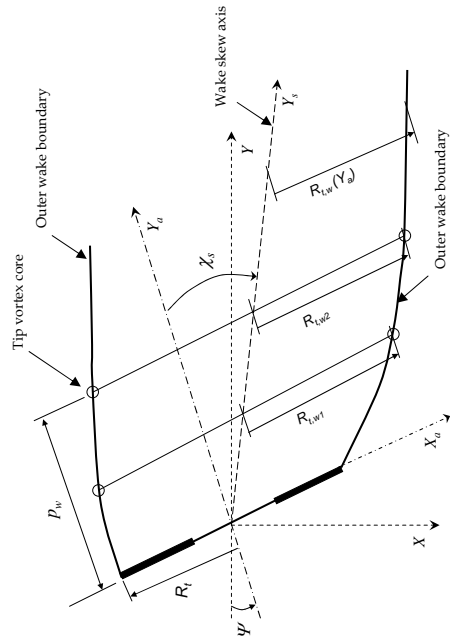


Fig. (a): Geometry for outer wake boundary of prescribed wake

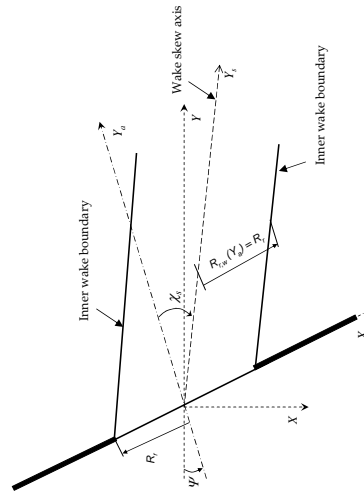


Fig. (b): Geometry for inner wake boundary of prescribed wake

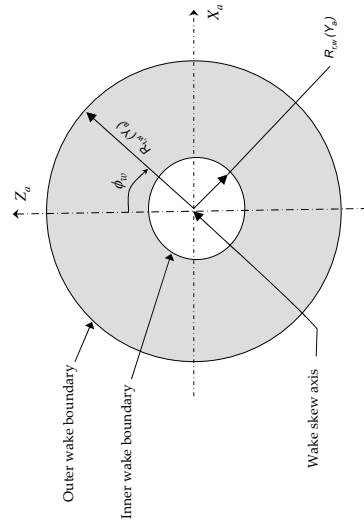


Fig. (c): Cross-section through prescribed wake at given Y_a

Figure 4.39 – Schematic diagrams describing how prescribed vortex wake was modelled

The rest of the helices ($i=1,2..n-2$) are allowed to expand in accordance with the following linear interpolating formula

$$r_w(Y_a) = R_{r,w}(Y_a) + \left(\frac{R_{t,w}(Y_a) - R_{r,w}(Y_a)}{R_t - R_r} \right) (r - R_r) \quad (4.47)$$

Since after one whole helical revolution, each helix will advance by one pitch (p_w), then the axial distance along the Y_a axis may be written in index form $(Y_a)_k$ as

$$(Y_a)_k = \frac{k \cdot p_w}{\tau_{tot}} \quad (4.48)$$

and Eq. 4.47 in index form is expressed by $(r_w)_{k,b,i}$ as

$$(r_w)_{k,b,i} = (R_{r,w})_{k,b,i} + \left(\frac{(R_{t,w})_{k,b,i} - (R_{r,w})_{k,b,i}}{R_t - R_r} \right) (r_i - R_r) \quad (4.49)$$

The angle ϕ_w at each wake node is determined from

$$(\phi_w)_{k,b} = (\phi)_\tau + \frac{2\pi b}{B} - k \cdot \Delta\phi \quad (4.50)$$

where τ is the index denoting the azimuth angle of the first blade and $\Delta\phi$ is the azimuthal step ($2\pi/\tau_{tot}$). The distance of each wake node along the wake skew axis may be written in index notation $(Y_s)_k$ as

$$(Y_s)_k = \frac{k \cdot p_w}{\tau_{tot} \cos(\chi_s)} \quad (4.51)$$

The position of each wake node on the vortex sheets is expressed in 3D Cartesian co-ordinates $[(X_a)_{k,b,i}, (Y_a)_k, (Z_a)_{k,b,i}]$ using the following transformation equations:

$$\begin{bmatrix} (X_a)_{k,b,i} \\ (Y_a)_k \\ (Z_a)_{k,b,i} \end{bmatrix} = \begin{bmatrix} (Y_a)_k \cdot \tan(\chi_s) + (r_w)_{k,b,i} \cdot \sin((\phi_w)_{k,b}) \\ (Y_a)_k \\ (r_w)_{k,b,i} \cdot \cos((\phi_w)_{k,b}) \end{bmatrix} \quad (4.52)$$

Finally, the wake node co-ordinates are transformed into the global fixed X-Y-Z frame of reference using the following transformation:

$$\begin{bmatrix} (X)_{k,b,i} \\ (Y)_{k,b,i} \\ (Z)_{k,b,i} \end{bmatrix} = \begin{bmatrix} \cos(\Psi) & \sin(\Psi) & 0 \\ -\sin(\Psi) & \cos(\Psi) & 0 \\ 0 & 0 & 1 \end{bmatrix}^{-1} \begin{bmatrix} (X_a)_{k,b,i} \\ (Y_a)_k \\ (Z_a)_{k,b,i} \end{bmatrix} \quad (4.53)$$

Wake Trailing Circulation Distribution

Γ_T represents the trailing circulation in the wake due to a spanwise variation in bound circulation. Each trailing vortex filament in the wake is denoted by $(\Gamma_T)_{k,b,i}$ and is connected to nodes (k,b,i) and $(k+1,b,i)$, refer to Fig. 4.38. When the turbine is operating in steady conditions with its axis parallel to the windspeed direction, the bound circulation at the blades is constant. Consequently, each helix of the wake vortex sheet will have a uniform circulation. For non-yawed conditions however, the bound circulation becomes a function of the blade azimuth angle (ϕ) . Thus, the circulation at each helix is varied from filament to filament, depending on its azimuth position of the filament, i.e. $(\phi_w)_{k,b}$. The assignment of the circulation at each trailing filament is carried out in accordance with the following relation:

$$(\Gamma_T)_{k,b,i} = (\Gamma_B)_{\tau,b,i-1} - (\Gamma_B)_{\tau,b,i} \quad (4.54a)$$

where

$$(\phi_w)_{b,k} = \phi_\tau + \frac{2\pi b}{B} \quad (4.54b)$$

Eq. 4.54(b) is used so that each filament is assigned a circulation calculated using the bound circulation when the blades are at the same azimuth angle as that of the filament.

Numerical Solution

Initially, a spanwise variation of bound circulation is prescribed to each blade of the modelled rotor as a function of rotor azimuth angle. The total number of helical revolutions for the prescribed wake ($nwRev$) is inputted and a whole rotor revolution is subdivided into n_{tot} equally spaced azimuth steps. The solution starts with an impulsive start of the rotor with the first blade initially at an azimuth angle of 0° . The axial distance of the plane parallel to the rotorplane at which the induced velocities are to be computed (Y_{ap}) is inputted. A number of calculations points on the plane are noted as shown in Fig. 4.40. The azimuthal spacing of the points is equal to $\Delta\phi$, while the number of radial locations at a fixed azimuth is equal to n . Each point in this plane is denoted by co-ordinates (X_p, Y_p, Z_p) and indices $(ip, \tau p)$ where $ip=0$ and $ip=n-1$ for $r=R_r$ and $r=R_t$, respectively and $\tau p=0$ for an azimuth angle of 0° .

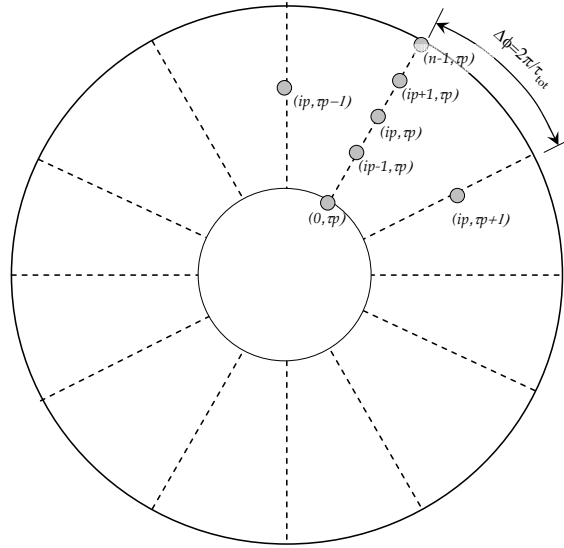


Figure 4.40 - Notation used for calculations points within plane distant Y_{ap} from rotorplane.

For each rotor time step τ , the following steps are carried out

- (1) the geometry of the wake vortex sheet due to each blade is modelled using Eqs. 4.46-4.53.
- (2) the trailing circulation at each wake filament is found using Eqs. 4.54(a), (b).
- (3) the Biot-Savart equations (Appendix C, Eqs. C.24..32) are applied to calculate the 3D induced velocity components at each calculation point $(ip, \tau p)$ due to all bound vortices at the blades and trailing vortex filaments in the wake, as follows:

$$\begin{aligned}
 (u_X)_{ip, \tau p} &= \sum_{b=0}^{B-1} \sum_{i=0}^{n-1} (\Gamma_B)_{\tau, b, i} * GXB_{ip, \tau p, \tau, b, i} + \sum_{k=0}^{ktot} \sum_{b=0}^{B-1} \sum_{i=0}^{n-1} (\Gamma_T)_{k, b, i} * GXT_{ip, \tau p, k, b, i} \\
 (u_Y)_{ip, \tau p} &= \sum_{b=0}^{B-1} \sum_{i=0}^{n-1} (\Gamma_B)_{\tau, b, i} * GYB_{ip, \tau p, \tau, b, i} + \sum_{k=0}^{ktot} \sum_{b=0}^{B-1} \sum_{i=0}^{n-1} (\Gamma_T)_{k, b, i} * GYT_{ip, \tau p, k, b, i} \\
 (u_Z)_{ip, \tau p} &= \sum_{b=0}^{B-1} \sum_{i=0}^{n-1} (\Gamma_B)_{\tau, b, i} * GZB_{ip, \tau p, \tau, b, i} + \sum_{k=0}^{ktot} \sum_{b=0}^{B-1} \sum_{i=0}^{n-1} (\Gamma_T)_{k, b, i} * GZT_{ip, \tau p, k, b, i}
 \end{aligned} \tag{4.55}$$

where GXB , GYB and GZB are the geometric influence coefficients due to the bound circulation vortices while GXT , GYT and GZT are the geometric influence coefficients for the trailing circulation vortices. The discretization equations for these coefficients are presented in Tables 4.2 and 4.3. A simple numerical cut-off method is used to de-singularise

$$\begin{aligned}
 GXB_{ip,\tau p,\tau,b,i} &= \frac{[(r_1)_{ip,\tau p,\tau,b,i} + (r_2)_{ip,\tau p,\tau,b,i}] \cdot [[(Y_p)_{ip,\tau p} - (Y_B)_{\tau,b,i+1}] [(Z_B)_{\tau,b,i+1} - (Z_B)_{ip,\tau p}] - [(Z_p)_{ip,\tau p} - (Z_B)_{\tau,b,i+1}] [(Y_B)_{\tau,b,i+1} - (Y_B)_{\tau,b,i}]]}{2\pi \cdot (r_1)_{ip,\tau p,\tau,b,i} \cdot (r_2)_{ip,\tau p,\tau,b,i} \cdot [(r_1)_{ip,\tau p,\tau,b,i} + (r_2)_{ip,\tau p,\tau,b,i}]^2 - [(L)_{\tau,b,i}]^2} \\
 GYB_{ip,\tau p,\tau,b,i} &= \frac{[(r_1)_{ip,\tau p,\tau,b,i} + (r_2)_{ip,\tau p,\tau,b,i}] \cdot [[(Z_p)_{ip,\tau p} - (Z_B)_{\tau,b,i+1}] [(X_B)_{\tau,b,i+1} - (X_B)_{\tau,b,i}] - [(X_p)_{ip,\tau p} - (X_B)_{\tau,b,i+1}] [(Z_B)_{\tau,b,i+1} - (Z_B)_{\tau,b,i}]]}{2\pi \cdot (r_1)_{ip,\tau p,\tau,b,i} \cdot (r_2)_{ip,\tau p,\tau,b,i} \cdot [[(r_1)_{ip,\tau p,\tau,b,i} + (r_2)_{ip,\tau p,\tau,b,i}]^2 - [(L)_{\tau,b,i}]^2]} \\
 GZB_{ip,\tau p,\tau,b,i} &= \frac{[(r_1)_{ip,\tau p,\tau,b,i} + (r_2)_{ip,\tau p,\tau,b,i}] \cdot [[(X_p)_{ip,\tau p} - (X_B)_{\tau,b,i+1}] [(Y_B)_{\tau,b,i+1} - (Y_B)_{\tau,b,i}] - [(Y_p)_{ip,\tau p} - (Y_B)_{\tau,b,i+1}] [(X_B)_{\tau,b,i+1} - (X_B)_{\tau,b,i}]]}{2\pi \cdot (r_1)_{ip,\tau p,\tau,b,i} \cdot (r_2)_{ip,\tau p,\tau,b,i} \cdot [[(r_1)_{ip,\tau p,\tau,b,i} + (r_2)_{ip,\tau p,\tau,b,i}]^2 - [(L)_{\tau,b,i}]^2]} \\
 (r_1)_{ip,\tau p,\tau,b,i} &= \sqrt{[(X_p)_{ip,\tau p} - (X_B)_{\tau,b,i}]^2 + [(Y_p)_{ip,\tau p} - (Y_B)_{\tau,b,i}]^2 + [(Z_p)_{ip,\tau p} - (Z_B)_{\tau,b,i}]^2} \\
 (r_2)_{ip,\tau p,\tau,b,i} &= \sqrt{[(X_p)_{ip,\tau p} - (X_B)_{\tau,b,i+1}]^2 + [(Y_p)_{ip,\tau p} - (Y_B)_{\tau,b,i+1}]^2 + [(Z_p)_{ip,\tau p} - (Z_B)_{\tau,b,i+1}]^2} \\
 (L)_{\tau,b,i} &= \sqrt{[(X_B)_{\tau,b,i+1} - (X_B)_{\tau,b,i}]^2 + [(Y_B)_{\tau,b,i+1} - (Y_B)_{\tau,b,i}]^2 + [(Z_B)_{\tau,b,i+1} - (Z_B)_{\tau,b,i}]^2}
 \end{aligned}$$

Table 4.2: Discretization equations for influence coefficients for bound circulation

$$\begin{aligned}
 GXI_{ip,\tau,p,k,b,i} &= \frac{[(r_1)_{ip,\tau,p,k,b,i} + (r_2)_{ip,\tau,p,k,b,i}] \cdot [[(Y_p)_{ip,\tau,p} - (Y)_{k+1,b,i}] [(Z)_{k+1,b,i} - (Z)_{k,b,i}] - [(Z_p)_{ip,\tau,p} - (Z)_{k+1,b,i}] [(Y)_{k+1,b,i} - (Y)_{k,b,i}]]}{2\pi \cdot (r_1)_{ip,\tau,p,k,b,i} \cdot (r_2)_{ip,\tau,p,k,b,i} \cdot [[(r_1)_{ip,\tau,p,k,b,i} + (r_2)_{ip,\tau,p,k,b,i}]^2 - [(L)_{k,b,i}]^2]} \\
 GYT_{ip,\tau,p,k,b,i} &= \frac{[(r_1)_{ip,\tau,p,k,b,i} + (r_2)_{ip,\tau,p,k,b,i}] \cdot [[(Z_p)_{ip,\tau,p} - (Z)_{k+1,b,i}] [(X)_{k+1,b,i} - (X)_{k,b,i}] - [(X_p)_{ip,\tau,p} - (X)_{k+1,b,i}] [(Z)_{k+1,b,i} - (Z)_{k,b,i}]]}{2\pi \cdot (r_1)_{ip,\tau,p,k,b,i} \cdot (r_2)_{ip,\tau,p,k,b,i} \cdot [[(r_1)_{ip,\tau,p,k,b,i} + (r_2)_{ip,\tau,p,k,b,i}]^2 - [(L)_{k,b,i}]^2]} \\
 GZI_{ip,\tau,p,k,b,i} &= \frac{[(r_1)_{ip,\tau,p,k,b,i} + (r_2)_{ip,\tau,p,k,b,i}] \cdot [[(X_p)_{ip,\tau,p} - (X)_{k+1,b,i}] [(Y)_{k+1,b,i} - (Y)_{k,b,i}] - [(Y_p)_{ip,\tau,p} - (Y)_{k+1,b,i}] [(X)_{k+1,b,i} - (X)_{k,b,i}]]}{2\pi \cdot (r_1)_{ip,\tau,p,k,b,i} \cdot (r_2)_{ip,\tau,p,k,b,i} \cdot [[(r_1)_{ip,\tau,p,k,b,i} + (r_2)_{ip,\tau,p,k,b,i}]^2 - [(L)_{k,b,i}]^2]} \\
 (r_1)_{ip,\tau,p,k,b,i} &= \sqrt{[(X_p)_{ip,\tau,p} - (X)_{k,b,i}]^2 + [(Y_p)_{ip,\tau,p} - (Y)_{k,b,i}]^2 + [(Z_p)_{ip,\tau,p} - (Z)_{k,b,i}]^2} \\
 (r_2)_{ip,\tau,p,k,b,i} &= \sqrt{[(X_p)_{ip,\tau,p} - (X)_{k+1,b,i}]^2 + [(Y_p)_{ip,\tau,p} - (Y)_{k+1,b,i}]^2 + [(Z_p)_{ip,\tau,p} - (Z)_{k+1,b,i}]^2} \\
 (L)_{k,b,i} &= \sqrt{[(X)_{k+1,b,i} - (X)_{k,b,i}]^2 + [(Y)_{k+1,b,i} - (Y)_{k,b,i}]^2 + [(Z)_{k+1,b,i} - (Z)_{k,b,i}]^2}
 \end{aligned}$$

Table 4.3: Discretization equations for influence coefficients for trailing circulation

the Biot-Savart equations. Note that in Eqts. 4.55 above, the induction components (u_x , u_y , u_z) are in the X-Y-Z reference frame. These are finally transformed into the moving x - y - z frame of reference using the following transformation:

$$\begin{bmatrix} (u_x)_{ip,\tau p} \\ (u_y)_{ip,\tau p} \\ (u_z)_{ip,\tau p} \end{bmatrix} = \begin{bmatrix} \cos((\phi)_{ip,\tau p}) & 0 & -\sin((\phi)_{ip,\tau p}) \\ 0 & 1 & 0 \\ \sin((\phi)_{ip,\tau p}) & 0 & \cos((\phi)_{ip,\tau p}) \end{bmatrix} \cdot \begin{bmatrix} \cos(\Psi) & \sin(\Psi) & 0 \\ -\sin(\Psi) & \cos(\Psi) & 0 \\ 0 & 0 & 1 \end{bmatrix} \cdot \begin{bmatrix} (u_x)_{ip,\tau p} \\ (u_y)_{ip,\tau p} \\ (u_z)_{ip,\tau p} \end{bmatrix} \quad (4.56)$$

where u_x , u_y and u_z are the tangential, axial and radial induction components respectively.

The above three steps are repeated for all rotor time steps ($\tau = 0..n_{tot}-1$). This yields a 3D induction distribution at the calculation plane at all azimuth steps of one whole rotor revolution.

4.3.4 Assessment of Wind Tunnel Blockage Effects

From the inflow measurements (refer to Figs. 4.18(a), 4.19 and 4.20, *see* section 4.2.2), it was required to derive the axial induced velocity components at the rotorplane by applying equation

$$u_a = w_a - U \cos(\Psi) \quad (4.57)$$

A major difficulty in finding the axial induced velocities was in establishing the true free-wind speed accurately (U) to be able to use it in Eq. 4.57. Due to the influences of tunnel blockage, the exit-jet velocity measured at three points using the pitot-static probes may be slightly different from the true-free wind speed. It will be shown later on in this section that a small difference in the value of U may yield to large errors in the derived axial induced velocities.

When a wind turbine is operating in a real open air environment, then the wake is allowed to expand freely, as illustrated in Fig. 4.41(a). Outside the wind turbine wake, the flow velocity may be considered to be uniform and equal to the free-wind speed. The flow characteristics across a wind turbine in a wind tunnel may therefore be considerably different than those that would be experienced if the same turbine is operating in an open air environment. This is because in a wind tunnel, the flow field is limited to a restricted flow channel. Such differences give rise to wind blockage effects. A major pre-requisite in wind tunnel testing is to achieve a flow environment that is as close as possible to that of an

open air environment. Precautions should therefore be taken to ensure that blockage influences are minimal. If not, then the measured results should be corrected. Physically, tunnel blockage is related to the momentum reduction in the wake. The amount of blockage will depend on the wind tunnel configuration used. In an open-jet wind tunnel (similar to the one used in this study), blockage effects are less than that in a closed section, since the turbine wake is less restricted from expanding (*see* Figs. 4.41(b) and (c)). Also, for a given tunnel configuration, tunnel blockage depends on the ratio of the cross-sectional area of the rotor to that of the test-section. The larger this ratio, the larger tunnel blockage effects tend to be. This ratio is often referred to the *blockage factor* (denoted here by B_F). For an open-jet tunnel, B_F is taken to be equal to A_{rotor}/A_{jet} . For this study on the TUDelft rotor, B_F was equal to 0.29.

Basically, two main blockage phenomena take place in an open-jet wind tunnel:

(1) Blockage due to Wake Boundary

If we consider a closed-section wind tunnel (*see* Fig. 4.41(b)), wake expansion is constrained by the tunnel walls. When the rotor is operating in a wind turbine state, the flow velocity w_a would be less than the free-stream velocity U . But since the same volume of air that passes any section upstream of the turbine must pass any section behind it, it follows that the velocity bypassing the rotor w_b (outside the slipstream) would be greater than U . In an open air environment, this w_b would be equal to U (Fig. 4.41(a)). For the closed test-section, the static pressure of the air bypassing the turbine would therefore be less than that of the undisturbed stream having velocity U . This influences the turbine so that it develops a thrust larger than would be developed in an unrestricted flow of the same speed with the same rotor angular speed and blade pitch. Alternatively, it can also be argued that the thrust developed would be equal to that produced when the turbine is operating in an open-air environment at a higher windspeed.

In an open-jet wind tunnel, the flow field is limited by the size of the jet. However, the jet is not constrained by walls and thus the turbine wake is allowed to expand more freely than in closed test section (*see* Fig. 4.41(c)). However if w_b at any point in the jet flow bypassing the turbine is not equal to U , then some wake boundary blockage will still be present. A simple first-order relation for w_b may be derived from basic actuator disk theory for a turbine in axial conditions in an inviscid and incompressible flow:

Consider two sections p and q in the fluid stream such that p is located far upstream from the rotor where the tunnel speed is equal to U while q is located at a downstream distance from the rotor (*see* Fig. 4.42). Let D_j be the diameter of the tunnel tube while D_j' be the diameter of the tunnel jet at section q . Let the diameter of the rotor wake at section q be D' . The flow velocity at section q is denoted by w_a' . Referring to Fig. 4.42

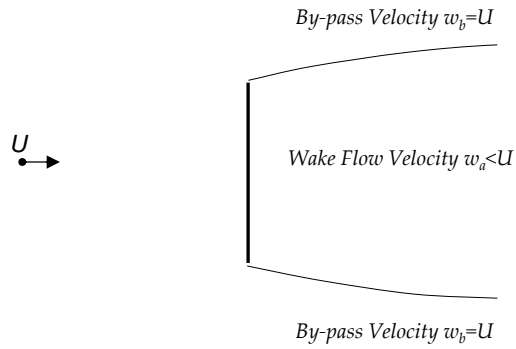


Fig (a) – Open air environment

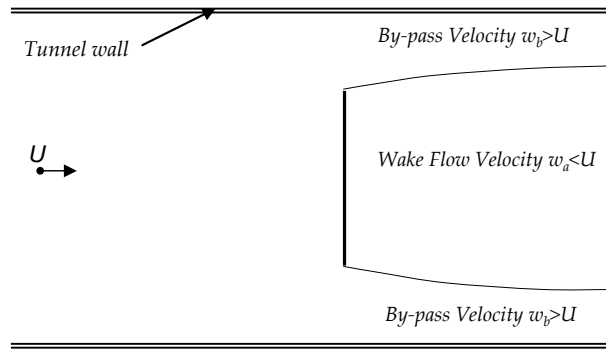


Fig (b) – Wind tunnel with closed test-section

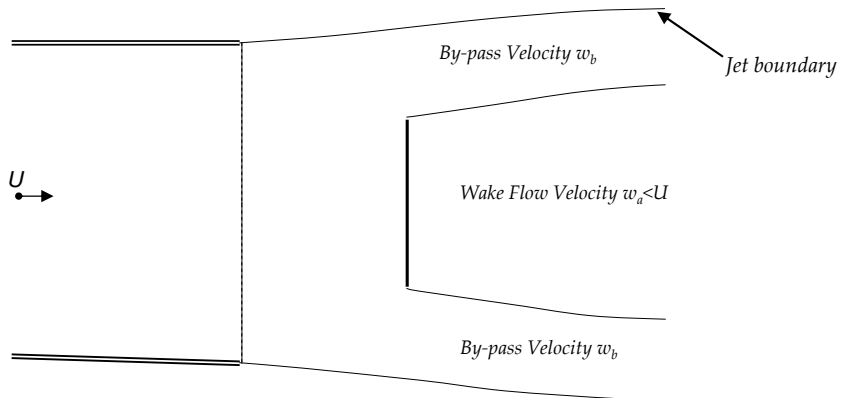


Fig (c) – Wind tunnel with open test-section

Figure 4.41: Wake developments in open air and in two different wind tunnel types (open and closed test-section).

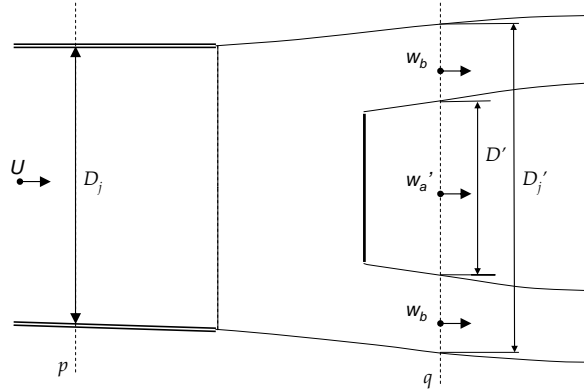


Figure 4.42 – Nomenclature for simple analysis of wind turbine in an open-jet wind tunnel.

and applying the volume continuity equation between sections p and q ,

$$D_j^2 U = D'^2 w_a' + (D_j'^2 - D'^2) w_b$$

$$\therefore w_b = \frac{U - \frac{D'^2}{D_j^2} w_a'}{1 - \frac{D'^2}{D_j^2}} \quad (4.58)$$

Let a_1' be the magnitude of the axial induction factor at section q

where

$$a_1' = \frac{w_a' - U}{U}$$

Dividing both sides of Eq. 4.58 by U and substituting for a_1' yields

$$\frac{w_b}{U} = \frac{1 - \frac{D'^2}{D_j^2} (1 + a_1')}{1 - \frac{D'^2}{D_j^2}} \quad (4.59)$$

It can be easily shown from Eq. 4.59 that for the wind turbine wake to reach the ideal wake boundary condition as that for an open air environment (i.e. $w_b/U=1$), the jet diameter at any distance from the rotorplane should expand in accordance with

$$D_j' = \frac{D_j}{\sqrt{1 + a_1'}} \quad (4.60)$$

Since for the normal operating state of a wind turbine $a_1' < 0$, then $D_j' > D_j$. Also from simple axial momentum considerations, a_1' will increase negatively downstream until it reaches a

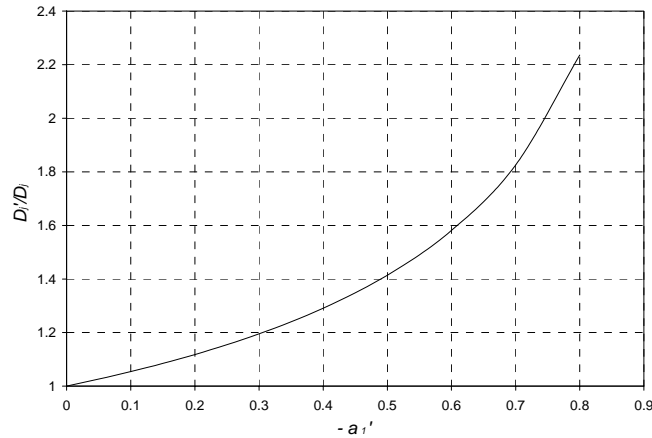


Figure 4.43 – Required open-jet expansion at different local axial induction factors as predicted by Eq. 4.60 to have the ideal situation where no wake blockage is present.

value that is double that at the rotorplane in the far wake. This implies that the tunnel jet diameter should increase gradually downstream in accordance with Eq. 4.60. Fig. 4.43 plots the required wake expansion with the local axial induction factor. In reality such a condition would be very difficult to obtain and consequently some wake blockage will always be present. Yet, the above analysis reveals that by having an open-jet tunnel instead of a tunnel with a closed test-section (where D_j' has to be maintained constant and equal to D_j), wake boundary blockage would be less significant. For yaw, the required jet expansion would be more complex (due to wake skew) and even more difficult to have.

(2) Blockage due to proximity of Rotor to Tunnel Exit Jet

When a wind turbine is placed in the jet of the wind tunnel, its presence will be also felt upstream of the rotorplane. In fact, the retardation of the flow starts way upstream from the rotor, as shown in Fig. 4.44. Thus if the rotor is placed close to the tunnel exit where the pitot readings (U_{jet}) are taken, the latter will not measure the true free-stream velocity. In addition, the rotor will cause the tunnel exit velocity distribution to become non-uniform. The non-uniformity becomes more complex when the rotor is yawed. This effect is illustrated pictorially in Figs. 4.45(a) and (b). This severity of this type of blockage depends on the blockage factor (B_F), the distance of the rotor from the tunnel exit, the rotor geometry and the operating condition. The rotor geometry and operating condition will determine the thrust exerted by the rotor on the fluid stream. A higher operating thrust will make the pitot-readings more susceptible to this type of blockage. In yawed conditions, this effect could be more severe for two reasons: first because the

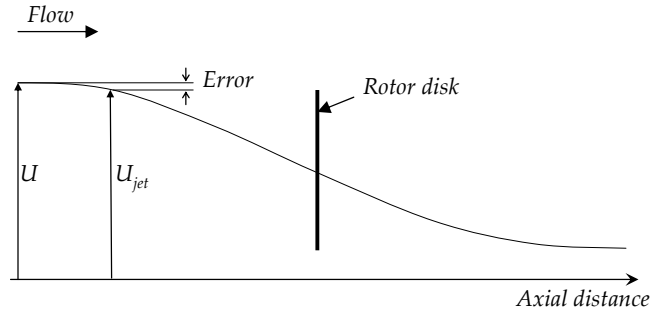


Figure 4.44 – Discrepancy between U_{jet} and U due to proximity of rotor to pitot-tubes.

upwind blade will be closer to the tunnel exit. Secondly, the skewed wake causes an uneven induction at the tunnel exit. The skewed wake induction at the blades causes the local axial thrust at the blades to be higher between azimuth angles 180° and 360° , than over the rest of the rotorplane. This may be observed in Fig. 4.46 where a predicted distribution of the local blade axial thrust (in dimensionless form) is shown as a function of blade azimuth angle for the TUDelft rotor at a yaw angle of 30° . This distribution was predicted using an acceleration potential code by van Bussel [15].

Ideally, the rotor should be placed well downstream of the tunnel exit such that it will not influence the jet velocity distribution at the tunnel exit. However, doing so will cause the inflow at the rotor to have a higher turbulence level. This is due to the fact that as the tunnel jet expands downstream, the turbulence level generally increases. In this study the rotor was placed 1m downstream of the tunnel exit.

In effect, the influences of tunnel blockage due to wake boundary and that due to the proximity of the rotor to the exit jet cannot be considered in isolation. In fact it is possible that the combined action of the two may reduce the uncertainty in taking U_{jet} equal to U . One physical explanation would be the following: Referring to Fig. 4.42, blockage due to wake boundary may cause w_b to be higher than U if the jet expansion remains small. This may cause the local flow at the pitot to become higher than U . On the other hand, tunnel blockage due to rotor proximity to the tunnel exit may cause the local flow at the pitot to become less than U . In this case the combined action will help in reducing uncertainty. However, it may happen that the proximity of the rotor to the jet may also help to speed up the flow at the pitot. As a result, both blockage types will increase uncertainty levels.

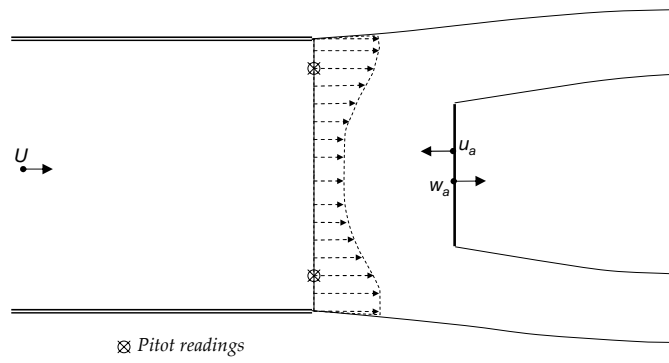


Fig (a) – Axial Conditions

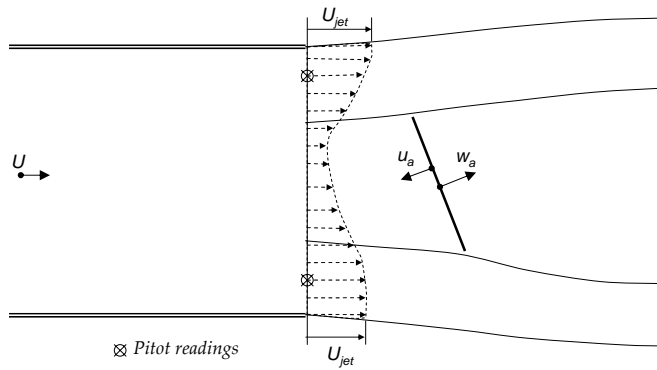


Fig (b) – Yawed Conditions

Figure 4.45 –Influence of rotor on tunnel exit jet velocity distribution.

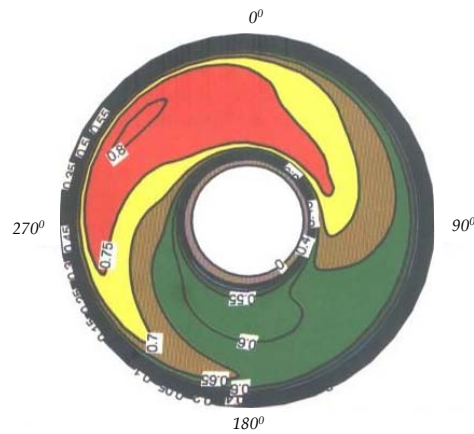


Figure 4.46 – Variation of the local axial thrust coefficient with blade azimuth angle for $\Psi=30^\circ$ for the TUDelft rotor as predicted by an acceleration potential method. (Source: van Bussel [15]).

Quantification of Error in the Computed Axial Induced Velocity due to Error in U_{jet}

As already outlined before, tunnel blockage makes it difficult to determine the true free-stream velocity. The true free-stream velocity at any point in the cross-section of the tunnel tube may differ from that measured using the pitot-static tubes at the tunnel exit jet. Using a simple actuator disk model, it may be shown mathematically that very large errors in the derived axial induced velocity may result when the latter is calculated on the assumption that the free-wind speed (U) is equal to that measured by the pitot-static tubes at the tunnel exit (U_{jet}):

Let k_c be equal to the ratio of the exit jet velocity to the true free stream velocity (i.e. $k_c=U_{jet}/U$). Let $w_{a,exp}$ be equal to the measured axial flow velocity at the rotor disk. Let u_a be the axial induced velocity at the rotor disk derived using the assumption that U_{jet} is equal to the true free-stream velocity (U). Let u_a^* be the axial induced velocity derived using the true free-stream velocity (U). Then

$$u_a = w_{a,exp} - U_{jet} \cos(\Psi) \quad (4.61a)$$

$$u_a^* = w_{a,exp} - U \cos(\Psi) \quad (4.61b)$$

$$= w_{a,exp} - \frac{U_{jet}}{k_c} \cos(\Psi) \quad (4.61c)$$

The percentage error introduced by finding the axial induced velocity using U_{jet} instead of U will then be equal to:

$$\mathcal{E}_{k_c} = \frac{u_a - u_a^*}{u_a^*} \cdot 100 \quad (4.62)$$

Substituting Eq. 4.61(c) in Eq. 4.62 yields

$$\mathcal{E}_{k_c} = \frac{U_{jet} \cos(\Psi)(1 - k_c)100}{k_c w_{a,exp} - U_{jet} \cos(\Psi)} \quad (4.63)$$

Since for a wind turbine the axial flow velocity decreases continuously downstream then $k_c w_{a,exp} < U_{jet} \cos(\Psi)$ where $k_c > 0$. If the tunnel blockage causes the local velocity at the pitot probes to be less than the true free windspeed, then $k_c < 1$. On the other hand if tunnel blockage causes a speed-up in the flow local to the probes, then $k_c > 1$. Fig. 4.47 plots the variation of error \mathcal{E}_{k_c} with k_c in accordance with Eq. 4.63 for $U_{jet}=5.5$ m/s and for different yaw angles and axial flow velocities (w_a). The error in the axial induced velocity will be larger at lower values of k_c , larger yaw angles and at higher measured values of w_a . Note that for $k_c=1$, the error is equal to zero since for this condition the exit jet velocity is equal to the true free-stream velocity. It can be easily observed from Fig. 4.47 that a small deviation of exit jet velocity from the true free-wind speed could possibly yield a large error in the

estimation of the axial induced velocity. For instance at yaw 45° , a 10% deviation of U_{jet} (i.e. $k_c=0.9$) from the true free-stream velocity may easily result in a 30% error in u_a . This provides evidence that special care should be taken when assuming U_{jet} to be equal to the free-stream velocity and that it is crucial to know the free-stream velocity accurately if accurate prediction of the induced velocity is to be estimated. A very important note to make is that, apart from tunnel blockage, the non-uniformity in velocity distribution of the tunnel exit jet (shown in Fig. 4.5, page 49) also cause the true-free windspeed to be different from that measured by the probes. It could be easily observed from Fig. 4.5, that a k_c value of 0.93 can be easily presented due to tunnel exit jet non-uniformity. If additionally tunnel blockage is present such that it contributes to a k_c value of 0.95, then the total effective k_c value would be equal to $0.93 \times 0.95 = 0.884$. From Fig. 4.47, it is seen that the later value yields a percentage error in u_a of around 20-25%, which is considerable.

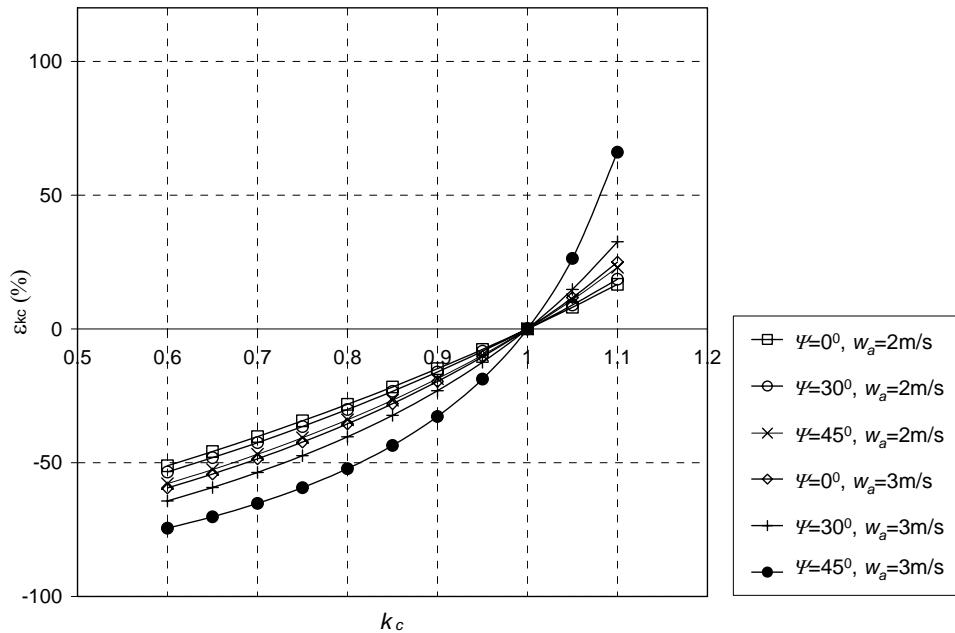


Figure 4.47 – Variation of ε_{k_c} with k_c for different yaw angles and measured inflow velocities ($w_{a,exp}$). The results are calculated for $U_{jet} = 5.5\text{m/s}$ since during all measurements, the tunnel speed was set such that the pitot-readings measured this wind speed.

Procedures for Assessing Influences due to Tunnel Blockage

Two separate computational procedures were adopted to assess the extent to which the inflow measurements on the TUDelft rotor could have been affected by tunnel blockage. The procedures are illustrated in Fig. 4.48. Both procedures make use of the prescribed

vortex model *HAWT_PVC* on the assumption that this model is reasonably accurate for modelling the wake inflow distributions for both axial and yawed conditions. Re-call that in this code a bound circulation (which may vary with blade azimuth angle) is prescribed to calculate the induced velocity distribution at a given plane.

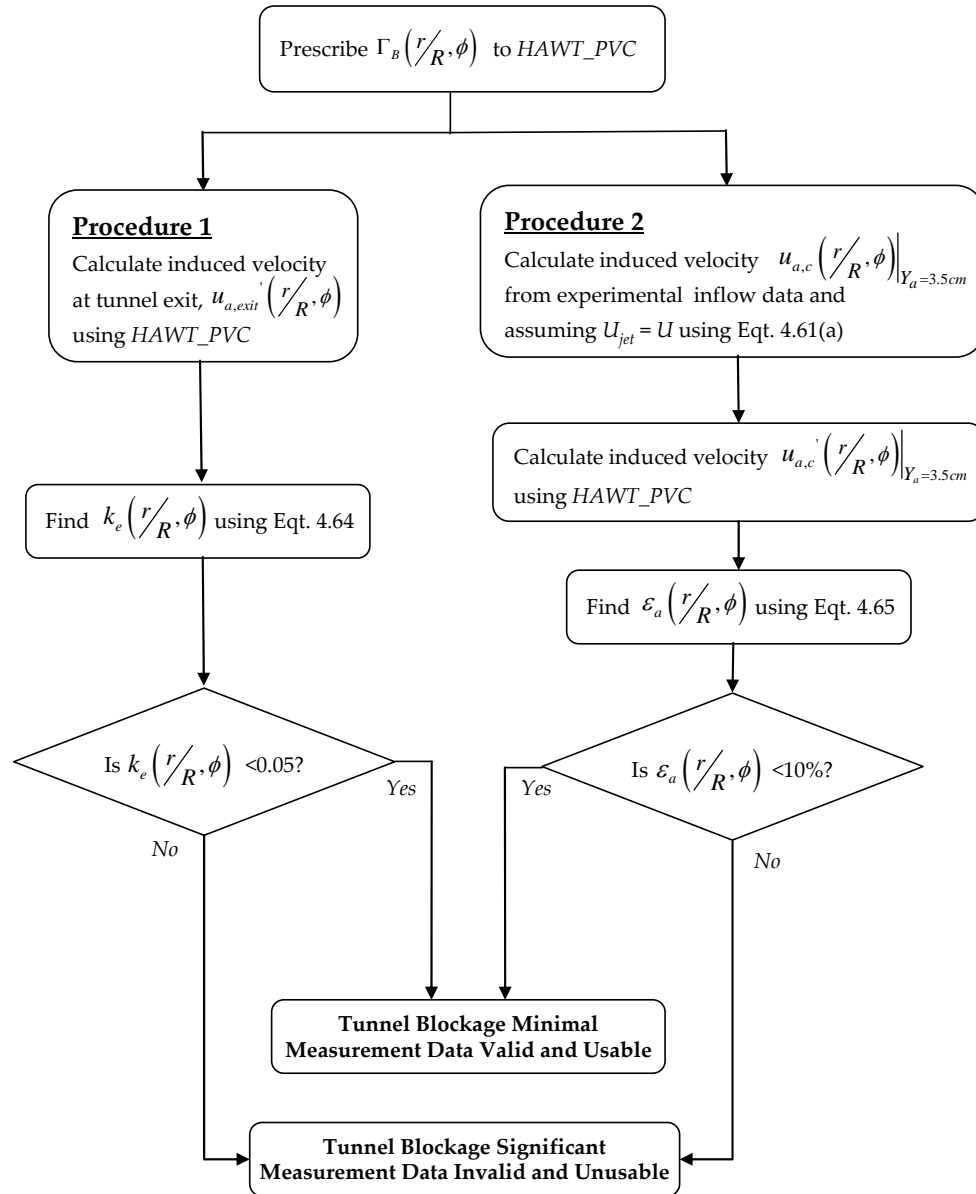


Figure 4.48 - Two procedures used to assess the inflow measurements for influences due to tunnel blockage.

Since in this code, the modelled vorticity is only due to the rotor, then it may be argued that the computed induced velocities are equivalent to those which would have been obtained should the rotor was operating in an open air environment (i.e. no blockage) with the same bound circulation at the blades.

In both assessment procedures, the bound circulation derived directly from the inflow measurements using *HAWT_LFIM* is prescribed to vortex code *HAWT_PVC*. In Procedure 1 the vortex code computes the tunnel exit axial velocity distribution, $u_{a,exit} \left(\frac{r}{R}, \phi \right)$. The ratio of this velocity to that measured using the pitot probes is evaluated using

$$k_e \left(\frac{r}{R}, \phi \right) = \left| \frac{u_{a,exit} \left(\frac{r}{R}, \phi \right)}{U_{jet}} \right| \quad (4.64)$$

In ideal conditions (no-blockage), this ratio should be equal to zero. But this would not be the case if blockage due to rotor proximity to the tunnel exit is present (refer to Fig. 4.44). Also tunnel non-uniformity may cause the velocity at some locations in the jet exit to be higher than U_{jet} . This would lead to a higher wake circulation whose induction is felt more at the tunnel exit. In this study, it was decided to limit k_e to 0.05. If it was higher, then the measurement data would be invalid and unusable or a correction to the data would be required.

In Procedure 2, the axial induced velocities at the 3.5cm downstream plane are derived from the experimental measurements using the assumption that the pitot U_{jet} is equal to the free-stream velocity (using Eq. 4.61(a)). These are then compared with that computed by *HAWT_PVC* for the same plane, $u_{a,c} \left(\frac{r}{R}, \phi \right)$. The two induced velocities are compared along the different points in the 3.5cm plane and the relative error is found using

$$\varepsilon_a \left(\frac{r}{R}, \phi \right) = \frac{u_{a,c} \left(\frac{r}{R}, \phi \right) \Big|_{y_a=3.5cm} - u_{a,c} \left(\frac{r}{R}, \phi \right) \Big|_{y_a=3.5cm}}{u_{a,c} \left(\frac{r}{R}, \phi \right) \Big|_{y_a=3.5cm}} \quad (4.65)$$

Assuming that the results for Γ_b derived in accordance with Fig. 4.33 and *HAWT_PVC* are reasonably accurate, the error in the equation above should mainly be in using Eq. 4.61(a) to find $u_{a,c} \left(\frac{r}{R}, \phi \right)$. Considering that the values for $w_{a,exp}$ are accurate, it follows that the main source of error in ε_a is due to the U_{jet} (i.e. the pitot reading). In ideal conditions, this should be zero. Note that in this assessment method, error ε_a is based on the induced velocities at 3.5cm downstream and not those at the rotorplane to reduce the uncertainties due to the linear interpolation that was required to estimate $w_{a,c}$ at the rotorplane (Eq. 4.7).

4.3.5 Quantification of Errors in Deriving Blade Loading due to Errors in Inflow Measurements

As already outlined before, in this work related to the TUDelft turbine, the main objective was to investigate an approach for deriving the aerodynamic loading distributions at the blades from hot-film inflow measurements in attached flow conditions. In this analysis, it was therefore very important to investigate the uncertainty in the derived blade loading resulting from errors in $w_{a,c}$ which is directly obtained from the hot-film measurements. It was also necessary to investigate how this uncertainty is influenced by other parameters such as the blade radial location and pitch angle.

Consider a blade element at a given blade azimuth position and yaw angle. Assume that the local angle of attack is small and does not exceed the stall angle. Neglecting the effects of unsteady flow over the blades, the lift coefficient may be approximated to $C_l=2\pi\alpha$. The local lift loading in N/m may then be expressed as

$$f_L = \frac{dL}{dr} = \rho\pi\alpha c V^2 \quad (4.66)$$

Taking $w_{a,c}$ as the axial flow velocity at the blade lifting line obtained from the measurements using linear interpolation (see Eq. 4.7 and Figs. 4.18(a), 4.19 and 4.20) and substituting Eq. 4.11 and 4.12 in Eq. 4.66,

$$f_L = \rho\pi c \left(w_{a,c}^2 + r^2\Omega^2 \right) \left(\tan^{-1} \left(\frac{w_{a,c}}{r\Omega} \right) - \theta \right) \quad (4.67)$$

Relation $\tan^{-1} \left(w_{a,c}/r\Omega \right)$ is equal to the local inflow angle (φ) and this can be expanded in series form as follows

$$\varphi = \tan^{-1} \left(\frac{w_{a,c}}{r\Omega} \right) = \frac{w_{a,c}}{r\Omega} - \frac{1}{3} \left(\frac{w_{a,c}}{r\Omega} \right)^3 + \frac{1}{5} \left(\frac{w_{a,c}}{r\Omega} \right)^5 - \frac{1}{7} \left(\frac{w_{a,c}}{r\Omega} \right)^7 + \dots \quad (4.68)$$

Since for the TUDelft turbine, $w_{a,c} \ll r\Omega$ at all radial locations, then we can neglect terms $\left(w_{a,c}/r\Omega \right)^3$ and higher. Thus Eq. 4.67 becomes

$$f_L \approx \rho\pi c r^2 \Omega^2 \left(1 + \frac{w^2}{r^2\Omega^2} \right) \left(\frac{w}{r\Omega} - \theta \right) \quad (4.69)$$

Neglecting the drag on the blades (this assumption is reasonable for $1 < \alpha < 12$ deg for the NACA0012 aerofoil), the axial thrust (N/m) and torque (Nm/m) loading at a given radial location on the blades as equal to

$$f_T = \frac{dT}{dr} = f_L \cos(\varphi) \quad (4.70a)$$

$$f_Q = \frac{dQ}{dr} = r \times f_L \sin(\varphi) \quad (4.70b)$$

where φ is the inflow angle. Terms $\cos(\varphi)$ and $\sin(\varphi)$ may also be expanded in series form as

$$\begin{aligned} \cos(\varphi) &= 1 - \frac{1}{2!} \left(\frac{w_{a,c}}{r\Omega} \right)^2 + \frac{1}{4!} \left(\frac{w_{a,c}}{r\Omega} \right)^4 - \dots \\ \sin(\varphi) &= \frac{w_{a,c}}{r\Omega} - \frac{1}{3!} \left(\frac{w_{a,c}}{r\Omega} \right)^3 + \frac{1}{5!} \left(\frac{w_{a,c}}{r\Omega} \right)^5 - \dots \end{aligned} \quad (4.71)$$

Substituting Eqts. 4.71 in Eqts. 4.70 and neglecting terms $(w_{a,c}/r\Omega)^3$ and higher, the axial thrust and torque loading can then be approximated to

$$f_T \approx \rho \pi c r^2 \Omega^2 \left(\frac{w_{a,c}}{r\Omega} - \theta - \frac{w_{a,c}^2 \theta}{2r^2 \Omega^2} \right) \quad (4.72)$$

$$f_Q \approx \rho \pi c r^2 \Omega w_{a,c} \left(\frac{w_{a,c}}{r\Omega} - \theta \right) \quad (4.73)$$

The percentage error in f_T due to an error in measured $w_{a,c}$ at a given radial location on a blade could be simply found from

$$\mathcal{E}_T = \frac{f_T|_{w_{a,c} + \delta w_{a,c}} - f_T|_{w_{a,c}}}{f_T|_{w_{a,c}}} 100 \quad (4.74)$$

Alternatively, for small values in $\delta w_{a,c}$ only, the percentage error \mathcal{E}_T is given by

$$\mathcal{E}_T \approx \frac{\partial f_T}{\partial w_{a,c}} \frac{\mathcal{E}_{w_{a,c}}}{f_T} w_{a,c} \quad (4.75)$$

where $\mathcal{E}_{w_{a,c}}$ is the percentage error in $w_{a,c}$ given by

$$\mathcal{E}_{w_{a,c}} = \frac{\delta w_{a,c}}{w_{a,c}} 100 \quad (4.76)$$

From Eqts. 4.72 and 4.75, it follows that

$$\mathcal{E}_T \approx \frac{\left(\frac{1}{r\Omega} - \frac{w_{a,c} \theta}{r^2 \Omega^2} \right) \mathcal{E}_{w_{a,c}} w_{a,c}}{\left(\frac{w_{a,c}}{r\Omega} - \theta - \frac{w_{a,c}^2 \theta}{2r^2 \Omega^2} \right)} \quad (4.77)$$

For the condition in which the local blade pitch angle, θ , is equal to zero, it can be concluded that $\mathcal{E}_T \approx \mathcal{E}_{w_{a,c}}$. This implies that when using the inflow measurements to find the axial thrust loading, the error in the loading remains approximately equal to that in $w_{a,c}$. This only holds when the local pitch angle is zero. For other pitch angles however, Eq. 4.77 shows that for constant speed Ω , the percentage error in the thrust loading, \mathcal{E}_T , is dependent on parameters $w_{a,c}$, r and θ . Fig. 4.49(a) shows that variation of \mathcal{E}_T with $\mathcal{E}_{w_{a,c}}$ at different values of θ and $w_{a,c}$ while keeping $r\Omega$ constant. It is noted that, at a given value of $\mathcal{E}_{w_{a,c}}$, error \mathcal{E}_T is very much dependent on the values of θ and $w_{a,c}$.

A more important observation concerns the fact that in many situations, a small error in $w_{a,c}$ may yield a significantly larger error in the derived loading. When $w_{a,c}/r\Omega$ becomes close to θ , \mathcal{E}_T becomes very large, even when $\mathcal{E}_{w_{a,c}}$ is small. In fact, this is the condition when the local angle of attack is small and thus the thrust loading (f_t) approaches zero. This is a very important issue that needs serious consideration when deriving blade loads from inflow measurements.

Therefore one can conclude that despite the fact that for attached flow conditions (low angles of attack at the blades), the uncertainty in the aerofoil data is small, the uncertainty in the derived loading due to measurement errors in $w_{a,c}$ may be large. On the contrary, when dealing with high angles of attack, the uncertainty due to $w_{a,c}$ is small, but that due to the aerofoil data may be large (especially when dealing with highly stalled flows).

Fig. 4.49(b) shows the spanwise variation of \mathcal{E}_T for $\mathcal{E}_{w_{a,c}} = 8\%$ and a pitch angle variation (θ) and speed (Ω) equal to those of the TUDelft rotor in the hot-wire measurements (i.e. $\Omega=720\text{rpm}$ and $\theta_{ip}=2^\circ$). The results are shown for two values of $w_{a,c}$ (equal to 2 and 3m/s) which are on the order of magnitude of those derived in the wind tunnel. It can be easily noted that a small variation in $w_{a,c}$ has a significant effect on \mathcal{E}_T and may cause it to be much larger than $\mathcal{E}_{w_{a,c}}$. In Figs. 4.49(a) and (b), the results for \mathcal{E}_T were computed both with the exact equation 4.74 and the approximate equation 4.77. But the results from the two equations were found to be nearly equal.

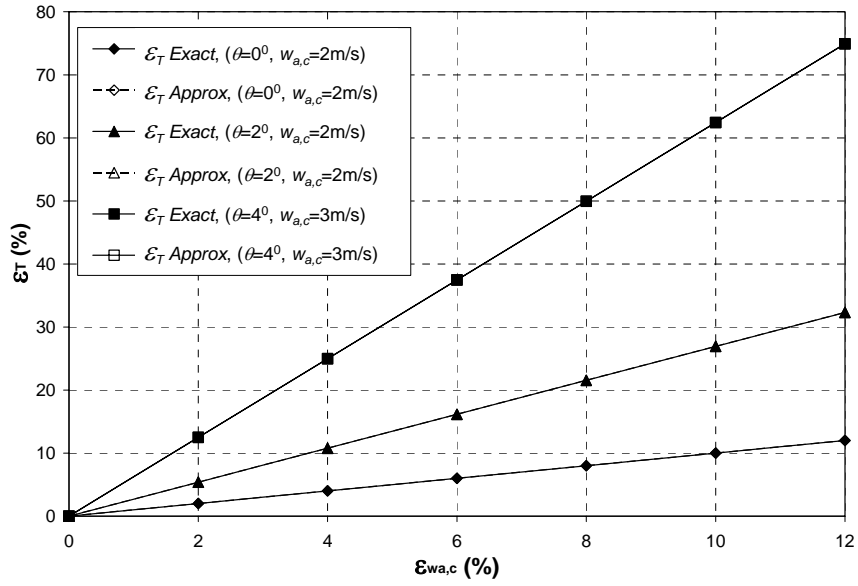


Figure 4.49(a) – Variation of error due to axial thrust loading against the error in $w_{a,c}$. $r/R=0.5$, $\Omega=720rpm$.

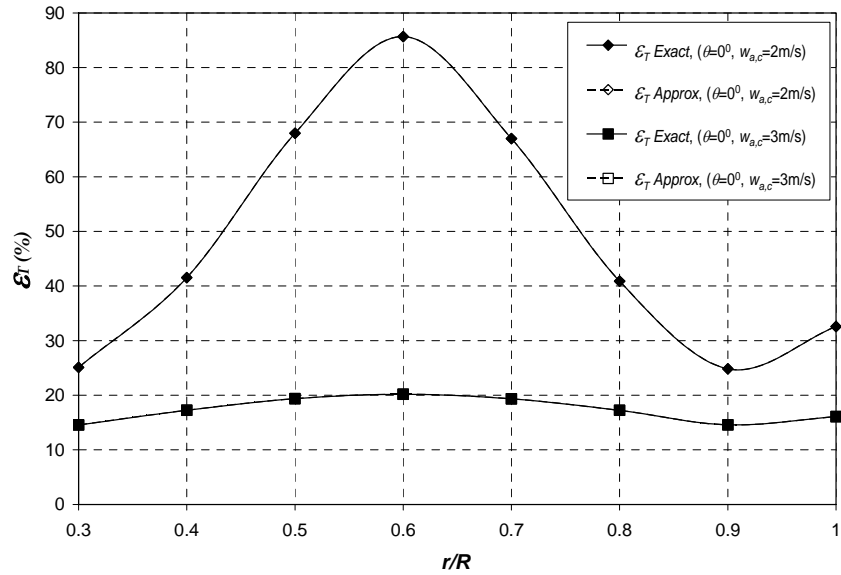


Figure 4.49(b) – Spanwise variation of the error due to axial thrust loading for $\mathcal{E}_{w_{a,c}}=8\%$. $\Omega=720rpm$. Spanwise variation of θ is equal to that of the TUDelft rotor with $\theta_{tip}=2^\circ$.

Applying a similar approach to the torque loading f_Q , the percentage error in f_Q due to an error in measured $w_{a,c}$ at a given radial location and blade could simply be found from

$$\varepsilon_Q = \frac{f_Q|_{w_{a,c} + \delta w_{a,c}} - f_Q|_{w_{a,c}}}{f_Q|_{w_{a,c}}} 100 \quad (4.78)$$

Alternatively, for small values in $\delta w_{a,c}$ only, the percentage error ε_Q is given by

$$\varepsilon_Q \approx \frac{\partial f_Q}{\partial w_{a,c}} \frac{\varepsilon_{w_{a,c}}}{f_Q} w_{a,c} \quad (4.79)$$

From Eqts. 4.73 and 4.79, it follows that

$$\varepsilon_Q \approx \frac{\left(\frac{2w_{a,c}}{r\Omega} - \theta \right) \varepsilon_{w_{a,c}}}{\left(\frac{w_{a,c}}{r\Omega} - \theta \right)} \quad (4.80)$$

It can be easily observed from the equation above that ε_Q is always larger than $\varepsilon_{w_{a,c}}$ which concludes that the error in the derived torque loading would always be larger than that in the inflow measurements. For the condition in which the local blade pitch angle, θ , is equal to zero, it can be concluded that $\varepsilon_Q \approx 2\varepsilon_{w_{a,c}}$. Thus the error is doubled. For a given radial location and operating condition, the error in torque loading due to $\varepsilon_{w_{a,c}}$ is therefore higher than that in the axial thrust loading. This result indicates more difficulties in maintaining accuracy when deriving the rotor torque and power coefficients from the inflow measurements. Figs. 4.50(a) and (b) are plots similar to Figs. 4.49(a) and (b) but ε_Q is shown instead. It can be observed that the values of ε_Q are larger than those of ε_T . In these figures, the results for ε_Q are computed both with the exact equation 4.78 and the approximate equation 4.80. The results from the two equations differ marginally, especially at larger values of $\varepsilon_{w_{a,c}}$. From Eq. 4.80, it can be shown that as $w_{a,c}/r\Omega$ approaches θ , then ε_Q becomes much larger than $\varepsilon_{w_{a,c}}$.

To summarise, from the above analysis it can be concluded that when deriving the axial thrust and torque loading distributions from measured inflow values ($w_{a,c}$), the uncertainties in these derived distributions due to errors in the inflow measurements is largest at low angles of attack. For a given inflow measurement error, the resulting error in the torque loading is larger than that for axial thrust. In a yawed rotor conditions, the values of $w_{a,c}$ at a fixed windspeed and rotor speed are smaller than for non-yawed

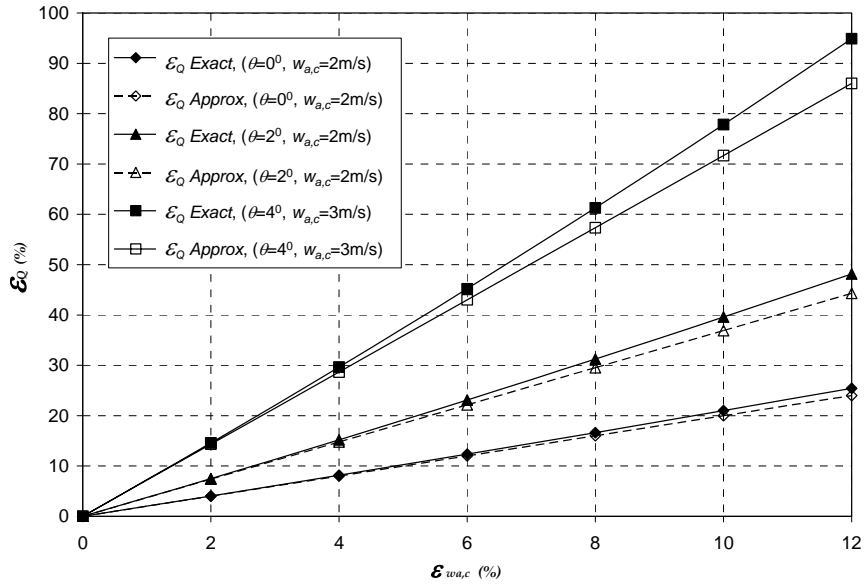


Figure 4.50(a) – Variation of error due to torque loading against the error in $w_{a,c}$. $r/R=0.5$, $\Omega=720\text{rpm}$.

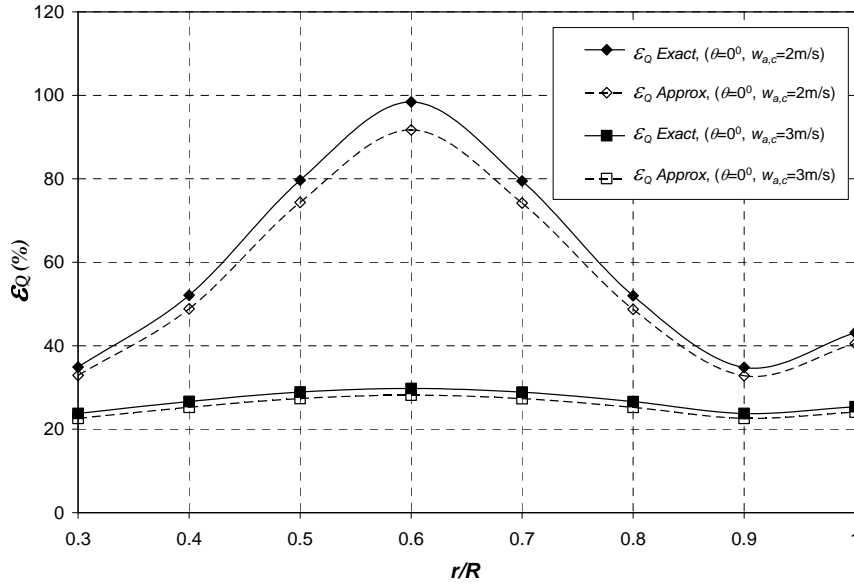


Figure 4.50(b) – Spanwise variation of the error due to axial thrust loading for $\mathcal{E}_{w_{a,c}}=8\%$. $\Omega=720\text{rpm}$. Spanwise variation of θ is equal to that of the TUDelft rotor with $\theta_{tip}=2^\circ$.

conditions. This results in a smaller angle of attack at some blade azimuth positions and hence the uncertainties in the derived loading due to errors in the inflow measurements would be larger. For this reason, it is more difficult to derive the loading distributions for inflow measurements when treating yawed conditions. Following this analysis, one might ask why the hot-film measurements carried out in this study were not accomplished with a lower rotor tip speed ratio (instead of $\lambda=8$) or at a smaller tip pitch angle (instead of $\theta_{tip}=2^\circ$) so as to increase the local angles of attack at the blades and hence reduce the uncertainties in the derived loading due to the measurement errors. The reasons for not doing so are two: first of all larger angles of attack could easily result in stall in some radial locations on the blades. This would generate high turbulence levels in the near wake which would otherwise increase the error in inflow measurements themselves. Secondly, it is very difficult to model the aerofoil data accurately in stalled conditions, especially when the rotor is yawed.

4.3.6 Results and Discussion

This section presents the results for aerodynamic flow parameters and blade loads that were derived for the TUDelft rotor using *HAWT_LFIM*. The wind tunnel inflow values for $w_{a,c}$ at the rotorplane estimated directly from the hot-film measurements by linear interpolation, (see Figs. 4.18(a), 4.19 and 4.20) were used in conjunction with the unsteady aerofoil model (described in section 4.3.2) in accordance with the procedure described in section 4.3.1. The parameters were computed for different azimuth positions (at 15° increments) over one whole revolution of the rotor.

A. Uncertainty Analysis

The first-order analysis of section 4.3.5 has shown that the uncertainty in the derived blade loading is very sensitive to the uncertainty in the inflow measurements used. In section 4.2.2 (page 67), the sources of error in the hot-film measurements were outlined and the uncertainty in these measurements was estimated to be in the order of 6-10% for $\Psi=0^\circ$. In the calculations using *HAWT_LFIM*, it was necessary to introduce a more elaborate uncertainty analysis to be able to quantify the resulting errors in each derived parameter (e.g. the derived angle of attack or aerodynamic thrust loading) due to errors in the measured data. Also the possible presence of significant tunnel blockage could only add to the uncertainty in the data. Tunnel blockage effects were however assessed and, as it will be explained later on, they were found to be negligible.

Uncertainty Analysis in Axial Conditions

For axial conditions, an uncertainty analysis was carried out by deriving the parameters at the different blade azimuth angles over one whole revolution (at 15° increments) taking into account the deviations in $w_{a,c}$. The mean value and standard deviation of each parameter across the whole revolution were then estimated for the different radial locations (40, 50, 60, 70, 80 and 90%R). The standard deviation was taken as a measure of the uncertainty due to measurement errors.

Uncertainty Analysis in Yawed Conditions

For yawed conditions, the uncertainty analysis is much more difficult to accomplish than in axial conditions because the parameters are known to be a function of ϕ . However, as already remarked in section 4.2.2 (page 68), it is reasonable to assume that the uncertainty in $w_{a,c}$ for yawed conditions would be equal to that in $\Psi=0^\circ$, i.e. in the range of 6-10%.

For the calculations with *HAWT_LFIM*, an uncertainty of $\pm 0.26\text{m/s}$ and $\pm 0.21\text{m/s}$ in $w_{a,c}$ was assumed at $\Psi=30^\circ$ and 45° , respectively. This is equivalent to about $\pm 8\%$ of the azimuthally averaged value of $w_{a,c}$ at each radial location. The calculations were performed for three

different sets of $w_{a,c}$ at the rotorplane: (1) with the values of $w_{a,c}$ shown in Figs. 4.19 and 4.20; (2) same as (1) but with each $w_{a,c}$ value increased by 0.26m/s and 0.21m/s at $\psi=30^\circ$ and 45° , respectively; (3) same as (1) but with each $w_{a,c}$ value decreased by 0.26m/s and 0.21m/s at $\psi=30^\circ$ and 45° , respectively.

B. HAWT_LFIM Results for Axial Conditions

This section presents the results that were obtained for the blade aerodynamic parameters in axial conditions (i.e. $\psi=0^\circ$). The mean values obtained over one whole revolution are plotted together with error bars denoting the corresponding \pm one standard deviation from the mean.

B.1 Derivation of spanwise distributions of angle of attack, flow relative velocity and bound circulation

Fig. 4.51 illustrates the angle of attack (α) distribution obtained for axial conditions using Eq. 4.11 computed at radial locations 40, 50, 60, 70, 80 and 90% R . The mean angle of attack is small at each radial location and is much smaller than the stalling angle for the NACA 0012 aerofoil (which is equal to 11° at a Reynolds number of 150,000). This provides evidence that the flow over the blades is fully attached. The corresponding flow relative velocity (V_r) distribution computed using Eq. 4.12 is shown in Fig. 4.52. For V_r , the standard deviation was found to be negligible due to the fact that for this study $r\Omega \gg U$ at all radial locations.

The angle of attack values of Fig. 4.51 were used in the unsteady aerofoil model presented in section 4.3.2. For axial conditions, the angle of attack was almost constant with blade

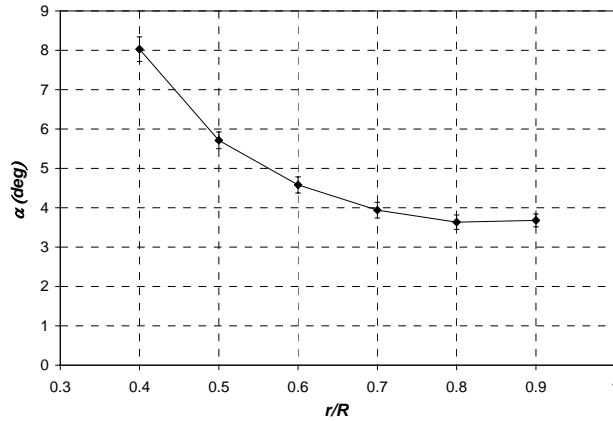


Figure 4.51 – Distribution of angle of attack ($U=5.5\text{m/s}$, $\Omega=700\text{rpm}$, $\theta_{ip}=2^\circ$).

azimuth angle, the slight fluctuations mainly being due to the non-uniformity in the tunnel exit jet. The lift coefficient could be approximated to the incompressible equation for attached flow: $C_l=2\pi\alpha$. The bound circulations at 40, 50, 60, 70, 80 and 90%R were then found from the Kutta-Joukowski law Eq. 4.13. These results are plotted in Fig. 4.53 where they are referred by curve ' $Y_a=0$ cm'.

As already outlined before, these results were calculated using the values for $w_{a,c}$ estimated at the rotorplane using linear interpolation of those at $Y_a=-6$ cm and at $Y_a=3.5$ cm. To investigate the sensitivity of $\Gamma_{B,2D}$ due to changes in $w_{a,c}$, the same calculations were also performed using the measured $w_{a,c}$ values at $Y_a=3.5$ cm. The resulting $\Gamma_{B,2D}$ values are also included in Fig. 4.53 where they are referred to by ' $Y_a=3.5$ cm'. Considerable differences

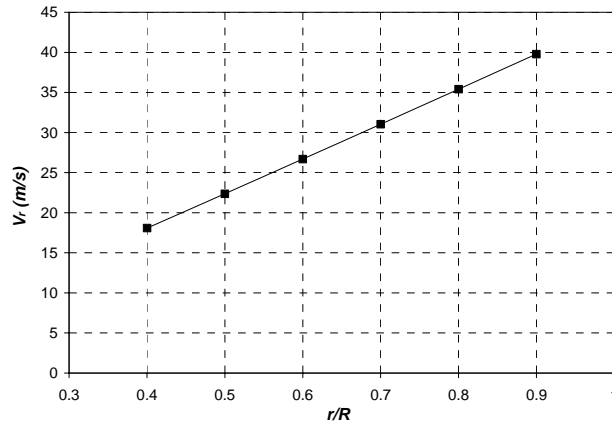


Figure 4.52 – Distribution of flow velocity relative to moving blades ($U=5.5$ m/s, $\Omega=700$ rpm, $\theta_{ip}=2^\circ$).

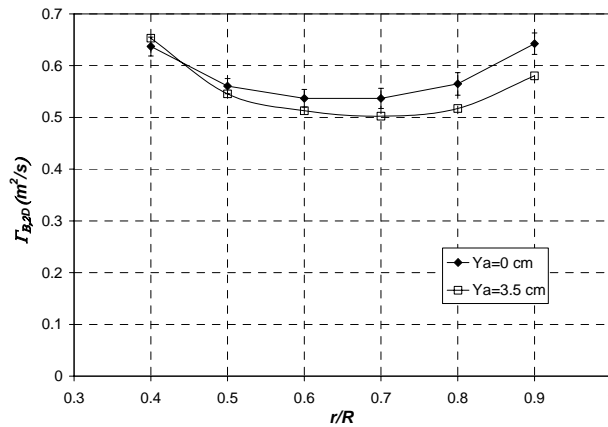


Figure 4.53 – Distribution of bound circulation distribution estimated using 2D lift coefficient ($U=5.5$ m/s, $\Omega=700$ rpm, $\theta_{ip}=2^\circ$).

were found, especially towards the outboard sections. This indicates the importance of estimating the inflow at the rotorplane using both upstream and downstream measurements. For the operating condition being tested, the change in $\Gamma_{B,2D}$ resulting from the use of $w_{a,c}$ values at $Y_a=3.5\text{cm}$ instead of those estimated for $Y_a=0\text{cm}$ is not mainly due to changes in V_r (since $r\Omega \gg w_{a,c}$), but due to the angle of attack that is sensitive to changes in $w_{a,c}$.

B.2 Extrapolated Bound Circulation Distribution Corrected for Tip and Root Loss

A major difficulty encountered was to derive an extrapolated bound circulation distribution across the whole blade span (from 30% to 100% R) from the point values at 40, 50, 60, 70, 80 and 90% R . The derived bound circulation at locations 40% and 90% R was found to be rather unrealistically high (see Fig. 4.53), even though the angle of attack was derived directly from the inflow measurements. This is because these two locations are very close to the blade tip and root and the highly 3D nature of the flow here will cause the lift coefficient to be less than $2\pi\alpha$. This phenomenon has been observed by Johansen *et al.* [40] when deriving lift and drag coefficients from detailed CFD computations and by Tangler [90] when deriving aerofoil data from pressure measurements on a rotating turbine blade using a vortex model. The same was observed in this project when analyzing the NREL Phase VI rotor (refer to Chapter 6, Fig. 6.19(a)).

To derive an extrapolated bound circulation distribution that accounts for tip/root loss ($\Gamma_{B,3D}$), two different methods were used:

In *method 1*, the estimated values of the bound circulation at 40% and 90% R were discarded and a cubic variation of bound circulation was prescribed between 30% and 40% R and between 80% and 100% R . The bound circulation at 30% and 100% R was set to zero. A spline interpolation was then applied to obtain a continuous bound circulation distribution across the whole blade using the technique described in Appendix D.

In *method 2*, a trial-and-error approach was used in conjunction with the prescribed-wake vortex model *HAWT_PVC* described in section 4.3.3. In this method, the axial induced velocity at the blades ($u_{a,c}$) at $Y_a=3.5\text{cm}$ was initially found by assuming that the free-stream velocity was equal to the ideal free-wind speed of 5.5 m/s (i.e. using results for $w_{a,c}$ in Figs. 4.18(a) in Eq. 4.57). This was justified since, as it will be explained later on in section B.3, blockage effects for axial conditions were found to be small. Then, a large number of different spanwise distributions for bound circulations were assumed and each was prescribed to *HAWT_PVC* to calculate the spanwise distributions $u_{a,c}$ at $Y_a=3.5\text{cm}$. Using a trial-and-error algorithm embedded in the code, the prescribed vortex model *HAWT_PVC* determined the bound circulation that yielded an induced velocity variation that is closest to that derived directly from measurements at $Y_a=3.5\text{cm}$. The vortex model parameters were set as shown in table 4.4. Parameters $R_{t,w1}$, $R_{t,w2}$ and p were obtained from the smoke visualization experiments (refer to section 4.2.3). The calculations were carried out for three

different values of n : $n=15, 21$ and 31 . The modelled helical wake geometry used for the vortex model is depicted in Fig. 4.54. Fig. 4.55 shows the derived distributions for $\Gamma_{B,3D}$ obtained using the two methods. For *method 2*, the distributions for $\Gamma_{B,3D}$ obtained for the three different values of n are shown. In fact, the difference between the resulting distributions is negligible. The induced velocities at $Y_r=0.035\text{cm}$ for such distributions using *HAWT_PVC* are shown in Fig. 4.56. These agree very well with those obtained for the measurements using Eq. 4.57. It is observed in Fig. 4.55 that the results from *methods 1* and *2* agree very well, thus providing confidence in the derived bound circulation along the blades. It should be noted that in *method 2*, no knowledge of aerofoil data for the lift coefficient is used.

Table 4.4: Parameters used for determining the bound circulation using *HAWT_PVC* for $\Psi=0^\circ$.

$nwRev$	10
π_{tot}	36
$\Delta\phi$	10°
$R_{t,w1}$	0.6398
$R_{t,w2}$	0.668
p	0.37
<i>ReleaseTip</i>	0.99
<i>ReleaseRoot</i>	0.305
δ	0.5mm

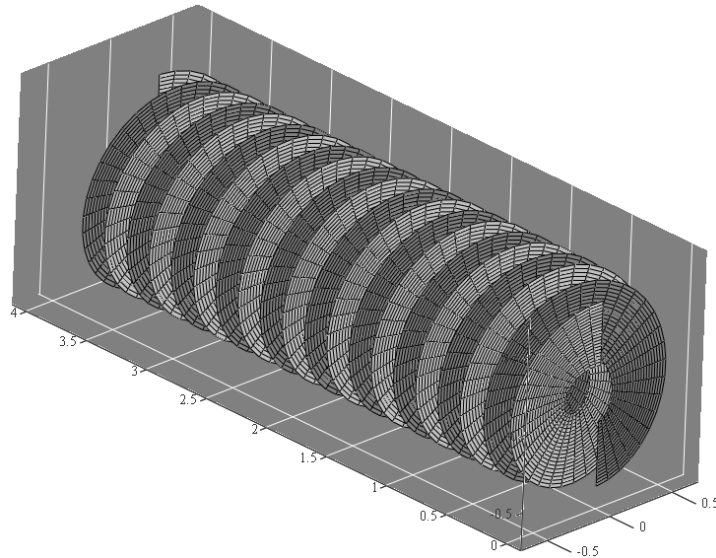


Figure 4.54 – Wake geometry for determining bound circulation distribution at blades using prescribed vortex model (*HAWT_PVC*) in *method 2*. ($n = 21$).

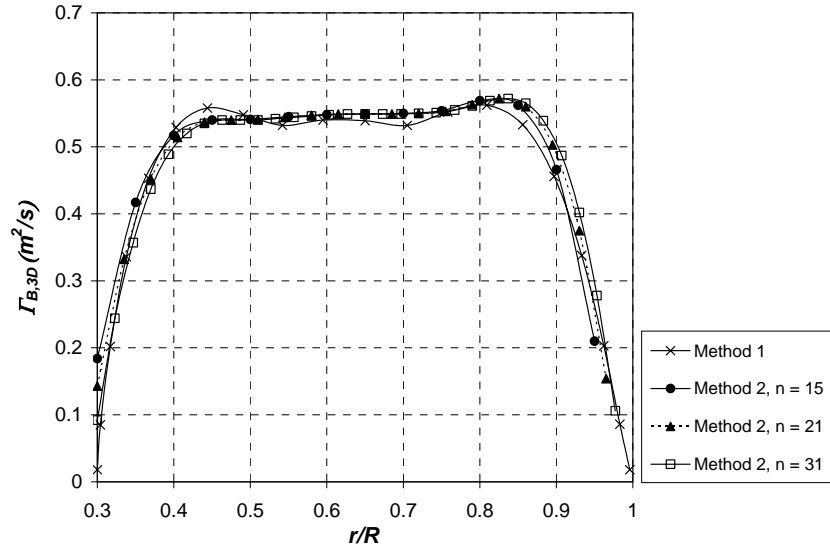


Figure 4.55 – Derived bound circulation distributions using methods 1 and 2.

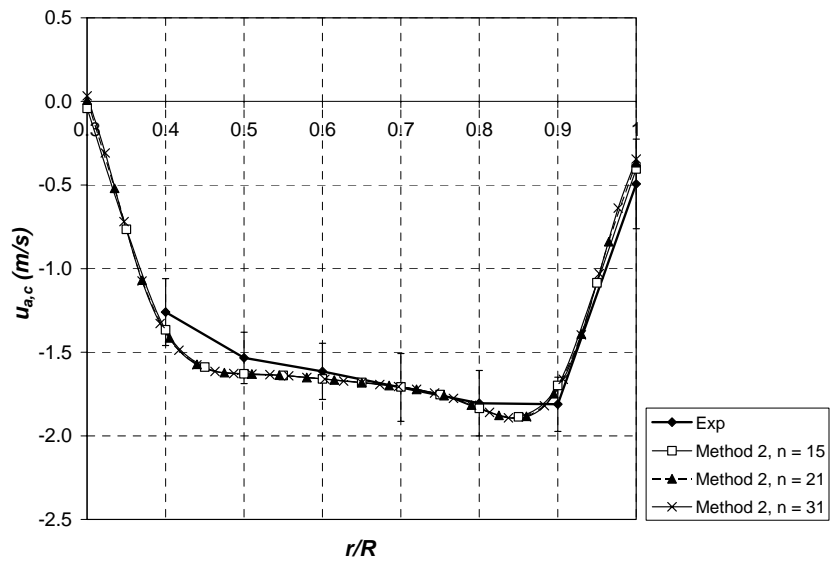


Figure 4.56 – Comparison of induced velocities at blades at $Y_a = 3.5\text{cm}$ computed using method 2 with that derived from experimental measurements ('Exp') using Eq. 4.57. The error bars in plot 'Exp' denote the \pm one standard deviations due to the uncertainty in the hot-film measurements.

B.3 Assessment of the Effects of Tunnel Blockage in Axial Conditions

To assess for blockage the two procedures described in section 4.3.4, Fig. 4.48 were applied. In both cases, the mean bound circulation derived using *method 1* (refer to section B.2) was prescribed to vortex model *HAWT_PVC* together with the parameters of table 4.4.

In *procedure 1*, *HAWT_PVC* calculated the axial induced velocities in line with the blades but at the tunnel exit (i.e. finding $u_{a,c}$ at $Y=-1\text{m}$) and the factor k_e were evaluated at all radial locations (using Eq. 4.64). The results are presented in Figs. 4.57(a) and (b). Note that since we are dealing with axial conditions, the calculations were carried out at only one rotor azimuth angle (at $\phi=0^\circ$). It can be observed that the induced velocity at the tunnel exit is very small. The highest value for k_e being predicted by *HAWT_PVC* is only 0.029 at $r/R=0.3$ (i.e. 2.9% of U_{jet}). k_e decreases continuously to 0.022 at the blade tip. These values for k_e are very small and are only on the order of magnitude of the standard deviations caused by tunnel jet non-uniformity. This provides evidence that tunnel blockage due to rotor proximity to the tunnel exit can be neglected.

To assess for tunnel blockage using *procedure 2* (see section 4.3.4, Fig. 4.48), the axial induced velocities at $Y=3.5\text{cm}$ were initially found by assuming that the free-stream velocity was equal to the ideal free-wind speed of 5.5 m/s (i.e. using results for $w_{a,c}$ of Fig. 4.18 in Eq. 4.57). Actually these are the same values as those of Fig. 4.56 (referred by 'Exp'). *HAWT_PVC* then calculated the induced velocity $u_{a,c}'$ at $Y=3.5\text{cm}$ resulting from the bound circulation estimated using *method 1*. The two induced velocities were compared and the percentage discrepancy (ϵ_a) was found in accordance with Eq. 4.65. The results are shown in Figs. 4.58(a) and (b). The induced velocities derived using the two different methods agree very well and this implies that it is justified to assume that $U_{jet} = U$ when applying Eq. 4.57. Thus it may be argued that blockage effects are small. However, one should keep in mind that in the blockage assessment, it is being assumed that the vortex model *HAWT_PVC* is suitably accurate in calculating the induction for a given bound circulation.

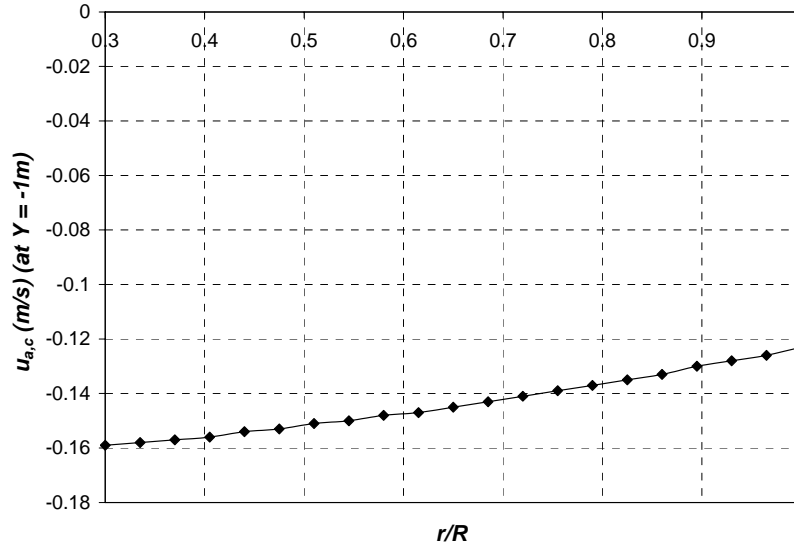


Figure 4.57(a) – Spanwise variation of $u_{a,c}$ calculated at the tunnel exit using HAWT_PVC ($n=21$).

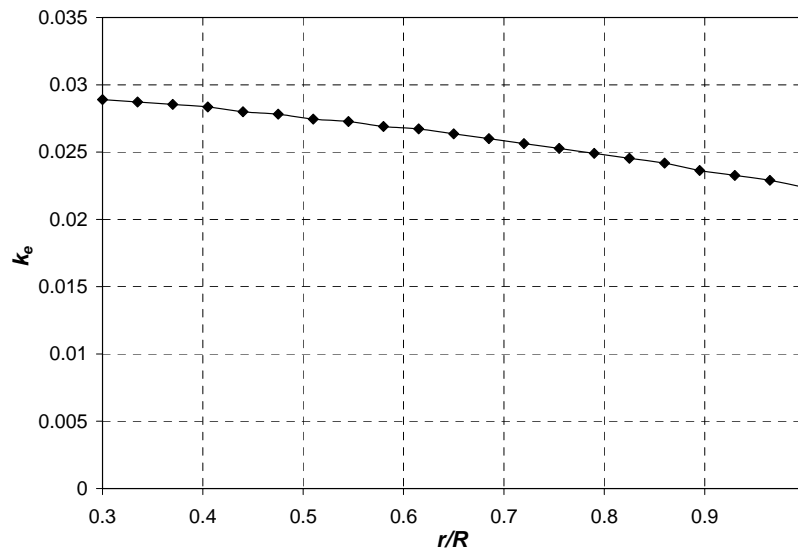


Figure 4.57(b) – Spanwise variation of k_e calculated using HAWT_PVC ($n=21$).

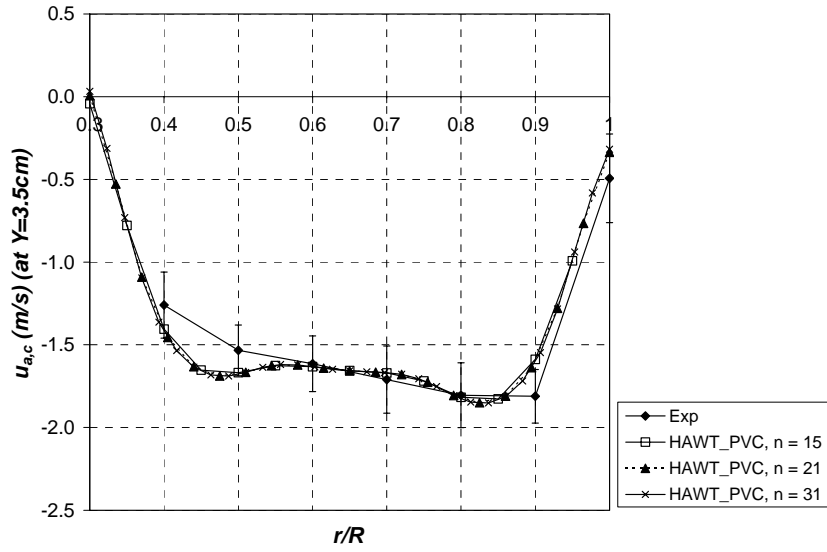


Figure 4.58(a) – Comparison of axial induced velocities at 3.5cm downstream of rotorplane calculated using measurements and assuming $U_{\text{ref}}=U$ with those calculated from HAWT_PVC.

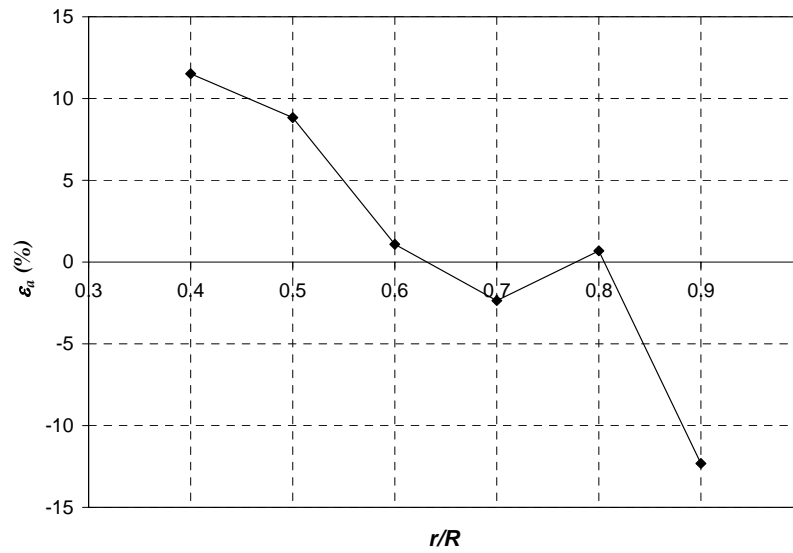


Figure 4.58(b) – Spanwise variation of percentage discrepancy calculated using Eq. 4.65.

B.4 Axial Induction Factor Distributions

Since the blockage effects were found to be small, then U can be taken to be equal to U_{jet} (5.5m/s). The axial induction distributions for $u_{a,c}$ at each measuring plane ($Y_a=6, 3.5, 6$ and 9cm) could be found using the measured values of $w_{a,c}$ in Fig. 4.18(a) and Eq. 4.57. The azimuthally averaged induced velocities (i.e. the average axial induced velocity over an annulus) at each radial location for a given rotor azimuth angle could be computed as follows: By knowing the axial flow velocity w_a at each probe position (denoted by indices (i,j)) and rotor azimuth angle (denoted by index τ) (refer to section 4.2.2, page 58), the azimuthally averaged axial flow velocity at a given radial location and rotor azimuth angle could be found from:

$$(w_{a,aver})_{i,\tau} = \frac{1}{j_{tot}} \sum_{j=0}^{j=j_{tot}} (w_a)_{\tau,i,j} \quad (4.81)$$

The azimuthally averaged axial induced velocities could then be found from

$$u_a = w_{a,aver} - U \quad (4.82)$$

The results for $u_{a,c}$ and u_a at the different measuring planes are shown in Figs. 4.59(a) and (b). The axial induction factors at the rotorplane ($a_{1,c}$ and a_1) were then be found by dividing the interpolated induced velocities at the rotorplane by 5.5m/s. The results are shown in Figs. 4.60(a) and (b). The bars indicated the +/-one standard deviations in the data across one whole revolution.

It can be observed from Figs. 4.60 and 4.61 that the standard deviations in a_1 are smaller than those in $a_{1,c}$. This is a result of the fact that averaging tends to damp out any fluctuations in velocity that tend to occur locally.

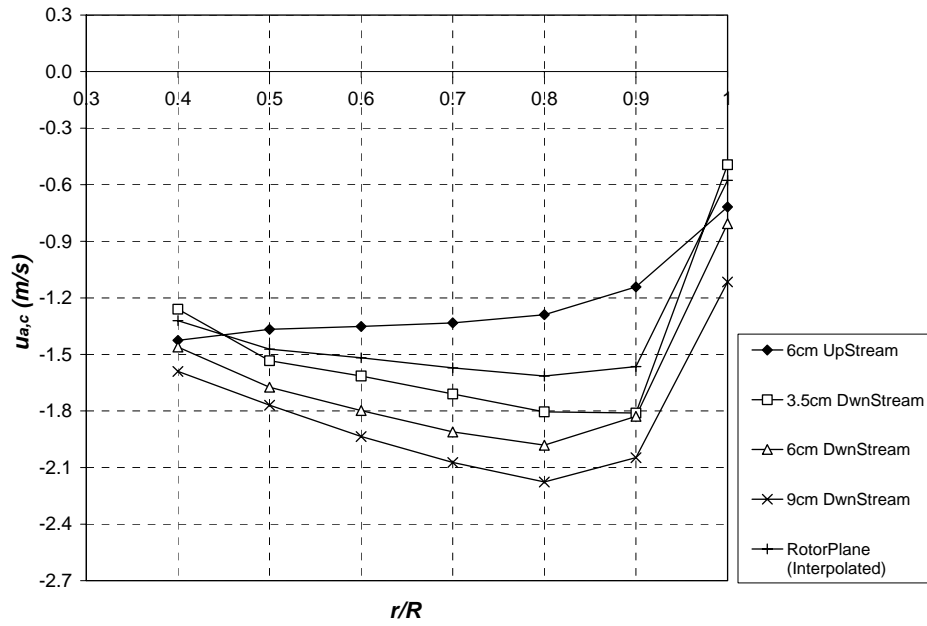


Figure 4.59 (a) – Spanwise variation of axial induced velocity at blade lifting line.

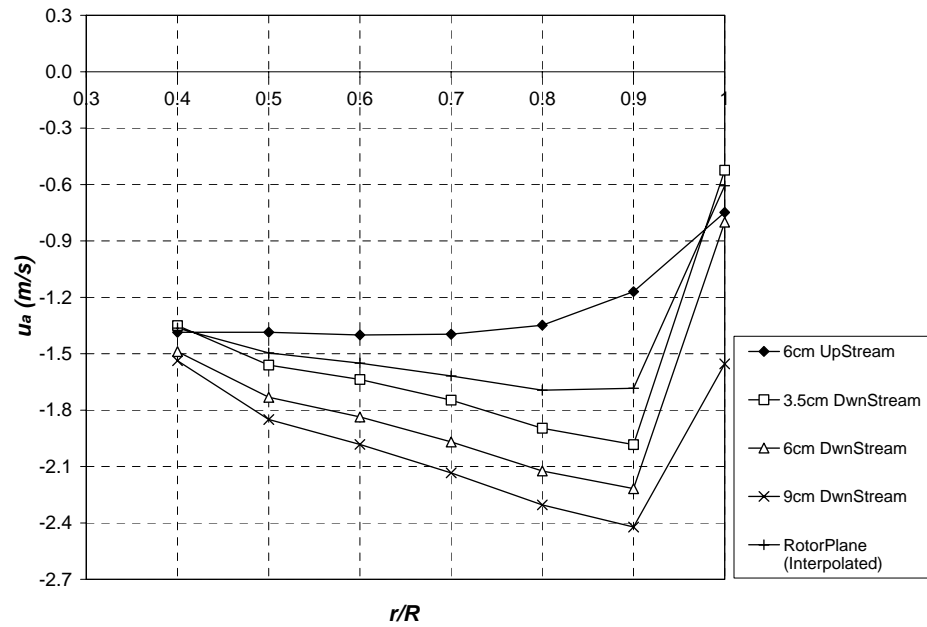


Figure 4.59 (b) – Spanwise variation of azimuthally averaged axial induced velocity at rotorplane.

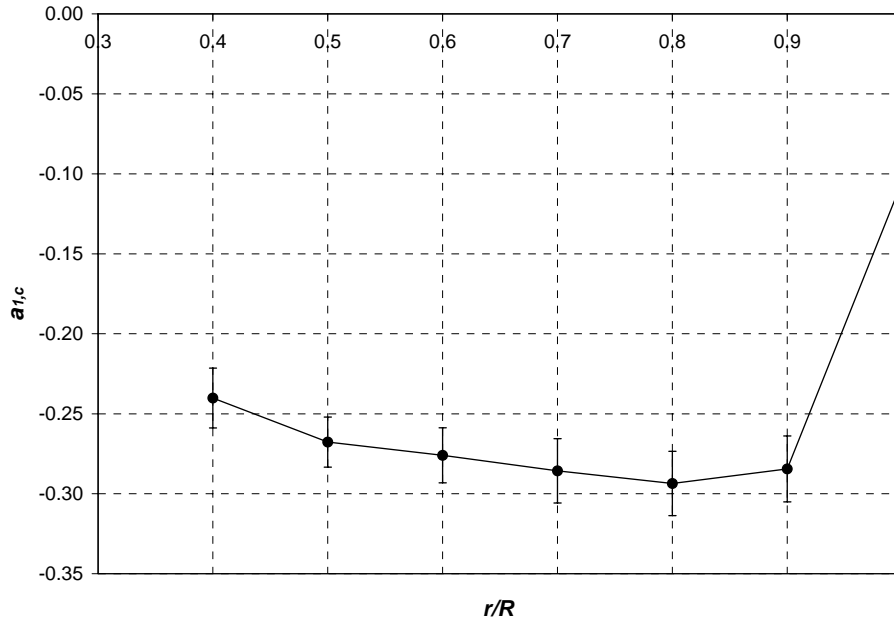


Figure 4.60 – Spanwise variation of axial induction factor at blade lifting line.

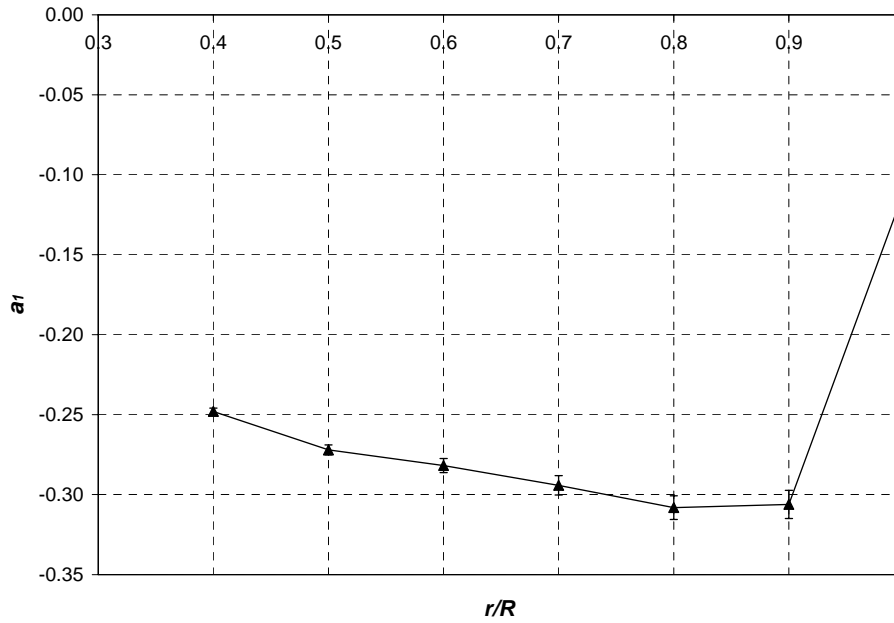


Figure 4.61 – Spanwise variation of azimuthally averaged axial induction factor at rotorplane.

B.5 Blade Load Distributions

Using the distribution for $\Gamma_{B,3D}$ calculated using *method 1* (see section B.2, page 131), the lift coefficient corrected for tip/root loss ($C_{l,3D}$) was calculated from Eq. 4.14 at radial locations 40, 50, 60, 70, 80 and 90%R. The drag coefficient was found from the 2D data for the NACA 0012 aerofoil. The drag coefficient was not corrected for tip/root loss. The error incurred was small, since the drag coefficient was very small. The results are shown in Figs. 4.62 and 4.63. Using *HAWT_LFIM*, the blade chordwise and normal loading values (dA_η and dA_c) at 40, 50, 60, 70, 80 and 90%R were found using the blade-element theory equations Eqts. 3.16 and the lift/drag coefficients of Figs. 4.62 and 4.63. Each rotor blade was discretized into 22 equally-spaced elements. The loading values at the blade tip and root were set to zero and a spline interpolation (as in Appendix D) was applied to estimate the loading values at each of the 22 blade sections. The results are displayed in Figs. 4.64 and 4.65. The blade thrust and torque loading distributions (dT_{3D} and dQ_{3D}) were estimated using a similar method, however using Eqts. 3.20 (refer to Figs. 4.66 and 4.67). In Figs. 4.62 – 4.67, the error bars denote the \pm one standard deviations resulting from the uncertainties in the inflow measurements. It was found that the maximum errors in dT_{3D} and dQ_{3D} due to the uncertainties in the inflow measurements ($w_{a,c}$) were equal to 7.4% and 13.6%. Re-call from section 4.2.2 (page 68) that the uncertainty in $w_{a,c}$ was found to be in the range 6-10% at $\psi=0^\circ$. It can therefore be concluded that the error in dT_{3D} remained in the same order of that of the inflow measurements from which it was derived. However the error in dQ_{3D} is higher than that for dT_{3D} and this consolidates what was found earlier in section 4.3.5 that $\varepsilon_Q > \varepsilon_T$.

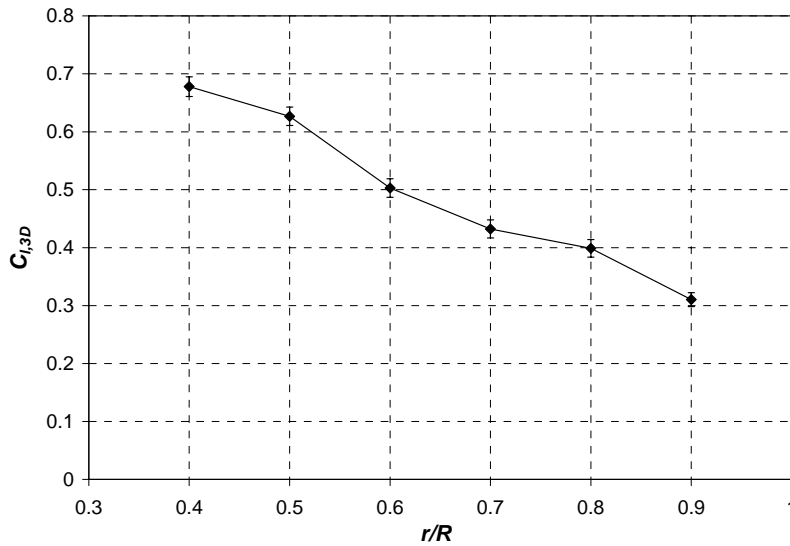


Figure 4.62 – Distribution of lift coefficient (corrected for tip/root loss).

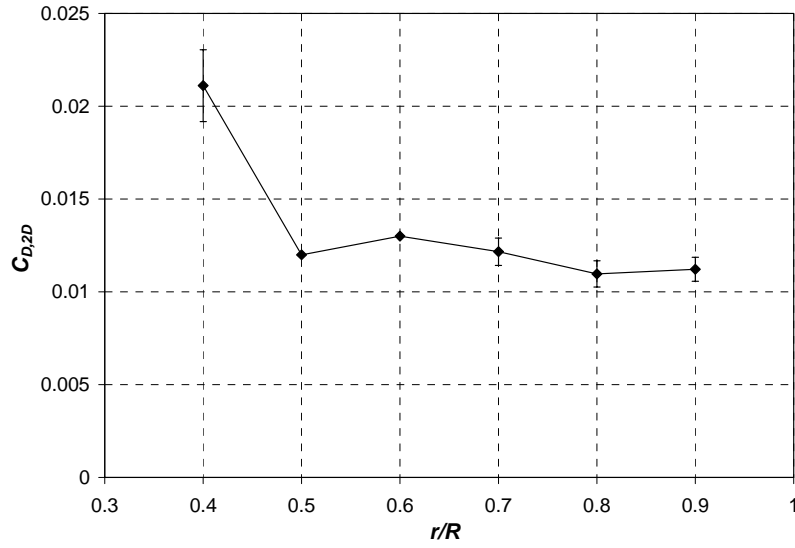


Figure 4.63 – Distribution of drag coefficient (not corrected for tip/root loss).

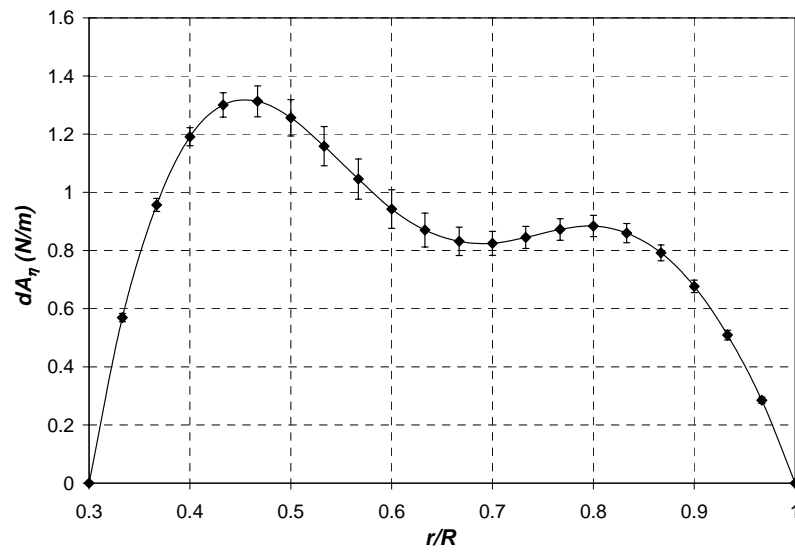


Figure 4.64 – Distribution of chordwise aerodynamic loading.

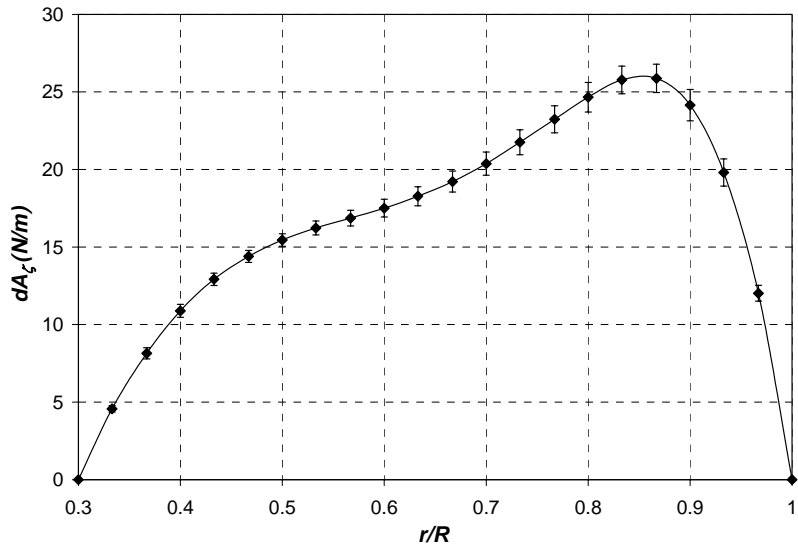


Figure 4.65 – Distribution of normal aerodynamic loading.

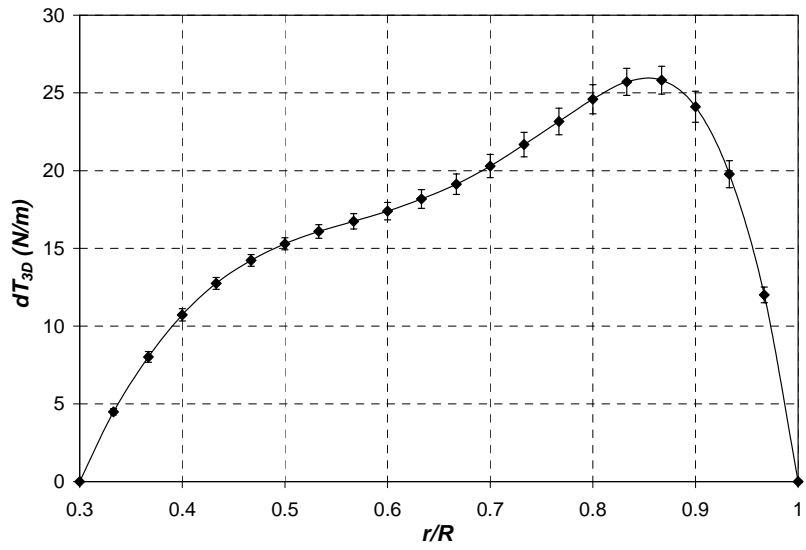


Figure 4.66 – Distribution of axial thrust aerodynamic loading.

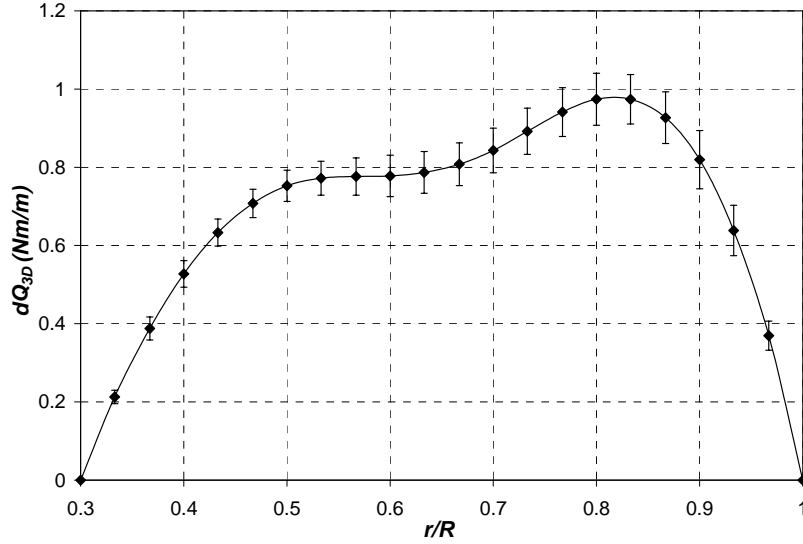


Figure 4.67 – Distribution of torque aerodynamic loading.

B.6 Comparison of Rotor Power and Axial Thrust Coefficients

HAWT_LFIM integrated the loading distributions of Figs. 4.64 and 4.65 using the procedure of Appendix B to determine the axial thrust and power coefficients for the rotor for $\lambda=8$ and $\theta_{tip}=2^\circ$. These were compared with those measured during the wind tunnel experiments by means of strain gauges (refer to Figs. 4.2, 4.3 and 4.26). The comparison is shown in table 4.5. Ideally the two readings should be the same. The percentage discrepancy is mainly due to various sources of error associated with the hot-film measurements. Another source of error is the uncertainty in the tip/loss correction used. The tip/root correction applied using the cubic extrapolation and using *HAWT_PVC* (methods 1 and 2, refer to section B.2) may underestimate the thrust loading a tip and root region, thus resulting in a lower value for C_T . One should also remark that the lifting line model used in *HAWT_LFIM* and *HAWT_PVC* is a 2D flow model and is rather limited in representing the 3D effects at the rectangular blade tip and root regions.

Table 4.5: Comparison of axial thrust and power coefficients derived by *HAWT_LFIM* using hot-film near wake measurements with those measured using strain gauge techniques.

	Measured using Strain Gauges	Derived from Inflow Measurements	Percentage Discrepancy
C_P	0.32	0.37	15.625
C_T	0.8	0.67	-16.25

C. HAWT_LFIM Results for Yawed Conditions

This section presents the results that were obtained for the blade aerodynamic parameters in yawed conditions ($\Psi=30^\circ$ and 45°) using HAWT_LFIM. Since in yaw the parameters are unsteady, the results are plotted as a function of blade or rotor azimuth angle (ϕ) over one whole revolution. The error bars in the plotted results denote the uncertainty bounds resulting from the estimated errors of $\pm 0.26\text{m/s}$ and $\pm 0.21\text{m/s}$ in $w_{a,c}$ at $\Psi=30^\circ$ and 45° , respectively. These errors are approximately equivalent to $\pm 8\%$ of the azimuthally averaged values of $w_{a,c}$.

C.1 Derivation of spanwise distributions of angle of attack, flow relative velocity and bound circulation

Figs. 4.68 and 4.69 show the variations of the local angle of attack (α) with blade azimuth angle (ϕ) derived using Eq. 4.11 for yaw angles 30° and 45° . The variations are periodic and the inboard blade sections experience the highest variations of both the mean and cyclic components of the angle of attack. The maximum angle of attack is about 10° and occurs at $\phi=0^\circ$, $r/R=0.4$ and $\Psi=30^\circ$. This is slightly less than the 2D stalling angle for the NACA0012 aerofoil which is about 11° at a Reynolds number of 150,000. Thus, at these yawed conditions the flow over the blades is fully attached. The uncertainty in α resulting from the assumed errors in $w_{a,c}$ is in the range of $\pm 0.8^\circ$ at $r/R = 0.4$ to $\pm 0.4^\circ$ at $r/R = 0.9$. A discontinuity in the variation of α with ϕ is observed between $330^\circ < \phi < 360^\circ$ and $0^\circ < \phi < 30^\circ$ at almost all radial locations. This results from the discontinuity observed in the inflow measurements which was already mentioned earlier in section 4.2.2, page 67 (see Figs. 4.19 and 4.20). Consequently this discontinuity has resulted in a discontinuity of the other parameters derived from the inflow measurements (e.g. lift and drag coefficients, bound circulation and aerodynamic loading), as will be noted later on. As already described, this behaviour between $330^\circ < \phi < 360^\circ$ and $0^\circ < \phi < 30^\circ$ is mainly due to the non-uniformity in the tunnel exit jet and possibly also from influences from the complex circulation in skewed flow caused by the yawed rotor. It could also be the case that the influences from the centrebody structure contribute to such a behaviour.

From the angle of attack variations of Figs. 4.68 and 4.69, it was possible to calculate the rate of change of the local angle of attack ($\dot{\alpha}$) with time as a function of ϕ using the inverse Adam-Bashfort method described in section 4.3.2 (page 95). The results are plotted in Figs. 4.70 and 4.71. In general, $\dot{\alpha}$ is negative for $0^\circ < \phi < 180^\circ$ and positive for $180^\circ < \phi < 360^\circ$. The highest rates of change of angle of attack are observed at the inboard blade sections and consequently higher local unsteady aerodynamic effects are experienced here.

Figs. 4.72 and 4.73 show the variations of the local flow relative velocities (V_r) with blade azimuth angle (ϕ) using Eq. 4.12. As in axial conditions, the uncertainty in this parameter due to errors in the measured flow velocities ($w_{a,c}$) is very small because $r\Omega \gg w_{a,c}$.

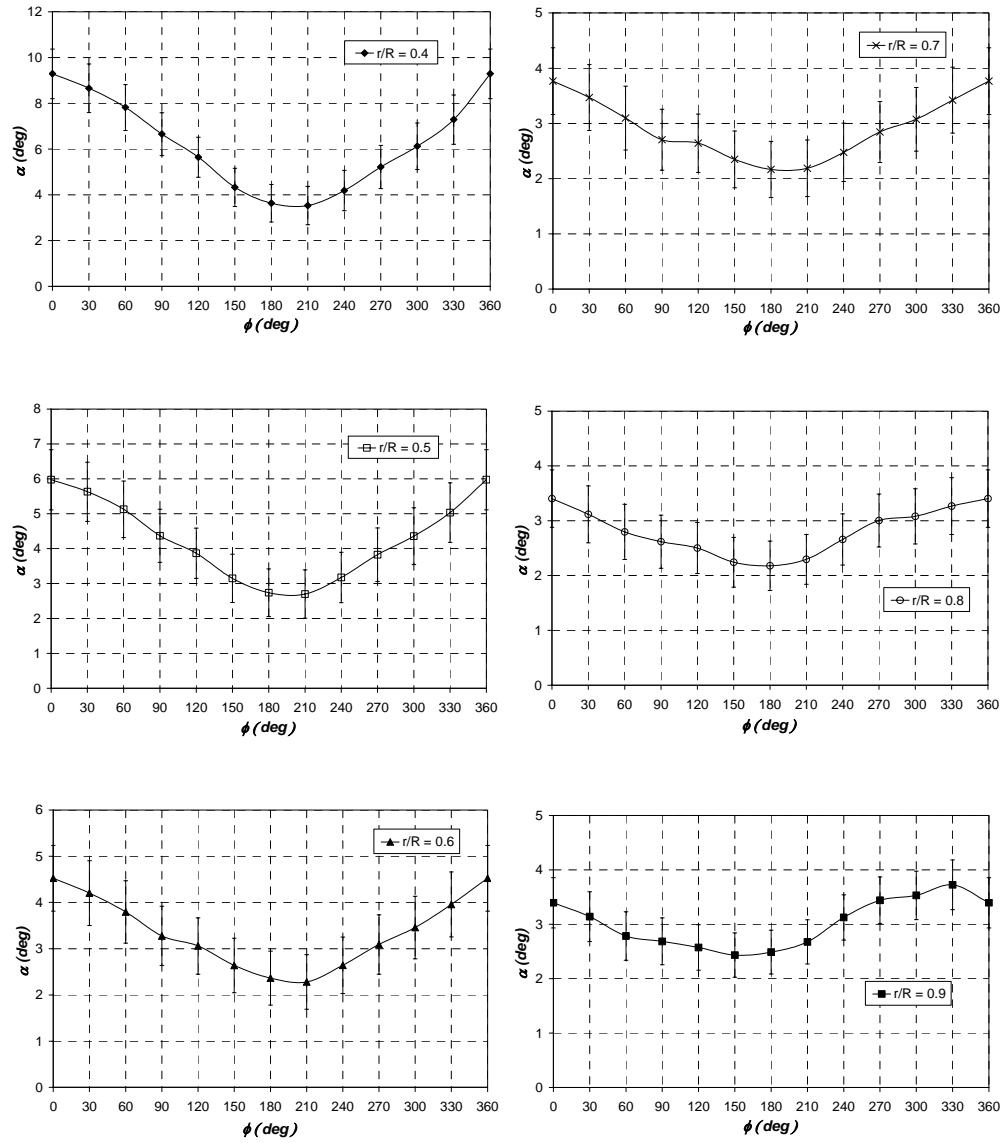


Figure 4.68 - Variation of angle of attack with blade azimuth angle at $\Psi=30^\circ$.

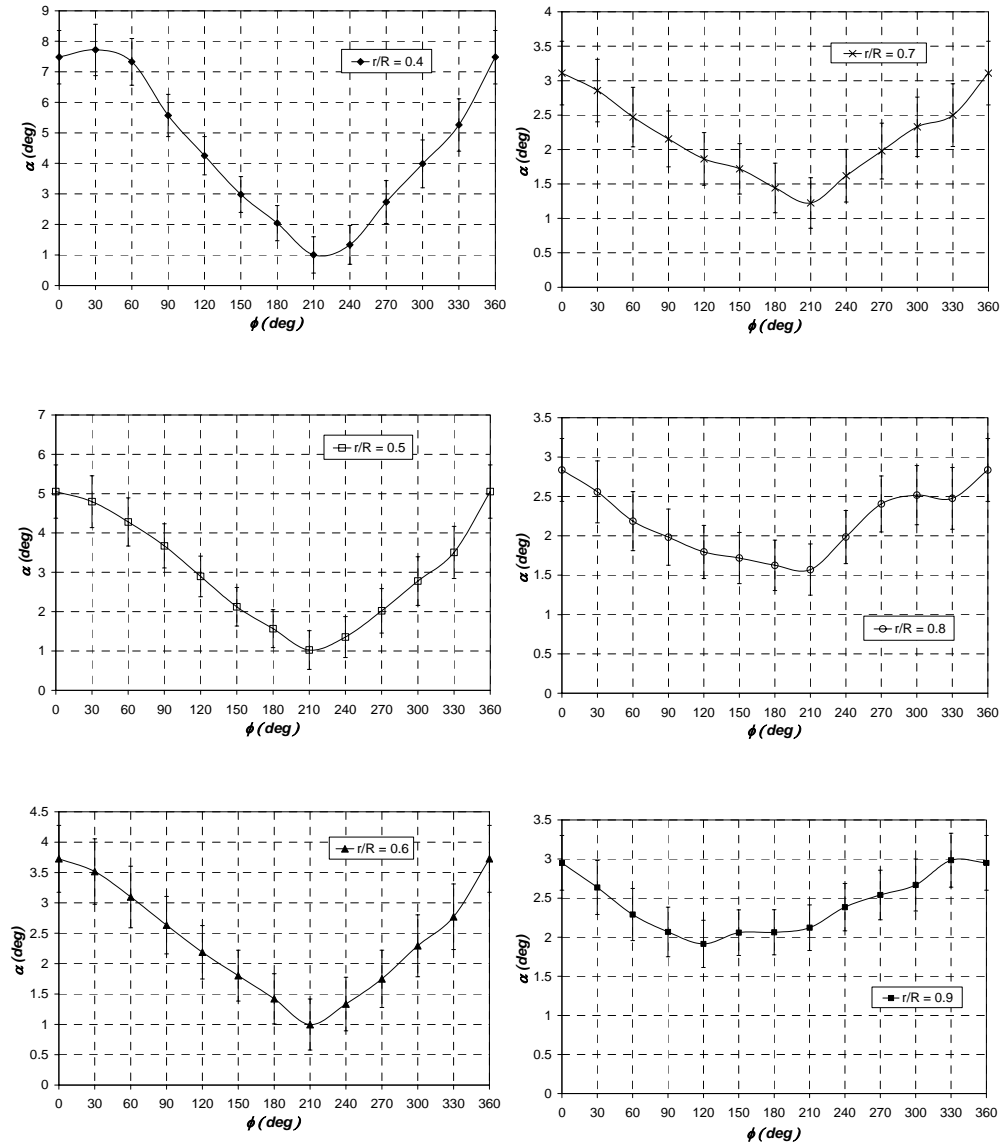


Figure 4.69 - Variation of angle of attack with blade azimuth angle at $\Psi=45^\circ$.

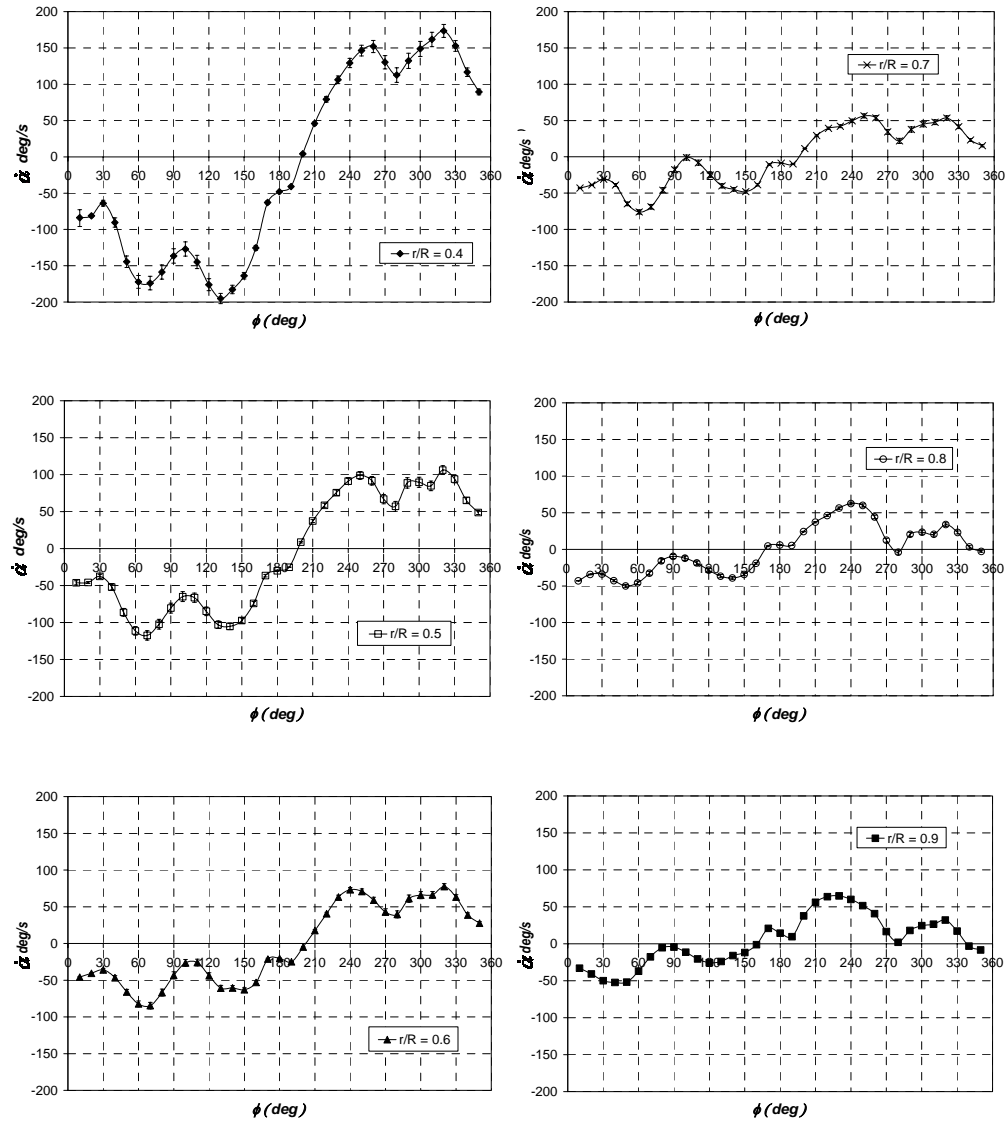


Figure 4.70 - Variation of time rate of change of angle of attack with blade azimuth angle at $\Psi=30^\circ$.

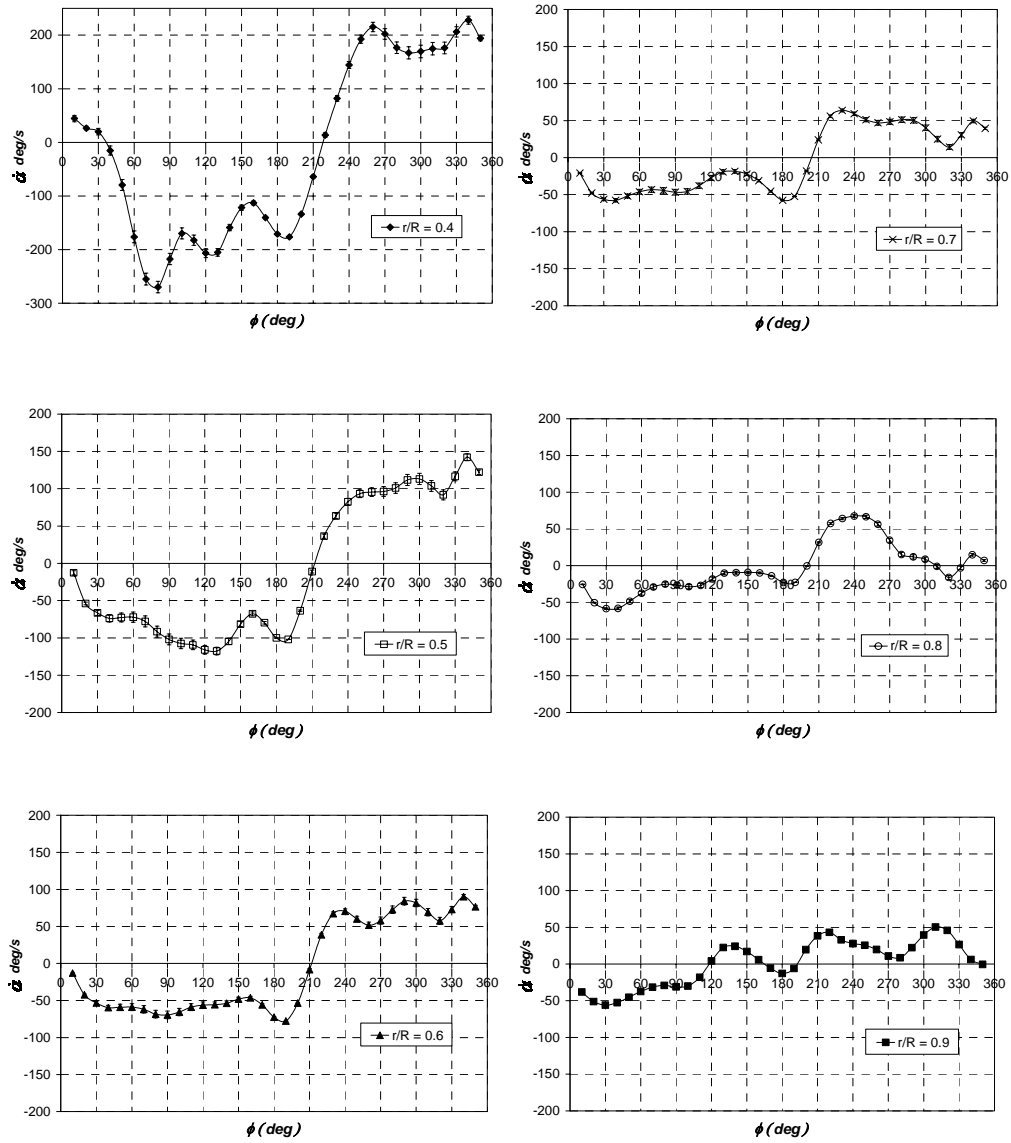


Figure 4.71 - Variation of time rate of change of angle of attack with blade azimuth angle at $\Psi=45^\circ$.

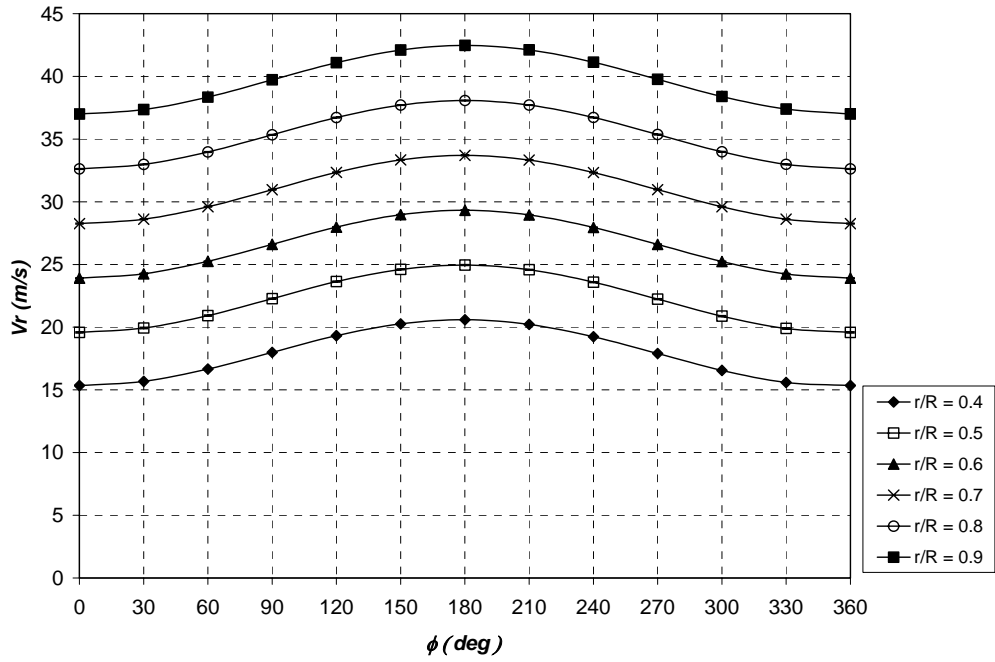


Figure 4.72 - Variation of flow relative velocity with blade azimuth angle at $\Psi=30^\circ$.

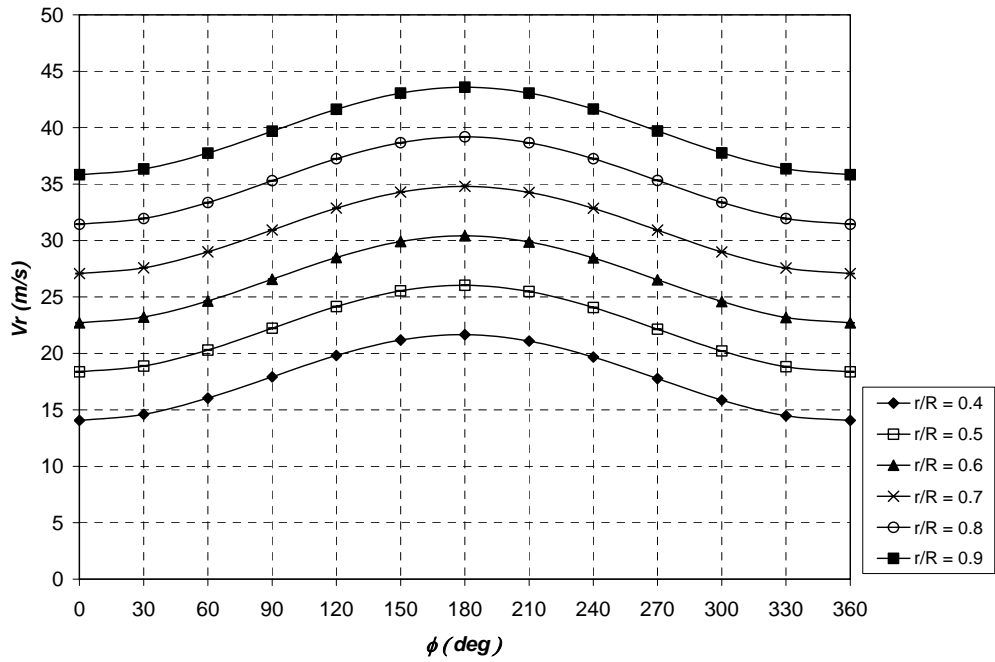


Figure 4.73 - Variation of flow relative velocity with blade azimuth angle at $\Psi=45^\circ$.

Figs. 4.74 and 4.75 plot the resulting spanwise bound circulation distributions ($\Gamma_{B,2D}$) for different blade azimuth angles (0° , 90° , 180° and 270°) as derived in accordance with the Kutta-Joukowski law (Eq. 4.13). The error bars for this parameter due to the estimated errors in $w_{a,c}$ are not included in these plots for the sake of clarity. But the error in $\Gamma_{B,2D}$ was found to be on the order of ± 0.071 and $\pm 0.055 \text{ m}^2/\text{s}$ at yaw angles 30° and 45° respectively. Unlike axial conditions, the bound circulation is a function of the blade azimuth angle and is therefore unsteady. Comparing Figs. 4.53, 4.74 and 4.75, it may be noted that the bound circulation level decreases as the yaw angle is increased, but the unsteadiness actually increases.

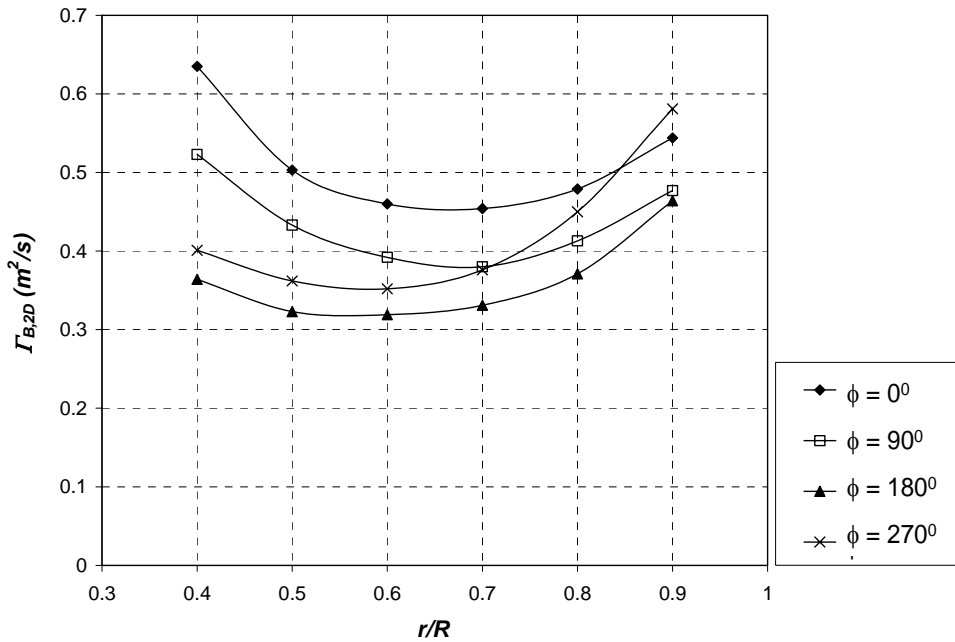


Figure 4.74 - Variation of bound circulation with blade azimuth angle at $\Psi=30^\circ$.

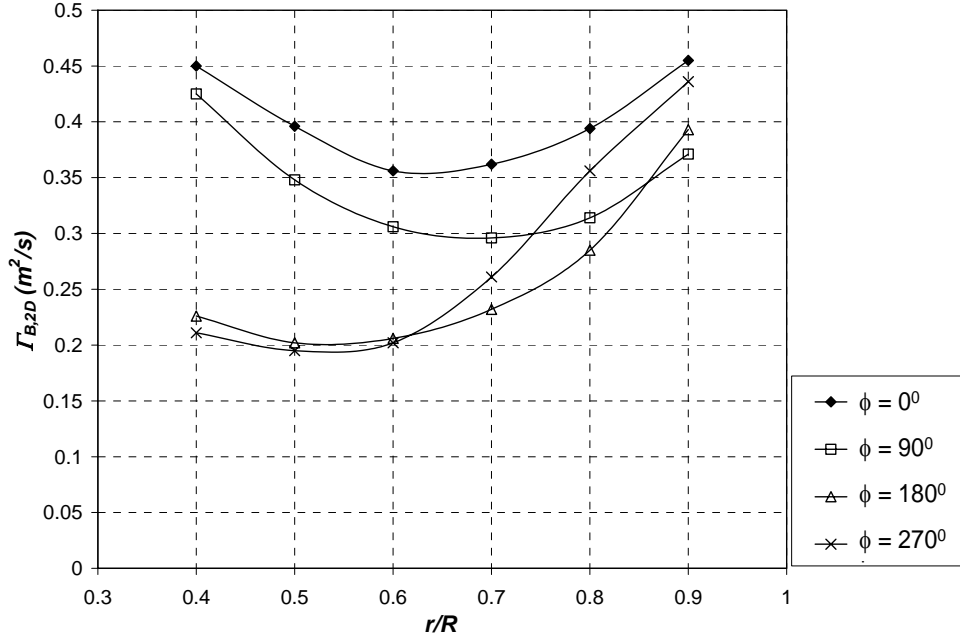


Figure 4.75 - Variation of bound circulation with blade azimuth angle at $\Psi=45^\circ$.

C.2 Extrapolated Bound Circulation Distributions Corrected for Tip and Root Loss

The section describes how the extrapolated distributions for the unsteady bound circulations for the whole blade span were derived from the point values at 40, 50, 60, 70, 80 and 90%R. Recall that in axial conditions the bound circulation values at 40% and 90%R were found to be unrealistically high (refer to section B.1, Fig. 4.53), even though the angle of attack was being derived from the inflow measurements. This presented a difficulty for deriving a bound circulation distribution across the whole blade span. The same problem was also expected to occur at yaw angles 30° and 45° , for the simple reason that the unsteady aerofoil model employed to derive the lift coefficient was a 2D model and does not cater for blade tip/root 3D effects. In axial conditions, the prescribed vortex model *HAWT_PVC* could easily be employed to derive the extrapolated bound circulation distributions corrected for tip/root loss using a trial-and-error approach (This approach is referred to as *method 2* in section B.2). This was possible because this vortex model was found to be very accurate when treating axial conditions. However, when it came to yawed conditions, it was found that the predicted results by *HAWT_PVC* for $u_{a,c}$ did not agree very well with the corresponding experimental results. Consequently the trial-and-error approach was very difficult to apply at both 30° and 45° yaw. The following alternate method was applied to obtain the unsteady extrapolated bound circulation distributions

that account for tip/root loss effects ($\Gamma_{B,3D}$): the estimated values of the bound circulation at 40% and 90% R were discarded (as they were expected to be high). The bound circulation at the blade root and tip (30% and 100% R) was set to zero. A spline interpolation was then employed to obtain a continuous bound circulation across the whole blade span using the method described in Appendix D. The results for such distributions at 30° and 45° yaw are shown in Figs. 4.76 and 4.77. In these plots, the distributions of the 2D uncorrected values ($\Gamma_{B,2D}$) of Figs. 4.74 and 4.75 are also included for the purpose of comparison. The difference between the $\Gamma_{B,2D}$ and $\Gamma_{B,3D}$ distributions is at the regions between 30% R and 50% R and between 80% R and 100% R , where the tip/root loss correction is applied together with the extrapolation. Figs. 4.78 and 4.79 show the same results for $\Gamma_{B,3D}$ but plotted as a function of the blade azimuth angle.

To derive an accurate tip/root loss correction for yawed conditions where no blade pressure measurements could be performed is not an easy task and requires a thorough modelling of 3D flows at the blade tips such as CFD. This was beyond the scope of the project. The fact of not carrying out this in-depth analysis and instead applying the simple spline extrapolation method described above introduces some level of uncertainty in the unsteady bound circulation values at the blade tip and root regions. It should be kept in mind that these derived bound circulations were required to validate the free-wake vortex model using the procedure described in Figs. 2.4 and 5.10. A high uncertainty due to the tip/root loss correction could have been detrimental to this validation exercise. Therefore, it was vital to assess the significance of this uncertainty. To do so, the vortex model *HAWT_PVC* was used. The uncorrected bound circulation distributions ($\Gamma_{B,2D}$) of Fig. 4.74 and 4.75 were extrapolated using the same method described above but the circulation values at 40% and 90% R were not discarded (i.e. no tip/root loss correction was applied). The two different extrapolated circulations, $\Gamma_{B,2D}$ and $\Gamma_{B,3D}$, were then prescribed to *HAWT_PVC* to calculate the axial induced velocities at the blades ($u_{a,c}$ at $Y_a=0$). The latter were compared, as shown in Figs. 4.80 and 4.81. Table 4.6 gives the parameters used in *HAWT_PVC*. In this table, parameters $R_{t,w1}$, $R_{t,w2}$, p , and χ_s were obtained from the smoke visualization experiments (refer to section 4.2.3). The calculations were performed at different values of n ($n = 11, 21$ and 31) to show that the numerical errors due to blade discretization are negligible. Figs. 4.82 and 4.83 illustrate the prescribed skewed wakes modelled by *HAWT_PVC*. The discrepancy between the induced velocities resulting from the two different circulations, $\Gamma_{B,2D}$ and $\Gamma_{B,3D}$, gives a first order indication of how significantly this uncertainty in the tip/root correction would influence the spanwise induced velocity distribution along the blades. Figs. 4.80 and 4.81 show that this uncertainty mainly influences only induced velocities at the blade tip and root region. The region between 50% and 80% R experience only a minor influence.

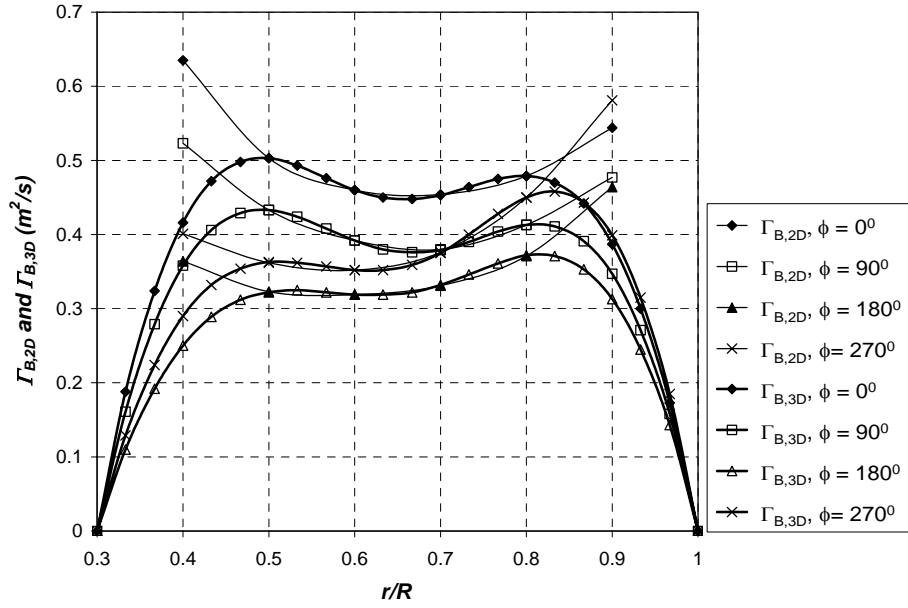


Figure 4.76 - Comparison of extrapolated bound circulation distributions corrected for tip/root loss ($\Gamma_{B,3D}$) with uncorrected distributions ($\Gamma_{B,2D}$) at $\Psi=30^\circ$.

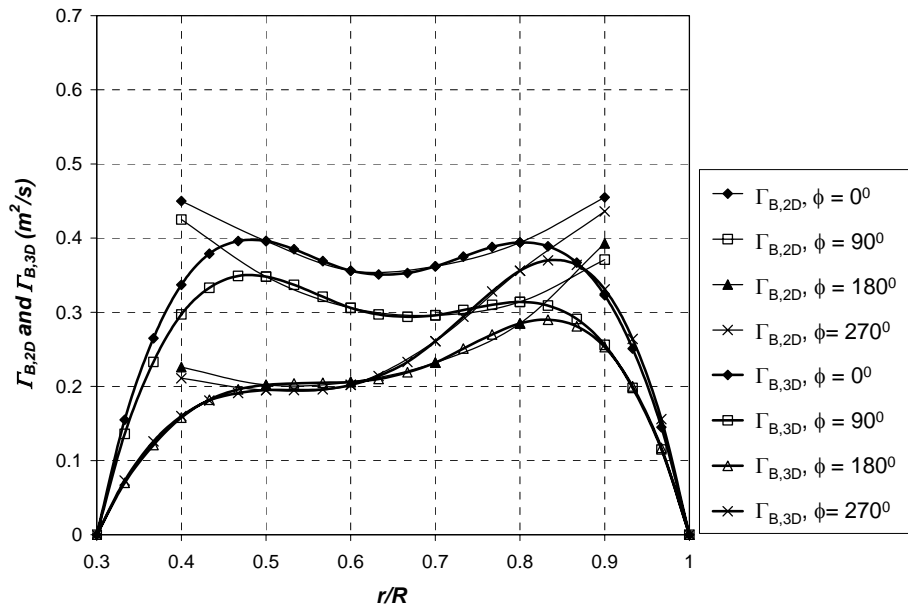


Figure 4.77 - Comparison of extrapolated bound circulation distributions corrected for tip/root loss ($\Gamma_{B,3D}$) with uncorrected distributions ($\Gamma_{B,2D}$) at $\Psi=45^\circ$.

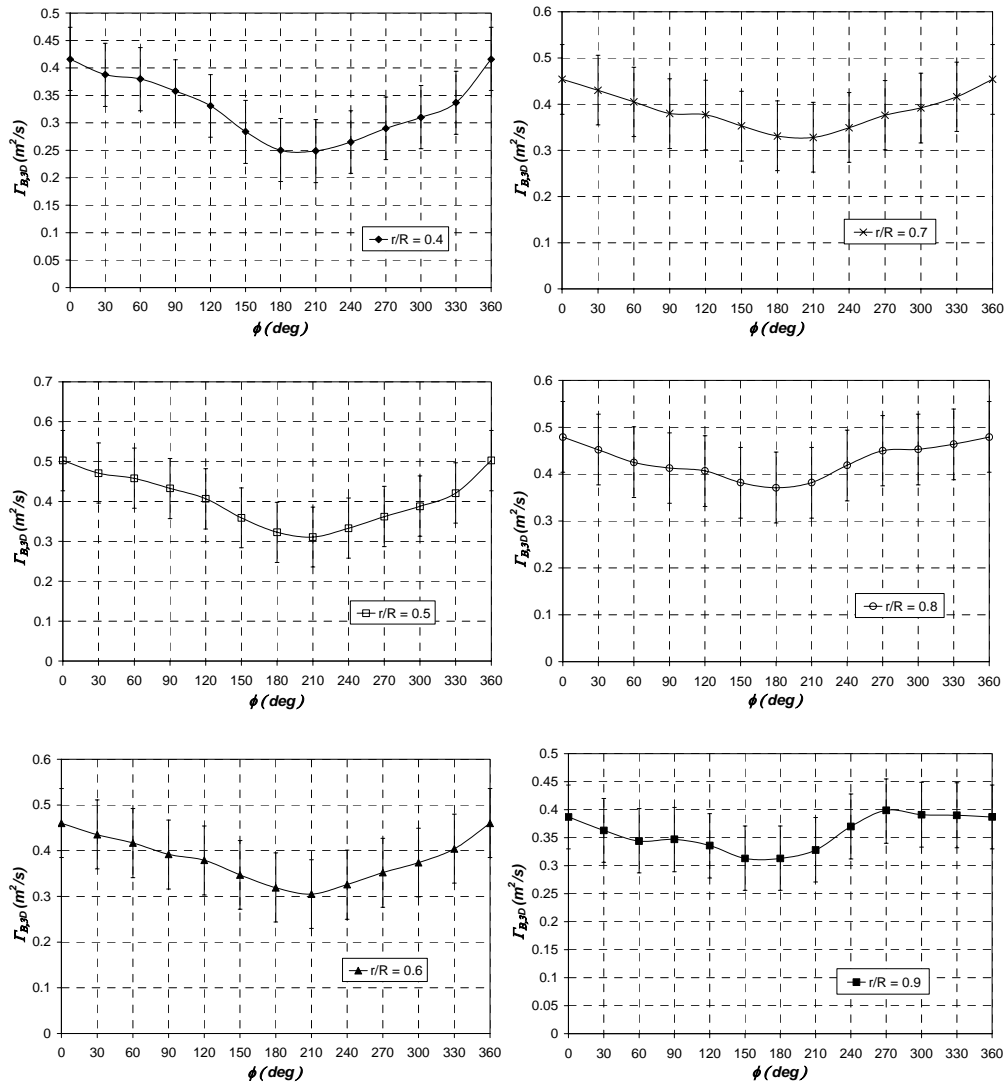


Figure 4.78 - Variation of the extrapolated bound circulation (corrected for tip/root loss) with blade azimuth angle at $\Psi=30^\circ$.

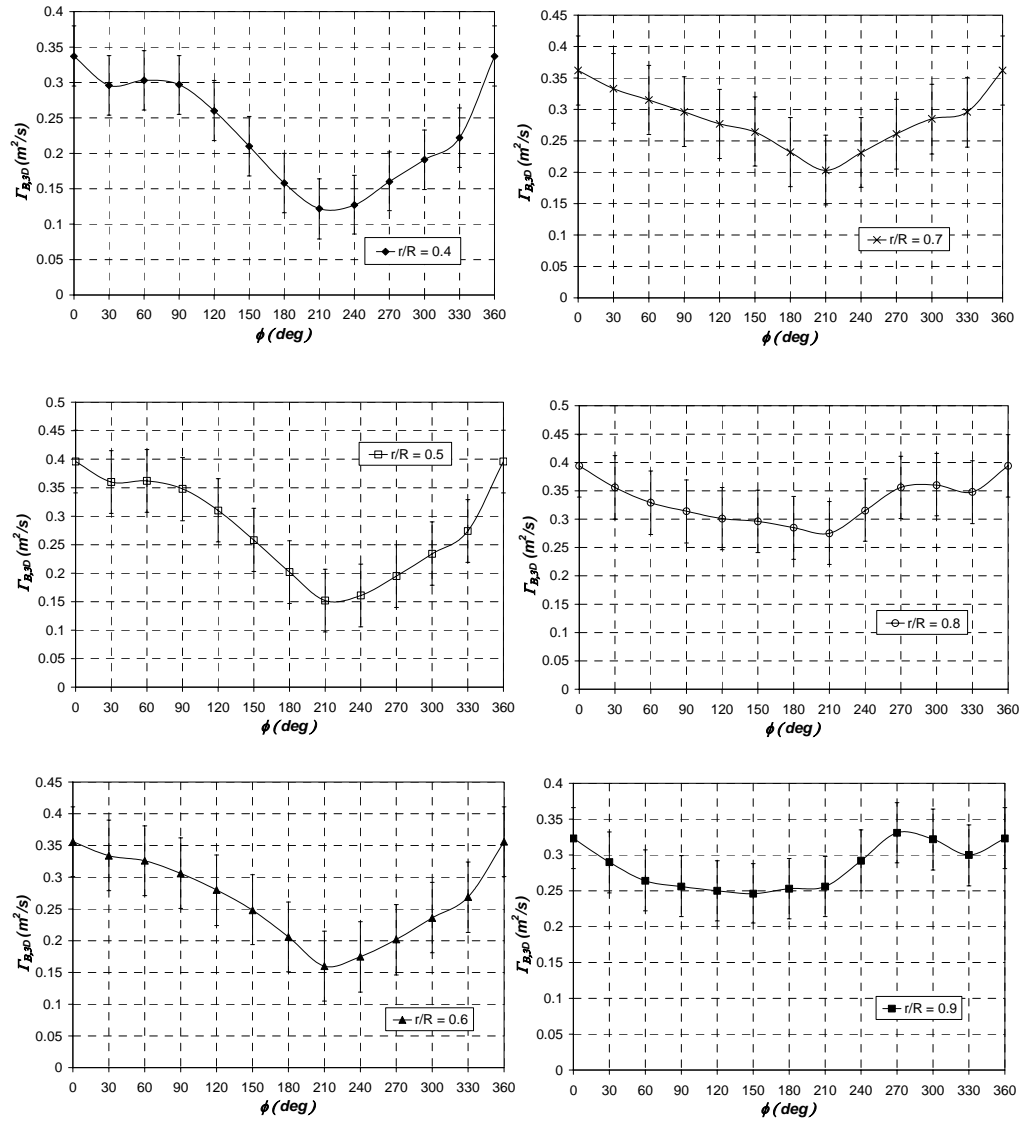


Figure 4.79 - Variation of the extrapolated bound circulation (corrected for tip/root loss) with blade azimuth angle at $\Psi=45^\circ$.

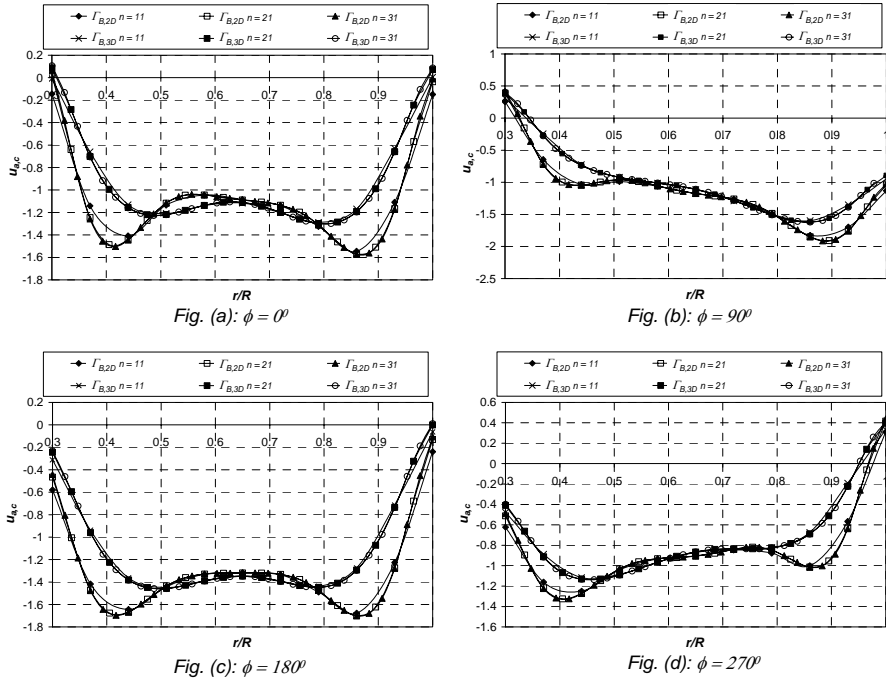


Figure 4.80 - Spanwise distributions of axial induced velocity at blades as predicted by HAWT_PVC

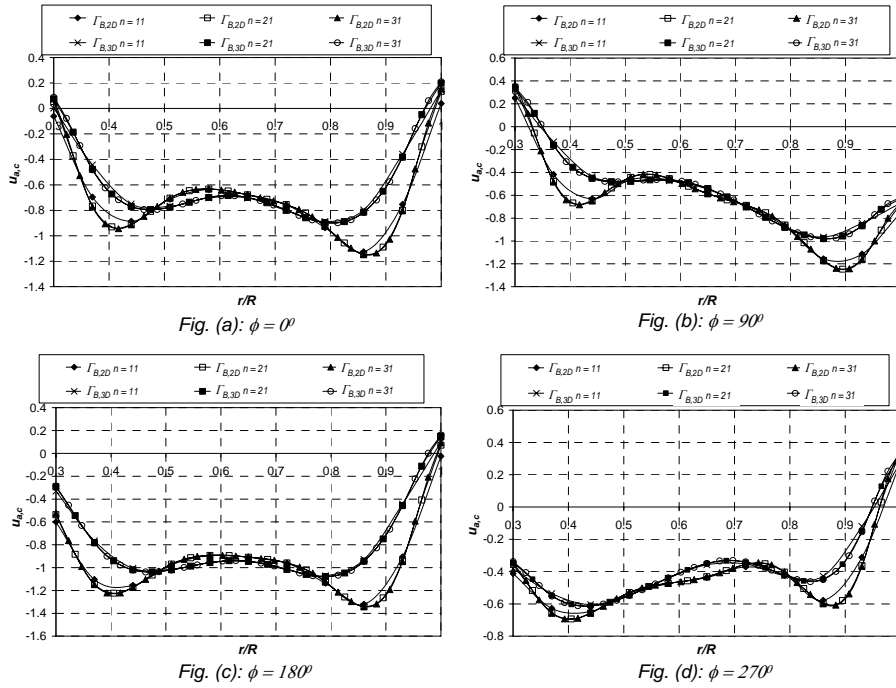


Figure 4.81 - Spanwise distributions of axial induced velocity at blades as predicted by HAWT_PVC

Table 4.6: Parameters used for the computations using HAWT_PVC for $\Psi = 30^\circ$ and 45° .

	$\Psi = 30^\circ$	$\Psi = 45^\circ$
$nwRev$	10	10
τ_{tot}	36	36
$\Delta\phi$	10°	10°
$R_{t,w1}$	0.61	0.60
$R_{t,w2}$	0.62	0.61
p	0.32	0.28
<i>ReleaseTip</i>	0.99	0.99
<i>ReleaseRoot</i>	0.305	0.305
χ^s	35°	48°
δ	0.5mm	0.5mm

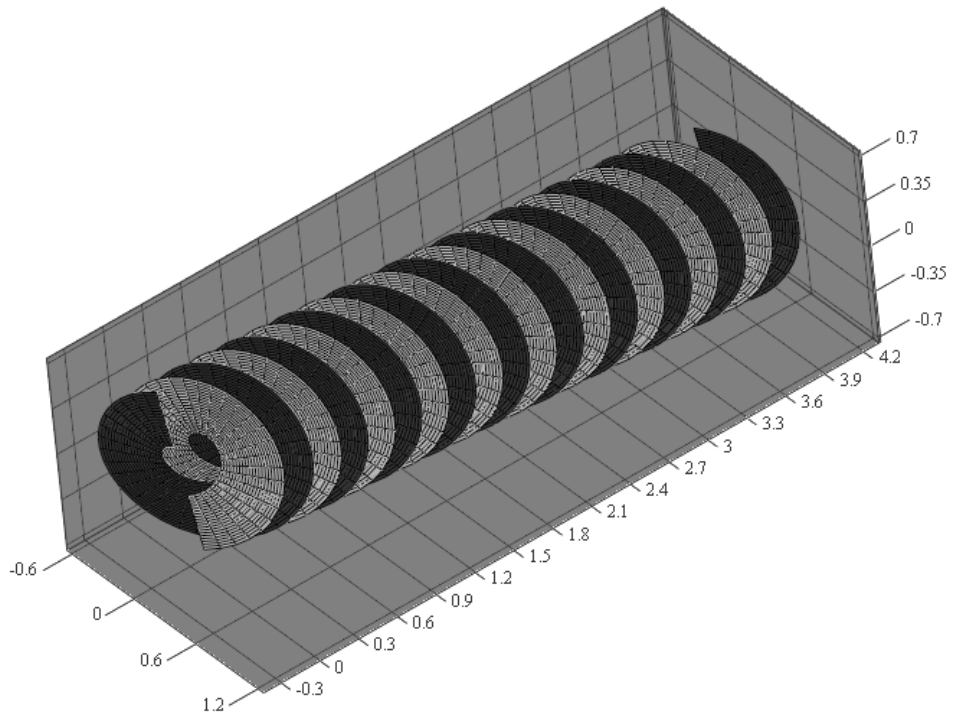


Figure 4.82 - Prescribed helical wake as modelled by HAWT_PVC at $\Psi=30^\circ$. $n=21$.

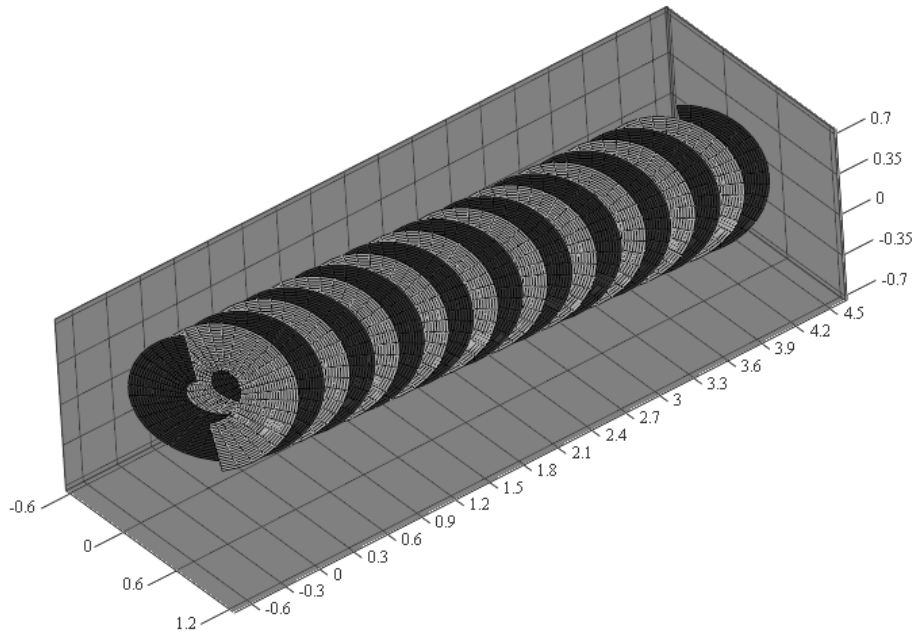


Figure 4.83 - Prescribed helical wake as modelled by HAWT_PVC at $\Psi=45^\circ$, $n=21$.

C.4 Assessment of the Effects of Tunnel Blockage in Yawed Conditions

To assess for tunnel blockage effects, *Procedure 1* described in Fig. 4.48 was applied. The bound circulation distributions shown in Figs. 4.78 and 4.79 were prescribed to HAWT_PVC to calculate the induced velocities at the wind tunnel exit (u_a tunnel exit) over a circular region having a diameter equal to that of the rotor. The parameters used for HAWT_PVC were the same as in table 4.6. The induced velocity was computed in a direction parallel to the tunnel jet. To obtain a conservative estimate, the upper limit of the circulation distributions was used for the calculations. Since yawed conditions were being considered, the computed induced velocity across the tunnel exit jet was uneven. The results are plotted in Fig. 4.84. It can be noted that the peak induced velocities are very small at both 30° and 45° yaw (-0.13 and -0.09 m/s, respectively). This is much less than the pitot-reading at the tunnel exit (5.5m/s). The equivalent values for k_e computed from Eq. 4.64 are 0.024 and 0.016, respectively. This was less than the acceptable limit of 0.05. Thus it may be concluded that in yawed conditions the tunnel blockage effects were also minimal.

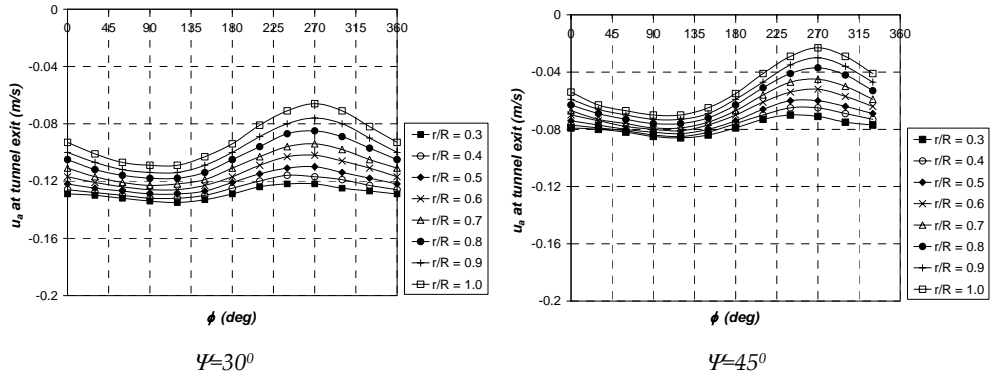


Figure 4.84 – Induced velocities computed using HAWT_PVC at tunnel exit across area equal to that of rotor ($n=21$).

C.5 Axial Induction Factor Distributions

Since wind tunnel blockage effects were found to be small, then it was justified to take U to be equal to U_{jet} (5.5m/s). The axial induction distributions for $u_{a,c}$ at each measuring plane ($Y_a=6, 3.5, 6$ and 9cm) could be found using the experimental values of $w_{a,c}$ in Figs. 4.19 and 4.20 (taking the smoothed values) and Eq. 4.57. The results for $u_{a,c}$ at 30° and 45° yaw are shown in Figs. 4.85 and 4.86.

The corresponding azimuthally averaged induction distributions could be found using the same method as for $\Psi=0^\circ$ (i.e. using Eqs. 4.81 and 4.82). The results for u_a at the different measuring planes are shown in Figs. 4.87 and 4.88. Linear interpolation was then used to estimate u_a at the rotorplane using an equation similar to Eq. 4.7. The distributions for u_a were smoothed using the Gaussian kernel technique described in Eq. 4.8. These smoothed distributions are also included in Figs. 4.87 and 4.88. It may be easily observed that for yawed conditions, u_a is not always constant with the rotor azimuth angle (ϕ). A cyclic variation in u_a is observed at the blade root and tip regions and is a consequence of the root and tip vortices in the wake. This variation has a frequency of twice the rotor angular speed for the simple reason that the rotor has two blades.

The axial induction factors at the rotorplane ($a_{1,c}$ and a_1) were found by dividing the interpolated induced velocities at the rotorplane by 5.5m/s. The results are shown in Figs. 4.89 and 4.90.

Chapter 4 – Aerodynamic Analysis of the TUDelft Model Turbine

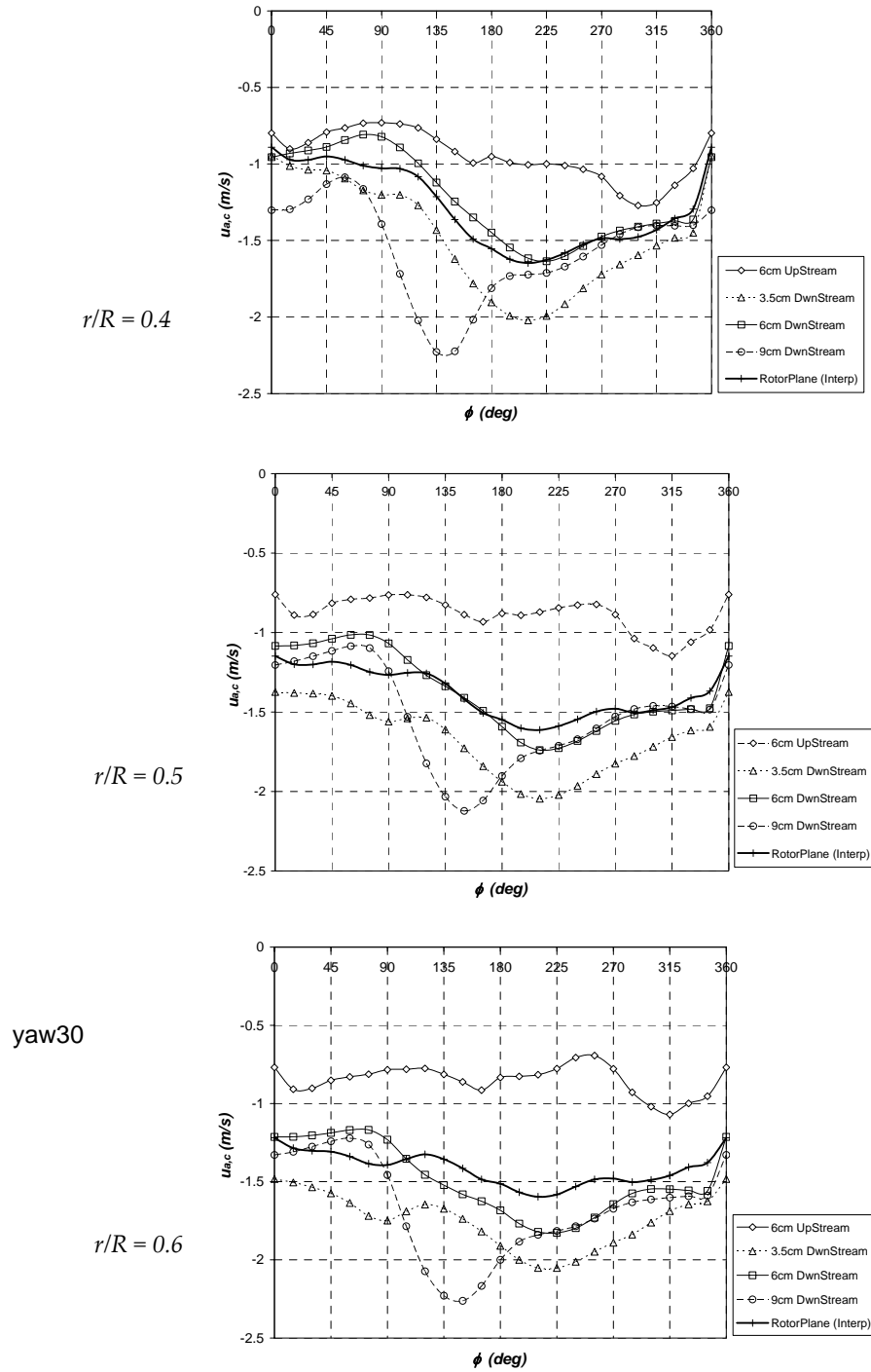


Figure 4.85 – Variation of axial induced velocity at blades with blade azimuth angle at different radial locations at $\Psi=30^\circ$.

Chapter 4 – Aerodynamic Analysis of the TUDelft Model Turbine

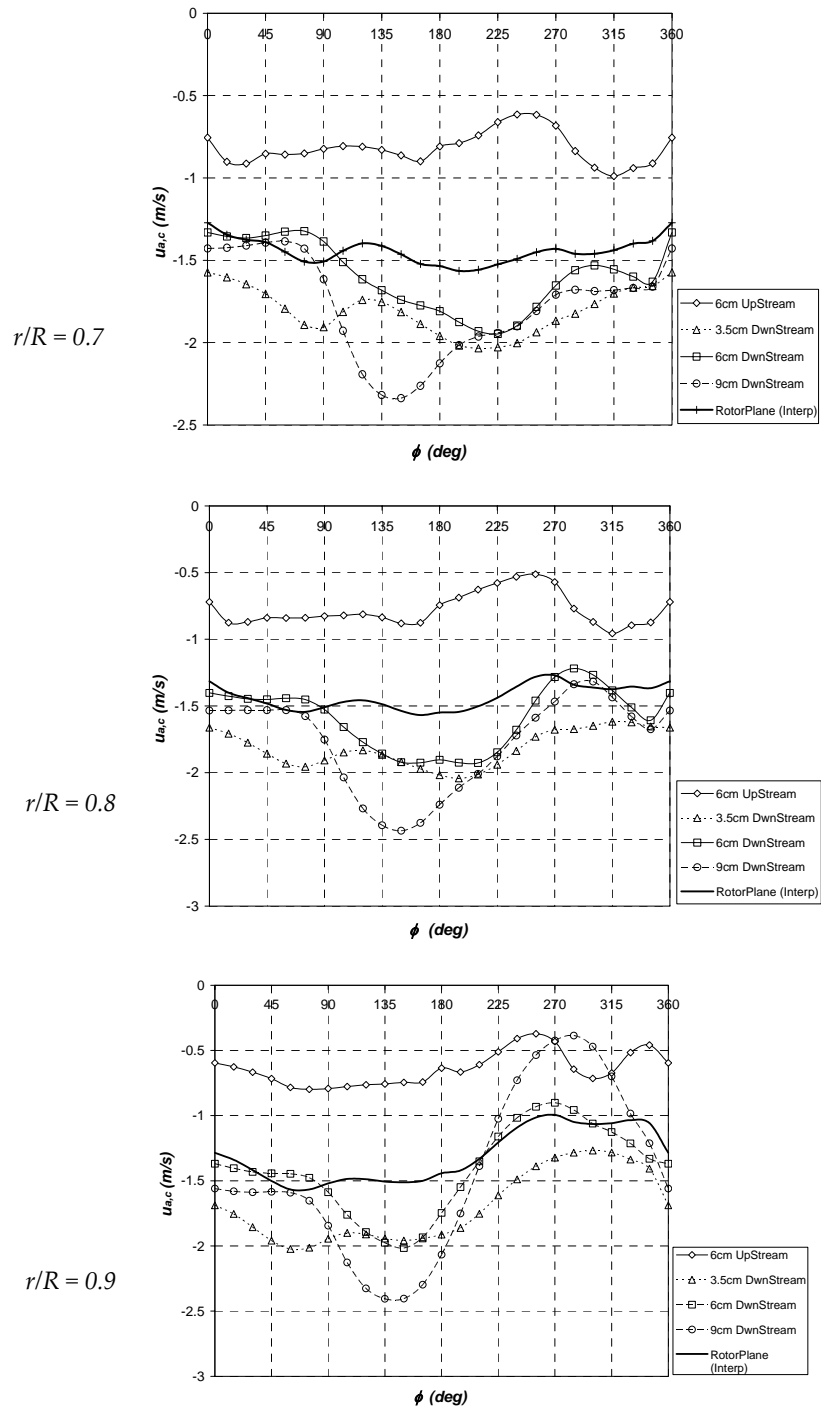


Figure 4.85 – contd. from previous page.

Chapter 4 – Aerodynamic Analysis of the TUDelft Model Turbine

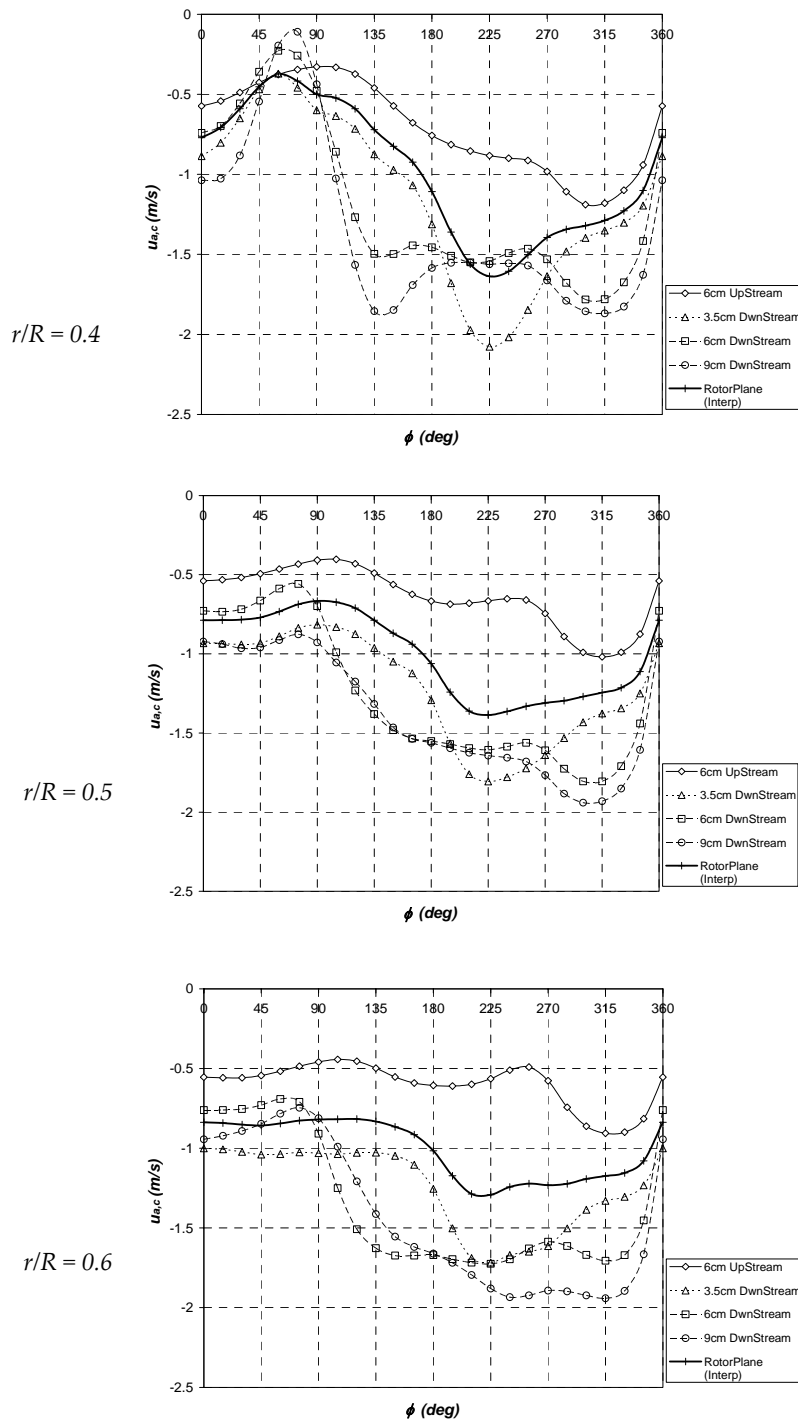


Figure 4.86 – Variation of axial induced velocity at blades with blade azimuth angle at different radial locations at $\Psi=45^\circ$.

Chapter 4 – Aerodynamic Analysis of the TUDelft Model Turbine

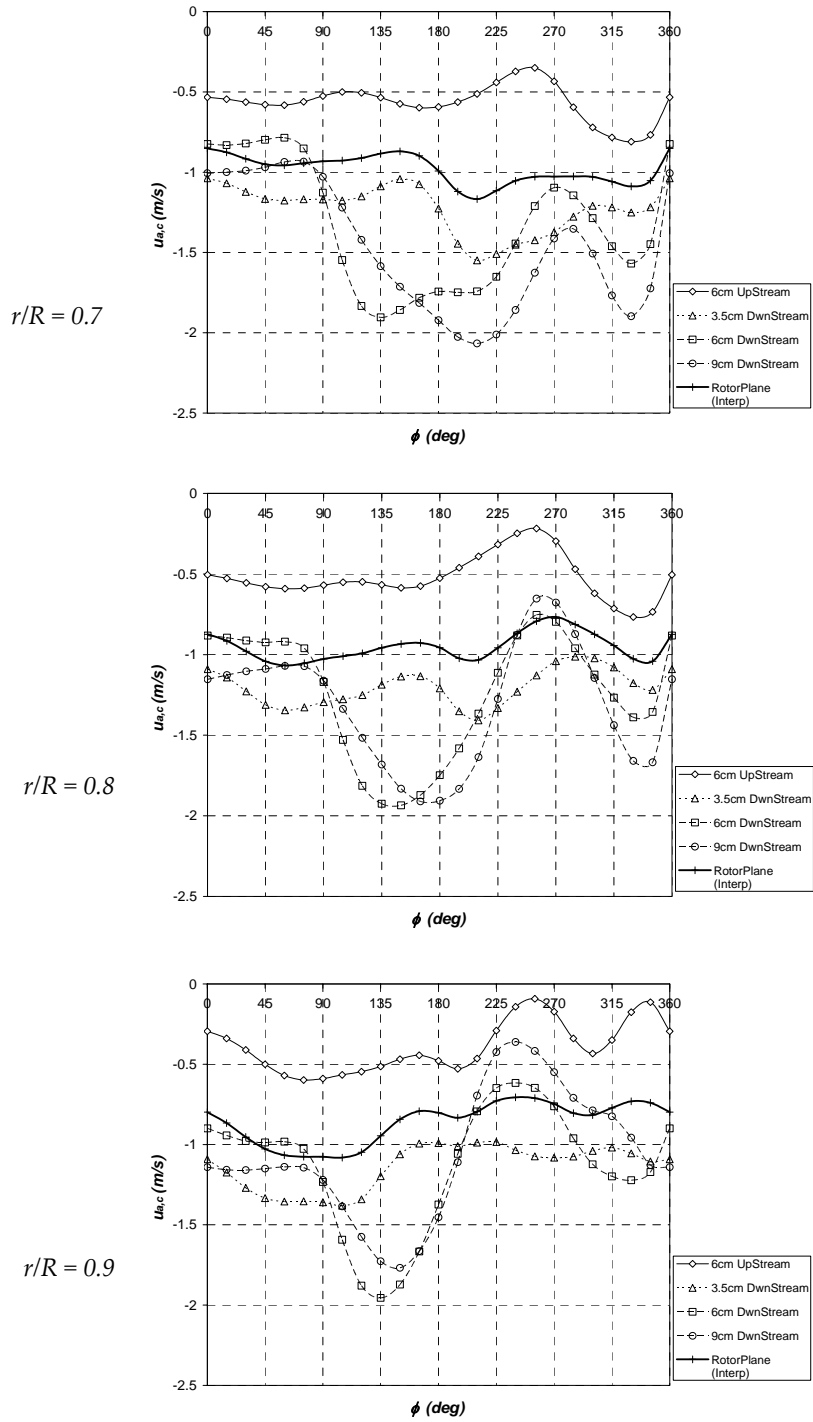


Figure 4.86 – contd. from previous page.

Chapter 4 – Aerodynamic Analysis of the TUDelft Model Turbine

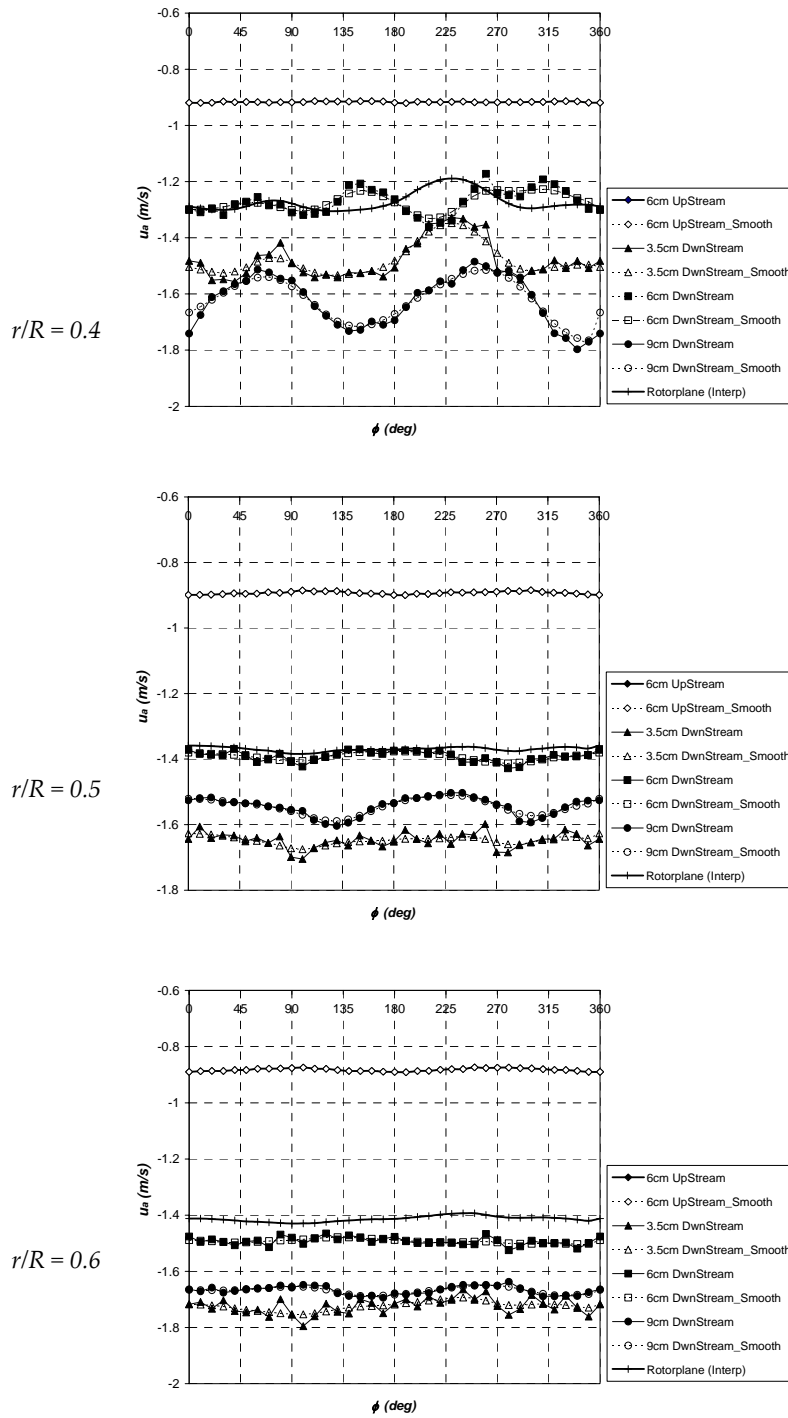


Figure 4.87 – Variation of azimuthally averaged axial induced velocity with blade azimuth angle at different radial locations at $\Psi=30^\circ$.

Chapter 4 – Aerodynamic Analysis of the TUDelft Model Turbine

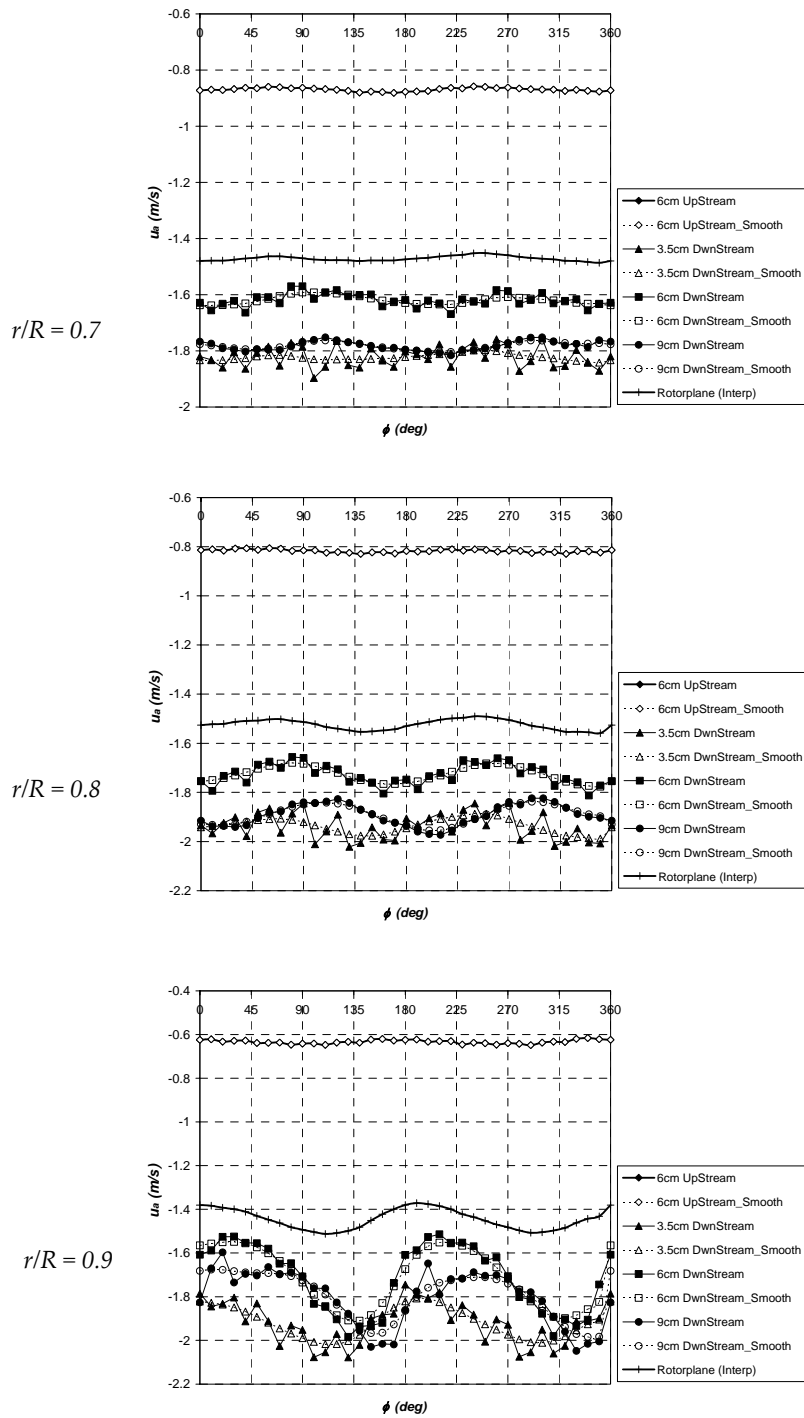


Figure 4.87 – contd. from previous page.

Chapter 4 – Aerodynamic Analysis of the TUDelft Model Turbine

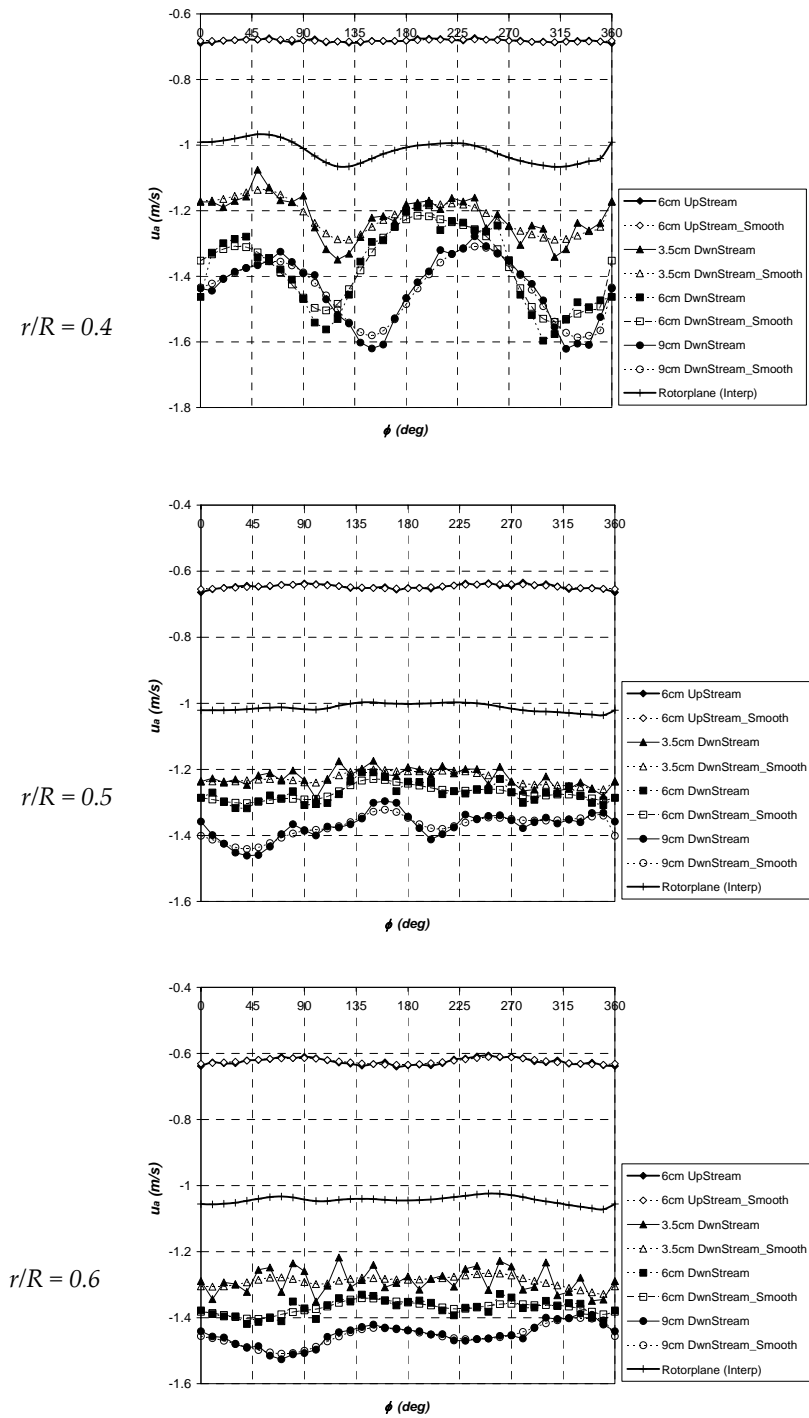


Figure 4.88 – Variation of azimuthally averaged axial induced velocity with blade azimuth angle at different radial locations at $\Psi=45^\circ$.

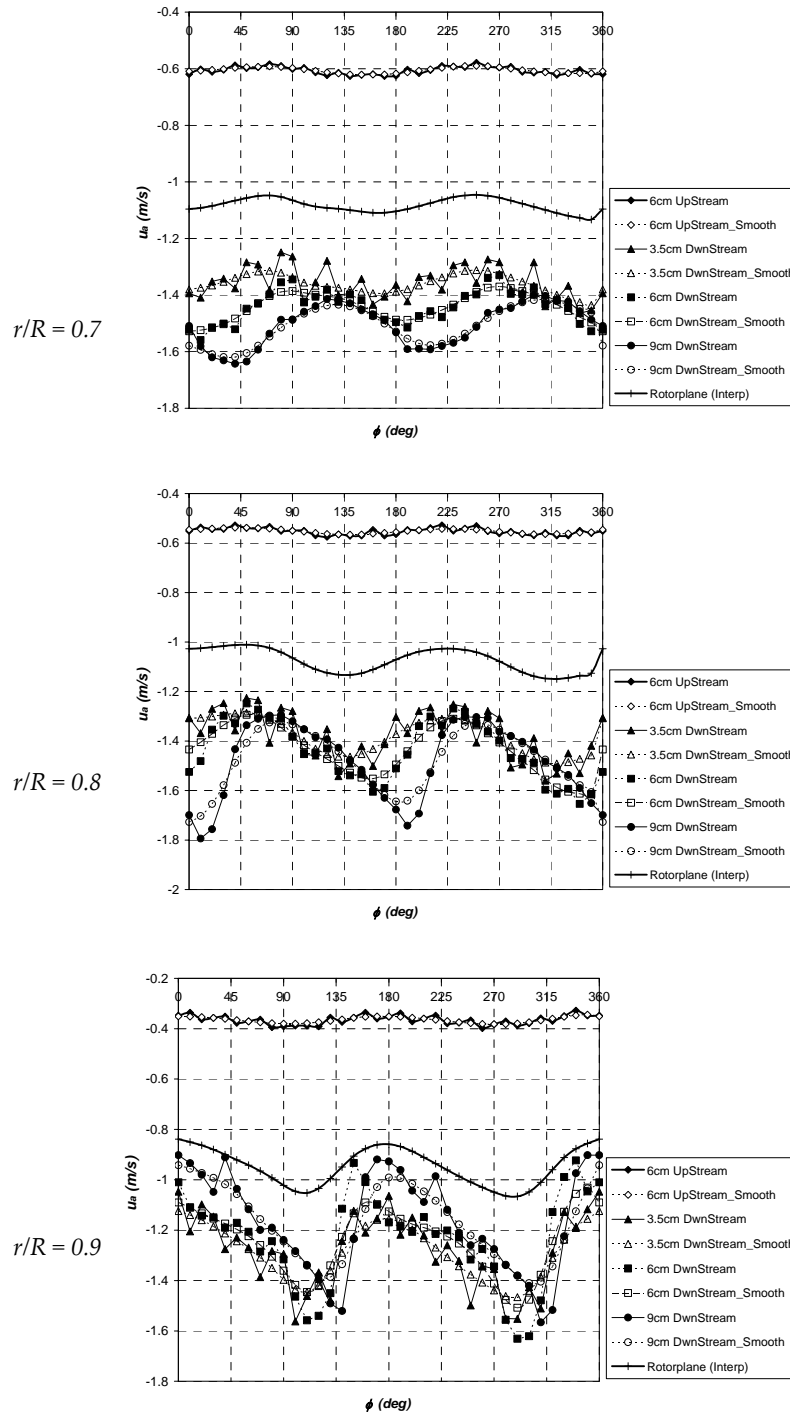


Figure 4.88 – contd. from previous page.

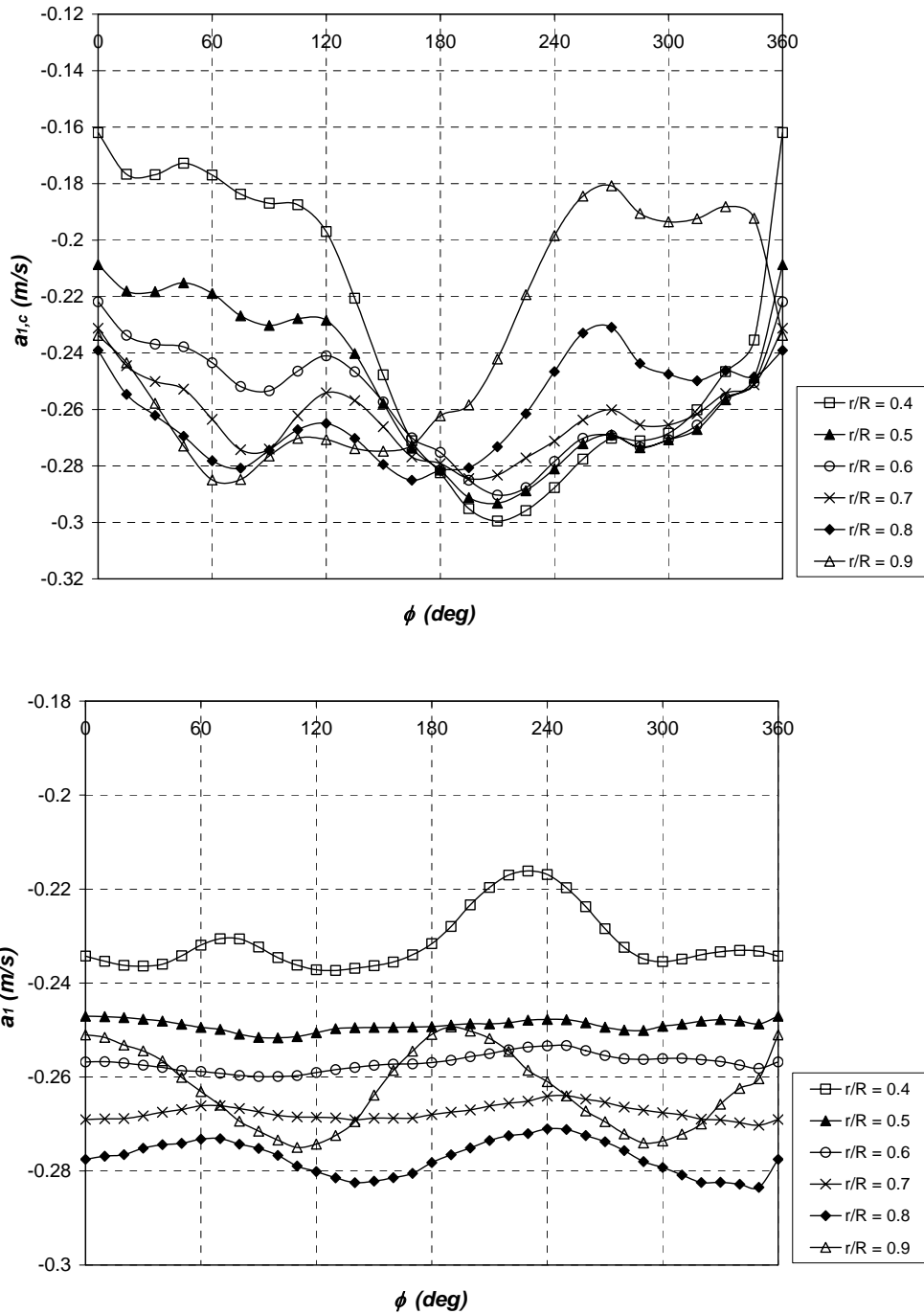


Figure 4.89 – Variation of the axial induction factor (at blade lifting line and azimuthally averaged) with blade/rotor azimuth angle at $\Psi=30^\circ$.

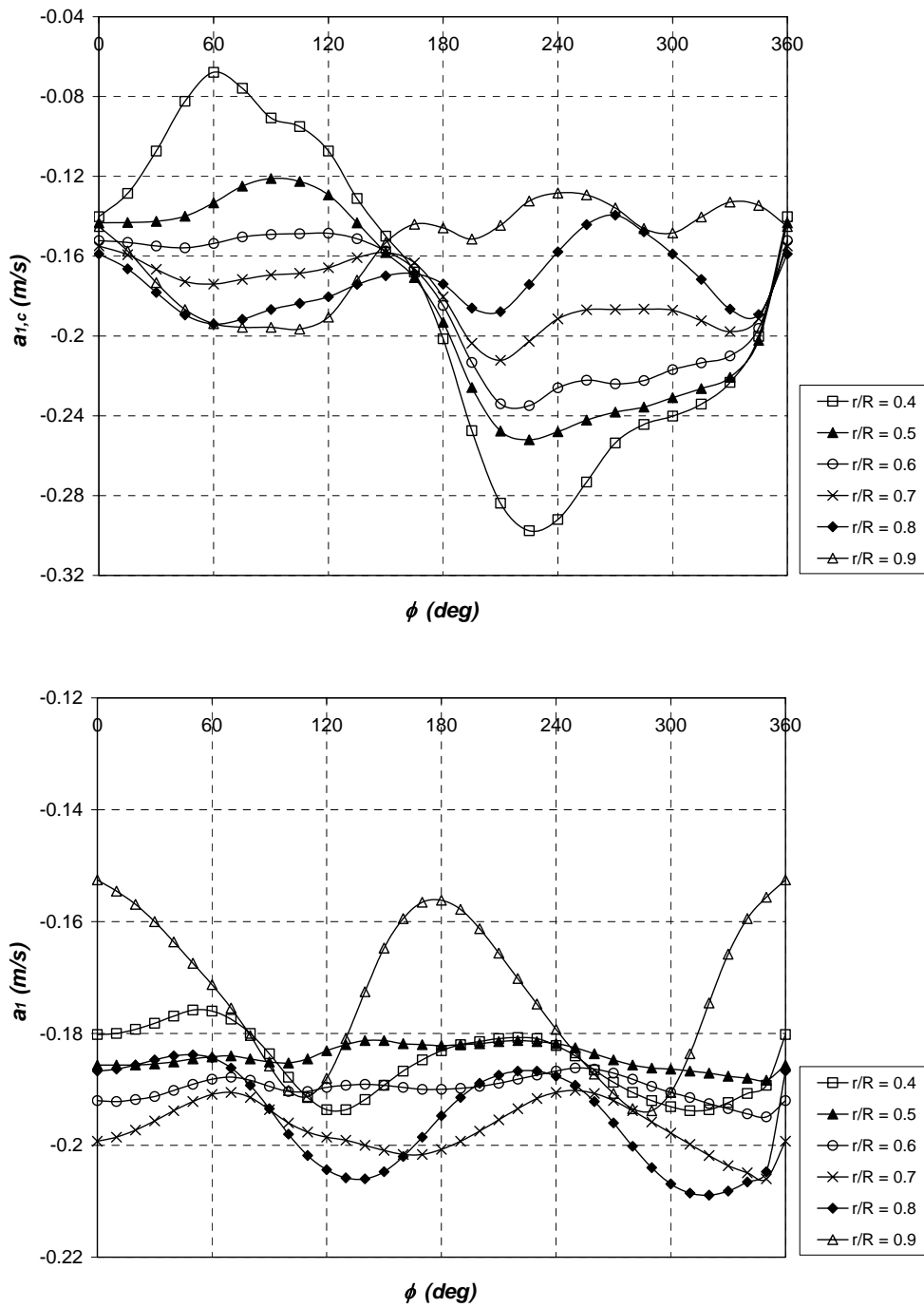


Figure 4.90 – Variation of the axial induction factor (at blade lifting line and azimuthally averaged) with blade/rotor azimuth angle at $\Psi=45^\circ$.

C.6 Comparison of Experimental Axial Induced Velocities with those from *HAWT_PVC*

Once the axial induced velocities were derived (section C.5), an attempt was made to assess the capability of the prescribed vortex model *HAWT_PVC* in treating yawed conditions at both 30° and 45° yaw. To do so, the parameters of table 4.6 were used together with the unsteady bound circulation distributions of Figs. 4.78 and 4.79. These distributions were prescribed to the model to compute the axial induced velocities ($u_{a,c}$) at 3.5cm downstream of the rotorplane. These were then compared with those obtained experimentally (of Figs. 4.85 and 4.86). The comparison is shown in Figs. 4.91 and 4.92. Note that comparison of the values at 3.5cm downstream is being made instead of that at the rotorplane so as to avoid any ambiguity resulting from the additional uncertainties in the linear interpolation (using Eq. 4.7). In Figs. 4.91 and 4.92, the error bars in the experimental values of $u_{a,c}$ are displayed. These are equal to $\pm 0.26\text{m/s}$ at 30° yaw and $\pm 0.21\text{m/s}$ at 45° yaw. The vortex model results also include error bars. These represent the uncertainty in the vortex model predictions for $u_{a,c}$ resulting from the uncertainties in the prescribed bound circulations. Recall from section C.1 that the prescribed bound circulations were derived from the inflow measurements and therefore these circulations are also subject to the uncertainties in the inflow measurements. Such uncertainties were displayed earlier in Figs. 4.78 and 4.79.

Despite the fact that in *HAWT_PVC* the wake was modelled using experimental data collected from the smoke visualization measurements, the correlation of the vortex model predictions with the experimental results was not as good as that achieved in axial conditions (Fig. 4.56). One reason for this is the fact that wake roll-up is not modelled in *HAWT_PVC*. Another reason is that shed circulation is also not included in the wake model embedded in this vortex code. However, in the validation work of the newly developed free-wake vortex model, *HAWT_FWC* (which accounts for both roll-up and shed circulation in the wake), it was discovered that there are other reasons for not obtaining a good correlation with the experimental measurements. The levels of shed circulation were found to be very small compared to trailing circulation. But it was discovered that it is very likely that the flow interference caused by the centrebody of the tunnel turbine should be blamed. Looking closely at Figs. 4.91 and 4.92 shows that for blade positions $0 < \phi < 180^\circ$, the correlation with the experimental values is relatively good, taking the uncertainty limits into account. The large disagreement only occurs for blade positions $180 < \phi < 360^\circ$. The smoke visualization photos revealed that in yaw, the tip vortex path was being obstructed by the centrebody on the upwind side of the rotor, i.e. for the same blade positions $180 < \phi < 360^\circ$. This interference was not modelled in *HAWT_PVC*. Further details of this investigation are given later on in Chapter 5, page 262.

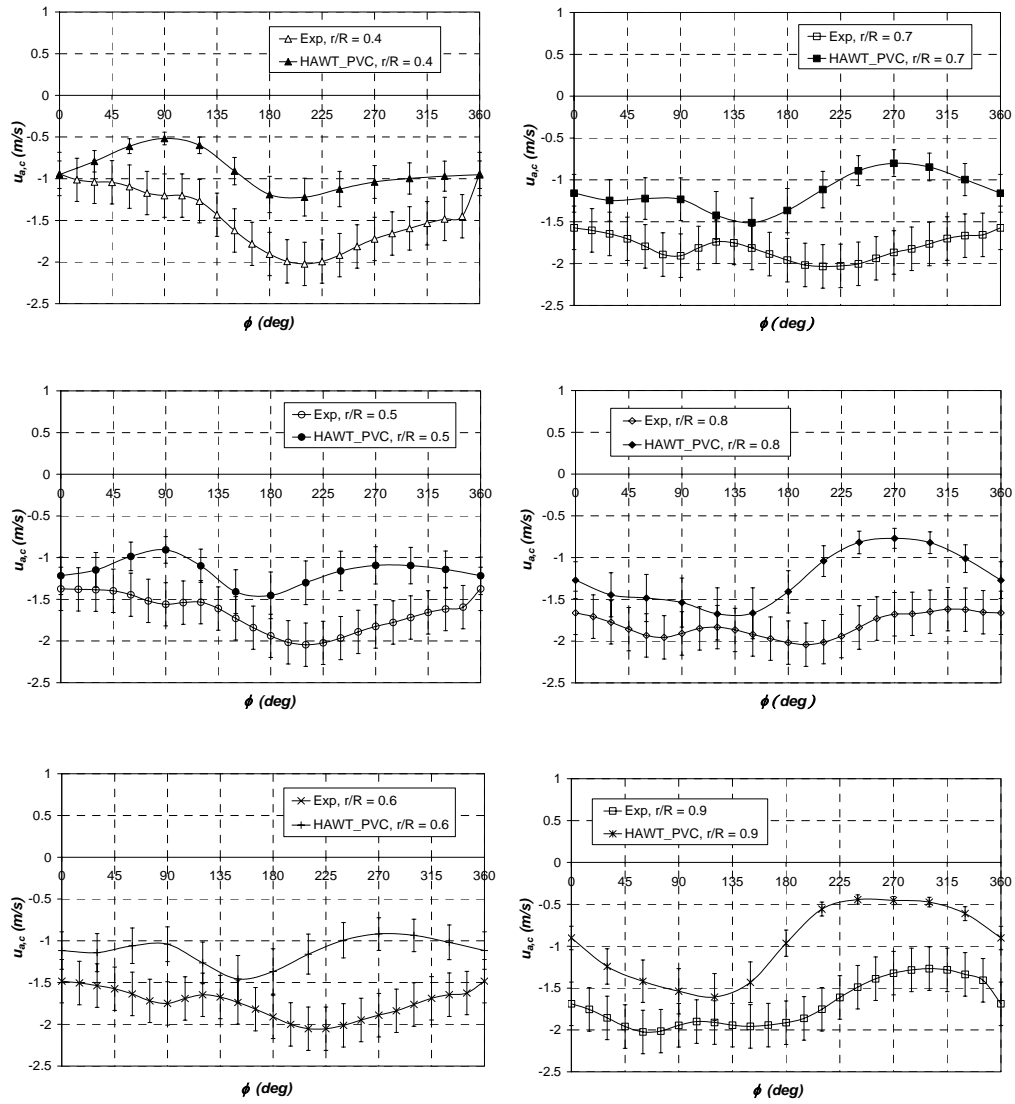


Figure 4.91 - Comparison of axial induced velocity distributions computed by HAWT_PVC with those obtained from the hot-film measurements at $\Psi=30^\circ$ at $Y_a=3.5\text{cm}$ downstream.

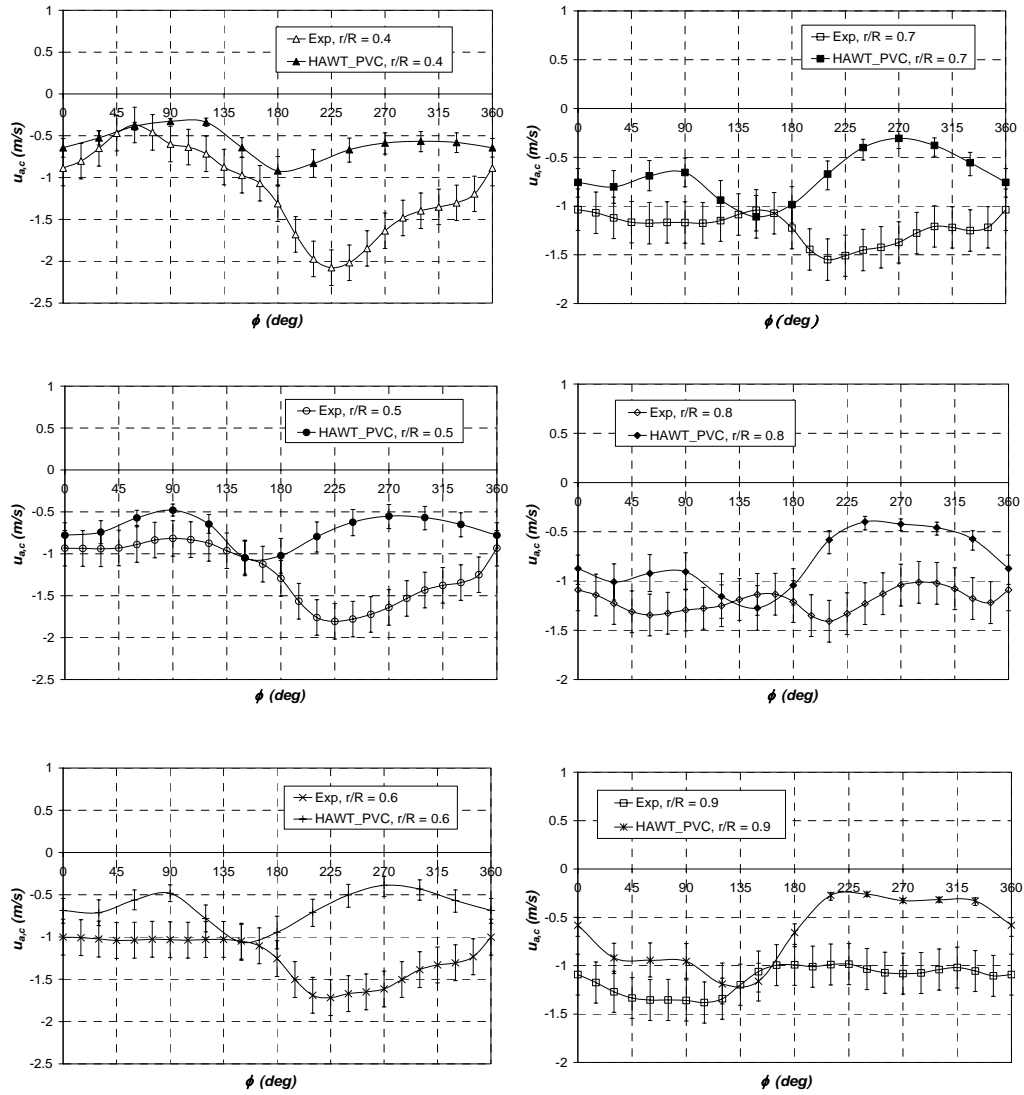


Figure 4.92 - Comparison of axial induced velocity distributions computed by HAWT_PVC with those obtained from the hot-film measurements at $\Psi=45^\circ$ at $Y_a=3.5\text{cm}$ downstream.

C.7 Blade Load Distributions

As for axial conditions, the values of $\Gamma_{B,3D}$ of Figs. 4.78 and 4.79 were used to determine the unsteady lift coefficient corrected for tip/root loss ($C_{l,3D}$) in accordance with Eq. 4.14 at radial locations 40, 50, 60, 70, 80 and 90%R and at different blade azimuth angles over one whole revolution of the rotor. Re-call that the calculations with *HAWT_PVC* (section C.2) have shown that radial locations 50, 60, 70, 80%R tend to be not affected by the tip/root loss correction and therefore $C_{l,3D}$ is equal to $C_{l,2D}$ as estimated by the unsteady aerofoil model described in section 4.3.2 and the angle of attack values of Figs. 4.68 and 4.69. The drag coefficient was determined from the 2D static data for the *NACA 0012* aerofoil and was not corrected for tip/root loss and unsteadiness. The error incurred was small since at low angles of attack, the C_d are very small compared with C_l (<5% of the C_l). Figs. 4.93 and 4.94 show the variations of the unsteady lift coefficient ($C_{l,3D}$) with angle of attack at different radial locations at 30° and 45° yaw. For the sake of clarity, the error bars are not displayed in these plots. Due to the unsteadiness at each radial location (i.e. each aerofoil section experiences time-dependent variations of V_r and α), hysteresis loops are formed. Since the angles of attack are small and the flow over the blades is attached, then no dynamic stall takes place. The loops are modelled by the unsteady aerofoil model and if static aerofoil data was used in the computations, no loops would be observed, but a simple straight line along which C_l and α will vary. As the level of unsteadiness increases with yaw angle, the loops are in general wider at $\psi=45^\circ$ than at $\psi=30^\circ$, even though the overall values of C_l and α are smaller.

Figs. 4.95 and 4.96 show the results obtained for the axial thrust loading as a function of the blade azimuth angle (ϕ). These results were computed using the same method as for axial conditions. At $\psi=30^\circ$, the error intervals by assuming a ± 0.26 m/s deviation in $w_{a,c}$ range from ± 1.2 N/m at $r/R=0.4$ to ± 2.8 N/m at $r/R=0.9$. This is approximately equivalent to an error \mathcal{E}_T in the range of ± 14 -25%. At $\psi=45^\circ$, the error intervals by assuming a ± 0.21 m/s deviation in $w_{a,c}$ range from ± 1.0 N/m at $r/R=0.4$ to ± 2.0 N/m at $r/R=0.9$. This is approximately equivalent to the percentage error \mathcal{E}_T being in the range of ± 16 - 35%. These error intervals are large, considerably larger than those of the inflow measurements from which they were derived. This consolidates what was proved analytically in section 4.3.5, i.e. the percentage error in the derived axial thrust loading (\mathcal{E}_T) is very sensitive to the error in the inflow at the blade lifting lines obtained from the inflow measurements, ($\mathcal{E}_{w_{a,c}}$). It can also be confirmed that the sensitivity increases at larger yaw angles. For the torque loading, the error intervals were found to be much larger, sometimes exceeding 100% of the azimuthally averaged thrust loading at some radial locations. This also consolidates what was shown in section 4.3.5, i.e. the error in the derived torque loading (\mathcal{E}_Q) resulting from the error in the inflow measurements is usually larger than that in the axial thrust loading (\mathcal{E}_T). This explains the limitation for this analysis, i.e. to derive the unsteady aerodynamic loads from hot-film measurements in the near wake. The accuracy of the results could only be improved by being able to measure the flow velocities more accurately.

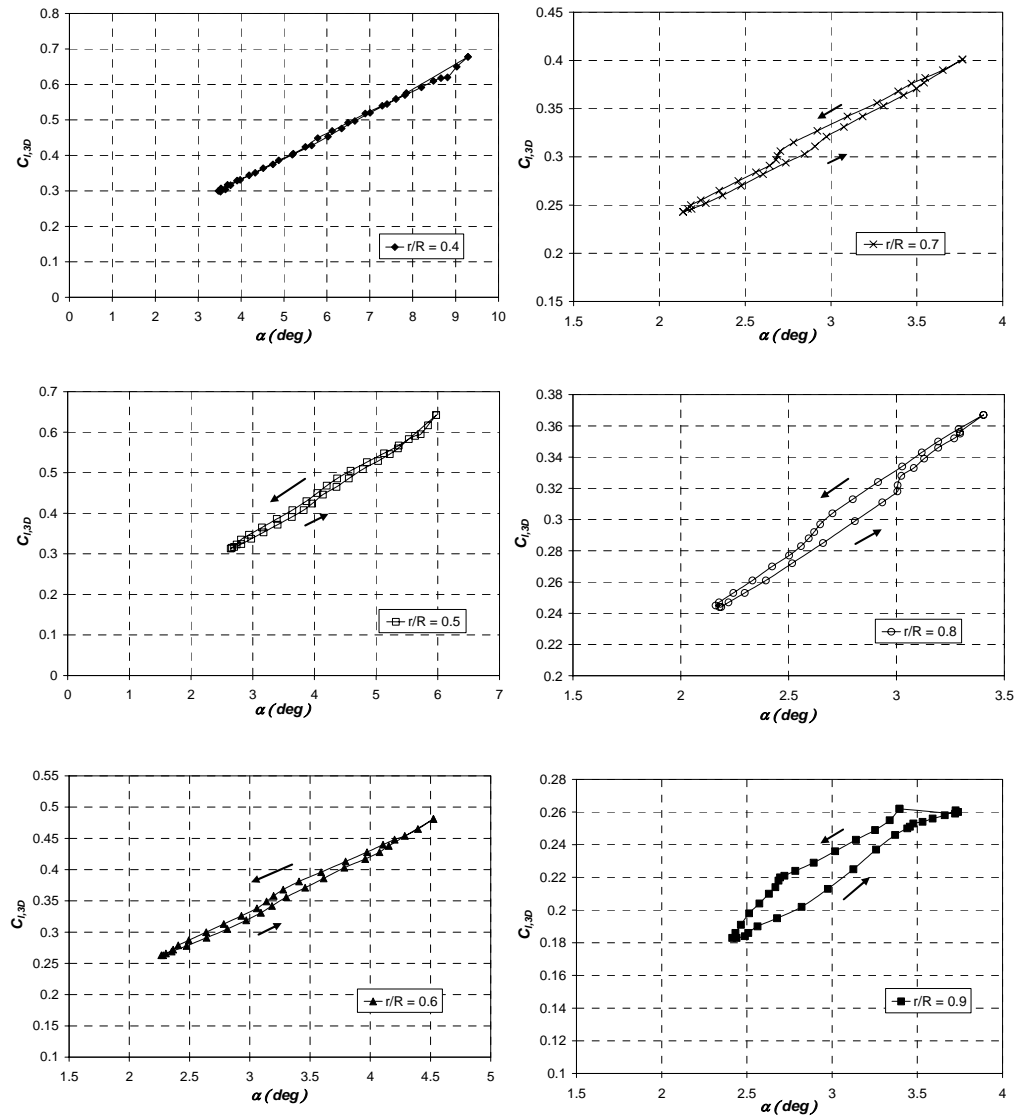


Figure 4.93 – Variation of unsteady lift coefficient with angle of attack at various radial locations at $\Psi=30^\circ$.

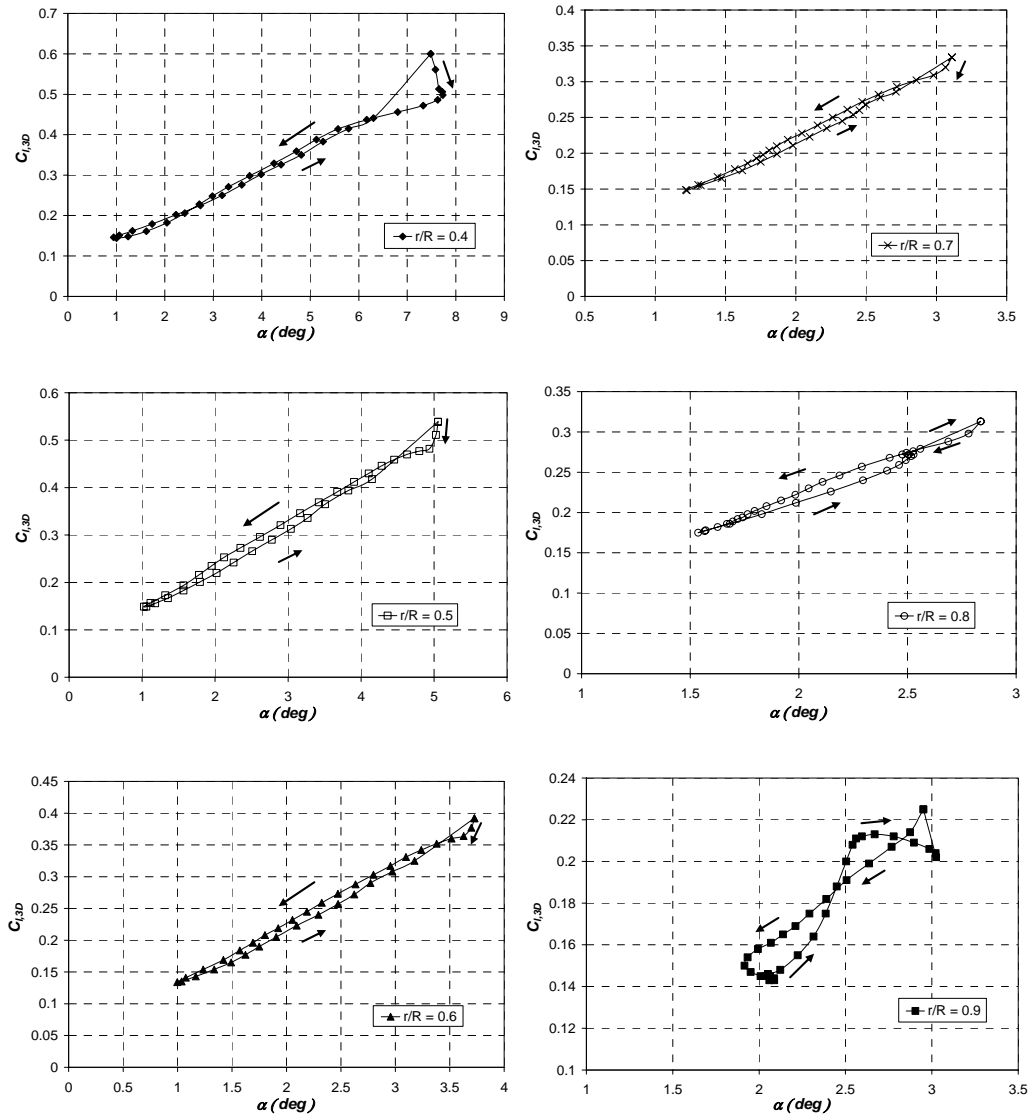


Figure 4.94 – Variation of unsteady lift coefficient with angle of attack at various radial locations at $\Psi=45^\circ$.

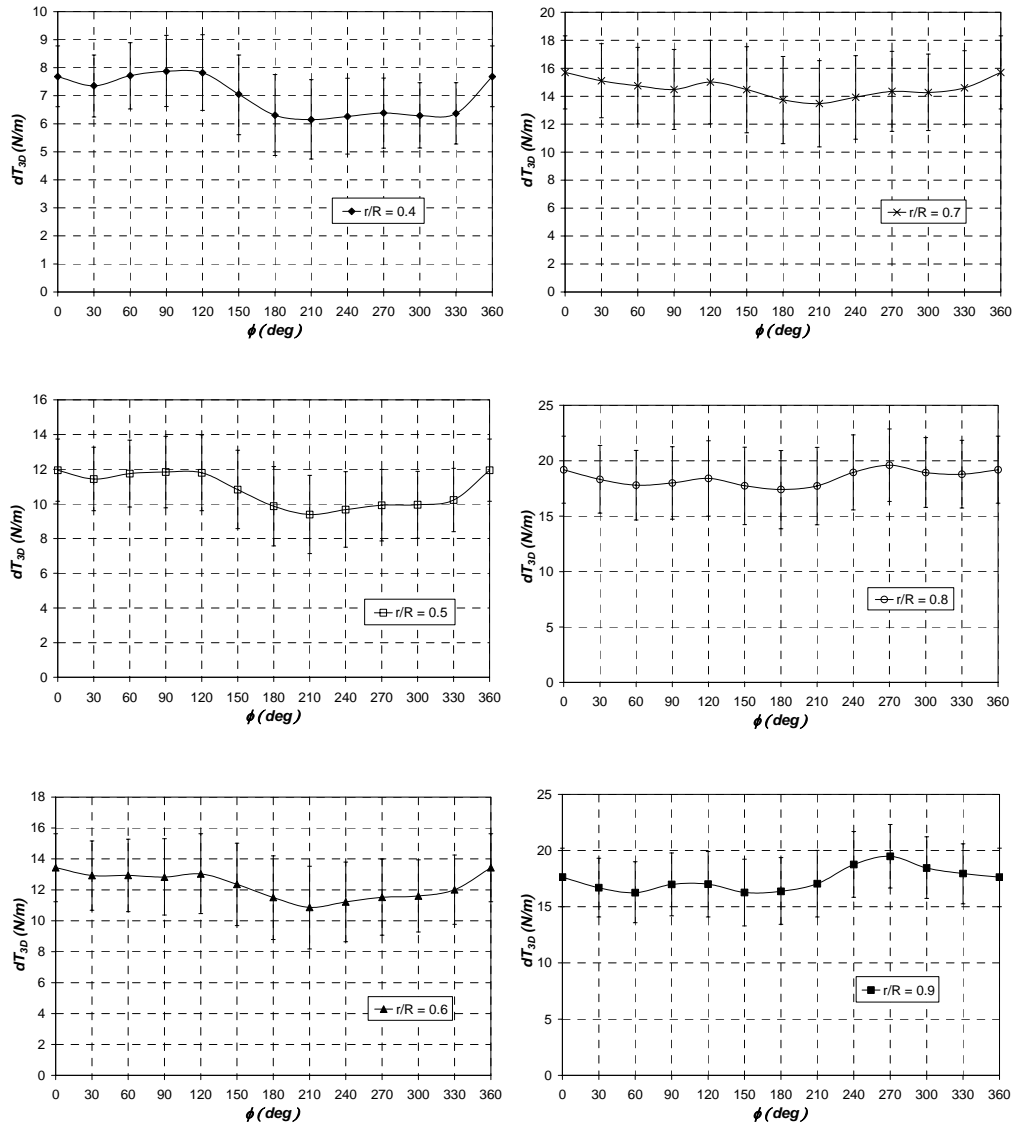


Figure 4.95 – Variation of unsteady axial thrust loading with blade azimuth angle at various radial locations at $\Psi = 30^\circ$.

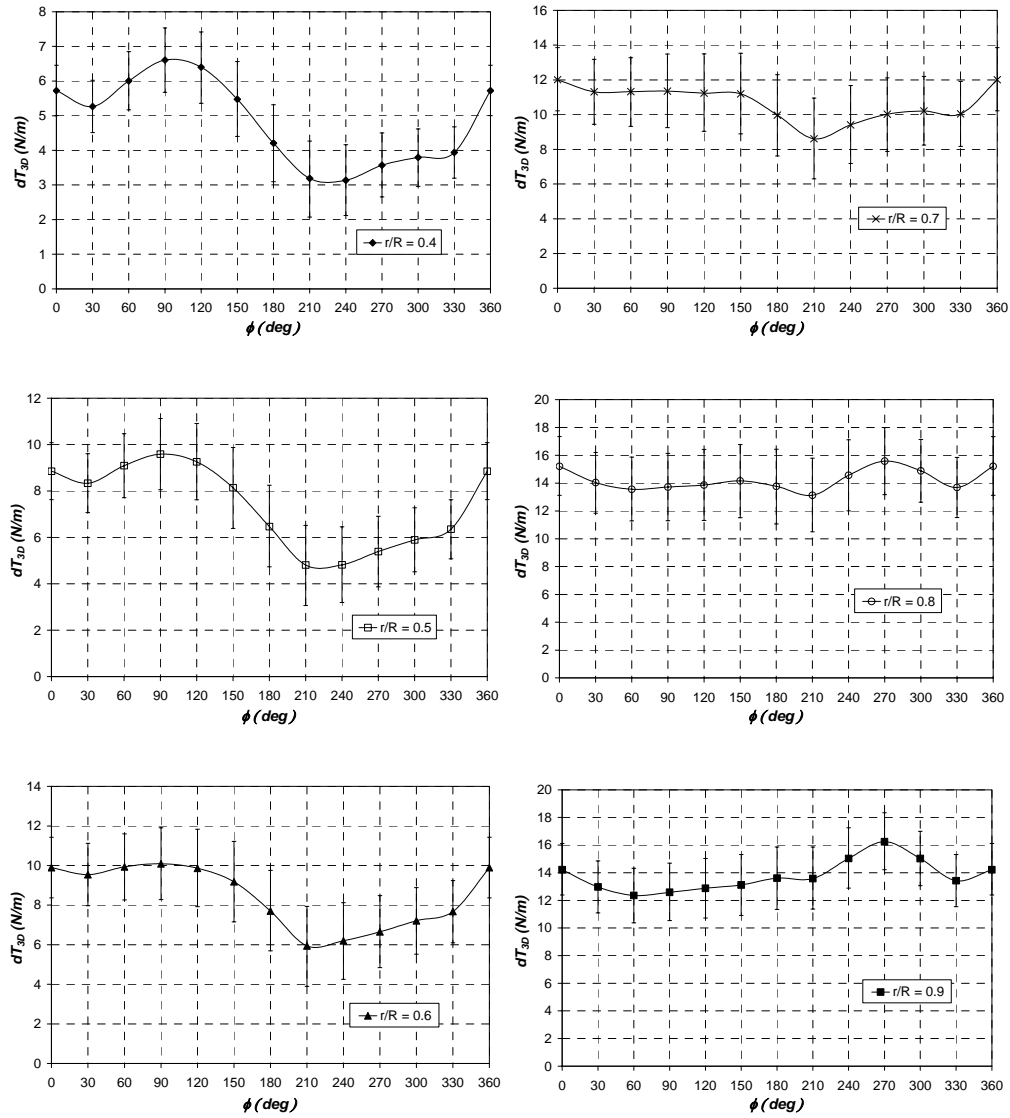


Figure 4.96 – Variation of unsteady axial thrust loading with blade azimuth angle at various radial locations at $\Psi=45^\circ$.

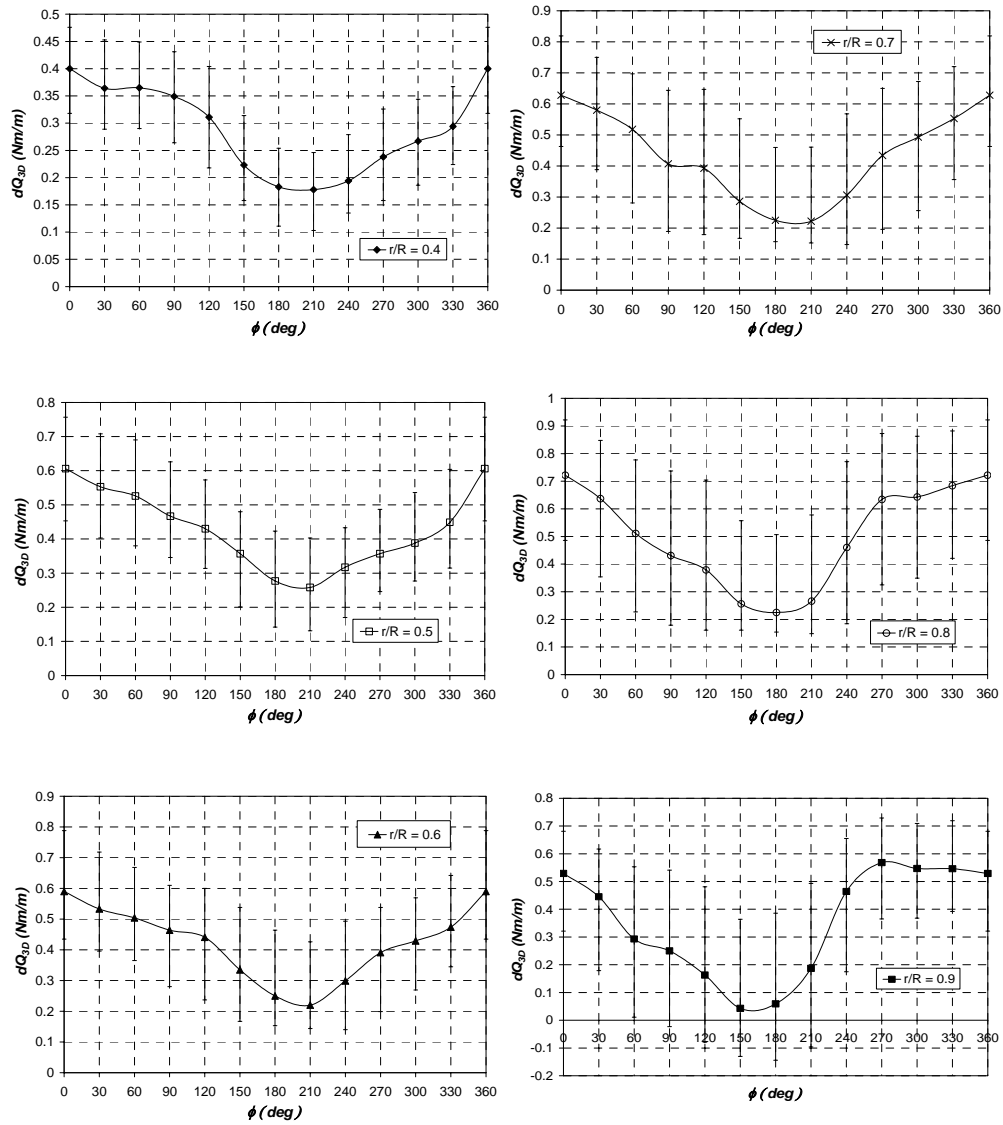


Figure 4.97 – Variation of unsteady torque loading with blade azimuth angle at various radial locations at $\Psi=30^\circ$.

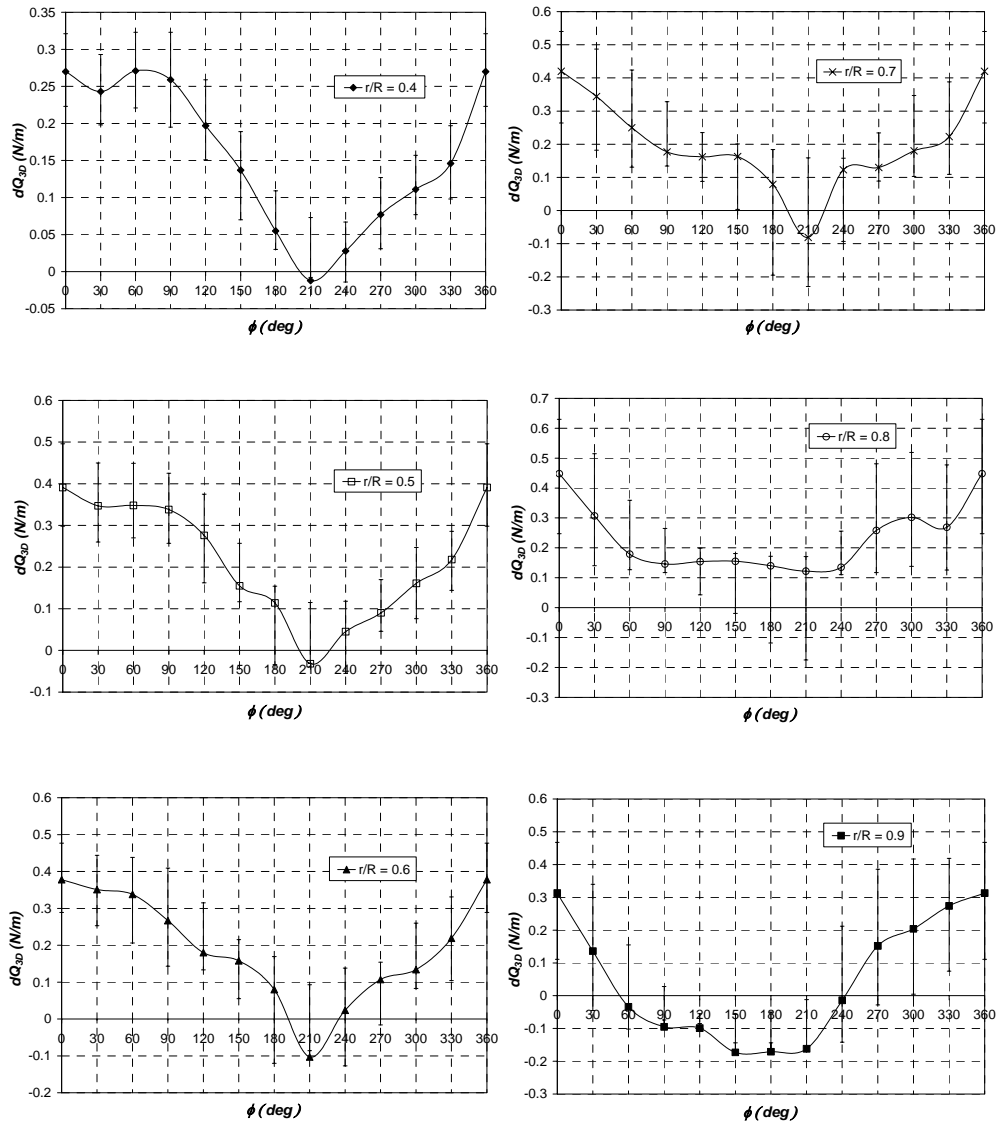


Figure 4.98 – Variation of unsteady torque loading with blade azimuth angle at various radial locations at $\Psi=45^\circ$.

C.8 Comparison of Axial Thrust Coefficients

The axial thrust coefficient at each yaw angle for $\lambda=8$ and $\theta_{ip}=2^\circ$ was computed by *HAWT_LFIM* by integrating numerically the axial thrust loading distributions of Figs. 4.95 and 4.96. These were compared with those measured using strain gauges in the wind tunnel experiments (refer section 4.2.3, Fig. 4.26). The comparison for C_T is given in table 4.7 below. Note that the azimuthal averaged value of C_T is being compared.

Table 4.7: Comparison of axial thrust coefficients derived by HAWT_LFIM using hot-film near wake measurements with those measured using strain gauge techniques. (Tip/root loss correction applied)

	<i>Measured using Strain Gauges</i>	<i>Derived from Inflow Measurements</i>	<i>Percentage Discrepancy</i>
$C_T (\Psi=30^\circ)$	0.693	0.472 ± 0.09	$-31.9 \pm 12.7\%$
$C_T (\Psi=45^\circ)$	0.514	0.347 ± 0.063	$-32.5 \pm 12.4\%$

In table 4.7, the percentage discrepancies relative to the measured values are given. The uncertainty intervals in C_T due to the assumed errors in $w_{a,c}$ are also included together with the corresponding uncertainties in the percentage discrepancy. The mean percentage discrepancy is found to be quite high (about -32%) which is considerably larger than that obtained for $\Psi=0^\circ$ (about -16%, refer to table 4.5). Even the range in the uncertainty resulting from the uncertainty in $w_{a,c}$ is very large (about 12%) and this shows that the C_T values derived using *HAWT_PVC* are very sensitive to the errors in $w_{a,c}$. Apart from the errors in $w_{a,c}$, another source of uncertainty is due to the tip/root loss correction used (described in section C.2).

To be able to assess the sensitivity of C_T to the applied tip/root loss correction, *HAWT_LFIM* computed the C_T values with no tip/root loss correction. The axial thrust loading (dT) values at radial locations 40, 50, 60, 70, 80 and 90%*R* were computed using the 2D values of C_l and C_d (i.e. no tip/root loss correction). For each blade azimuth angle, the spanwise distributions were then extrapolated by applying the boundary condition that at 30 and 100%*R* dT is zero and applying a spline interpolation (using method of Appendix D). Such distributions were integrated to yield C_T . These results were compared with the measured values, as shown in table 4.8 below.

In table 4.8, it is noted that the mean percentage discrepancy is lower than that with no tip/loss correction (-20% instead of -32%) indicating that the uncertainty in this correction has a considerable influence on the derived values for C_T . Yet the uncertainty resulting from errors in $w_{a,c}$ arising from the hot-film measurements is larger. Another important point is that the uncertainty in the tip/root loss correction is not expected to influence the loading distributions over the middle blade sections (between 50% and 80%*R*).

Table 4.8: Comparison of axial thrust coefficients derived by HAWT_LFIM using hot-film near wake measurements with those measured using strain gauge techniques. (Tip/root loss correction not applied)

	<i>Measured using Strain Gauges</i>	<i>Derived from Inflow Measurements</i>	<i>Percentage Discrepancy</i>
$C_T (\Psi=30^\circ)$	0.693	0.55 ± 0.1	$-20.6 \pm 14.0\%$
$C_T (\Psi=45^\circ)$	0.514	0.41 ± 0.07	$-20.2 \pm 13.6\%$

4.4 Investigating the Limitations of the BEM Theory for Axial/Yawed Wind Turbines

This section describes the work in which the hot-film inflow measurements and the derived aerodynamic loading distributions on the blades were used to assess the limitations of the BEM theory when modelling wind turbines in both axial and yawed conditions. This study demonstrated the importance of knowing the experimental blade aerodynamic loading distributions (apart from the inflow measurements) to be able to carry out a more detailed assessment of the limitations of BEM-based models. However, one should bear in mind the fact that, for the TUDelft rotor, the blade loads were derived from the inflow measurements (as documented in section 4.3). It was found that the uncertainty in such loads was found to be considerably large, especially when the rotor was yawed. This uncertainty was a major stumbling block to perform an accurate quantitative assessment of the actual deficiencies of the BEM theory. The uncertainty in the tip/root correction also presented difficulties, but this tended to influence only radial locations $r/R < 50\%$ and $r/R > 80\%$.

This assessment was only restricted to the operating conditions at which the inflow measurements on the TUDelft rotor were carried out ($\lambda=8$, $\theta_{tip}=2^\circ$ and $\Psi=0, 30$ and 45°), and for which the flow behaviour over the blades is known to be fully attached (i.e. no blade stall). Two separate approaches were used: *Approach A* and *Approach B*.

(i) *Approach A* is an original approach that made use of inflow measurements to check the BEM Eq. 3.21 when modelling both axial and yawed conditions. The inflow measurements and the unsteady aerofoil model described in section 4.3.2 were used to calculate separately the blade-element theory and momentum parts denoted by F_{A1} and F_{A2} where

$$F_{A1} = \frac{c}{2\pi r} \left\{ \sum_{b=0}^{B-1} V_r C_L(\alpha, \text{Re}) [V_\eta \cos\theta - V_\zeta \sin\theta] + \sum_{b=0}^{B-1} V_r C_D(\alpha, \text{Re}) [V_\zeta \cos\theta + V_\eta \sin\theta] \right\} \quad (4.83a)$$

$$F_{A2} = -4(u_a) \sqrt{(U \cos\Psi + u_a)^2 + U^2 \sin^2\Psi} \quad (4.83b)$$

The capability of the BEM theory to simulate yawed conditions depends on the discrepancies between the values of F_{A1} and the corresponding values of F_{A2} . These two so-called BEM parameters were computed at different radial positions, rotor azimuth angles and yaw angles. A large discrepancy implied a deficiency of the BEM theory to simulate such conditions for the model wind turbine. Actually, this approach investigated the validity of the momentum equation for axial thrust (Eq. 3.6a).

For this case study with the TUDelft rotor, the linearly interpolated values of $w_{u,c}$ within the rotorplane (Figs. 4.18(a), 4.19 and 4.20) were used to compute F_{A1} . The azimuthally-averaged axial induced velocities obtained from the inflow measurements (Fig. 4.59(b), 4.87 and 4.88) were used to compute F_{A2} . The lift coefficient values corrected for tip/root loss at $r/R=40\%$ and 90% ($C_{l,3D}$) were used for computing F_{A1} (see Figs. 4.62, 4.93 and 4.94). 2D NACA0012 static aerofoil data for the drag coefficient was used but this was not corrected for tip/root loss.

(ii) In *Approach B*, the aerodynamic parameters predicted by the developed BEM code *HAWT_BEM* were compared with those derived directly from the experimental data (using the computer code *HAWT_LFIM* as described in the previous section 4.3). For a description of *HAWT_BEM*, refer to section 3.6. This BEM model implements both the tip and root tip losses using the Prandtl equations (Eqts. 3.10). The lift and drag coefficients were modelled using the same method as for the calculations with *HAWT_LFIM*, i.e. using the unsteady aerofoil model of section 4.3.2 for the lift coefficient ($C_{l,2D}$) and 2D NACA0012 static aerofoil data for the drag coefficient. In the modelling, the blades were discretized using 22 elements. Skewed wake effects in yawed rotor conditions were modelled by using Glauert's model (Eq. 3.28) and Coleman's equation (given in table 3.1) for the K factor.

4.4.1 Results from Approach A

Axial Conditions

Fig. 4.99 compares parameters F_{A1} with F_{A2} for $\psi=0^\circ$. The two parameters are very close to each other, proving the reliability of the BEM equation (Eq. 3.21) in axial conditions. The mean values obtained over one whole rotor revolution are plotted and the error bars represent \pm one standard deviations in the data over one whole revolution.

Yawed Conditions

Figs. 4.100 and 4.101 compare F_{A1} and F_{A2} at $\psi=30^\circ$ and 45° . Since unsteady conditions are considered due to rotor yaw, the results are being plotted as a function of rotor azimuth angle (ϕ). The error bars represent the uncertainties in both F_{A1} and F_{A2} due to the $\pm 8\%$ uncertainty in the hot-film measurements for w_u . It is easily noted that these error bars are considerably wide and this indicates that, like the derived aerodynamic loads, parameters F_{A1} and F_{A2} are also very sensitive to the errors in the hot-film measurements. This causes ambiguity in comparing F_{A1} and F_{A2} , as may be easily observed in Figs. 4.100 and 4.101 unless the errors in the inflow measurements are kept very small. Yet, a considerable discrepancy which increases with yaw angle may still be observed between these two parameters, demonstrating the limitation of the momentum equation (Eq. 3.6a) when modelling yawed conditions. Actually this limitation yields an incorrect prediction for the

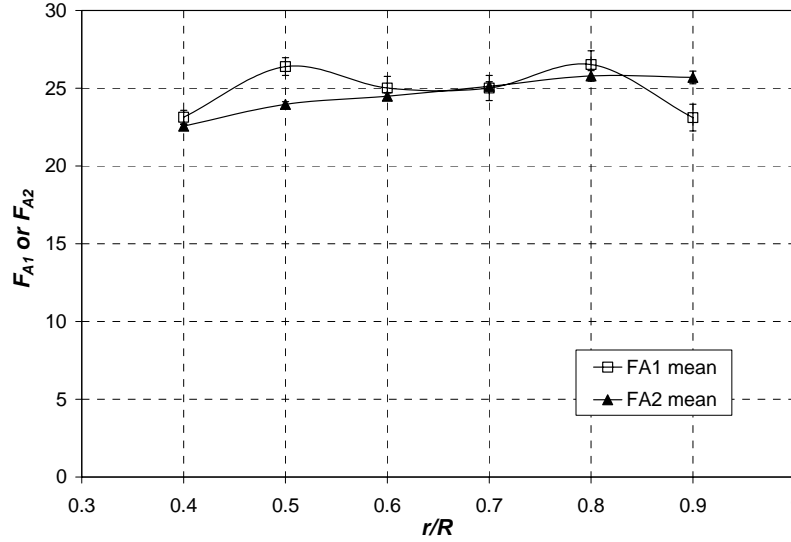


Figure 4.99 – Comparison of BEM parameters F_{A1} and F_{A2} at $\Psi=0^\circ$.

azimuthally averaged axial induced velocity (u_a) in BEM codes when Eq. 3.6a is used. The discrepancy between F_{A1} and F_{A2} should be corrected if BEM predictions in yaw are to be improved. One way of doing so is to include another correction parameter k_a to the BEM equation such that

$$k_a \times 4(u_a) \sqrt{(U \cos \Psi - u_a)^2 + U^2 \sin^2 \Psi} = \frac{c}{2\pi r} \left\{ \sum_{b=0}^{B-1} V_{rel} C_L(\alpha, Re) [V_\eta \cos \theta - V_\zeta \sin \theta] + \sum_{b=0}^{B-1} V_{rel} C_D(\alpha, Re) [V_\zeta \cos \theta + V_\eta \sin \theta] \right\} \quad (4.84)$$

k_a is a function of several parameters, including rotor geometry, operating conditions, radial location (r/R) and rotor azimuth position (ϕ).

In state-of-art BEM-based design codes, the implemented correction models for skewed wake effects in yaw (*Type I* engineering models described in Chapter 3, page 35) only correct the ratio of local blade element induced velocity to the annular average induced velocity. No correction is applied to the annular averaged induced velocity. The fact that Figs. 4.100 and 4.101 indicate a considerable discrepancy between F_{A1} and F_{A2} shows that correcting only this ratio may be insufficient, even when treating attached flow conditions (low angles of attack). The inclusion of parameter k_a as in Eq. 4.84 should result in better estimates for u_a and thus improve BEM predictions. An engineering model for this parameter may be derived from experiments that include both unsteady inflow measurements (to obtain the inflow at the rotorplane) and unsteady aerodynamic load measurements. F_{A1} and F_{A2} may then be found from the measurements to estimate k_a using

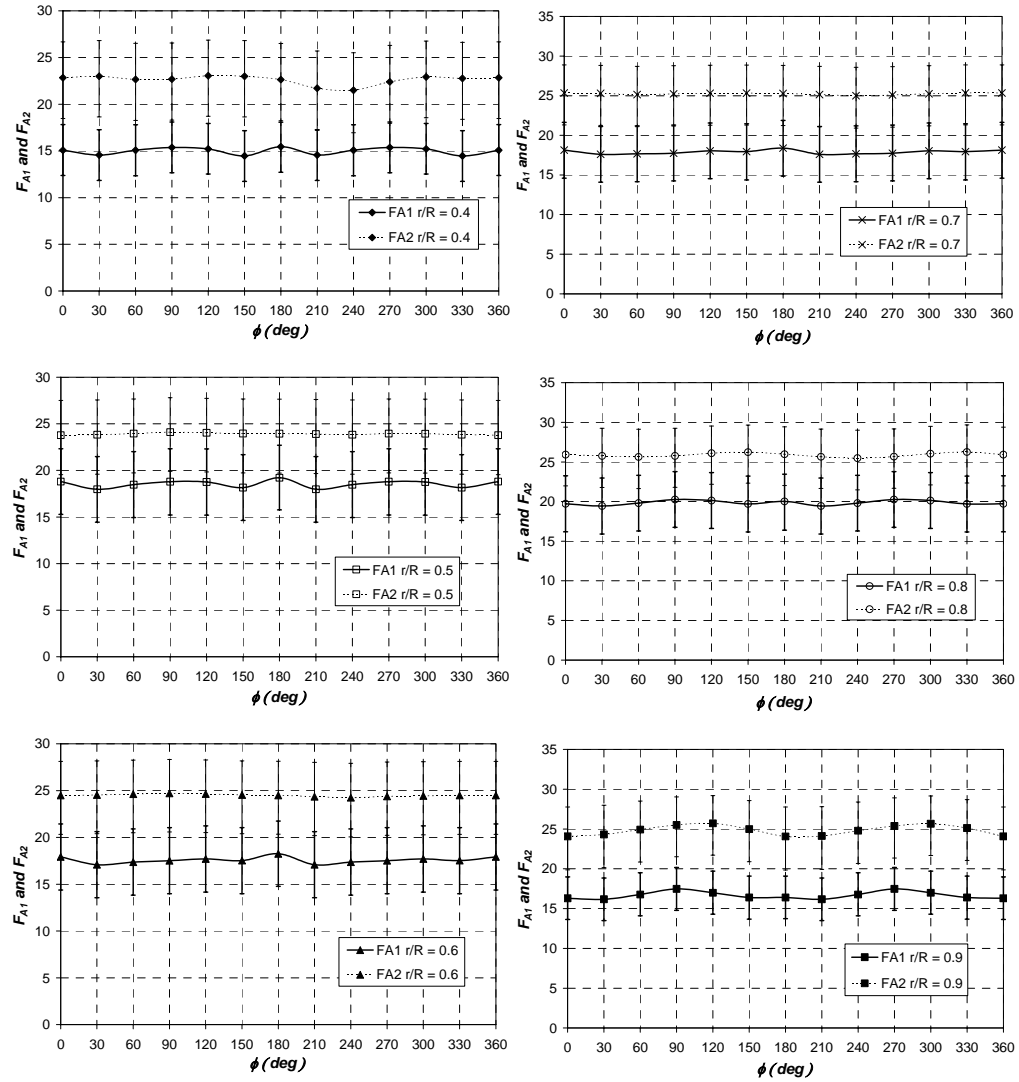


Figure 4.100 – Comparison of BEM parameters F_{A1} and F_{A2} at $\Psi=30^\circ$.

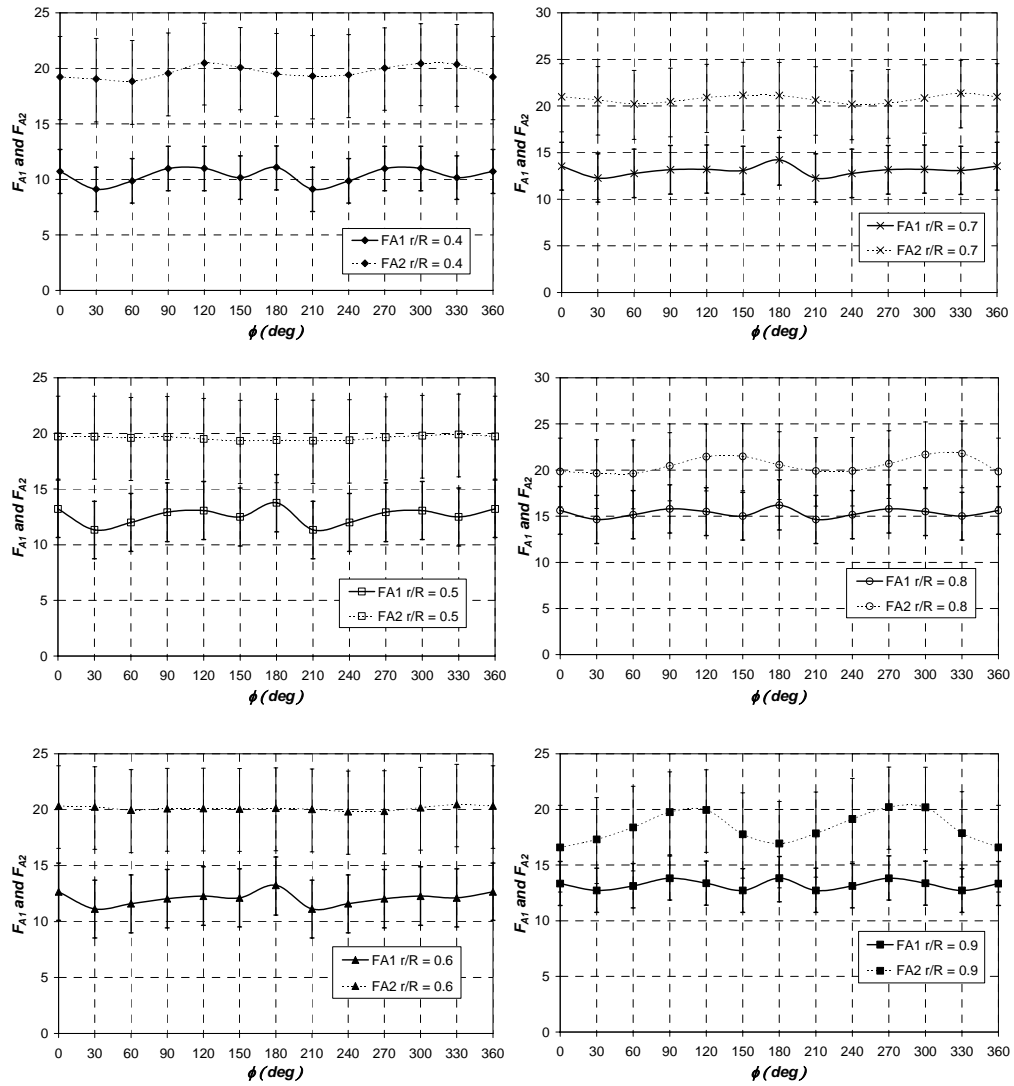


Figure 4.101 – Comparison of BEM parameters F_{A1} and F_{A2} at $\Psi = 45^\circ$.

the formula

$$(k_a)_{\tau,i} = \frac{(F_{A1})_{\tau,i}}{(F_{A2})_{\tau,i}} \tag{4.85}$$

Alternatively, an engineering model may be derived with the help of more advanced aerodynamic models such as vortex models and CFD.

In this study on the TUDelft rotor, an attempt was made to derive reasonable values for k_a at $\Psi=30^\circ$ and 45° from the results for F_{A1} and F_{A2} plotted in Figs. 4.100 and 4.101 (i.e. from the results derived from the inflow measurements). Eq. 4.85 was applied and k_a was found to be relatively constant with the rotor azimuth angle (ϕ). At each yaw angle, an averaged value for k_a was obtained by averaging both azimuthally and radially. The values are plotted in Fig. 4.102. The uncertainties in k_a due to the errors in the inflow measurements are also included. It is noted that these uncertainties are very large and thus make it very difficult to establish realistic values for k_a . At $\Psi=0^\circ$, F_{A1} and F_{A2} are nearly equal (see Fig. 4.99) and thus k_a is very close to unity in accordance with Eq. 4.85. One can still observe that larger yaw angles cause the value of k_a to decrease and this reflects the increased deficiency of the momentum equation (Eq. 3.6a) when increasing the rotor yaw angle.

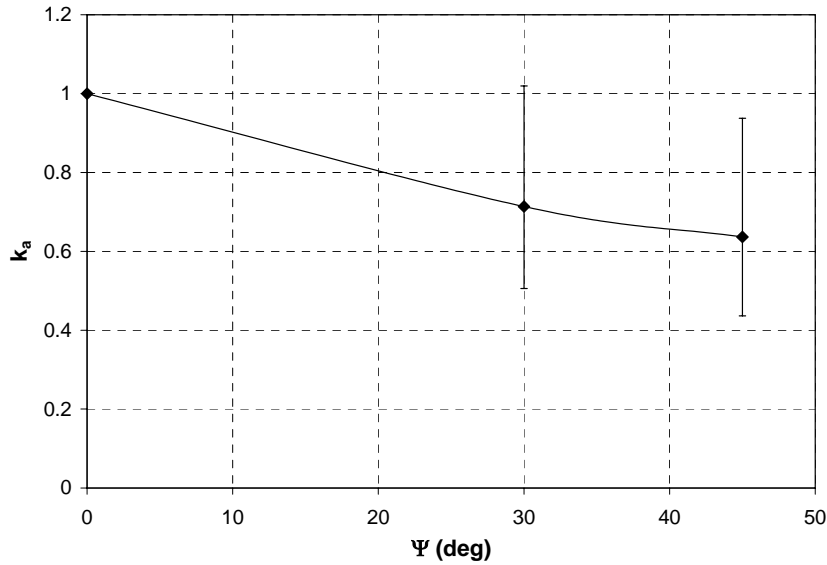


Figure 4.102 – Variation of k_a with yaw angle for the TUDelft rotor with λ and θ_{tip} maintained constant at 8 and 2° , respectively.

4.4.2 Results from Approach B

The results from BEM code *HAWT_BEM* are now compared with those obtained from the hot-film inflow measurements and unsteady aerofoil model using *HAWT_LFIM*.

Axial Conditions

This section presents the comparison for $\Psi=0^\circ$. In the case of the results from *HAWT_LFIM* (denoted in graphs by ‘Exp’), the mean values are plotted (mean over one whole rotor revolution), and the error bars represent the corresponding \pm one standard deviations. The results from *HAWT_BEM* are denoted in the graphs by ‘BEM’.

Figs. 4.103 and 4.104 compare the distributions of the axial induction factor at the blade lifting line ($a_{1,c}=u_{a,c}/U$) and the azimuthally averaged values (annular averaged, i.e. $a_1=u_a/U$), respectively. The correlation for a_1 is very good even at the sections close to the blade root and tip (40 and 90% R), see Fig. 4.104. However the correlation for $a_{1,c}$ is not good and the discrepancy between the experimental and BEM results increases towards the blade tip and root, see Fig. 4.103. In the BEM model for $\Psi=0^\circ$, $a_{1,c}$ is computed from a_1 using the equation $a_{1,c} = a_1/f$ where f is the Prandtl tip/root loss factor in accordance with Eqs. 3.10 and 3.27 (taking parameter F_{sa} equal to unity since we are dealing with axial flow). This indicates that the discrepancy in Fig. 4.103 is due to f . Also good agreement is achieved between the distribution of f predicted by the BEM model and that derived from the inflow measurements (i.e. using Eqs. 3.10 with the inflow angle (φ) obtained from the inflow measurements), see Fig. 4.105. It may therefore be concluded that the discrepancy in Fig. 4.103 is due to the intrinsic deficiency of the Prandtl tip/root loss model itself. This model corrects for the decreased aerodynamic loading at the blade tip and root regions by artificially increasing $a_{1,c}$ here to reduce the local angle of attack and thus also reduce the local 2D lift and drag coefficients. This is physically not accurate since it results in an incorrect prediction for the axial induction factor at the blade tip and root. It is important to emphasize the fact that in many state-of-art BEM design codes, 2D aerofoil data is still used at the blade tip and root regions. However recall the fact that, in this study with the TUDelft rotor, an unrealistically high bound circulation resulted at the blade tip and root region when using an angle of attack derived directly from the near wake inflow measurements and applying a 2D lift coefficient (refer to section 4.3.6, B.1 and Fig. 4.53). This suggests that for BEM codes to predict more accurately the induction at the blade tip and root while at the same time modelling the loading distribution at the tip and root correctly, modified 3D aerofoil data should be used instead. Thus, rather than artificially increasing the induction locally to reduce the angle of attack, a better tip/root loss correction model should modify the 2D aerofoil data to 3D values in a way to reduce the loading at the tip and root.

Figs. 4.106, 4.107 and 4.108 compare the distributions of V_r , α , and C_l . Excellent agreement was obtained in V_r at all radial locations along the blades, but this is only due to the simple

reason that $r\Omega \gg U$ and therefore the error in the computed induction has negligible influence on V_r . Still it is observed that there is a notable disagreement at the blade tip and root in both α and C_l . Again this results from the inadequacy of the Prandtl tip/root loss correction. It is noted that this correction over-predicts the lift coefficient at the tips. Fig. 4.109 and 4.110 compare the axial thrust and torque loading distributions. This over-prediction of the lift coefficient at the tips results in a high tip loading.

It can be concluded from this analysis that for axial conditions in attached flow over the blades, the predictions by *HAWT_BEM* correlated very well with those derived from the

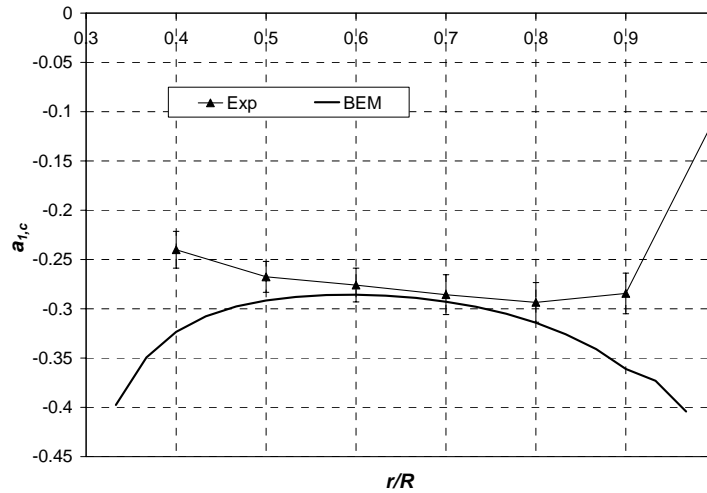


Figure 4.103 – Comparison of $a_{1,c}$ at $\Psi=0^\circ$.

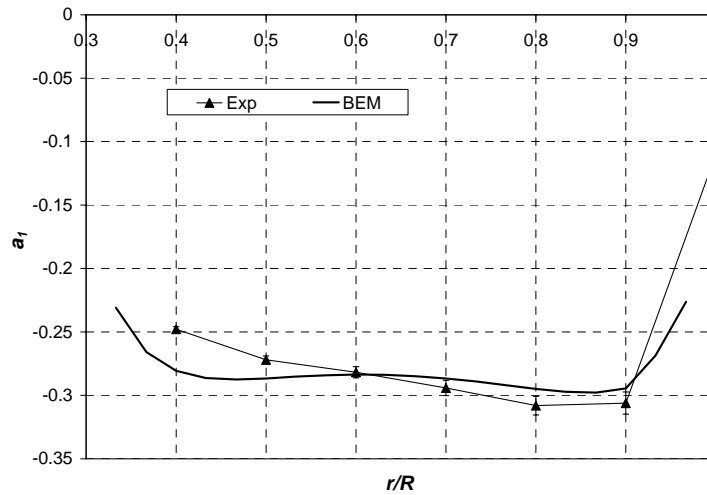


Figure 4.104 – Comparison of a_1 at $\Psi=0^\circ$.

experiments at the middle blade sections. However this cannot be stated for the tip/root regions due to the deficiency of the Prandtl correction. The significance of this deficiency depends on the aspect ratio of the blades. The higher the blade aspect ratio, the less influential this deficiency will be.

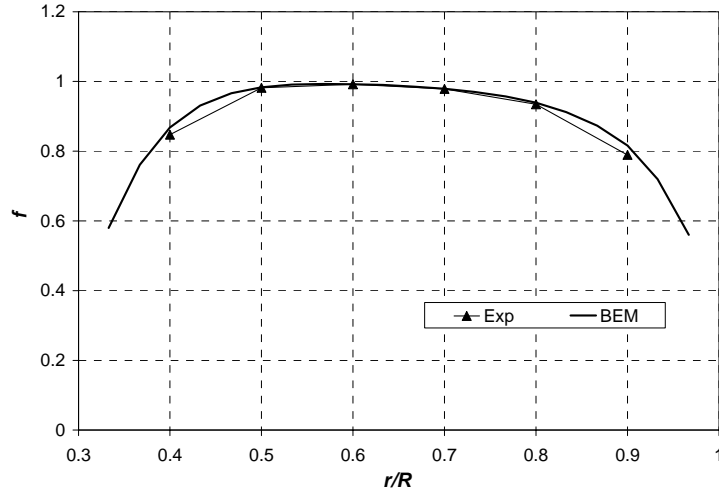


Figure 4.105 – Comparison of Prandtl tip loss factor at $\Psi=0^\circ$.

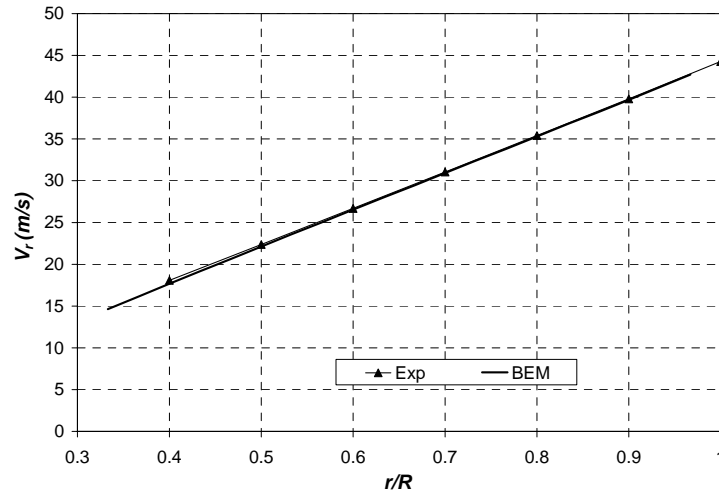


Figure 4.106 – Comparison of V_r at $\Psi=0^\circ$.

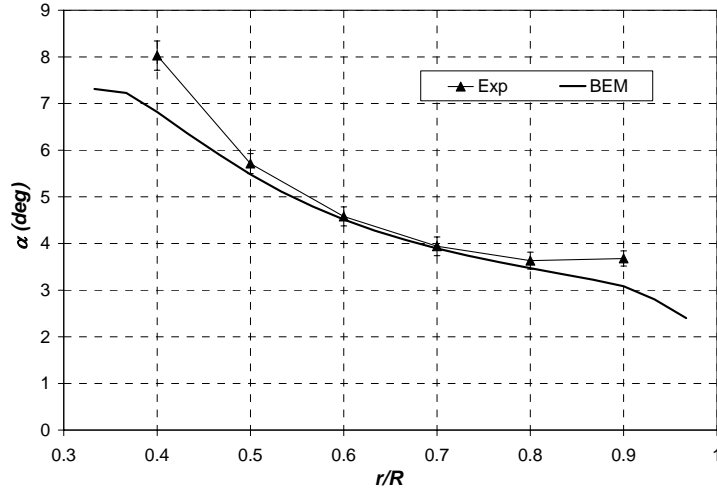


Figure 4.107 – Comparison of α at $\Psi=0^\circ$.

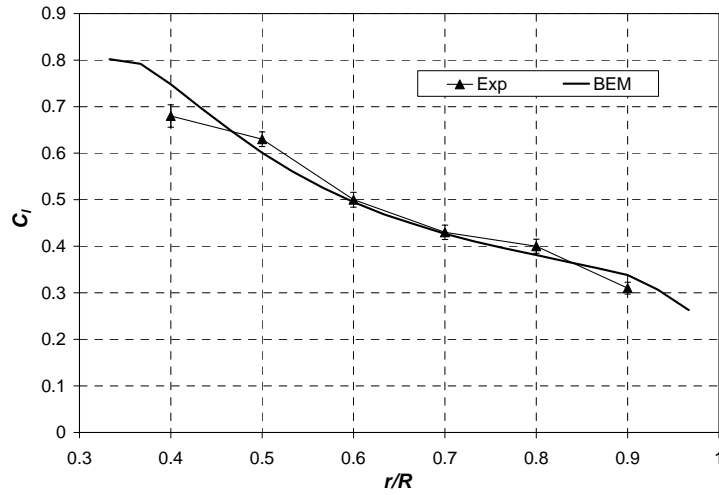


Figure 4.108 – Comparison of C_t at $\Psi=0^\circ$.

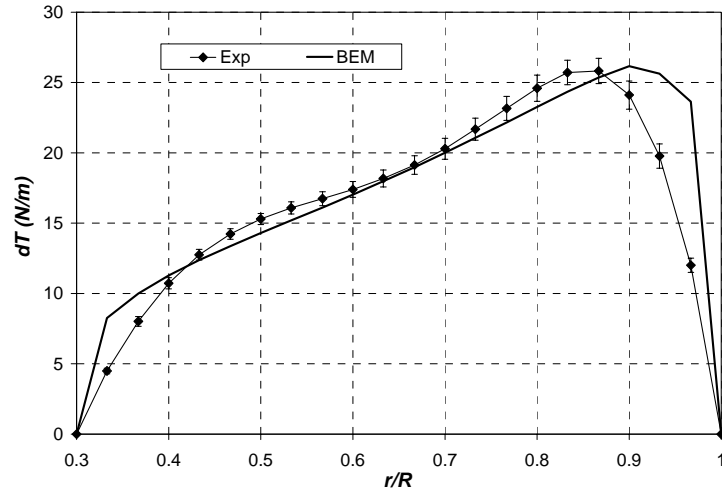


Figure 4.109 – Comparison of dT at $\Psi=0^\circ$.

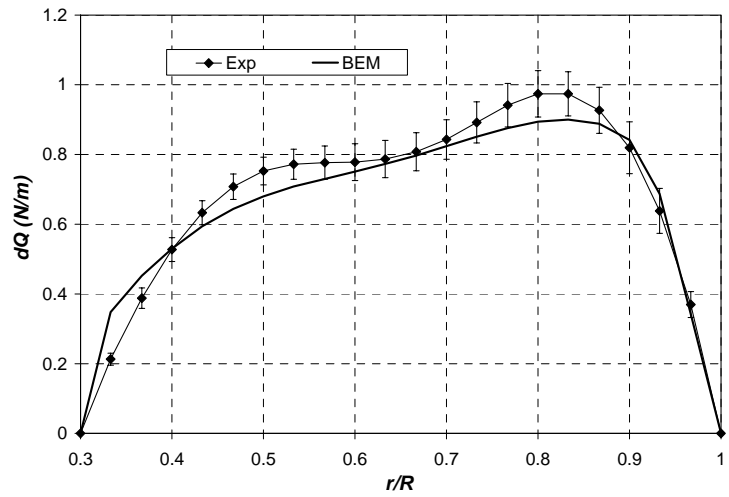


Figure 4.110 – Comparison of dQ at $\Psi=0^\circ$.

Yawed Conditions

This section presents the comparison for $\Psi=30^\circ$ and 45° . The results are plotted as a function of the blade/rotor azimuth angle (ϕ). The results from *HAWT_LFIM* are denoted in graphs by ‘Exp’. The error bars in these plots denote the uncertainty resulting from the assumed errors in the inflow measurements (i.e. $\pm 0.26\text{m/s}$ at $\Psi=30^\circ$ and $\pm 0.21\text{m/s}$ at $\Psi=45^\circ$). The results from *HAWT_BEM* are denoted by ‘BEM’.

Figs. 4.111 and 4.112 compare the results for $a_{1,c}$ at $\Psi=30^\circ$ and 45° , respectively. Remember that in the BEM calculations, skewed wake effects were modelled using Glauert’s model (Eq. 3.23) with the Coleman model for the factor K . This model yields a sinusoidal variation of $a_{1,c}$ with ϕ with the axial induction reaching the maximum and minimum negative values at 90° and 270° respectively. A qualitative comparison with the measurements in Figs. 4.111 and 4.112 clearly demonstrates large differences between Glauert’s predictions and the experimental results. These differences are largest towards the inboard regions of the blades and are mainly due to root vorticity which in reality causes the induction at the inboard blade sections to be higher at blade positions $180^\circ < \phi < 360^\circ$. As already outlined in section 3.5, Glauert’s model only accounts for the tip vorticity in skewed flows and excludes the presence of root vorticity. However on the subject rotor, it was found that the high negative induction measured at the inboard blade sections for blade positions $180^\circ < \phi < 360^\circ$ was not only due to the presence of considerable root vorticity but also because of influences of flow obstruction from the centrebody of the turbine model. Due to the complex geometry of this centrebody structure, it was very difficult to model such influences in *HAWT_BEM*.

Figs. 4.113 and 4.114 compare the results for a_1 . It is observed that the BEM code tends to under predict the value of a_1 at almost all radial locations both at $\Psi=30^\circ$ and 45° . The disagreement with the experimental values is not only a consequence of the deficiency of Glauert’s equation but also due to the limitation of the axial momentum Eq. 3.6a when treating yawed conditions. The issue that the deficiency in this equation brings about an inaccurate prediction for u_a (and hence also in a_1) has already been brought forward earlier in section 4.4.1. Better predictions for a_1 could have been achieved but modifying the momentum equation for thrust as Eq. 4.84 with a suitable engineering model for k_a . This was already shown in an earlier study documented in [67].

An incorrect prediction for the induction factors obviously results also from the inappropriate Prandtl tip/root correction. This issue was brought forward earlier in this section when comparing the $\Psi=0^\circ$.

Incorrect predictions for $a_{1,c}$ and a_1 yield incorrect predictions for the angles of attack, aerofoil coefficients and also for the blade loading distributions. Figs. 4.115 – Figs. 4.122 compare the results for the unsteady parameters α , C_i , dT and dQ from *HAWT_BEM* with those derived from the measurements using *HAWT_LFIM*. Unfortunately the large uncertainties in the results derived from the measurements (resulting from uncertainties in

the hot-film measurements) make it very difficult to quantify the discrepancies between the results of *HAWT_BEM* and *HAWT_LFIM*. However it is clear that, given that BEM codes incorporate accurate engineering models for skewed wake effects (i.e. better models for parameter F_{sa} in Eq. 3.27) together with engineering models to correct for the deficiency of the momentum equation in yaw (i.e. the inclusion of model for parameter k_a in Eq. 4.84), their reliability will be improved when modelling yawed conditions. Yet we should keep in mind the fact that in this study on the TUDelft rotor, we are limiting ourselves to attached flow conditions only for which the time-dependent angles of attack at the blades are known to be small. For such conditions, the aerofoil data used in the calculations is known to be reasonably accurate. When dealing with turbine operating conditions in which the angles of attack are large (i.e. where stall-delay and dynamic stall take place), the reliability of the aerofoil data used in BEM codes also becomes an important issue.

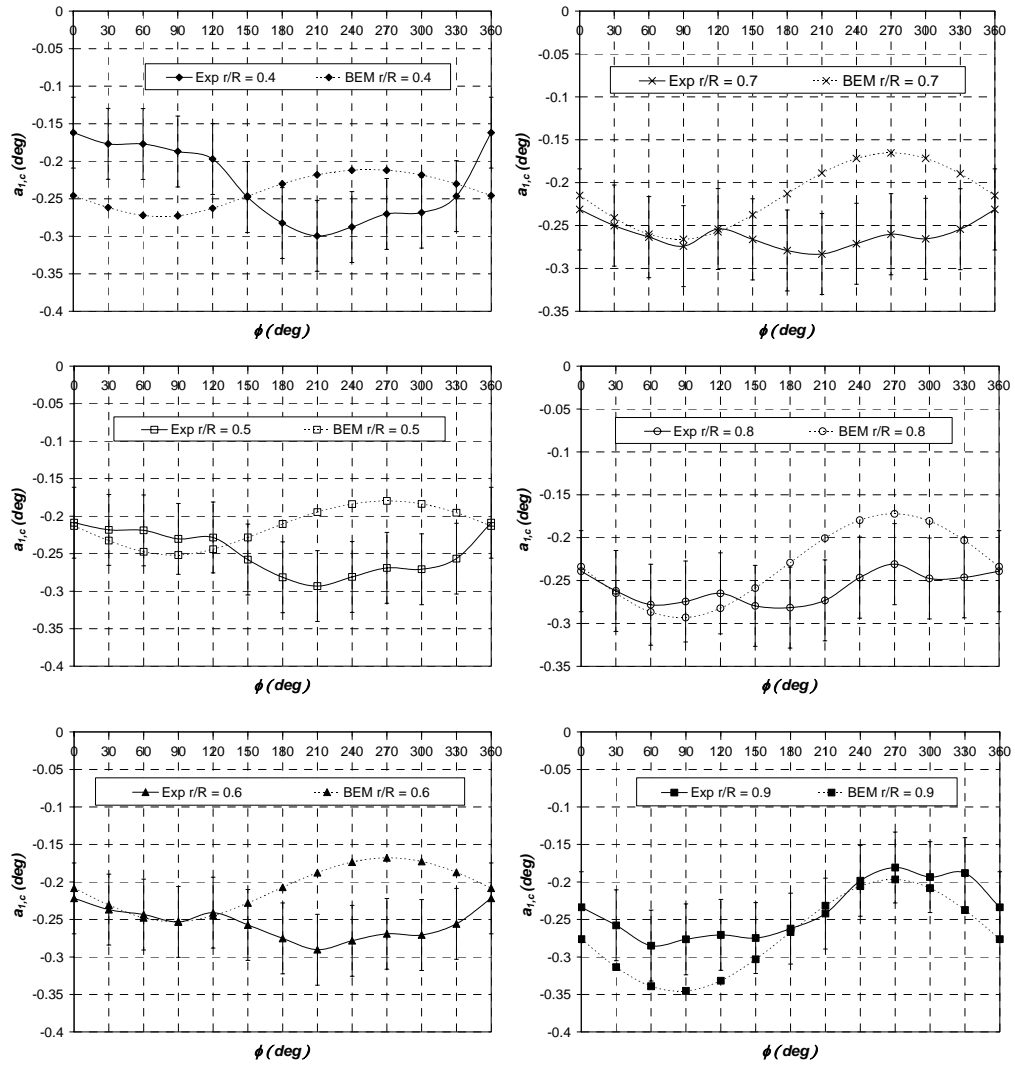


Figure 4.111 – Comparison of $a_{1,c}$ at $\Psi=30^\circ$.

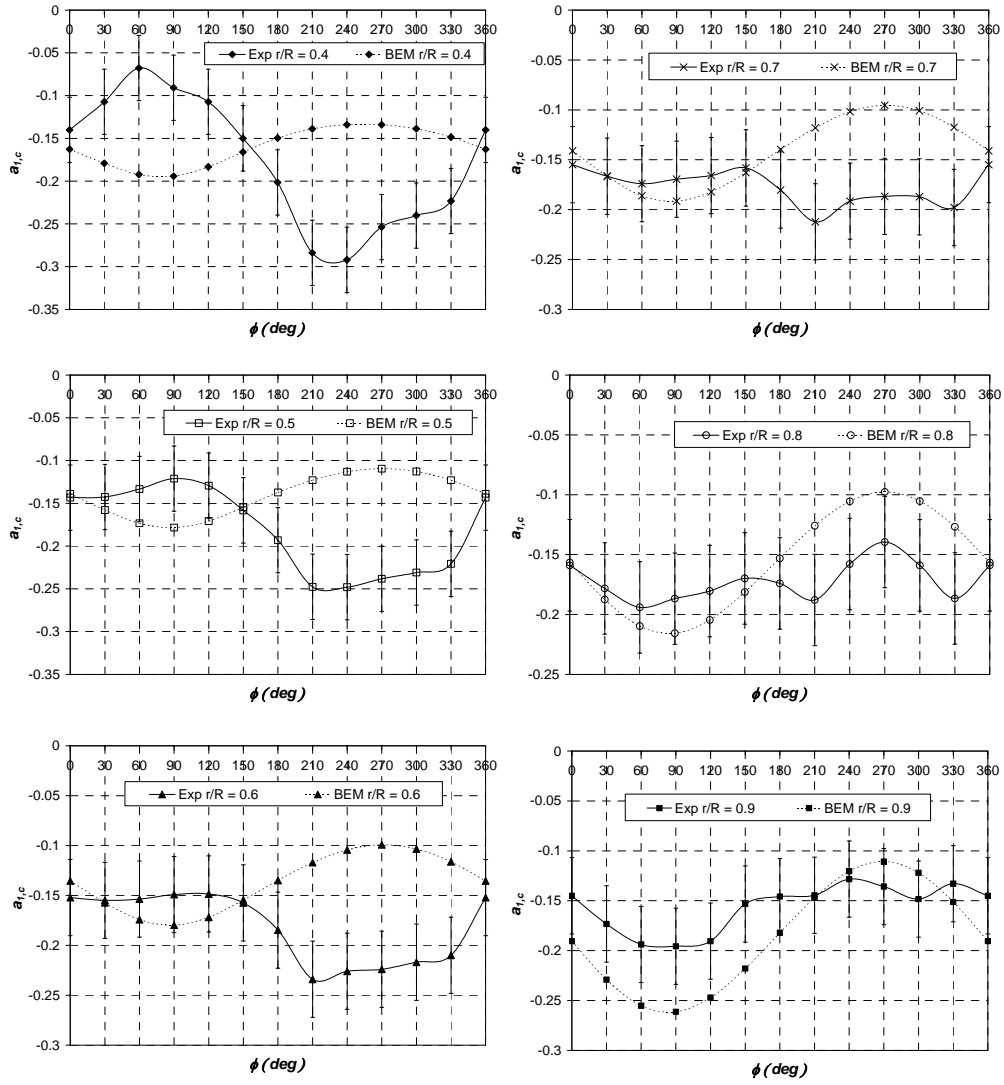


Figure 4.112 – Comparison of $a_{1,c}$ at $\Psi=45^\circ$.

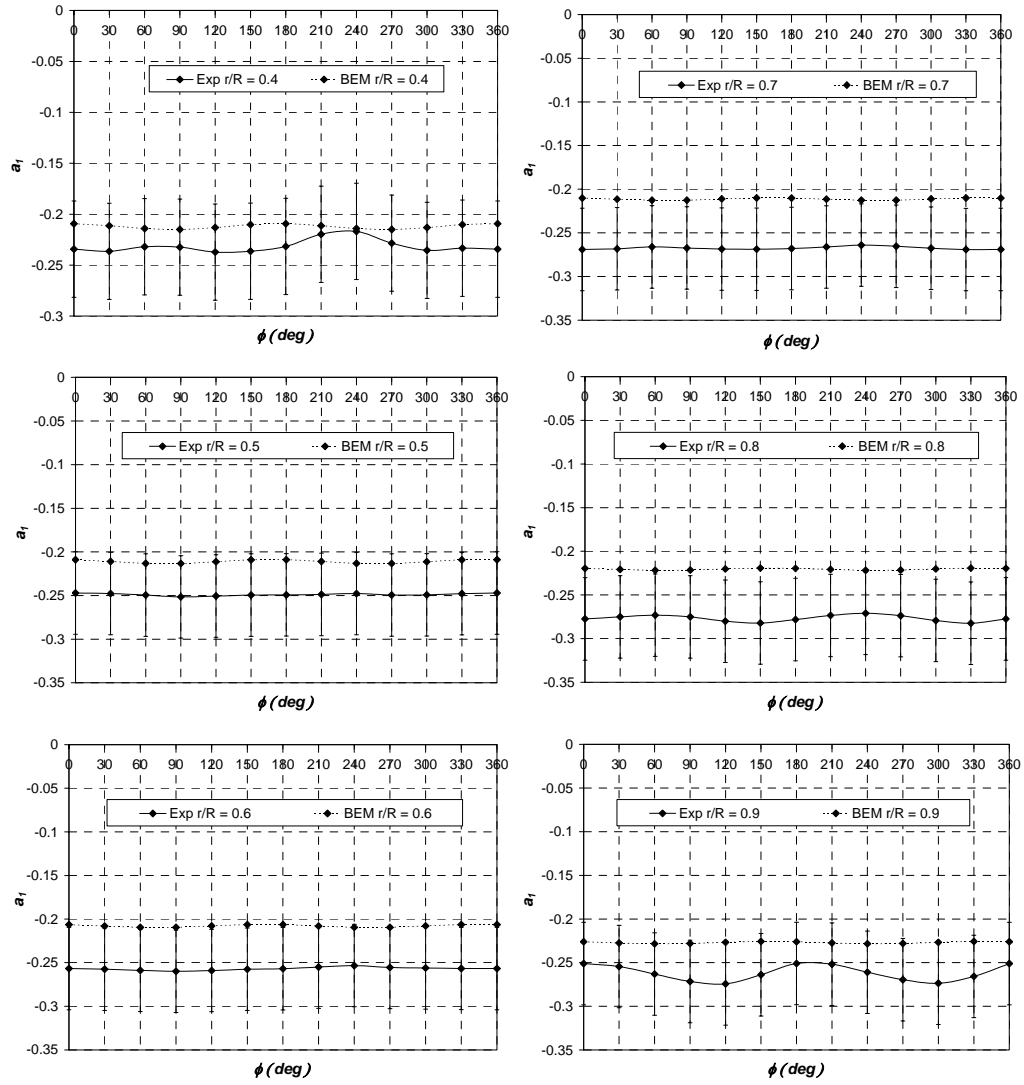


Figure 4.113 – Comparison of a_1 at $\Psi=30^\circ$.

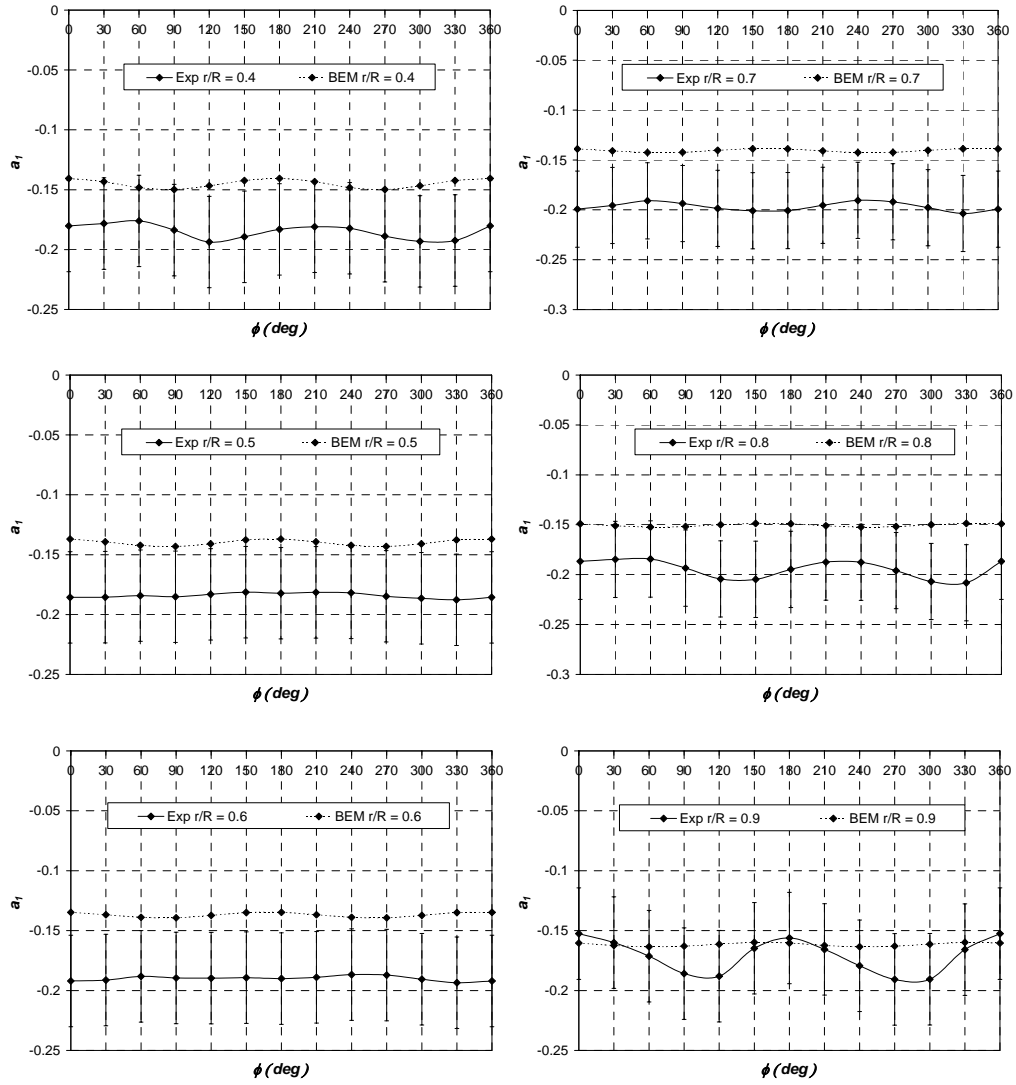


Figure 4.114 – Comparison of a_1 at $\Psi=45^\circ$.

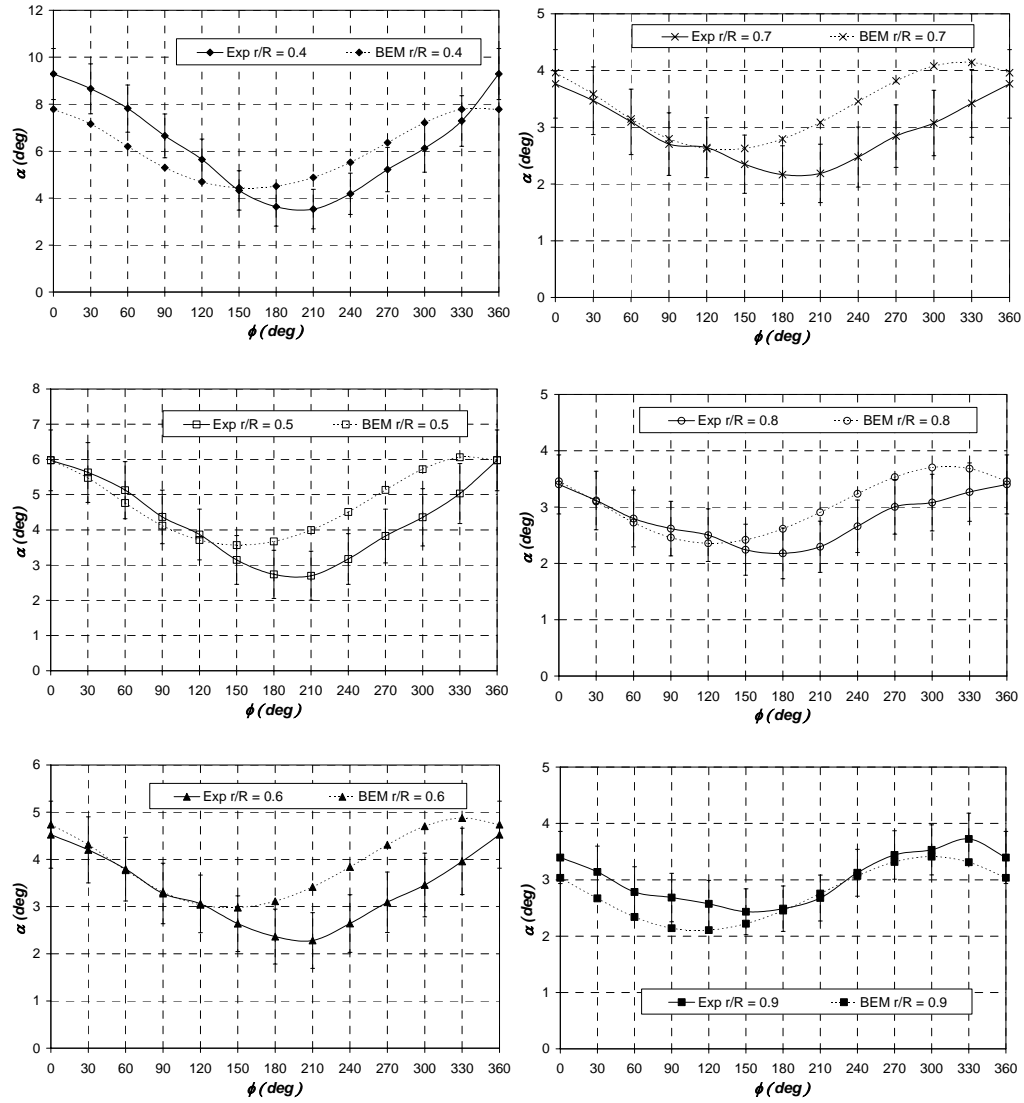


Figure 4.115 – Comparison of α at $\Psi=30^\circ$.

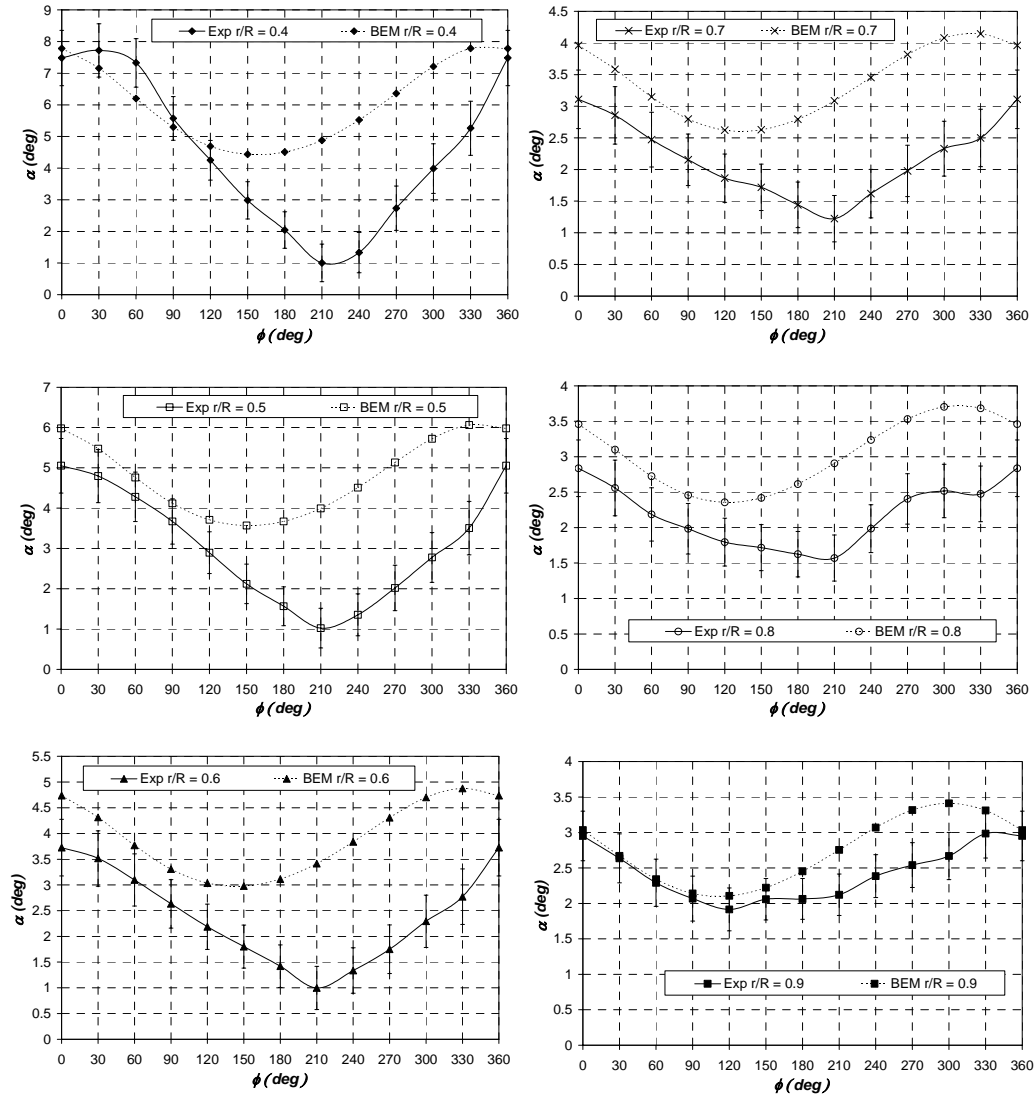


Figure 4.116 – Comparison of α at $\Psi=45^\circ$.

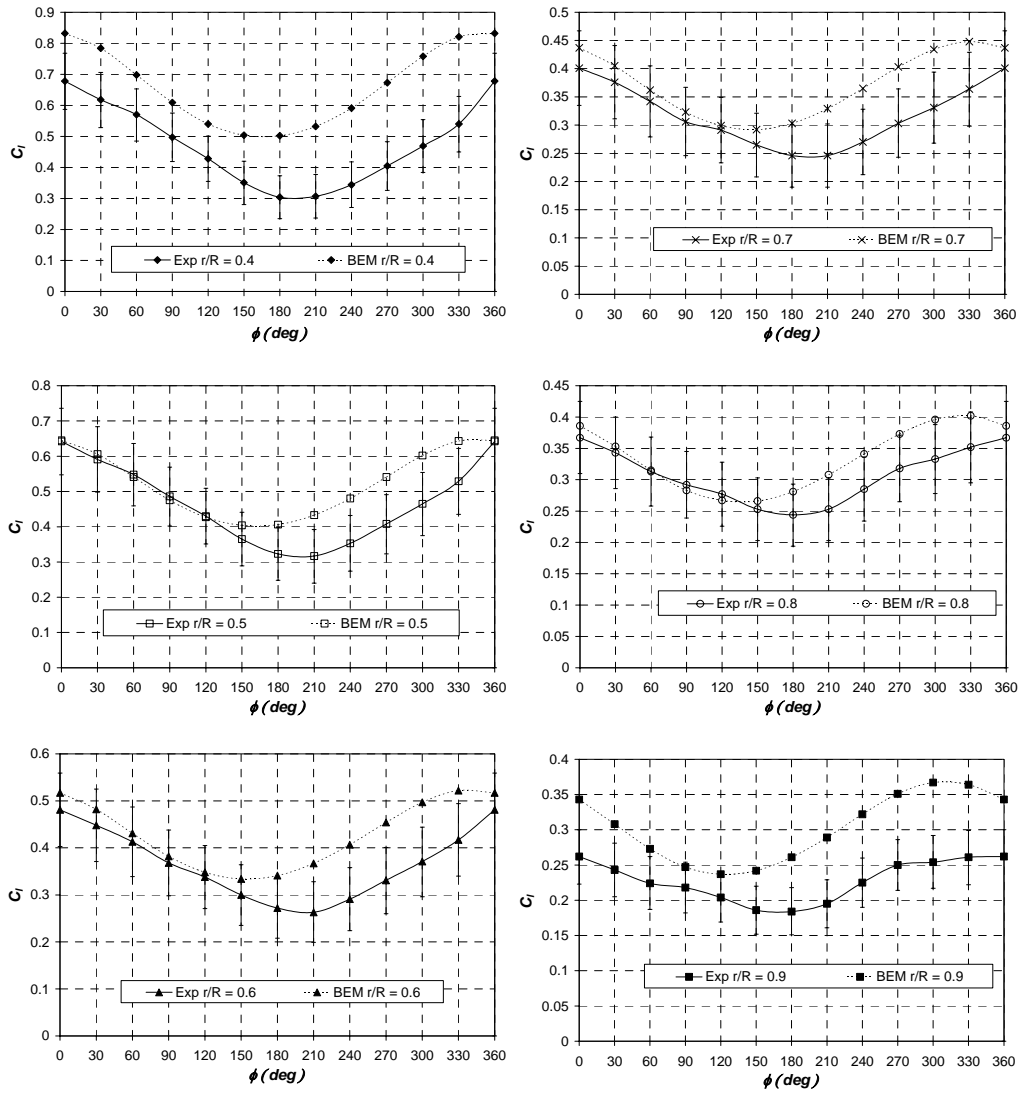


Figure 4.117 – Comparison of C_l at $\Psi=30^\circ$.

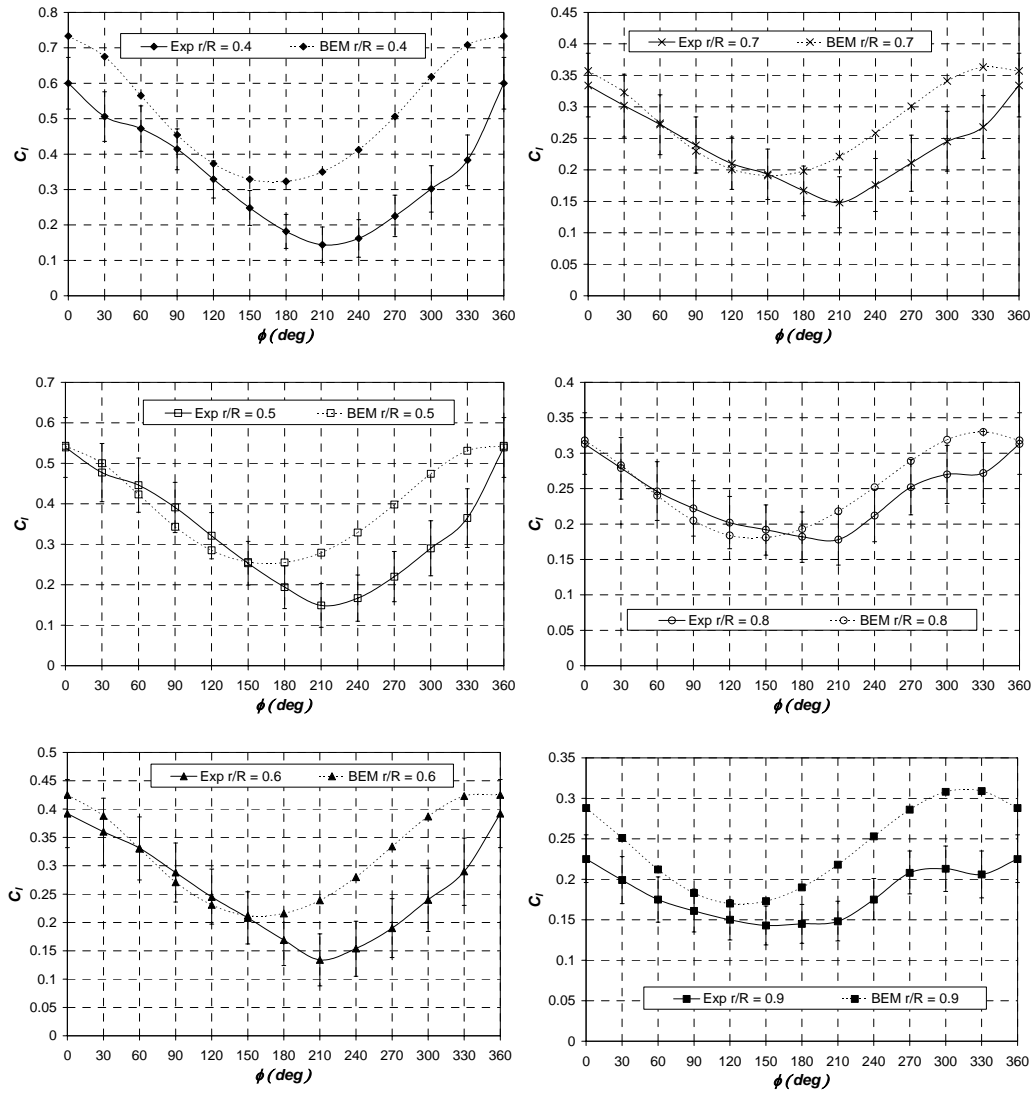


Figure 4.118 – Comparison of C_l at $\Psi=45^\circ$.

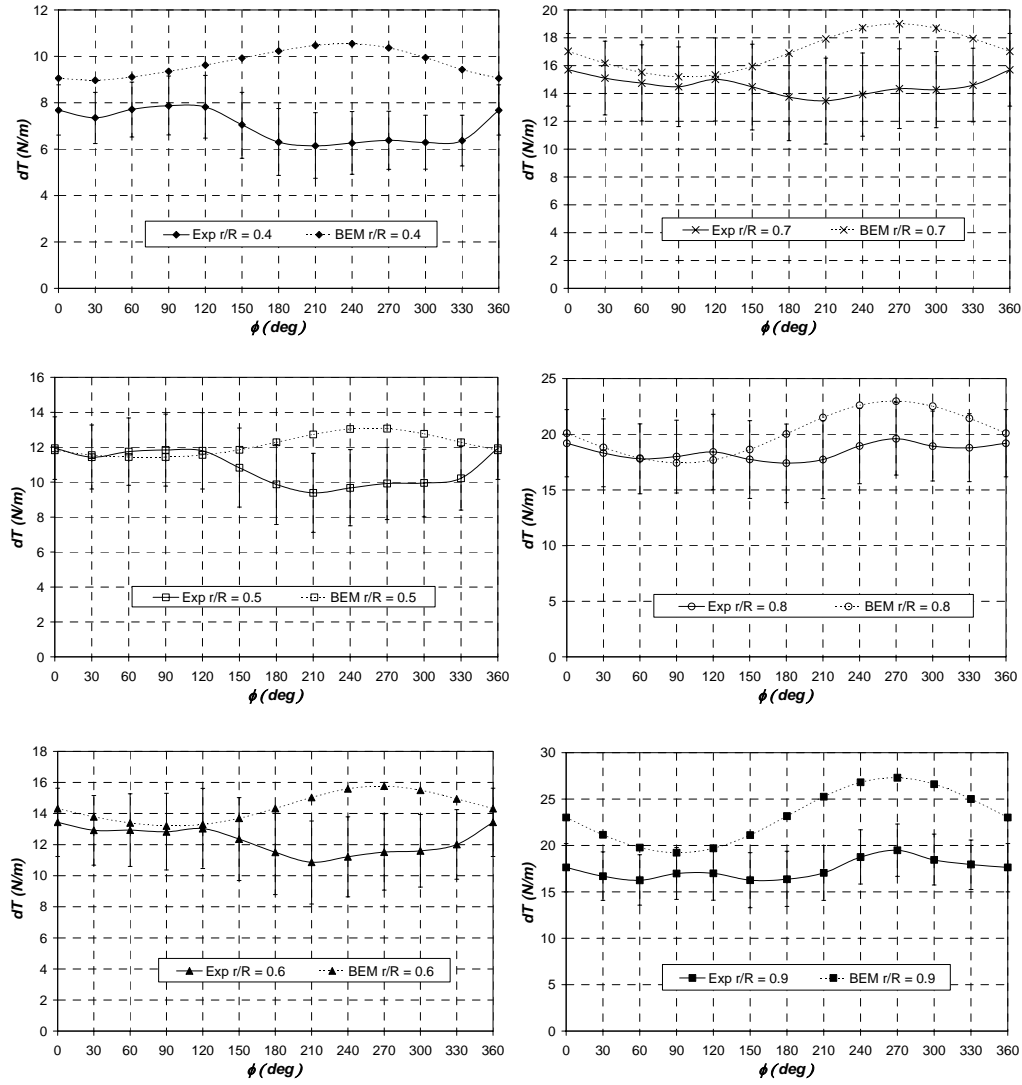


Figure 4.119 – Comparison of dT at $\Psi=30^\circ$.

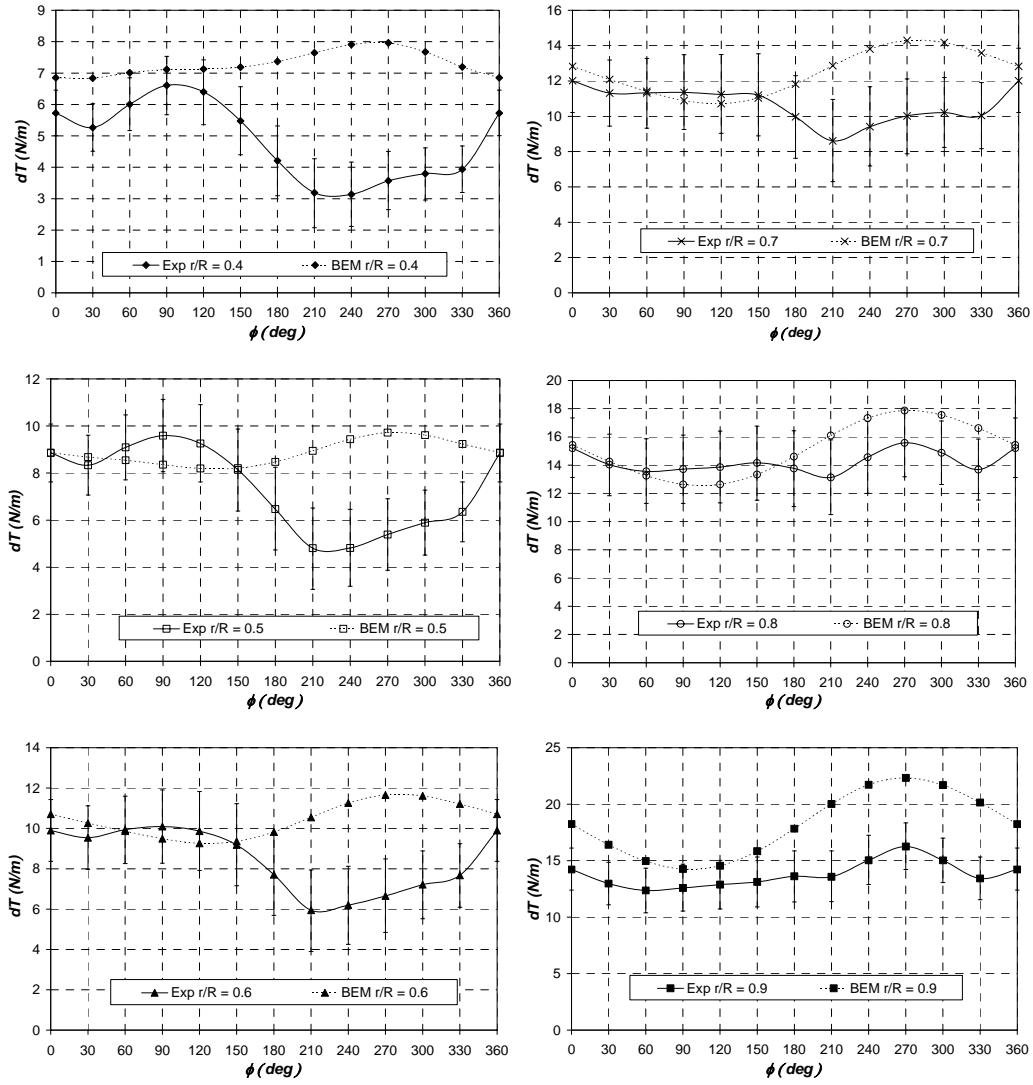


Figure 4.120 – Comparison of dT at $\Psi=45^\circ$.

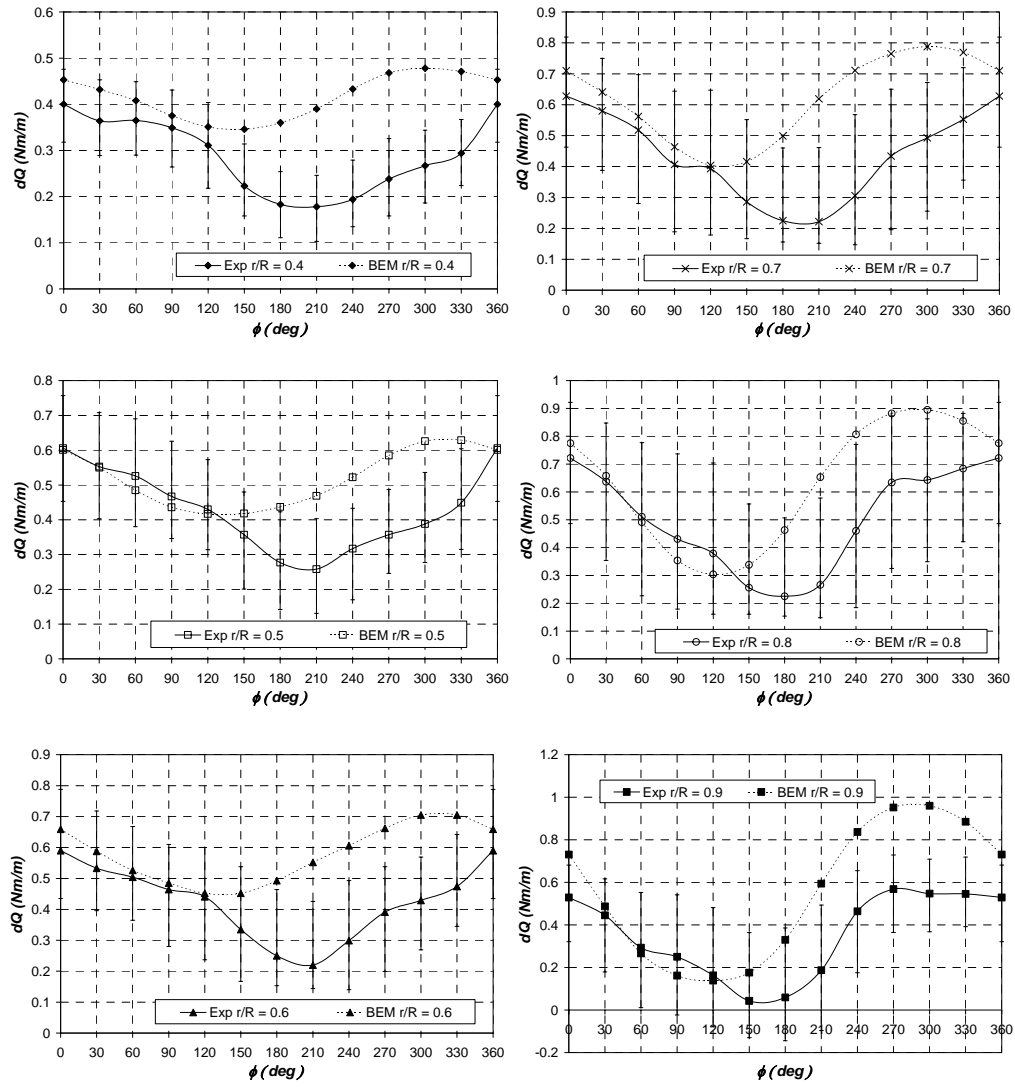


Figure 4.121 – Comparison of dQ at $\Psi=30^\circ$.

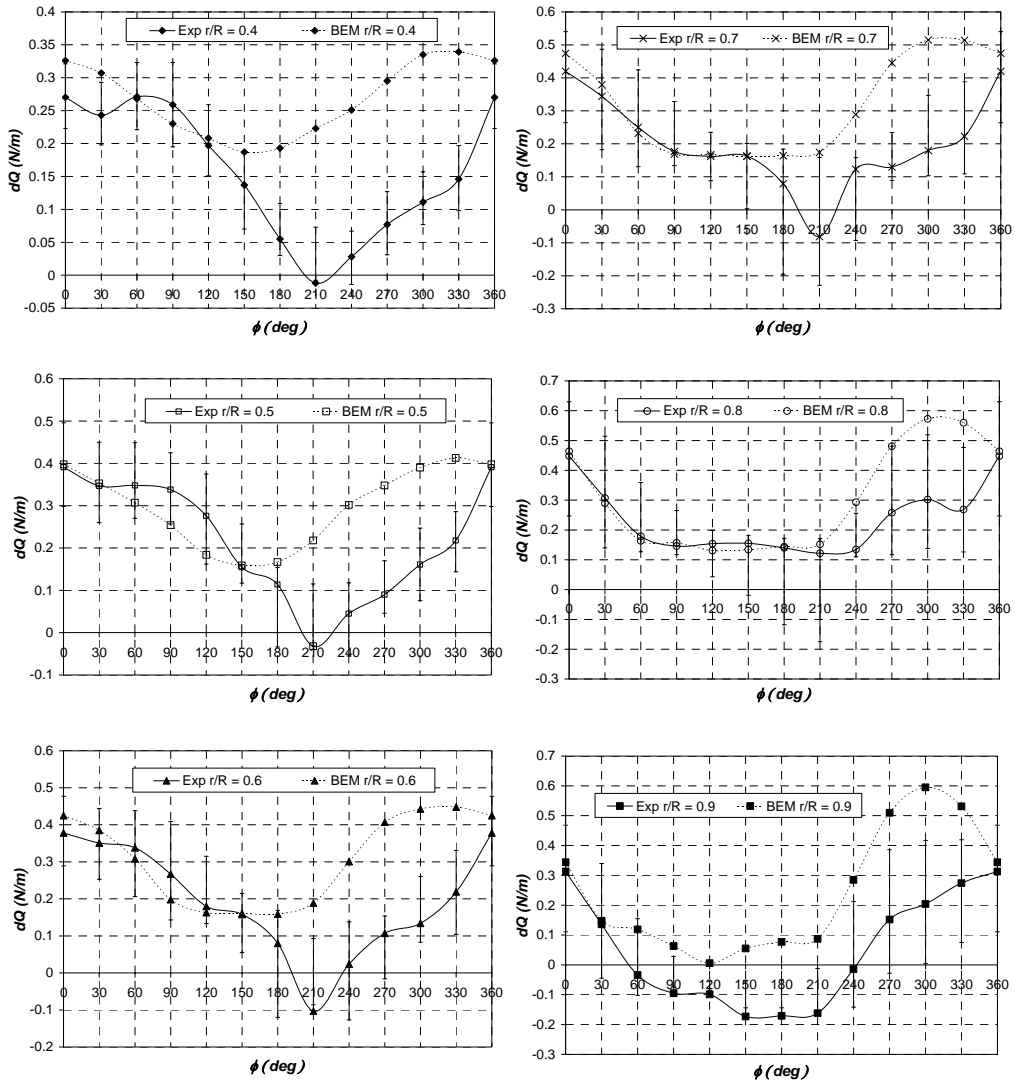


Figure 4.122 – Comparison of dQ at $\Psi=45^\circ$.

4.5 Conclusions

Wind tunnel measurements were taken on the TUDelft model turbine carried out in an open-jet facility with close collaboration with Wouter Haans, a Phd colleague carrying out research in the same field. Two different measurement campaigns were carried out: (1) detailed hot-film measurements in the near wake of the rotor, at various planes parallel to the rotorplane; (2) smoke visualization measurements to track the tip-vortex paths of the rotor wake together with measurements of the rotor axial thrust. A methodology was applied for deriving the unsteady aerodynamic loading distributions at the blades from the hot-film measurements using an unsteady aerofoil model, developed by Leishman [49]. Despite the fact that the analysis was only restricted to attached flow conditions at the blades (for which the unsteady aerofoil model is considerably accurate), this methodology was found to be quite challenging to apply due to the following drawbacks:

- (1) The derived aerodynamic loads are very sensitive to the errors in the hot-film measurements. In other words, a small percentage error in the inflow measurements may result into a significantly larger error in loading. Two main conclusions can be made: (a) the uncertainty in the derived loading distributions resulting from inflow measurement errors increases with yaw angle and (b) the uncertainty in the torque loading is normally larger than that for the axial thrust loading. This could be shown through a simple analytical analysis and was actually proved when applying an uncertainty analysis with the hot-film measurements taken on the TUDelft rotor. The percentage error of these measurements was estimated to be in the range 6-10% and this was mainly due to the non-uniformity in the tunnel exit jet of the wind tunnel, positioning errors of the traversing system, errors in calibrating the hot-film probes and errors in the data-reduction of the velocity components. When treating axial conditions, the error in the derived aerodynamic loading resulting from errors in the hot-film data did not exceed 20%, which is considered to be reasonable. In yawed conditions the error was larger. The maximum errors in the axial thrust loading at $\psi=30^\circ$ and $\psi=45^\circ$ were found to be 25% and 35%, respectively. The corresponding errors in the torque loading were found to exceed 100% and this mainly occurred when this loading was close to zero.

It is important to point out again the fact that due to physical restrictions, it is impossible to measure the inflow velocities directly at the rotorplane with hot-films. In this study, linear interpolation was used to estimate such velocities from the measurements taken upstream and downstream of the rotor. This introduced an additional uncertainty in the derived loading which was not included in the calculations. This uncertainty could not be determined as it was not possible to take the measurements at the rotorplane with the equipment available.

- (2) A tip/root correction is required. It was found that the bound circulation derived using the employed unsteady aerofoil model was unrealistically high at the blade tip and root regions, even though the angle of attack was estimated directly from the inflow measurements. This was due to the fact that the unsteady aerofoil model used is a 2D model and thus does not cater for the highly 3D flow phenomena taking place at the blade tip and root. The importance of the tip/root correction depends on the aspect ratio of the blade and also on the blade geometry. For blades having a small aspect ratio and a rectangular tip and root as that of the TUDelft rotor, then 3D effects are more prominent and this correction could not be ignored.

In this study, a prescribed-wake vortex model was developed to determine whether tunnel blockage influences were significant. Luckily, these influences were found to be very small.

Recommendations for future work

This work on the TUDelft rotor has revealed the various difficulties associated with deriving the steady/unsteady aerodynamic load distributions on a wind turbine blade from detailed hot-film measurements in the near wake in axial/yawed conditions. In certain cases, blade pressure measurements are not possible and alternatively the loads have to be derived from the near wake measurements. The detailed hot-film measurements in this study have proved to be very time consuming and the following recommendations from lessons learnt are being made for future work:

- The rotor should have a high aspect ratio to minimize the uncertainty in the tip/root loss correction.
- The uncertainty in the measurements should be kept very low (<3% is being recommended) so that errors in the derived loading are minimized. It is advisable to use higher windspeeds for the same tip speed ratio to avoid having small flow velocities at the blades that could yield large percentage errors.
- The hot-film measurement equipment should be automated as much as possible. In this way it would be possible to take more repetitive measurements for the same period of time available for the wind tunnel testing.
- It should be considered to use Particle Imaging Velocimetry (PIV) instead of hot-film anemometry since the former has the capability to measure the inflow directly at the rotorplane. PIV is very efficient since measurements at different points may be taken simultaneously and very quickly.

Investigation of the limitations of BEM Codes

The results derived from the inflow measurements on the TUDelft rotor were used to carry out a detailed investigation of a typical BEM code (*HAWT_BEM*) when modelling axial and

yawed turbines. Despite that attached flow conditions were only being treated and also the fact that the results derived from the inflow measurements had a high level of uncertainty in general, it was still possible to have a better understanding of the limitations of BEM-based design codes and obtain further intuition of how these may be improved. Various conclusions could be drawn, but these will be discussed in Chapter 7, together with other conclusions drawn from a similar investigation on the NREL Phase VI rotor described in Chapter 6.

5. Development of A Free-wake Vortex Model

5.1 Introduction

A special class of rotor aerodynamic models that are less computationally demanding than CFD techniques but are more reliable than BEM methods, are the so-called free-wake vortex methods. These methods are based on the principle that, for flows that may be assumed to be incompressible and inviscid, vorticity formed at the blades is convected into the wake as trailing and shed vorticity (as shown in Fig. 1.4) with a local velocity that is the vectorial sum of the free stream velocity and that induced by all vorticity sources in the wake and from the blades. These methods are typically unsteady in nature: vorticity in the wake is allowed to diffuse freely and the evolution of the wake is calculated in time. Circulation in the wake is modelled by a series of vortex filaments that may take the form of lines (Afjeh *et al.* [1], Bareiß *et al.* [6], Leishman *et al.* [51], Garrel [26]) or particles (Lee *et al.* [46], Voutsinas *et al.* [101]). Circulation around the blades is modelled with a lifting line or lifting surface representation. The induced velocity at different points in the wake is computed using the Biot-Savart law.

In this project, a new free-wake vortex model, named *HAWT_FWC* (*FWC* meaning *Free-Wake Code*), was developed. The model is applicable to both axial and yawed conditions. It was specifically designed to model HAWT rotor wakes from knowledge of the aerodynamic loads at the blades. Unlike other free-wake models, it does not directly rely on the availability of aerofoil data to iteratively determine the blade loading. The input to this code is a prescribed spanwise distribution of bound circulation that may be time-dependent. From this prescription, the code generates a wake and then calculates the 3D induced velocities at different points in the flow field of the rotor. As already outlined in Chapter 2, the main reason for developing this code was to use it in the novel approach being proposed for deriving the angle of attack distributions in HAWTs from blade pressure measurements. This novel method will be presented in detailed in Chapter 6.

This chapter is organized in two sections:

- A. Section 5.2 describes the numerical model implemented in the free-wake code *HAWT_FWC*, together with the program structure.
- B. Section 5.3 describes the verification and validation work carried out on *HAWT_FWC* using the experimental data obtained for the TUDelft rotor.

5.2 Free-wake Numerical Model

5.2.1 Blade Model

In this model, each rotor blade is represented by a lifting line consisting of a fixed number of piecewise constant spanwise segments located at the quarter-chord location ($c/4$). The arrangement of the segmentation is illustrated in Fig. 5.1. The number of segments is equal to n while i is an index representing each particular segment. An important requirement of this piecewise constant representation is that the spanwise segments be small enough so that any variation in the prescribed bound circulation, blade chord and twist is approximately represented by the straight-line segments between i and $i+1$.

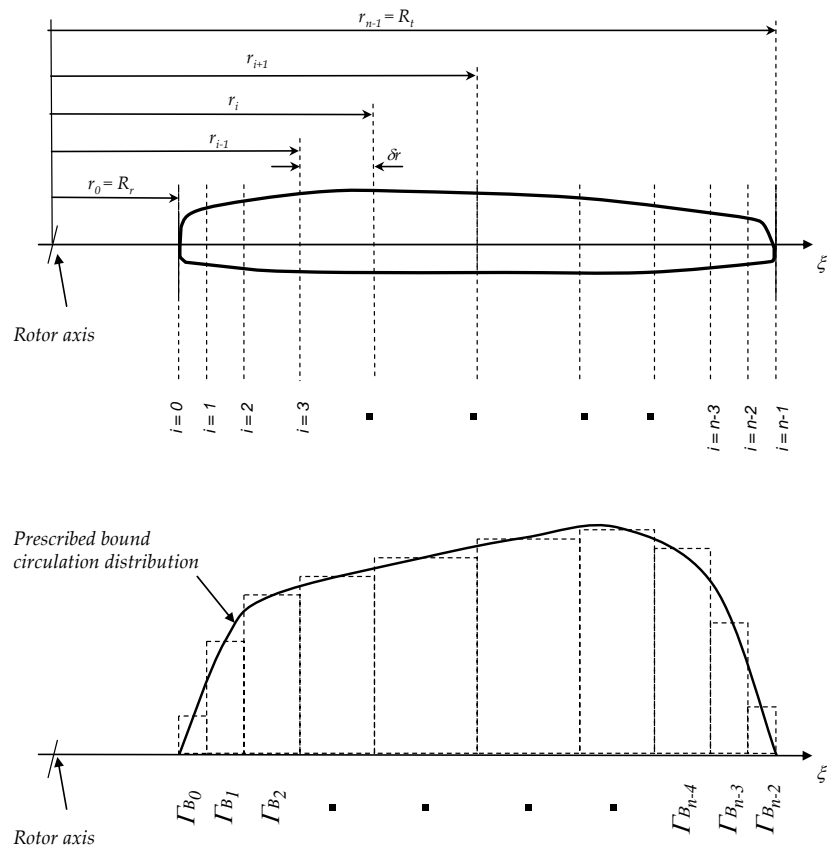


Figure 5.1 – Discretization of Blade and Bound Circulation Distribution.

A cosine radial segmentation is adopted to use smaller segments towards the blade tip and root such that

$$r_i = \left(\frac{R_r + R_t}{2} \right) - \left(\frac{R_t - R_r}{2} \right) \cos(\gamma_i) \quad (5.1)$$

$$\gamma_{i+1} = \gamma_i + \frac{\pi}{n-1} \quad \text{where } 0 \leq i \leq n-1; \quad \gamma_0 = 0 \text{ rad} \quad (5.2)$$

This cosine segmentation increases the numerical accuracy in vortex codes [26, 90] especially towards the blade tip and root, where the bound circulation varies rapidly with radial position.

5.2.2 Near Wake Model

The near wake is modelled as vortex sheets, one for each blade. Figure 5.2 illustrates how the each vortex sheet is discretized by means of straight-line vortex filaments, the latter being interconnected by nodes to form vortex nodes. The time step is denoted by m . a represents the vortex age. Filaments having $a=0$ are the oldest filaments while those having $a=m$ are the youngest ones that have just formed at the blades at time step m . At a given time step, each node in the wake is identified by a dual numbering system (i,a) . The number of trailing vortex filaments emerging from each blade is equal to the number of blade stations (n). Γ_T represents the trailing circulation in the wake due to spanwise variation in bound circulation at the blades. Each trailing vortex filament is attached to two nodes numbered (i,a) and $(i,a+1)$, (see Fig. 5.2). When the turbine is operating with its shaft parallel to a uniform windspeed, the trailing vortex segments from the same blade radius have a constant strength downstream. This is not the case when the turbine is operating in unsteady environments. Γ_s represents the shed circulation resulting from the time-dependent variation in bound circulation experienced in unsteady environments. Each shed vortex filament is attached to two nodes numbered (i, a) and $(i+1, a)$.

To satisfy the Kutta condition, the wake must be shed at the trailing edge of a blade. Thus the wake nodes should leave the blades from the trailing edges, from which they advance after each time step way downstream with a local velocity that is equal to the vectorial sum of the free-stream velocity and the vorticity induced velocity. At each time step, a new set of trailing and shed vortex filaments are modelled to be shed from the blade trailing edge. These filaments are numerically represented as follows:

$$\text{Trailing vortex filament:} \quad (\Gamma T_b)_{i,m} = (\Gamma B_b)_{i,\tau} - (\Gamma B_b)_{i+1,\tau} \quad (5.3a)$$

$$\text{Shed vortex filament:} \quad (\Gamma S_b)_{i,m} = (\Gamma B_b)_{i,\tau} - (\Gamma B_b)_{i,\tau-1} \quad (5.3b)$$

The wake filaments are convected downstream depending on the absolute velocity of the nodes to which they are connected. The total induced velocity at a given node is due to the bound, trailing and shed vortices from all rotor blades.

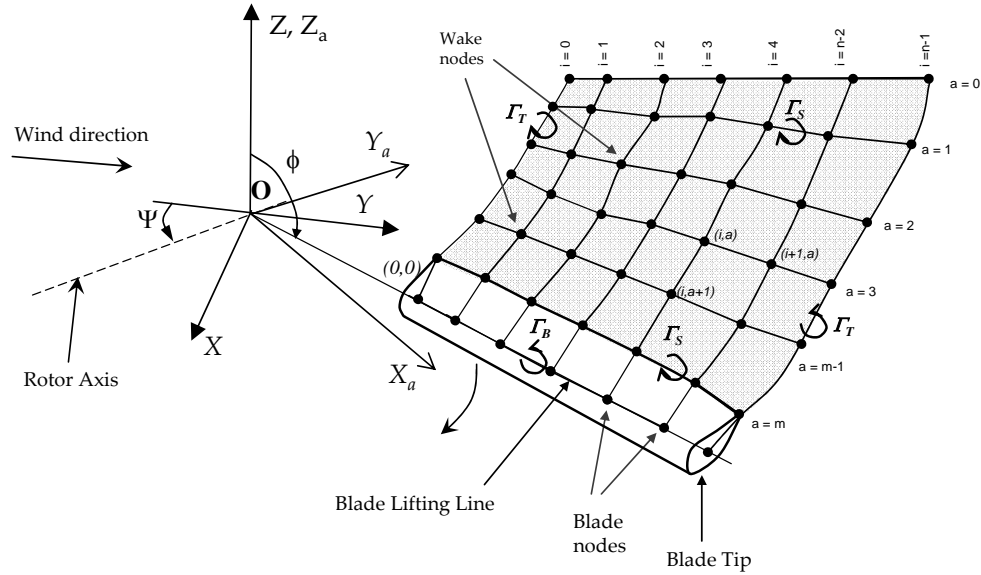


Figure 5.2 – Modelling of blades and near wake in free-wake vortex model.

The induced velocity induced at each node due to a vortex is computed from the Biot-Savart equation:

$$d\vec{u} = \frac{\Gamma}{4\pi} \frac{d\vec{s} \times \vec{r}}{|\vec{r}|^3} \quad (5.4)$$

Treatment of viscous effects in the near wake model

Viscous effects in rotor wakes usually occur at much smaller scales than potential flow phenomena. However, these effects may be significant in yawed conditions due to the formation of complex and unsteady blade-to-wake interactions and skewed wake effects. Leishman *et al.* [51] modify the Biot-Savart equation to account for viscous effects by introducing a viscous parameter, K_v , such that

$$d\vec{u} = K_v \frac{\Gamma}{4\pi} \frac{d\vec{s} \times \vec{r}}{|\vec{r}|^3} \quad (5.5)$$

where

$$K_v = \frac{h^2}{(r_c^{2z} + h^{2z})^{1/z}} \quad (5.6)$$

Eq. 5.6 is a viscous core model in which the inner part of the vortex, denoted as the core region ($r < r_c$), almost rotates as a solid body. The outer region (outside the core, $r > r_c$) almost behaves as a potential flow. h is the perpendicular distance of the evaluation point from the vortex element while r_c is the viscous core radius of the vortex. In effect, K_v desingularizes the Biot-Savart equation as \vec{r} tends to zero. Fig. 5.3 illustrates how this vortex core model modifies the swirl velocity distribution predicted by the Biot-Savart law close to the filament.

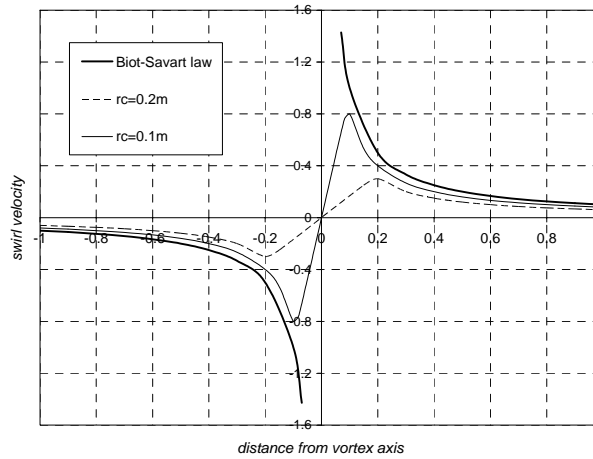


Figure 5.3 – Modification of the swirl velocity distribution at a vortex filament predicted by the Biot-Savart law using a core model (Eq. 5.6) to account for viscous effects.

In Eq. 5.6, parameter z defines the form of velocity profile. If $z = 1$, the Scully model is obtained and if $z = 2$ then an algebraic approximation to the Lamb-Oseen vortex model is obtained (refer to references [49], [51]). In Leishman’s free-wake model [51], the wake is modelled by using a single concentrated helical tip vortex per blade. In *HAWT_FWC*, the wake is modelled by vortex sheets from each blade each consisting of a mesh of straight-line filaments and Eq. 5.6 is applied to each of the trailing and shed filaments. The Lamb - Oseen viscous core model is used.

The viscous diffusion of vorticity in this free-wake model is handled by applying a core growth model. A core growth model was adopted from Ananthan *et al.* [2] and is applied to every trailing and shed vortex filament. The one-dimensional laminar Navier-Stokes equations reveal that the viscous vortex core radius grows with time in accordance with ([2], [10] [49], [51]):

$$r_c(t) = \sqrt{4\alpha\delta_v vt} \quad (5.7)$$

where α is a constant equal to 1.25643. δ_v is the turbulent viscosity coefficient that is added to Eq. 5.7 by Leishman ([49], pp 441) to account for the increased vorticity diffusion in turbulent flows. Experimental investigations ([2], [10]) suggest that δ_v is about 10 for small-scale rotors and is higher for full-scale rotors (on the order 100 to 1000). Current research intends to develop relations for δ_v . In Eq. 5.7, $t=0$ refers to the moment at which a vortex is shed from the blade’s trailing edge. Due to the formation of a boundary layer on the blade surfaces, viscous effects are present at the trailing edge. Consequently, each vortex sheet in the free-wake model should therefore have some thickness here within which viscous effects are considerable. The following relation is used in the subject free-wake code to increase the core radius gradually with time:

$$r_c(t) = \sqrt{4\alpha\delta_v v(t + S_c)} \quad (5.8)$$

S_c is a time-offset parameter that sets a non-zero viscous core radius for vortices that are just released from the trailing edge of each blade. Fig. 5.4 shows a typical variation of the viscous core radius with time as modelled by Eq. 5.8. In a free-wake solution the wake nodes are allowed to convect freely, thereby causing the vortex filaments to be strained. This results in a change in the vorticity content of the individual filaments which in turn modifies the induced velocity field around the vortex core. To account for filament straining, the core radius estimated by Eq. 5.8 is corrected using:

$$r_{c_{eff}} = r_c \left(\frac{1}{\sqrt{1 + \varepsilon}} \right) \quad (5.9)$$

where ε is the vortex filament strain. The derivation of Eq. 5.9 is presented in Appendix E and is based on Helmholtz’s third law stating that the net strength of a vortex should remain constant.

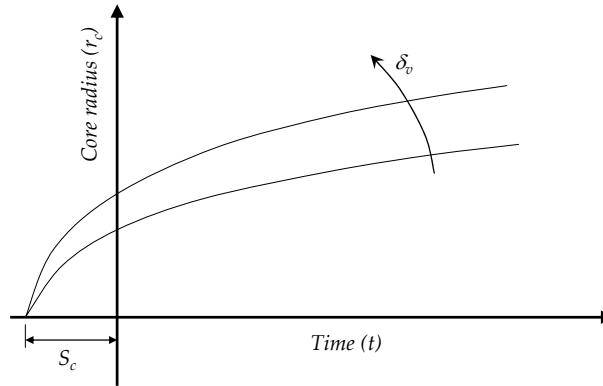


Figure 5.4 – Typical variation in the vortex core radius as modelled by core growth model Eq. 5.8.

Computation of 3D induced velocities at a point

The wake filaments travel downstream depending of the absolute velocity of the nodes to which they are connected. This total induced velocity at a given node is due to the bound, trailing and shed vortices of all the rotor blades. This velocity has three components and may be found with the application of the Biot-Savart equations (see Appendix C, Eqts. C.24 – C.32). For this numerical model, the total induced velocity at each particular wake node when the rotor is at time step τ is mathematically expressed in the X-Y-Z reference frame in terms of the following equations:

$$\begin{aligned}
 (u_x)_{bp,ip,ap} &= \sum_{b=0}^{B-1} \sum_{i=0}^{n-2} K_V * (\Gamma B_b)_{i,\tau} * IBX_{b,i,\tau,bp,ip,ap} + \dots \\
 &\dots + \sum_{b=0}^{B-1} \sum_{i=0}^{n-1} \sum_{a=0}^m K_V * (\Gamma T_b)_{i,a} * ITX_{b,i,\tau,bp,ip,ap} + \sum_{b=0}^{B-1} \sum_{i=0}^{n-2} \sum_{a=0}^m K_V * (\Gamma S_b)_{i,a} * ISX_{b,i,\tau,bp,ip,ap} \\
 (u_y)_{bp,ip,ap} &= \sum_{b=0}^{B-1} \sum_{i=0}^{n-2} K_V * (\Gamma B_b)_{i,\tau} * IBY_{b,i,\tau,bp,ip,ap} + \dots \\
 &\dots + \sum_{b=0}^{B-1} \sum_{i=0}^{n-1} \sum_{a=0}^m K_V * (\Gamma T_b)_{i,a} * ITY_{b,i,\tau,bp,ip,ap} + \sum_{b=0}^{B-1} \sum_{i=0}^{n-2} \sum_{a=0}^m K_V * (\Gamma S_b)_{i,a} * ISY_{b,i,\tau,bp,ip,ap} \\
 (u_z)_{bp,ip,ap} &= \sum_{b=0}^{B-1} \sum_{i=0}^{n-2} K_V * (\Gamma B_b)_{i,\tau} * IBZ_{b,i,\tau,bp,ip,ap} + \dots \\
 &\dots + \sum_{b=0}^{B-1} \sum_{i=0}^{n-1} \sum_{a=0}^m K_V * (\Gamma T_b)_{i,a} * ITZ_{b,i,\tau,bp,ip,ap} + \sum_{b=0}^{B-1} \sum_{i=0}^{n-2} \sum_{a=0}^m K_V * (\Gamma S_b)_{i,a} * ISZ_{b,i,\tau,bp,ip,ap}
 \end{aligned}
 \tag{5.10}$$

where indices (bp,ip,ap) denote the particular wake node at which the total induced velocity is being evaluated. The parameters IBX, IBY, IBZ are the geometric influence coefficients for the bound vortices, ITX, ITY, ITZ are the geometric influence coefficients for the trailing vortices and ISX, ISY, ISZ are the geometric influence coefficients for the shed vortices. The numerical equations for these influence coefficients are given in tables 5.1, 5.2 and 5.3. In table 5.1, X_B, Y_B and Z_B denote the node co-ordinates on the lifting line of a blade b at radial location i and rotor azimuth position τ .

$$\begin{aligned}
 IBX_{b,i,\tau,lp,ip,ap} &= \frac{[(r_1)_{lp,ap,ip,\tau,b,i} + (r_2)_{lp,ap,ip,\tau,b,i}] \cdot [[(Z)_{lp,ip,ap} - (Z_B)_{\tau,b,i+1}] [(Y)_{\tau,b,i+1} - (Y_B)_{lp,ip,ap} - (Y_B)_{\tau,b,i+1} - (Z_B)_{\tau,b,i}] [(Z)_{\tau,b,i+1} - (Z_B)_{\tau,b,i}]]}{2\pi \cdot (r_1)_{lp,ap,ip,\tau,b,i} \cdot (r_2)_{lp,ap,ip,\tau,b,i} + (r_2)_{lp,ap,ip,\tau,b,i} \cdot [[(r_1)_{lp,ap,ip,\tau,b,i}]^2 - [(L)_{\tau,b,i}]^2]} \\
 IBY_{b,i,\tau,lp,ip,ap} &= \frac{[(r_1)_{lp,ap,ip,\tau,b,i} + (r_2)_{lp,ap,ip,\tau,b,i}] \cdot [[(X)_{lp,ip,ap} - (X_B)_{\tau,b,i+1}] [(Z)_{\tau,b,i+1} - (Z_B)_{lp,ip,ap} - (Z_B)_{\tau,b,i+1} - (X_B)_{\tau,b,i}]] [(X)_{\tau,b,i+1} - (X_B)_{\tau,b,i}]]}{2\pi \cdot (r_1)_{lp,ap,ip,\tau,b,i} \cdot (r_2)_{lp,ap,ip,\tau,b,i} + (r_2)_{lp,ap,ip,\tau,b,i} \cdot [[(r_1)_{lp,ap,ip,\tau,b,i}]^2 - [(L)_{\tau,b,i}]^2]} \\
 IBZ_{b,i,\tau,lp,ip,ap} &= \frac{[(r_1)_{lp,ap,ip,\tau,b,i} + (r_2)_{lp,ap,ip,\tau,b,i}] \cdot [[(Y)_{lp,ip,ap} - (Y_B)_{\tau,b,i+1}] [(X_B)_{\tau,b,i+1} - (X_B)_{lp,ip,ap} - (X_B)_{\tau,b,i+1} - (Y_B)_{\tau,b,i}]] [(Y)_{\tau,b,i+1} - (Y_B)_{\tau,b,i}]]}{2\pi \cdot (r_1)_{lp,ap,ip,\tau,b,i} \cdot (r_2)_{lp,ap,ip,\tau,b,i} + (r_2)_{lp,ap,ip,\tau,b,i} \cdot [[(r_1)_{lp,ap,ip,\tau,b,i}]^2 - [(L)_{\tau,b,i}]^2]} \\
 (r_1)_{lp,ip,ap,\tau,b,i} &= \sqrt{[(X)_{lp,ip,ap} - (X_B)_{\tau,b,i}]^2 + [(Y)_{lp,ip,ap} - (Y_B)_{\tau,b,i}]^2 + [(Z)_{lp,ip,ap} - (Z_B)_{\tau,b,i}]^2} \\
 (r_2)_{lp,ip,ap,\tau,b,i} &= \sqrt{[(X)_{lp,ip,ap} - (X_B)_{\tau,b,i+1}]^2 + [(Y)_{lp,ip,ap} - (Y_B)_{\tau,b,i+1}]^2 + [(Z)_{lp,ip,ap} - (Z_B)_{\tau,b,i+1}]^2} \\
 (L)_{\tau,b,i} &= \sqrt{[(X_B)_{\tau,b,i+1} - (X_B)_{\tau,b,i}]^2 + [(Y_B)_{\tau,b,i+1} - (Y_B)_{\tau,b,i}]^2 + [(Z_B)_{\tau,b,i+1} - (Z_B)_{\tau,b,i}]^2}
 \end{aligned}$$

Table 5.1: Discretization equations for geometric influence coefficients for bound circulation

$$\begin{aligned}
 ITX_{hp,ip,ap,ba} &= \frac{[(r_1)_{hp,ap,ip,ba} + (r_2)_{hp,ap,ip,ba}] \cdot [[(Z)_{hp,ip,ap} - (Z)_{b,i,a-1}][(Y)_{b,i,a-1} - (Y)_{hp,ip,ap} - (Y)_{b,i,a-1}][(Z)_{b,i,a-1} - (Z)_{b,i,a}]]}{2\pi \cdot (r_1)_{hp,ap,ip,ba} \cdot (r_2)_{hp,ap,ip,ba} \cdot [(r_1)_{hp,ap,ip,ba} + (r_2)_{hp,ap,ip,ba}]^2 - [(L)_{b,i,a}]^2}
 \end{aligned}$$

$$\begin{aligned}
 ITY_{hp,ip,ap,ba} &= \frac{[(r_1)_{hp,ap,ip,ba} + (r_2)_{hp,ap,ip,ba}] \cdot [[(X)_{hp,ip,ap} - (X)_{b,i,a-1}][(Z)_{b,i,a-1} - (Z)_{b,i,a}] - [(Z)_{hp,ip,ap} - (Z)_{b,i,a-1}][(X)_{b,i,a-1} - (X)_{b,i,a}]]}{2\pi \cdot (r_1)_{hp,ap,ip,ba} \cdot (r_2)_{hp,ap,ip,ba} \cdot [(r_1)_{hp,ap,ip,ba} + (r_2)_{hp,ap,ip,ba}]^2 - [(L)_{b,i,a}]^2}
 \end{aligned}$$

$$\begin{aligned}
 ITZ_{hp,ip,ap,ba} &= \frac{[(r_1)_{hp,ap,ip,ba} + (r_2)_{hp,ap,ip,ba}] \cdot [[(Y)_{hp,ip,ap} - (Y)_{b,i,a-1}][(X)_{b,i,a-1} - (X)_{b,i,a}] - [(X)_{hp,ip,ap} - (X)_{b,i,a-1}][(Y)_{b,i,a-1} - (Y)_{b,i,a}]]}{2\pi \cdot (r_1)_{hp,ap,ip,ba} \cdot (r_2)_{hp,ap,ip,ba} \cdot [(r_1)_{hp,ap,ip,ba} + (r_2)_{hp,ap,ip,ba}]^2 - [(L)_{b,i,a}]^2}
 \end{aligned}$$

$$(r_1)_{hp,ip,ap,ba} = \sqrt{[(X)_{hp,ip,ap} - (X)_{b,i,a}]^2 + [(Y)_{hp,ip,ap} - (Y)_{b,i,a}]^2 + [(Z)_{hp,ip,ap} - (Z)_{b,i,a}]^2}$$

$$(r_2)_{hp,ip,ap,ba} = \sqrt{[(X)_{hp,ip,ap} - (X)_{b,i,a-1}]^2 + [(Y)_{hp,ip,ap} - (Y)_{b,i,a-1}]^2 + [(Z)_{hp,ip,ap} - (Z)_{b,i,a-1}]^2}$$

$$(L)_{b,i,a} = \sqrt{[(X)_{b,i,a-1} - (X)_{b,i,a}]^2 + [(Y)_{b,i,a-1} - (Y)_{b,i,a}]^2 + [(Z)_{b,i,a-1} - (Z)_{b,i,a}]^2}$$

Table 5.2: Discretization equations for geometric influence coefficients for trailing circulation

$$\begin{aligned}
 ISX_{hp,ip,ap,b,i,a} &= \frac{[(r_1)_{hp,ap,ip,b,i,a} + (r_2)_{hp,ap,ip,b,i,a}] \cdot [[(Z)_{hp,ap,ip} - (Z)_{b,a,i+1}][(Y)_{b,a,i+1} - (Y)_{hp,ap,ip} - (Y)_{b,a,i+1} - (Z)_{b,a,i}]]}{2\pi \cdot (r_1)_{hp,ap,ip,b,i,a} \cdot (r_2)_{hp,ap,ip,b,i,a} \cdot [[(r_1)_{hp,ap,ip,b,i,a} + (r_2)_{hp,ap,ip,b,i,a}]^2 - [(L)_{b,i,a}]^2]}
 \end{aligned}$$

$$\begin{aligned}
 ISY_{hp,ip,ap,b,i,a} &= \frac{[(r_1)_{hp,ap,ip,b,i,a} + (r_2)_{hp,ap,ip,b,i,a}] \cdot [[(X)_{hp,ap,ip} - (X)_{b,a,i+1}][(Z)_{b,a,i+1} - (Z)_{hp,ap,ip} - (Z)_{b,a,i+1} - (X)_{b,a,i}]]}{2\pi \cdot (r_1)_{hp,ap,ip,b,i,a} \cdot (r_2)_{hp,ap,ip,b,i,a} \cdot [[(r_1)_{hp,ap,ip,b,i,a} + (r_2)_{hp,ap,ip,b,i,a}]^2 - [(L)_{b,i,a}]^2]}
 \end{aligned}$$

$$\begin{aligned}
 ISZ_{hp,ip,ap,b,i,a} &= \frac{[(r_1)_{hp,ap,ip,b,i,a} + (r_2)_{hp,ap,ip,b,i,a}] \cdot [[(Y)_{hp,ap,ip} - (Y)_{b,a,i+1}][(X)_{b,a,i+1} - (X)_{hp,ap,ip} - (X)_{b,a,i+1} - (Y)_{b,a,i}]]}{2\pi \cdot (r_1)_{hp,ap,ip,b,i,a} \cdot (r_2)_{hp,ap,ip,b,i,a} \cdot [[(r_1)_{hp,ap,ip,b,i,a} + (r_2)_{hp,ap,ip,b,i,a}]^2 - [(L)_{b,i,a}]^2]}
 \end{aligned}$$

$$(r_1)_{hp,ip,ap,b,i,a} = \sqrt{[(X)_{hp,ip,ap} - (X)_{b,i,a}]^2 + [(Y)_{hp,ip,ap} - (Y)_{b,i,a}]^2 + [(Z)_{hp,ip,ap} - (Z)_{b,i,a}]^2}$$

$$(r_2)_{hp,ip,ap,b,i,a} = \sqrt{[(X)_{hp,ip,ap} - (X)_{b,i+1,a}]^2 + [(Y)_{hp,ip,ap} - (Y)_{b,i+1,a}]^2 + [(Z)_{hp,ip,ap} - (Z)_{b,i+1,a}]^2}$$

$$(L)_{b,i,a} = \sqrt{[(X)_{b,i+1,a} - (X)_{b,i,a}]^2 + [(Y)_{b,i+1,a} - (Y)_{b,i,a}]^2 + [(Z)_{b,i+1,a} - (Z)_{b,i,a}]^2}$$

Table 5.3: Discretization equations for geometric influence coefficients for shed circulation

5.2.3 Far Wake Model

In order to account for the influence of the far-field on the near wake, a far wake model is incorporated. This vortex model is very similar to the prescribed-wake vortex model *HAWT_PVC* (see section 4.3.3), with the difference that only a single tip vortex helical model per blade is modelled. Also, each helix has a constant diameter and is attached to the outboard end of the corresponding near wake, i.e. to near wake node with co-ordinate $(0, n-1)$, see Fig. 5.2. Thus at this node, the near wake vortex sheet is modelled to roll-up immediately into a concentrated tip vortex. Each helix is segmented into straight-line vortex filaments and the discretized Biot-Savart equations (Appendix C, Eqts. C.24 – C.32) are applied with a simple numerical cut-off method. As the rotor model is set to rotate, the vortex sheet of the near wake starts growing with time and consequently the far-wake helical tip vortices are convected downstream.

In this far wake model, the helical pitch (pfw) and the number of helical revolutions ($nfwRev$) need to be prescribed by the code user. When modelling yawed conditions, the far wake tip helices are skewed, similar to *HAWT_PVC* and the wake skew angle (χ_s) also needs to be prescribed. Fig. 5.5 depicts a typical plot of the modelled helical tip vortex far-wake due to a single blade.

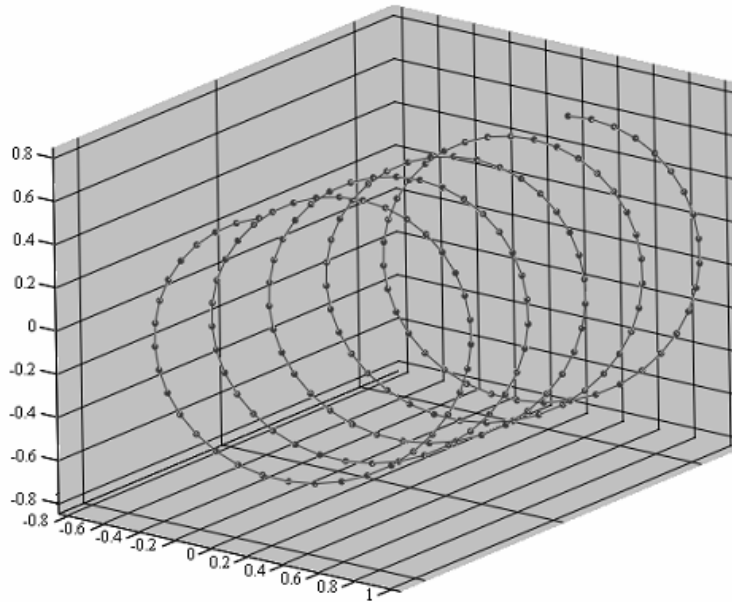


Fig. 5.5 – Typical helical tip vortex geometry for far wake model for one blade. $\chi_s = 35^\circ$ and $nfwRev=5$.

5.2.4 Numerical Solution

The procedure for obtaining the unsteady free near wake solution for this model is now described. A time-marching algorithm was implemented with the solution started by an impulsive start of the rotor. Fig. 5.6 presents a flowchart for this solution.

A boundary condition used specifies that each trailing and shed vortex filament should be attached to the blade trailing edge at the point of origin. Initially, the following data has to be inputted to the model:

- i. *Rotor geometry parameters:* blade tip and root radii (R_t and R_r), rotor number of blades (B) and radial distributions of blade chord and twist (c and θ).
- ii. *Operating condition parameters:* rotor parameters (angular speed (Ω), blade pitch angle (Θ), and yaw angle (Ψ) and wind speed (U)).
- iii. *Bound circulation distributions* at different blade azimuth angles over one whole revolution corresponding to the operating conditions being considered.
- iv. *Viscous modelling parameters for near wake:* S_c and δ_v . These are maintained constant throughout the solution.
- v. *Far wake model parameters:* tip vortex pitch (pfw), number of revolutions for helical tip vortices ($nfwRev$), wake skew angle (χ_s) and numerical cut-off parameter.

Prior to commencing the free-wake solution, one whole rotor revolution is divided into a fixed number of azimuth positions (equal to τ_{tot}) as in Fig. 3.7, Chapter 3. The time step is equal to $\Delta\tau$ and is calculated by Eq. 4.31, Chapter 4. The number of rotor rotations ($nRev$) to generate the free (near) wake is inputted. The total number of rotor time steps for the solution is then given by M_{tot} where $M_{tot}=nRev \times \tau_{tot}$. Initially, the first blade is set at the zero azimuth position (blade vertical pointing upwards) and there is no near wake, but only the prescribed far wake consisting of a vortex helix emerging from each blade tip. In the far wake, the number of filaments per helical revolution is set equal to τ_{tot} and this remains constant throughout the whole computation. The rotor then starts rotating at constant speed (Ω). At each time step, trailing and shed vortex filaments are shed from the blades' trailing edges with a circulation calculated from the spanwise and time variations of the bound circulation distributions at the blades. This will eventually form a near wake that will extend downstream.

Fig. 5.7 illustrates the growth (formation) of the near free wake after each time step m . Initially, ($m = 0, \tau = 0$), shed vortices are placed at the trailing edge of each blade with a circulation strength equal and opposite to the bound circulation in order to satisfy Kelvin's condition. At each time step m , the following steps are made:

- i. newly formed trailing and shed vortices are placed at the trailing edge of the blades. Their circulation strength is computed from the local radial and time variations in bound circulation using Eqts. 5.3.

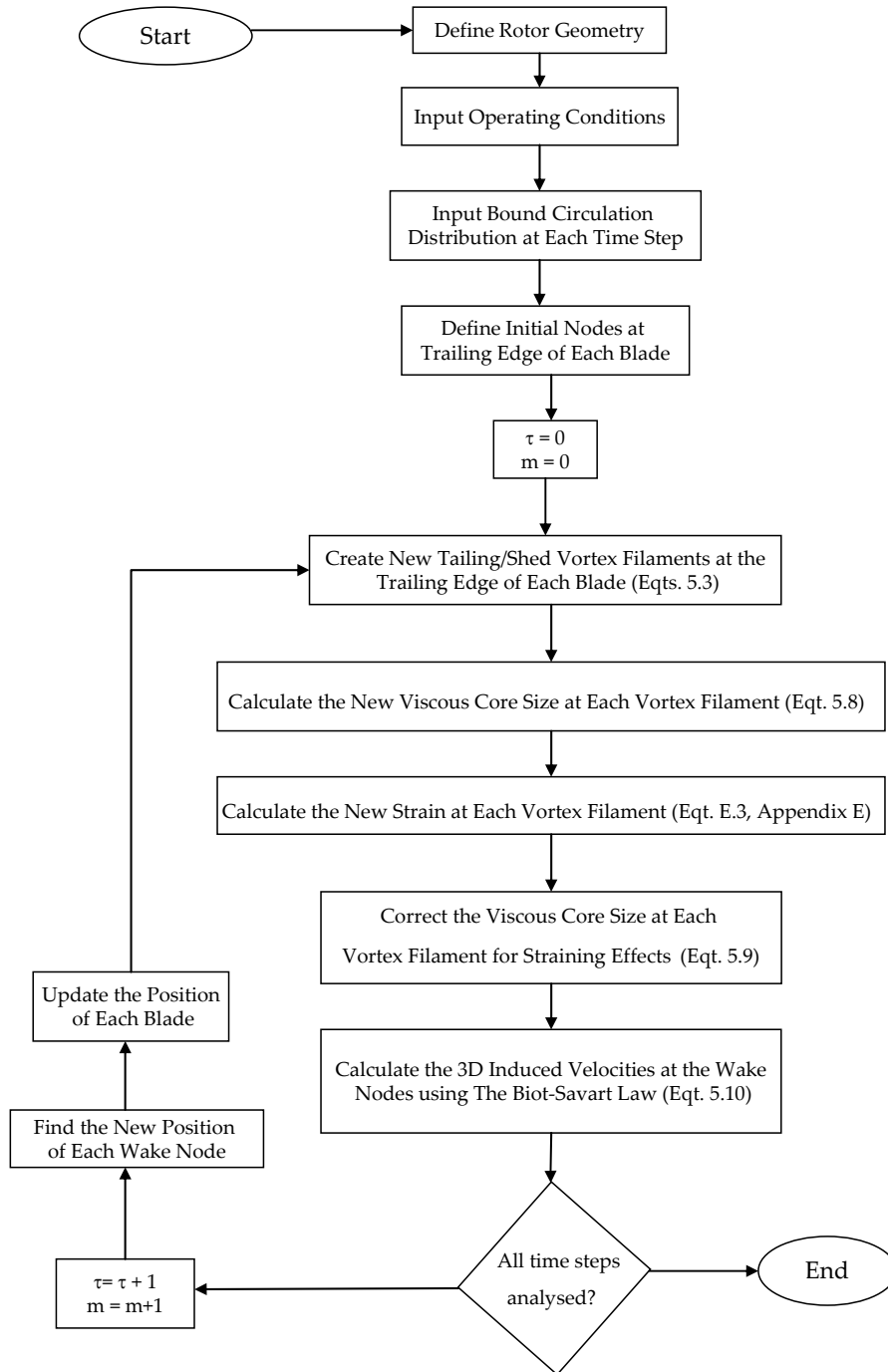


Figure 5.6 – Flowchart describing the numerical solution for generating near free-wake.

- ii. a core size is determined for all wake shed and trailing filaments accounting for viscous growth and filament straining using Eqts. 5.8 and 5.9.
- iii. the 3D induced velocities at each wake node due to bound, trailing and shed circulation are calculated using Eqts. 5.10.

- iv. the absolute velocity at each wake node, \vec{W} , is determined by vectorially adding the flow free stream velocity and the local induced velocities using the formula:

$$\vec{W} = \vec{U} + \vec{u} \quad (5.11)$$

Eq. 5.11 is written in the X-Y-Z reference frame and considering a uniform free windspeed it is expressed as

$$\begin{bmatrix} W_x \\ W_y \\ W_z \end{bmatrix} = \begin{bmatrix} 0 \\ U \\ 0 \end{bmatrix} + \begin{bmatrix} u_x \\ u_y \\ u_z \end{bmatrix} \quad (5.12)$$

- v. the position of each wake node in 3D space is determined using the Euler explicit time-integrating scheme:

$$\vec{r}_{\tau+1} = \vec{r}_{\tau} + \frac{1}{2} (\vec{W}_{\tau+1} + \vec{W}_{\tau}) * \Delta \tau \quad (5.13)$$

- vi. the rotor azimuth position and time step are updated (τ and m).

The above process is repeated until m is equal to M_{tot} . During the last rotor revolution, (i.e. from time step $m=(M_{tot}-n_{tot})$ to $m=M_{tot}$, the Biot-Savart law is applied to both the generated near free wake and the prescribed far wake to compute the 3D induced velocities at a selected plane parallel to the rotorplane. These 3D induced velocities are obtained in the x - y - z reference frame for different rotor azimuth positions (τ). The discretization of points in this selected plane is determined in a similar way to *HAWT_PVC*, as shown in Fig. 4.40 (page 107). It can be noted that in the time-integrating scheme using Eq. 5.13, the absolute velocity of each node is taken to be equal to the average of the newly calculated value and that of the previous time step. This averaging procedure improves the numerical accuracy and stability of the time integrating scheme, as noted in [5].

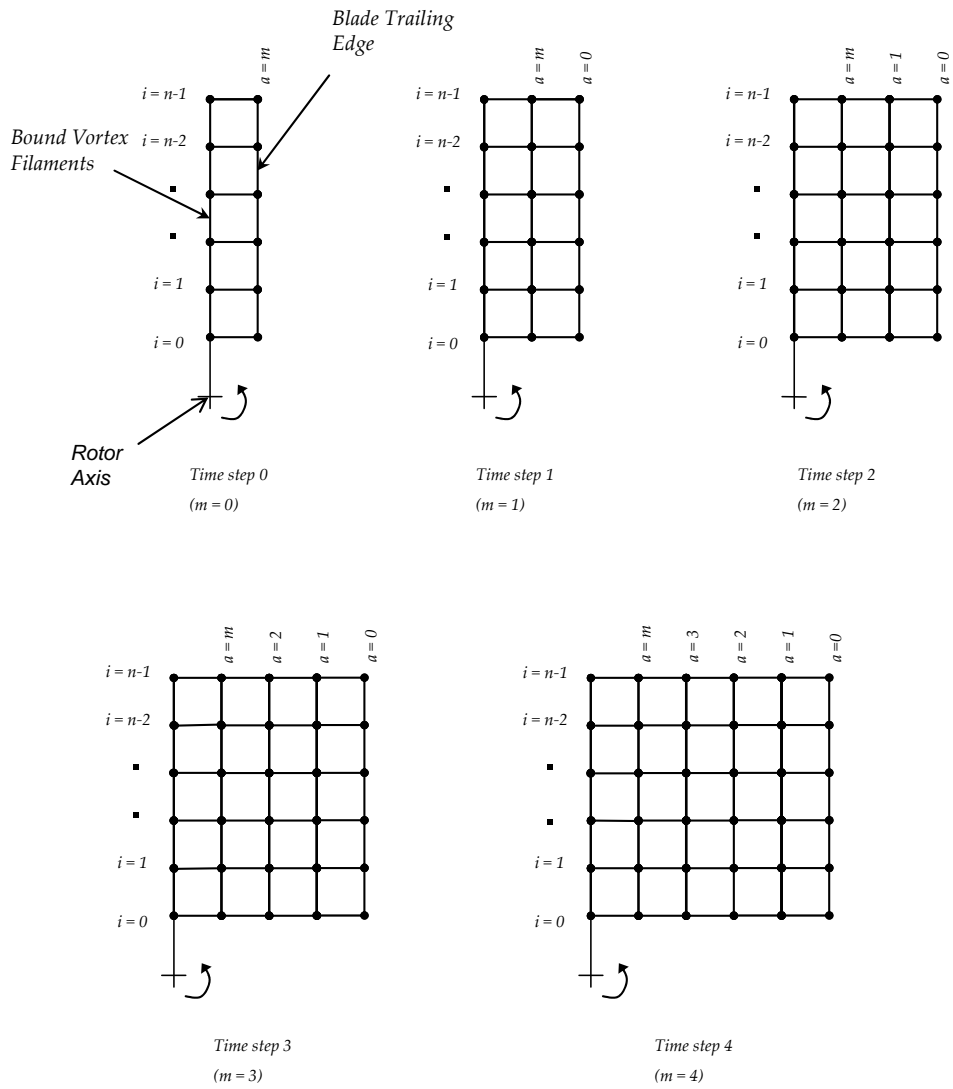


Figure 5.7 - Time-marching sequence for vortex lattice formation of the near wake due to each blade. The first five time steps are shown.

5.2.5 Program Structure

HAWT_FWC was written in MathCad© version 11. Fig. 5.8 describes the structure of the program. Like the other developed codes, there are three main modules: the *Data Input Module*, in which the parameters describing the rotor geometry and operating condition are inputted, together with the prescribed steady/unsteady bound circulation distributions. The far wake model parameters (pfw , $nfwRev$ and χ_s) are also prescribed here. The distance from the rotorplane of the plane at which the 3D induced velocities are to be computed is also inputted. The *Data Processing Module* implements the vortex model and the time-marching solution using the Biot-Savart equations as described in sections 5.2.1, 5.2.2, 5.2.3 and 5.2.4 to generate the free-wake and calculate the 3D induced velocities at a plane parallel to the rotorplane. Given that the aerofoil data are known, this module also calculates the steady/unsteady aerodynamic blade loading distributions using the BET equations (Eqts. 3.16 and 3.20, Chapter 3) as well as the 3D global aerodynamic loads induced at the yaw bearing (using procedure described in Appendix B). The *Data Output Module* outputs the free-wake geometry, together with the trailing and shed circulation in the wake and the 3D induced velocities in the required plane for different rotor azimuth positions. The blade aerodynamic load distributions and the global loads at the yaw bearing are also outputted as a function of blade/rotor azimuth angle.

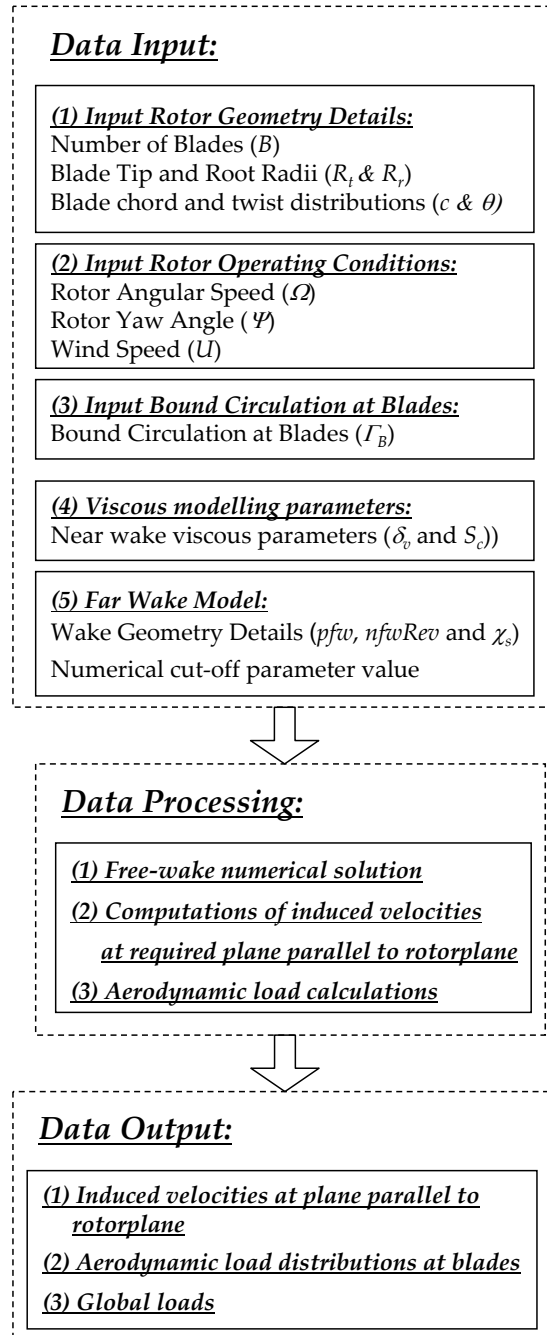


Figure 5.8 – Structure of computer code HAWT_FWC.

5.3 Verification and Validation of Free-wake vortex model

As with all numerical models, assessing the accuracy and reliability of the solution in reproducing results observed in the real world is an indispensable requirement. This section describes the verification and validation work carried out on the newly developed free-wake lifting-line code *HAWT_FWC* for modelling wind turbines in both axial and yawed conditions. This work was indispensable in order to be able to assess the reliability of the new method being proposed in Chapter 6 for deriving the angle of attack and inflow distributions in the turbine wake from blade pressure measurements.

Although free-wake models have reached a reasonably good level of maturity, more rigorous validation efforts are still required. It is important to remark here the distinction between verification and validation. As defined by Oberkampf *et al.* [59], *Verification* is the process of quantifying the numerical error in solving a conceptual model. In doing so, the accuracy of the computational solution is measured relative to two types of highly accurate solutions: analytical solutions and highly accurate solutions. *Validation*, on the other hand, is the assessment of accuracy of a computational solution when compared with the real world, i.e. the experimental data. In verification the comparison of the computational results with the experimental data is *not* an issue. In validation this comparison *is* an issue. Briefly speaking, verification is primarily a mathematics issue while validation is a physics issue. In this study on *HAWT_FWC*, validation is based on direct comparison of near wake inflow measurements. This makes the validation more rigorous than when comparing blade loads. The reason for this regards the basic fact that free-wake lifting line vortex methods still rely on the blade-element theory for computing the aerodynamic loads on the blades. The accuracy in load calculations will depend on the accuracy of the induced velocities computed by the free-wake code as well as the aerofoil data used. At low induction conditions however, a large error in the calculated induced velocities can still yield considerably accurate loads. But this would not mean that the free-wake model is accurate. Also errors in the aerofoil data may mask errors in the induced velocities computed by the free-wake code.

5.3.1 Verification & Validation Methodology

This section describes the procedures used to verify and validate vortex code *HAWT_FWC*.

A. Verification

An essential condition of a computational solution is that it should be convergent both in discretizing (*blade and wake discretization convergence*) and iterating (*iterative convergence*). Since in the subject free-wake code *HAWT_FWC*, the bound circulation is prescribed directly instead of determined iteratively using aerofoil data, there are no iterative

procedures here. Consequently, solution convergence is only due to insufficient blade and vortex sheet (i.e. wake) discretization. Blade and wake discretization convergence implies that, by systematically using a finer discretization, the solution should eventually converge asymptotically to an exact solution which is the *calculus limit*.

The blade lifting line discretization is determined by n alone. Increasing n will make blade discretization finer as it will represent more accurately the chord and twist variations along the blade span. A larger n will also yield a more accurate representation of the prescribed bound circulations (refer to Fig. 5.1). The discretization of the near wake is determined by the number of vortex filaments to make up the mesh to represent the vortex sheet/s extending downstream from the rotor plane. This discretization is dependent on modelling parameters n , $\Delta\phi$ and $nRev$. $\Delta\tau$ is directly related to $\Delta\phi$ ($\Delta\tau = \Delta\phi/\Omega$). For a fixed number of rotor revolutions ($nRev$), increasing n and using a smaller $\Delta\phi$ will increase the number of filaments, thus making the wake discretization finer. Another parameter is the distance to which the near wake extends downstream of the rotorplane. For fixed values of n and $\Delta\tau$, increasing M_{tot} will make the near wake extend more downstream. The discretization of the far wake is determined by the number of straight-line segments taken to represent the prescribed number of helices as well as $\Delta\phi$.

To be physically meaningful, the required outputs from the free-vortex solution should ideally be insensitive to discretization. In verification, a convergence study is conducted by numerical experiments in which a systematic refinement is applied with one discretization parameter at a time while holding the others constant. In this way, one may determine the most appropriate values that should be assigned to the discretization parameters in order to achieve acceptable levels of numerical accuracy. Another fact that should be taken into account is computational cost. A major drawback of free-wake models is the very rapid increase in computational cost as the number of vortex filaments is increased. Compromise should therefore be reached between numerical accuracy and computational cost. It is imperative that the verification procedure demonstrates the computational expenses required to achieve the required numerical accuracy.

The higher the number of discretization parameters, the more complex the convergence study will be. Yet there is another problem that complicates things further: apart from the discretisation parameters, there are other modelling parameters that are included to make the conceptual (mathematical) model more realistic. The problem is that we do not know exactly which values for such parameters to use for a simulation. It is best to leave the choice arbitrary and to the subjective decision of code user. It is validation *not* verification that will help us identify the most realistic values to use in a simulation. There are two sets of such arbitrary parameters in the subject free-wake model: (1)Viscous core modelling parameters (δ_c and S_c) and (2)Far wake modelling parameters (cut-off parameter, prescribed pitch (pfw) and number of rotations for which the helices extend downstream ($nfwRev$)). In this situation, the verification procedure should ideally check whether the *discretization convergence* criterion is met over a wide range of values of the arbitrary parameters.

In this verification procedure, the computed axial induced velocity at the blades is used as a basis for comparison. Apart from providing the necessary evidence of discretization convergence and correct implementation of the conceptual model, the verification process will provide insight into the numerical behaviour of the code and how the different parameters will influence the results.

To verify the free-wake model, two different case studies were considered. In the first case study, the free wake code modelled a single elliptical blade rotating at a very large radius compared to its span. This approximated an elliptical wing moving linearly at constant speed. An elliptical bound circulation was prescribed to the blade as shown in Fig. 5.9 and the calculated downwash was compared with that from the analytical solution which states that the downwash is constant along the wing span and equal to ([3], [42]):

$$u_{a,c} = -\frac{\Gamma_{B,max}}{2b_s} \quad (5.14)$$

The blade geometric and operating parameters were set as shown in table 5.4. The far wake model was not included in this case study.

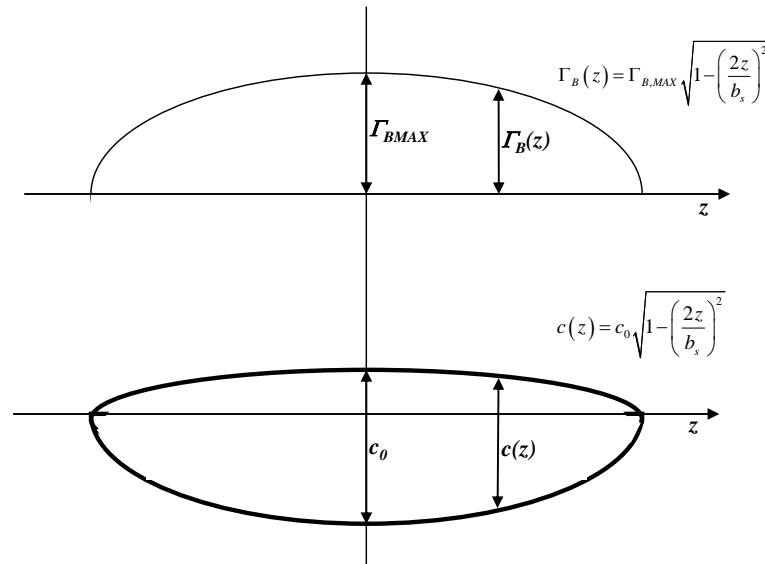


Figure 5.9 – Elliptical wing with a prescribed bound circulation distribution.

Table 5.4 – Blade geometry and operating condition parameters for elliptical wing.

<u>Blade Geometry Parameters</u>	
<i>B</i>	1
<i>R</i>	1000m
<i>Blade span</i>	10m
θ	3deg
<i>c₀</i>	2m
<u>Operating Conditions</u>	
<i>U</i>	0 m/s
Ω	0.1 rev/min
ρ	1.225kg/m ³

For the second case study, the verification was carried out concurrently with the validation process (see Part. B) when modelling the TUDelft wind tunnel turbine whose geometric details are given table 4.1, page 46. *HAWT_FWC* modelled the TUDelft rotor for the same conditions as those used for hot-film inflow measurements (with $U=5.5\text{m/s}$, $\lambda=8$ and $\theta_{ip}=2^\circ$). The verification was carried out for $\psi=0^\circ$ and 45° . The bound circulation distributions obtained from *HAWT_LFIM* using the inflow measurements and the unsteady aerofoil theory (see Figs. 4.55 (*method 1*) and 4.79 (uncertainty limits not included), Chapter 4) were prescribed to *HAWT_FWC* to generate the near free-wake and compute the induced velocities at the rotorplane or at 3.5cm downstream. The axial induced velocities were computed for different values for the discretization parameters n , $\Delta\phi$ and $nRev$ and the numerical accuracies were computed and analyzed. To limit the complexity resulting from a large number of variables to be analyzed separately while maintaining the other constant, the far wake modelling parameters whether kept constant through the verification study.

The disadvantage of doing verification and validation concurrently is that any errors due to insufficient numerical convergence may mask other errors when comparing with experimental data. To avoid this problem, it was assured in this study that appropriate numerical convergence was achieved before comparing with experimental data.

B. Validation

As already outlined in Chapter 2 (Fig. 2.4), the experimental data from the TUDelft wind tunnel turbine model was used for the validation work on the free-wake vortex model. The validation was performed for $\psi=0^\circ$, 30° and 45° . The bound circulation distributions obtained from *HAWT_LFIM* using the inflow measurements and the unsteady aerofoil theory (see Figs. 4.55, 4.78 and 4.79, Chapter 4) were prescribed to *HAWT_FWC* to generate

the free-wake and compute the induced velocities at the rotorplane or at 3.5cm downstream at different values for viscous parameters (δ_v , S_c). Two independent procedures were then adopted for the validation: in the first procedure, the induced velocities from the free-wake model were compared with those derived from the hot-film measurements (see Figs. 4.59, 4.85 and 4.86); in the second procedure, the tip vortical locations from the free-wake model were compared with those from the smoke visualization (see Figs. 4.24, 4.27 and 4.28, Chapter 4). A limitation of this validation process is that it only considers attached flow conditions. Validation of *HAWT_FWC* for stalled flow conditions over the blades is not performed.

Fig. 5.10 summarizes the procedure for the verification and validation work of *HAWT_FWC* when modelling the TUDelft rotor.

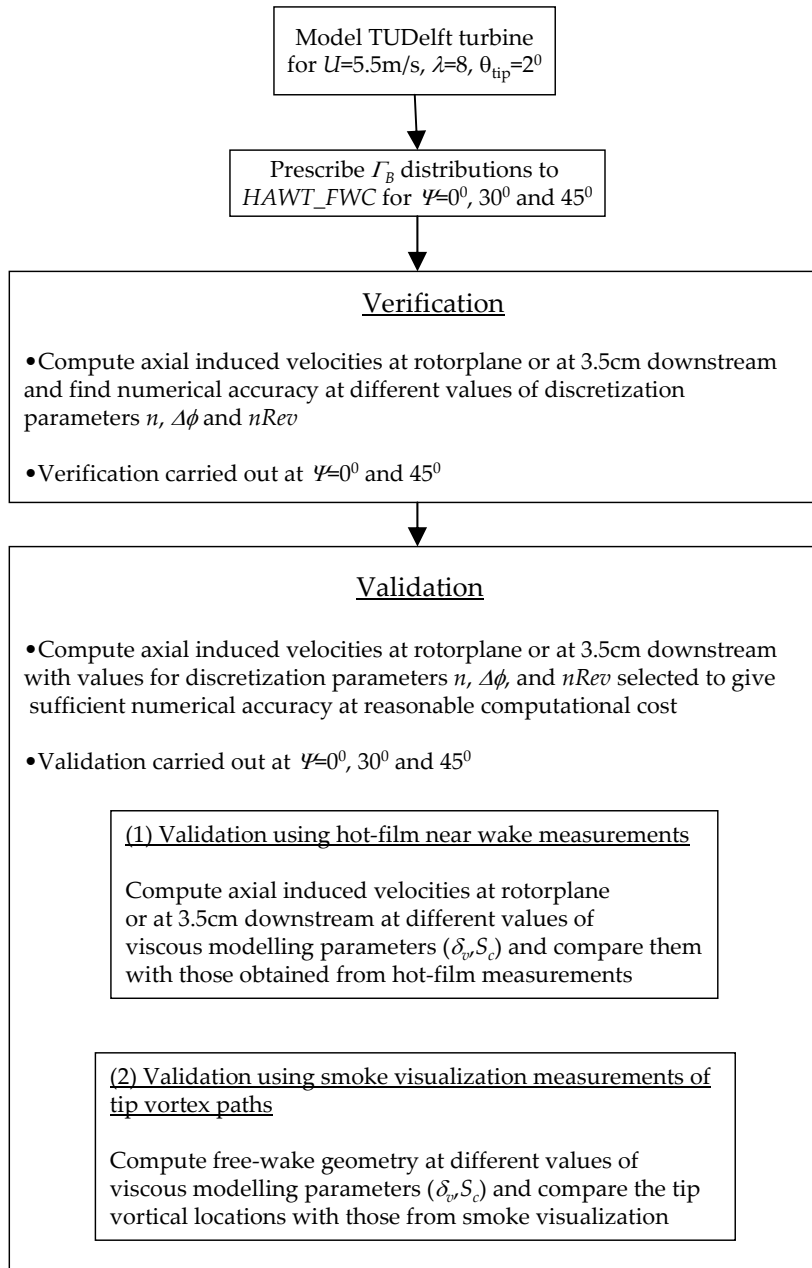


Figure 5.10 – Procedure for Verification and Validation of HAWT_FWC using the TUDelft rotor model.

5.3.2 Results and Discussion

This section describes the results obtained from this verification and validation study on *HAWT_FWC*. The results are organized in two parts: *Part A* describes the results obtained from the verification study which modelled the elliptical wing; *Part B* describes the results from the verification and validation which modelled the TUDelft wind tunnel turbine for the operating condition $\lambda=8$, $\theta=2^\circ$ at $\psi=0^\circ, 30^\circ$ and 45° .

A. Verification by Modelling Elliptical Wing

A constant elliptical circulation distribution (time-independent) was prescribed at the blade rotating at the very large radius with $\Gamma_{B,Max}$ in Eq. 5.14 set to $10\text{m}^2/\text{s}$. The blade was rotated until a constant spanwise distribution for the downwash was obtained at the lifting line ($u_{a,c}$). It was found that by rotating the blade by only 3° was enough to yield a downwash at the lifting line that was independent of vortex sheet length. This was equivalent to ratio y/c_0 equal to about 26 where y is the distance travelled by the wing. Since the bound circulation is constant with time, there are no shed vortex filaments in the wake except those included at the first time step to account for Kelvin's condition. For $\Gamma_{B,Max}$ equal to $10\text{m}^2/\text{s}$, the analytical value for the downwash at the lifting line as given by Eq. 5.14 is equal to -0.5m/s . Fig. 5.11 shows a typical downwash distribution predicted by the free-wake code at different values of n . It can be observed that the predictions are very close to the analytical result. The free-wake numerical solution predicts a downwash that is fairly constant for most of the span except at the wings tips where the downwash increases rapidly to positive values.

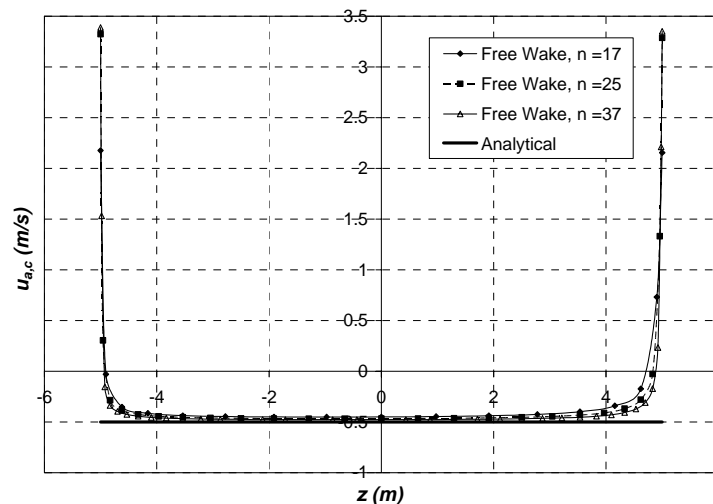


Figure 5.11 - Spanwise distribution of downwash for elliptical wing. Free-wake code results computed for $M_{tot}=30$, $\Delta\phi=0.1^\circ$, $\Delta\tau=0.167\text{s}$, $\delta=10$, $S_c=1$.

A finer discretization for the lifting line (i.e. using a larger n) reduces the deviation from the analytical result at all radial locations, especially the wing tips. The discrepancies between the analytical and the free-wake code results are mainly due to the fact in the analytical solution, the wake is assumed to be rigidly flat. In the free-wake solution, the wake is allowed to develop freely in 3D space under the action of the self induced velocity and that from the blade lifting line. The resulting free wake is not flat, especially towards the wing tips where there are higher levels of trailing vorticity.

Fig. 5.12 shows the build-up of downwash $u_{a,c}$ at the lifting line as the wing is suddenly set into motion at constant speed and with a constant elliptical bound circulation. As the wing moves, it leaves a wake behind that causes an evolving downwash at the wing. At start-up, the downwash is zero but this is followed by an instantaneous increase due to the shedding of the starting shed vortex. With time, the starting vortex moves away from the wing and the downwash approaches to the steady values.

Fig. 5.13 displays a typical resulting wake plot from the free-wake solution. The presence of roll-up of the vortex sheet at the wing tips is evident and the tip vortex formation at each wing tip shows up unmistakably.

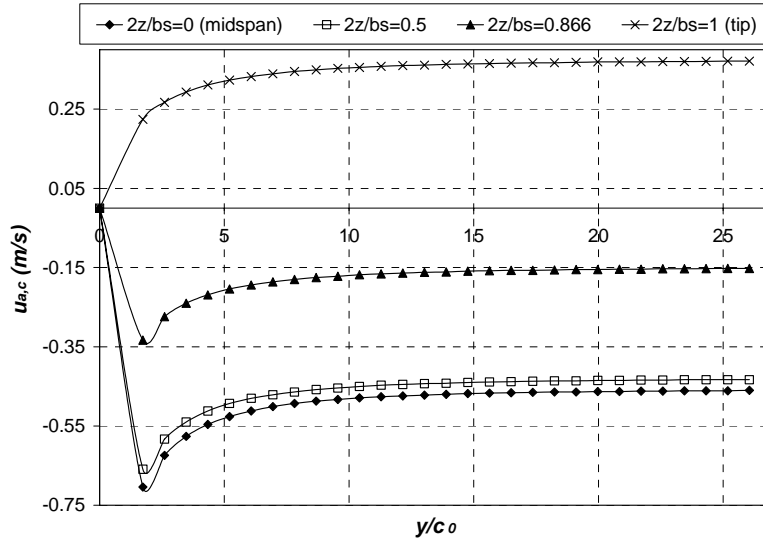


Figure 5.12 – Build-up of downwash at different spanwise locations as predicted by free-wake code. $n=25$, $M_{tot}=30$, $\Delta\phi=0.1^\circ$, $\Delta\tau=0.083s$, $\delta_i=500$, $S_c=10$.

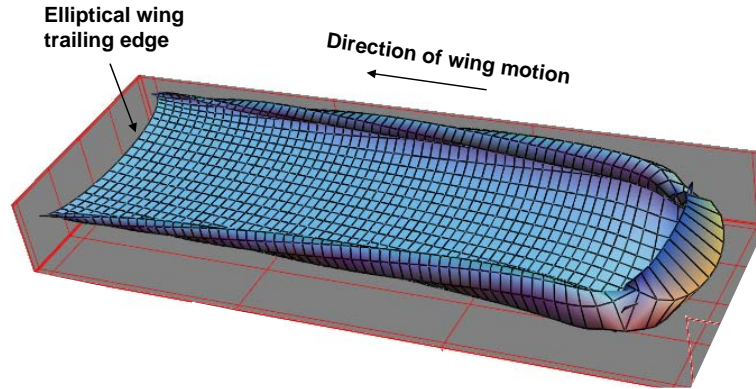


Figure 5.13 –Typical free-wake plot for elliptical wing.

B. Verification and Validation by Modelling TUDelft Wind Tunnel Turbine Model

B.1. Axial Conditions

The results obtained from the verification and validation procedures applied for the TUDelft turbine at $\psi \neq 0^\circ$ are now presented. The bound circulation distribution of Fig. 4.55 (using *method 1*) was prescribed to *HAWT_FWC* and the computations were carried out for different values of $nRev$, $\Delta\phi$, n , δ and S_c . The computed axial induced velocities were compared with those obtained experimentally (Figs. 4.59(a) and (b)). The wake vortical locations predicted by the free-wake code were compared with the tip vortex locations measured during the smoke visualization experiments.

To limit the number of variables in the verification and validation study, the prescribed far wake model parameters in *HAWT_FWC* (pitch (pfw), number of helical revolutions ($nfwRev$) and cut-off distance) were kept constant throughout the study. To determine an appropriate pitch (pfw) for the far wake, preliminary free-wake computations were carried out at different far wake pitch values and the pitch value was extracted from the computed near free-wake geometry. The number of helical revolutions ($nfwRev$) was kept constant at 5. A constant cut-off distance of 0.5mm was used.

Verification

Effect of $nRev$ and far wake model

In order to obtain realistic results for the induced velocities at the blade lifting lines, one should make sure that the free-wake (i.e. the near wake in this context) extends far enough downstream from the rotor. When treating rotors in steady axial flows, two conditions

must be satisfied before applying the Biot-Savart law to compute the inflow distribution at the rotorplane: *Condition 1* is that the computed induced velocity distribution at the blades should ideally be independent of the number of revolutions ($nRev$) used to generate the free-wake; *Condition 2* is that this velocity distribution should ideally be independent of the far-wake, i.e. the computed induced velocities at the rotorplane with and without the far-wake vortex model should be the same. This is because the far-wake model is only a prescribed wake vortex model and is therefore less reliable. *Condition 1* is met by selecting $nRev$ large enough to reach a suitable degree of wake periodicity. Wake periodicity is achieved if, when computing the inflow at the rotorplane during the last rotor revolution, the induced velocity at the blade lifting line of the first blade at a rotor azimuth angle of 360° is equal to that at a rotor azimuth angle of 0° . A suitable degree of wake periodicity is achieved if the relative error is close to zero. The percentage relative error for wake periodicity is defined here as

$$\xi_{wp} = \frac{u_{a,c}|_{\phi=0^\circ} - u_{a,c}|_{\phi=360^\circ}}{u_{a,c}|_{\phi=360^\circ}} \times 100 \quad (5.15)$$

Condition 2 is also met by using a sufficiently large value for $nRev$. Increasing $nRev$ will push the far-wake helical vortex model away from the rotor and thus its contribution to the total induction at the blades is less influential.

In investigating quantitatively the effect of $nRev$ and the far-wake, free-wake computations were computed at different values of $nRev$ (equal to 1, 2, 3, 4 and 5) while keeping the other parameters, n , $\Delta\phi$, δ_v and S_c , constant (at 21, 10° , 10 and 5 respectively). The reasons for selecting the latter values for such parameters will be discussed later. The induced velocities at the blades were computed with and without the far-wake model included. Note however that the far wake model was still included to generate the near wake. Fig. 5.14 shows the computed axial induced velocity distributions at the blade lifting lines for the different $nRev$ values. Fig. 5.15 shows the corresponding variation of the relative percentage error for wake periodicity against $nRev$ computed using Eq. 5.15. From this figure, it may be observed that wake periodicity is achieved rapidly after the first three rotor revolutions and the percentage discrepancy converges steadily towards zero over the following revolutions. With $nRev$ equal to 3, the relative percentage error is below 5 percent at all radial blade locations. Fig. 5.16 illustrates the increase in computational time when increasing $nRev$ from 1 up to 5. The Relative Computational Time Factor (*RCTF*) is plotted here instead of the actual computational time in hours, since the latter varies depending on the computer processor speed. In this case, the *RCTF* is defined as the time required to compute the free-wake solution with a given value of $nRev$ divided by the time required to do the same computation with $nRev$ set to one. The rapid increase in computational time is evident from Fig. 5.16. Selecting $nRev$ equal to 4 instead of 3 will reach a higher degree of wake periodicity but this also implies that more than double the computation time is required (*RCTF* is 36 instead of 16).

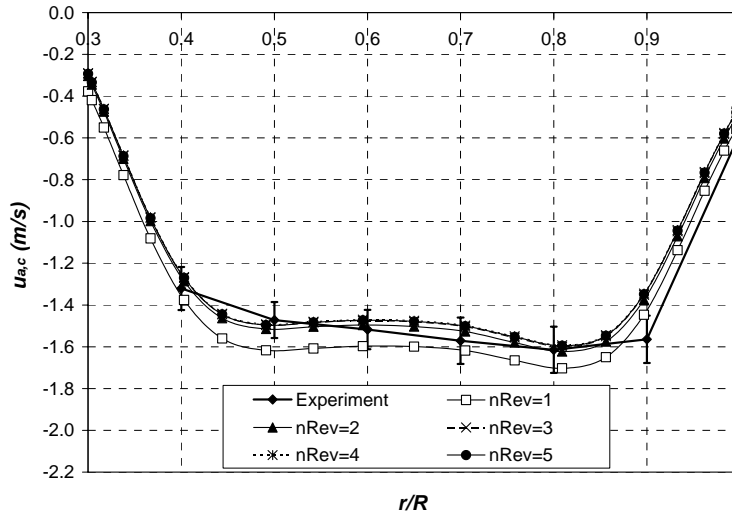


Figure 5.14 – Axial induced velocity distribution at blade lifting line computed by free-wake code for different values of $nRev$. Blade is at 360° azimuth. (Far wake model included in velocity calculations). Bars in experimental curve represent \pm one standard deviation in the experimental data.

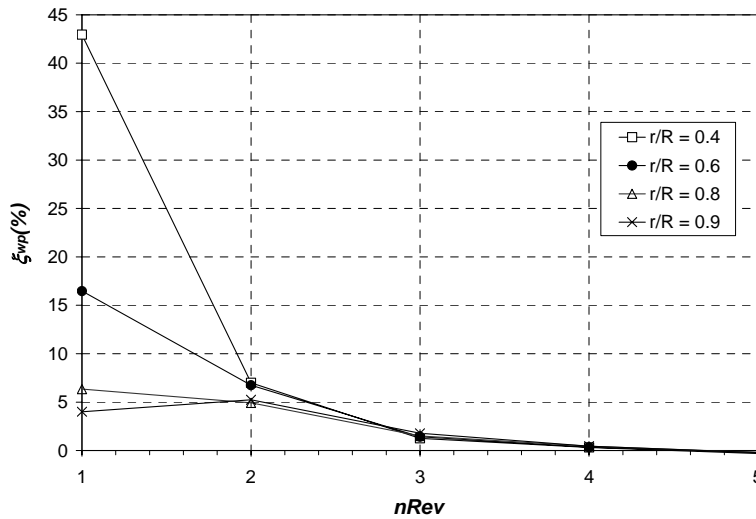


Figure 5.15 – Variation of Relative Percentage Error in Wake Periodicity with $nRev$.

Although good agreement was achieved with the experimental data when including the far wake model in the induced velocity calculations for all $nRev$ (as shown in Fig. 5.14), the agreement was not as good when performing the same calculations excluding the far wake model (refer to Fig. 5.17). Yet, in Fig. 5.17 better agreement with the experiments was still

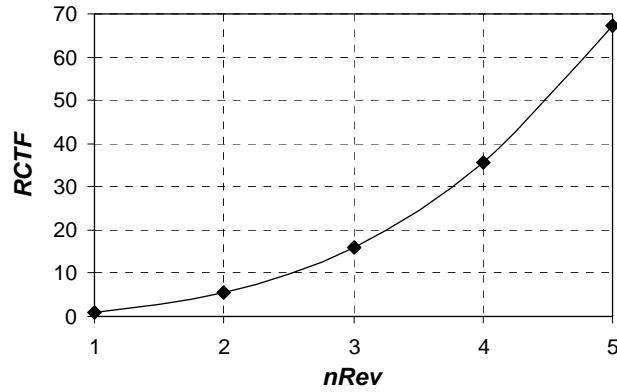


Figure 5.16 – Variation of Relative Computational Time Factor with nRev

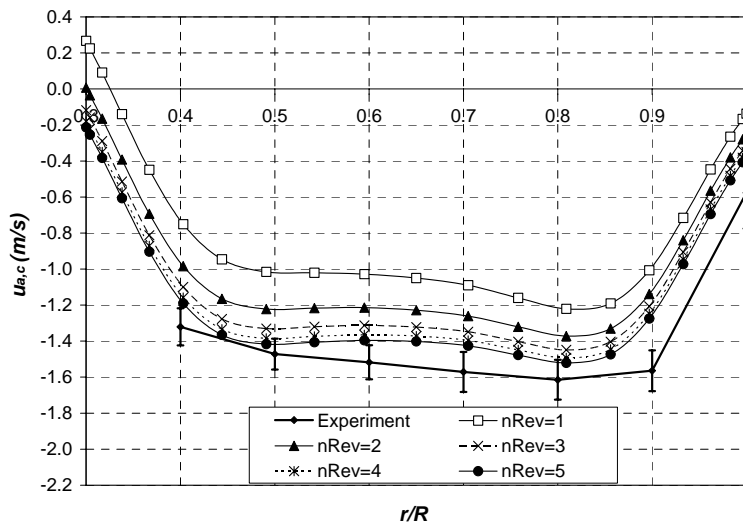


Figure 5.17 - Axial induced velocity distribution computed by free-wake code for different values of nRev (Far wake not included). Bars in experimental curve represent +/- one standard deviation in the experimental data.

obtained as nRev was increased. In analyzing the discrepancy in calculating the induction with and without the far-wake model at different nRev values, the results of Figs. 5.14 and 5.17 were used to calculate the percentage relative error given by:

$$\xi_{fw} = \frac{u_{a,c}|_{with\ far\ wake} - u_{a,c}|_{without\ far\ wake}}{u_{a,c}|_{without\ far\ wake}} \times 100 \quad (5.16)$$

The errors are plotted in Fig. 5.18. As expected, as the number of near wake revolutions is increased, the relative error decreases and convergences steadily to approach zero. This is due to the reduced influence of the far wake on the rotorplane induction as the former is convected downstream by the growing near wake. It should be noted that at each value of $nRev$, the relative errors in Fig. 5.18 are significantly larger than those in Fig. 5.15. This implies that, as $nRev$ is increased, *condition 1* (i.e. that wake periodicity is reached) is satisfied before *condition 2* (i.e. independence of far-wake model). This proves that selecting $nRev$ based on satisfying *condition 1* alone is insufficient, unless *condition 2* is also satisfied.

In this analysis, the criterion to meet *conditions 1* and *2* are based on $nRev$ because the latter is directly related to computational cost. In this way one could obtain insight regarding the computational cost required to reach different levels of wake periodicity and far-wake independence. But one should realize the fact that this also depends on the operating condition of the rotor, in particular the tip speed ratio (λ). A safer criterion is to base the selection on the distance the near wake should extend downstream from the rotor. The higher the tip speed ratio, the smaller is the pitch of the vortex sheet and therefore a higher $nRev$ would be required to extend the near wake suitably downstream. In this sense, free-wake models request higher computational costs when modelling high tip speeds than for lower values. In this study, in which the rotor was operating at $\lambda=8$, the corresponding near wake distance from the rotorplane for $nRev$ equal to 1, 2, 3, 4 and 5 are $0.33d$, $0.75d$, $1d$, $1.25d$, and $1.5d$ respectively.

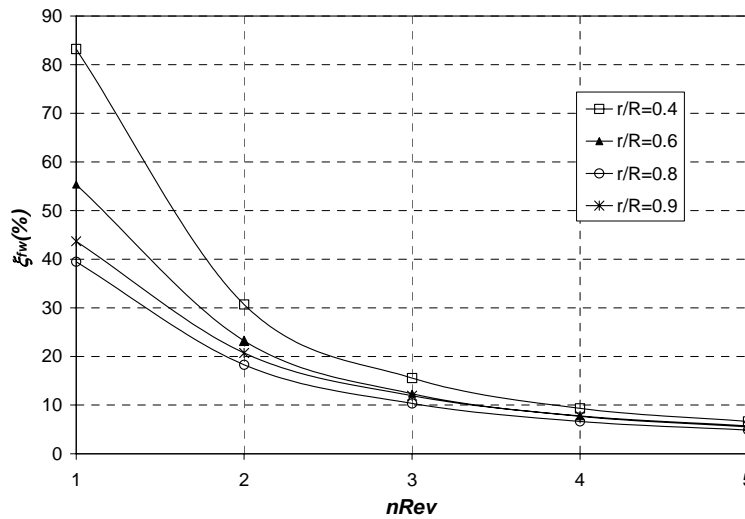


Figure 5.18 – Variation of Relative Percentage Error (ξ_w) for discrepancies between computations for $u_{a,c}$ carried out with and without far wake model.

This verification study therefore suggests that to reach wake periodicity and far wake independence with an error of less than 10% at all radial locations at the blades, the near wake should at least extend 1.25 diameters before computing the induced velocities at the blade lifting lines.

Effect of $\Delta\phi$

To investigate the influence of the time step size on the computed induced velocities at the blades, the calculations using *HAWT_FWC* were carried out using the bound circulation of Fig. 4.55 (using *method 1*) for different values of $\Delta\phi$, keeping the other parameters fixed. Four values for $\Delta\phi$ were chosen, equal to 7.5, 10, 15 and 30° while keeping parameters n , $nRev$, δ_0 and S_c fixed at 21, 3, 10 and 5 respectively. In these calculations, the induced velocity at the blades was computed, taking into account also the contribution from the far wake. The results are displayed in Fig. 5.19. The differences are very small, the largest being when $\Delta\phi$ is equal to 30°.

To quantify these differences, the relative percentage error was found using the equation:

$$\xi_{\Delta\phi} = \frac{u_{a,c}|_l - u_{a,c}|_s}{u_{a,c}|_s} \times 100 \tag{5.17}$$

where suffix s and l denote the small and large value of $\Delta\phi$ respectively. Eq. 5.17 was applied by taking (s,l) successively equal to (7.5°, 10°), (10°, 15°) and (15°, 30°). The spanwise variation of $\xi_{\Delta\phi}$ at the different values of (s,l) is shown in Fig. 5.20. It may be observed that the relative error is small, reaching a maximum towards the blade root and tip.

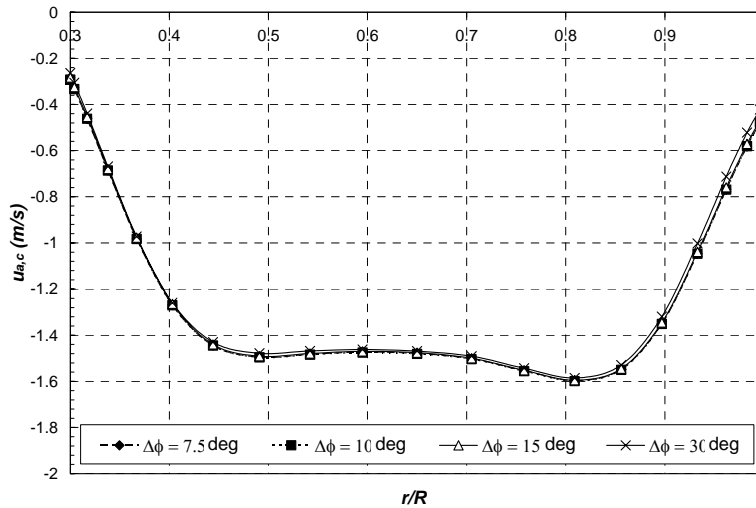


Figure 5.19 – Axial induced velocity distribution at blade lifting line computed by free-wake code for different values of $\Delta\phi$. Blade is at 360° azimuth. (Far wake model included in velocity calculations).

$\xi_{\Delta\phi}$ becomes smaller and approaches zero as smaller values of (s,l) are used. This happens at all spanwise blade positions and provides evidence of discretization convergence in the numerical free-wake model when using gradually smaller rotor time steps. Reducing the value of $\Delta\phi$ improves numerical accuracy because it reduces the time step ($\Delta\tau$) used in the time-marching scheme. Also at a given value of $nRev$, by using smaller values for $\Delta\phi$, the wake vortices are segmented into smaller segments. This improves the accuracy with which the vortex system represents the rotor wake as discussed Gupta *et al.* [34]. Unfortunately, a reduced time step will require increased computational costs, as illustrated in Fig. 5.21. The RCTF is defined here as the time taken to carry out the free-wake with a given value of $\Delta\phi$ divided by the time taken for the same computation with $\Delta\phi$ equal to 7.5° .

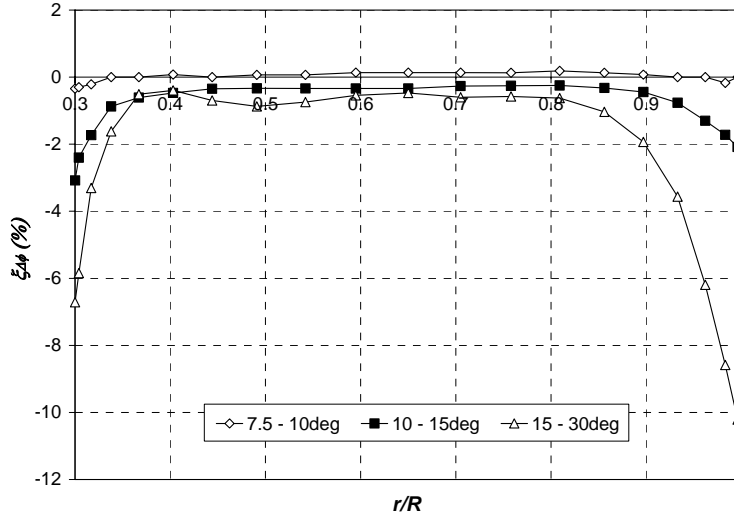


Figure 5.20 – Spanwise distribution of percentage relative error resulting from different values of $\Delta\phi$.

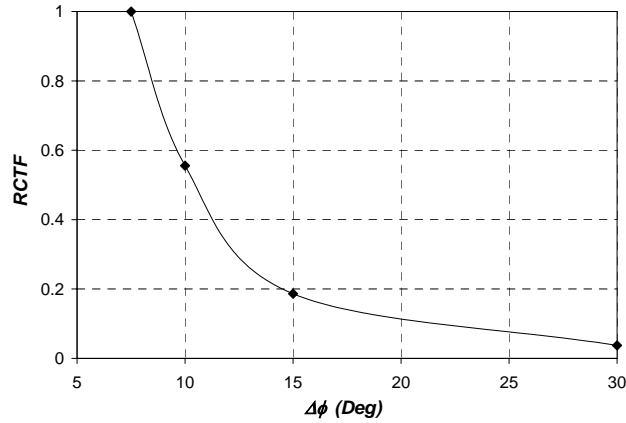


Figure 5.21 – Variation of Relative Computational Time Factor with $\Delta\phi$.

Effect of n

The free-wake calculations using *HAWT_FWC* were also carried out at different values of n (equal to 11, 21 and 31) while maintaining $nRev$ and $\Delta\phi$ constant (3 revolutions and 10° respectively). At each value of n , different sets of values for the viscous parameters (δ_v, S_c) were taken. The main objective of these calculations was to provide evidence of discretization convergence when increasing n over a wide range of values of (δ_v, S_c). Fig. 5.22 shows the axial induced velocity distribution at the blade lifting line calculated for the three values of n with (δ_v, S_c) taken as (10, 5). The presence of discretization convergence is apparent, since the discrepancy between the distributions at $n=21$ and $n=31$ is less than that between $n=11$ and $n=21$.

The Relative Computation Time Factor (*RCTF*) variation is displayed in Fig. 5.23. In this case, the *RCTF* is defined as the computation time required for a given n value divided by that required to carry out the same computation with $n=11$. It is important to note that the computational time is not affected by the choice of (δ_v, S_c) because these parameters are not blade or wake discretization parameters. Taking n equal to 21 instead of 31 reduces the computational time required by about 60% and while decreasing the numerical accuracy by only a maximum of 4% at all radial locations.

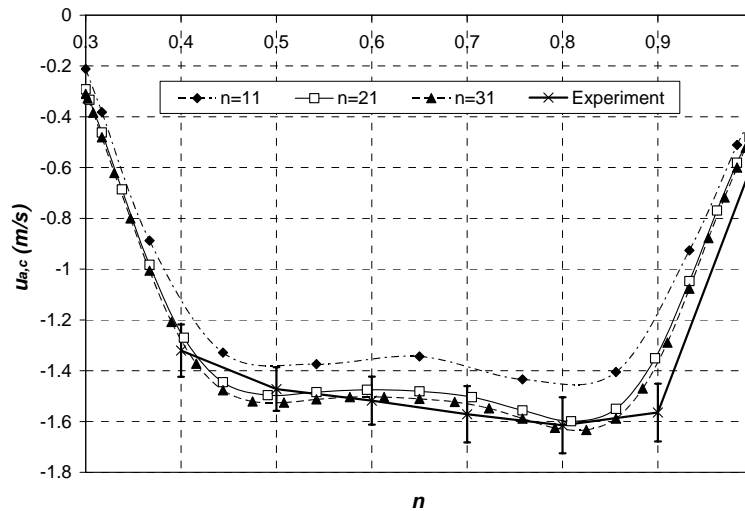


Figure 5.22 – Axial induced velocity distribution at blade lifting line computed by free-wake code for different values of n . (δ_v, S_c) are equal to (10, 5).

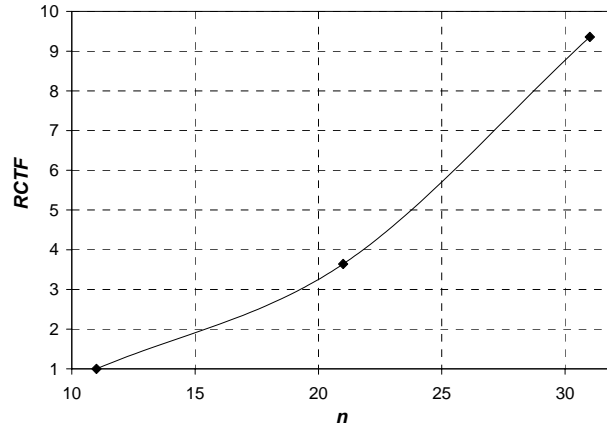


Figure 5.23 – Variation of Relative Computational Time Factor with n .

Figs. 5.24(a) and (b) illustrate how the calculated value of $u_{a,c}$ at the blade lifting line (at $r/R=0.65$) varies with n at different values of (δ_v, S_c) . Convergence was observed at all values of (δ_v, S_c) . Similar convergence trends were seen at other blade spanwise locations. Higher convergence rates are achieved at larger values of δ_v and S_c . To quantify the differences in $u_{a,c}$ through varying n , the relative percentage error was found using the equation:

$$\xi_n = \frac{u_{a,c}|_l - u_{a,c}|_s}{u_{a,c}|_s} \times 100 \quad (5.18)$$

where suffix s and l denote the small and large value of n respectively. Eq. 5.18 was applied by taking (s,l) successively equal to (21,11) and (31,21) for the different values of (δ_v, S_c) . Figs. 5.24 (a) and (b) also show the resulting values of ξ_n . The decreased relative error from (21,11) to (31,21) provides evidence of numerical convergence.

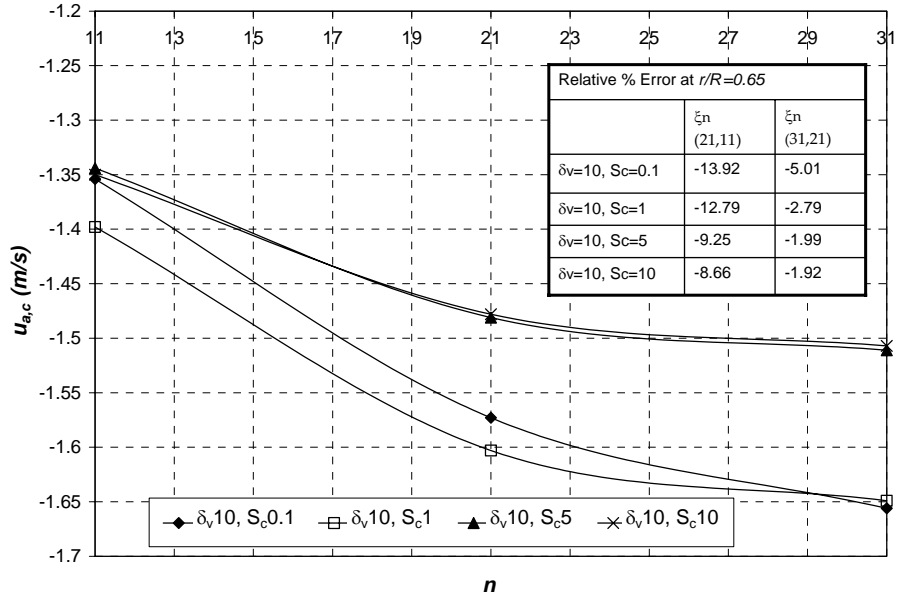


Figure 5.24(a) – Variation of computed induced velocity at blade lifting line at $r/R=0.65$ with n for different values of S_c keeping δ_v constant. ($n=11, 21$ and 31).

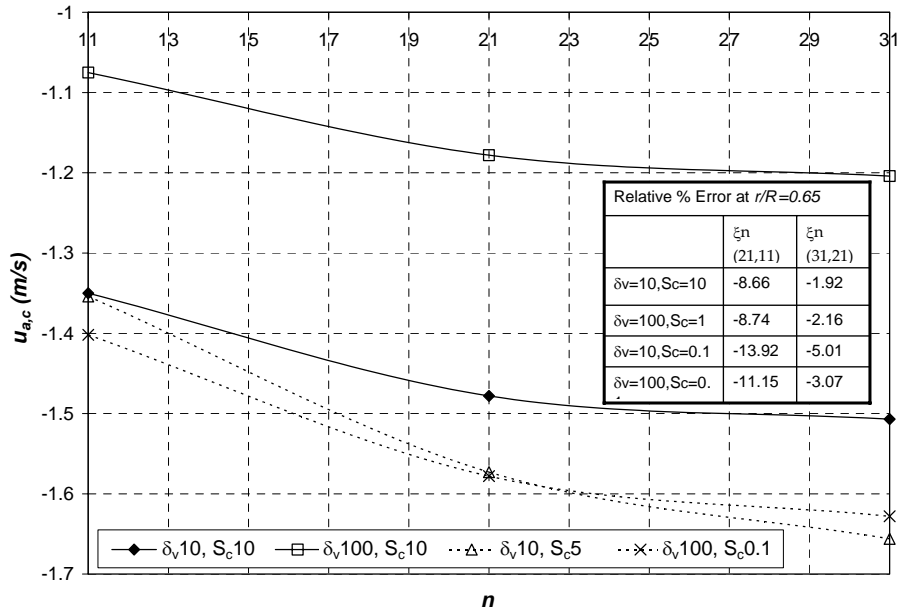


Figure 5.24(b) – Variation of compute induced velocity at blade lifting line at $r/R=0.65$ with n for different values of δ_v keeping S_c constant at 10 and then at 0.1. ($n=11, 21$ and 31).

Validation

After investigating the convergence trends in $u_{a,c}$ when increasing n , a study was then carried out to determine how different values of (δ_v, S_c) influence the correlation with the experimental data of Figs. 4.59(a) and (b). Figs. 5.25(a) and (b) show the spanwise distributions of the axial induced velocity at the blade lifting lines at different (δ_v, S_c) . The experimental results of Figs. 4.59(a) and (b) are also included in these plots. The following observations were noted:

- Very good agreement was obtained with the experiments for the middle blade sections (from $r/R=0.55$ to 0.75) at all (δ_v, S_c) values, except that at $(10,10)$. In fact, at these middle sections, the calculated induced velocity is quite insensitive to values of δ_v ranging from 1 to 10 and to values of S_c ranging from 0.01 to 10 seconds.
- The agreement is not good at the blade tip and root region. High sensitivity to δ_v and S_c is observed at the blade root and tip regions.
- When assigning small values of δ_v and S_c , the induced velocity distribution will tend to a converged distribution.

With reference to Eq. 5.8, increasing both δ_v and S_c increase the viscous core radius of the vortex filaments that model the near wake. As it may be noted from Figs. 5.25(a) and (b), when assigning small values for these parameters (i.e use small core radii), the induced velocity distribution at the blade will converge to one that is very close to the real (experimental) values at the middle blade sections, but over-predicts the induced velocities at the blade tip and root. On the other hand, when assigning increasing values for δ_v and S_c , the discrepancy at the blade tip and root is reduced. But if these two parameters are increased too much, the induced velocities will reduce to unrealistic low values at all positions along the blades.

In an attempt to determine a realistic estimation of δ_v and S_c , Eq. 5.8 was used together with the assumption that the thickness of the viscous layer of the vortex sheet at the point when it is shed from the trailing edge of each blade is on the order of the blade thickness. This is equal to $0.12c$ for the rotor considered in this case study. Based on this assumption, the core radii of the vortex filaments emerging from the blades (i.e. at $t = 0$) would therefore be approximately equal to half the blade thickness. Using these criteria, Eq. 5.8 then yields that the product of $\delta_v \times S_c$ equals 0.332. Given that δ_v is fixed at 10 (to follow the guidelines in references [2, 10] for small-scale rotors), then S_c would be equal to 0.0332 seconds. This implies that the axial induced velocity distribution would be somewhere between those at $(10, 0.01)$ and $(10, 0.1)$. Therefore, referring to Fig. 5.25(a), the distribution would have good agreement with the experimental one at the middle blade sections but not at the blade tip and root. Although there is some level of uncertainty in the computed induced velocity due to the fact that the bound circulation distribution (refer to Fig. 4.55) at the blade tip and root region was extrapolated (refer to section 4.3.6), one should also recall that the flow at blade tip/root regions is highly 3D in character and modelling the blade as a lifting line is insufficient here. This is a major limitation of lifting-line methods, as opposed to the more

accurate lifting-surface methods which cater for the 3D effects around the blade ends. The significance of the error from the lifting-line methods at the blade tip/root is dependent on the aspect ratio of the rotor blades: the higher the aspect ratio, the less is the significance of the error. For this study, the rotor blades had a low aspect ratio (equal to 5.25) and the blade root/tips were rectangular in shape. Consequently these errors are large. Luckily enough, modern wind turbine (and helicopter) blades have higher aspect ratios and consequently this limitation of lifting-line models is not highly influential.

Figs. 5.26(a) and (b) plot the azimuthally averaged axial induced velocities at the rotorplane. This plot shows a similar behaviour as for the induced velocity at the lifting line, i.e. there is a low sensitivity for δ_v and S_c at the middle blade sections, but a high sensitivity at the blade tip and root regions.

In effect, δ_v and S_c determine the viscous core radius of the wake filaments at different vortex ages. The variation of the core radius with vortex age (i.e. time) at various values of δ_v and S_c may be observed in Fig. 5.27. S_c controls the initial core size at the point where a vortex is shed from the blade. δ_v controls the initial core size as well as the rate of core growth with time. Recall that a is an index denoting the vortex age and the lower its value, the older is the age of the vortex. It may be observed from Fig. 5.27 that the older vortices suffer from large changes in core radius. This is because they lie on the edge of the near wake vortex sheet, close to the interface with the far wake where large filament strains are experienced. This abrupt variation is quite unrealistic and is only due to the limitation in which the wake is being modelled.

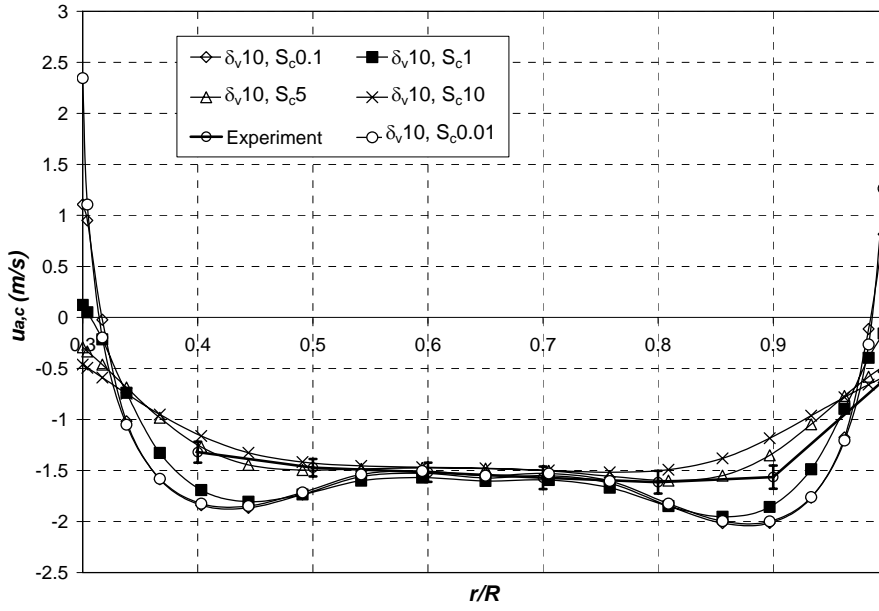


Figure 5.25(a) – Axial induced velocity distribution at blade lifting line computed by free-wake code for different values of S_c keeping δ_v constant. ($n=21$).

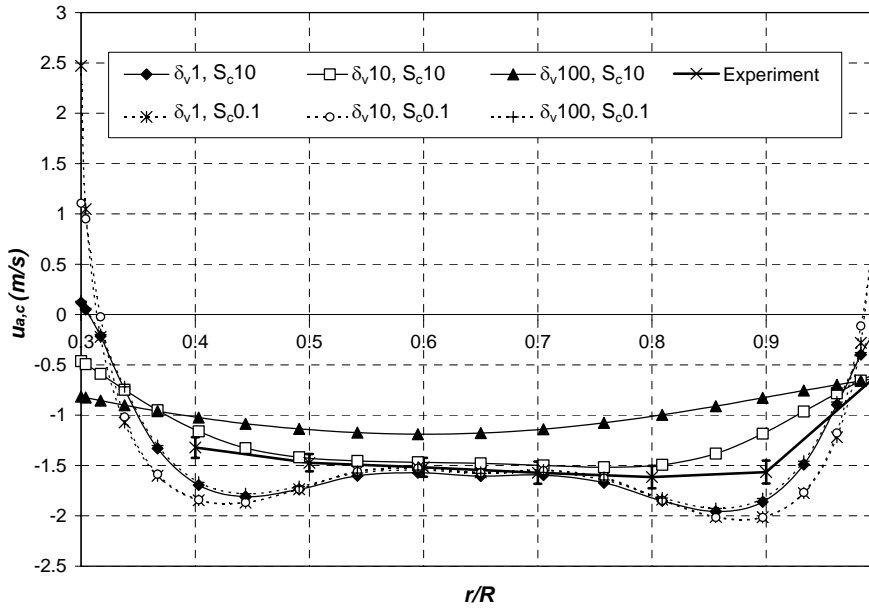


Figure 5.25(b) – Axial induced velocity distribution at blade lifting line computed by free-wake code for different values of δ_v keeping S_c constant at 10 and then at 0.1. ($n=21$).

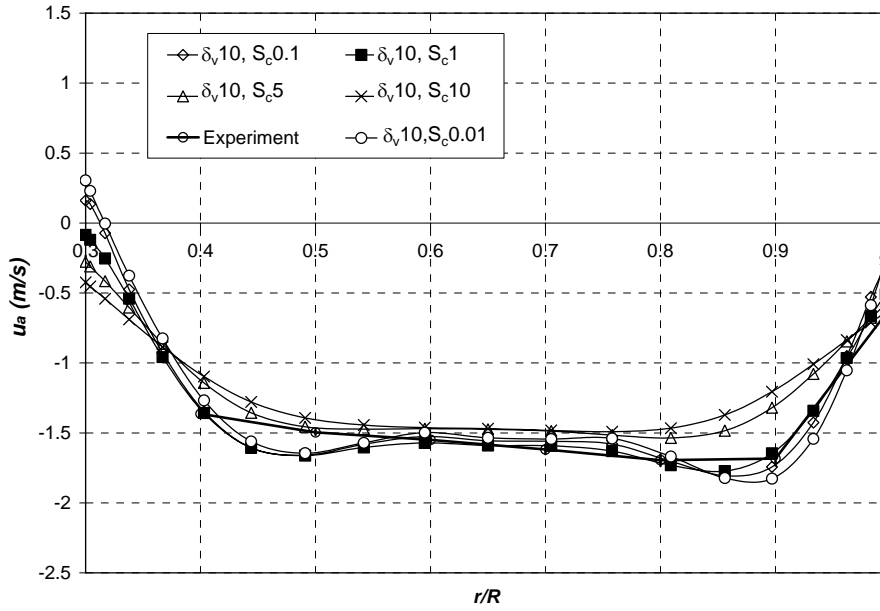


Figure 5.26(a) – Azimuthally-averaged axial induced velocity distribution at rotorplane computed by free-wake code for different values of S_c keeping δ_v constant. ($n=21$).

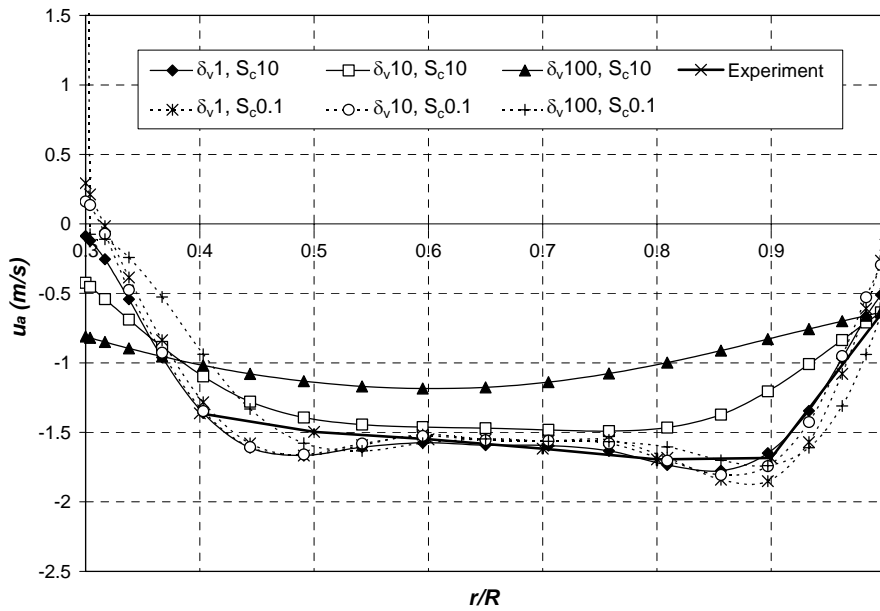


Figure 5.26(b) – Azimuthally-averaged axial induced velocity distribution at rotorplane computed by free-wake code for different values of δ_v keeping S_c constant at 10 and then at 0.1. ($n=21$).

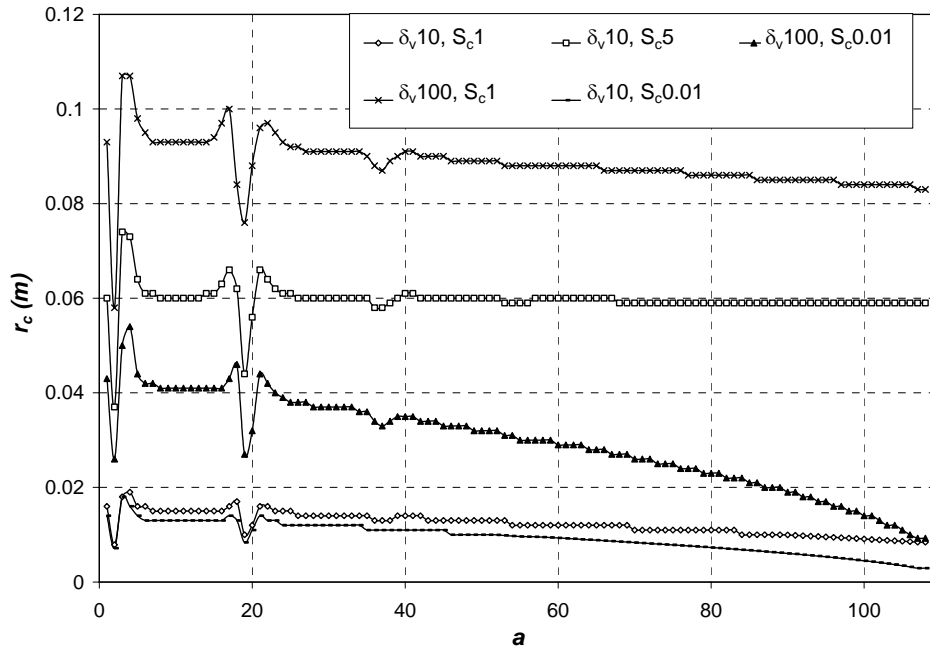


Figure 5.27 – Variation of viscous core radius of near wake trailing vortex filaments with vortex age at $r/R=0.65$. ($n=21$, $\Delta\phi=10^\circ$, $nRev=3$).

Figs. 5.28(a) and (b) plot the azimuthal distribution of the axial induced velocity for $r/R=0.6$ and 0.9 at 3.5cm downstream from the rotorplane for a fixed blade position at $\phi=0^\circ$. The free-wake results from *HAWT_FWC* are plotted at different viscous parameters and are compared with those measured in the wind tunnel. As a repeatability check of the experimental data, two measured traces are shown: at rotor azimuth positions 0° and 180° , since these should be the same in a two-bladed rotor. It may be noted in Fig. 5.28(a) that, although the computed induced velocity in line with the blade lifting line at $r/R=0.6$ agrees well with the experimental value, the comparison of the peak-to-peak velocity is not good. The peak-to-peak signal predicted by the lifting line model is only a fraction of the measured value. The main reason for this is the fact that the measured velocity signal includes the effects of a real blade section passing by. Thus the effects of section thickness and a non-zero chord length are present in the measurements. In Mast *et al.* [55], these effects are quantified and a method is proposed to adapt the measured velocities accordingly. As one moves away from the rotorplane, the peak-to-peak velocity predicted by the lifting line becomes more realistic. In fact, better predictions were obtained when computing the same velocity traces further downstream, at 9cm from the rotorplane (refer to Figs. 5.29 (a) and (b)).

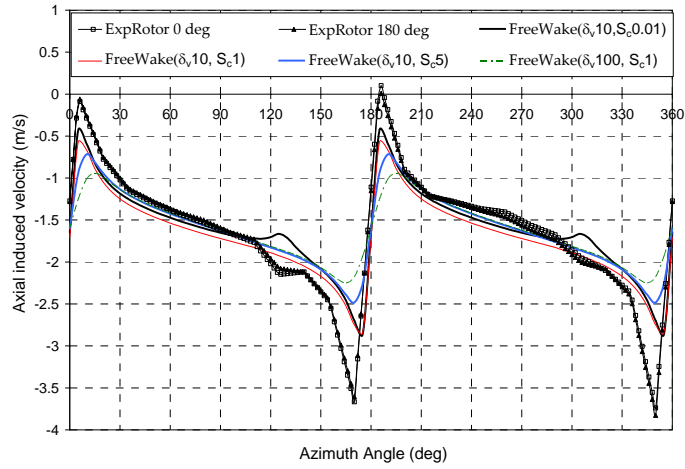


figure (a): $r/R = 0.6$

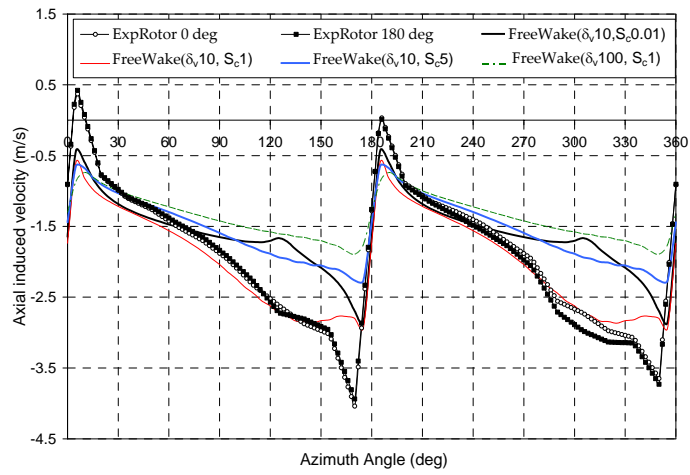


figure (b): $r/R = 0.9$

Figure 5.28 – Comparison of axial induced velocity traces computed by free-wake model with that measured by hot-film at 3.5cm downstream from rotorplane. Rotor blade is at 0/180 degrees azimuth. fig.(a): $r/R=0.6$; fig (b): $r/R=0.9$. ($n=21$, $\Delta\phi=10^\circ$, $nRev=3$).

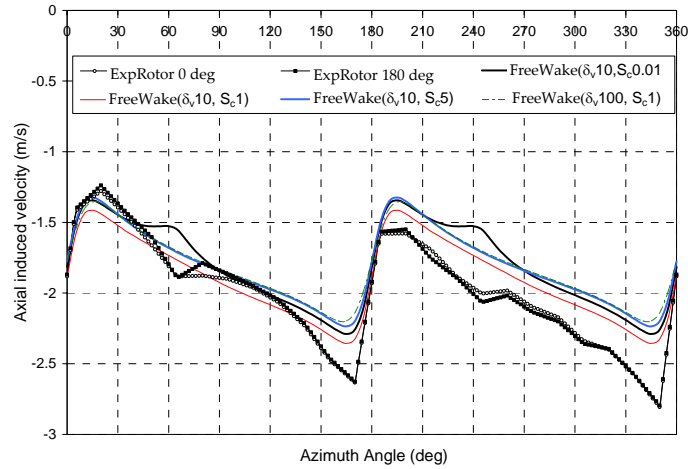


figure (a): $r/R = 0.6$

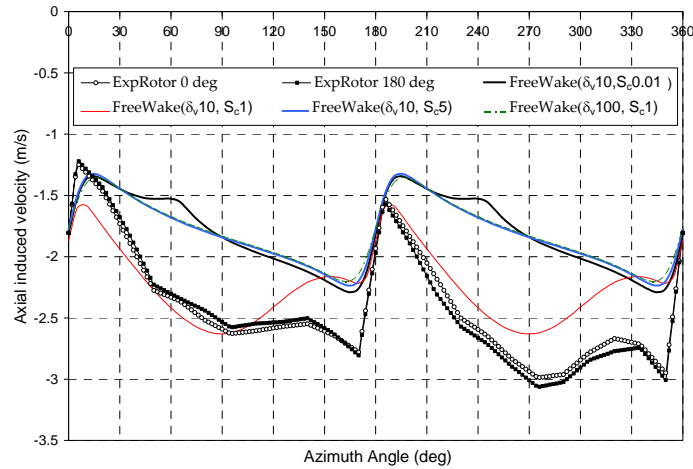


figure (b) $r/R = 0.9$

Figure 5.29 – Comparison of axial induced velocity traces computed by free-wake model with that measured by hot-film at 9cm downstream from rotorplane. Rotor blade is at 0/180 degrees azimuth. fig.(a): $r/R=0.6$; fig. (b): $r/R=0.9$. ($n=21$, $\Delta\phi=10^\circ$, $nRev=3$).

Fig. 5.30 compares the vortical wake positions predicted by HAWT_FWC for different values of (δ, S_c) with the tip-vortex locations measured using the smoke visualization experiments (see section 4.2.3). It may be easily observed that for (δ, S_c) equal to (10,0.1), very good agreement is obtained for the wake expansion, even though such parameters did not yield an accurate prediction for the axial induced velocity at the blade root and tip (refer to Figs. 5.25(a) and (b)). Recall that the selection of (10, 5) resulted in a better correlation for

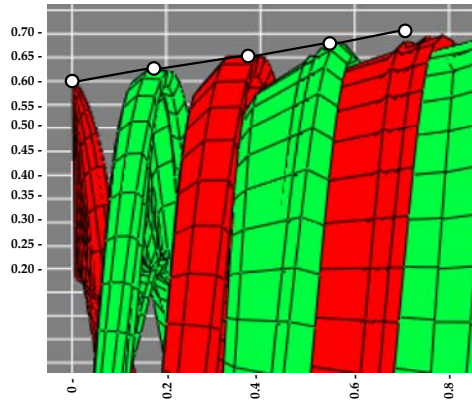


Figure (a): $(\delta_v, S_c) = (10, 0.1)$

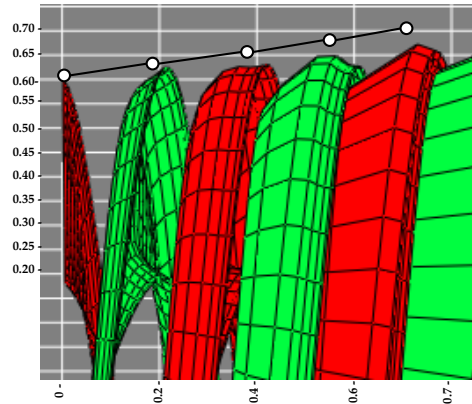


Figure (b): $(\delta_v, S_c) = (10, 5)$

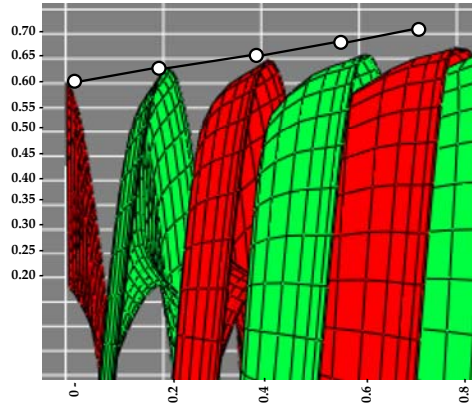


Figure (c): $(\delta_v, S_c) = (100, 1)$

Figure 5.30 – Comparison of tip vortical wake positions computed by free-wake code at different (δ_v, S_c) with measured tip vortex locations measured using smoke visualizations (represented by white dots). $n=21$, $\Delta\phi=10^\circ$, $nRev=3$.

the induced velocity at the blade root and tip. Yet this does not yield a better prediction for the wake expansion, as seen in Fig. 5.30(b). In effect, parameters (δ, S_c) control the amount of roll-up and expansion in the computed free-wake geometry. Increasing both (δ, S_c) reduce the wake roll-up as well as the wake expansion.

Wake circulation distribution

Fig. 5.31 illustrates the free-wake plot resulting from the bound circulation at the blades given in Fig. 4.55 (*method 1*). Colour coding is introduced in the plot to denote the trailing circulation in the wake. The plot provides a better understanding of how the bound circulation at the blades is eventually diffused into the wake. The figure shows that the highest circulation occurs at the blade tip and root, with the circulation at the tip being positive, while that at the root being negative.

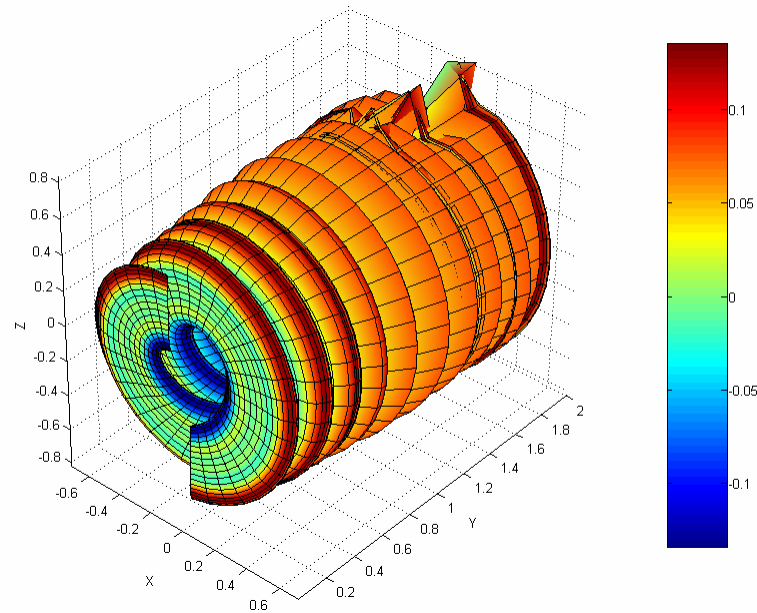


Figure 5.31 – Free-wake plot with $(\delta, S_c) = (10, 5)$ and $n=21$, $\Delta\phi=10^\circ$, $nRev=5$. Colour coding represents trailing circulation in wake.

B.2. Yawed Conditions

This section describes the results from verification and validation process of *HAWT_FWC* by modelling the TUDelft rotor in yawed conditions. Throughout this process, the far wake model parameters were kept constant. The number of the far wake helical revolutions (n_{fwRev}) was set equal to 10. To determine reasonable values for the prescribed helical pitch (p_{fw}) and wake skew angle (χ_s) for the far wake model at both $\Psi=30^\circ$ and 45° , preliminary calculations were carried out with the same free-wake model and an estimate was obtained from the near wake geometry. The cut-off distance was kept equal to 0.5mm.

The verification as carried out only for $\Psi=45^\circ$ while the validation was accomplished at both $\Psi=30^\circ$ and 45° .

Verification

The verification of *HAWT_FWC* at $\Psi=45^\circ$ was performed using an approach similar to that applied for axial conditions. The unsteady bound circulation distribution of Fig. 4.79 (Chapter 4), were prescribed to the vortex model. The uncertainty limits of this distribution were not considered in the calculations required for this verification process. Parameters $nRev$, $\Delta\phi$ and n were varied one at a time, while keeping all the other parameters constant. The induced velocities at the blade lifting lines ($u_{a,c}$) at $Y_a=3.5\text{cm}$ were used as a basis for comparison. In all these calculations, the far wake contribution was included when computing both the near wake geometry and the induced velocities at the lifting lines.

Effect of $nRev$

As in axial conditions, when modelling a rotor operating in yaw at constant speed and in a uniform wind speed, the free-wake solution should attain a reasonable level wake periodicity to be realistic. Therefore parameter $nRev$ should be large enough to obtain the axial induced velocity at the lifting line of the first blade at a rotor azimuth angle of 360° equal to that at 0° and hence have wake periodicity. $nRev$ should also be large enough to push the far wake more downstream and thus reducing its influence on the induction at the blades. In investigating the effect of $nRev$, the free-wake computations with *HAWT_FWC* were computed at different values of $nRev$ (equal to 1, 2, 3, 4 and 5) while keeping the other parameters n , $\Delta\phi$, δ_v and S_c fixed at 21, 10° , 10 and 5, respectively. Figs. 5.32 and 5.33 compare the induced velocities at the blade lifting lines (at $Y_a=3.5\text{cm}$) for the different values of $nRev$. To quantify the level of wake periodicity attained at each value of $nRev$, the error ξ_{wp} was calculated using Eq. 5.15 at various radial locations. Some of the results are shown in Fig. 5.34 where it may be realised that wake periodicity is achieved rapidly, similar to what was found in axial conditions (see Fig. 5.15). Yet, when comparing the

results of Fig. 5.34 with those of Fig. 5.15 it is found that the values of ξ_{wp} at $nRev=1$ are much higher at $\Psi=45^\circ$ than at $\Psi=0^\circ$. This is because of the skewed wake effect in yaw where a larger value of $nRev$ is required to achieve a given level of wake periodicity than in axial conditions.

Note that in these calculations, the far wake model was included both to generate the free-wake geometry and to compute the induced velocities at the blades. The same calculations were repeated but excluding the far wake when finding the induced velocities at the blades and the error ξ_{fw} was determined using Eq. 5.16. The results also had the trends very similar to those obtained in axial conditions.

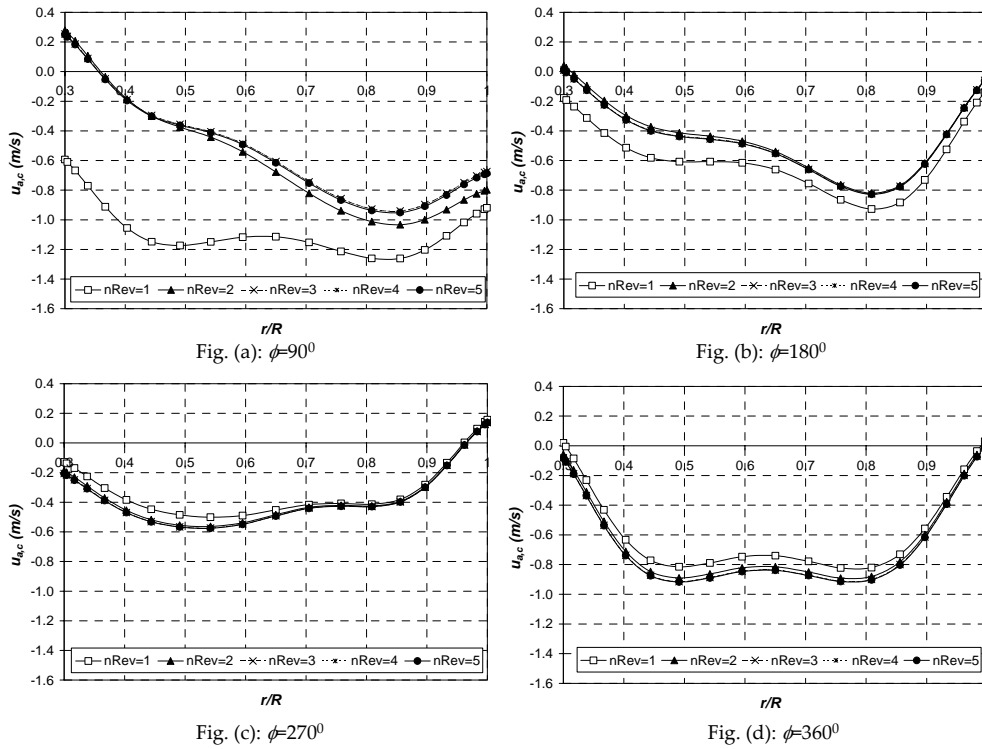


Figure 5.32 – Spanwise distributions of the axial induced velocities at the blades at $Y_w=3.5cm$ calculated by free-wake code at $\Psi=45^\circ$ for different values of $nRev$. The distributions are shown for different blade azimuth angles.

Effect of $\Delta\phi$

To investigate the influence of the time step size on the computed induced velocities at $\Psi=45^\circ$, the free-wake computations were performed at different values of $\Delta\phi$ while keeping all other parameters fixed. Four values of $\Delta\phi$ were chosen, equal to 7.5° , 10° , 15° and 30° . Parameters n , $nRev$, δ and S_c were set equal to 31, 3, 10 and 5 respectively. The results are shown in Fig. 5.35. The differences are small, similar to what was observed at $\Psi=0^\circ$ (see Fig. 5.19). To quantify these differences, the relative percentage error $\xi_{\Delta\phi}$ was found at different radial locations and blade azimuth angles using Eq. 5.17. This equation was applied taking (s,l) successively equal to $(7.5^\circ, 10^\circ)$, $(10^\circ, 15^\circ)$ and $(15^\circ, 30^\circ)$. The variations of $\xi_{\Delta\phi}$ with ϕ at various radial locations for the different values of (s,l) is shown in Fig. 5.36. It is evident that the numerical accuracy is improved as small values of $\Delta\phi$ are used, thus showing discretization convergence in the numerical free-wake model when using gradually smaller rotor time steps. However, when comparing the values for $\xi_{\Delta\phi}$ obtained for $\Psi=0^\circ$ (Fig. 5.20) and 45° (Fig. 5.36), it can be seen that the relative errors for $\Psi=45^\circ$ are in general higher than the corresponding values at $\Psi=0^\circ$.

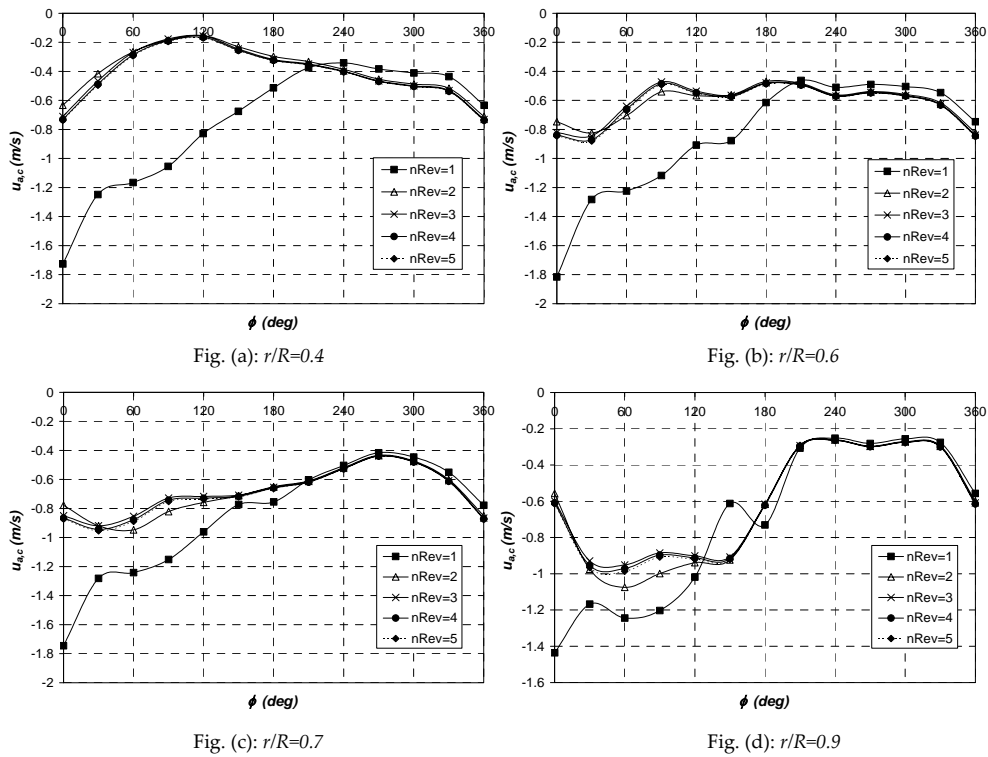


Figure 5.33 – Variations of the axial induced velocities at the blades at $Y_a=3.5\text{cm}$ as a function of blade azimuth angle as calculated by free-wake code at $\Psi=45^\circ$. The results are shown for different values of $nRev$.

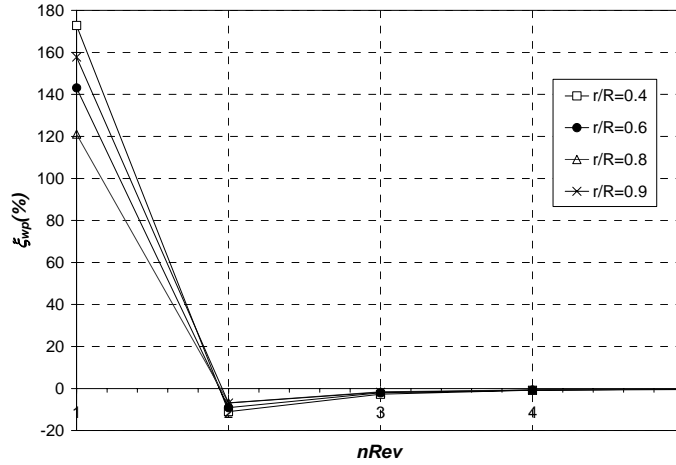


Figure 5.34 – Variation of the relative percentage error in wake periodicity with $nRev$ at $\Psi=45^\circ$.

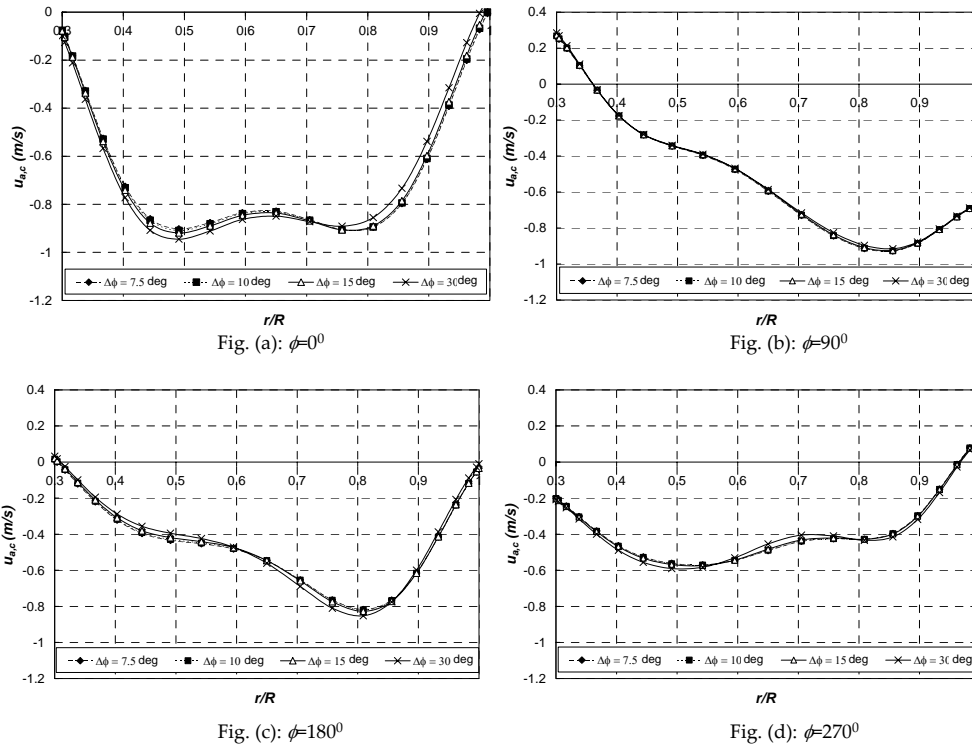


Figure 5.35 – Spanwise distributions of the axial induced velocities at the blades at $Y_a=3.5cm$ calculated by free-wake code at $\Psi=45^\circ$ for different values of $\Delta\phi$. The distributions are shown for different blade azimuth angles.

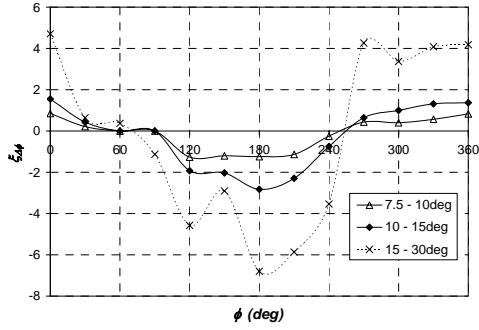


Fig. (a): $r/R=0.4$

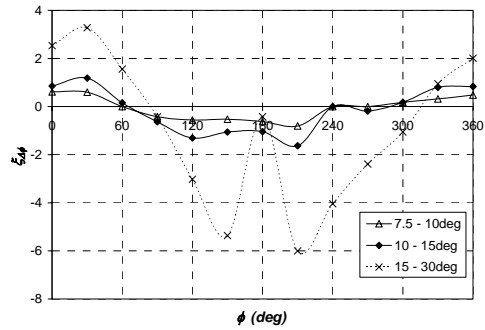


Fig. (b): $r/R=0.6$

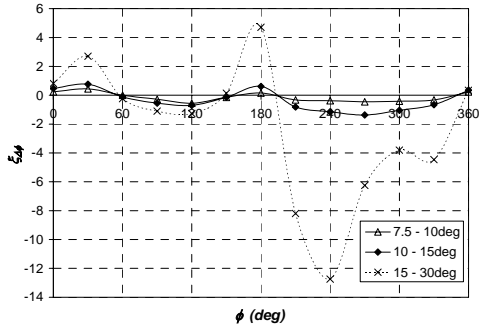


Fig. (c): $r/R=0.7$

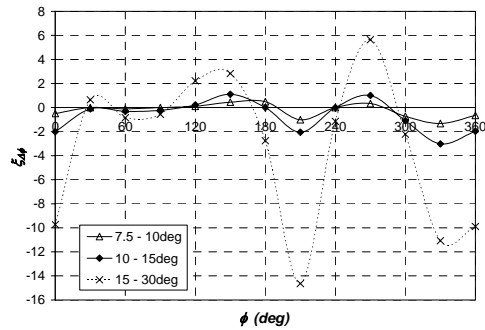


Fig. (d): $r/R=0.9$

Figure 5.36 – Variations of the percentage relative error resulting from different values of $\Delta\phi$ as a function of blade azimuth angle as calculated by free-wake code at $\Psi=45^\circ$.

Effect of n

The free-wake computations were then carried out at values of n (11, 21 and 31) while maintaining $nRev$ and $\Delta\phi$ constant at 3 and 10° , respectively. Viscous modelling parameters (δ_v, S_v) were kept at (10, 5). Fig. 5.37 shows the axial induced velocity distributions at the blades at $Y_i=3.5\text{cm}$ for the different values of n . The presence of discretization convergence when increasing n is clear. Eq. 5.18 was applied to determine the relative error ξ_n at the different blade azimuth angle and radial locations. The results are displayed in Fig. 5.38. The values for ξ_n were in general found to be of the same order as those obtained at $\Psi=0^\circ$.

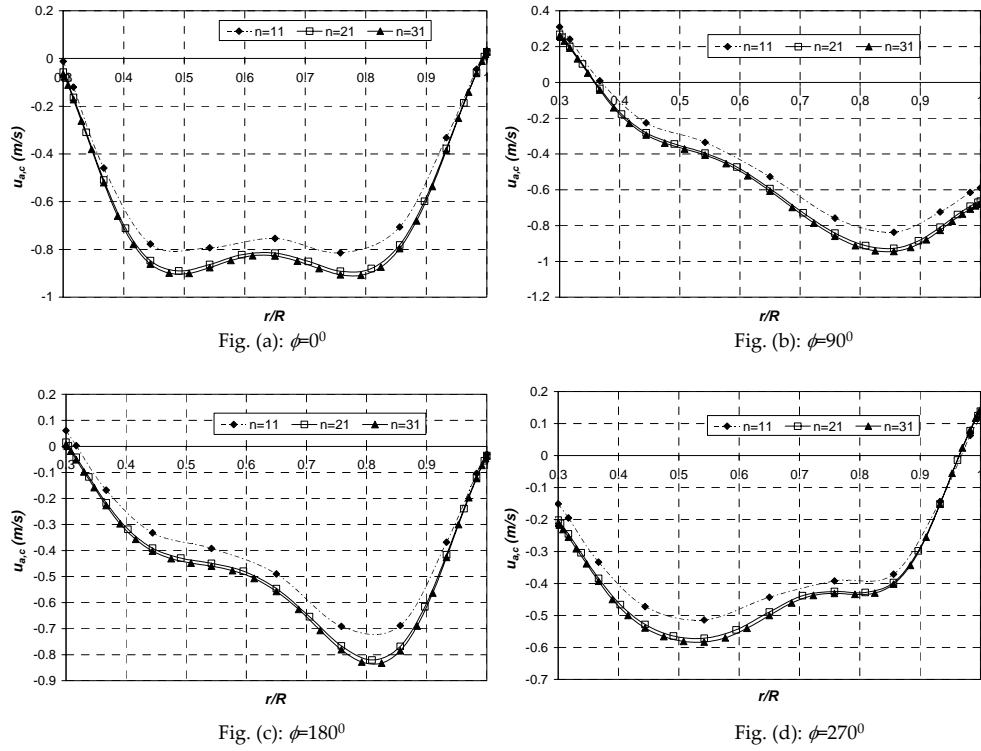


Figure 5.37 – Spanwise distributions of the axial induced velocities at the blades at $Y_w=3.5\text{cm}$ calculated by free-wake code at $\Psi=45^\circ$ for different values of n . The distributions are shown for different blade azimuth angles.

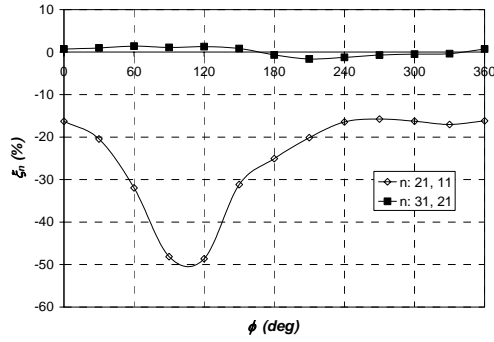


Fig. (a): $r/R=0.4$

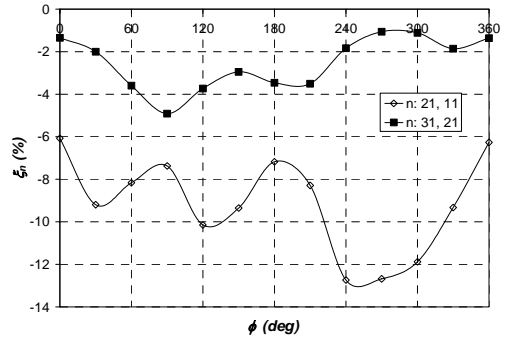


Fig. (b): $r/R=0.6$

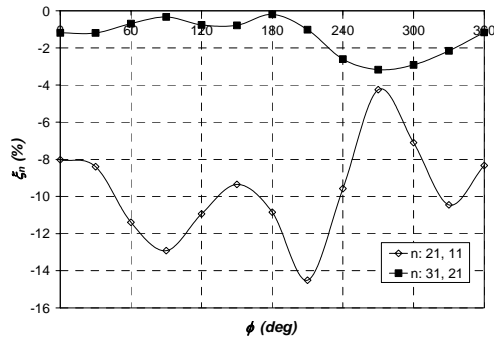


Fig. (c): $r/R=0.7$

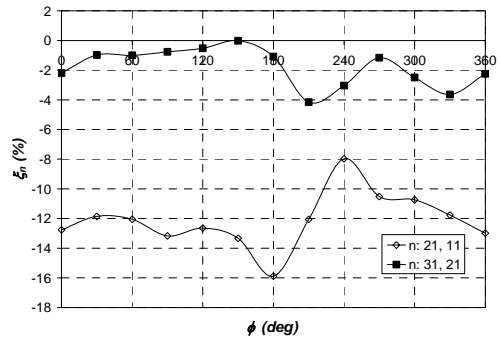


Fig. (d): $r/R=0.8$

Figure 5.38 – Variations of the percentage relative error resulting from different values of n as a function of blade azimuth angle as calculated by free-wake code at $\Psi=45^\circ$.

Validation

We now compare the axial induced velocity distributions at the blade lifting lines predicted by *HAWT_FWC* at $\Psi=30^\circ$ and 45° with those obtained from the hot-film measurements. A disadvantage of the approach for the validation lies in the basic fact that the bound circulation distributions used were derived from unsteady aerofoil theory and inflow measurements. As already discussed in Chapter 4, these derived circulation distributions (refer to Figs. 4.78 and 4.79) are subject to considerable uncertainties. Re-call that such uncertainties resulted from experimental errors in $w_{a,c}$ which were estimated to be approximately $\pm 0.26\text{m/s}$ for $\Psi=30^\circ$ and $\pm 0.21\text{m/s}$ for $\Psi=45^\circ$, see section 4.3.6, page 128). To avoid any ambiguity in the validation using the hot-film measurements in yawed conditions, the bound circulations distributions of Figs. 4.78 and 4.79 were prescribed with their uncertainty estimates, i.e. for each yaw angle (30° and 45°), three different bound circulation distributions were prescribed separately: (1) *central* Γ_B distribution, i.e. circulation that was computed assuming no uncertainty in the $w_{a,c}$ values derived at the rotorplane from the inflow measurements, (2) *upper* Γ_B distribution, i.e. assuming a 0.26m/s or 0.21m/s uncertainty (for $\Psi=30^\circ$ and $\Psi=45^\circ$, respectively) in the $w_{a,c}$ values and (3), *lower* Γ_B distribution i.e. assuming a -0.26m/s or -0.21m/s uncertainty (for $\Psi=30^\circ$ and $\Psi=45^\circ$, respectively) in the $w_{a,c}$ values. In each computation, *HAWT_FWC* parameters n , $\Delta\phi$ and $nRev$ were set equal to 21, 10° and 5 respectively. To be able to investigate the influence of the viscous parameters, these computations were also repeated for different values of (δ_v, S_c) , equal to (10, 0.1), (10, 5) and (100, 1). Throughout this validation, the values of $u_{a,c}$ at 3.5cm downstream (which is one of the measurement planes at which the hot-film measurements were taken) were used for the comparison rather than those exactly on the blade lifting lines.

Figs. 5.39 and 5.40 compare the *HAWT_FWC* results for $u_{a,c}$ at $Y_a=0.035\text{cm}$ with the corresponding experimental results for $\Psi=30^\circ$ and $\Psi=45^\circ$. In these plots, the spanwise variation of $u_{a,c}$ is plotted at four different blade azimuth angles ($0^\circ, 90^\circ, 180^\circ$ and 270°). The free-wake model results for different values of (δ_v, S_c) are shown. It is noted that, similar to what was observed in axial conditions, the free-wake model results for the middle blade sections are insensitive to viscous parameters (δ_v, S_c) . But considerable sensitivity is present at the blade root and tip regions. However, unlike for axial conditions, there is in general considerable disagreement between the free-wake model results and those from the experiments. Quantitatively, this disagreement is significantly larger than the differences obtained in the model predictions due to different values of (δ_v, S_c) .

Figs. 5.41 and 5.42 plot the variations of $u_{a,c}$ at $Y_a=0.035\text{cm}$ with the blade azimuth angle (ϕ) at different radial locations as predicted by the free-wake model for $\Psi=30^\circ$ and 45° . The results are shown for the three different bound circulation distributions (central, upper and lower distributions). Thus it is possible to analyse the uncertainty in induced velocities predicted by *HAWT_FWC* resulting from the uncertainty in the prescribed bound

circulations (which uncertainty is due to errors in the hot-film measurements). Figs. 5.41 and 5.42 include also the experimental distributions, together with their respective error bars. It is noted that the vortex model predictions and the experimental results agree very well at $\phi=0^\circ$. But for the other blade positions, the disagreement is not that good and the percentage discrepancy may sometimes be above 100%. The percentage discrepancy can be very high for the simple reason that the induced velocities are very small and close to zero. Yet it should be emphasized that this percentage discrepancy is very sensitive to the level of uncertainty estimated in the hot-film measurements. It should be kept in mind that the two uncertainties both arise due to the errors in the measurements. The upper uncertainty value for the inflow velocity $w_{a,c}$ (i.e. $w_{a,c} + 0.26$ or $+0.21$ m/s, for $\Psi=30^\circ$ and 45° respectively) resulted in a higher bound circulation distribution, which in turn predicted a higher (negative) distribution for $u_{a,c}$. Also, this upper uncertainty yielded the lower distribution for $u_{a,c}$ (as derived by Eq. 4.57). For this reason, in Figs. 5.41 and 5.42 we compare the vortex model

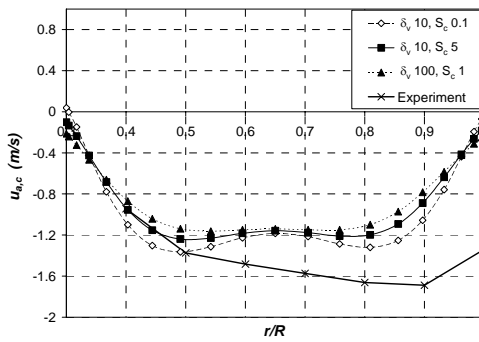


Fig. (a): $\phi=0^\circ$

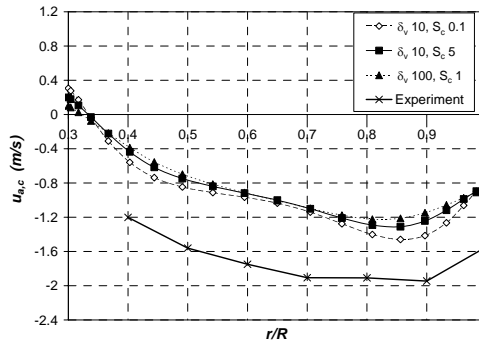


Fig. (b): $\phi=90^\circ$

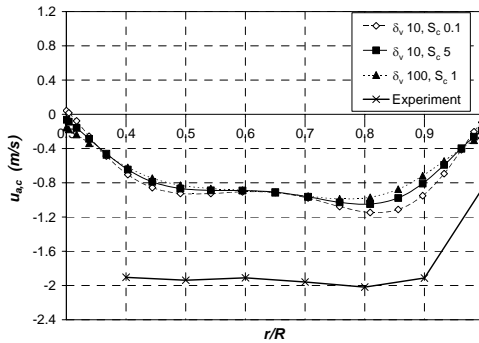


Fig. (c): $\phi=180^\circ$

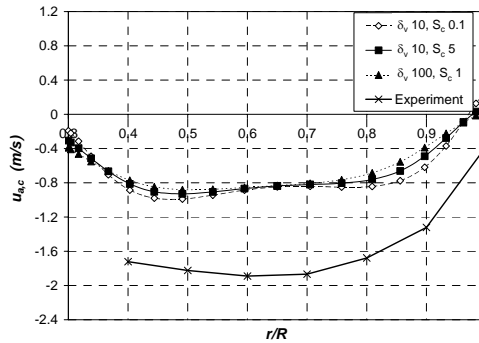


Fig. (d): $\phi=270^\circ$

Figure 5.39 – Comparison of the spanwise distributions of $u_{a,c}$ at $Y_a=3.5$ cm predicted by free-wake vortex model with experimental results for $\Psi=30^\circ$. Vortex model results are shown for different blade azimuth angles and different values for (δ_v, S_c) . The central Γ_B distribution is used for computations with $n=21$, $\Delta\phi=10^\circ$, $nRev=5$.

results “HAWT_FWC_Upper” with the upper extreme value of the experimental values, then the correlation of the vortex model results with the experimental values improves considerably. In some cases, the uncertainty limits of the HAWT_FWC prediction and those of the experimental results overlap one another. This is a positive factor that provides more confidence that, given the uncertainties in the hot-film measurements were smaller the agreement could have been better. This overlapping is mostly observed at $\Psi=45^\circ$ (Fig. 5.42) between blade azimuth angles 0° and 180° . However, between blade azimuth angles 180° and 360° , the agreement is still not good even when the uncertainties in the hot-film measurements are taken in account. This is because the amount of disagreement is considerably larger than the uncertainty levels. However there is considerable evidence to show that the large disagreement is due to the flow obstruction from the centre body structure of wind tunnel model resulting from rotor yaw. The photos of the smoke visualisation help support this evidence.

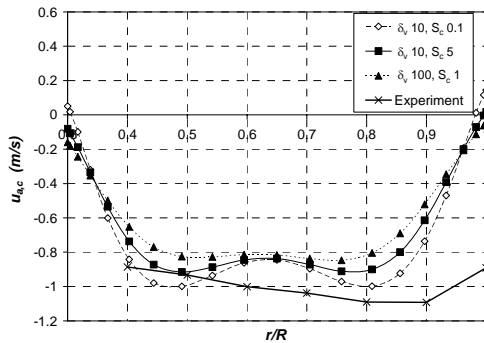


Fig. (a): $\phi=0^\circ$

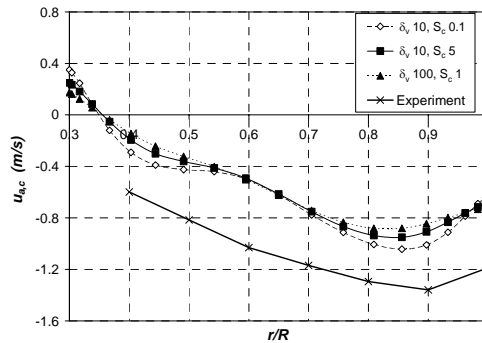


Fig. (b): $\phi=90^\circ$

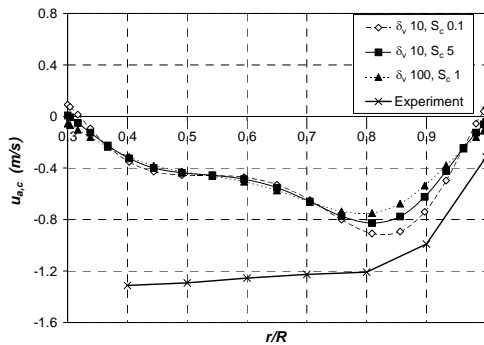


Fig. (c): $\phi=180^\circ$

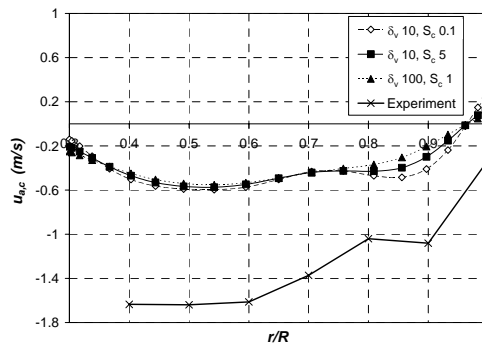


Fig. (d): $\phi=270^\circ$

Figure 5.40 – Comparison of the spanwise distributions of $u_{a,c}$ at $Y_a=3.5\text{cm}$ predicted by free-wake vortex model with experimental results for $\Psi=45^\circ$. Vortex model results are shown for different blade azimuth angles and different values for (δ_v, S_c) . The central Γ_B distribution is used for computations with $n=21$, $\Delta\phi=10^\circ$, $nRev=5$.

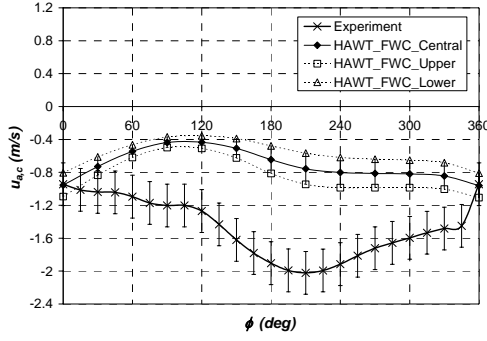


Fig. (a): $r/R=0.4$

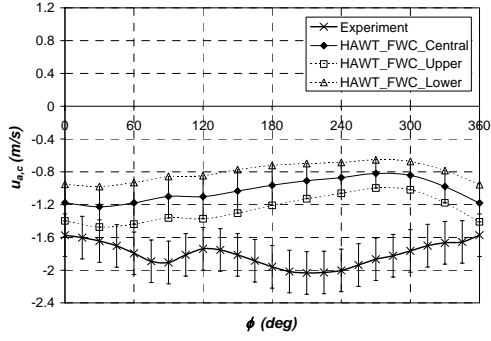


Fig. (d): $r/R=0.7$

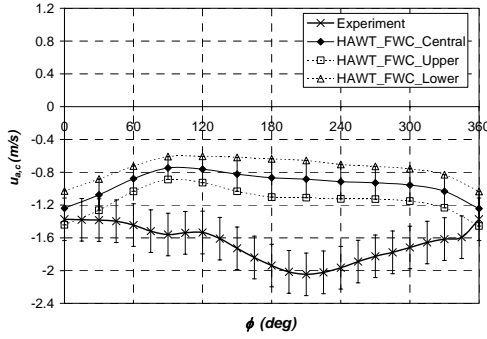


Fig. (b): $r/R=0.5$

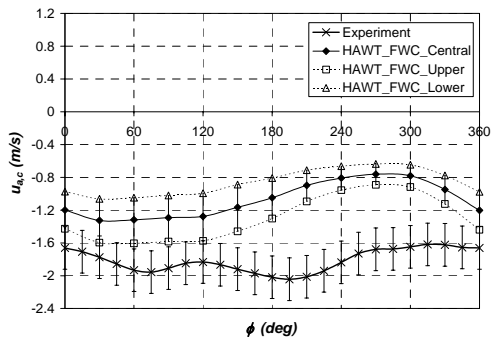


Fig. (e): $r/R=0.8$

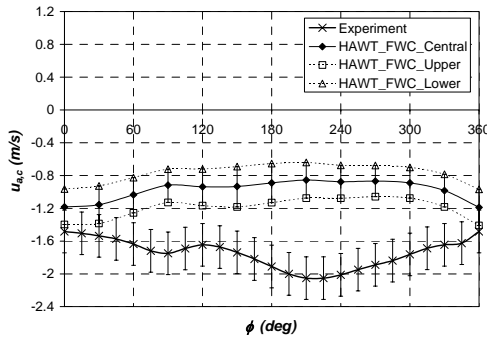


Fig. (c): $r/R=0.6$

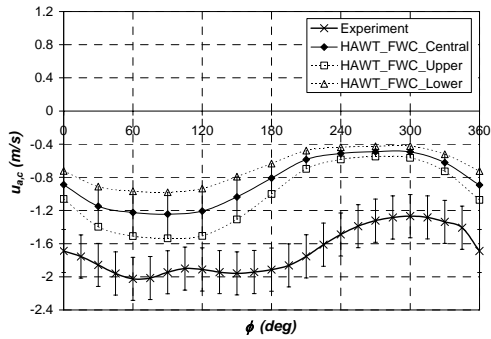


Fig. (f): $r/R=0.9$

Figure 5.41 – Comparison of the distributions of $u_{a,c}$ with ϕ at $Y_a=3.5\text{cm}$ predicted by free-wake vortex model with experimental results for $\Psi=30^\circ$. Vortex model results are shown as a function of blade azimuth angle and at different radial location. The central, upper and lower Γ_b distributions are used for computations with $n=21$, $\Delta\phi=10^\circ$, $n\text{Rev}=5$, $(\delta_r, S_c)=(10,5)$.

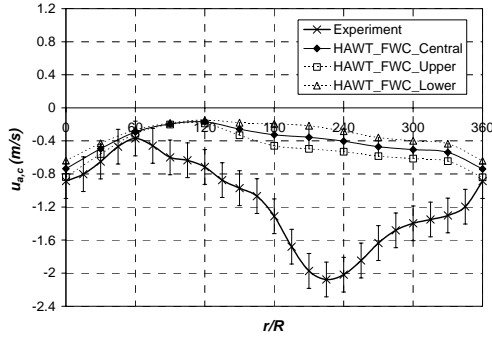


Fig. (a): $r/R=0.4$

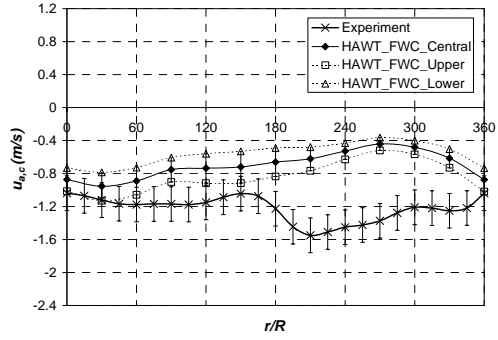


Fig. (d): $r/R=0.7$

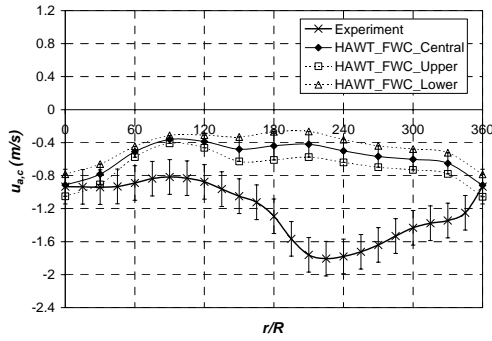


Fig. (b): $r/R=0.5$

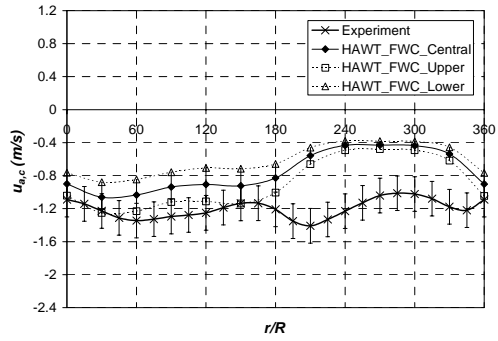


Fig. (e): $r/R=0.8$

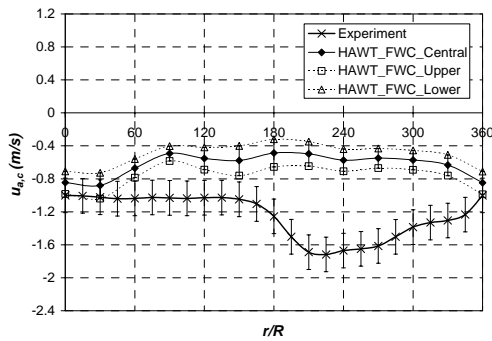


Fig. (c): $r/R=0.6$

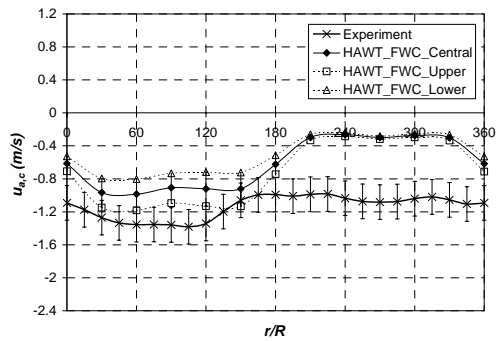


Fig. (f): $r/R=0.9$

Figure 5.42 – Comparison of the distributions of $u_{a,c}$ with ϕ at $Y_a=3.5\text{cm}$ predicted by free-wake vortex model with experimental results for $\Psi=45^\circ$. Vortex model results are shown as a function of blade azimuth angle and at different radial location. The central, upper and lower Γ_b distributions are used for computations with $n=21$, $\Delta\phi=10^\circ$, $n\text{Rev}=5$, $(\delta_r, S_c)=(10,5)$.

The photo in Fig. 5.43 shows that for a positive yaw angle of $\psi=45^\circ$, at blade positions $\phi=180^\circ$ and 360° , the tower structure lies within the tip vortex path. It is shown in this photo that the third tip vortex core, around which there is a considerably high vorticity content, is in fact colliding with the tower structure. This vortex core is still too close to the rotorplane (within an axial distance of about one R). A simple application of the Biot-Savart law on the vortex core suggests that this vortical location influences considerably the total induced at the rotorplane, and even more at $Y_a=3.5\text{cm}$, at which the comparison of the induced velocities is being made.

The obstruction from the model centrebody caused a reduction in the flow velocities on the upwind side of the rotor. Consequently the values for $w_{a,c}$ obtained from the hot-film experiments between $\phi=180^\circ$ and 360° (see Fig. 4.19 and 4.20, Chapter 4) are lower than what would have been measured if no such centrebody structure was not present. This resulted in lower experimental axial induced velocities ($u_{a,c}$) when applying Eq. 4.57. This is the reason why in Figs. 5.41 and 5.42 the experimental values are considerably lower than the *HAWT_FWC* predictions between $\phi=180^\circ$ and 360° and thus resulting in a large disagreement. The interference of the turbine centrebody was not modelled in the free-wake vortex model. Looking at Fig. 5.43 explains that for the upwind side, the inboard radial locations of the blade suffer the most from the flow obstruction since these are closer to turbine centrebody. This is in fact noted in Fig. 5.42 for $\psi=45^\circ$, where it is evident that the inboard radial locations ($r/R= 0.4, 0.5$ and 0.6 , Figs. (a), (b), (c)) have the largest disagreement between $\phi=180^\circ$ and 360° , larger than the disagreement obtained at the outboard blade regions (Figs. (d), (e), (f)). On the other hand, for blade azimuth angles between $\phi=0^\circ$ and 180° (i.e. on the downwind side of rotor plane), the tip vortices are not obstructed by the centrebody (as may be seen in Fig. 5.43). This explains why a much better correlation was achieved between the experimental and free-wake vortex model results.

The above arguments provide more confidence that the free-wake vortex model is reasonably accurate even in yawed conditions, despite the fact that considerable disagreements with the induced velocities from the experiments were found.

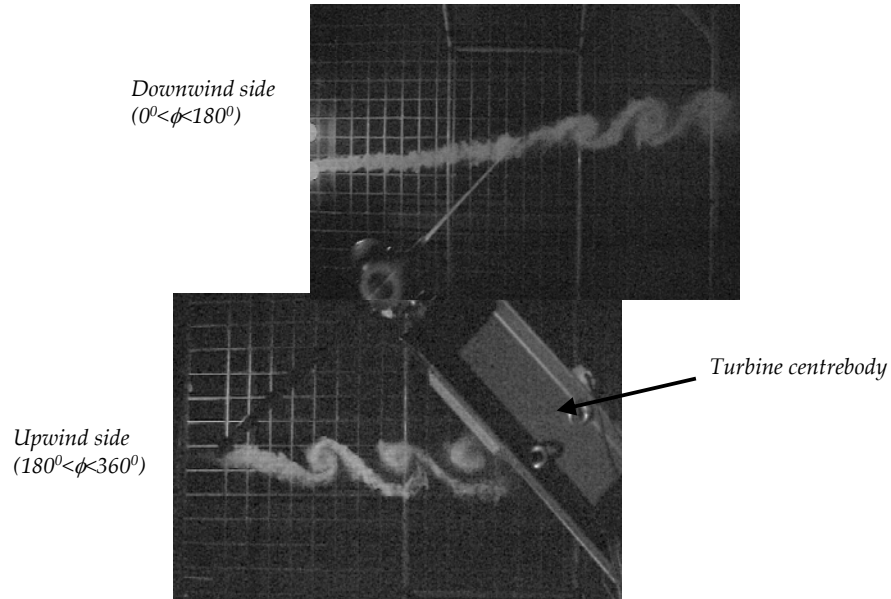


Figure 5.43 – Smoke visualization photos of the TUDelft turbine at $\Psi=45^\circ$. Note that on upwind side, the tip vortex core trajectory is obstructed by the centrebody of the turbine.

The tip vortical locations predicted by *HAWT_FWC* are now compared with the tip vortex core locations measured during the smoke visualisation experiments. The vortex plots at $\Psi=30^\circ$ and 45° are shown in Figs. 5.44 and 5.45, respectively. The white dots in these plots indicate the tip vortex core locations measured from the smoke visualization. The free-wake vortex plots are shown for the instant in which the first and second blades are located at $\phi=90^\circ$ and 180° , and thus at the same positions at which the smoke visualisation photos were taken. In these vortex model computations, parameters n , $\Delta\phi$ and $nRev$ were set equal to 21, 10° and 3.5 respectively and the central bound circulation distribution were used, without taking the corresponding uncertainties into account. To investigate the influence of the viscous parameters, these computations were also repeated for different values of (δ, S_c) , equal to (10, 0.1), (10, 5) and (100,1). As already explained before, for axial conditions parameters (δ, S_c) control the amount of roll-up in the modelled free-wake. The larger their values, the less is the roll-up and the deformation of the wake. It can be noted from Figs. 5.44 and 5.45 that the vortex sheet pitch is well predicted at all the three sets of values of (δ, S_c) . Yet it is seen that, at both $\Psi=30^\circ$ and 45° , (δ, S_c) values equal to (10,0.1) yield the best predicted wake expansion correlation with the experimental measurements. Re-call that the same was already noted earlier in axial conditions, *see* Fig. 5.30. Re-call also that from the validation for axial conditions (section 5.3.2, page 246) that parameter δ_0 was taken equal to

Fig. (a):
 $(\delta_v, S_c) = (10, 0.1)$

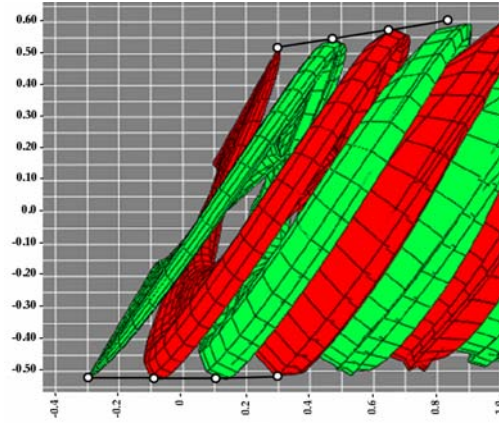


Fig. (b):
 $(\delta_v, S_c) = (10, 5)$

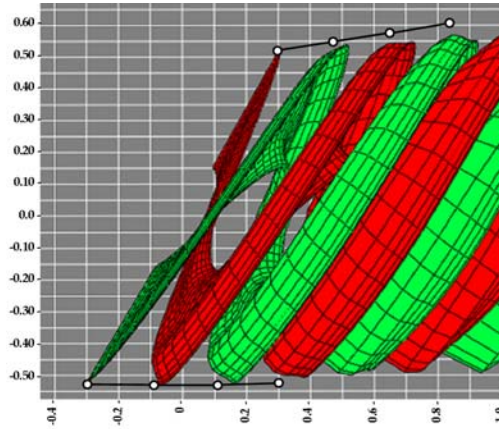


Fig. (c):
 $(\delta_v, S_c) = (100, 1)$

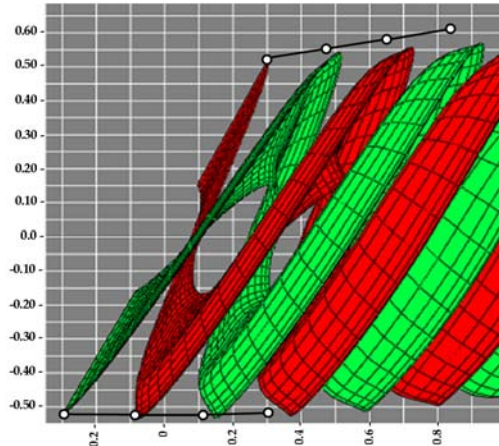


Figure 5.44 – Comparison of tip vortical wake positions computed by free-wake code at different (δ_v, S_c) with tip vortex locations measured using smoke visualizations (represented by white dots) at $\Psi=30^\circ$, $n=21$, $\Delta\phi=10^\circ$, $nRev=3.5$.

Fig. (a):
 $(\delta_v, S_c) = (10, 0.1)$

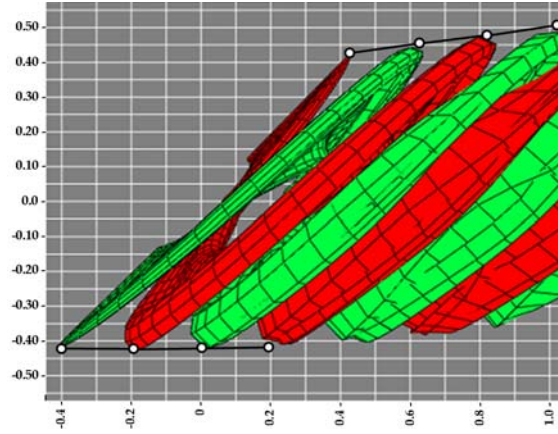


Fig. (b):
 $(\delta_v, S_c) = (10, 5)$

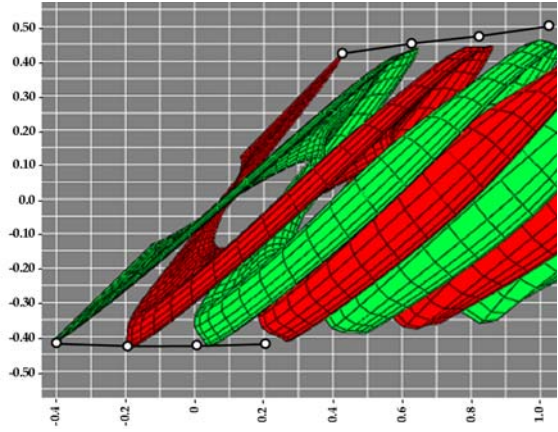


Fig. (c):
 $(\delta_v, S_c) = (100, 1)$

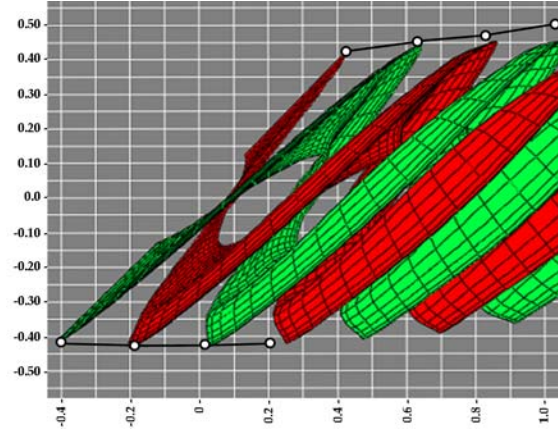


Figure 5.45 – Comparison of tip vortical wake positions computed by free-wake code at different (δ_v, S_c) with tip vortex locations measured using smoke visualizations (represented by white dots) at $\Psi=45^\circ$, $n=21$, $\Delta\phi=10^\circ$, $nRev=3.5$.

10 based on the results from references [2, 10]. S_c was taken equal to 0.1 in order to yield a vortex sheet viscous layer thickness at the blades' trailing edges approximately equal to the blade thickness.

The very good agreement achieved in the correlation of tip vortical locations with the smoke visualisation measurements adds to the confidence about the validity of the newly developed free-wake vortex model *HAWT_FWC*.

Wake circulation distribution

Figs. 5.46 and 5.47 show the free wake plots from the unsteady bound circulation at the blades (Figs. 4.78 and 4.79, uncertainty limits not taken into account) at $\psi=30^\circ$ and 45° . Colour coding is used to represent the trailing or shed circulation distribution in the wake. For each yaw angle, the wake plot is shown twice: Fig. (a) illustrates the trailing circulation while Fig. (b) illustrates the shed circulation in the near free wake. Two observations can be made here. First of all, the trailing circulation tends to be concentrated at the tip and root regions, with the circulation at the tip being positive while that at the root being negative. This is very similar to what was seen in axial conditions (*see* Fig. 5.31). Secondly, since yawed conditions are being dealt with and also because the bound circulation at the blades is unsteady, some shed circulation results in the wake. However, in general, the shed circulation levels are much smaller than the trailing circulation, as it may be seen in Figs. 5.46 and 5.47.

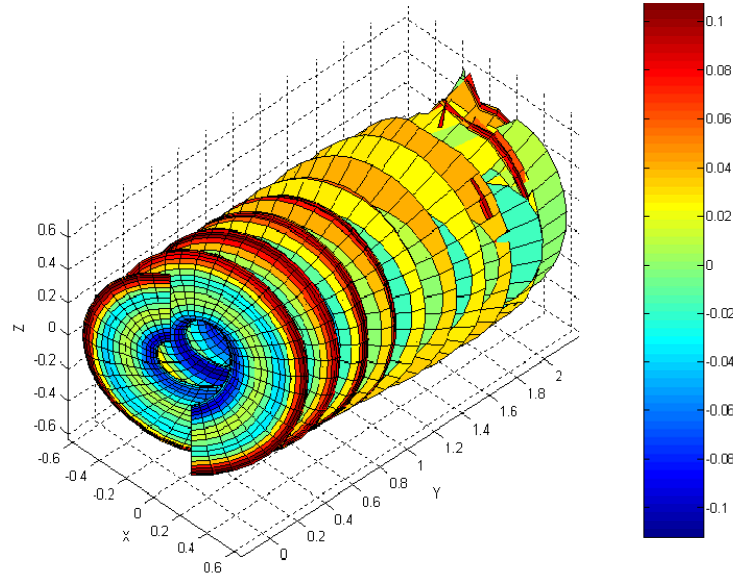


Fig. (a) -Trailing circulation

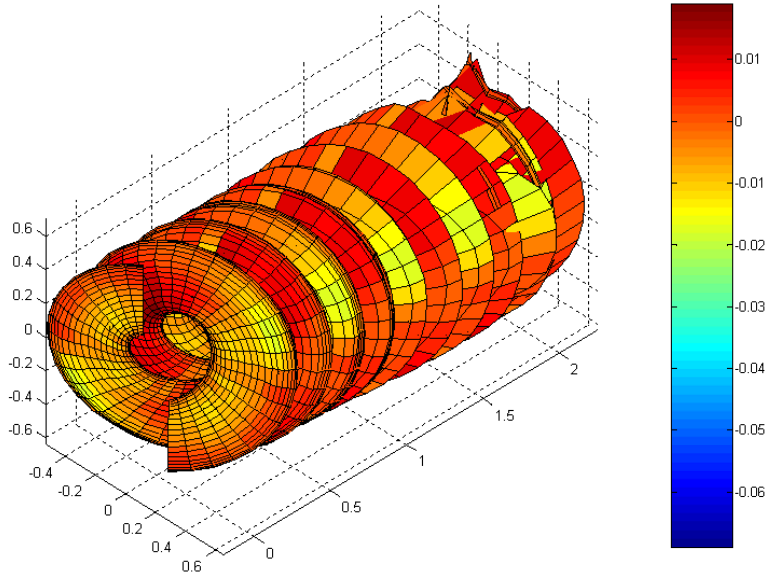


Fig. (b) - Shed circulation

Figure 5.46 – Free-wake plot with $(\delta, S_c) = (10, 5)$ and $n=21$, $\Delta\phi=10^\circ$, $nRev=5$ at $\Psi=30^\circ$. Colour coding represents the trailing or shed circulation in wake.

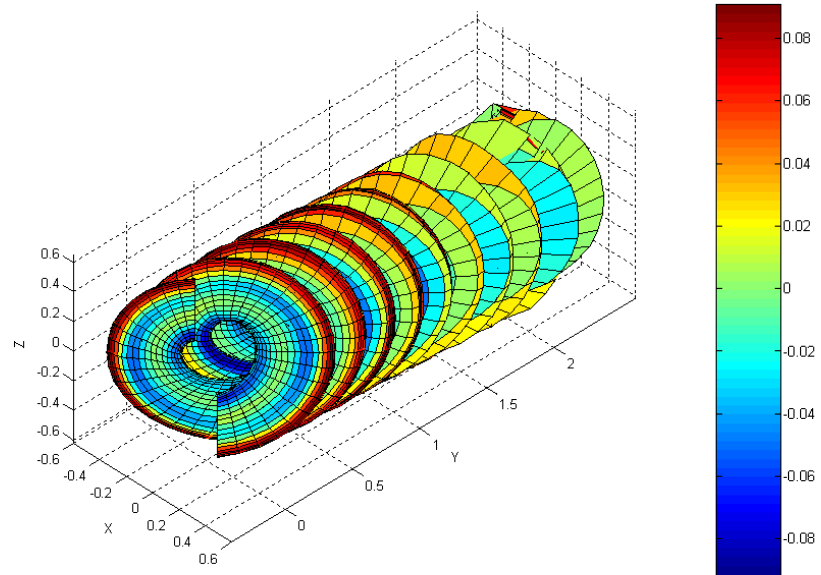


Fig. (a) -Trailing circulation

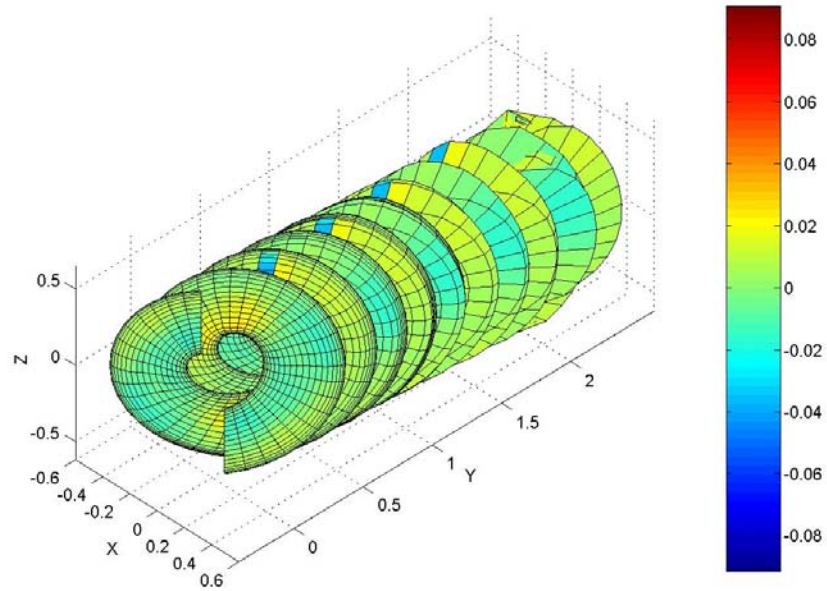


Fig. (b) - Shed circulation

Figure 5.47 – Free-wake plot with $(\delta, S_c) = (10, 5)$ and $n=21$, $\Delta\phi=10^\circ$, $nRev=5$ at $\Psi=45^\circ$. Colour coding represents the trailing or shed circulation in wake.

5.4 Conclusions

A free-wake vortex model developed in this project was verified and validated by modelling the TUDelft model turbine in axial and yawed conditions. In both the verification and validation, the bound circulation estimated from the hot-film inflow measurements and the unsteady aerofoil model (as described in section 4.3.1) was prescribed to the vortex model to generate a free-wake plot and calculate the induced velocities at the rotorplane or at 3.5cm downstream. In the verification, a parametric analysis was carried out to quantify the numerical errors and computational time of the vortex model at different levels of blade and wake discretization. In the validation, the results from the free-wake vortex model were compared with the experimental data obtained from the measurements taken in the open-jet wind tunnel. Two separate comparisons were carried out: (1) the induced velocities from the free-wake model were compared with those obtained from the inflow measurements; (2) the tip vortical locations from the free-wake model plots were compared with the tip vortex location obtained in the smoke visualization measurements. A disadvantage of the approach adopted for this validation was that the prescribed bound circulation distribution was derived from the inflow measurements. Thus, the free-wake vortex model predictions were not fully independent of the experimental data. For axial conditions, the derived bound circulation was reliable but for yawed cases considerable uncertainty was present due to errors in the inflow measurements. To avoid ambiguity, in the validation in yawed cases (at $\psi=30^\circ$ and 45°), the induced velocities from the free-wake model were computed taking into account the uncertainty limits of the prescribed bound circulations that resulted from errors in the inflow measurements.

The validation process examined how the choice of viscous modelling parameters influences the accuracy of the calculated induced velocities when comparing it with the experimental data. It was found that, for the middle blade sections, the calculated induced velocities at the blade lifting lines are quite insensitive to a wide range of values of the viscous parameters. However, high sensitivity to the viscous parameters was noted at the blade root/tip regions. This behaviour was observed in both axial and yawed conditions of the rotor.

When modelling axial conditions, very good correlation with the experimental induced velocities data was obtained at the middle sections of the blade. However, at the blade tip and root regions, this correlation was very much dependent on the arbitrary choice of viscous parameters. In the blade tip and root regions, the flow is highly 3D by nature and this is not usually catered for accurately by lifting-line blade models. Luckily, this source of inaccuracy is not very problematic when modelling blades with a high aspect ratio.

In yaw, the correlation of the induced velocities predicted by the free-wake model with the corresponding experimental values was not as good as in axial conditions. The correlation was reasonably good for blade azimuth positions $0 < \phi < 180^\circ$ (downwind side of rotor disc).

But for $180^\circ < \phi < 360^\circ$ (upwind side of rotor disc), the free-wake predictions were considerably different than those from the experiments at both $\psi = 30^\circ$ and 45° . The experimental induced velocities were higher than the free-wake values and it is very probable that this resulted from the blockage from the centrebody structure of the model turbine. The smoke visualization photos revealed that the centrebody obstructed the flow for $180^\circ < \phi < 360^\circ$ (upwind side of rotor disc) when the rotor was yawed. This flow interference was not included in the free-wake vortex modelling.

Finally, the vortical locations of the free wake geometries predicted at different values of viscous modelling parameters were compared with the tip vortex locations measured using smoke visualization experiments. In general, the agreement was very good, although it was better for those calculated using low values of the viscous parameters that correspond to smaller filament core radii.

6. Aerodynamic Analysis of the NREL Phase VI Wind Turbine

6.1 Introduction

This chapter describes in detail the aerodynamic analysis carried out on the NREL Phase VI rotor. The experimental data collected in the NASA Ames wind tunnel during the UAE experiments was used for the analysis. This data mainly consisted of blade pressure measurements from which the normal and tangential coefficients (C_n and C_t) could be found, together with the local flow angle measurements (*LFA*) (see Figs. 2.1 and 2.2, Chapter 2). Torque and blade bending moment measurements, taken using strain-gauge techniques, were also used for the analysis.

In this chapter, a novel approach is described for coupling the blade pressure measurements and a free-wake vortex model to derive the angle of attack distributions at the blades together with the inflow distribution at rotorplane. The developed free-wake vortex model *HAWT_FWC* (see Chapter 5) was used for this analysis. Both axial (i.e. steady) and yawed (i.e. unsteady) conditions were investigated.

The angle of attack distributions and inflow distributions at the rotorplane derived from the blade pressure measurements using *HAWT_FWC* were used to obtain new aerofoil data for BEM-based codes. For yawed conditions, new inflow corrections were also derived, apart from the aerofoil data. The new aerofoil data and inflow corrections (for yawed conditions) were then used in BEM code *HAWT_BEM* to re-compute the aerodynamic loads on the NREL rotor. The results from the BEM code were compared with those measured in the tunnel. In this way, it was possible to assess the reliability of the BEM theory when more accurate aerofoil data and inflow correction models are available. The derived aerofoil data and inflow corrections could be very useful to develop improved engineering models for BEM-based design codes as will be explained later on in Chapter 7.

The new aerofoil data is more accurate than that from 2D static wind tunnel experiments since the former was directly derived from the rotor experimental measurements. It accounts for both rotational augmentation (stall-delay) and unsteady effects (e.g. dynamic stall) at high angles of attack. Thus the new aerofoil data can be regarded as 3D aerofoil data. Yet the reliability of this new data depends on the accuracy with which the free-wake vortex model calculates the angle of attack from the known blade pressure measurements. Although the free-wake vortex model was already verified and validated earlier using the

TU Delft rotor (see Chapter 5), it was felt that additional tests were required to evaluate the method being proposed to find the angle of attack. The following tests were carried out:

1. For each operating condition on the NREL rotor in both axial and yawed conditions, the free-wake model computed the local inflow angles (*LFA*) at the positions where inflow probes were installed. The *LFA*'s predicted by the free-wake model were compared with those measured by the inflow probes.
2. For axial conditions only, the new 3D aerofoil data derived by *HAWT_FWC* was compared with that derived from CFD at Riso by Johansen *et al.* [40].
3. For one operating condition in yaw, the inflow distribution by *HAWT_FWC* was compared with that predicted by *AWSM*, a free-wake vortex model developed at ECN [26].

This chapter is being organized in three parts:

- A. Section 6.2 describes briefly the NREL Phase VI experiments in the NASA Ames tunnel and the experimental data selected for this study.
- B. Section 6.3 describes in detail the approach used for finding the angle of attack from the blade pressure measurements using the free-wake vortex model *HAWT_FWC*. The results for the angle of attack, aerofoil data and inflow distributions are presented and discussed.
- C. Section 6.4 presents the calculations performed on the BEM model *HAWT_BEM* with the new aerofoil data and inflow corrections. The results are compared with those performed with standard 2D static aerofoil data.

6.2 NASA/Ames UAE Wind Tunnel Data Used

The NREL Phase VI rotor is a two-bladed 10.1 m diameter wind turbine rotor with a rated power of 19.8kW (Fig. 6.1). The blade geometry is based on the S809 aerofoil. Fig. 6.2 gives the chord and twist distributions of the blade. Further details regarding the blade design may be found in [29]. One of the blades was equipped with pressure taps at $0.30R$, $0.47R$, $0.63R$, $0.80R$ and $0.95R$ to acquire detailed surface pressure data (Fig. 6.3). At each of the full pressure tap distributions, pressures were integrated to obtain C_n , C_t and C_m . The blade was also equipped with five-hole pressure probes at $0.34R$, $0.51R$, $0.67R$, $0.84R$ and $0.91R$ to measure the local inflow angle (*LFA*) (see Fig. 6.3 and 6.4). Various loads were measured using strain-gauge techniques. These included the blade root flap and edge moments and the low-speed shaft torque.



Figure 6.1 – The NREL Phase VI wind turbine in the NASA Ames wind tunnel (Source: [35]).

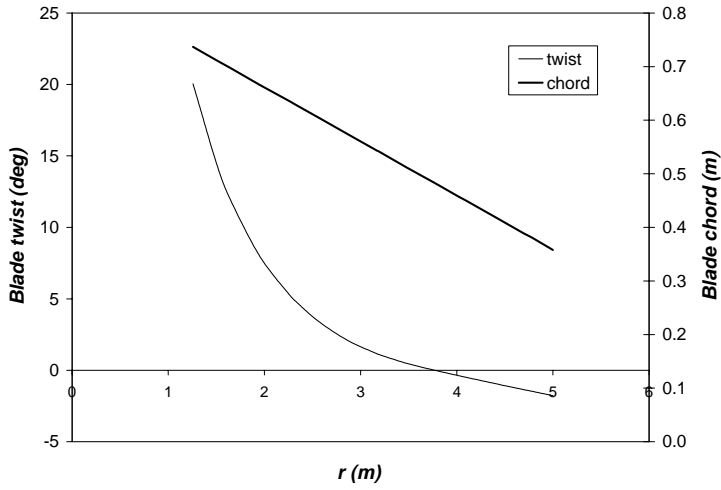


Figure 6.2 – Blade twist and chord distributions (Source: [35]).

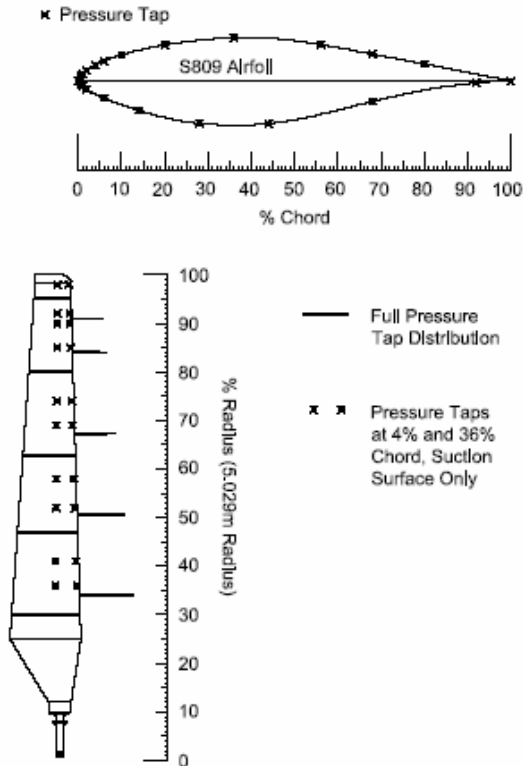


Figure 6.3 – Location of blade surface pressure tapplings and five-hole probes (Source: [35]).

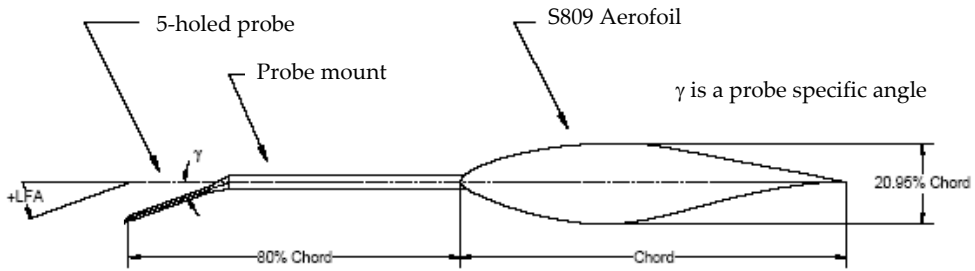


Figure 6.4 - Installation of five-hole pressure probe (Source: [35]).

In the UAE Phase VI experiments, the turbine was tested over a very wide range of operating conditions. Details of these experimental campaigns may be found in references [35, 73]. This study considered both axial and yawed conditions with the rotor operated in the upwind configuration for the cases shown in table 6.1. The blade pitch angle was set to 3° and the rotor coning angle was 0° . Yaw angles above 30° were not included in this study since their measurements were expected to be considerably affected by the flow disturbances from the box/boom installed upstream of the rotor. This study only considered the experimental data collected with the 'S' and 'H' configurations (refer to reference [35]).

Table 6.1 – Operational conditions considered in this study.

Data File	Yaw Angle	Air Density (kg/m^3)	Windspeed (m/s)	Rotational Speed (rpm)	Tip Speed Ratio	Measured Rotor Thrust Coefficient	Measured Rotor Power Coefficient
S0500000	0°	1.244	5.0	71.7	7.58	0.563	0.361
S0700000	0°	1.246	7.0	71.9	5.43	0.481	0.362
S1000000	0°	1.246	10.0	72.1	3.81	0.344	0.207
S1300000	0°	1.227	13.1	72.1	2.91	0.245	0.092
S1500000	0°	1.224	15.1	72.1	2.53	0.208	0.054
S2000000	0°	1.221	20.1	72.0	1.90	0.153	0.021
S2500000	0°	1.220	25.1	72.1	1.52	0.126	0.015
S0500300	30°	1.244	5.0	71.7	7.58	0.43	0.23
S0700300	30°	1.246	7.0	71.8	5.43	0.4	0.26
S1000300	30°	1.246	10.1	72.0	3.81	0.29	0.17
S1300300	30°	1.227	13.0	72.2	2.91	0.23	0.11
S1500300	30°	1.225	15.1	72.2	2.53	0.19	0.07

In the table above, the values shown for the thrust and power coefficients are the averaged values of those measured over one whole rotor revolution.

For each operating condition, data records of the surface pressures were taken for 36 individual rotor rotations (cycles). Fig. 6.5 shows typical variations for C_n obtained at each individual cycle at $0.3R$ at yaw 30° and a wind speed of 15m/s . In this figure, data from five different cycles are shown. It may be observed that for blade azimuth angles between approximately 120° and 240° , the cycle-to-cycle variation is very small. As it will be noted later on, at this region of blade azimuth angle, the angle of attack is small and the flow is attached. For the other blade azimuth angles, the cycle-to-cycle variation is large and this is due to the high angles of attack where flow separation influences reduce the repeatability of the measured data. In all cases, the mean (indicated by the solid black line in Fig. 6.5) is considered for the analysis using the free-wake code.

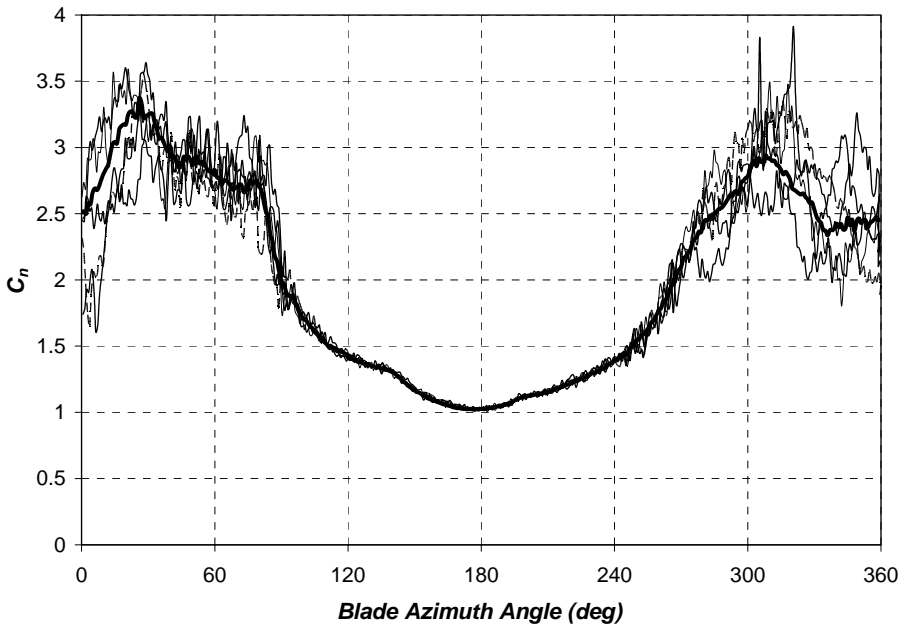


Figure 6.5 – Variation of the normal coefficient (derived from blade surface pressure measurements) with blade azimuth angle for yaw 30° , $U = 15\text{m/s}$ and $r/R = 0.3$. The values for five separate cycles are shown and the cycle mean is indicated by the bold curve.

6.3 Estimating the Angle of Attack from Blade Pressure Measurements using the Free-wake Vortex Model

6.3.1 Methodology

The computational procedure used to derive the unsteady angle of attack using the NREL experimental data and the free-wake model is now described. The method was applied to both axial and yawed conditions. In the latter conditions, the situation is unsteady and the derived angle of attack is a function of the blade azimuth angle (ϕ). The experimental data was only available for one blade. The same data was applied for the other blade, obviously taking into account the respective blade azimuth angles. The procedure is illustrated in Fig. 6.6. It consisted of the following steps:

Step 1: The measured values of Q_{NORM} , C_n and C_l at the different radial locations and blade azimuthal angles were first loaded into the code from the NREL experimental database ('S' configuration [35]).

Step 2: An angle of attack distribution was then assumed and the equation shown in Fig. 2.1 (refer to Chapter 2) was used to obtain an estimate for C_l at the different radial locations and blade azimuthal angles.

Step 3: The relative flow velocity at the blades, V_r , was found from Q_{NORM} using the equation for dynamic pressure given by

$$Q_{NORM} = \frac{1}{2} \rho V_r^2 \quad (6.1)$$

Step 4: The Kutta-Joukowski theorem for a lifting line was used to find the bound circulations at the pressure measurement stations:

$$\Gamma_B = \frac{1}{2} C_l V_r c \quad (6.2)$$

Step 5: A double interpolation was made to obtain a bound circulation at the blades as a function of radial position and blade azimuth position ($\Gamma_B[r/R, \phi]$), with the bound circulation at the blade tip and root set to zero. For interpolating, a spline interpolation was initially used to obtain Γ_B as a function of r/R . But it was found that the number of pressure measuring stations along the blade (equal to 5) was not enough to give an accurate representation of the bound circulation distribution along the blade with a spline method. This caused the spline method to yield unrealistic 'jumps'. Alternatively, a linear interpolating method had to be adopted. A spline interpolation was used only to interpolate for different blade azimuth positions.

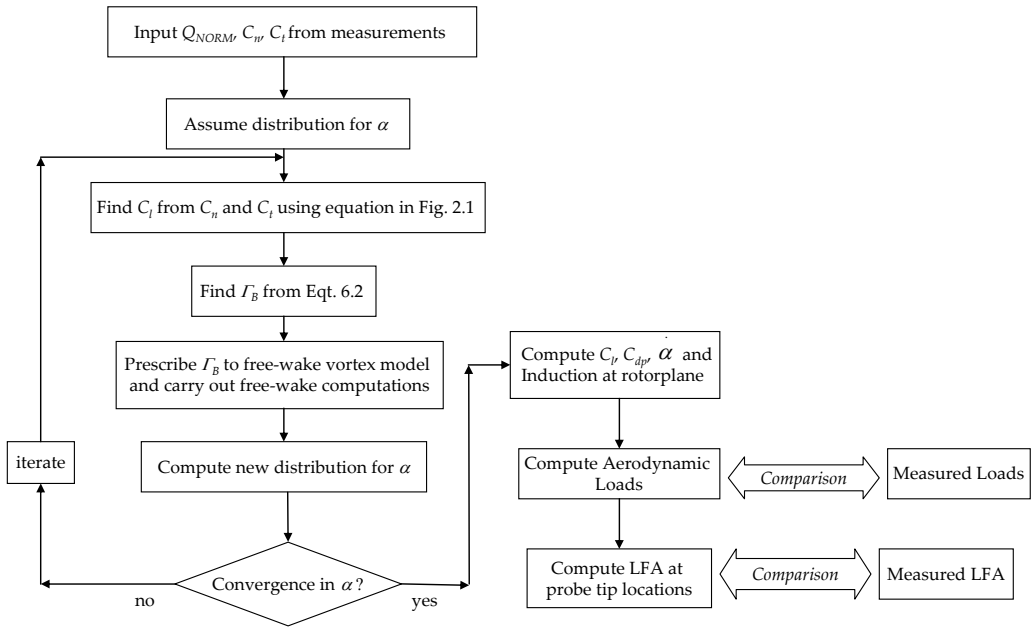


Figure 6.6 – Computational procedure used to derive the angle of attack from C_n and C_t using free-wake vortex model.

Step 6: the interpolated bound circulation distribution $(\Gamma_B[r/R, \phi])$ was then prescribed to the free-wake code and the modelled rotor was set to rotate to generate the free-wake extending downstream for a given number of rotations. This was used to calculate the unsteady 3D induced velocities at the lifting line of each rotor blade from which a new angle of attack estimate was obtained using the equation derived from Fig. 2.1 (Chapter 2):

$$\alpha = \tan^{-1} \left(\frac{V_n}{V_t} \right) \quad (6.3)$$

Step 7: the new angle of attack was used in Eq. 6.2 to yield a new bound circulation distribution and the whole process was repeated until convergence in the angle of attack was obtained at all radial locations and rotor azimuth angles.

Once a converged solution was obtained, the final distributions of the unsteady values of C_t and C_{dp} were derived in accordance with the equations of Fig. 2.1. From knowledge of the angle of attack variations with rotor azimuth angle, it was possible to derive the time-rate of change of angle of attack, together with the hysteresis loops for $C_t-\alpha$ and $C_{dp}-\alpha$. The computed free-wake geometries were used to calculate the unsteady induction distributions at the rotorplane. The latter were then used together with the derived lift and drag

coefficients to evaluate the rotor/blade loads as a function of rotor azimuth angle. These loads were compared with those measured during the wind tunnel experiments. Finally, using the free-wake vortex model, it was possible to compute the local inflow angles (*LFA*) at the measuring tip of the flow direction probes. These were also compared with the corresponding experimental values ('H' configuration [35]). The *LFA* was computed using the same equation for the angle of attack (Eq. 6.3) but with flow components V_n and V_t calculated at a point on the chordline $0.8c$ in front of the leading edge (refer to Figs. 2.1, 2.2 and 6.4)

The above procedure was repeated for each of the operating conditions listed in table 6.1 (page 281). In these calculations the flow disturbances due to the tower and nacelle were ignored. Structural dynamic influences were also neglected.

6.3.2 Axial Conditions

This section describes the computational work carried out for axial conditions ($\Psi=0^\circ$) for windspeeds $U=5, 7, 10, 13, 15, 20$ and 25m/s .

A. Selecting Free-Wake Model Parameters

Selection of HAWT_FWC parameters n , $\Delta\phi$ and $nRev$

In all the free-wake computations at $\Psi=0^\circ$, n and $\Delta\phi$ were chosen to be equal to 21 and 10° , respectively. These values were found to be sufficient to minimize the errors due to the numerical solution [68]. As explained in Chapter 5 (section 5.3.2, page 236), in selecting the required value of $nRev$, two conditions need to be satisfied: *Condition 1* is that the induced velocity at the rotorplane is independent of $nRev$; *Condition 2* is that the induced velocity at the rotoplane due to the far wake is negligible compared with that due to the near wake. To satisfy *Condition 1*, wake periodicity should be achieved such that the induced velocity at the blade lifting line of the first blade at an azimuth angle of 360° should be equal to that at an azimuth angle of 0° . The relative error for wake periodicity (ξ_{wp}) computed given by Eq. 5.15 should ideally be equal to zero.

$nRev$ was set equal to 3 for windspeeds equal to 13m/s and higher. For lower windspeeds ($5, 7$ and 10m/s), the pitch of the wake vortex sheets is smaller due to a higher tip speed ratio. Consequently $nRev$ had to be increased to be able to generate a near wake that extended enough downstream. For $U=5\text{m/s}$, $nRev$ was set equal to 5 while for $U=7$ and 10m/s , $nRev$ was set to 4. With these values for $nRev$, the near wake extended downstream by $3.6R, 4R, 6R, 6R, 7R, 9.4R, 12R$ at windspeeds $5, 7, 10, 13, 15, 20$ and 25m/s respectively. At these distances, the values for ξ_w at all radial locations were $<1.5\%$. Also, the contribution

of the far wake to the axial induction at the lifting lines was found to be only <3% of the total axial induction. Thus it may be assumed that the total induction is due to the near wake alone.

Selection of HAWT_FWC parameters δ_v and S_c

It should be appreciated that, considering the limitations of vortex models to cater for viscous effects, it is very difficult to select the optimum values for (δ_v, S_c) . Due to this difficulty, an analysis was therefore carried out in this study to investigate the sensitivity of $u_{a,c}$ to different values of (δ_v, S_c) . The analysis was performed at a windspeed of 13m/s. Four different sets of values of (δ_v, S_c) were used: $(10,0.1)$, $(100,1)$, $(500,1)$ and $(500,10)$.

Figs. 6.7(a) and (b) display the axial induced velocities at the blade lifting line and the corresponding azimuthally averaged values computed using the four sets of values for (δ_v, S_c) . For the case shown, n was kept fixed at 21. At the middle blade sections, extending for most of the blades (from $0.4R$ to $0.85R$), the calculated induced velocity was found to be almost insensitive to changes in (δ_v, S_c) . High sensitivity was noted though in the blade root and tip regions, the reason being the high trailing circulation in the near wake that results from rapid radial changes in bound circulation. Since it is very difficult to establish realistic values of (δ_v, S_c) , the insensitivity of the free-wake solution for the induced velocities for most of the blade span is a very positive factor.

As outlined in Chapter 5, page 246, increasing both the value of δ_v and S_c will increase the core radius of the modelled trailing and shed vortices of the near wake. S_c determines the initial core size at the point a vortex is shed from a blade's trailing edge. δ_v controls not only the initial core size but more over the rate of core growth with time. Fig. 6.8 shows a typical variation of the viscous core radius with the vortex age index a on the NREL rotor. In fact this figure is similar to Fig. 5.27. Recall that the higher the value of a , the lower is the vortex age. As it may be observed, the older wake vortices have a larger core radius, as modelled by the free-wake solution. The oldest vortices suffer large changes in their core radius. This is because they lie on the edge of the vortex sheet of the near wake where large vortex filament strain is predicted. This abrupt variation is not physical and is only due to the way the wake is modelled.

Both δ_v and S_c control the amount of deformation of the free-wake geometry, especially at the inboard and outboard edges of the vortex sheets where roll-up is known to occur. The higher their values, the less is the deformation. Figs. 6.9(a) and (b) illustrate two wake plots of the near wake computed using the free wake code for two different sets of values for (δ_v, S_c) . The reduced wake roll-up with larger values of these two arbitrary parameters is evident.

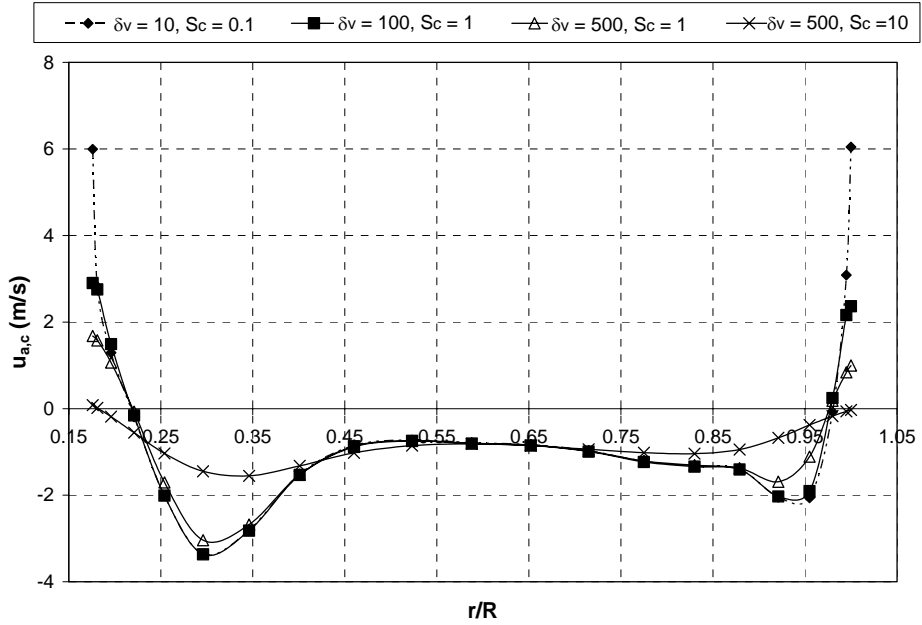


Figure 6.7(a) – Variation of induced axial velocity at blade lifting line for $n = 21$ at different values of (δ_v, S_c) .

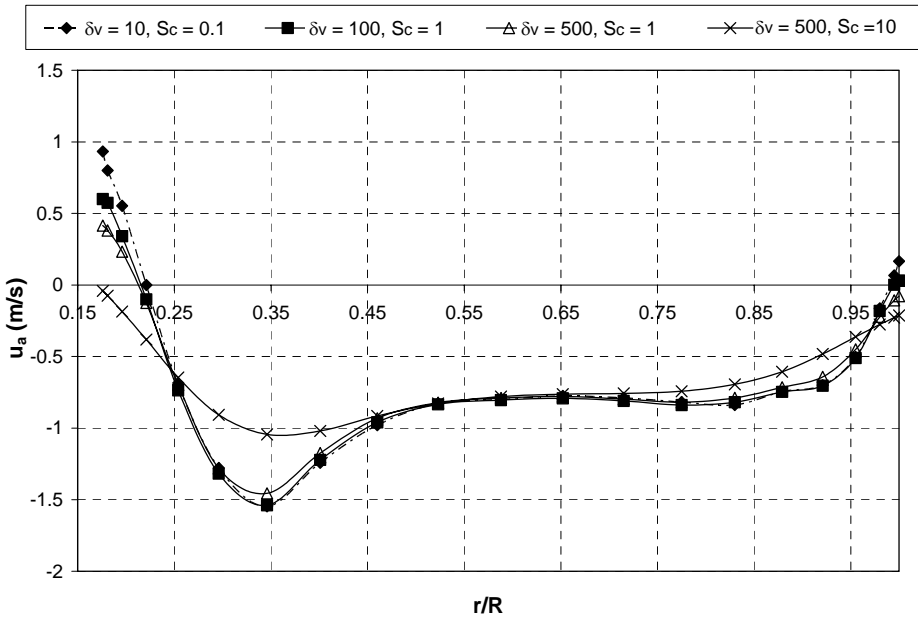


Figure 6.7(b) – Variation of the azimuthally averaged axial induced velocity at blade lifting line for $n = 21$ at different values of (δ_v, S_c) .

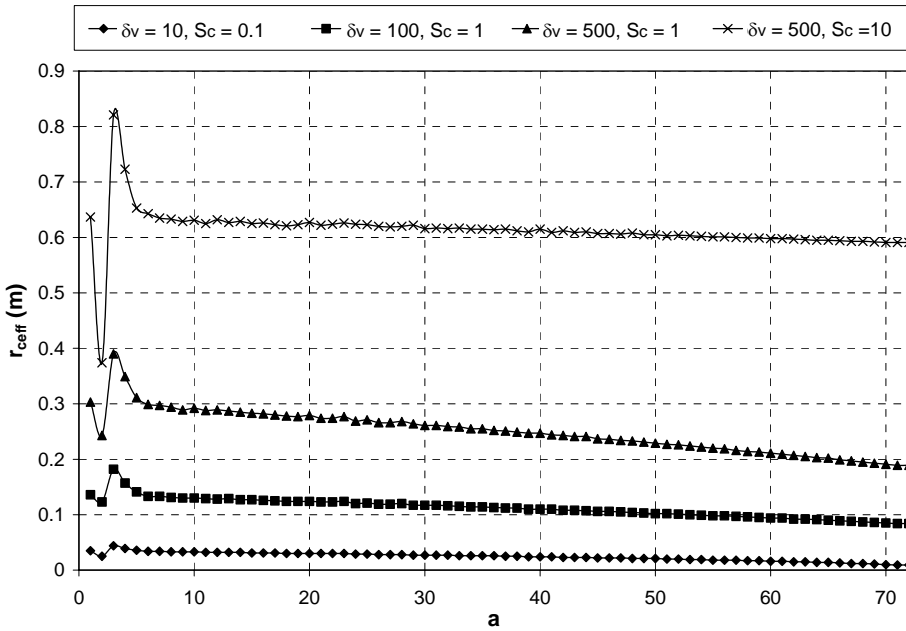


Figure 6.8 – Variation of viscous core radius of near wake trailing vortex filaments at $r/R=0.712$.

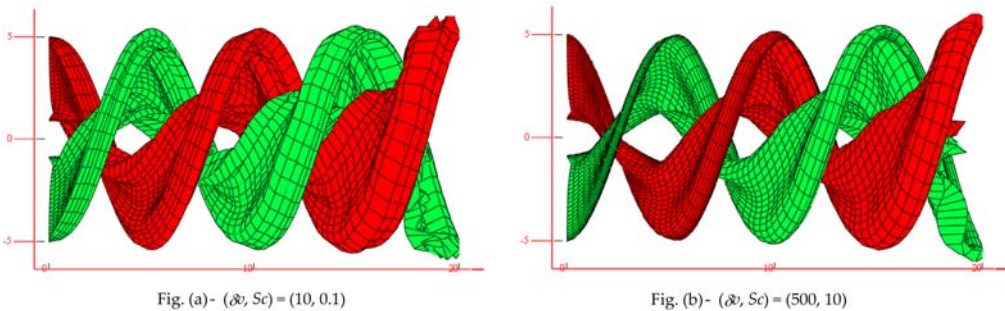


Figure 6.9 – Wake plots computed with $n=31$ for different values of (δ_v, S_c) .

Due to the wake deformation, the vortex filaments experience strain. This strain is mostly significant in the tip and root regions of the vortex sheets. Fig. 6.10 plots the variation of the strain with the vortex age experienced by the trailing vortex filaments originating from $r/R = 0.9$. The strain is computed using Eq. E.3, Appendix E. The variation is plotted at different values of (δ_v, S_c) . Since larger values of (δ_v, S_c) yield less roll-up (as illustrated in Fig. 6.9), it follows that they also cause the filaments to experience less strain.

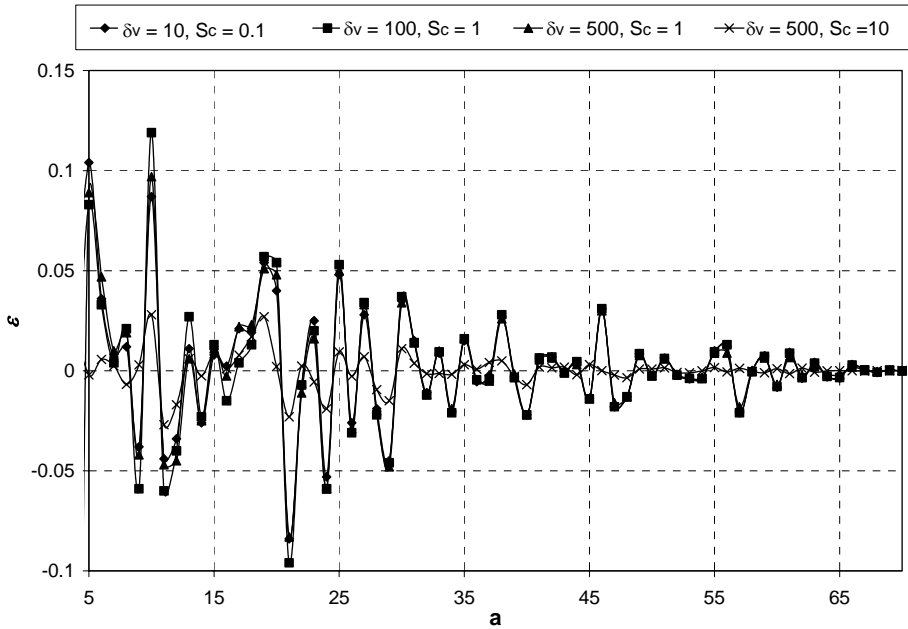


Figure 6.10 – Variation of strain of near wake trailing vortex filaments at $r/R=0.96$.

In attempting to select realistic values for these viscous parameters (δ_v , Sc) for this study, it was assumed that twice the value of r_c at the blade trailing edge (i.e. at time $t=0$) should approximately be equal to the thickness of the viscous layer of the wake vortex sheets. This thickness depends on the boundary layers formed on the upper and lower surfaces of the aerofoil which are in turn a function of the local Reynolds number and the angle of attack. The blade sections of the rotor at the operating conditions stated in table 6.1 have a local Reynolds number in the range $0.6 - 1.4 \times 10^6$. For attached flow conditions for which the angles of attack are small, the boundary layers are thin. It was estimated using *RFOIL* [63] that, for this Reynolds number range, the maximum boundary layer thickness at the trailing edge is only $7.82 \times 10^{-3}c$ up to an angle of attack of 10° . Consequently, the thickness of the viscous layer of the vortex sheet at the blade's trailing edge in attached flow conditions is also small and it does not exceed the local blade thickness ($20.95c\%$) (see Fig. 6.11). At high angles of attack however, flow separation on the blade's upper surface may cause the thickness of the viscous layer to be larger than the local blade thickness. The maximum angle of attack observed during the subject experiments was about 43° at $U=25\text{m/s}$ and $r/R=0.3$ (refer to Fig. 6.13)). At this angle of attack, however it is unlikely that the thickness of the viscous layer exceeds the blade chord length. Detailed investigations of the blade surface pressure distributions on NREL rotor [74, 75] revealed that as the angle of attack increases and the flow separation point arrives at the blade leading edge, boundary layer reattachment commences at the same time due to a high suction at the aft region of the

upper blade surface. This phenomenon is referred to shear layer impingement [75] and the resulting flow topology is illustrated in Fig. 6.11. Consequently the flow reattachment causes the thickness of the viscous layer of the vortex sheet to become thin again at the blade trailing edge.

The values of 2^*r_c at the trailing edge ($t=0$) predicted by Eq. 5.8 (Chapter 5) for the different sets of values of (δ_v, S_c) were compared with the blade thickness (which is equal to 20.95% c for the S809 aerofoil) and the blade chord spanwise distributions. This comparison is illustrated in Fig. 6.12. It is shown that parameters $(500, 10)$ yield a value of 2^*r_c that is much larger than the maximum blade chord. This is not realistic. Thus, a lower value of 2^*r_c was suggested for this study. Values $(500, 1)$ tend to be suitable for separated flow conditions since the resulting value of 2^*r_c is between 20.95% c and c . For attached flow conditions the values δ_v and/or S_c should strictly speaking be decreased so as to reduce 2^*r_c to be less than 20.95% c . However, since this does not affect considerably the calculated distributions of $u_{a,c}$ (refer to Fig. 6.7), (δ_v, S_c) were set to $(500, 1)$ for attached flow conditions also.

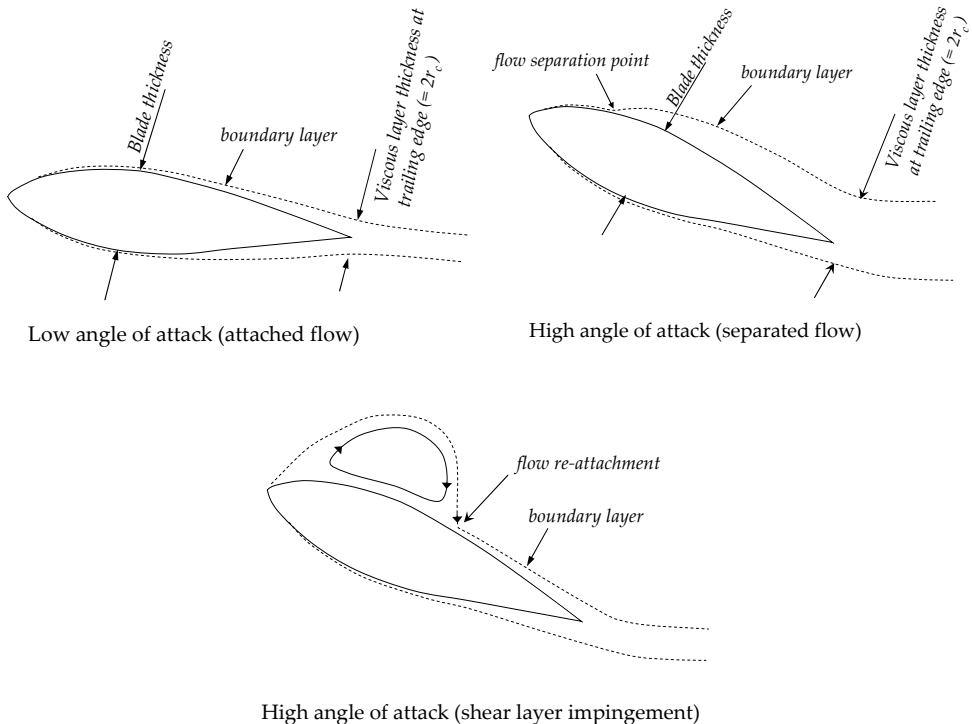


Figure 6.11 - Influence of the angle of attack on the variation of the viscous layer thickness of the wake vortex sheet at the trailing edge.

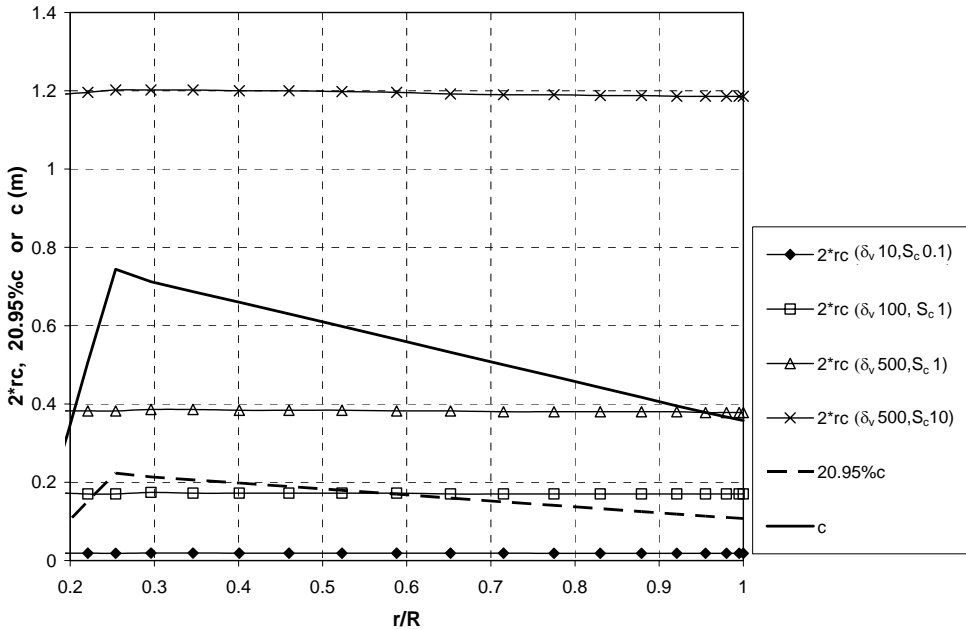


Figure 6.12 – Comparison of $2*r_c$ calculated at different values for viscous parameters (δ_v, S_c) with the spanwise distribution of blade thickness ($20.95*c$) and blade chord (c).

Selection of HAWT_FWC parameters for the far wake model

As regards the far wake parameters, the azimuthal step was always equal to $\Delta\phi$ (i.e. 10°), while the number of helical revolutions (n_{fwRev}) was kept constant equal to 10 for all calculations. The prescribed helical pitch (pfw) was varied depending on the windspeed. To determine a reasonable value for the prescribed helical pitch, preliminary calculations were carried out with the same free-wake model and an estimate was obtained from the near wake geometry.

B. Results and Discussion

This section presents the results obtained by applying the iterative procedure (Fig. 6.6) for finding the angle of attack on the NREL rotor for $U = 5, 7, 10, 13, 15, 20$ and 25m/s at $\psi = 0^\circ$. The parameters given in section A above were used in *HAWT_FWC*.

It was found that, for all the seven operating windspeeds, only two iterations were necessary to obtain a converged angle of attack distribution at the blades with 5% maximum error. The converged angle of attack distributions are shown in Fig. 6.13. The corresponding bound circulation distributions are shown in Fig. 6.14. These distributions are very similar to those derived by Tangler [90] using a prescribed-wake vortex code. In Fig. 6.13, a rise in the angle of attack is noted at the blade tip. This results from the viscous effects being modelled in the rolling up vortex sheet of the free-wake vortex code. At a windspeed of 15m/s , a rise in the bound circulation is observed in the middle section of the blades. This increases the trailing vorticity towards the middle sections of the blades. The operating range of Reynolds numbers is around $0.6 - 1.4 \times 10^6$ as shown in Fig. 6.15. In checking the calculations, the flow relative velocity variations, V_r , were estimated using the induced velocities outputted by the free-wake model and these were compared with those derived experimentally from Q_{NORM} (from Eq. 6.1). Good agreement was obtained, as may be seen in Fig. 6.16.

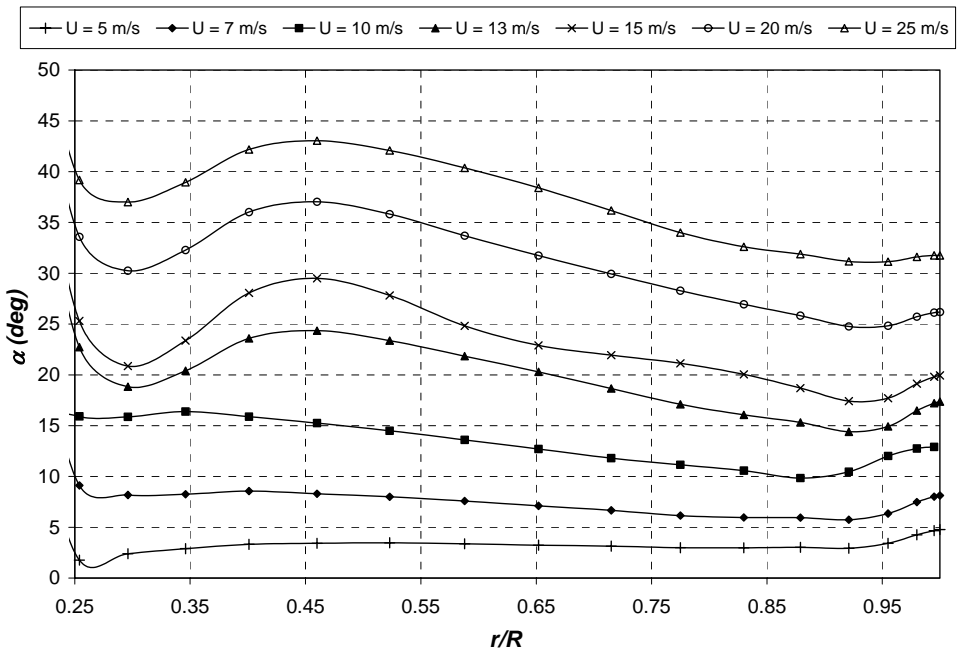


Figure 6.13 – Converged angle of attack distributions at different windspeeds.

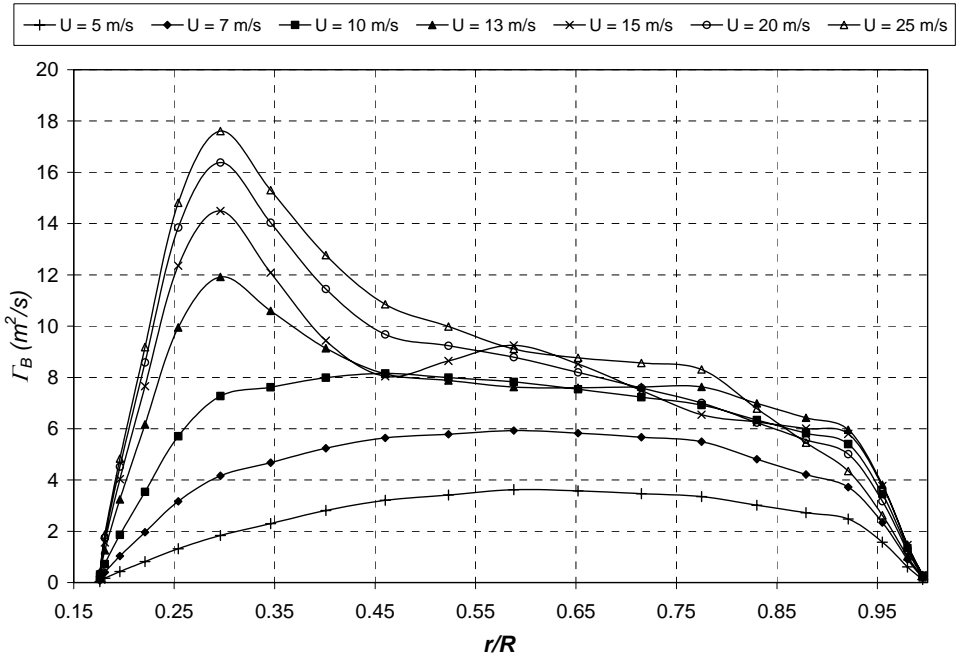


Figure 6.14 – Converged bound circulation distributions at different windspeeds.

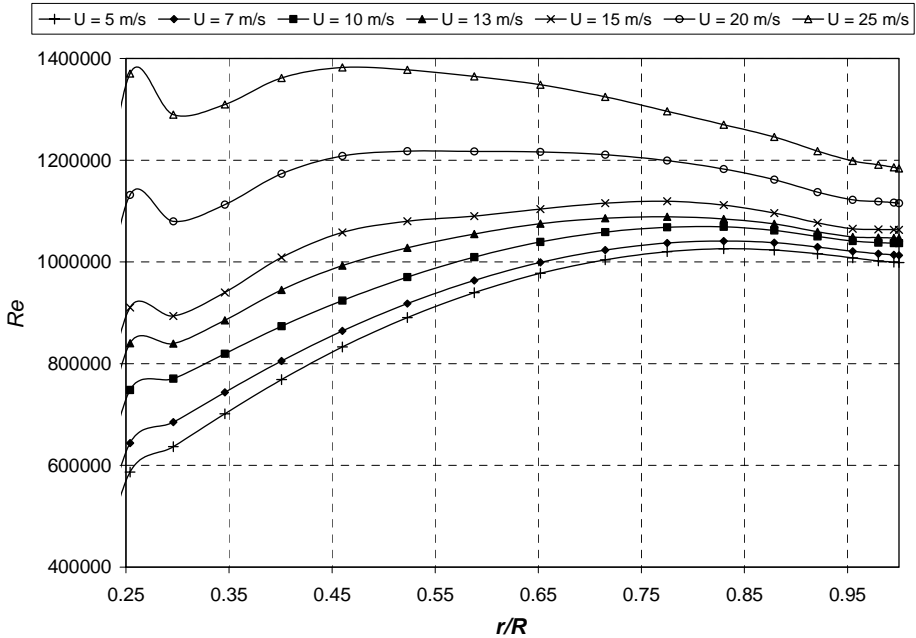


Figure 6.15 – Variation of Reynolds number at blades for different windspeeds.

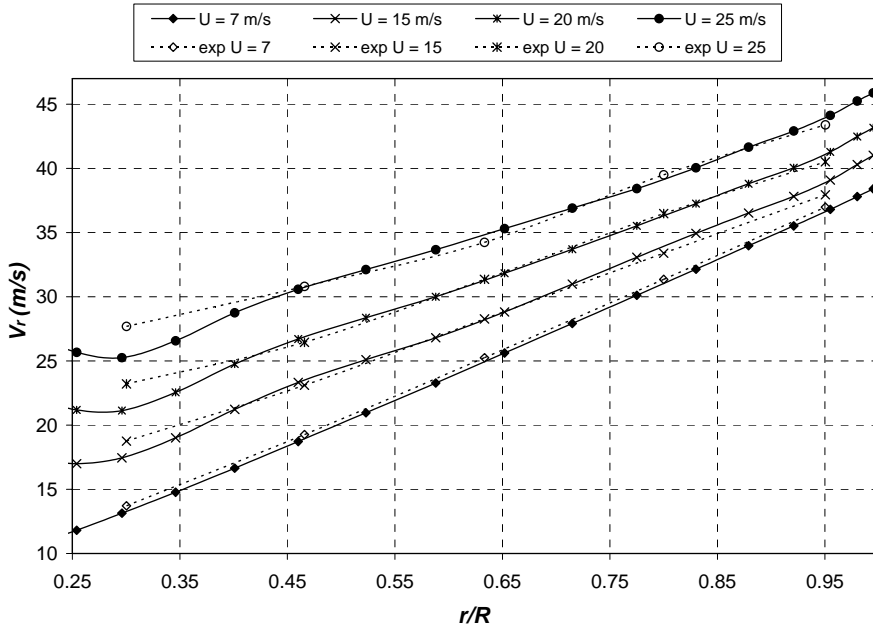


Figure 6.16 – Comparison of V_r calculated by the free-wake model with that derived from Q_{NORM} (denoted by 'exp').

Wake Plots

The resulting near wake plots computed by the free-wake code are illustrated for each windspeed in Figs. 6.17(a)-(g). Color coding is used to represent the circulation distribution in the wake. Such computations not only give insight on the wake geometry developed but also provide a pictorial representation of how the bound circulation formed around the blades (see Fig. 6.14) is eventually diffused into the wake under the action of complex 3D flows. Since all plots are for axial flow conditions, then the wake only consists of trailing circulation. In these plots, high positive trailing circulation is displayed in red, while high negative trailing circulation is displayed in blue. At low wind speeds ($U=5$ and 7 m/s), the wake trailing circulation tends to be concentrated at the blade tip and root locations. In Figs. 6.17(a) and (b) high positive trailing circulation in red is not always visible due to the folding of the vortex sheets resulting from roll-up. At higher wind speeds however ($U=10$ m/s and higher), considerable levels of trailing circulation are released for the middle sections of the blades in the form of horse-shoe vortices.

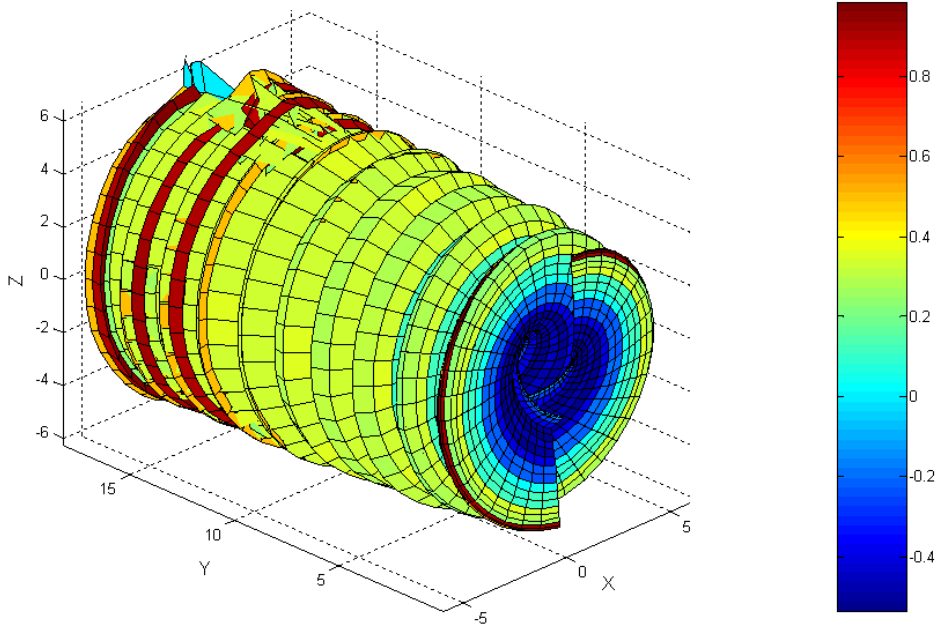


Figure 6.17(a) – Free-wake plot at $U = 5 \text{ m/s}$.

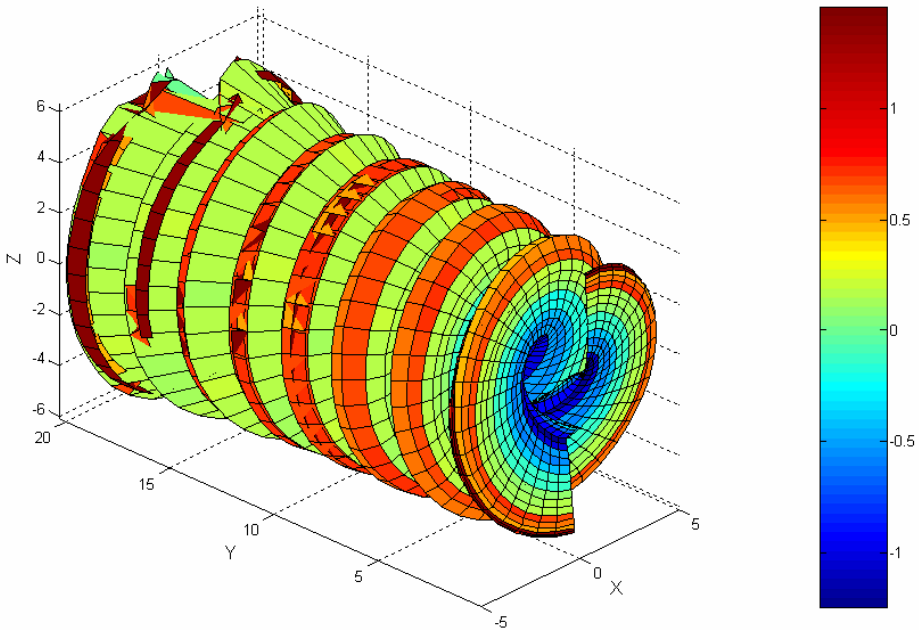


Figure 6.17(b) – Free-wake plot at $U = 7 \text{ m/s}$.

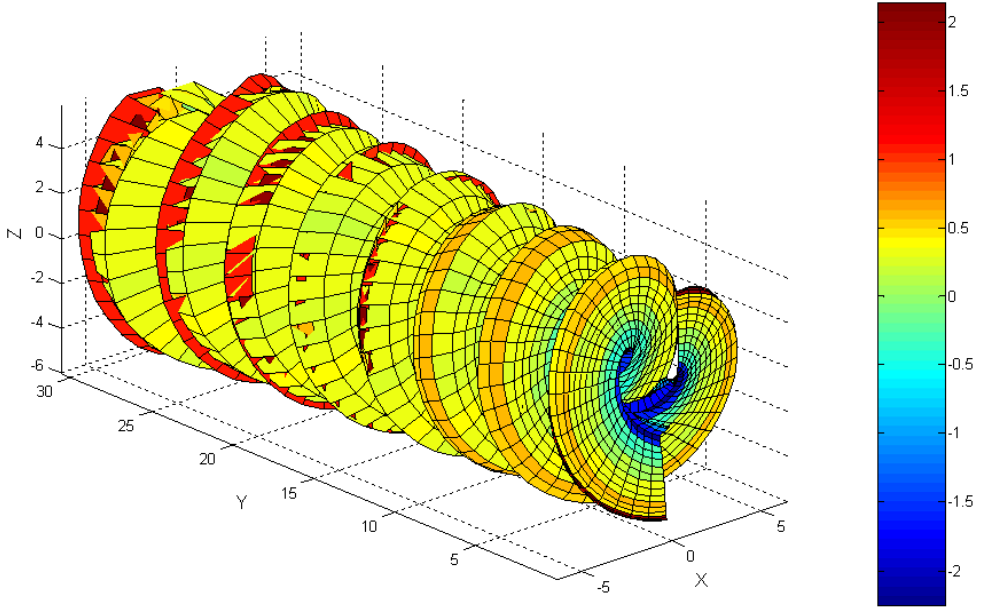


Figure 6.17(c) – Free-wake plot at $U = 10\text{m/s}$.

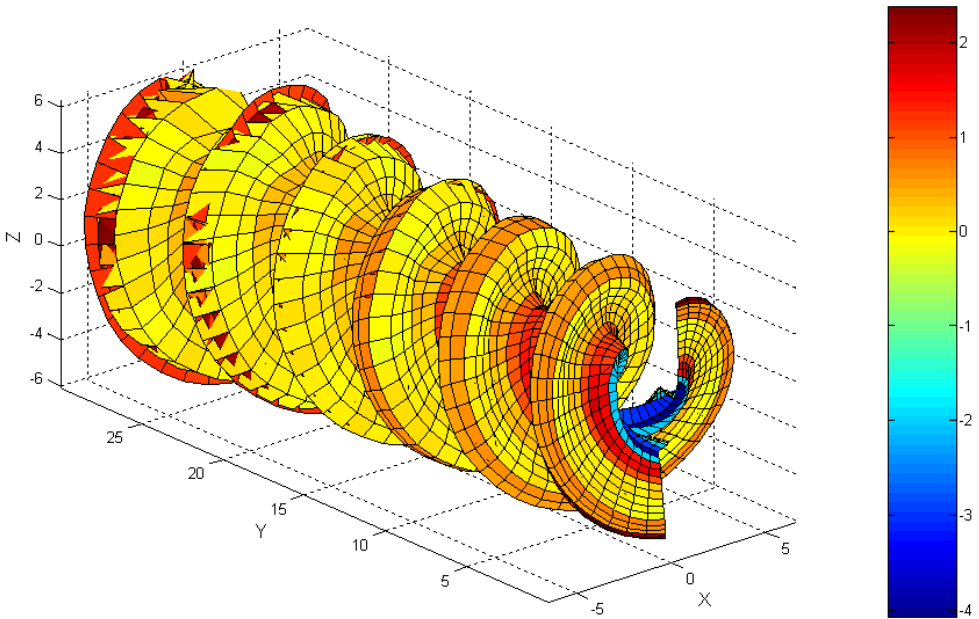


Figure 6.17(d) – Free-wake plot at $U = 13\text{m/s}$.

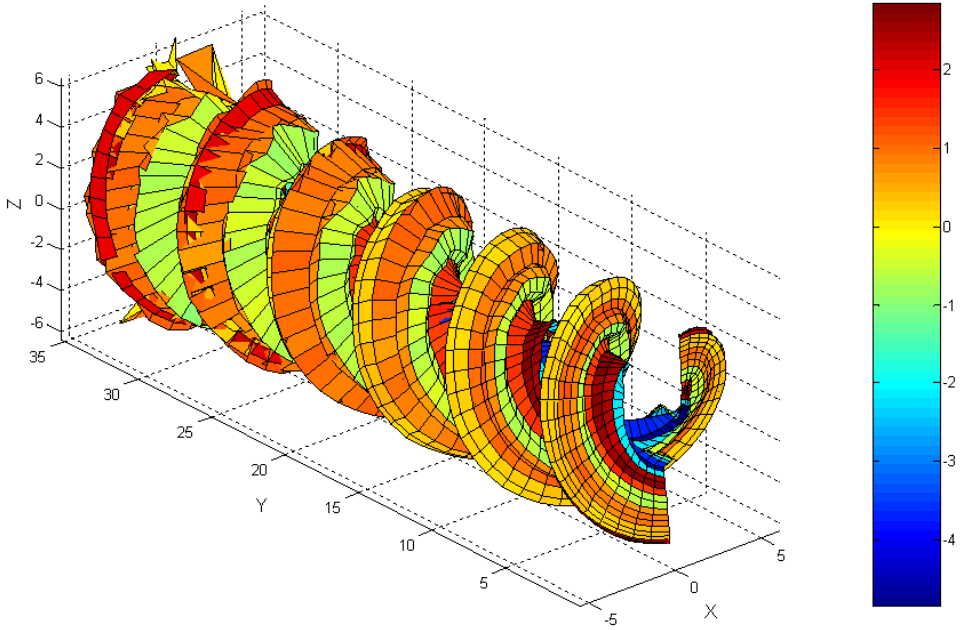


Figure 6.17(e) – Free-wake plot at $U = 15\text{m/s}$.

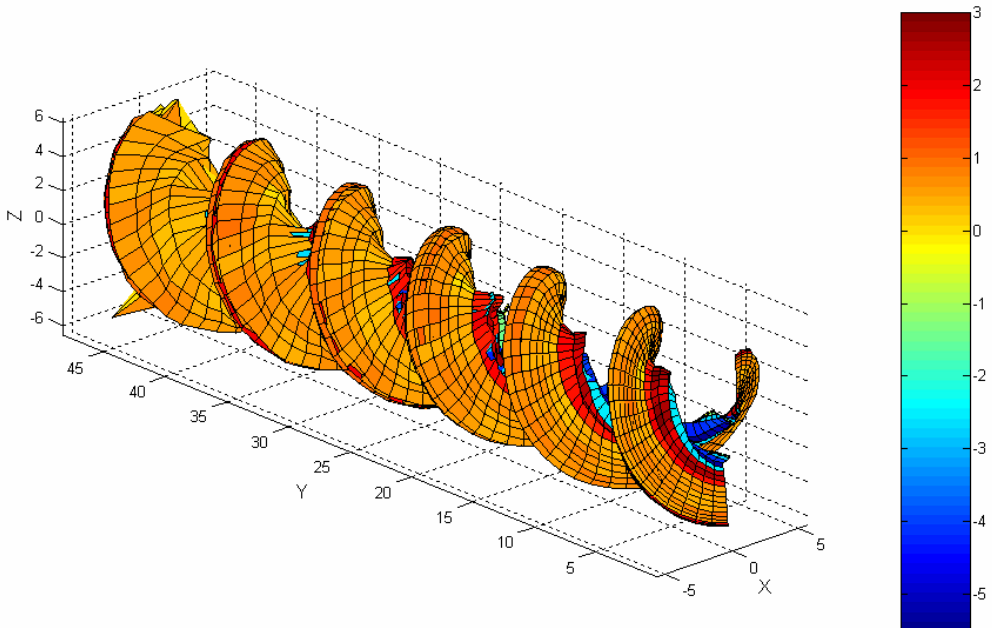


Figure 6.17(f) – Free-wake plot at $U = 20\text{m/s}$.

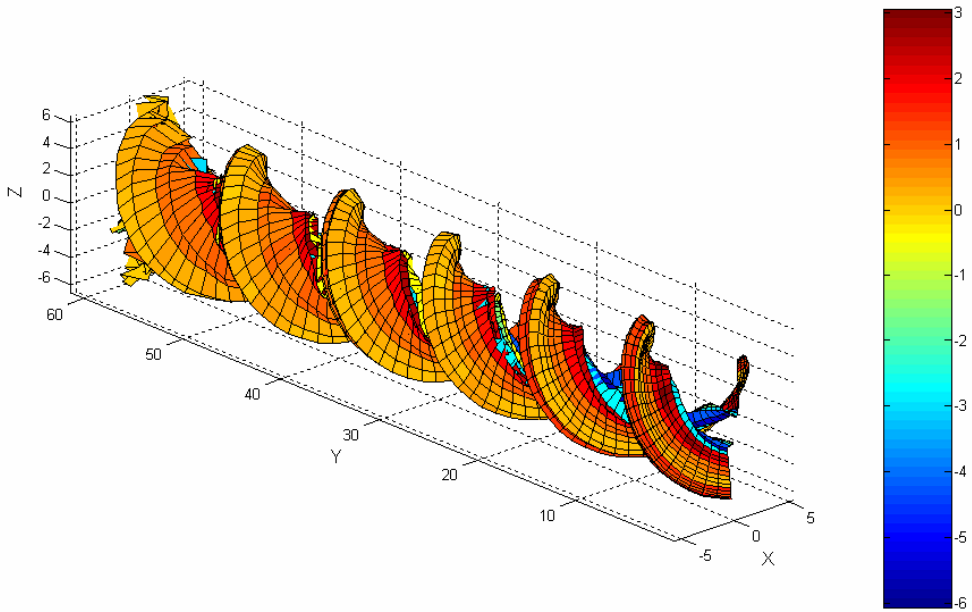


Figure 6.17(g) – Free-wake plot at $U = 25\text{m/s}$.

A summary of the vortex sheet pitch variation derived from the above free-wake geometries is shown in Figs. 6.18. Fig. 6.18(a) shows the variation of the pitch against the tunnel windspeed while Fig. 6.18(b) is a similar plot but with the non-dimensional values being shown instead. It may be noted that the vortex pitch increases almost linearly with windspeed. Wake expansion in the vicinity of the rotorplane was found to be small and hardly to quantify accurately from the free-wake plots. This small wake expansion is a consequence of the fact that the rotor was operating at low axial thrust coefficients.

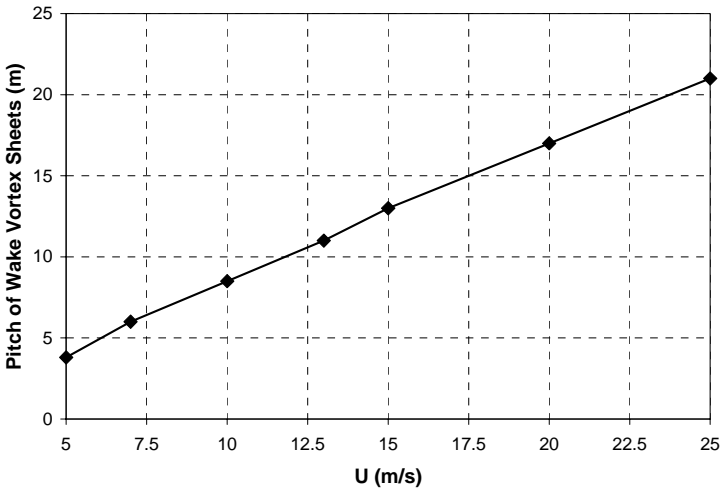


Figure 6.18(a) – Vortex sheet pitch variation with tunnel windspeed as estimated from free-wake plots at $\Psi=0^\circ$.

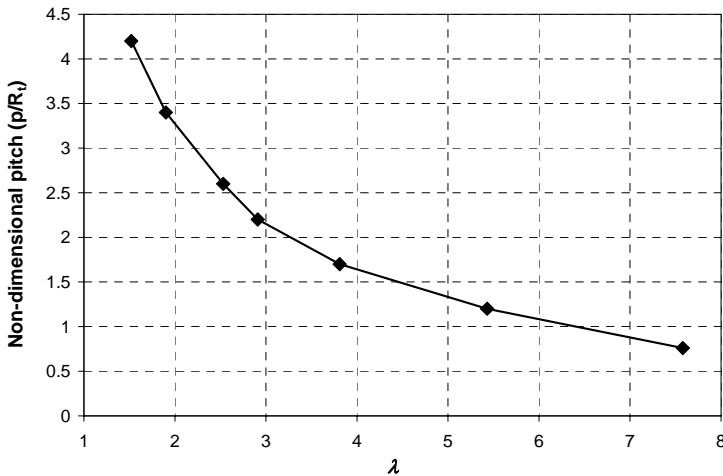


Figure 6.18(b) – Non-dimensional vortex sheet pitch variation (p/R_t) with rotor tip speed ratio (λ) as estimated from free-wake plots at $\Psi=0^\circ$.

Aerofoil Coefficients

The derived aerofoil data are summarized in Figs. 6.19(a) and (b). Both the lift and drag coefficients are dependent on the radial location. The Delft 2D aerofoil data for the S809 is plotted for a Reynolds number of 1×10^6 . At low angles of attack, the inboard blade sections have a lower lift coefficient than the 2D values, but this increases continuously for high angles of attack. The presence of stall delay is evident at the inboard blade sections. However, the tip region has the lowest lift coefficients, considerably lower than the 2D values. This is observed even for small angles of attack. This reduction in C_l at the blade tip results from the 3D flow effects in this region as well as induction effects from the strong tip vortex. Apart from increasing C_l , stall delay also increases C_{dp} . This increase is also more significant at the inboard sections. Lower values for C_{dp} are obtained for the tip region at $0.95R$.

3D Induction at Rotorplane

HAWT_FWC calculated the 3D induced velocity fields across the whole rotorplane for different blade azimuth angles for the blade pressure measurements taken in the tunnel. The contour plots displaying the induced velocity fields for $U=5$ and 15m/s are plotted in Fig. 6.20. In these plots, the positions of the blades (lifting lines) is recognized from the negatively large axial induced velocities (u_y) (dark blue zone). From such plots it was possible to obtain the axial induction factor distributions at the blade lifting lines together with the corresponding azimuthally (annular) averaged induction factors. These induction factor distributions at each wind speed ($U=5, 7, 10, 13, 15, 20$ and 25m/s) are illustrated in Figs. 6.21(a)-(f). The axial, tangential and radial induction factors at the blade lifting lines are shown in Figs. (a)–(c), while Figs. (d)–(f) show the corresponding azimuthally averaged values at each radial location. In general, higher windspeeds reduce the axial induction factors at the rotorplane. This is a consequence of the fact that, for a fixed rotor angular speed, higher windspeeds increase the pitch of the tip vortices and this reduces the axial induction experienced by the rotor. When looking at Figs. (a) and (d), it can be noted that, for the blade root and tip regions, the axial induction factor at the blades is considerably higher than the azimuthally averaged value. This is caused by the tip and root vortices that, at any instant, are closer to the blades than to the other regions in the rotorplane not occupied by the blades. The higher induction eventually reduces the blade loading at the tip and root regions.

The tangential induction at each blade section increases with windspeed, reaching the highest values at the blade root. However the tangential induction factor remains small compared to the axial induction factor at all windspeeds.

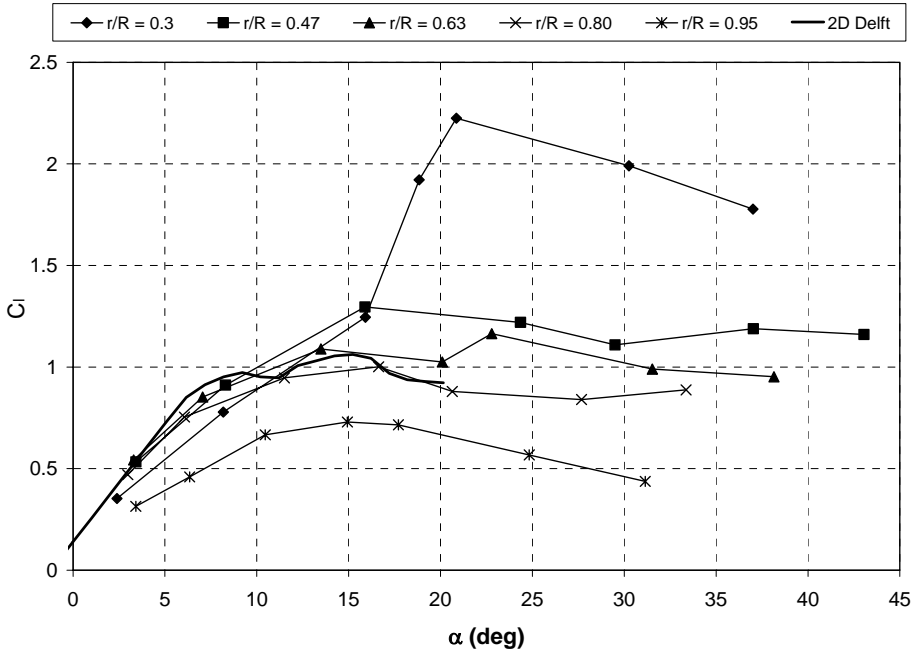


Figure 6.19(a) – Derived lift coefficients for different radial positions.

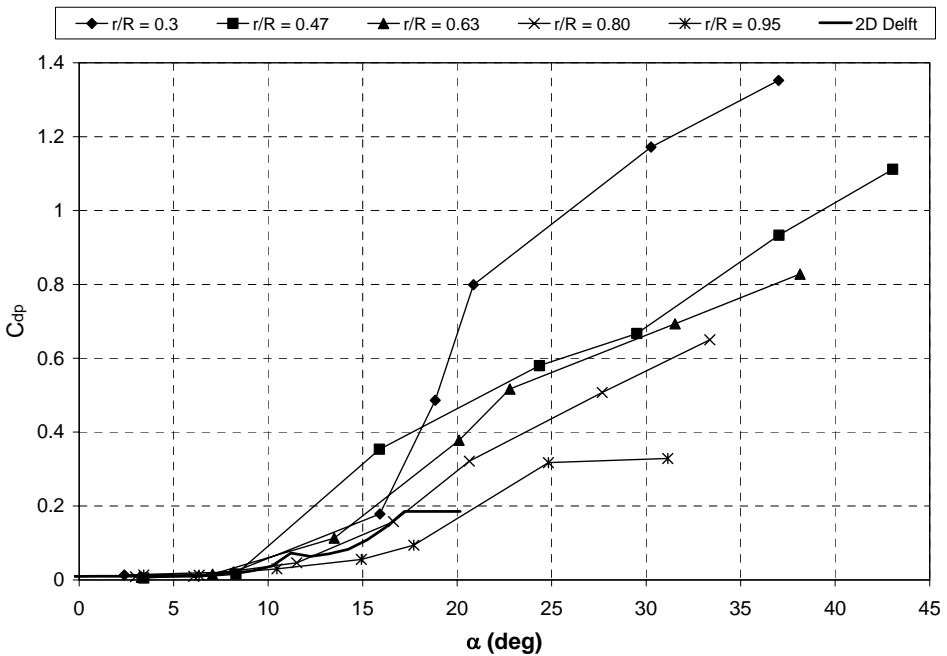
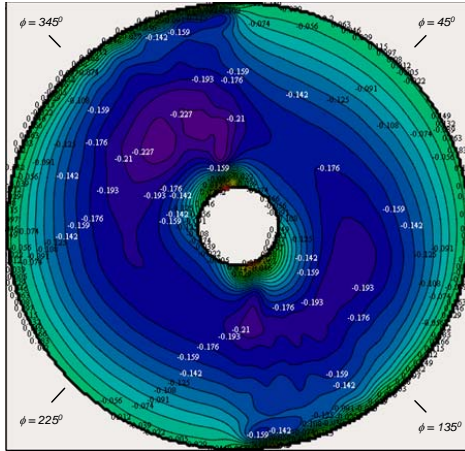
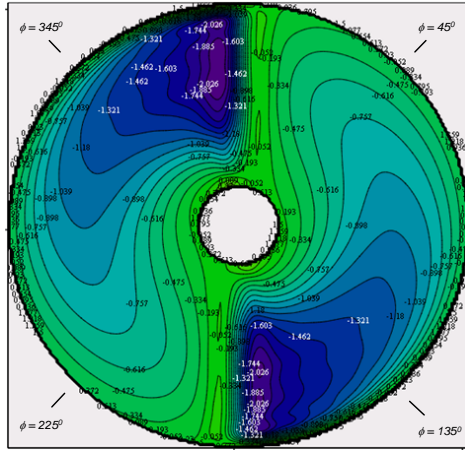


Figure 6.19(b) – Derived drag coefficients for different radial positions.

Tangential induced velocity field (u_x)



Axial induced velocity field (u_y)



Radial induced velocity field (u_z)

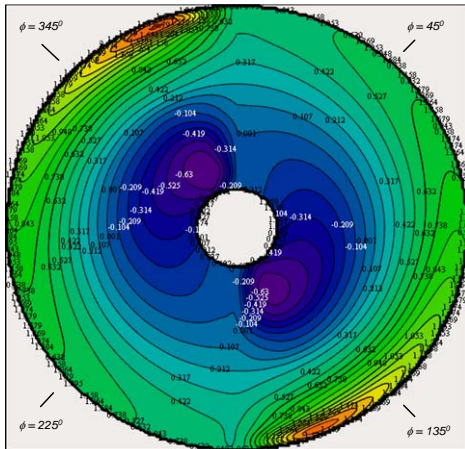
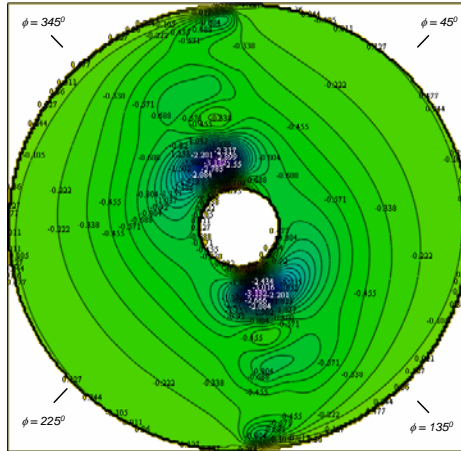
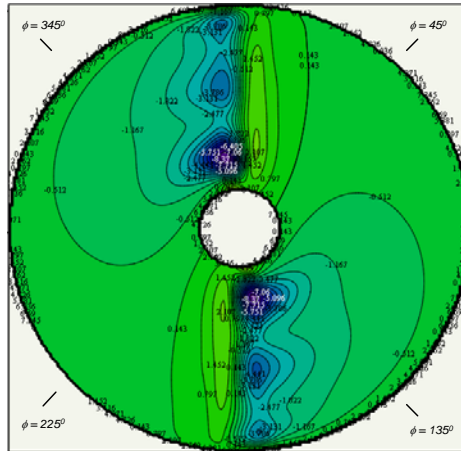


Figure 6.20(a) – 3D induced velocity field at rotorplane at $U=5\text{m/s}$, $\Psi=0^\circ$. Blade is at an azimuth angle of $0/180^\circ$. View is looking upstream from behind the rotorplane.

Tangential induced velocity field (u_x)



Axial induced velocity field (u_y)



Radial induced velocity field (u_z)

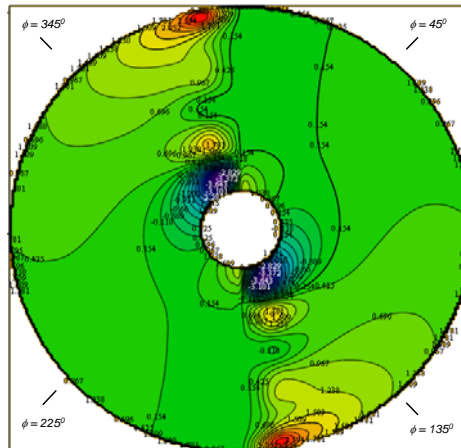


Figure 6.20(b) – 3D induced velocity field at rotorplane at $U=15\text{m/s}$, $\Psi=0^\circ$. Blade is at an azimuth angle of $0/180^\circ$. View is looking upstream from behind the rotorplane.

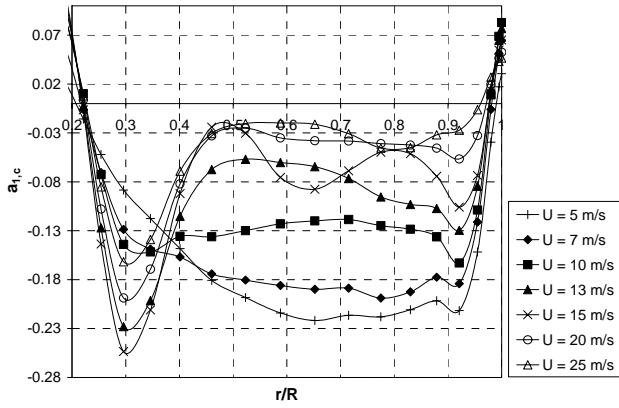


Figure 6.21(a) – variation of axial induction factor at blade lifting line.

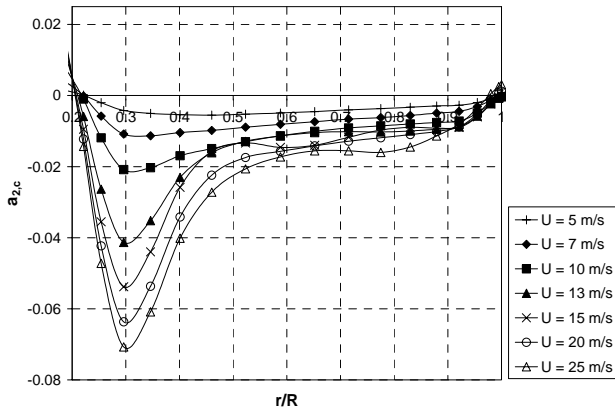


Figure 6.21(b) – variation of tangential induction factor at blade lifting line.

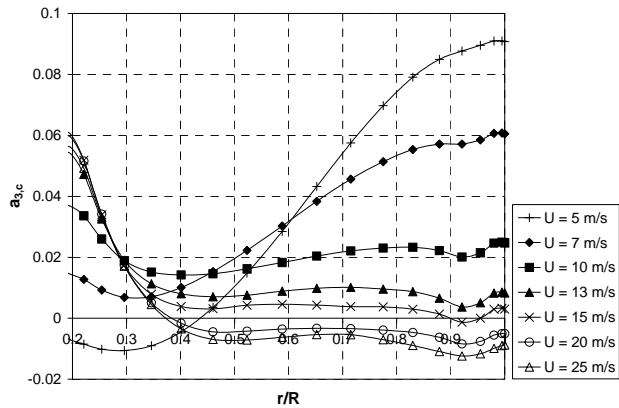


Figure 6.21(c) – variation of radial induction factor at blade lifting line.

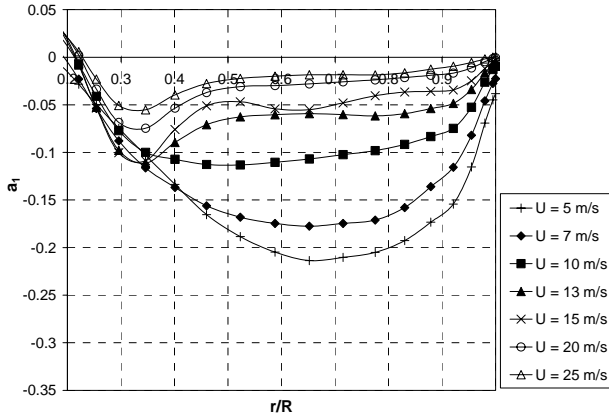


Figure 6.21(d) – variation of azimuthally averaged axial induction factor.

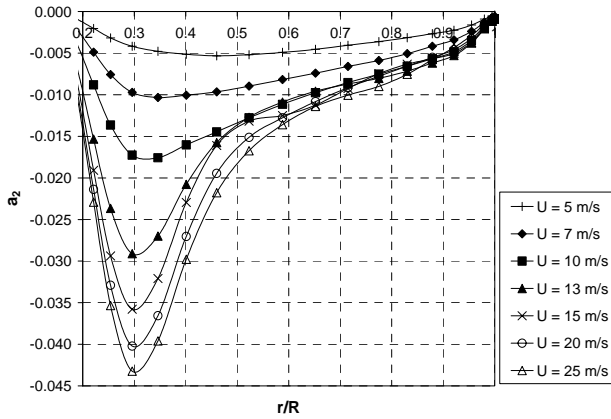


Figure 6.21(e) – variation of azimuthally averaged tangential induction factor.

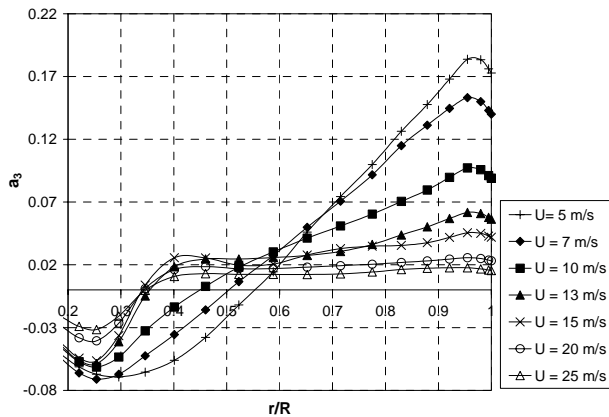


Figure 6.21(f) – variation of azimuthally averaged radial induction factor.

With reference to Fig. (f), the free-wake code is predicting an azimuthally averaged radial induction factor that is positive at the outboard sections, but negative at the inboard sections for 5, 7 and 10m/s. A positive radial induction factor means that radial flow is outwards towards the rotor tip radius and vice versa. This factor therefore gives an indication on the way the wake is expanding at the rotorplane. It appears that for low wind speeds (5, 7 and 10m/s), the flow at the outer radial positions is expanding outwards while that at the inner radial positions is expanding inwards in the direction of the rotor hub. For the higher windspeeds (13m/s and above), the vortex code is predicting lower values for a_3 and wake expansion is outwards. It can be noted from Fig. (c) that at the blade lifting lines, the radial induction is in general much lower in magnitude than the azimuthally averaged value. A more detailed study would be necessary to investigate how the wake-induced radial flow patterns influence the aerodynamic behaviour of the blades at both low and high angles of attack.

Global loads

The lift and drag coefficients and the induced velocities derived by the free-wake vortex model were used to calculate the low-speed shaft torque and the blade flap/edgewise bending moments using the blade-element theory Eqs. 3.16. These results are shown in Figs. 6.22 (a)-(c) where they are noted by plots 'Free-wake'. As a cross-check for these calculations, the same loads were computed directly from the experimental data at each rotor/blade time step τ by using a linear interpolation to obtain a distribution for C_n , C_t and Q_{NORM} across the whole blade span and using the following equations:

$$LSSTQ_\tau = \int_{b=0}^{b=B-1} \int_{R_{hub}}^{R_{tip}} Q_{NORM}_{\tau_{b,i}} \times \left(C_{t_{\tau_{b,i}}} * \cos(\theta_i) + C_{n_{\tau_{b,i}}} * \sin(\theta_i) \right) \times c_i \times r_i \times dr \quad (6.4)$$

$$RFM_\tau = \int_{R_{hub}}^{R_{tip}} Q_{NORM}_{\tau_{b,i}} \times \left(C_{n_{\tau_{b,i}}} * \cos(\theta_i - \theta_{tip}) - C_{t_{\tau_{b,i}}} * \sin(\theta_i - \theta_{tip}) \right) \times c_i \times \left(r_i - r_{strain\ gauge} \right) \times dr \quad (6.5)$$

$$REM_\tau = \int_{R_{hub}}^{R_{tip}} Q_{NORM}_{\tau_{b,i}} \times \left(C_{n_{\tau_{b,i}}} * \cos(\theta_i - \theta_{tip}) + C_{t_{\tau_{b,i}}} * \sin(\theta_i - \theta_{tip}) \right) \times c_i \times \left(r_i - r_{strain\ gauge} \right) \times dr \quad (6.6)$$

where $r_{strain\ gauge}$ is the radial location of the strain gauges measuring the blade root flap/edge moments. θ_{tip} is included in the above equations because the strain gauges installed at one of the rotor blades were oriented such that they measure the flapping moment about an axis parallel to the chordline of the blade tip section [35]. In the linear interpolation, C_n and C_t at the blade tip/root were set equal to zero. The trapezium rule was adopted for integrating

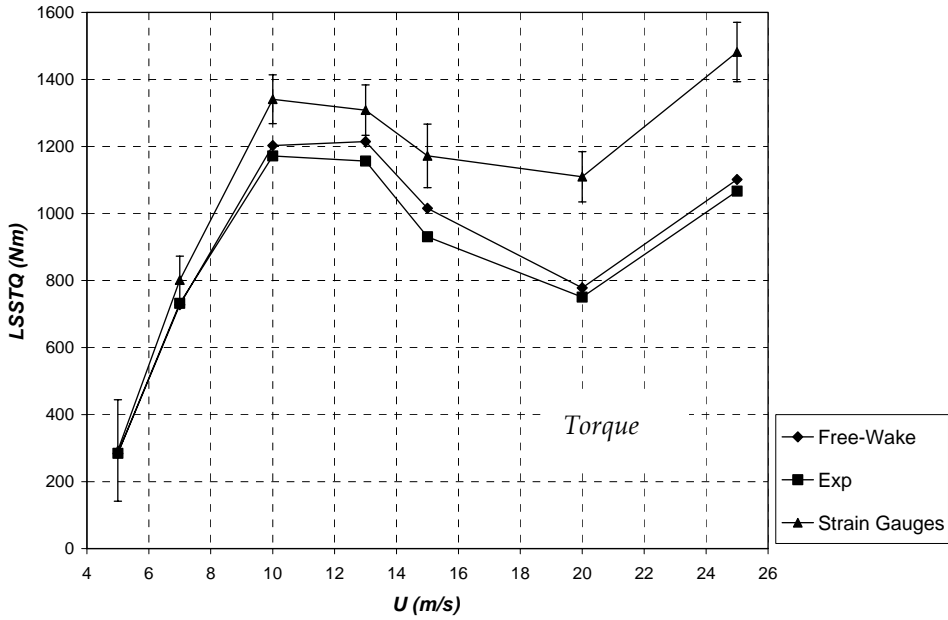


Figure 6.22(a) – Variation low speed shaft torque with windspeed.

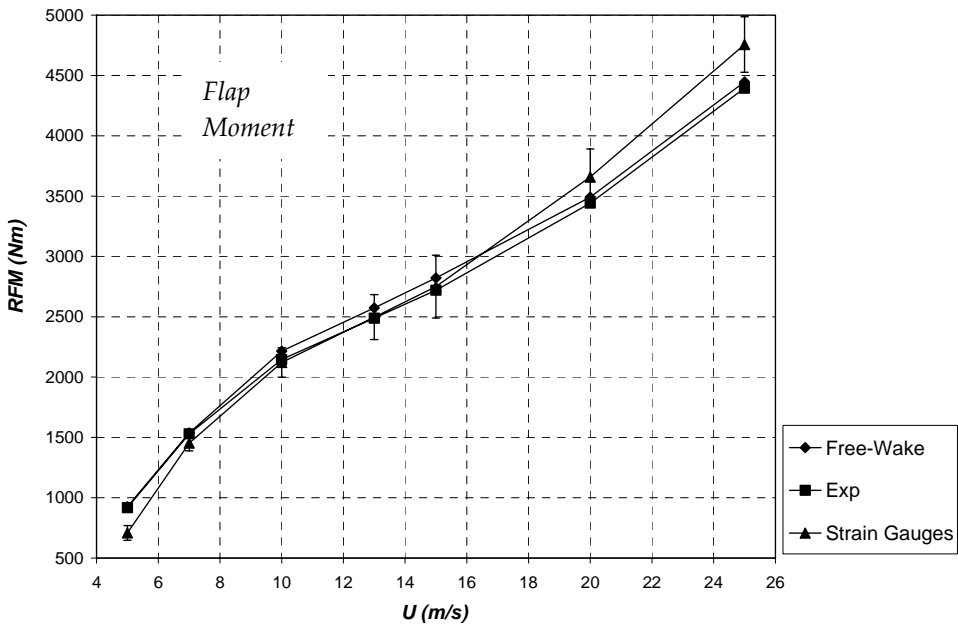


Figure 6.22(b) – Variation of blade root flap moment with windspeed.

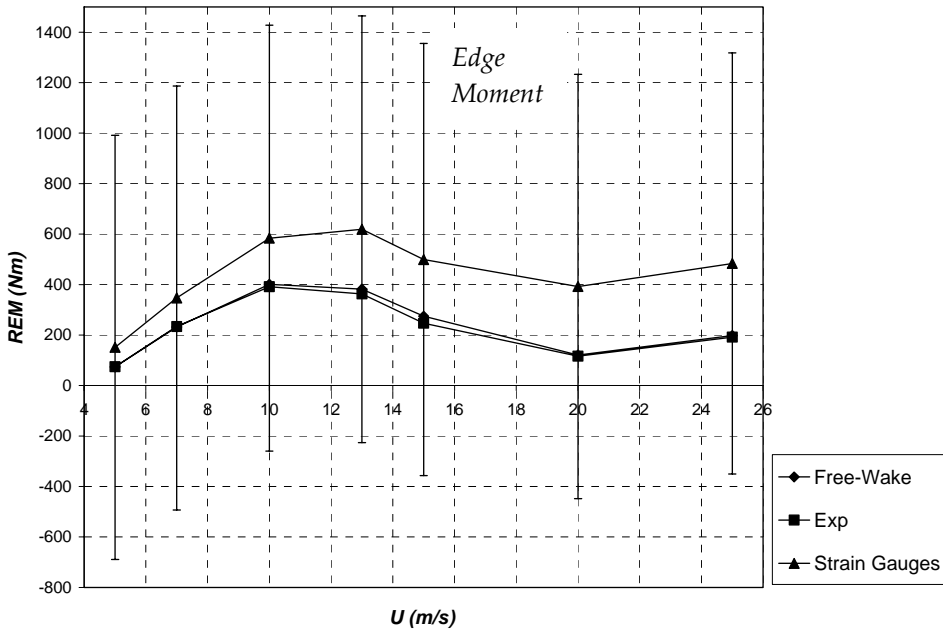


Figure 6.22(c) – Variation of blade root edge moment with windspeed.

numerically across the whole blade span. These results are included in Figs. 6.22 and are referred to ‘Exp’. The loads measured directly using strain-gauges are also included in Figs. 6.22. These are plotted together with the corresponding +/-one standard deviation. The large standard deviations in the REM were due to the cyclic gravitational loads. The results calculated by the free-wake model and those derived directly from the pressure measurements (‘Exp’) agree very well. However for the LSSTQ and REM, agreement with the loads measured by the strain gauges is not as good especially at higher wind speeds. Although one cannot ignore the fact that structural dynamic effects of the rotating rotor could have influenced the loads measured by the strain gauges, a more probable source of error was in measuring C_t . When investigating the variation of the measured C_t values with blade azimuth angle over a whole revolution, a considerably large standard deviation was found. Another possible source of error was due to the fact that the pressure measurements were only performed at five radial locations. Thus the linear extrapolated distributions of the experimental data used in the free-wake model could yield numerical errors.

Comparison of Inflow Angle

The local flow angles (*LFA*) predicted by *HAWT_FWC* are now compared with those measured by the flow direction probes during the wind tunnel experiments (see Fig. 6.4). The comparison is shown in Figs. 6.23(a)-(g). The angle of attack is also included. Ideally the *HAWT_FWC* predictions for the *LFA* should be equal to those measured by the probes. But this is not always the case, as it may be seen in Figs. 6.23. One source of error could be because the blades were modelled as rigid in *HAWT_FWC* and during the experiments blade deflection effects could influence the *LFA* measurements. However calculations performed by the ECN on aeroelastic code *PHATAS* confirm that the deflection of the blades was small, even at the high windspeeds (maximum blade tip deflection < 10cm), (ECN, Gerard Schepers, personal communication). To assess the uncertainty due to arbitrary choice of viscous parameters, the *LFA* distribution at $U = 25\text{m/s}$ was computed using the free-wake vortex model at two extreme sets of values of (δ_i, S_c) : at (10, 0.1) and (500, 1). The maximum deviation in the *LFA* due to the different (δ_i, S_c) values was found to be only 0.34° at $r/R=0.91$.

At all windspeeds, the free-wake vortex model predicts an *LFA* that is larger than the derived angle of attack. This is due to the presence of upwash created by the bound circulation at the blade. This is consistent with the measured values of *LFA* since these are also larger than the angle of attack being predicted by the vortex model. The correlation of the *LFA* is very good at low windspeeds ($U=5$ and 7m/s) at which the angle of attack is small across the whole blade span. At higher windspeeds, the agreement does not remain good, especially at the inboard sections. At $U=25\text{m/s}$, the largest discrepancy between the predicted and measured *LFA* is about 9° which is considerably high.

It was found that *HAWT_FWC* is accurate in predicting the *LFA* when at the outboard blade sections ($r/R > 0.67$), even at the high windspeeds where the local angle of attack exceeds the 2D stalling angle (around 10°). But at the inboard blade sections, the capability of the code in predicting the *LFA* accurately degrades steadily at larger windspeeds. The problem is most likely to be associated with the way the vortex model models circulation around the blades. In *HAWT_FWC*, the blades are modelled as lifting lines and the bound circulation is forced to leave from the trailing edge as a single vortex sheet (see Fig. 6.24(a)). The lift and bound circulation are related by the Kutta-Joukowski law (Eq. 6.2). Such a model works well where the flow over the blades is fully attached. Yet it is known that this model has limited accuracy when it comes to modelling high angles of attack where the flow over the upper blade surface experiences separation. In such conditions, not all bound circulation is released into the wake through the trailing edge. More accurate vortex models exist, as described in [42, pp 505-516]. Such models would include more than just one bound vortex, with all the bound vortices distributed around the blades surface (refer to Fig. 6.24(b)). In addition, to account for flow separation, a secondary vortex sheet in the near wake is included emerging from the upper blade surface. As already described in section 6.3.2,

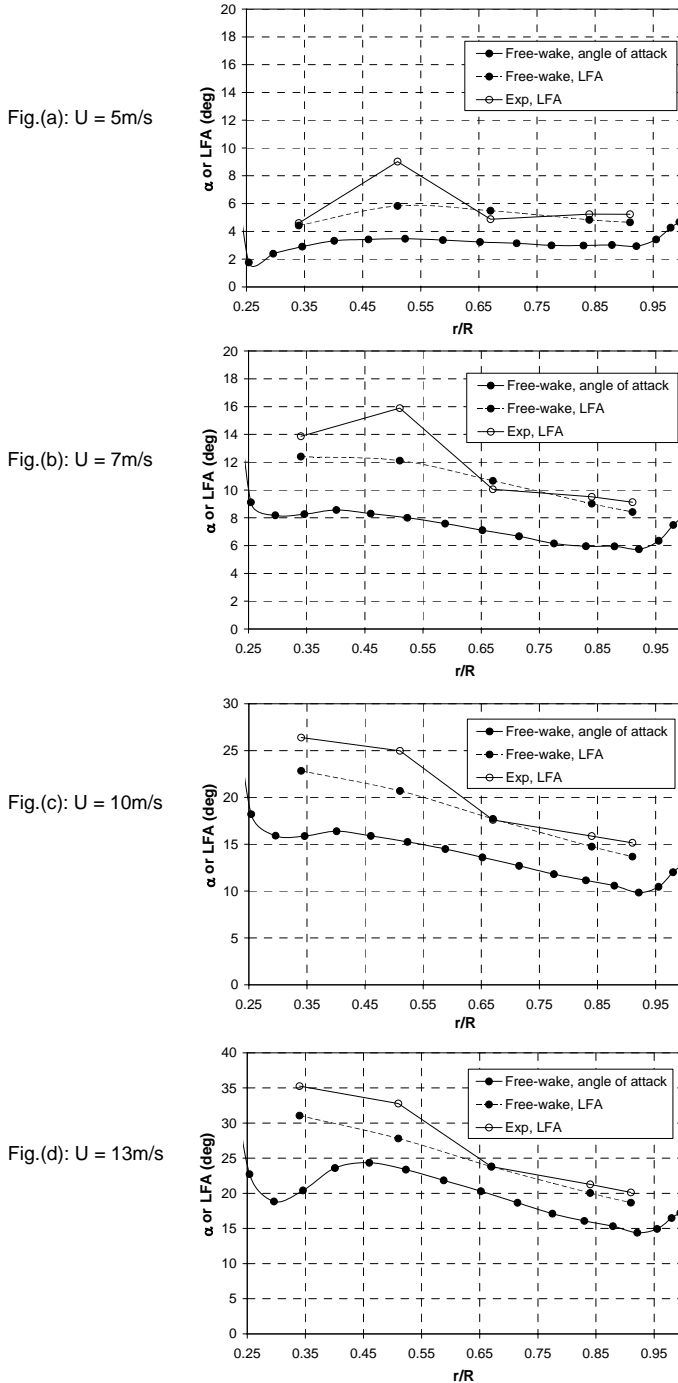


Figure 6.23 – Comparison of LFA distribution predicted by HAWT_FWC with those measured by five-hole probe. Angle of attack distribution computed by HAWT_FWC is also shown.

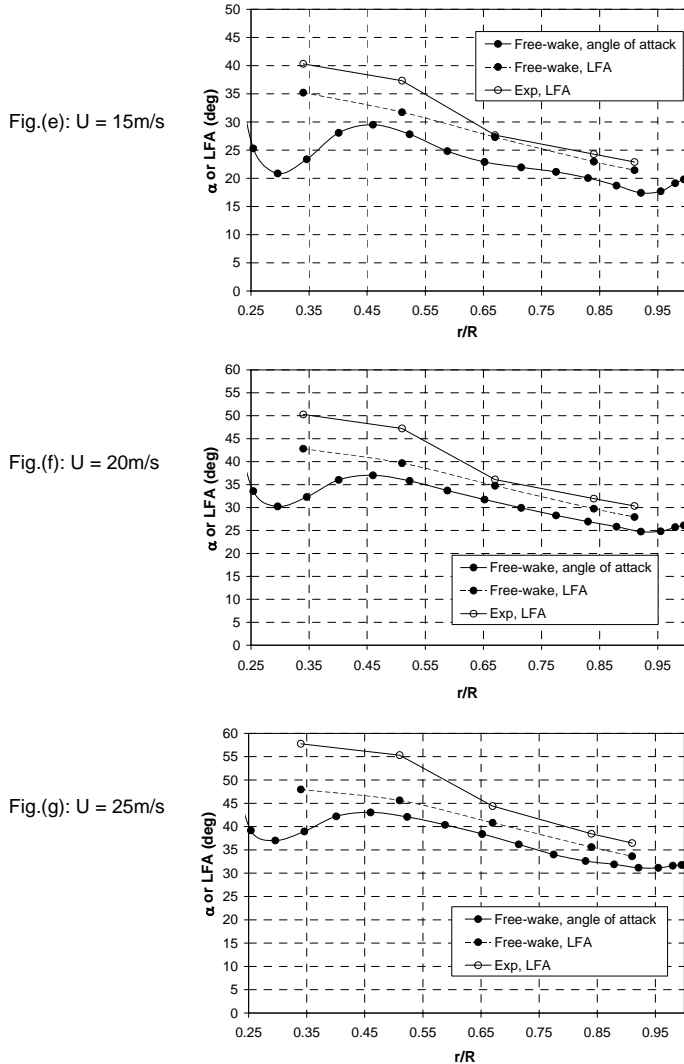


Figure 6.23 – Contd. from previous page.

various studies on the subject NREL Phase VI experiments [74, 75] however concluded that at sufficiently high angles of attack, the flow topology over the inboard sections of the blades is that of an impinging shear layer (see Fig. 6.11). The vortex lifting line model embedded in *HAWT_FWC* is also limited for modelling this situation. A more accurate vortex model could be with a second wake vortex sheet that emerges from the blade's leading edge and re-attaching itself with the blade's upper chamber at a defined position, as depicted in Fig. 6.24(c).

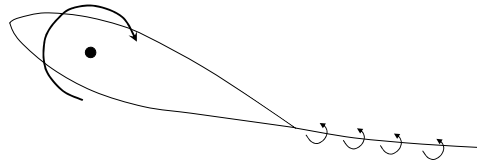


Fig. (a)

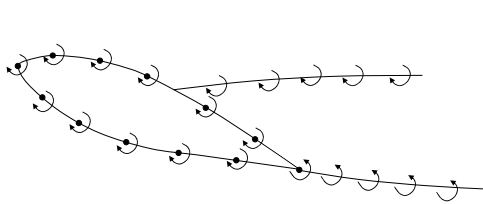


Fig. (b)

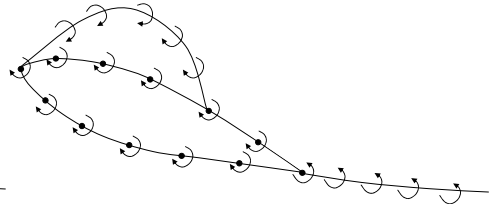


Fig. (c)

Figure 6.24 - Three different vortex models used to model flow over blades. Fig. (a) shows the vortex lifting line model embedded in HAWT_FWC; Fig. (b) is a more accurate vortex model for high angles of attack where separation only occurs. Fig. (c) is a more accurate vortex model for high angles of attack where flow separation at the leading edge is followed by a shear layer impingement.

Comparison with Results from EllipSys3D

The NREL Phase VI rotor has been modelled by Johansen *et al.* [40] using the CFD code *EllipSys3D* which is used to model wind turbine rotors. The code was developed by Michelsen *et al.* [57, 58] and Sørensen *et al.* [87]. In the code, a multiblock finite volume discretization of the incompressible Reynolds Averged Navier-Stokes equations is adopted. The code uses a collocated variable arrangement, and Rhei/Chow interpolation is used to avoid odd/even pressure decoupling. The SIMPLE algorithm is used to enforce the pressure/velocity coupling. The momentum equations are solved using a second order upwind interpolation scheme (SUDS) for the convective terms. The turbulence is modelled using the Detached-Eddy Simulation (DES) model according to Stretlets [89]).

Johansen *et al.* [40] used the results from *EllipSys3D* for the NREL rotor to derive 3D aerofoil coefficients (C_l and C_{dp}) for BEM models at different wind speeds (U) for $\Psi=0^\circ$. The azimuthally (annular) averaged axial flow velocity as a function of axial distance from the rotorplane was obtained from the CFD wake computations. The axial velocity at the rotorplane could then be obtained, together with the azimuthally averaged axial induction factor (a_1). The tangential induction factor was taken as zero since it was found to be negligibly small. a_1 was then used to evaluate the angle of attack (α). Using C_n and C_t with the derived α , the aerofoil coefficients for the different radial locations were derived using

the equations in Fig. 2.1. The angle of attack was determined using a similar method as for *HAWT_FWC* with the only difference that it was based on the azimuthally averaged axial induction factor (a_1) instead of that at the lifting line of the blades ($a_{1,c}$).

The results from *HAWT_FWC* are now compared with those obtained using *EllipSys3D* for $\psi=0^\circ$ and wind speeds $U=7, 10, 13, 15, 20$ and 25m/s . It is important to recall that *HAWT_FWC* makes use of the experimental data (C_n , C_t and Q_{NORM}) to be able to find the angle of attack and induction factor distributions. On the other hand, *EllipSys3D* is totally independent and does not require such experimental data as input. The analysis started by comparing the spanwise distributions of C_n and C_t . The comparison is illustrated in Figs. 6.25 and 6.26. In these plots, experimental data from NREL is shown. The mean values for C_n and C_t are plotted (mean over one whole blade revolution) together with the errors bars denoting the \pm one standard deviations. The distributions for C_n and C_t (extrapolated using linear interpolation as explained already in section 6.3.1) that were inputted to *HAWT_FWC* are also shown. In general, the predictions for C_n and C_t by *EllipSys3D* agree very well with the measurements and this demonstrates the capability of CFD methods in capturing stall-delay phenomena at the inboard blade sections. It is noted in Figs. 6.25 and 6.26 that the agreement is best at $U=7\text{m/s}$, for which the flow is known to be attached. At higher wind speeds however, C_n predictions by *EllipSys3D* tend to be slightly over-predicted at the inboard sections. This is attributed to the flow turbulence model embedded in the CFD code. At 10m/s , a dip in both C_n and C_t is predicted between $r/R = 0.5$ and 0.7 by *EllipSys3D*. However in the measured data, this dip is not observed in C_n . This may be due to the deficiencies of the CFD models in modelling accurately laminar-to-turbulent transition of the flow on the upper blade surface.

The induction factors a_1 and $a_{1,c}$ obtained by *HAWT_FWC* (plotted in Figs. 6.21(a) and (d)) were compared with a_1 derived by *EllipSys3D*. The comparison is presented in Fig. 6.27. At the low wind speed of $U=7\text{m/s}$ (small angles of attack), the agreement in a_1 predicted by the two different codes is very good (see Fig. 6.27(a)). But discrepancies in a_1 are observed at higher windspeeds. Since such discrepancies are only found at high windspeeds which cause large angles of attack at the blades, it is expected that the discrepancies are due to the deficiencies of the vortex model embedded in *HAWT_FWC*. As already described in the previous section, a vortex model in which the blades are modelled as lifting lines with only a single vortex sheet emerging from the blades' trailing edge may be insufficient to model the flow around the blades at high angles of attack, especially when the flow is massively separated (see Fig. 6.24). Recall also that the largest discrepancies in the *LFA* comparison (refer to previous section) were also noted at the higher windspeeds. On the other hand, CFD is more physically comprehensive in modelling the flow locally around the blades at high angles of attack.

Since the angle of attack in *HAWT_FWC* is based on $a_{1,c}$ while that in *EllipSys3D* is based on a_1 , then the differences between these induction factors (see Fig. 6.27) result in different

spanwise distributions for the angle of attack. The latter distributions are shown in Fig. 6.28. Because the results for $a_{i,c}$ from *HAWT_FWC* and a_i in *EllipSys3D* differ considerably from each other (especially at high windspeeds), it is expected that the angle of attack distribution would be very much different. On the other hand, these differences are negligible for $r/R > 0.5$ at all windspeeds. This is because the induced velocities are very small compared to U and $r\Omega$.

Fig. 6.29 compare the C_t - α and C_d - α curves for the different spanwise locations being predicted by *HAWT_FWC* and *EllipSys3D*. In general, the relations were found to be reasonably close. It should be kept in mind that the two codes use a different definition for the angle of attack. But since for $r/R > 0.5$ the angles of attack from both methods are very close (see Fig. 6.28), then the C_t and C_d values can be compared. This is not the case for spanwise locations $r/R = 0.3$ and 0.47 since differences in α result in differences in C_t and C_d .

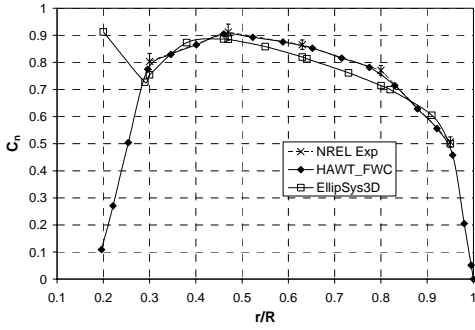


Fig. (a): $U = 7\text{m/s}$

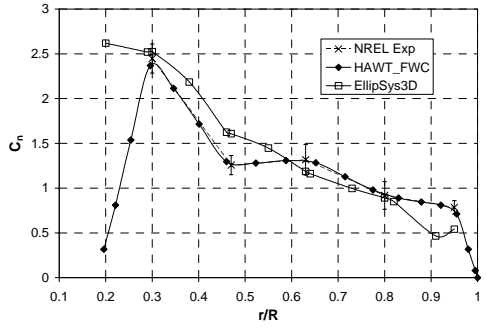


Fig. (d): $U = 15\text{m/s}$

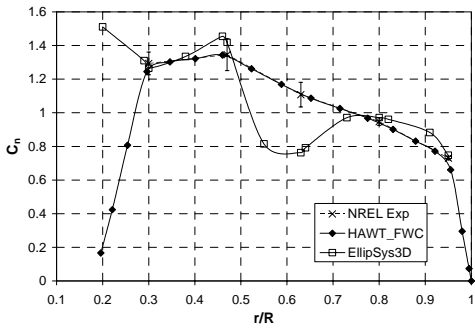


Fig. (b): $U = 10\text{m/s}$

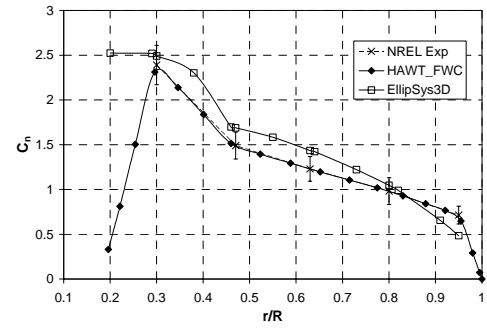


Fig. (e): $U = 20\text{m/s}$

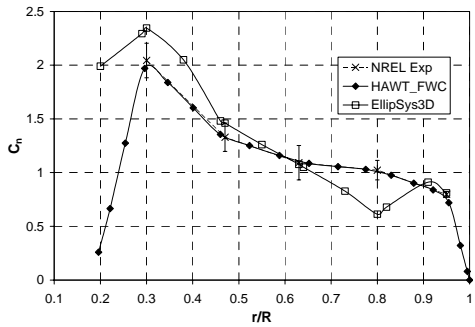


Fig. (c): $U = 13\text{m/s}$

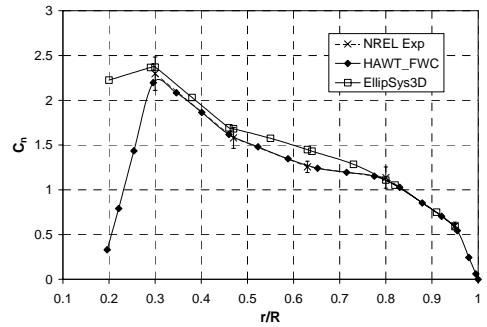


Fig. (f): $U = 25\text{m/s}$

Figure 6.25 – Comparison of the spanwise distributions of the normal coefficient along the blades at $\psi=0^\circ$.

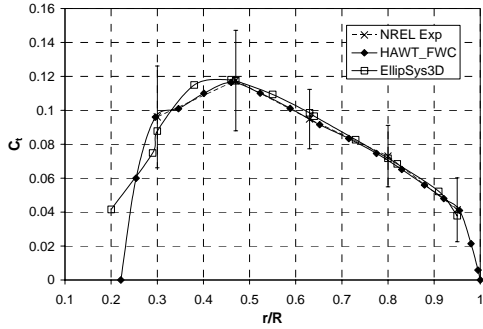


Fig. (a): $U = 7\text{m/s}$

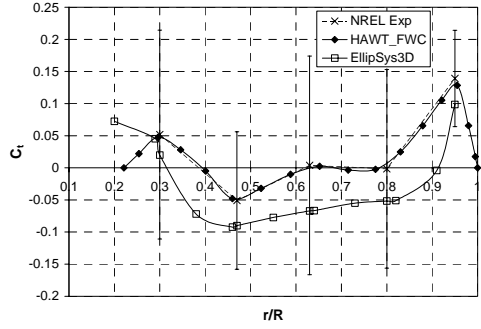


Fig. (d): $U = 15\text{m/s}$

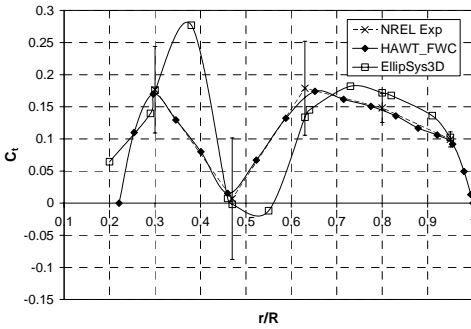


Fig. (b): $U = 10\text{m/s}$

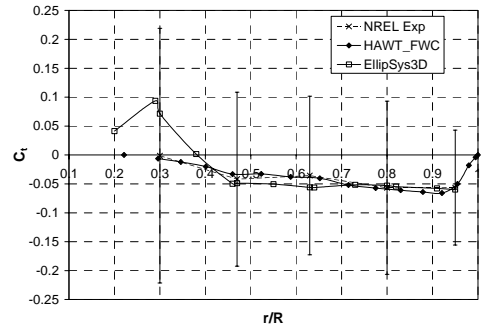


Fig. (e): $U = 20\text{m/s}$

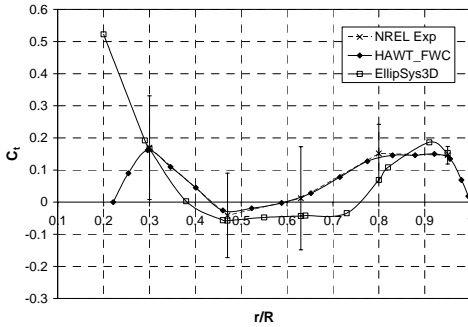


Fig. (c): $U = 13\text{m/s}$

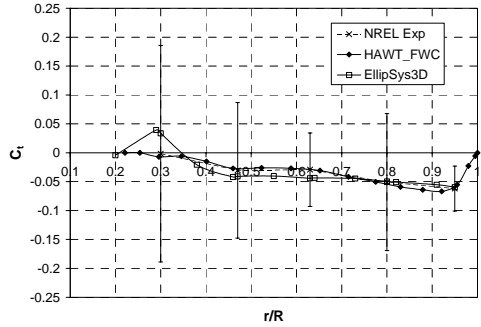


Fig. (f): $U = 25\text{m/s}$

Figure 6.26 – Comparison of the spanwise distributions of the tangential coefficient along the blades at $\Psi=0^\circ$.

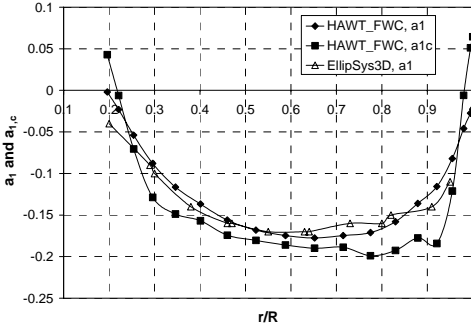


Fig. (a): $U = 7\text{m/s}$

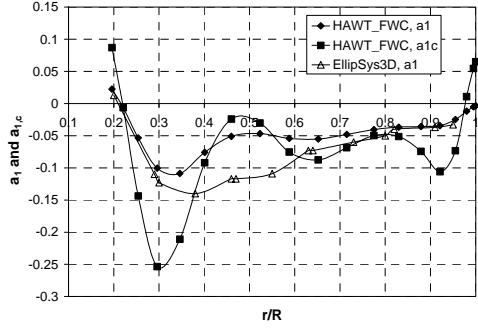


Fig. (d): $U = 15\text{m/s}$

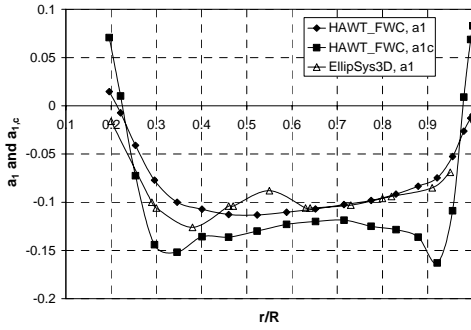


Fig. (b): $U = 10\text{m/s}$

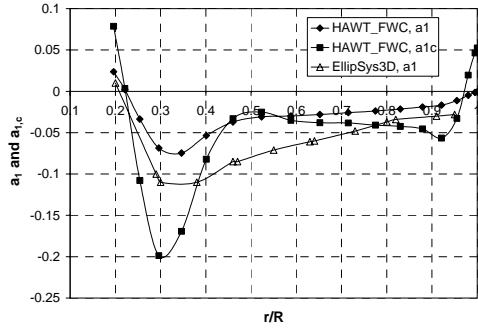


Fig. (e): $U = 20\text{m/s}$

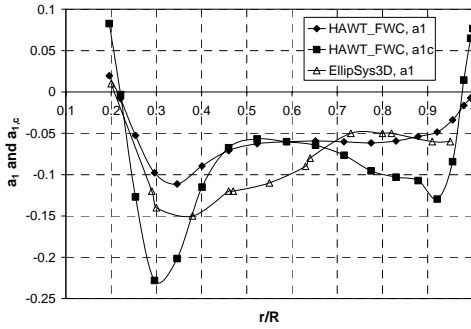


Fig. (c): $U = 13\text{m/s}$

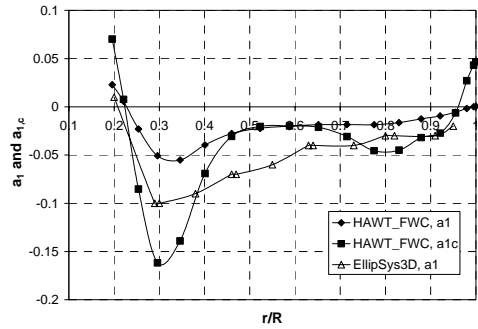


Fig. (f): $U = 25\text{m/s}$

Figure 6.27 – Comparison of the spanwise distributions of the induction factors along the blades at $\psi=0^\circ$.

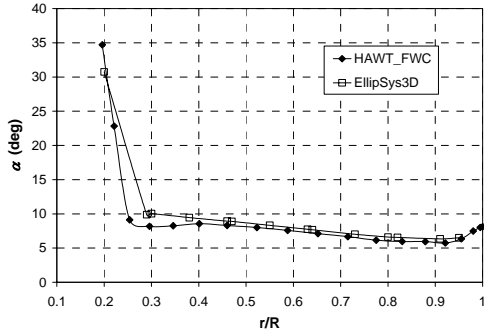


Fig. (a): $U = 7\text{m/s}$

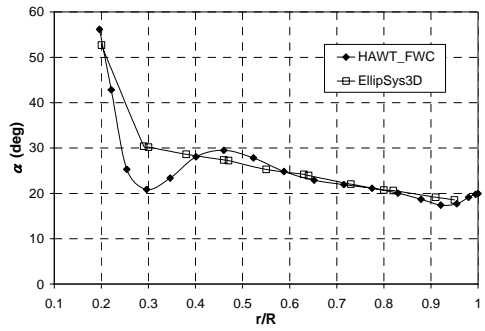


Fig. (d): $U = 15\text{m/s}$

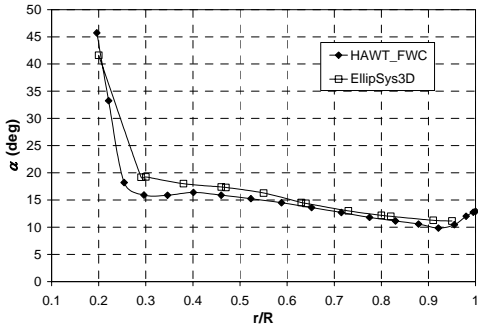


Fig. (b): $U = 10\text{m/s}$

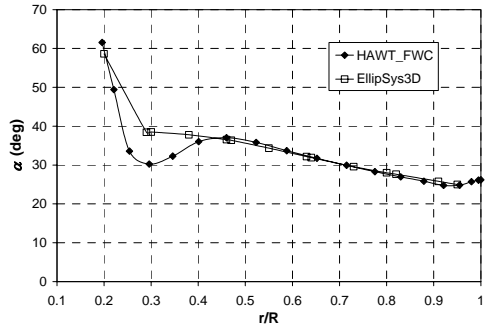


Fig. (e): $U = 20\text{m/s}$

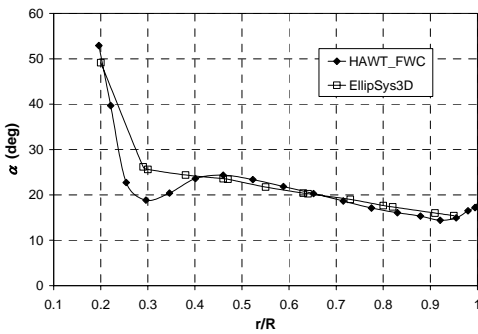


Fig. (c): $U = 13\text{m/s}$

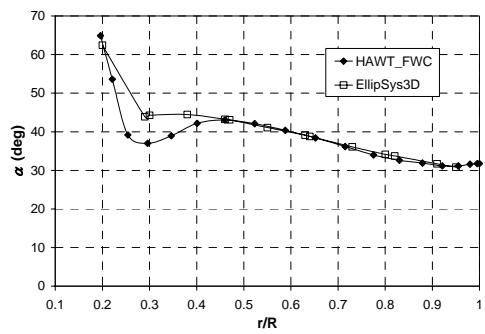


Fig. (f): $U = 25\text{m/s}$

Figure 6.28 – Comparison of the spanwise distributions of the angle of attack along the blades at $\psi=0^\circ$.

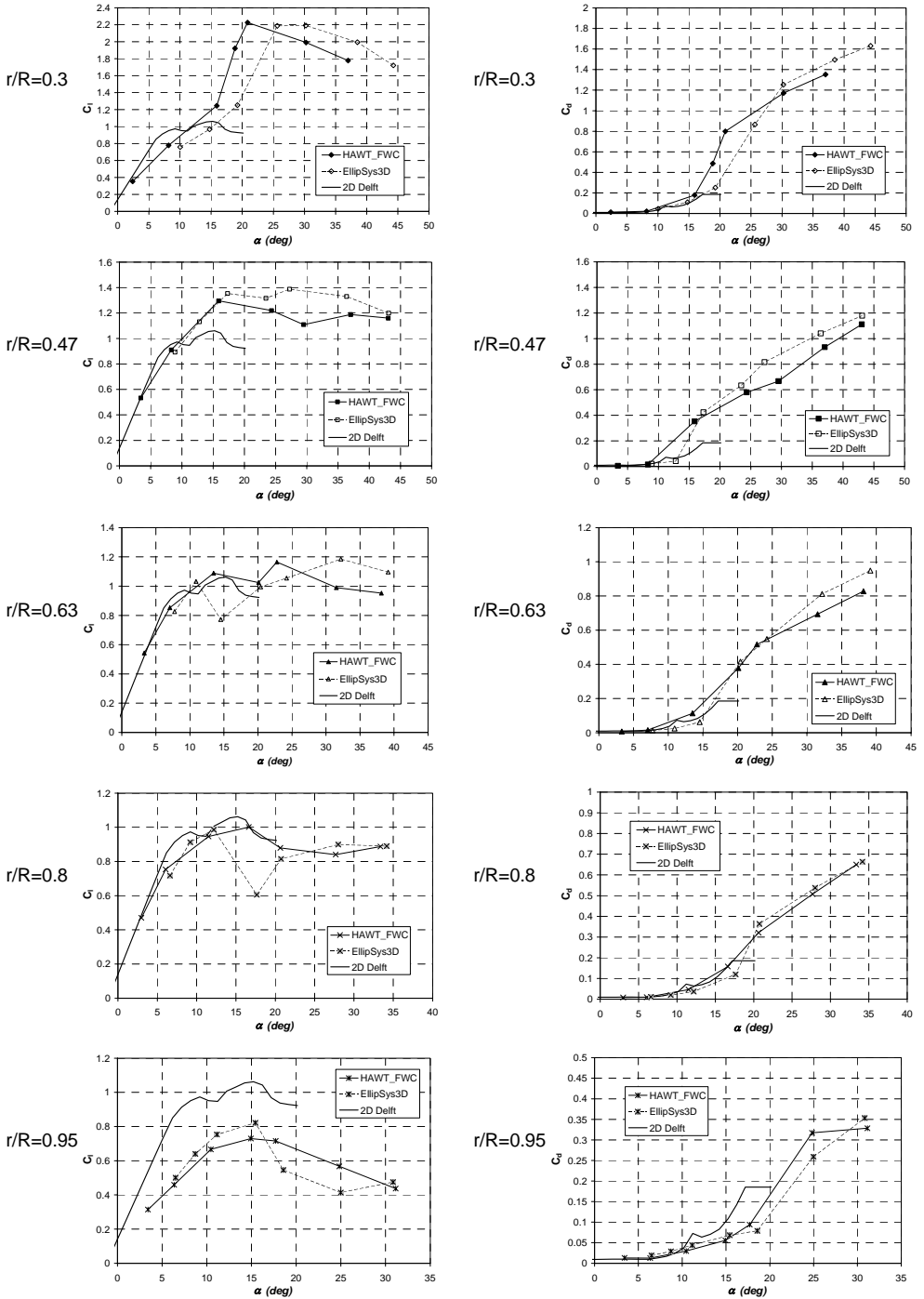


Figure 6.29 – Comparison of the derived aerofoil data at $\Psi=0^\circ$.

6.3.3 Yawed Conditions

This section describes the computational work carried out for yawed conditions ($\Psi=30^\circ$) for windspeeds $U = 5, 7, 10, 13$ and 15m/s .

A. Selecting Free-Wake Model Parameters

Selection of HAWT_FWC parameters n , $\Delta\phi$ and $nRev$

In all the free-wake computations at $\Psi=30^\circ$, n and $\Delta\phi$ were chosen to be equal to 21 and 10° , respectively. These values were found to provide sufficient numerical accuracy, even in yawed conditions. The following values for $nRev$ were found to be adequate: For $U=5\text{m/s}$, $nRev$ was set to 5. For $U=7\text{m/s}$ and 10m/s , $nRev$ was set to 4 while for $U=13$ and 15m/s , $nRev$ was set to 3. With these values, the near wake extended downstream (along the Y -axis) by $3.6R, 4.4R, 6R, 6R$ and $7R$ at $U=5, 7, 10, 13, 15\text{m/s}$ respectively. The resulting values for the percentage discrepancy for wake periodicity (ξ_{wp} , computed using Eq. 5.15, Chapter 5) at all radial locations were $<1.5\%$ while the far wake was enough downstream such that its contribution to the induction at the rotorplane was kept below 3% of the total induction.

Selection of HAWT_FWC parameters δ_v and S_c

As discussed already in section 6.3.2, Part A, it is very difficult to select the optimum values for (δ_v, S_c) used in the vortex models to cater for viscous effects. This is even more difficult when modelling yawed conditions in which these effects become subject to dynamic flow influences. Due to this difficulty, an analysis was therefore carried out to investigate the sensitivity of $u_{a,c}$ to different values of (δ_v, S_c) using a similar approach as that performed in axial conditions. The analysis was performed at two windspeeds (7 and 13m/s) which yielded attached flow and separated flow conditions at the blades, respectively. Four different sets of values of (δ_v, S_c) were used: (10,0.1), (100,1), (500,1) and (500,10). Figs. 6.30 and 6.31 illustrate the resulting spanwise variations at different blade azimuth positions ($0^\circ, 120^\circ$ and 240°). It is observed that the sensitivity of $u_{a,c}$ at the first 3 sets of values of (δ_v, S_c) is very small. But a notable relative discrepancy is seen for (500,10). However, as explained in section 6.3.2, Part A. (see Fig. 6.12), the values (500,10) are too large to be realistic and in all the free-wake computations at $\Psi=30^\circ$, (δ_v, S_c) were also taken to be equal to (500,1), as for axial conditions.

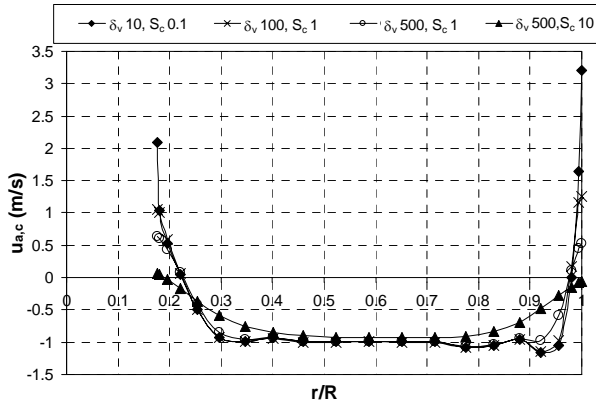


Fig (a): $\phi = 0 \text{ deg}$

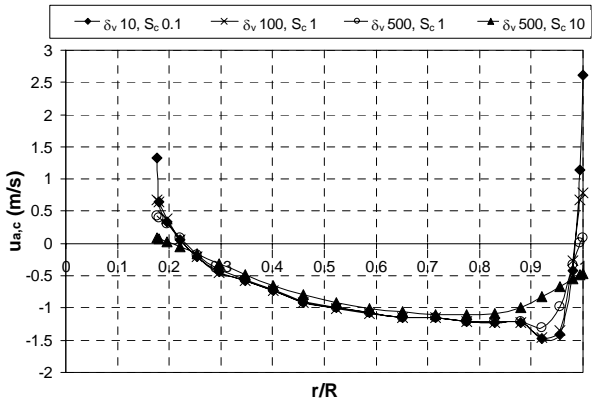


Fig (b): $\phi = 120 \text{ deg}$

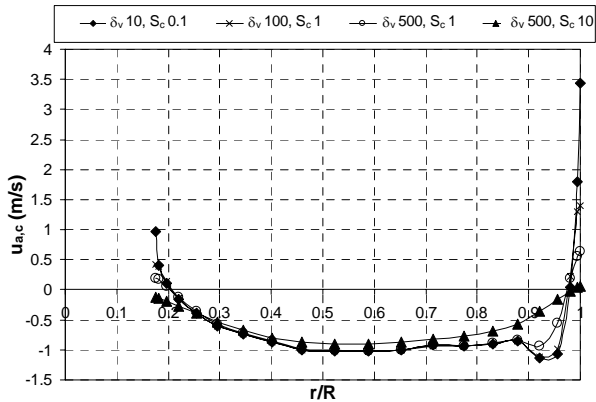


Fig (c): $\phi = 240 \text{ deg}$

Figure 6.30 – Effect of viscous parameters (δ_v, S_c) on the spanwise distribution of $u_{a,c}$ at different blade azimuth angles, $U=7\text{m/s}$.

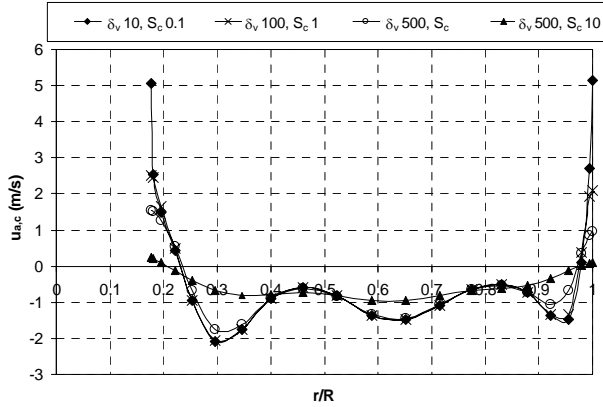


Fig (a): $\phi = 0 \text{ deg}$

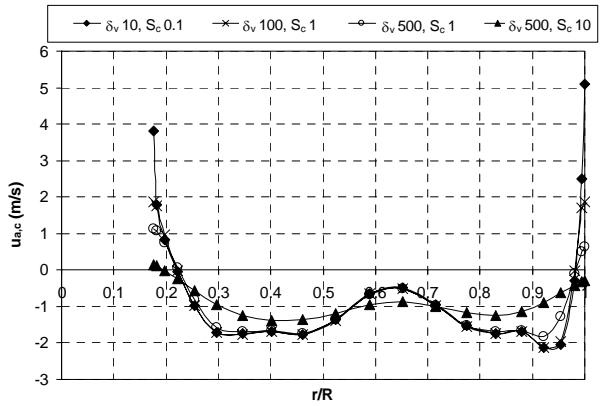


Fig (b): $\phi = 120 \text{ deg}$

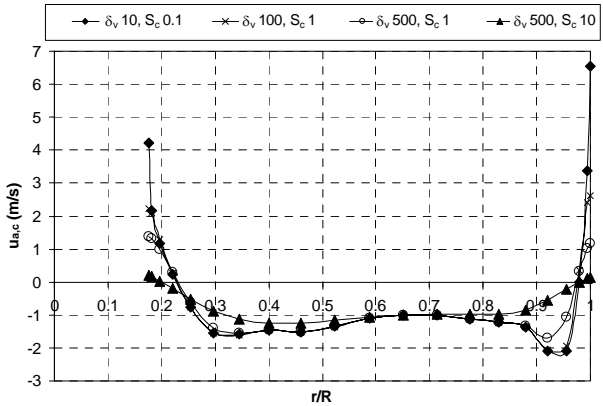


Fig (c): $\phi = 240 \text{ deg}$

Figure 6.31 – Effect of viscous parameters (δ_v, S_c) on the spanwise distribution of $u_{a,c}$ at different blade azimuth angles, $U=13 \text{ m/s}$.

Selection of HAWT_FWC parameters for the far wake model

For the far wake parameters, the azimuthal step was always equal to $\Delta\phi$ (i.e. 10°), while the number of helical revolutions (*nfwRev*) was kept constant equal to 10 for all calculations. The prescribed helical pitch (*pfw*) and wake skew angle (χ_s) were varied depending on the windspeed. To determine reasonable values for the prescribed helical pitch and wake skew angle, preliminary calculations were carried out with the same free-wake model and an estimate was taken from the near wake geometry.

B. Results and Discussion

This section describes the results obtained from a converged solution in the angle of attack from the NREL blade pressure measurements at windspeeds 5, 7, 10, 13 and 15m/s and at a yaw angle of 30° using the procedure of Fig. 6.6. The parameters given in section A. above were used in *HAWT_FWC*.

Variation of α , $\dot{\alpha}$, C_l and C_{dp} with blade azimuth angle (ϕ)

Figs. 6.32(a)-(e) illustrate the variations of the converged angle of attack, the rate of change of the angle of attack and the lift and drag coefficients with the blade azimuth angle at each of the different tunnel wind speeds. For all windspeeds, the angle of attack varies periodically with the blade azimuth angle. At $U=5\text{m/s}$, a gradual phase shift is observed in the angle of attack when moving outboard from $r/R=0.3$ to 0.95 . At $r/R=0.3$, the angle of attack is minimum at 210° while at $r/R=0.95$ the minimum occurs at 120° . For the higher windspeeds however ($U=7, 10, 13$ and 15m/s), this phase shift is not noted and the angle of attack is minimum when the blade is approximately at the 180° position and reaches a maximum when the blade is at the $0/360^\circ$ position. For a particular wind speed, both the mean and cyclic components of the angle of attack are larger at the inboard blade sections, implying that the inboard sections experience higher unsteady effects and are first to experience stall. Increasing the windspeed increases both the mean and cyclic components of the angle of attack.

In Figs. 6.32(a)-(e) it may also be noted that the time rate of change of angle of attack ($\dot{\alpha}$) varies also periodically with blade azimuth angle at all wind speeds. The rate of change of angle of attack is negative during approximately blade angles 0° to 180° while it is positive from about 180° to 360° . The inboard blade sections tend to experience the highest rates of change in the angle of attack, occurring at approximately blade angles 90° and 270° . Increasing the windspeed while keeping the rotor shaft speed constant results in higher values for $\dot{\alpha}$. At $U=5\text{m/s}$, $\dot{\alpha}$ at $r/R=0.3$ is equal to about $\pm 25\text{deg/s}$ while at $U=15\text{m/s}$, this reaches maximum values of about $\pm 200\text{deg/s}$.

With regards to the variation of the lift coefficient with blade azimuth angle, it may be observed that, at each windspeed, the inboard regions of the blades experience higher values in both the mean and cyclic components of C_l . At low windspeeds ($U=5, 7$ and 10m/s), the variation of C_l with ϕ is periodic and quite regular, reaching a maximum value at blade position $0/360^\circ$ and a minimum value at about 180° . At the higher wind speeds, ($U= 13$ and 15m/s), the variation is no longer regular.

The pressure drag coefficients (C_{dp}) are very small at low wind speeds ($U=5$ and 7m/s). But as the windspeed is increased, the pressure drag coefficient values increase rapidly, the highest values being at the inboard blade sections at blade angles $0\text{-}120^\circ$ and $240\text{-}360^\circ$.

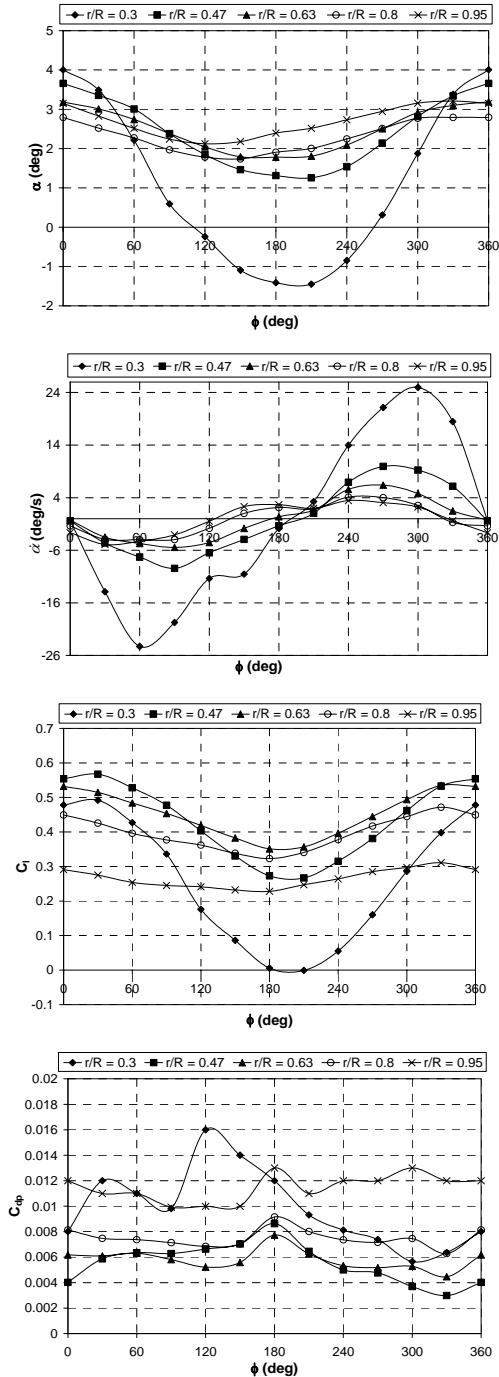


Fig. 6.32(a): α , $\dot{\alpha}$, C_l and C_{dp} at $U = 5\text{m/s}$

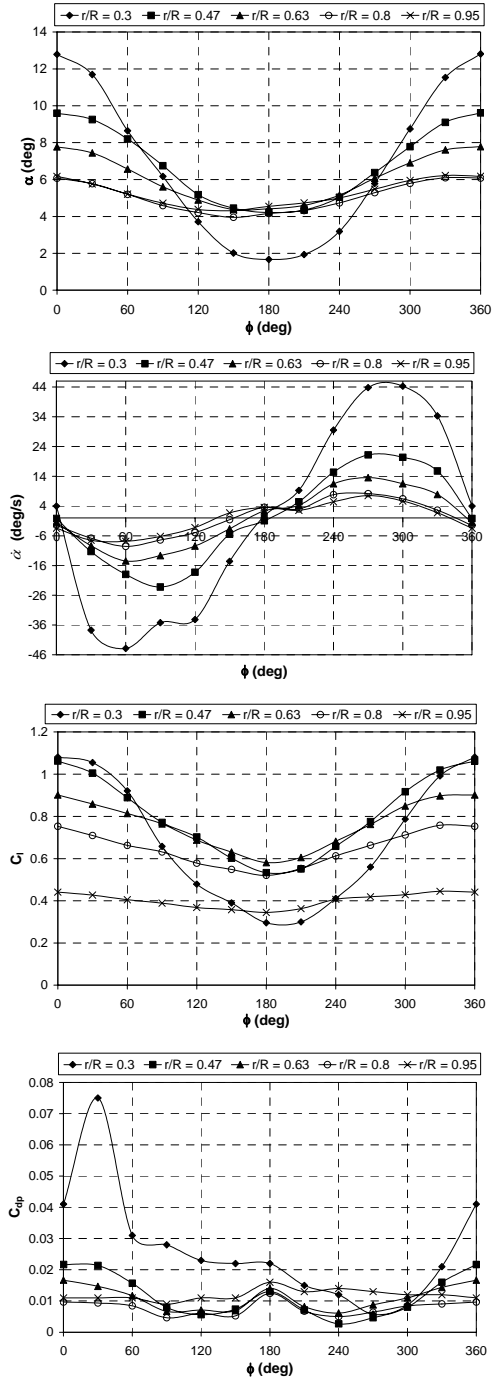


Fig. 6.32(b): α , $\dot{\alpha}$, C_l and C_{dp} at $U = 7\text{m/s}$

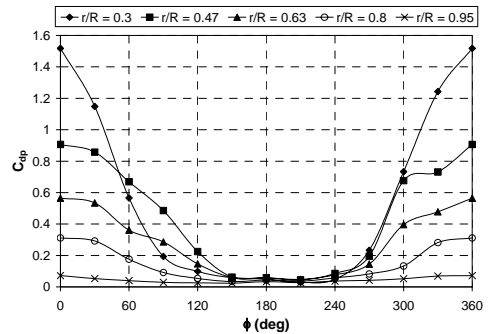
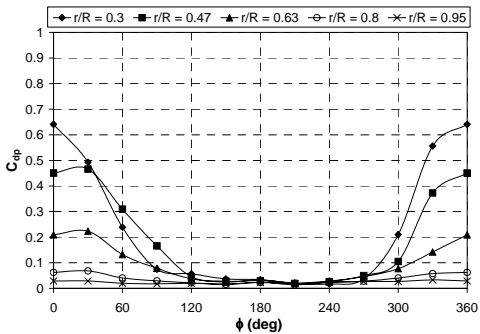
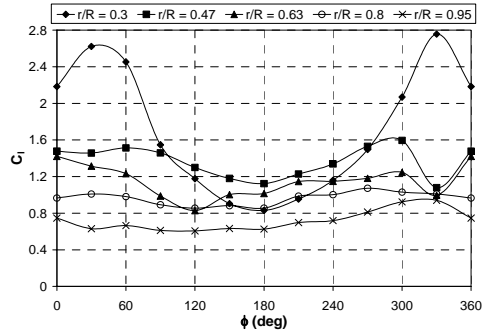
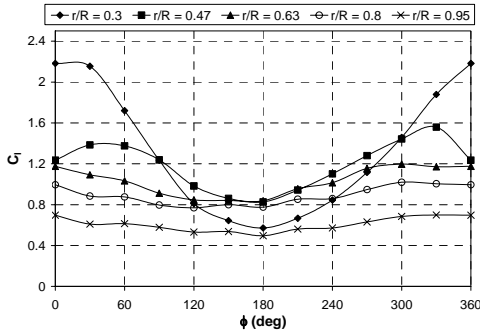
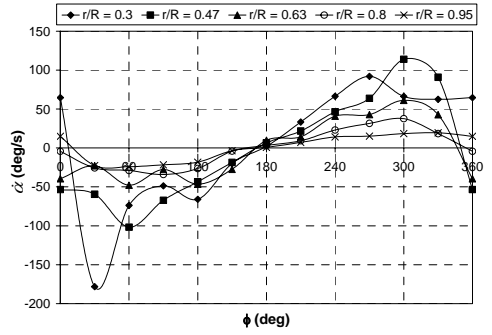
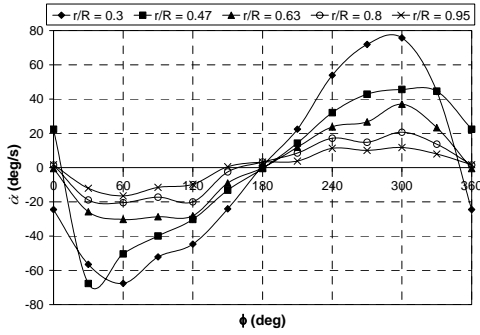
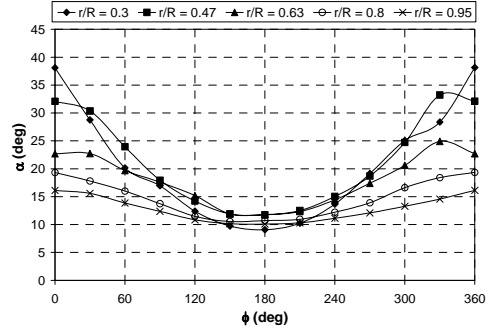
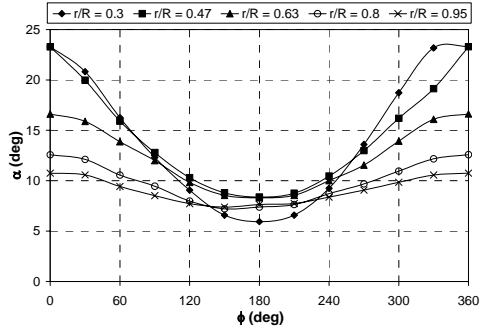


Fig. 6.32(c): α , $\dot{\alpha}$, C_i and C_{dp} at $U = 10$ m/s

Fig. 6.32(d): α , $\dot{\alpha}$, C_i and C_{dp} at $U = 13$ m/s

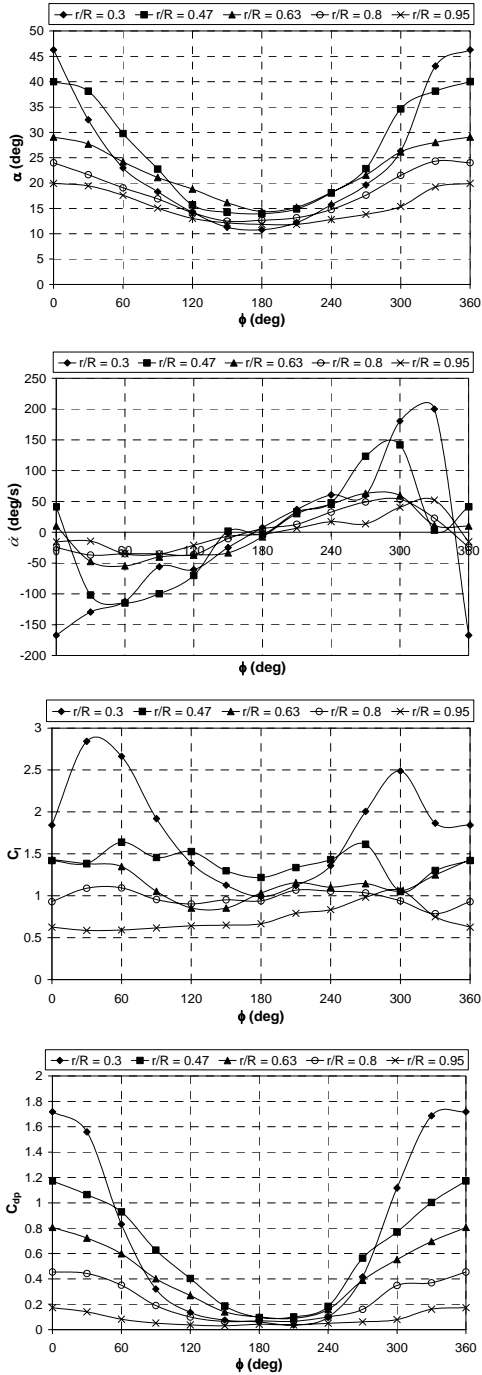


Fig. 6.32(e): α , $\dot{\alpha}$, C_t and C_{dp} at $U = 15\text{m/s}$

Hysteresis loops C_l - α and C_{dp} - α

From the data presented in Figs. 6.32, it is possible to derive the unsteady aerofoil hysteresis loops for C_l - α and C_{dp} - α . Figs. 6.33(a)-(j) illustrate the hysteresis loops for the different wind speeds and radial locations. The 2D steady aerofoil data obtained from the Delft wind tunnel experiments are also shown. The 3D steady aerofoil data, which were derived using the blade pressure measurements for non-yawed conditions together with the free-wake code (see Figs. 6.19) are also included. The hysteresis plots are helpful in establishing whether any particular blade section is operating in an attached or stalled-flow regime. One should keep in mind that in a yawed rotor, these loops are not only due to cyclic pitch variations, but also due to a cyclic variation of the flow velocity relative to the blades. In each of these hysteresis plots, the reduced frequency k is included. k is a parameter characterizing the degree of unsteadiness at which an aerofoil is operating. The reduced frequency is given by the equation:

$$k = \frac{\Omega c}{2V_r} \quad (6.7)$$

where V_r is the relative flow velocity at the aerofoil. When $k=0$, the flow is steady. In accordance with Leishman ([49], page 306), when $0 < k < 0.05$, the unsteadiness in the flow is minimal and the flow may be assumed to be quasi-steady. Higher values of k are considered unsteady. Values of k equal to 0.2 and above are considered highly unsteady.

At $U=5\text{m/s}$ (Figs. 6.33(a) and (b)), the angles of attack are small at all radial locations. Consequently the flow over the blades is fully attached throughout the whole blade revolution. Both the lift and drag hysteresis loops are considerably wide at the inboard sections ($r/R=0.3, 0.47$) which indicates that unsteady effects here are significant even though no stall is present. At the other radial locations ($r/R=0.63, 0.8$ and 0.95), the loops are very narrow and therefore unsteady effects here are negligible. At $U=7\text{m/s}$, the blades are operating at higher angles of attack. No stall is yet present, even though the 2D static stall angle is exceeded at the inboard regions ($r/R=0.3, 0.47$ and 0.63). The C_l - α loops are located around the 3D steady values which explains the fact that stall-delay is present, even in an unsteady environment. At the higher windspeeds ($U=10, 13$ and 15m/s), the angle of attack goes beyond the 3D steady stalling angle, resulting in dynamic stall. It may be observed that much larger phase variations in C_l and C_{dp} are present than for attached flow conditions ($U=5, 7\text{m/s}$). This is a result of significant hysteresis in the flow structures. The values of C_l and C_{dp} at the same angle of attack will vary on whether the flow is separating or re-attaching. In some severe cases however, flow re-attachment may not take place since the minimum angle of attack will be too high. Figs. 6.33 (e)-(j) indicate that dynamic stall is most severe at the inboard blade sections. One may observe that the unsteady lift and drag coefficients may well exceed not only the 2D steady values, but also the 3D steady values derived for non-yawed conditions.

Some important comments concerning the derived hysteresis loops are:

- at each wind speed the hysteresis loops for both C_l and C_{dp} are larger at the inboard blade sections and unsteady effects are less pronounced at the outboard regions. However severe unsteady effects may still take place at the blade tip regions, especially at high angles of attack (refer to Figs. 6.33(g) and (i) for $r/R=0.95$)
- in general, both the C_l and C_{dp} hysteresis loops are closer to the 3D steady values than to the corresponding 2D steady values. This is observed at both attached and stall conditions and it implies that 3D effects have a significant role in the unsteady flow behaviour of wind turbine blades, in particular stall-delay. This implies that a correction for 3D effects is also necessary when correcting 2D static aerofoil data for unsteady aerodynamic conditions.
- The hysteresis loops often change direction from counter-clockwise to clockwise when moving outboard from $r/R=0.3$ to 0.95. This is mainly observed in the lift hysteresis loops at $U = 10$ and 15m/s (see Figs. 6.33(c) and (e)).

Figs. 6.33 show that the obtained values for k at the different radial locations and wind speeds of the NREL rotor. Since in a yawed rotor the flow relative velocity at each blade section (V_r) is a function of blade azimuth angle (ϕ), then the maximum and minimum values are included. The maximum and minimum values of k occur at approximate blade azimuth angles of 0° and 180° respectively. It may be observed that the highest reduced frequencies occur at low r/R values. However, changing the windspeed does not alter significantly the reduced frequencies at each radial position significantly. This is a consequence of the fact that the rotor angular speed is kept constant and the wind tunnel speed is much smaller than the rotor angular speed ($U \ll r\Omega$).

More detailed analysis of the unsteady aerodynamic effects may be carried out by analyzing these derived hysteresis loops in conjunction with the analysis of the unsteady chordwise blade pressure distributions measured in the wind tunnel. The latter analysis is very helpful in identifying the flow characteristics of the blades at each angle of attack, as described by Schreck *et al.* [74, 76].

Bound Circulation Distributions at Blades

Fig. 6.34 illustrates 3D plots of the bound circulation distributions at the blades as a function of radial position (r/R) and blade azimuth angle (ϕ). For low wind speeds ($U=5, 7\text{m/s}$), at which the flow over the blades is considerably attached, the 3D plot takes the form of a saddle. At each blade azimuth angle, the peak bound circulation occurs close to the middle blade section. Also, the peak circulation is highest at blade position equal to $0/60^\circ$ and is lowest at about 180° . At high wind speeds, where separated flow conditions are known to occur ($U=10, 13, 15\text{m/s}$), the saddle-shaped distribution is no longer present and a rather

irregular distribution occurs. The peak bound circulation tends to shift towards the root region of the blade, where in fact the highest lift coefficients are noted. However the peak bound circulation is still observed at blade position $0/360^\circ$. It may be observed from Fig. 6.34 that high windspeeds result in higher levels of bound circulation.

Chapter 6 – Aerodynamic Analysis of the NREL Phase VI Wind Turbine

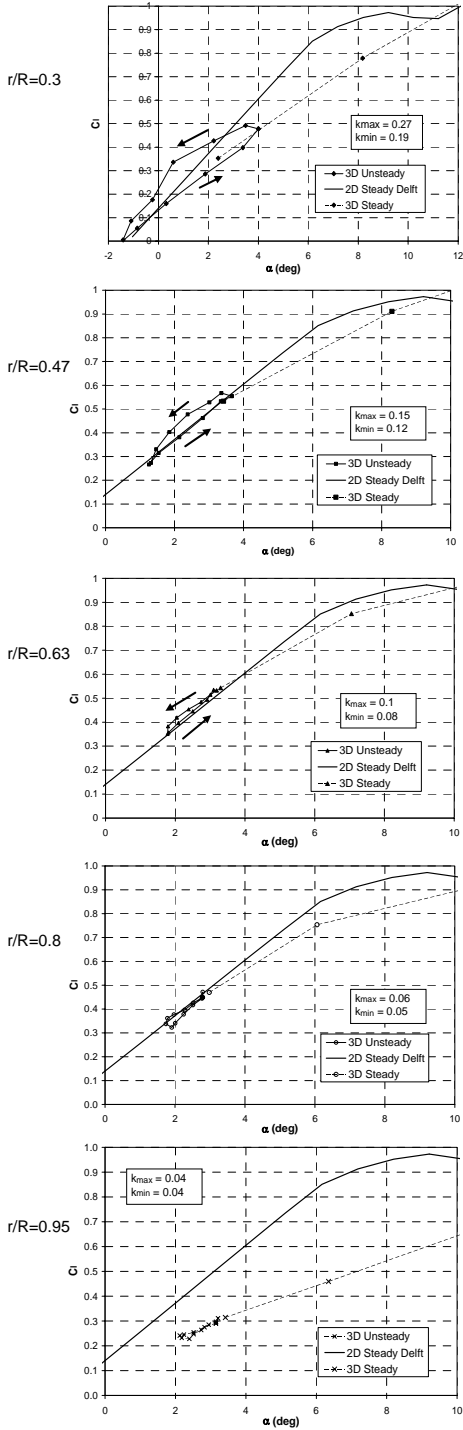


Fig. 6.33(a): C_t - α hysteresis loops at $U=5\text{m/s}$

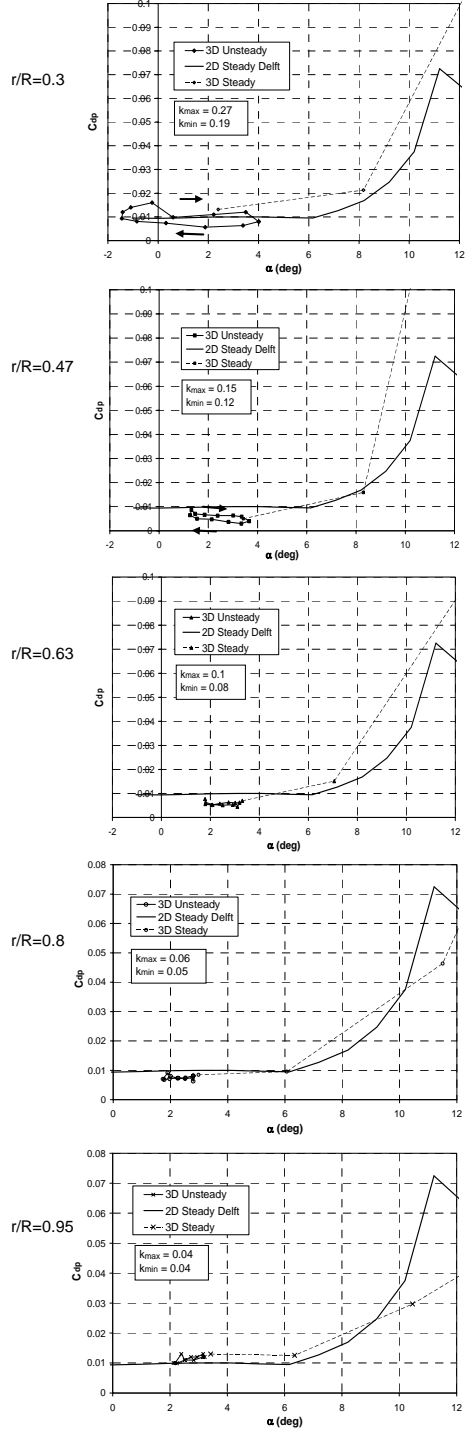


Fig. 6.33(b): C_{dp} - α hysteresis loops at $U=5\text{m/s}$

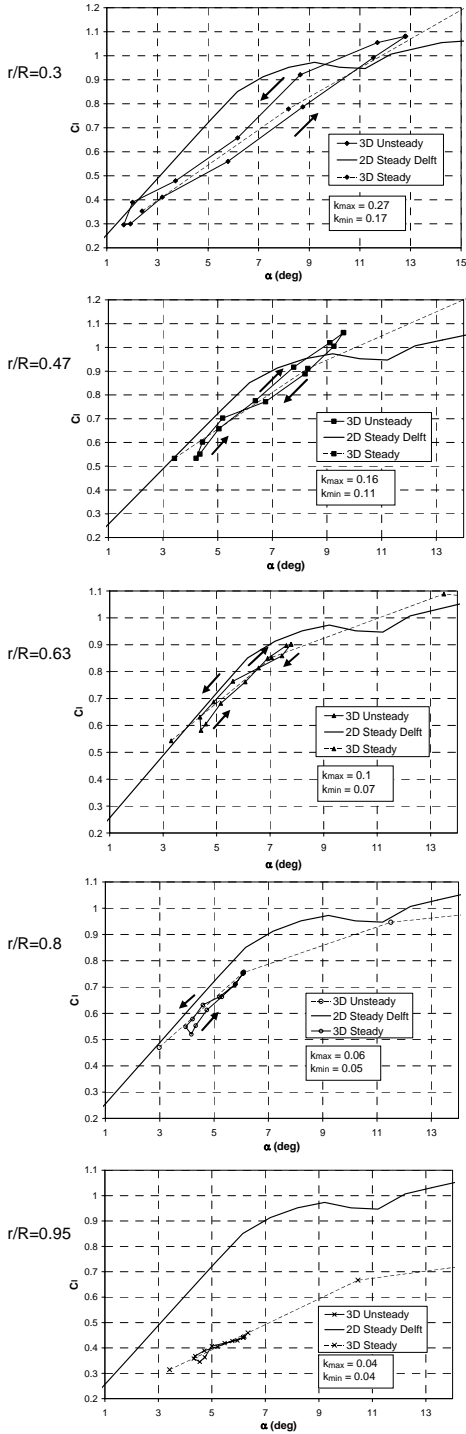


Fig. 6.33(c): C_l - α hysteresis loops at $U=7\text{m/s}$

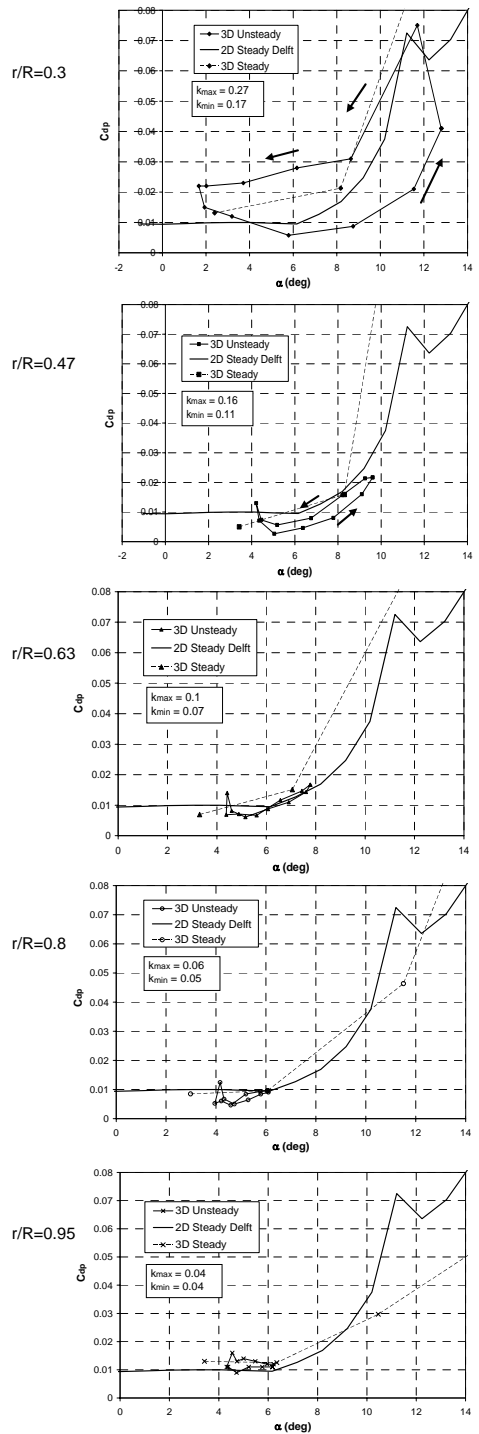


Fig. 6.33(d): C_{dp} - α hysteresis loops at $U=7\text{m/s}$

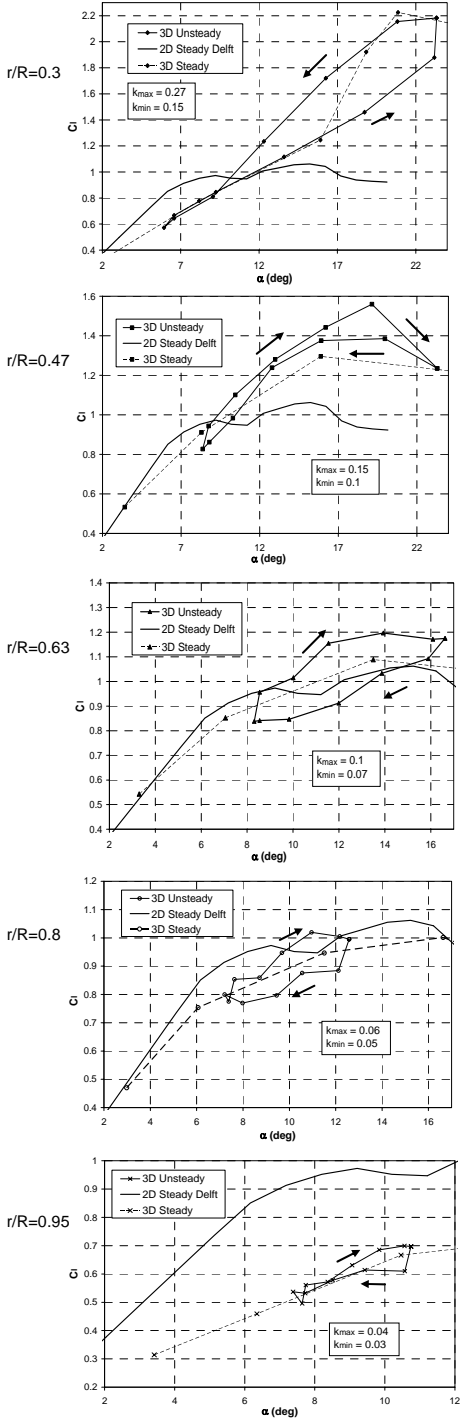


Fig. 6.33(e): C_t - α hysteresis loops at $U=10\text{m/s}$

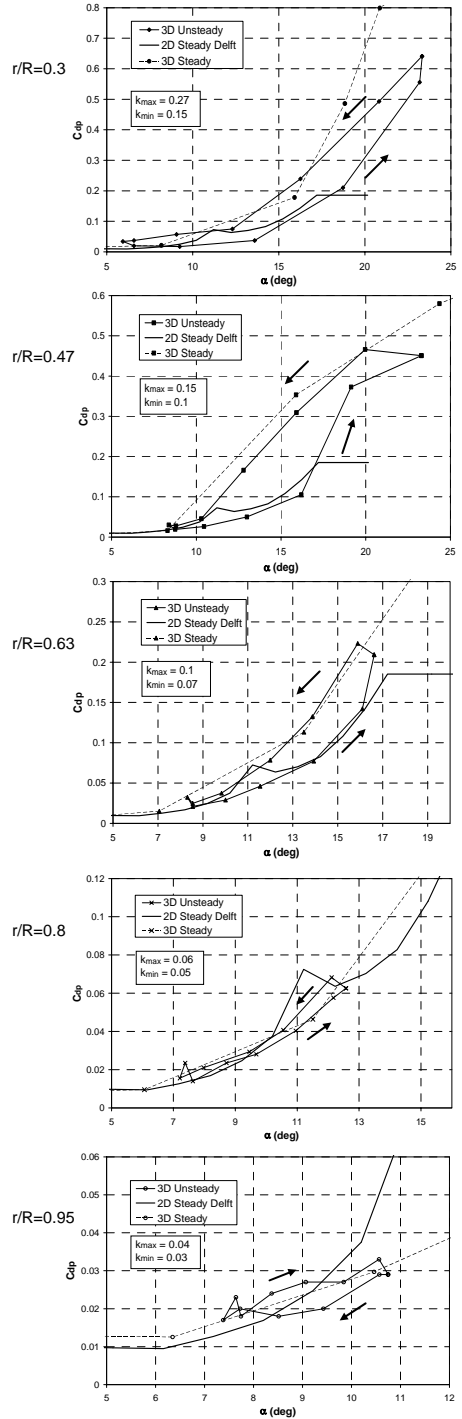


Fig. 6.33(f): C_{dp} - α hysteresis loops at $U=10\text{m/s}$

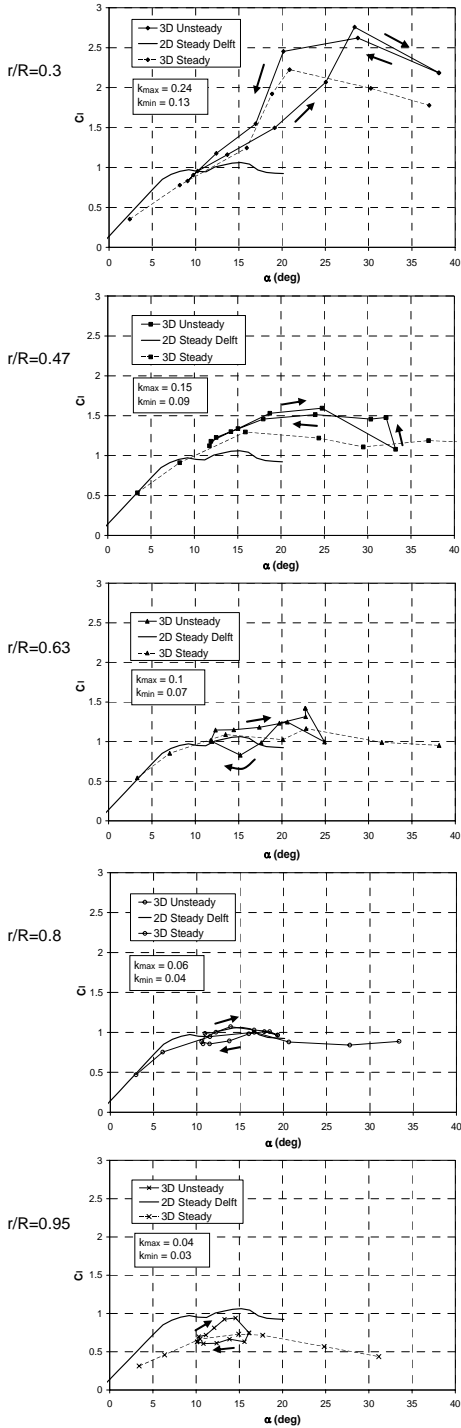


Fig. 6.33(g): C_l - α hysteresis loops at $U=13\text{m/s}$

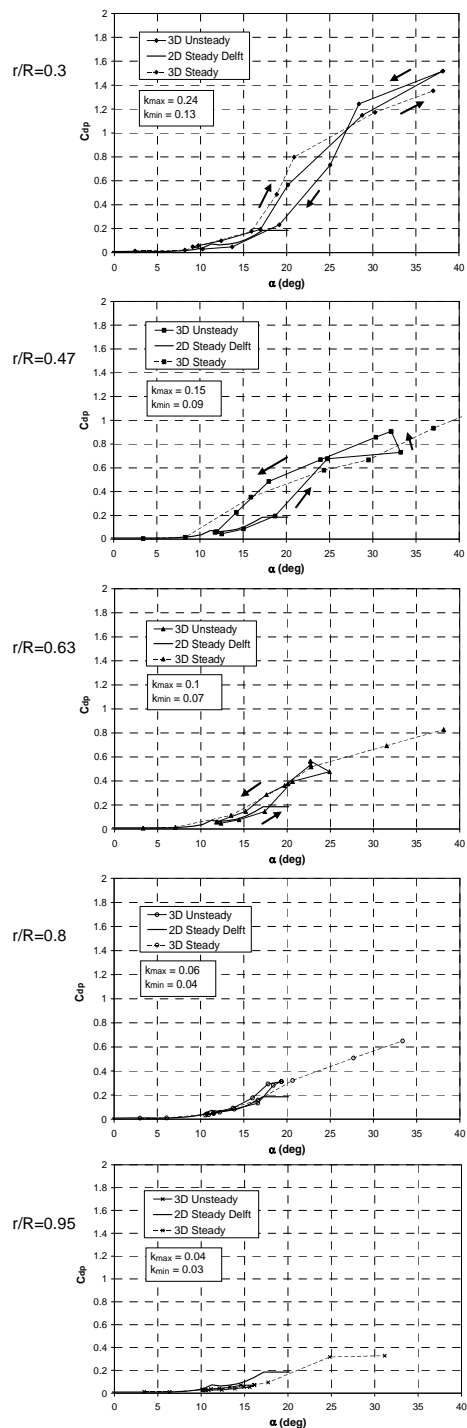


Fig. 6.33(h): C_{dp} - α hysteresis loops at $U=13\text{m/s}$

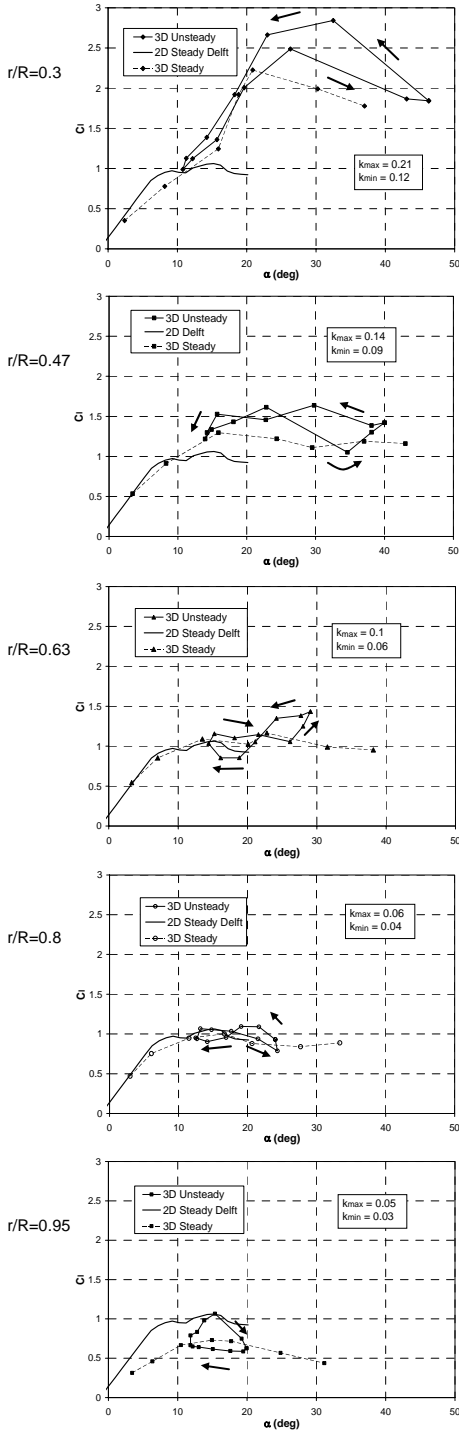


Fig. 6.33(i): C_l - α hysteresis loops at $U=15\text{m/s}$

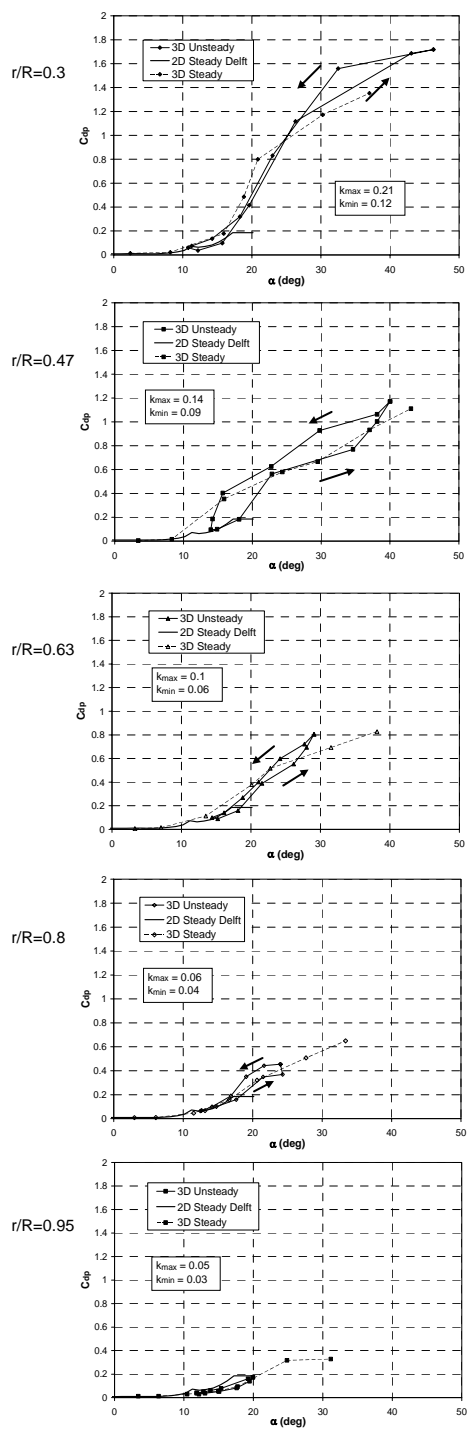


Fig. 6.33(j): C_{dp} - α hysteresis loops at $U=15\text{m/s}$

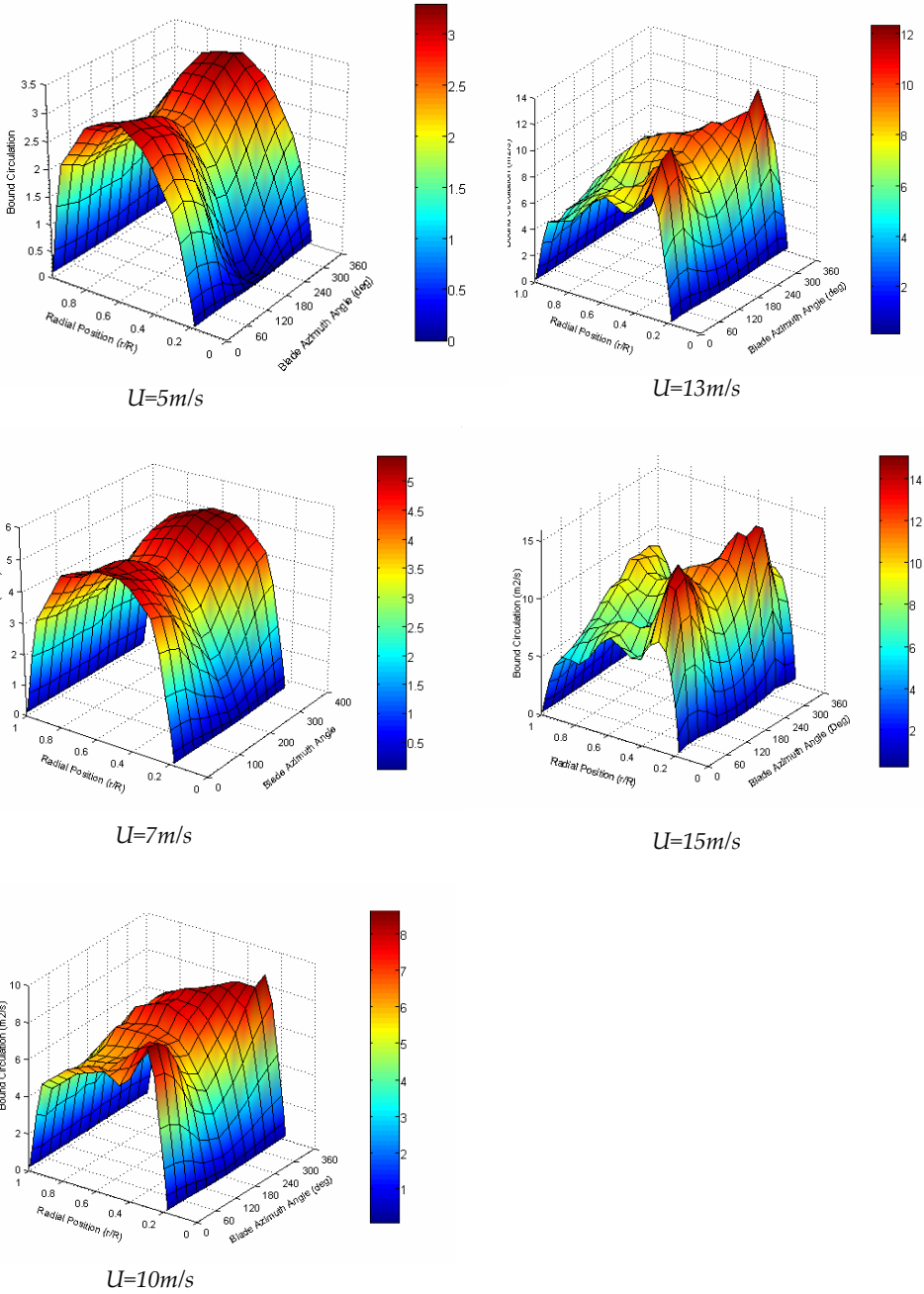


Figure 6.34 - Variation of bound circulation at blades with radial location and blade azimuth angle.

Wake Plots

Figs. 6.35(a)-(j) present the free-wake plots derived from the measured aerodynamic loading on the blades. Colour coding is used to denote the trailing and shed circulation in the near wake. For each windspeed, two plots are presented: one for trailing circulation, the other for shed circulation. From the wake geometry, it is possible to derive the approximate pitch of the wake vortex sheets. In the study this was derived by taking a cross-sectional plane through the free-wake, with the plane being horizontal and passing through the rotor hub. Fig. 6.36 illustrates the derived variation of the wake vortex sheet pitch with the windspeed for yaw angle of 30° . Due to wake skewness resulting from rotor yaw, the wake vortex sheet pitch on the upstream side of the wake is different from that on the downstream side. In Fig. 6.36, the corresponding vortex sheet pitch variation for non-yawed conditions from Fig. 6.18(a) is also included. In both non-yawed and yawed conditions, the vortex sheet pitch increases approximately linearly with wind speed. For the yawed case, the pitches on the upstream and downstream side of the wake tend to be very close. However it may be observed that, for all wind speeds, the rotor yaw decreases the vortex sheet pitch below that for zero yaw. It was very difficult to derive the wake expansion from the wake geometry since this was noted to be very small.

The colour coding in Figs. 6.35 is very helpful in understanding better how the unsteady bound circulation at the blades (refer to Fig. 6.34) eventually diffuses into the wake downstream of the rotor in the form of trailing and shed circulation. The presence of roll-up of the vortex sheets is apparent. Since in a yawed rotor, the bound circulation is a function of rotor azimuth angle, then the wake trailing and shed circulation will be time dependent. Looking at Figs. 6.35 will reveal that, at low windspeeds ($U=5, 7\text{m/s}$), the trailing circulation in the wake tends to be concentrated towards the blade tip and root regions. This is a result of the fact that the bound circulation at the blades is highest at the middle sections, but then decreases steadily to zero towards the blade tip and root (refer to Figs. 6.34). The trailing circulation at the tip region is positive, while it is negative at the root region. For high windspeed conditions however, the bound circulation distribution is irregular and this yields considerable levels of 'horse-shoe' trailing circulation to be released from the middle blade sections. This is especially observed at $U=15\text{m/s}$ (Fig. 6.35(i)). Consequently, the trailing circulation is more dispersed though the wake. The shed circulation levels are small at low wind speeds ($U=5, 7\text{m/s}$) when compared with the trailing circulation. At higher windspeeds ($U=10, 13, 15\text{ m/s}$), higher shed circulation levels are observed at local spots of the wake vortex sheets. However the shed circulation across most of the vortex sheets remains small in magnitude in comparison with the trailing circulation. At low windspeeds, the helical shape of the vortex sheets is well defined, but at the higher windspeeds, the vortex sheets become distorted. This distortion is induced by the unsteady separated air flow formed around the blades which then ends up into the wake.

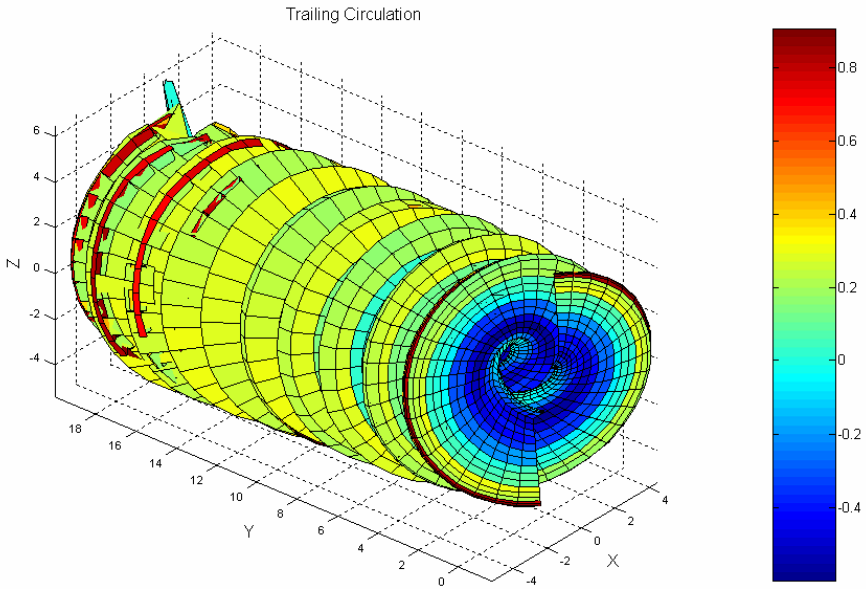


Figure 6.35(a) - Trailing circulation (m^2/s) distribution in wake at $U=5m/s$.

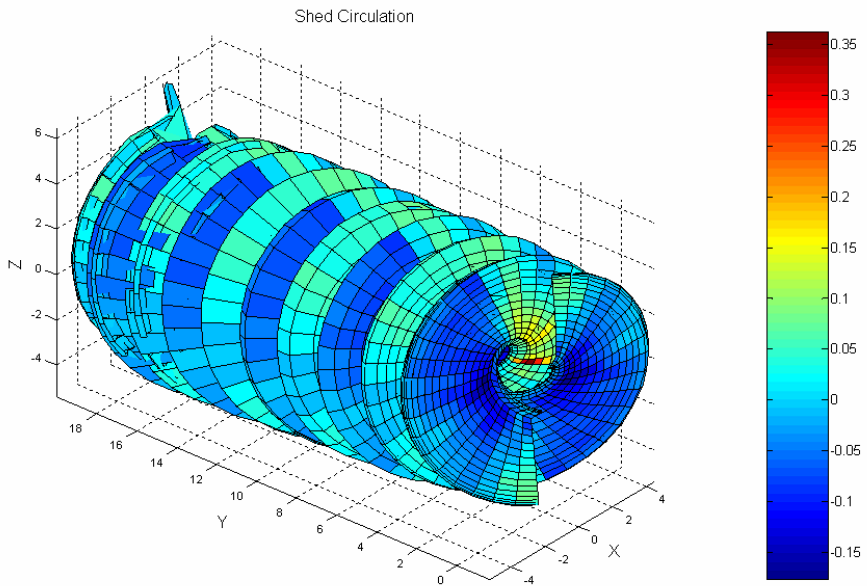


Figure 6.35(b) - Shed circulation (m^2/s) distribution in wake at $U=5m/s$.

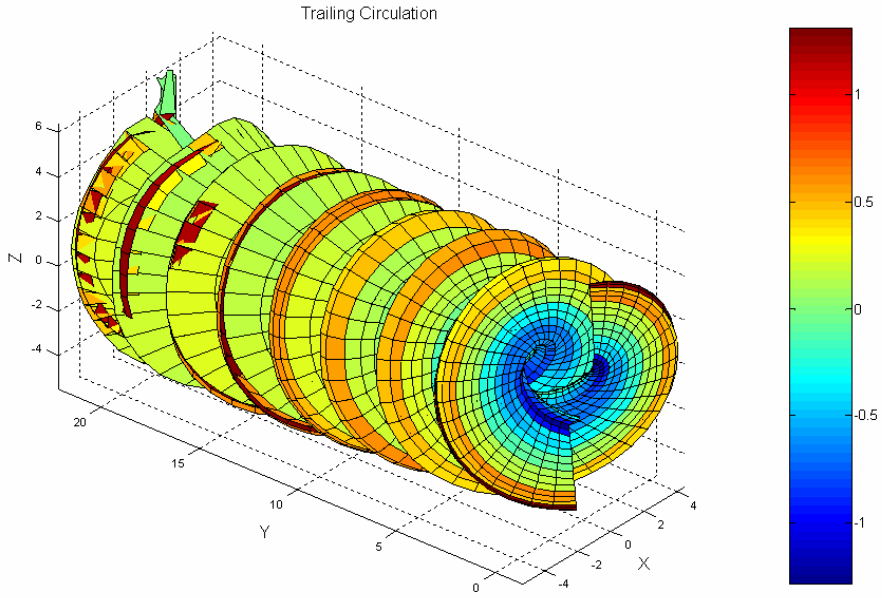


Figure 6.35(c) - Trailing circulation (m^2/s) distribution in wake at $U=7m/s$.

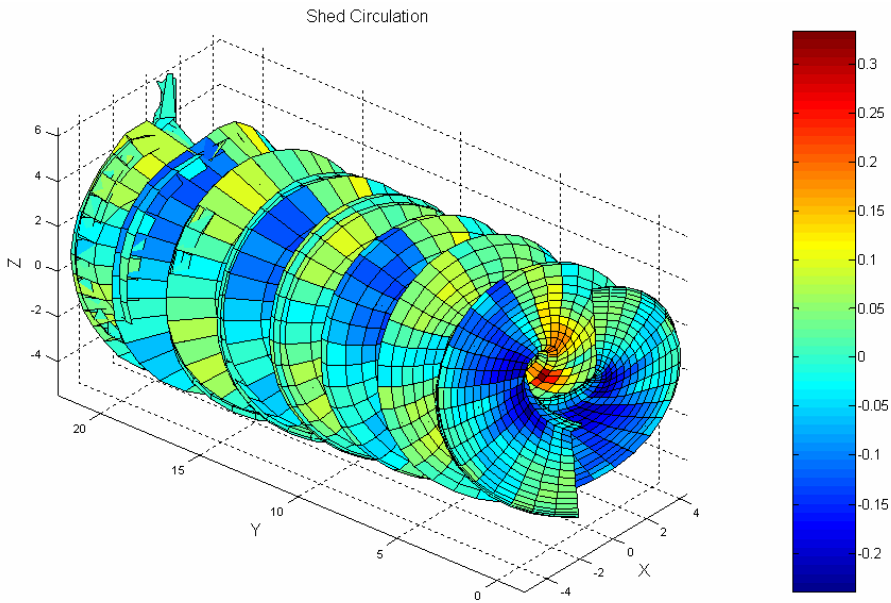


Figure 6.35(d) - Shed circulation (m^2/s) distribution in wake at $U=7m/s$.

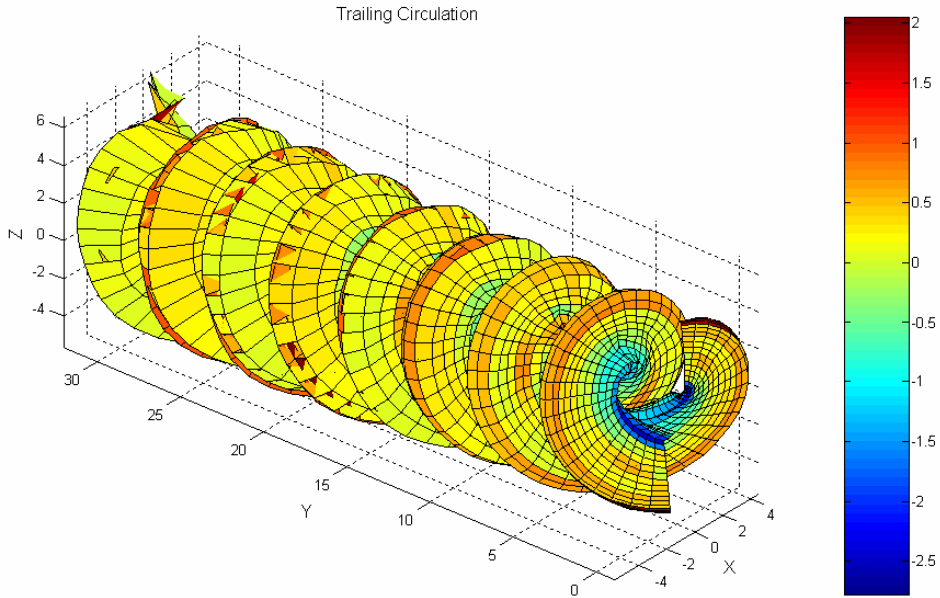


Figure 6.35(e) - Trailing circulation (m^2/s) distribution in wake at $U=10\text{m/s}$.

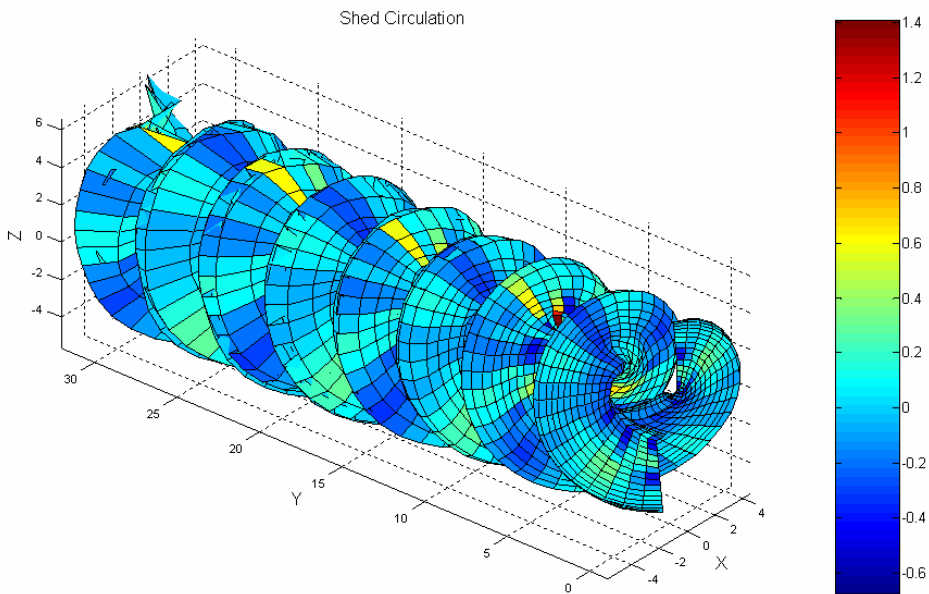


Figure 6.35(f) - Shed circulation (m^2/s) distribution in wake at $U=10\text{m/s}$.

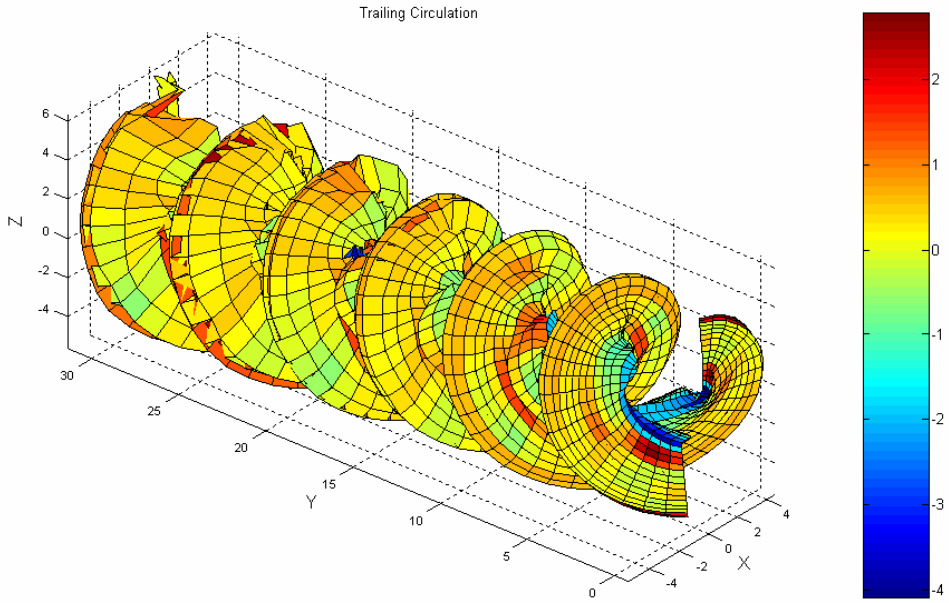


Figure 6.35(g) - Trailing circulation (m^2/s) distribution in wake at $U=13m/s$.

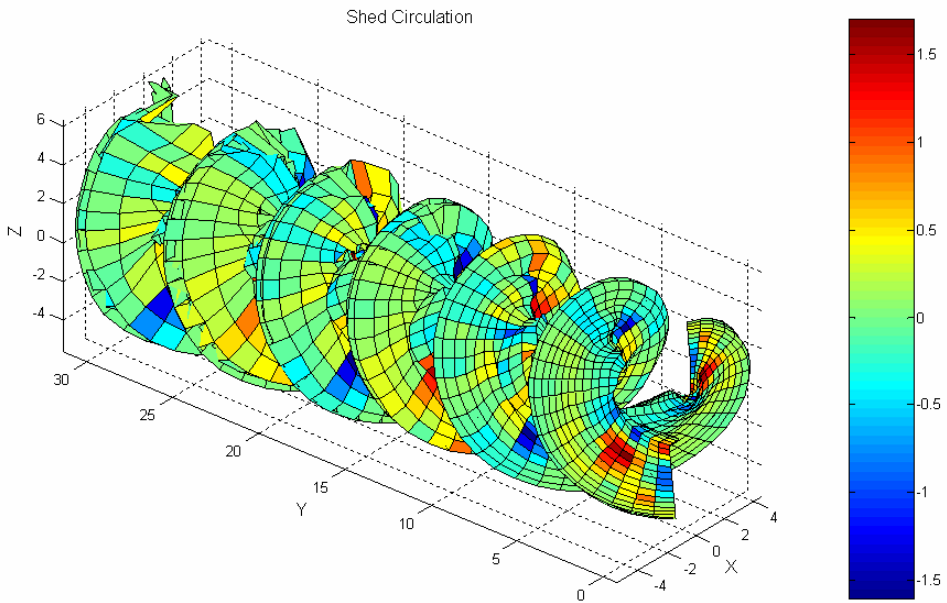


Figure 6.35(h) - Shed circulation (m^2/s) distribution in wake at $U=13m/s$.

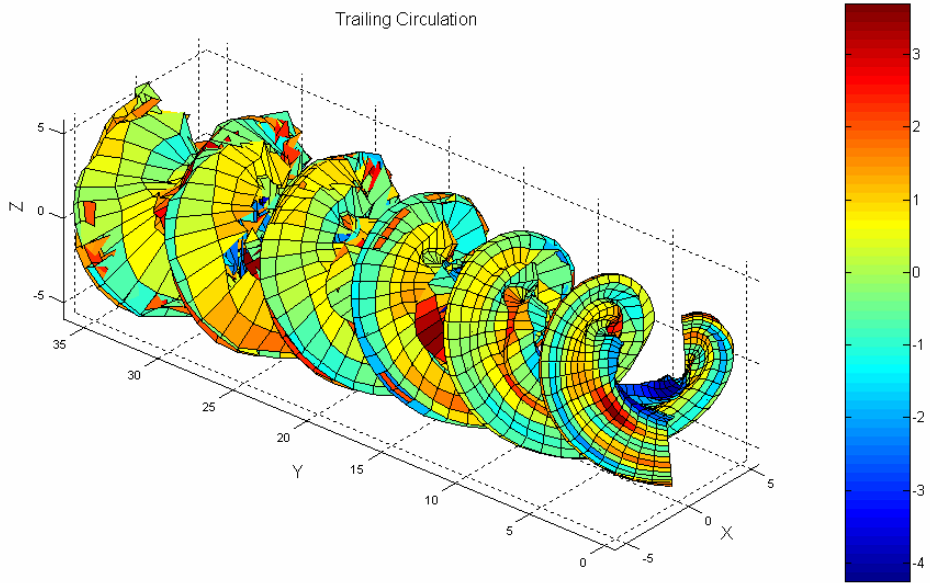


Figure 6.35(i) - Trailing circulation (m^2/s) distribution in wake at $U=15m/s$.

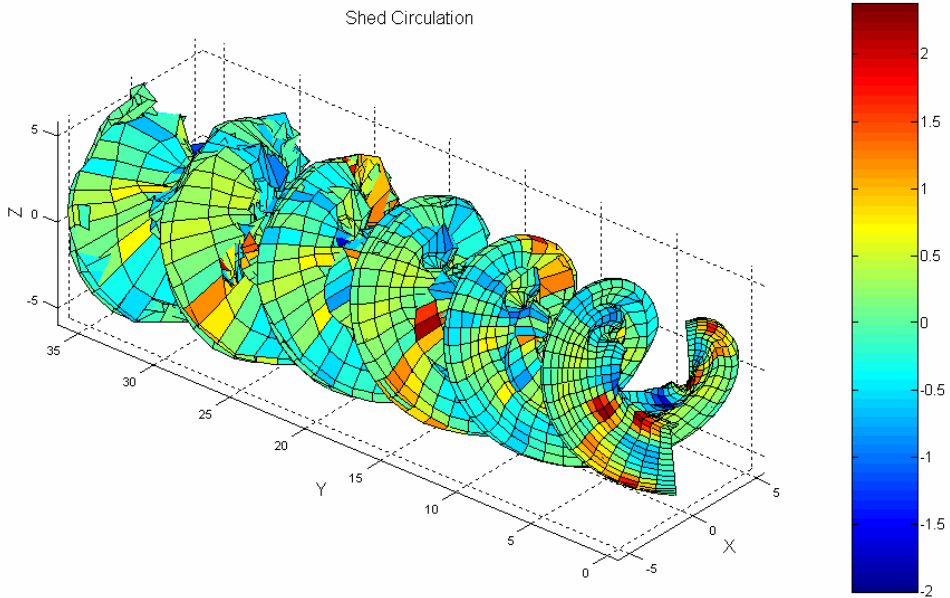


Figure 6.35(j) - Shed circulation (m^2/s) distribution in wake at $U=15m/s$.

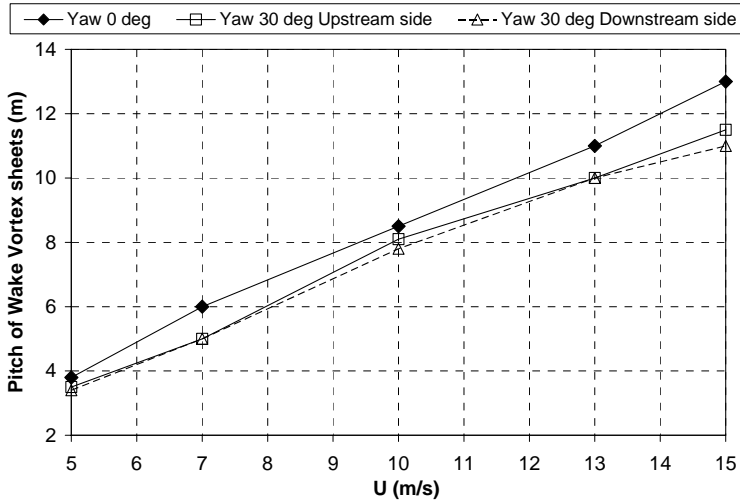


Figure 6.36 – Vortex sheet pitch variation as estimated from free-wake plots at $\Psi=0^\circ$ and $\Psi=30^\circ$.

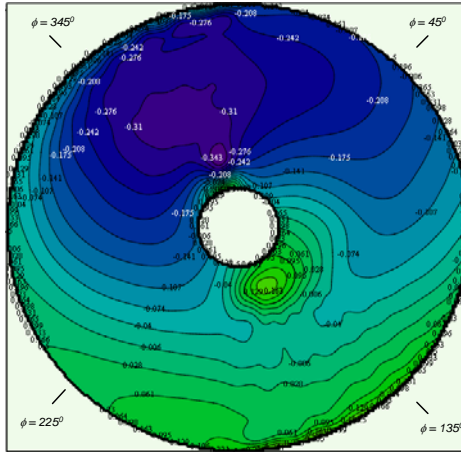
Induced Velocities at Rotorplane

HAWT_FWC calculated the 3D unsteady induced velocity fields across the whole rotorplane for different blade azimuth angles from the time-dependent distributions of C_{tr} and C_{lr} obtained from the blade pressure measurements. The contour plots displaying the induced velocity fields for $U=5$ and 15m/s at $\Psi=30^\circ$ for $\phi=0^\circ$ are plotted in Figs. 6.37. The asymmetry in the flow field at the rotorplane resulting from the skewed wake may be easily noted in these plots.

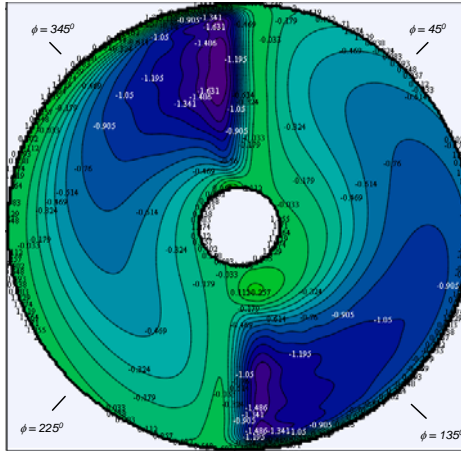
Figs. 6.38 and 6.39 illustrate the unsteady axial induction factors at the rotorplane as predicted by the free-wake plot in accordance with the blade pressure measurements taken in the wind tunnel. Figs. 6.38 (a)-(e) show the variation of the azimuthally-averaged axial induction factor (i.e. annular averaged axial induction factor, a_1) at the rotorplane with rotor azimuth angle for different radial locations. Figs. 6.39 (a)-(e) show the variation of the axial induction factor at the blade lifting line ($a_{1,e}$) with blade azimuth angle for different radial locations. The corresponding tangential and radial induction factors were also calculated but these are not included in this paper as they were found to be very small compared to the rotor angular speed.

When the windspeed is low ($U=5, 7\text{m/s}$), the free wake model predicts an azimuthally-averaged axial induction factor that is almost constant with rotor azimuth angle. Increasing the windspeed further increases the cyclic variation of a_1 . The cyclic component is highest at the inboard blade sections. The cyclic variation has frequency equal to $2p$ and this is because the rotor has two blades.

Tangential induced velocity field (u_x)



Axial induced velocity field (u_y)



Radial induced velocity field (u_z)

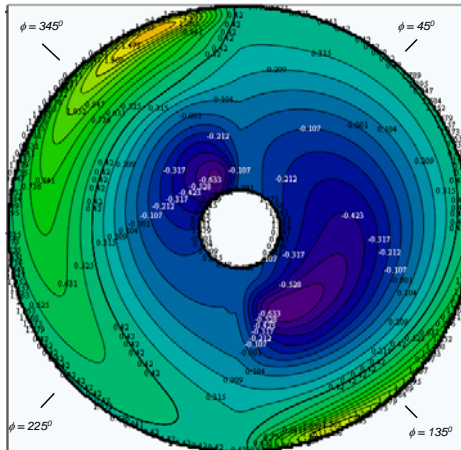
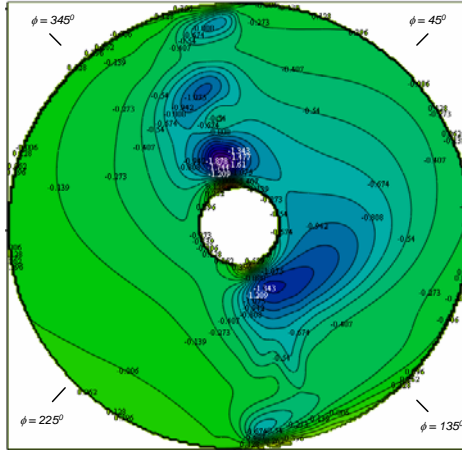
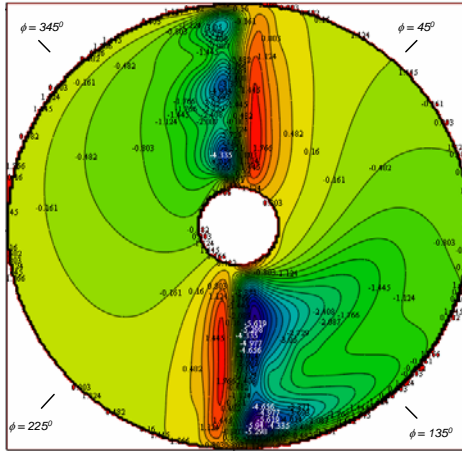


Figure 6.37(a) – 3D induced velocity field at rotorplane at $U=5\text{m/s}$, $\Psi=30^\circ$. Blade is at an azimuth angle of $0/180^\circ$. View is looking upstream from behind the rotorplane.

Tangential induced velocity field (u_x)



Axial induced velocity field (u_y)



Radial induced velocity field (u_z)

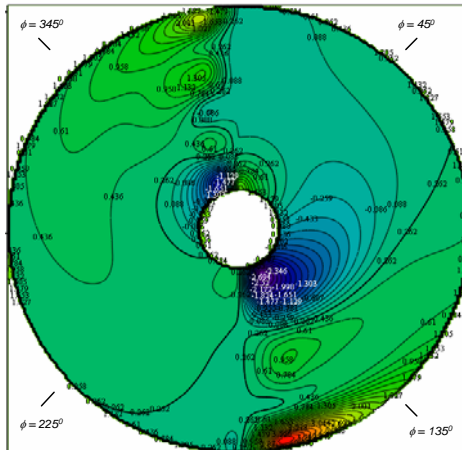


Figure 6.37(b) – 3D induced velocity field at rotorplane at $U=15\text{m/s}$, $\Psi=30^\circ$. Blade is at an azimuth angle of $0/180^\circ$. View is looking upstream from behind the rotorplane.

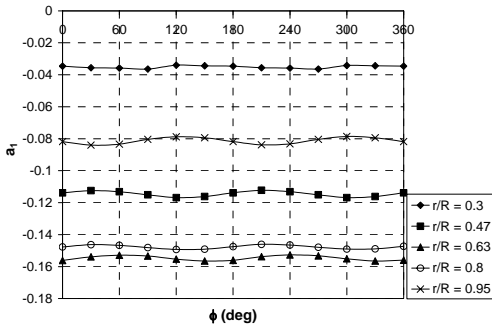


Fig. (a): $U = 5\text{m/s}$

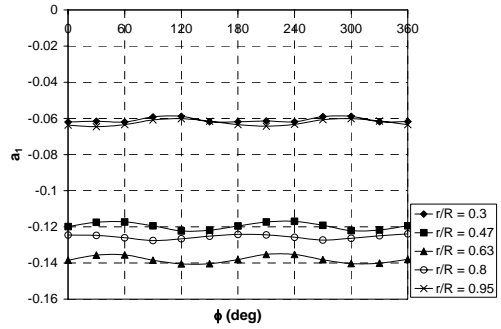


Fig. (b): $U = 7\text{m/s}$

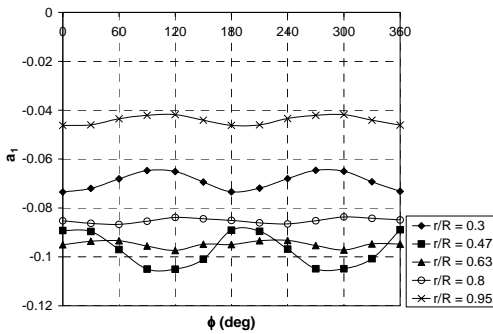


Fig. (c): $U = 10\text{m/s}$

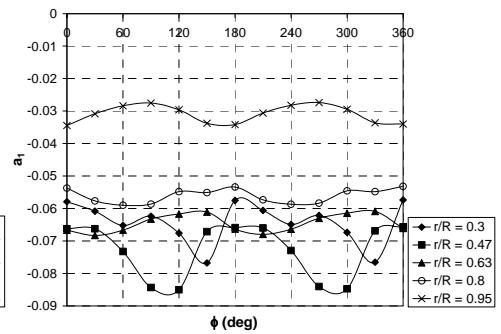


Fig. (d): $U = 13\text{m/s}$

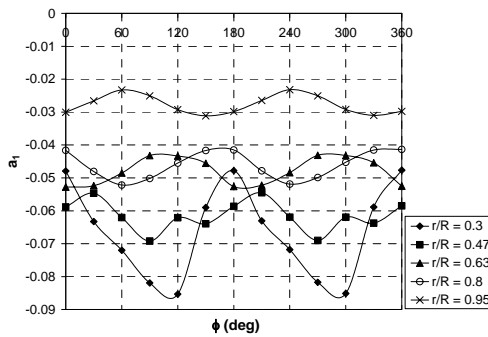


Fig. (e): $U = 15\text{m/s}$

Figure 6.38 - Variation of azimuthally averaged axial induction factor a_1 with rotor azimuth angle (ϕ) at $\Psi=30^\circ$ and $U=5, 7, 10, 13$ and 15m/s .

The variation of the axial induced velocity at the blade lifting line with the blade azimuth angle is periodic and regular at low wind speeds ($U=5, 7\text{m/s}$), especially at the outboard regions of the blades (see Figs. 6.39(a) and (b)) but then becomes very irregular at higher windspeeds ($U=10, 13, 15\text{m/s}$; see Figs. 6.39(c),(d) and (e)). At low wind speeds, the periodic variation $a_{1,c}$ with ϕ has a phase angle that changes depending on the radial position (r/R) of the blade section. This is due to the fact that in a skewed wake, the proximity of the blades to the wake circulation is a function of both blade azimuth angle and radial location. Recall from Fig. 6.35 (a) and (c) that at the low windspeeds, the trailing circulation in the wake tends to be concentrated at the tip and root regions. The outboard blade sections are in general closer to the wake circulation that is originating from the blade tips at blade azimuth position of 90° than at 270° . Consequently the induced velocity at the outboard blade sections is higher at 90° than at 270° , as in fact depicted in Figs. 6.39(a) and (b). As one moves inboard, the proximity of the blade sections to the wake circulation originating from the tip decreases, but this is followed by an increased proximity to the wake circulation originating from the blade roots. This causes the maximum induced velocity to occur at a different blade azimuth angle, thus changing the phase angle of the variation of $a_{1,c}$ with ϕ . At higher windspeeds ($U=10, 13$ and 15m/s), the presence of ‘horse-shoe’ trailing circulation levels at the middle blade sections remove the regular variation of $a_{1,c}$ with ϕ at all radial locations, making it very irregular.

From the results of this study, one can easily remark the following deficiencies of Glauert’s Eq. 3.23 (and similar models described in Chapter 3, section 3.5):

- Glauert’s model assumes that the azimuthally-averaged axial induced velocity (a_1) does not vary with rotor azimuth angle. Although this assumption may be realistic at low windspeeds, it does not necessarily apply for high windspeed conditions where the flow is separated.
- Glauert’s model does not cater for the phase angle change with radial location of the variation $a_{1,c}$ with ϕ , resulting from root circulation. Also as noted in references [83, 84] root circulation effects create an induced velocity distribution that has a higher harmonic content than only $1p$.
- Glauert’s model is invalid for high windspeeds with stalled flows where the variation $a_{1,c}$ with ϕ becomes very irregular.

As already described in Chapter 5, in the free vortex computations with *HAWT_FWC*, the induction at the lifting line of the blades is due to the free-wake trailing and shed circulation and due to the trailing circulation of the prescribed far wake model. The induction at the lifting line due to bound circulation from the two blades is zero. This is a consequence of the fact that a lifting line model is used to represent the blades and also because both lifting lines are in-line with one another (no blade coning). As already mentioned in section A. (page 320), in the free-wake calculations, the near wake parameter $nRev$ was selected large enough so that the induction contributed by the far wake is very small. Thus it may be assumed that the total induction is due to trailing and shed

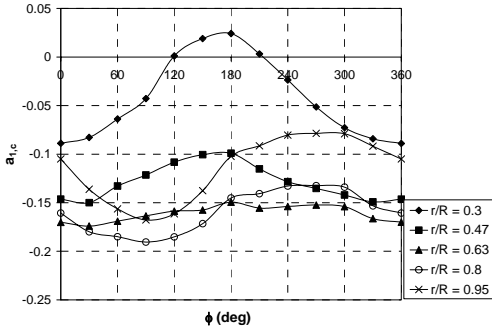


Fig. (a): $U = 5\text{m/s}$

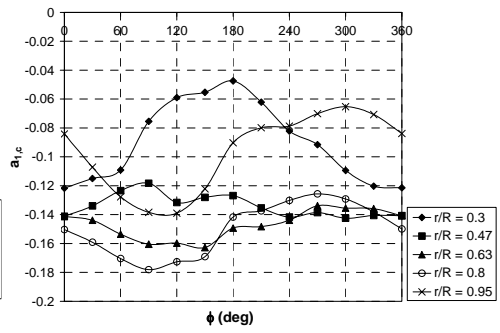


Fig. (b): $U = 7\text{m/s}$

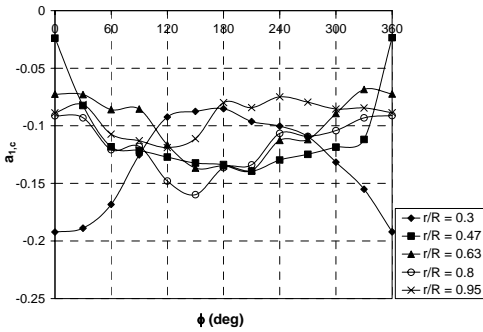


Fig. (c): $U = 10\text{m/s}$

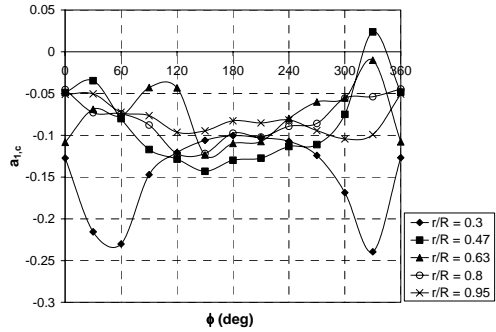


Fig. (d): $U = 13\text{m/s}$

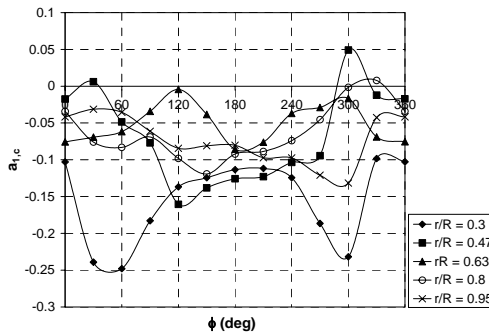


Fig. (e): $U = 15\text{m/s}$

Figure 6.39 - Variation of axial induction factor $a_{1,c}$ with blade azimuth angle (ϕ) at $\Psi=30^\circ$ and $U=5, 7, 10, 13$ and 15m/s .

circulation of the near wake only. Using this free-wake model, it is possible to calculate the induced velocity components resulting from the near wake trailing and shed circulation separately. In this way it would be possible to determine which circulation type has the greater influence on the flow at the blades. The induced velocities of Fig. 6.39 are shown again in Figs. 6.40 for $U=5$ and 15m/s , but including the individual induced velocity components due to trailing and shed circulation. The induced velocity by the shed circulation is in general very small. This is observed even at $U=7, 10$ and 13m/s . This proves that the trailing circulation is by far more dominant than the shed counterpart. The induction component due to the far wake alone is also included in Fig. 6.40 and as it may be observed it is very small compared to the total induction.

Global Loads

The unsteady lift and drag coefficients and induced velocities derived by the free-wake vortex model were used to calculate the low-speed shaft torque and the blade flap/edgewise bending moments using the blade-element theory equations 3.16. These results are shown in Figs. 6.41, 6.42 and 6.43 where they are noted by plots 'Free-wake'. As a cross-check for these calculations, the same loads were computed directly from the experimental data by using a linear interpolation to obtain a distribution for C_n , C_t and Q_{NORM} across the whole blade span and using Eqts. 6.4, 6.5 and 6.6. In the linear interpolation, C_n and C_t at the blade tips were set equal to zero. The trapezium rule was adopted for integrating numerically across the whole blade span. These results are included in Figs. 6.41, 6.42 and 6.43 and are referred to 'Exp'. The loads measured directly using strain-gauges are also included in these figures. The results calculated by the free-wake model and those derived directly from the pressure measurements ('Exp') agree very well. However agreement with the loads measured by the strain gauges is not as good. The reasons for the discrepancies are the same as those explained for axial conditions (*see* page 306). Gravitational loads are not included and thus the computed edgewise moment does not include the cyclic component induced by the blade weight. This leads to a large discrepancy in Figs. 6.43.

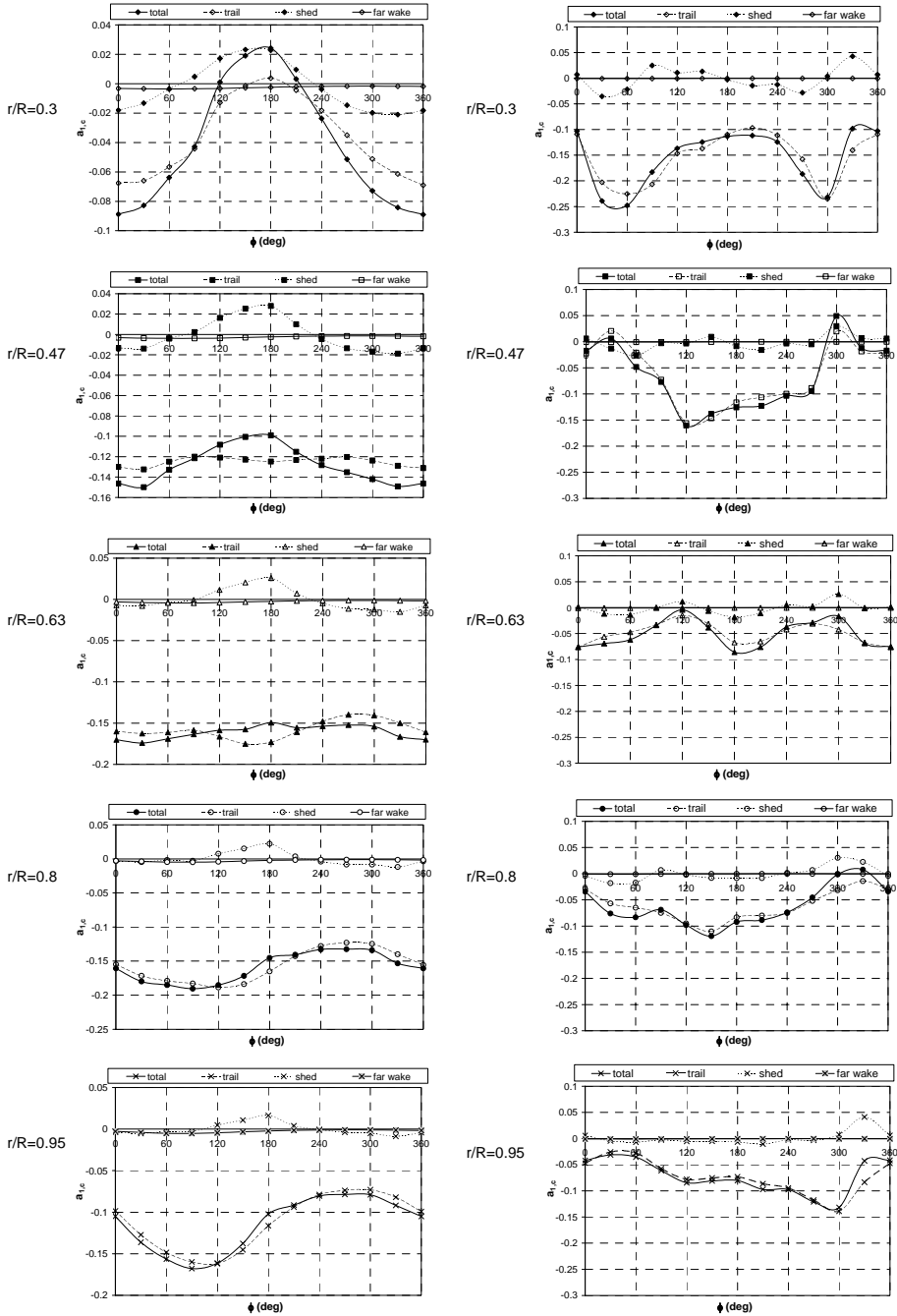


Fig. 6.40(a): contribution of circulation components from near and far wake to induction factor at blade lifting line at $U = 5 \text{ m/s}$

Fig. 6.40(b): contribution of circulation components from near and far wake to induction factor at blade lifting line at $U = 15 \text{ m/s}$

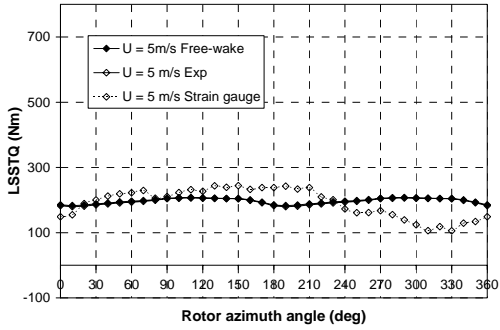


Fig. (a): $U = 5\text{ m/s}$

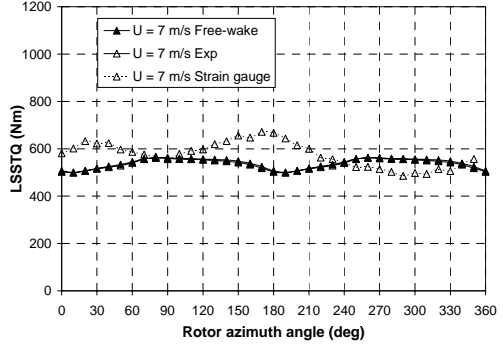


Fig. (b): $U = 7\text{ m/s}$

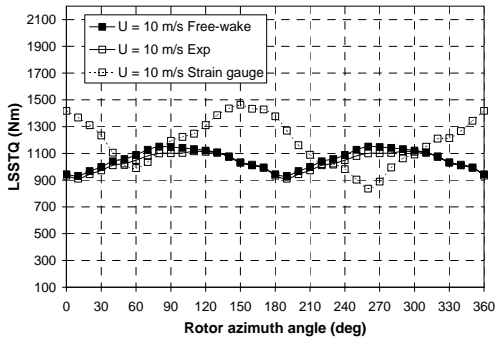


Fig. (c): $U = 10\text{ m/s}$

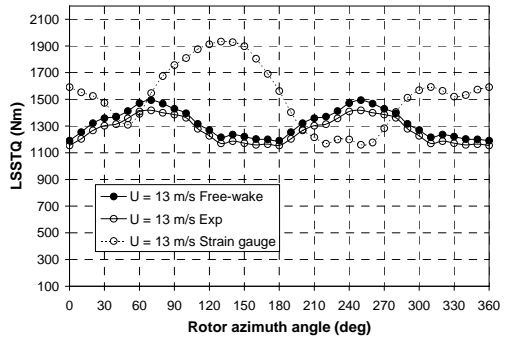


Fig. (d): $U = 13\text{ m/s}$

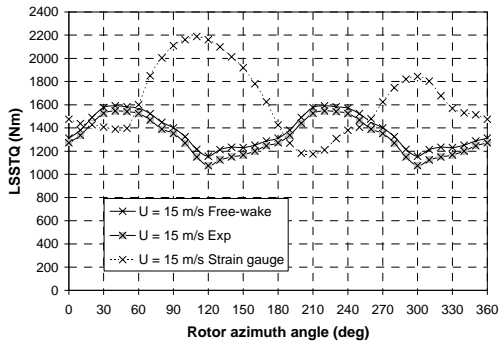


Fig. (e): $U = 15\text{ m/s}$

Fig. 6.41 - Variation of low-speed shaft torque with rotor azimuth angle (ϕ) at $U = 5, 7, 10, 13$ and 15 m/s .

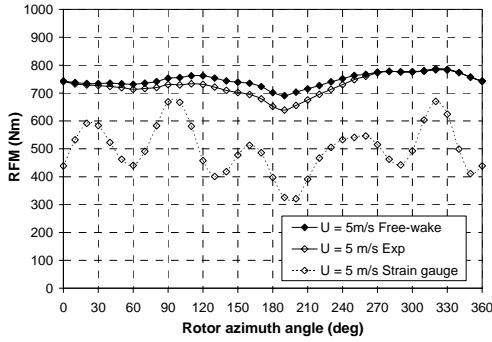


Fig. (a): $U = 5\text{m/s}$

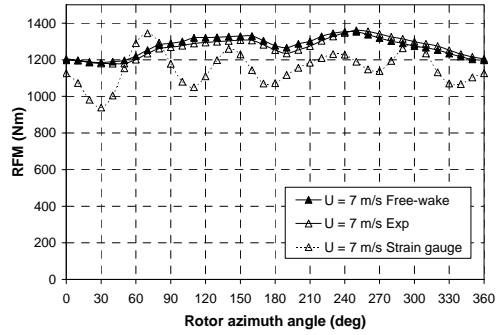


Fig. (b): $U = 7\text{m/s}$

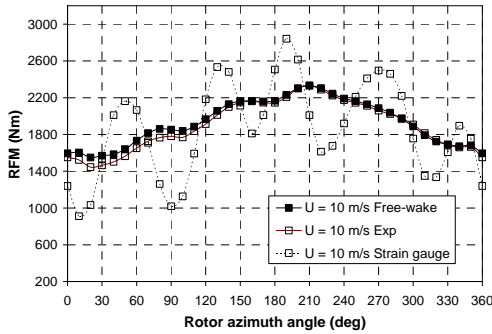


Fig. (c): $U = 10\text{m/s}$

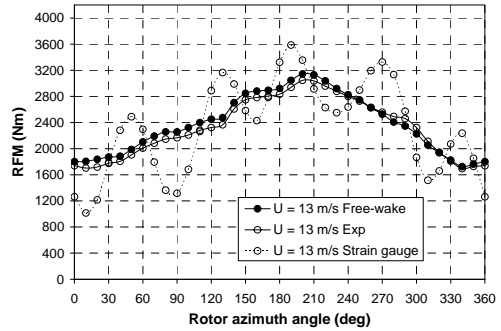


Fig. (d): $U = 13\text{m/s}$

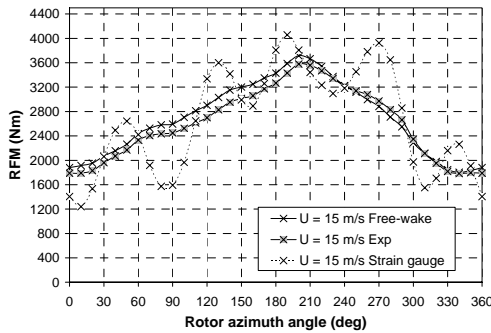


Fig. (e): $U = 15\text{m/s}$

Fig. 6.42 - Variation of blade root flap bending moment with rotor azimuth angle (ϕ) at $U = 5, 7, 10, 13$ and 15m/s .

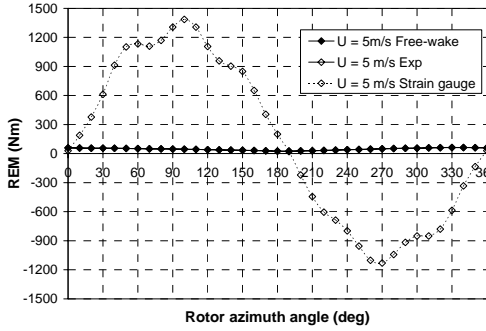


Fig. (a): $U = 5\text{ m/s}$

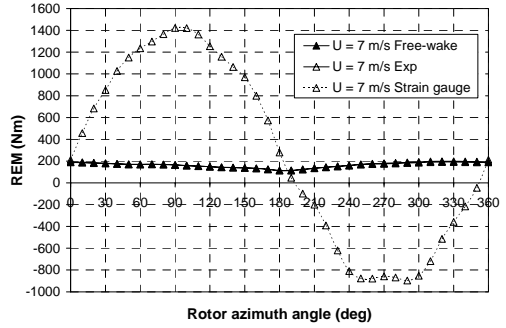


Fig. (b): $U = 7\text{ m/s}$

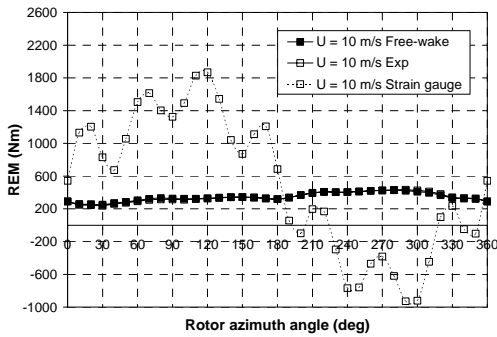


Fig. (c): $U = 10\text{ m/s}$

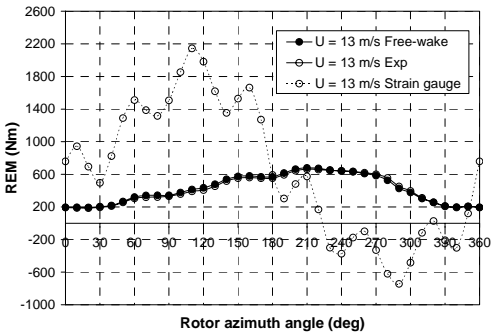


Fig. (d): $U = 13\text{ m/s}$

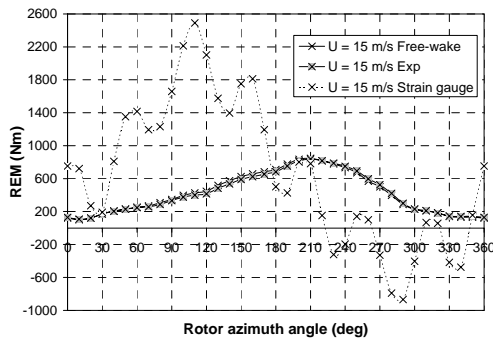


Fig. (e): $U = 15\text{ m/s}$

Fig. 6.43 - Variation of blade root edge bending moment with rotor azimuth angle (ϕ) at $U = 5, 7, 10, 13$ and 15 m/s .

Comparison of Inflow Angle

Figs. 6.44 – 6.48 compare the local inflow angles (*LFA*) predicted by *HAWT_FWC* with those measured by the flow direction probes during the wind tunnel experiments (see Fig. 6.4) at $\psi=30^\circ$ and windspeeds $U=5, 7, 10, 13$ and 15m/s . The angle of attack derived by *HAWT_FWC* from the blade pressure measurements is also included. In the ideal situation the *LFA* values computed by *HAWT_FWC* and those measured by the probes in the tunnel should be equal. But the correlation is not always good due to the various reasons explained already when describing the results for axial conditions (see page 309). The influence of blade deflection is small, even at yawed conditions and could not be considered as a major source of error. A calculation on the ECN aeroelastic code *PHATAS* confirm that blade deflection is small at $\psi=30^\circ$ (maximum blade tip deflection $<10\text{cm}$), (ECN, Gerard Schepers, personal communication). Also, as it may be noted from Figs. 6.44 – 6.48, good correlation in the *LFA* was achieved at the outboard blade sections ($r/R>0.67$) where blade deflection is normally largest. Surprisingly, this good correlation in the outboard blade sections is observed even at the high windspeeds at which the angle of attack exceeds the 2D static stalling angle (which is around 10°).

At the inboard sections, the discrepancy between the *HAWT_FWC* and experimental values of the *LFA* is sometimes large at the windspeeds ($U=10, 13$ and 15m/s), reaching a value of about 10° . The most probable reasons for this discrepancy are two: (1) the deficiency of the lifting line model implemented in *HAWT_FWC* to model 3D effects on the blades, as already noted already when treating axial conditions; (2) the fact at $\psi=30^\circ$, the probe was subjected to highly unsteady flow situations which are most prominent at the inboard blade sections. At $U=10\text{m/s}$, *HAWT_FWC* estimates that the time rate of change of angle of attack reaches a peak of about $\pm 78\text{deg/s}$ at $r/R=0.3$. At $U=15\text{m/s}$, this value exceeds $\pm 180\text{deg/s}$ (see Figs. 6.32(c), (d) and (e)). Further work is required to establish the accuracy with which five-hole pressure probes manage to measure the *LFA* at such high levels of unsteadiness.

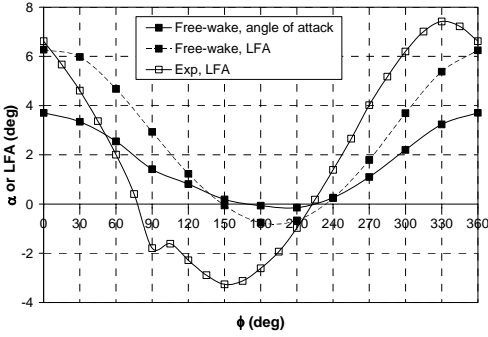


Fig. (a): $r/R = 0.34$

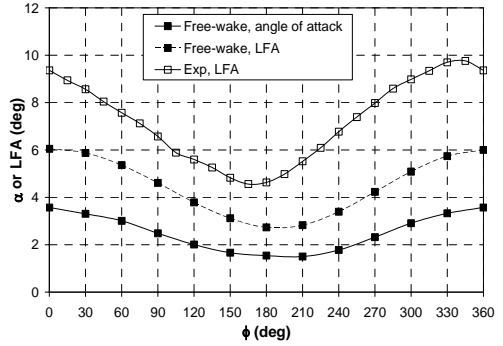


Fig. (b): $r/R = 0.51$

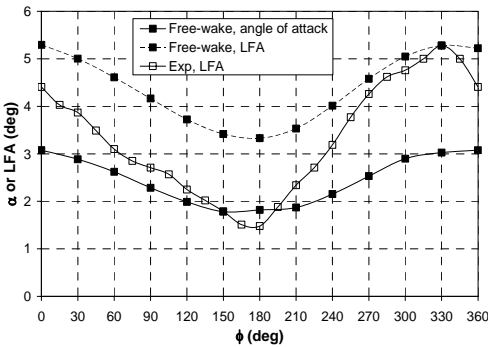


Fig. (c): $r/R = 0.67$

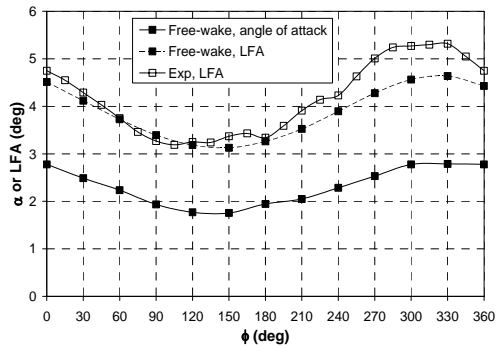


Fig. (d): $r/R = 0.84$

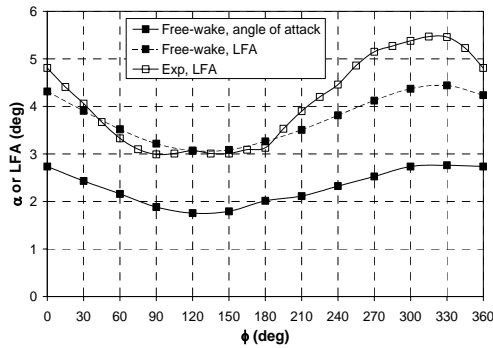


Fig. (e): $r/R = 0.91$

Fig. 6.44 - Variation of LFA and α with blade azimuth angle (ϕ) at $U = 5\text{m/s}$ and $\Psi = 30^\circ$.

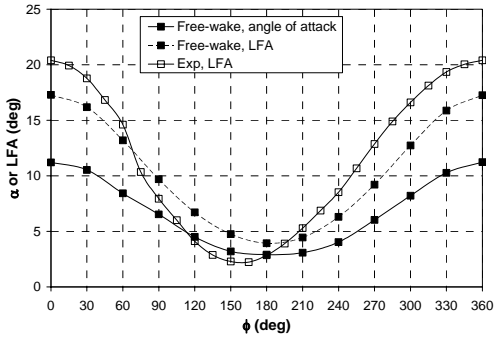


Fig. (a): $r/R = 0.34$

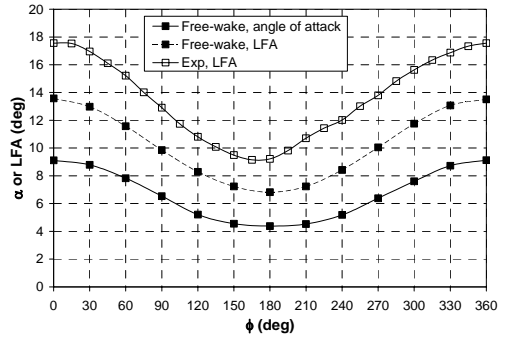


Fig. (b): $r/R = 0.51$

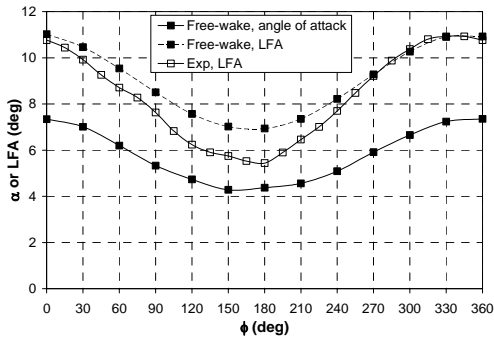


Fig. (c): $r/R = 0.67$

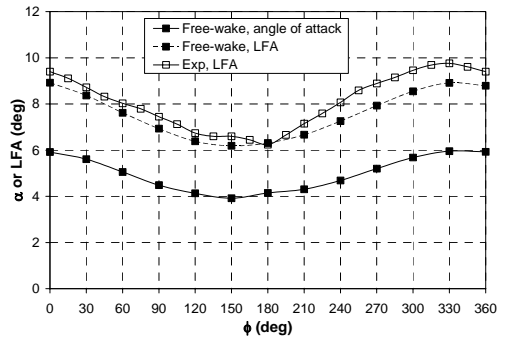


Fig. (d): $r/R = 0.84$

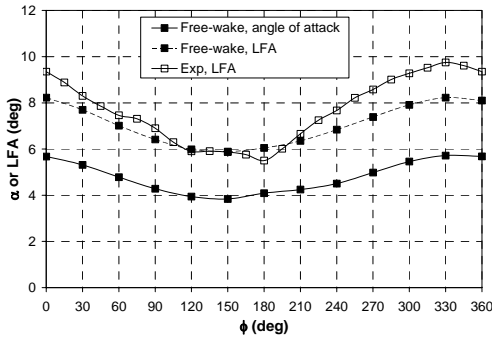


Fig. (e): $r/R = 0.91$

Fig. 6.45 - Variation of LFA and α with blade azimuth angle (ϕ) at $U = 7\text{m/s}$ and $\Psi = 30^\circ$.

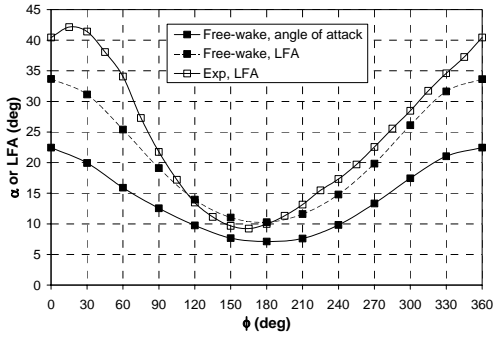


Fig. (a): $r/R = 0.34$

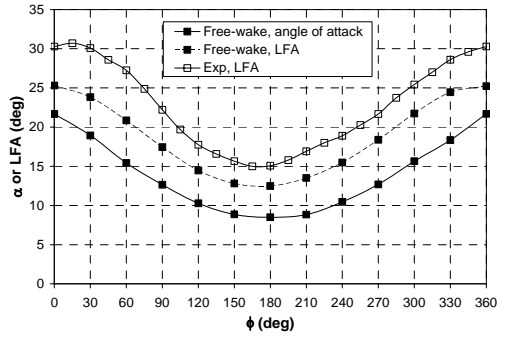


Fig. (b): $r/R = 0.51$

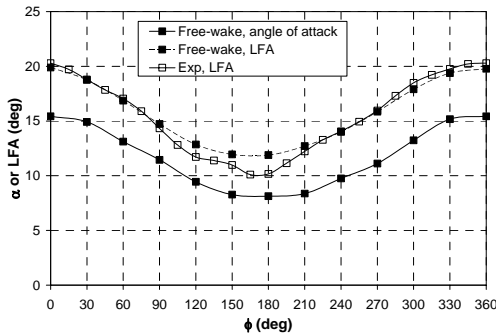


Fig. (c): $r/R = 0.67$

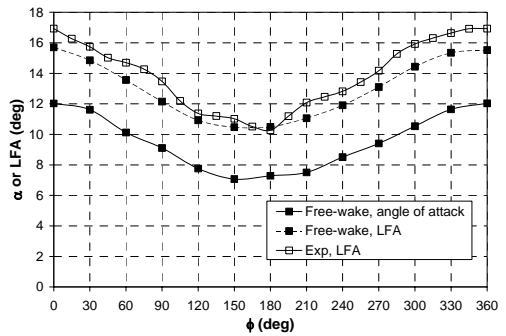


Fig. (d): $r/R = 0.84$

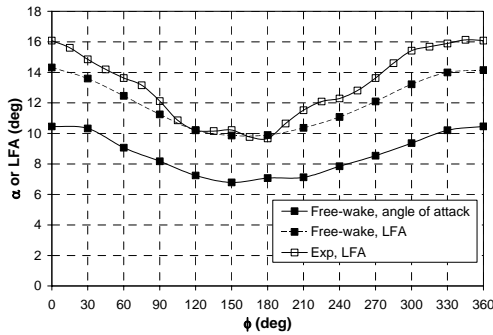


Fig. (e): $r/R = 0.91$

Fig. 6.46 - Variation of LFA and α with blade azimuth angle (ϕ) at $U = 10\text{m/s}$ and $\Psi = 30^\circ$.

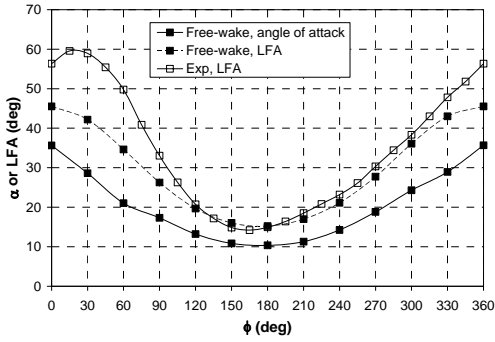


Fig. (a): $r/R = 0.34$

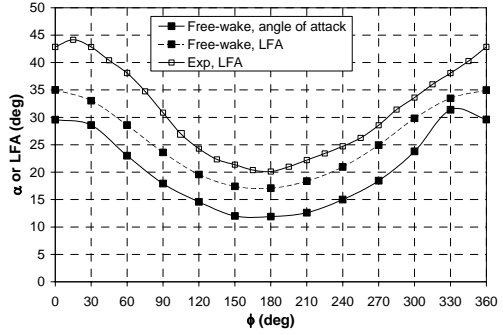


Fig. (b): $r/R = 0.51$

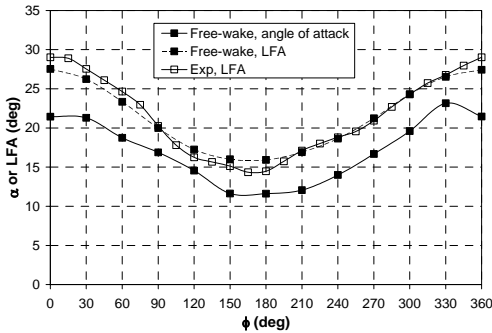


Fig. (c): $r/R = 0.67$

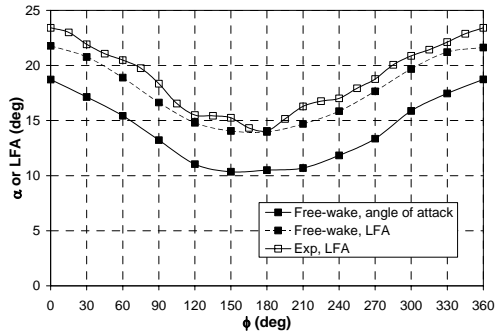


Fig. (d): $r/R = 0.84$

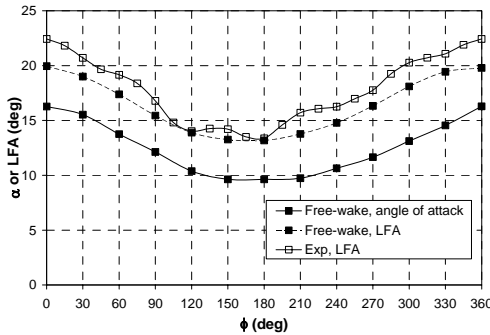


Fig. (e): $r/R = 0.91$

Fig. 6.47 - Variation of LFA and α with blade azimuth angle (ϕ) at $U = 13\text{m/s}$ and $\Psi = 30^\circ$.

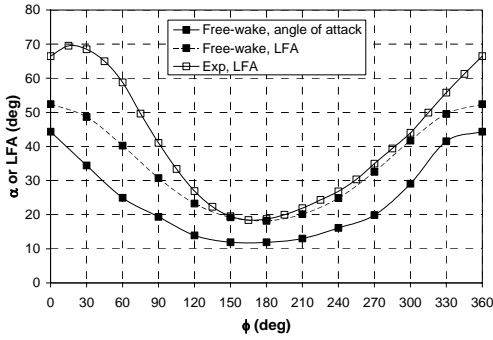


Fig. (a): $r/R = 0.34$

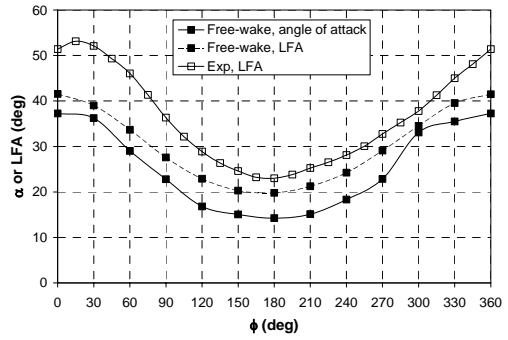


Fig. (b): $r/R = 0.51$

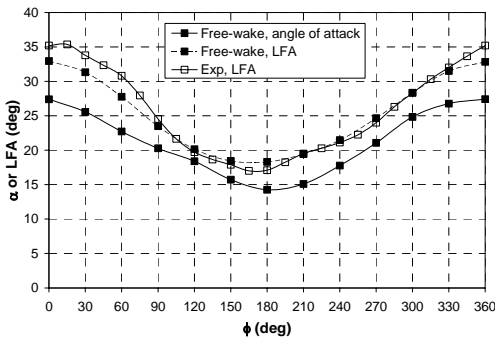


Fig. (c): $r/R = 0.67$

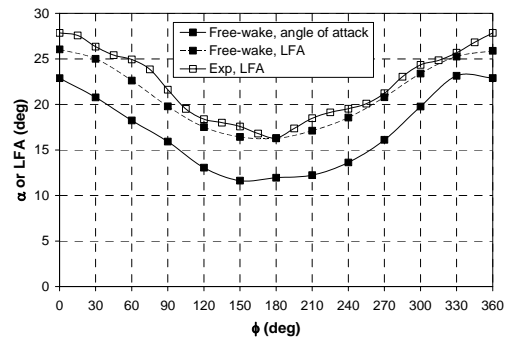


Fig. (d): $r/R = 0.84$

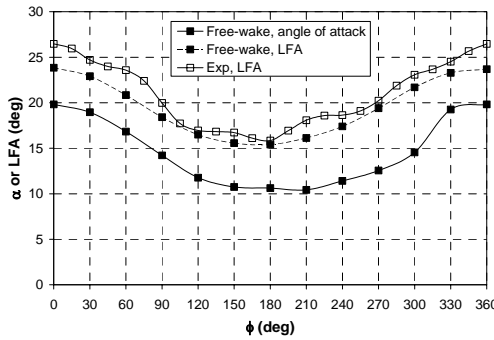


Fig. (e): $r/R = 0.91$

Fig. 6.48 - Variation of LFA and α with blade azimuth angle (ϕ) at $U = 15\text{m/s}$ and $\Psi = 30^\circ$.

Comparison of Results with those of Free-Wake Vortex Model AWSM

To further evaluate the reliability of the results from *HAWT_FWC*, a blind comparison was performed with the results predicted by another free-wake vortex model, *AWSM* developed by van Garrel at ECN [26]. *AWSM* is also a free-wake vortex model that models the blades as lifting lines and the wake as sheets, each consisting of a mesh of straight-line vortex filaments to account for both trailing and shed circulation. The main difference from *HAWT_FWC* is mainly that *AWSM* makes use of aerofoil data (C_l and C_d as function of α) to determine iteratively the aerodynamic loads and induction at the rotorplane. Recall that in *HAWT_FWC*, no aerofoil data is used, but the wind tunnel measurements of C_n and C_t . Further details on *AWSM* may be found in [26]. The comparison was limited to $U=5\text{m/s}$ and $\psi=30^\circ$ only, for which the static 2D S809 aerofoil data used in *AWSM* is reasonably close to that observed in the NASA Ames tunnel experiments. The results for the axial induction factor at the blade lifting line ($a_{l,c}$) from the two codes are compared in Fig. 6.49. It was found that the results agree very well. This is very encouraging and this gives more confidence in the results present earlier derived using *HAWT_FWC*.

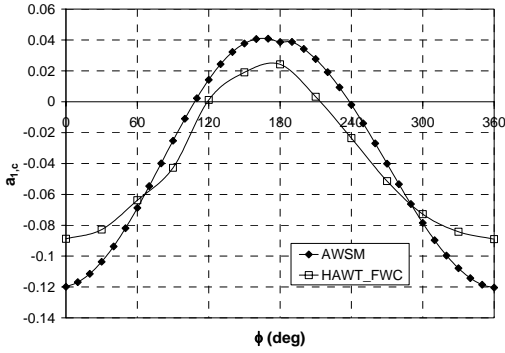


Fig. (a): $r/R = 0.3$

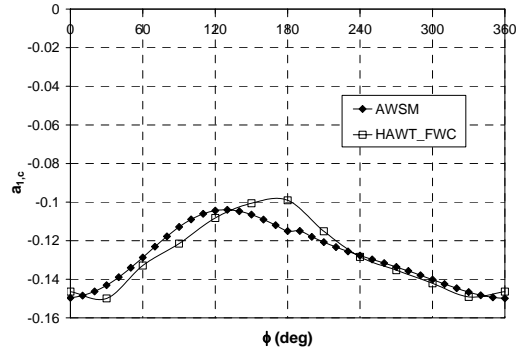


Fig. (b): $r/R = 0.47$

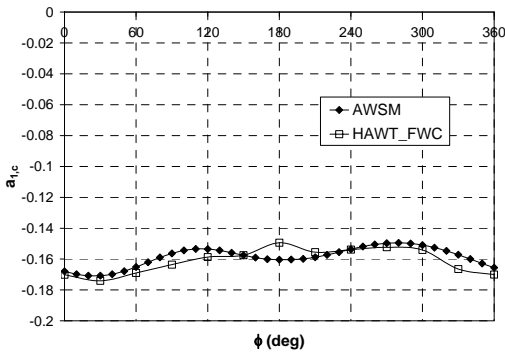


Fig. (c): $r/R = 0.63$

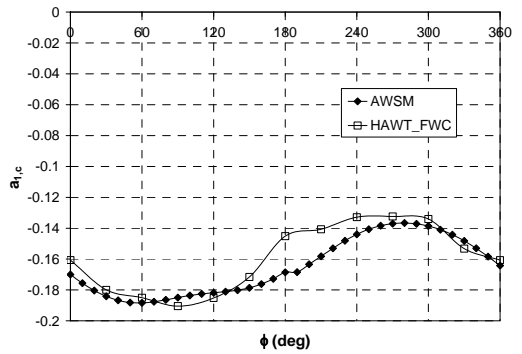


Fig. (d): $r/R = 0.8$

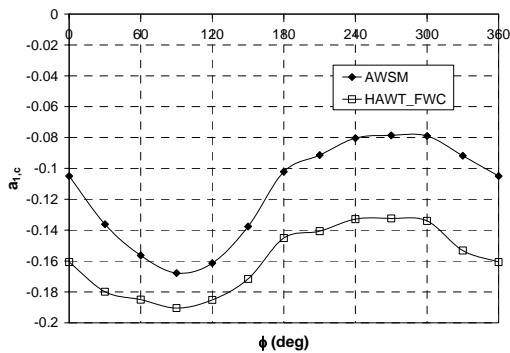


Fig. (e): $r/R = 0.95$

Fig. 6.49 – Comparison of the axial induction factor distribution at the blade lifting line ($a_{1,c}$) computed by HAWT_FWC with those from free-wake vortex model AWSM at $U = 5\text{ m/s}$ and $\Psi = 30^\circ$. AWSM results from ECN (Gerard Schepers, personal communication).

6.4 BEM Predictions for the NREL Phase VI Rotor with New Aerofoil Data and Inflow Corrections

As already outlined in section 6.1, the main objectives for this analysis on the NREL rotor was to improve BEM-based design codes. The new aerofoil data derived from the blade pressure measurements in conjunction with *HAWT_FWC* (see Figs. 6.19 for $\psi=0^\circ$ and Figs. 6.33 for $\psi=30^\circ$) were used in the Blade-Element-Momentum (BEM) theory to model the NREL Phase VI rotor in both axial and yawed conditions. For yawed conditions, inflow corrections for BEM codes were derived from the inflow results of *HAWT_FWC* (see Figs. 6.38 and 6.39). In this analysis, the BEM model developed in this project (*HAWT_BEM*) was used for the computations. The results computed by this BEM code were repeated with different aerofoil data (with 2D static data/with new 3D data from *HAWT_FWC*) and in the case of yawed conditions also with different inflow corrections (with/without inflow corrections from *HAWT_FWC*). In this way it was possible to assess both quantitatively and qualitatively the improvements in BEM predictions if the new aerofoil data and inflow corrections are used.

An important point to make is that in the following BEM computations with the new aerofoil data derived from the NREL blade pressure measurements and *HAWT_FWC*, the drag coefficient is only due to blade pressure (i.e. C_{dp}). Hence the drag coefficient due to skin friction is being ignored.

This analysis is divided into two parts: section 6.4.1 will consider axial conditions only ($\psi=0^\circ$) while section 6.4.2 is solely dedicated to yawed conditions ($\psi=30^\circ$).

6.4.1 Axial Conditions

The 3D aerofoil data derived from the NREL blade pressure measurements in conjunction with *HAWT_FWC* for $\Psi=0^\circ$ (Figs. 6.19 (a) and (b)) were double interpolated to yield the aerofoil data as a function of two variables, i.e. the aerofoil data at different radial locations and angles of attack (i.e. in the form $C_l, C_d(r/R, \alpha)$). A cubic spline interpolation as described in Appendix D was used to obtain the aerofoil data as a function of r/R with the boundary conditions that both C_l and C_d are zero at the blade tip and root. A spline interpolation was selected since unlike linear interpolation, this was found to yield more realistically smooth variation of loading at the blade tip and root.

To be able to assess the improvement in the BEM predictions when using the new 3D aerofoil data, each operating condition on the NREL rotor was modelled with *HAWT_BEM* using both the standard 2D static aerofoil data from the Delft wind tunnel and the new aerofoil data. Table 6.2 lists the different computations performed.

*Table 6.2: Computations performed on NREL rotor for $\Psi=0^\circ$ using *HAWT_BEM**

Computation Reference	BEM Code Configuration
BEM1	<ul style="list-style-type: none"> • 2D static aerofoil data (from Delft wind tunnel) extrapolated using Viterna-Corrigan model (Fig. 6.50) • Prandtl tip/root correction factor included
BEM2	<ul style="list-style-type: none"> • New 3D static aerofoil data obtained from NREL blade pressure measurements and <i>HAWT_FWC</i> (Fig. 6.19) • Prandtl tip/root correction factor included
BEM3	<ul style="list-style-type: none"> • New 3D static aerofoil data obtained from NREL blade pressure measurements and <i>HAWT_FWC</i> (Fig. 6.19) • Prandtl tip/root correction factor NOT included

Whether to include a Prandtl tip/root loss correction or not with the newly derived aerofoil data is contradicting and subject to dispute. On one hand in the free-wake model a 2D definition for the angle of attack was used since the effect of the wake was removed. This suggests that the tip/root loss should be included. On the other hand it should be kept in mind that the measured values of C_n and C_t from which the new aerofoil data was derived are 3D values which already include tip/root effects. For this reason it could be argued that the tip/root loss factor should not be introduced. In this study, the BEM calculations were therefore performed both with and without Prandtl tip/root loss correction factor.

For the computations with the BEM1 configuration (see table 6.2), the 2D static wind tunnel aerofoil data was extrapolated for high angles of attack using the Viterna-Corrigan empirical model which was described earlier in Chapter 3, section 3.5. The 2D Delft Wind

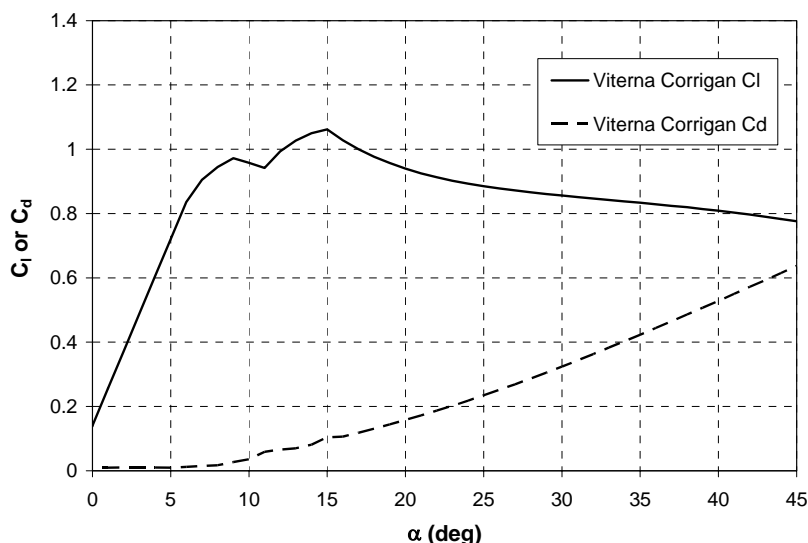


Figure 6.50 – 2D static aerofoil data from Delft wind tunnel (for $Re=1000000$) extrapolated for high angles of attack using the Viterna-Corrigan model.

tunnel aerofoil data extrapolated using the above Viterna-Corrigan model is plotted in Fig. 6.50.

A. Comparison of spanwise distributions of aerodynamic loading and induction factors

The results from the three different BEM computations (BEM1, BEM2 and BEM3, see table 6.2) for different wind speeds of the NREL rotor ($U=5, 10, 15, 20$ and 25m/s) are presented in Figs. 6.51, 6.52, 6.53, 6.54 and 6.55, respectively. For each windspeed, the spanwise variations of normal and tangential aerodynamic loading (dA_z and dA_η) from *HAWT_BEM* are compared with the corresponding values obtained by NREL using pressure measurements in the NASA Ames wind tunnel. It is easily noted from Figs. 6.51-6.55(a) and (b) that the BEM results for dA_z and dA_η improve significantly when the new 3D aerofoil data is used instead of the 2D aerofoil data with the Viterna-Corrigan extrapolation (compare results of BEM1 and BEM2). This improvement is observed at all wind speeds, even at the extreme windspeed of 25m/s . This proves that given the appropriate aerofoil data, the BEM theory can model aerodynamic loading augmentation at the inboard blade sections really well. An important comment to make concerns the Prandtl tip/root loss: the comparison obtained from BEM2 and BEM3 results reveals that the effect of including the Prandtl tip/root loss correction is very small. This consolidates the reason that this correction is not very important any more because the new aerofoil data can handle tip loss correction. This is a consequence of the fact that the loading parameters C_n and C_t from which the new aerofoil data was originally derived already accounts for tip and root loss.

Figs. 6.51-6.55(c) and (d) display the spanwise variations of the azimuthally (annular) averaged axial induction factor (a_1) and the axial induction factor at the blade lifting line ($a_{1,c}$) obtained by BEM. These are compared with those obtained by the free-wake model (*HAWT_FWC*) (which were already shown earlier in Figs. 6.21). Despite the fact that the aerodynamic loading distributions improved considerably at all windspeeds when the new aerofoil data was used, no improvement was observed in the BEM2 and BEM3 predictions for a_1 and $a_{1,c}$ at high windspeeds ($U=10, 15, 20$ and 25m/s) at radial locations where the local angle of attack is known to be large. This is likely to originate from the inherent limitation of the lifting-line model in *HAWT_FWC* used to derive the aerofoil data and induction from the blade pressure measurements at large angles of attack and not due to the BEM theory itself. In fact, in the work of Johansen *et al.* [40] where new aerofoil data was derived for BEM from CFD computations (*see* page 312), a good agreement was achieved when comparing the BEM predictions for a_1 with those from CFD.

As regards the spanwise variations of $a_{1,c}$, the BEM1 predictions yield a negative rise in this parameter at the blade tip, which is far different from that predicted by the free-wake vortex model. This is a limitation of the Prandtl correction and was already discussed when modelling the TUDelft rotor (section 4.4.2). With the inclusion of the new aerofoil data this negative rise at the blade tip is no longer present.

Figs. 6.51-6.55 show that the Prandtl tip/root correction has a notable influence on distributions for $a_{1,c}$, especially at high windspeeds and at the blade tip and root regions. This influence on the aerodynamic loads is however only marginal because the induction factors are generally small.

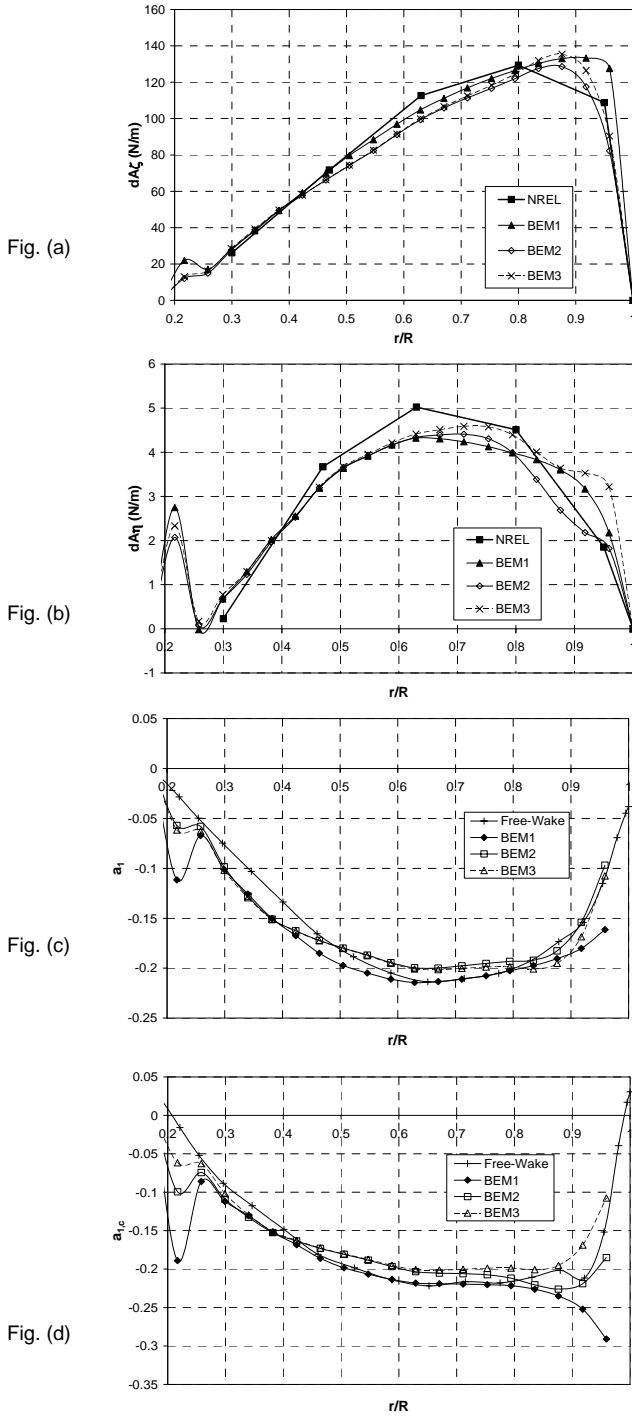


Figure 6.51 – Comparison of BEM predictions for $U = 5\text{m/s}$, $\Psi = 0^\circ$.

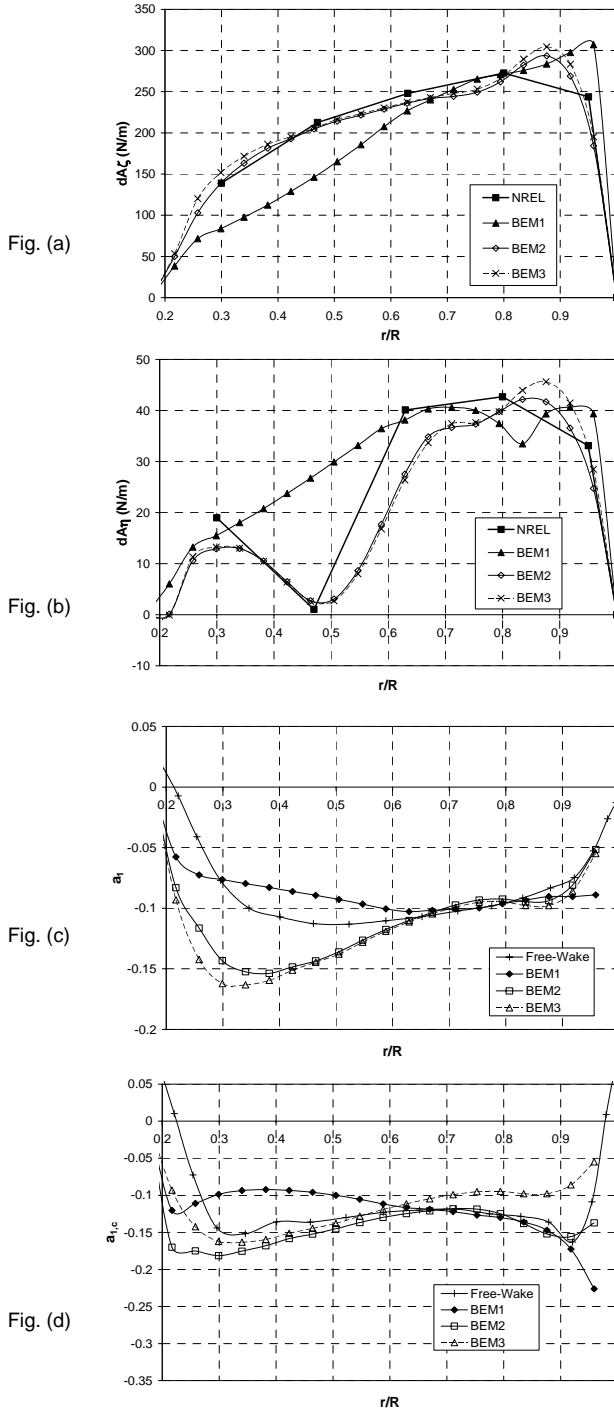


Figure 6.52 – Comparison of BEM predictions for $U = 10\text{m/s}$, $\Psi=0^\circ$.

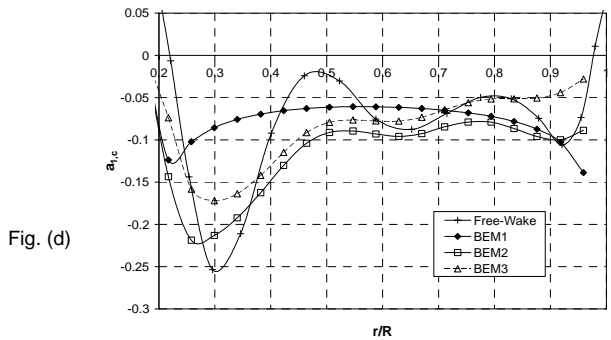
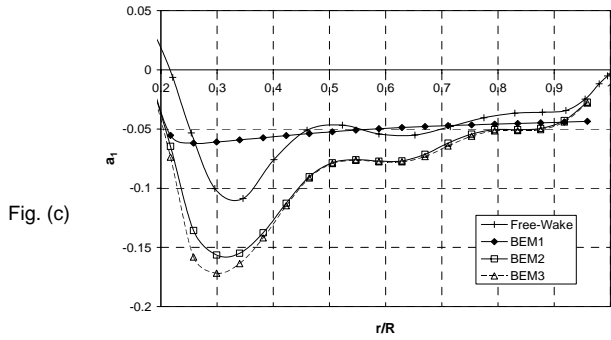
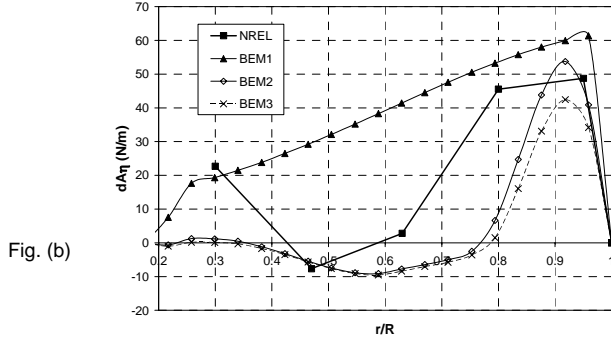
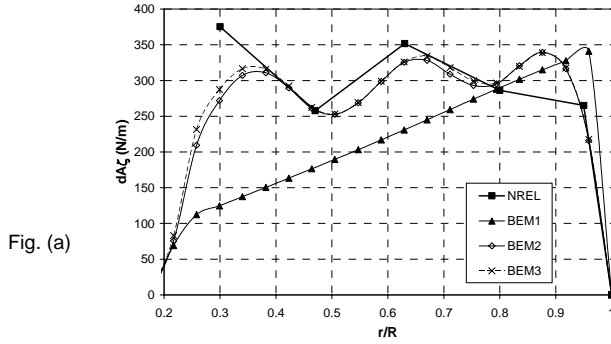


Figure 6.53 – Comparison of BEM predictions for $U = 15\text{m/s}$, $\Psi = 0^\circ$.

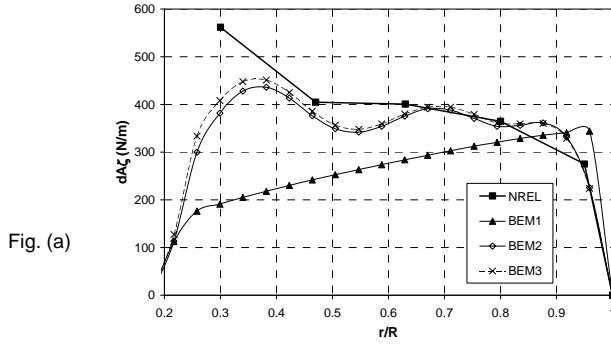


Fig. (a)

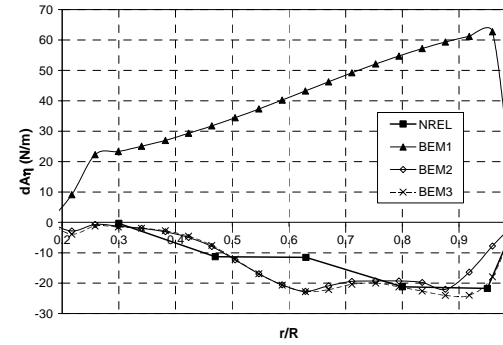


Fig. (b)

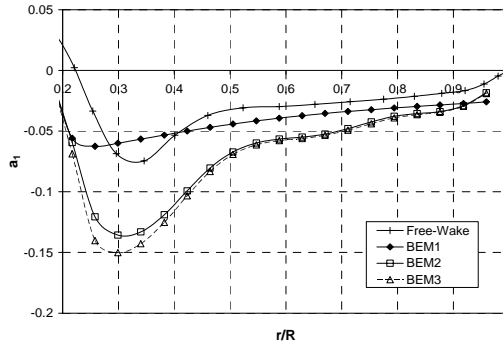


Fig. (c)

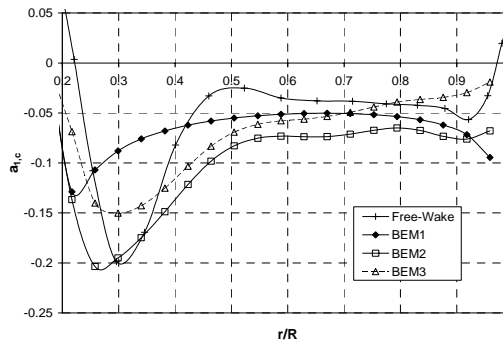


Fig. (d)

Figure 6.54 – Comparison of BEM predictions for $U = 20\text{m/s}$, $\Psi = 0^\circ$.

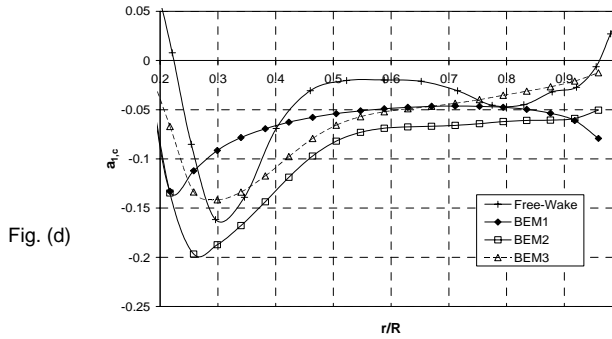
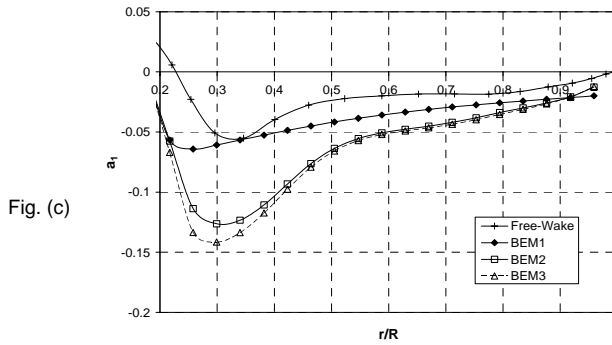
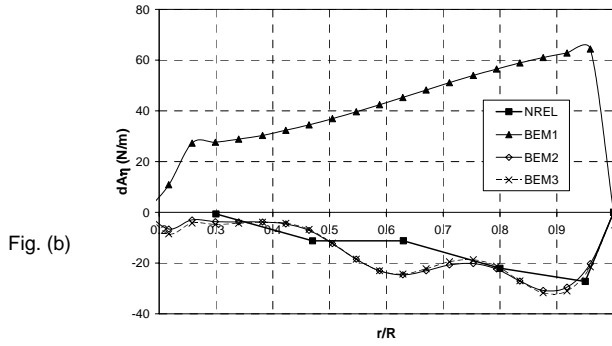
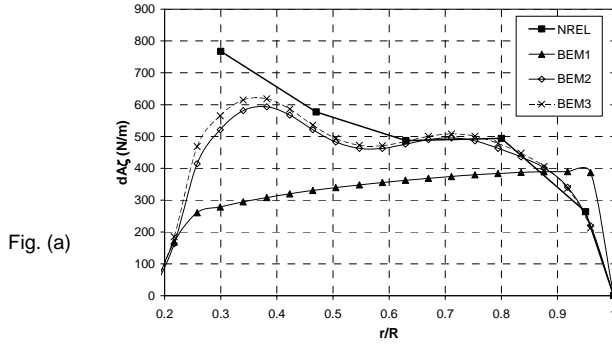


Figure 6.55 – Comparison of BEM predictions for $U = 25\text{m/s}$, $\Psi = 0^\circ$.

B. Comparison of Global loads

Figs. 6.56(a), (b) and (c) compare the aerodynamic global loads (low-speed shaft torque and the blade root flap and edge moments) predicted by the three different BEM computations (BEM1, BEM2 and BEM3) for windspeeds $U= 5, 7, 10, 13, 15, 20$ and 25m/s . These plots also show the results shown in Fig. 6.22, i.e. the global loads derived directly from the measurements using Eqts. 6.4, 6.5 and 6.6 (denoted by ‘Exp’) and those predicted by *HAWT_FWC* (denoted by ‘Free-wake’). At low windspeeds ($U= 5, 7, 10\text{m/s}$), the BEM predictions with 2D static aerofoil data (BEM1 computations) are within acceptable accuracy. However this is not the case at high windspeeds and this is due to the inconsistencies of the Viterna-Corrigan model. The radical improvement in the BEM predictions when using the new aerofoil data (BEM2 and BEM3 computations) is easily noted in Figs. 6.56(a), (b) and (c). Whether to include the Prandtl tip/root loss correction or not has negligible influence on the calculation of global loads since only very small differences are seen between the BEM2 and BEM3 results.

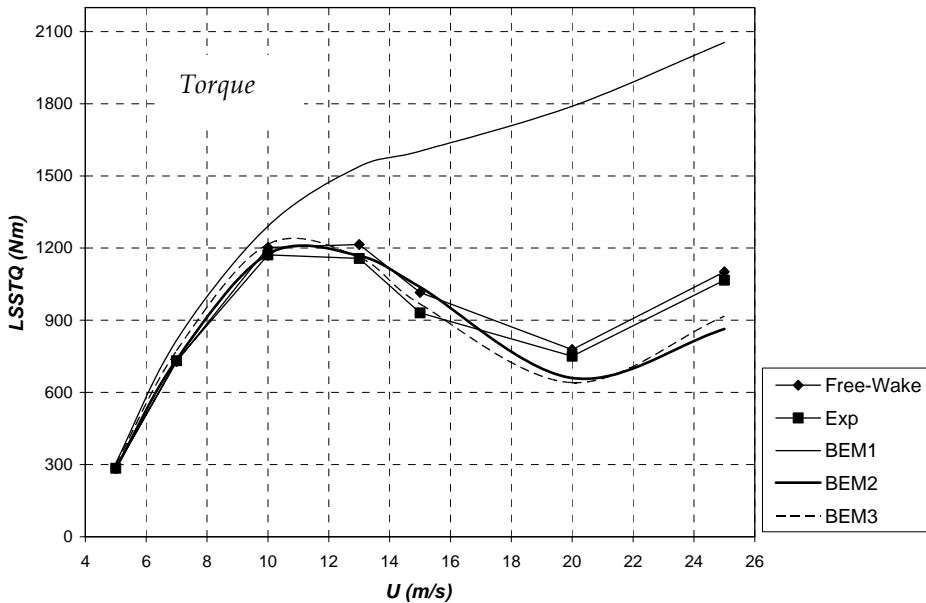


Figure 6.56(a) – Variation low speed shaft torque with windspeed.

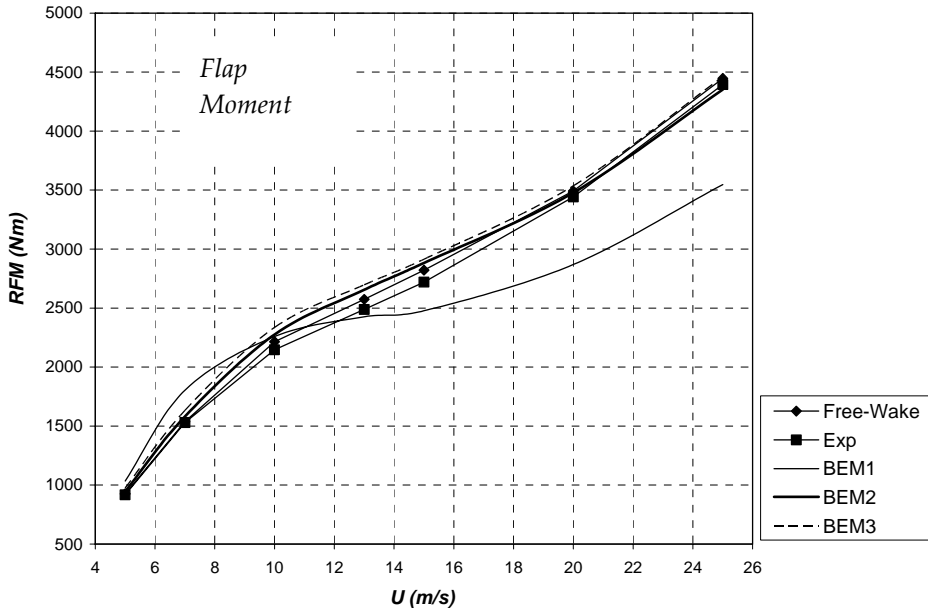


Figure 6.56(b) –Variation of blade root flap moment with windspeed.

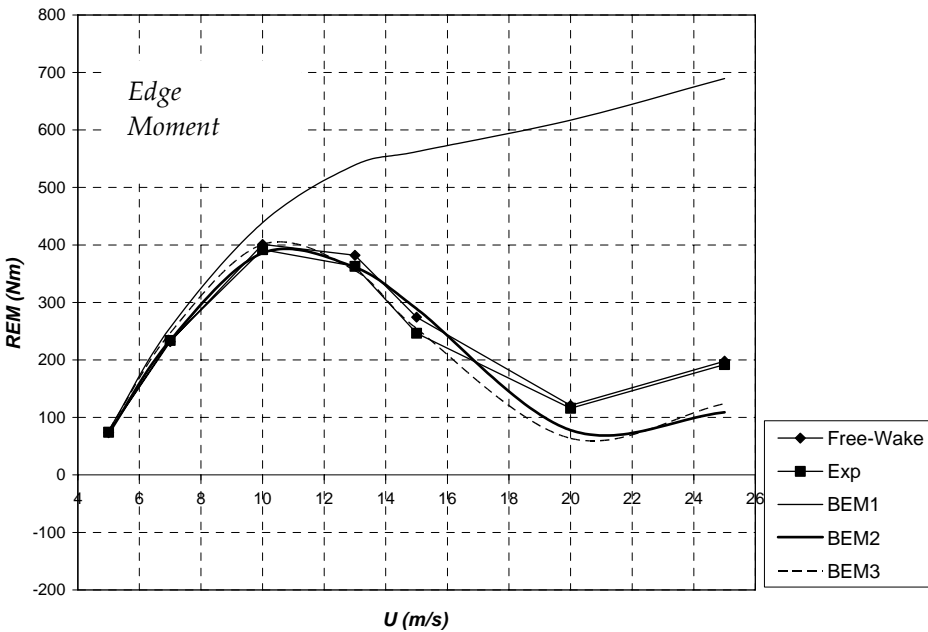


Figure 6.56(c) –Variation of blade root edge moment with windspeed.

6.4.2 Yawed Conditions

As for axial conditions, the newly derived aerofoil data for unsteady conditions in yaw was also interpolated to be able to use it for the BEM calculations. Strictly speaking, unsteady aerofoil data for 3D rotor applications should be interpolated with variables r/R , α , $\dot{\alpha}$, \dot{V} and k , i.e. $C_l, C_d \left\{ \frac{r}{R}, \alpha, \dot{\alpha}, \dot{V}, k \right\}$. But since the only scope for this analysis was to assess the improvement in BEM predictions only rather than developing a new engineering model, then it was possible to simply use a double interpolation using only two variables r/R and ϕ , i.e., $C_l, C_d \left\{ \frac{r}{R}, \phi \right\}$. A double interpolation was performed separately at each windspeed. The variation of C_l and C_d with r/R at any ϕ was fitted with a cubic spline interpolation (see Appendix D) with the boundary conditions that at the blade tip and root both C_l and C_d are zero.

To derive the inflow correction factor (denoted by F_{sa}) to account for the uneven induced velocity at the rotor disk in yaw the following method was used: recall from Eq. 3.27 (see section 3.5) that F_{sa} corrects only the axial induced velocity at the blade lifting lines. Making F_{sa} in Eq. 3.27 subject of the formula yields:

$$F_{sa} = \frac{u_{a,c}}{u_a} f \quad (6.8)$$

For each wind speed ($U= 5, 7, 10, 13$ and 15m/s at $\Psi=30^\circ$), parameters $u_{a,c}$ and u_a at each blade azimuth angle (ϕ) and radial location (r/R) were derived from the induced velocity distributions obtained from *HAWT_FWC* (Figs. 6.38 and 6.39). The Prandtl tip/root loss factor f could also be derived from *HAWT_FWC*, from knowledge of the inflow angle, ϕ , and using Eqts. 3.10. The results for F_{sa} at $U= 5, 10$ and 15m/s are plotted in Fig. 6.57. A cubic double spline interpolation was then done to obtain the inflow correction factor F_{sa} as a function of each blade azimuth angle and radial location, i.e. $F_{sa} \left(\frac{r}{R}, \phi \right)$.

The BEM computations were performed using different aerofoil data and with/without inflow corrections. The different BEM configurations are listed in table 6.3. They were selected in such a way that it was possible to determine quantitatively whether improvement is due to:

- a. the use of 3D static aerofoil data alone (by comparing BEM1 and BEM2 computations)
- b. the effect of including unsteady effects (including dynamic stall) by having 3D unsteady aerofoil data instead of 3D static data (by comparing BEM2 and BEM3 computations)
- c. the Coleman’s correction (see Eqts. 3.23, 3.24 and table 3.1) while at the same time having 3D unsteady aerofoil data (comparing BEM3 and BEM4)
- d. replacing Coleman’s correction with the newly derived corrections (Figs. 6.57) obtained from *HAWT_FWC* (comparing BEM4 and BEM5)

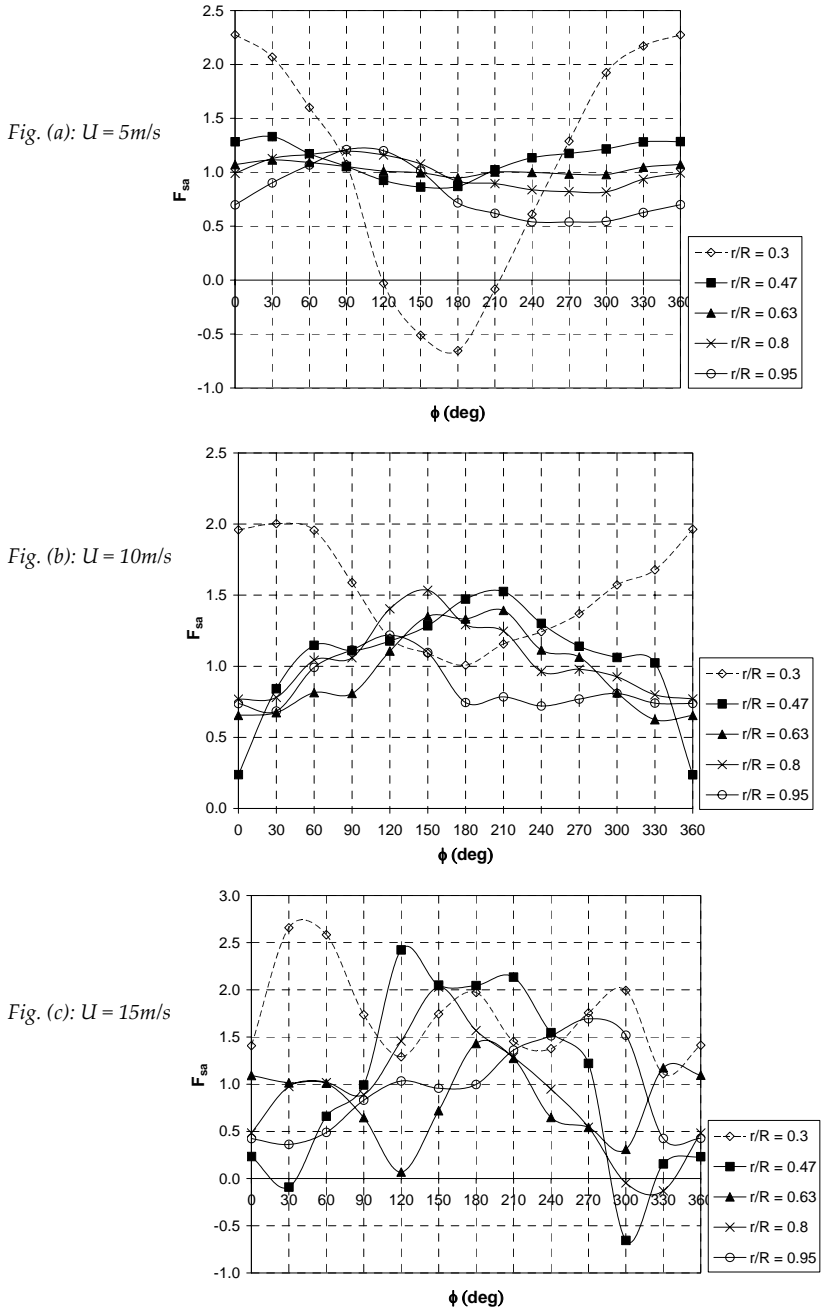


Figure 6.57 – Variations of the inflow correction factor F_{sa} derived by HAWT_FWC with blade azimuth angle and radial location.

By adopting this methodology it was possible to investigate whether improvement in the BEM code predictions is driven by the use of the new aerofoil data or by the new inflow correction or by both.

In all the different BEM computations, the Prandtl tip/root loss correction was used. When using the new inflow corrections (in the BEM5 configuration), this loss correction had to be included because its effect was accounted for when deriving the values for F_{sa} (see Eq. 6.8).

Table 6.3: Computations performed on NREL rotor for $\Psi=30^\circ$ using HAWT_BEM

Computation Reference	BEM Code Configuration
BEM1	<ul style="list-style-type: none"> • 2D static aerofoil data (from Delft wind tunnel) extrapolated using Viterna-Corrigan model (Fig. 6.50) • Correction for inflow in yaw NOT included • Prandtl tip/root correction factor included
BEM2	<ul style="list-style-type: none"> • New 3D static aerofoil data obtained from NREL blade pressure measurement and HAWT_FWC for axial conditions (Figs. 6.19) • Correction for inflow in yaw NOT included • Prandtl tip/root correction factor included
BEM3	<ul style="list-style-type: none"> • New 3D unsteady aerofoil data obtained from NREL blade pressure measurement and HAWT_FWC for yawed conditions (Figs. 6.33) • Correction for inflow in yaw NOT included • Prandtl tip/root correction factor included
BEM4	<ul style="list-style-type: none"> • New 3D unsteady aerofoil data obtained from NREL blade pressure measurement and HAWT_FWC for yawed conditions (Figs. 6.33) • Coleman correction for inflow in yaw included • Prandtl tip/root correction factor included
BEM5	<ul style="list-style-type: none"> • New 3D unsteady aerofoil data obtained from NREL blade pressure measurement and HAWT_FWC for yawed conditions (Figs. 6.33) • New inflow corrections for inflow in yaw obtained from NREL blade pressure measurement and HAWT_FWC for yawed conditions (Figs. 6.57) • Prandtl tip/root correction factor included

A. Comparison of induction factor distributions

Figs. 6.58, 6.59 and 6.60 compare the distributions for the azimuthally-averaged axial induction factor (a_i) for the different BEM computations (BEM1, BEM2, BEM3, BEM4 and BEM5) with those from the free-wake model *HAWT_FWC* (from Fig. 6.38) at windspeeds $U=5, 10$ and 15m/s . In each plot, the variation of a_i against rotor azimuth angle (ϕ) is plotted at radial locations $r/R=0.3, 0.47, 0.63, 0.8$ and 0.95 . In Figs. 6.61, 6.62 and 6.63, the axial induction factor at the blade lifting line ($a_{l,c}$) is shown. The predictions from *HAWT_FWC* for $a_{l,c}$ from Figs. 6.39 are included. Figs. 6.58, 6.59 and 6.60 show that, in most cases, the results for a_i from all five BEM computations are in close agreement with those from the free-wake model. Nonetheless the results for $a_{l,c}$ from the BEM computations differ considerably from each other, as noted in Figs. 6.61, 6.62 and 6.63. Recall from table 6.3 that the first three BEM computations (BEM1, BEM2 and BEM3) have no inflow correction to account for the uneven induction at the rotorplane created by the skewed helical wake. The results for $a_{l,c}$ from these three BEM computations are very much different from those predicted by the *HAWT_FWC*. This provides necessary evidence that the inflow correction in BEM computations is necessary to obtain a more realistic induction distribution at the blades. The BEM4 computation includes the Coleman correction for the inflow but in most cases the predictions for $a_{l,c}$ are still not in good agreement with those of the free-wake model (see Figs. 6.61, 6.62 and 6.63). The Coleman correction yields good agreement only at $U=5\text{m/s}$ and at the outboard blade sections $r/R=0.8$ and 0.95 . The best predictions for $a_{l,c}$ are those from the BEM5 computations since the inflow corrections used here were directly derived from the free-wake vortex model itself.

B. Comparison of aerodynamic loading distributions

The BEM results for the normal and tangential loading on the blades are now compared. The results for the normal loading (dA_n) are plotted against blade azimuth angle (ϕ) for wind speeds $U=5, 10$ and 15m/s in Figs. 6.64, 6.65 and 6.66, respectively. The corresponding results for the tangential loading (dA_t) are given in Figs. 6.67, 6.68 and 6.69. The experimental results obtained from the blade pressure measurements are included. It is shown that little improvement in the loading predictions is achieved by BEM when using the new 3D static aerofoil data obtained for axial conditions instead of the 2D static data (compare BEM1 and BEM2 results). However a radical improvement in the correlation with the experimental data is achieved when introducing the new unsteady 3D aerofoil data (compare BEM2 and BEM3 results). This provides evidence that with the use of reliable unsteady 3D aerofoil data, BEM predictions in yawed conditions can be significantly improved. The BEM4 and BEM5 results for loading differ only marginally from those of BEM3. This explains the fact that the influence of the inflow correction is very small and that the reason for this is that for the operating conditions being studied, the induction factors are small. It is expected that for other operating conditions, especially those for

which the tip speed ratio is high, the axial induction factors are larger and in such circumstances the inflow correction becomes more important.

C. Comparison of global loads

Figs. 6.70, 6.71 and 6.72 compare the low-speed shaft torque and the blade root flap and edge moments from the five different BEM computations with those derived from the blade pressure measurements using Eqts. 6.4 – 6.6. It can be noted that the use of the new 3D unsteady aerofoil data yields best correlation with the experimental data. The inclusion of the inflow correction due to yaw leaves only a small influence on the calculated global loads, as already observed in the loading results of Figs. 6.64 - 6.69.

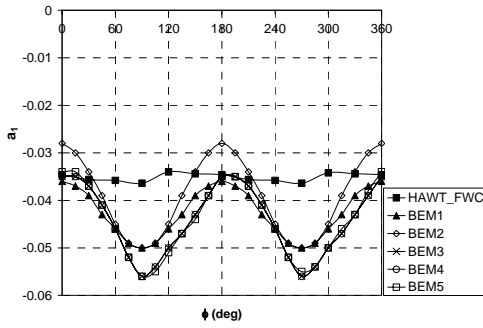


Fig. (a): $r/R=0.3$

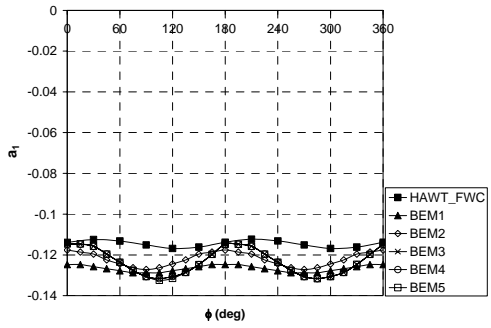


Fig. (b): $r/R=0.47$

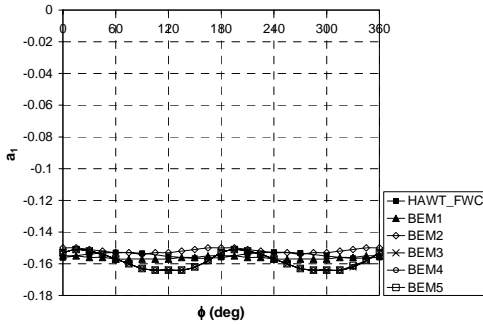


Fig. (c): $r/R=0.63$

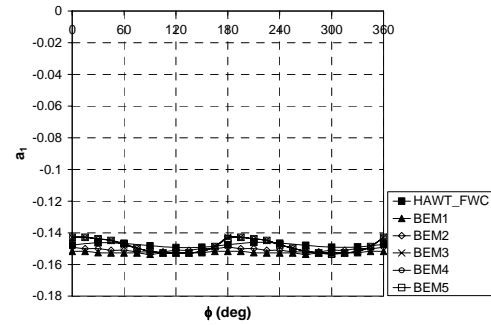


Fig. (d): $r/R=0.8$

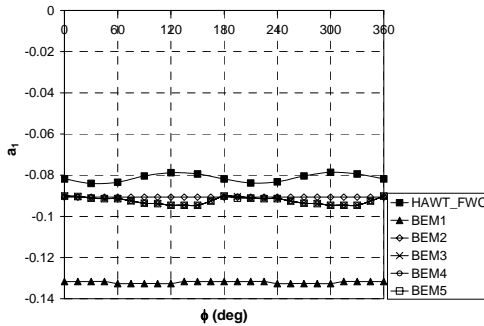


Fig. (e): $r/R=0.95$

Figure 6.58 – Variations of the azimuthally-averaged axial induction factor with blade azimuth angle at $U = 5\text{m/s}$, $\Psi = 30^\circ$.

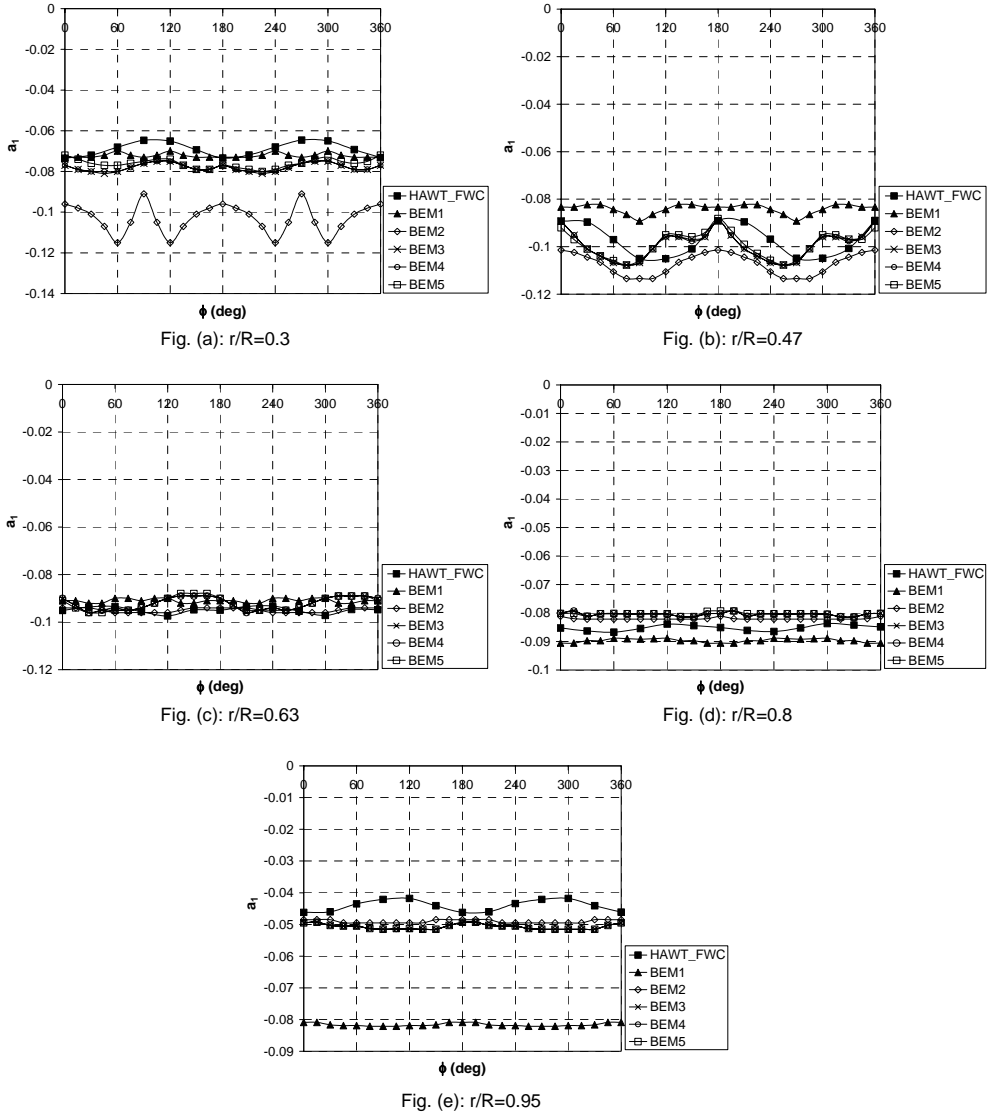


Figure 6.59 – Variations of the azimuthally-averaged axial induction factor with blade azimuth angle at $U = 10\text{m/s}$, $\Psi = 30^\circ$.

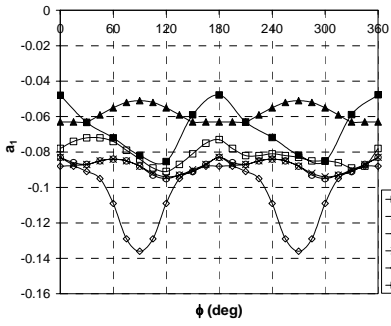


Fig. (a): $r/R=0.3$

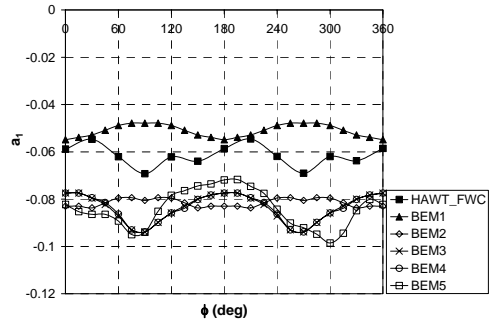


Fig. (b): $r/R=0.47$

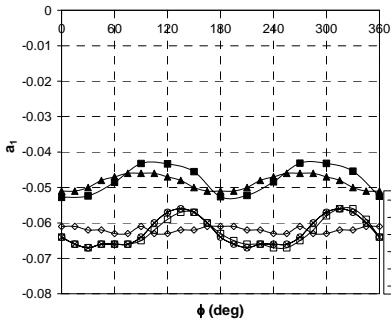


Fig. (c): $r/R=0.63$

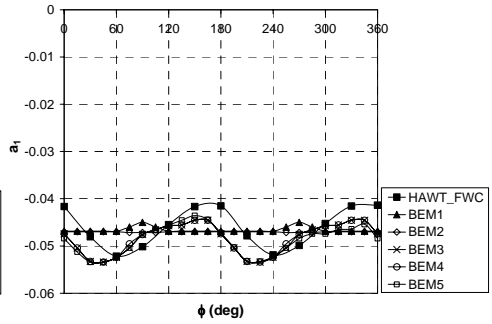


Fig. (d): $r/R=0.8$

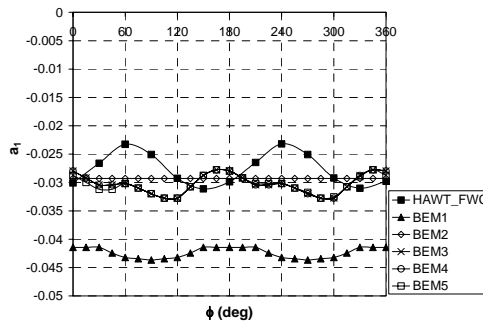


Fig. (e): $r/R=0.95$

Figure 6.60 – Variations of the azimuthally-averaged axial induction factor with blade azimuth angle at $U = 15\text{m/s}$, $\Psi = 30^\circ$.

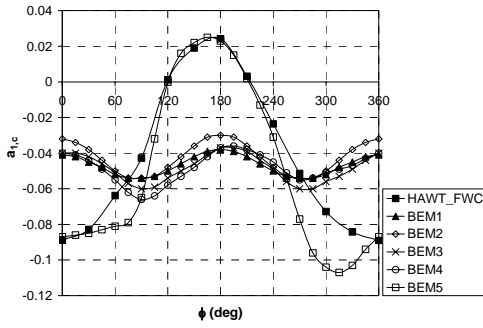


Fig. (a): $r/R=0.3$

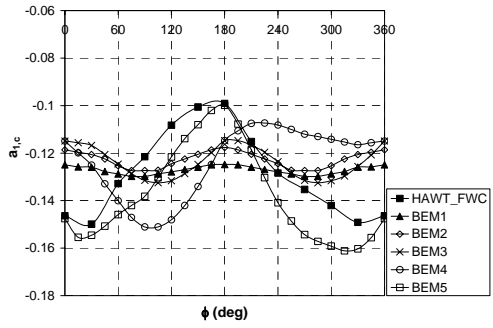


Fig. (b): $r/R=0.47$

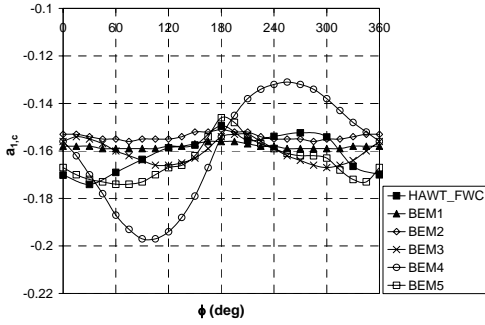


Fig. (c): $r/R=0.63$

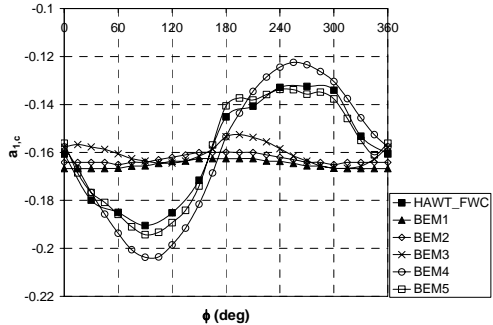


Fig. (d): $r/R=0.8$

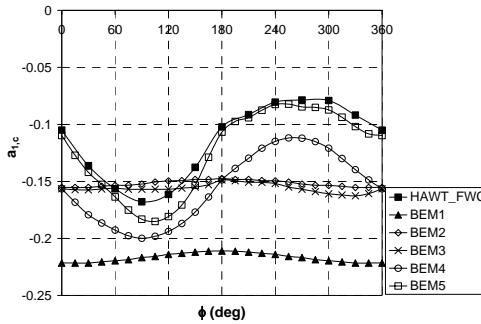


Fig. (e): $r/R=0.95$

Figure 6.61 – Variations of the axial induction factor at the blade lifting line with blade azimuth angle at $U = 5\text{m/s}$, $\Psi = 30^\circ$.

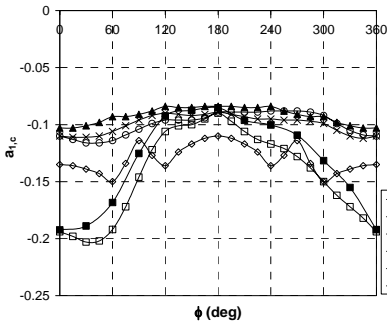


Fig. (a): $r/R=0.3$

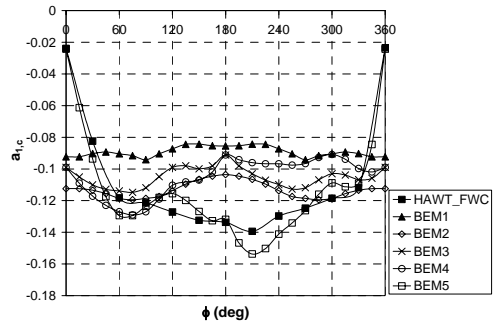


Fig. (b): $r/R=0.47$

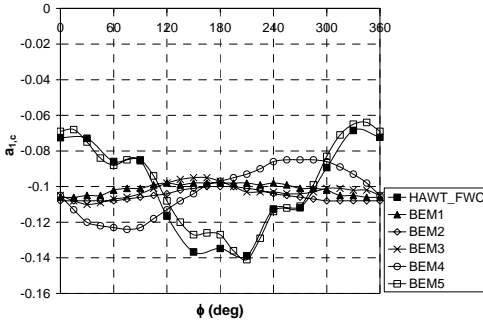


Fig. (c): $r/R=0.63$

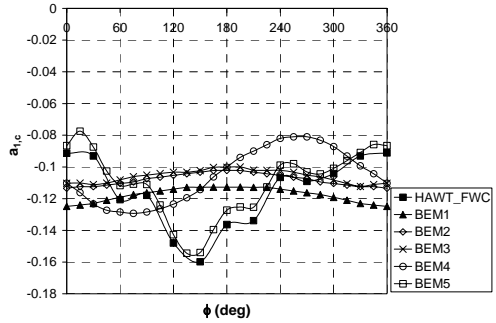


Fig. (d): $r/R=0.8$

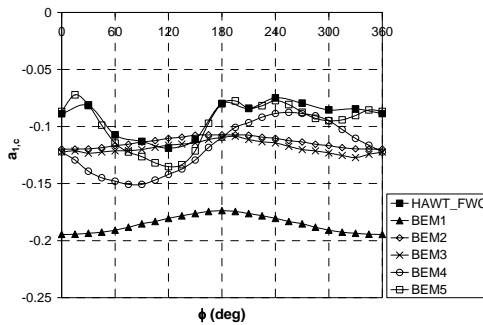


Fig. (e): $r/R=0.95$

Figure 6.62 – Variations of the axial induction factor at the blade lifting line with blade azimuth angle at $U = 10\text{m/s}$, $\Psi = 30^\circ$.

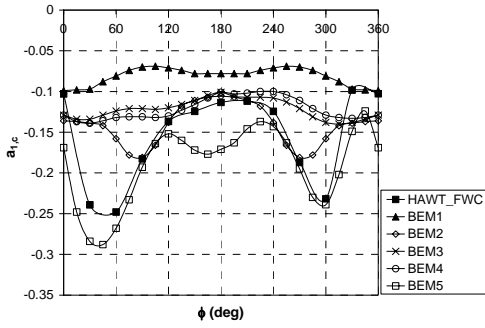


Fig. (a): $r/R=0.3$

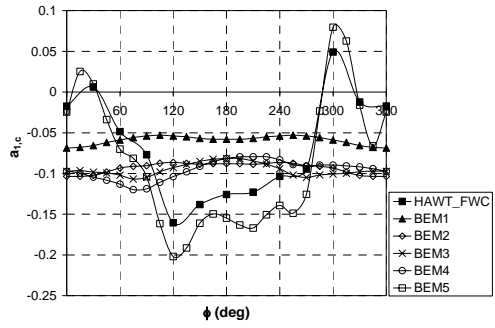


Fig. (b): $r/R=0.47$

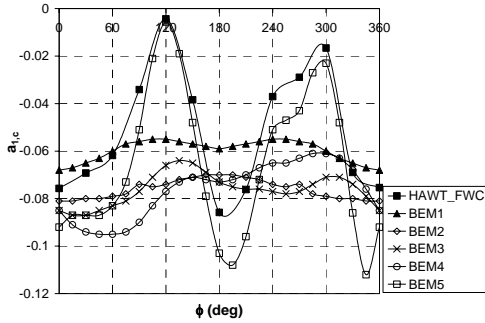


Fig. (c): $r/R=0.63$

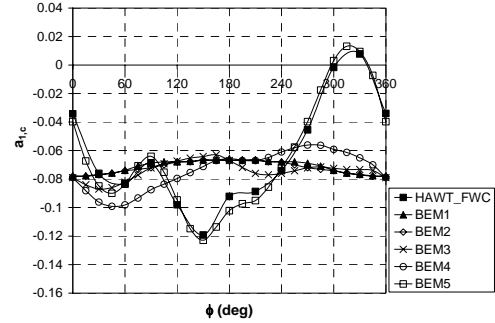


Fig. (d): $r/R=0.8$

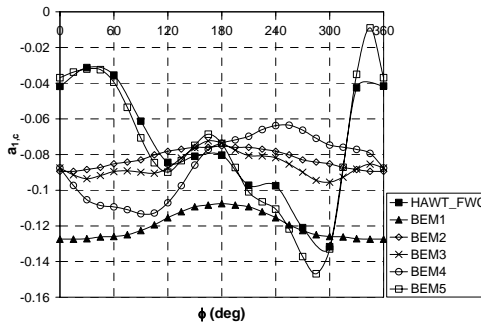


Fig. (e): $r/R=0.95$

Figure 6.63 – Variations of the axial induction factor at the blade lifting line with blade azimuth angle at $U = 15\text{m/s}$, $\Psi = 30^\circ$.

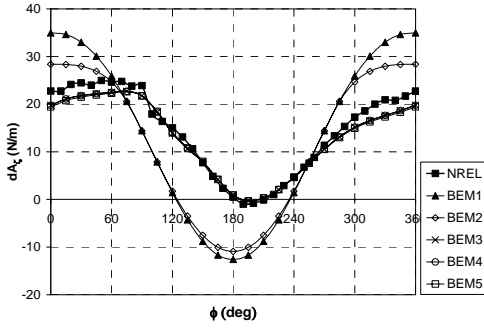


Fig. (a): $r/R=0.3$

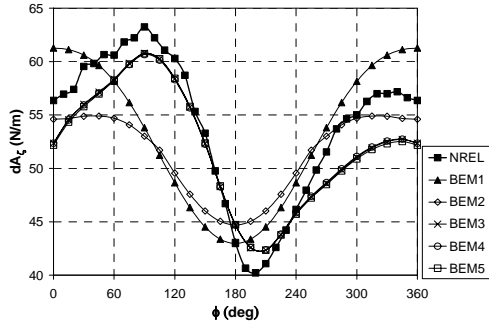


Fig. (b): $r/R=0.47$

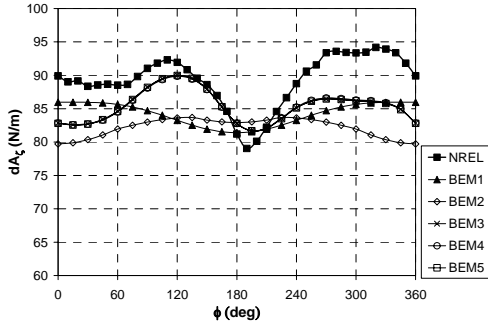


Fig. (c): $r/R=0.63$

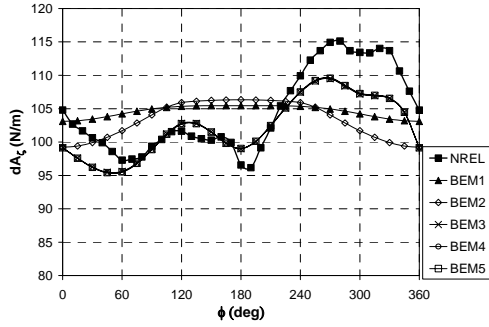


Fig. (d): $r/R=0.8$

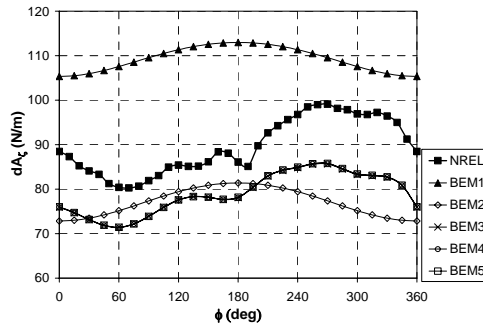


Fig. (e): $r/R=0.95$

Figure 6.64 – Variations of the normal loading at the blade lifting line with blade azimuth angle at $U = 5\text{m/s}$, $\Psi = 30^\circ$.

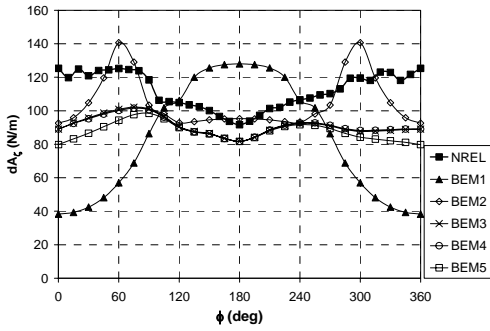


Fig. (a): $r/R=0.3$

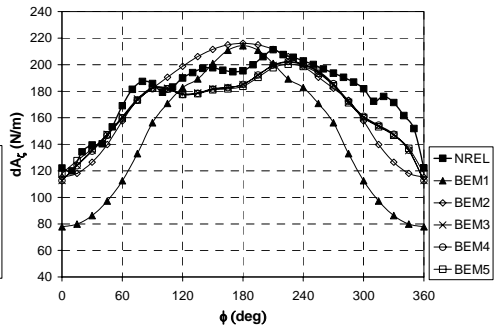


Fig. (b): $r/R=0.47$

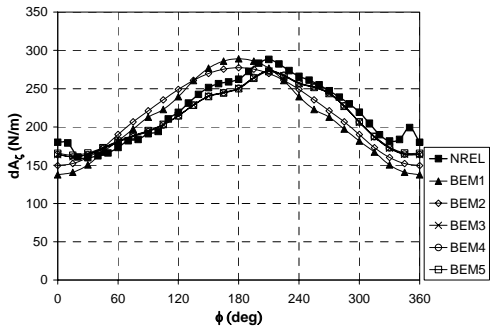


Fig. (c): $r/R=0.63$

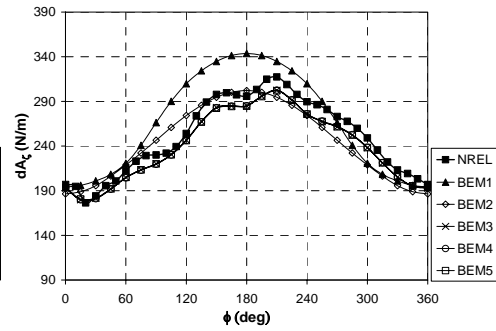


Fig. (d): $r/R=0.8$

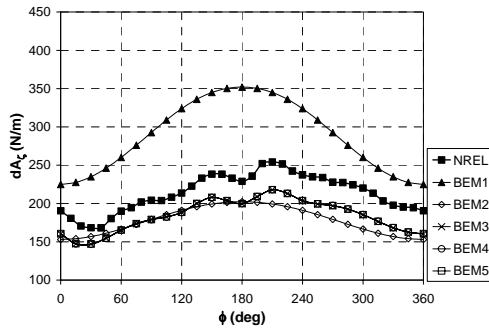


Fig. (e): $r/R=0.95$

Figure 6.65 – Variations of the normal loading at the blade lifting line with blade azimuth angle at $U = 10\text{m/s}$, $\Psi = 30^\circ$.

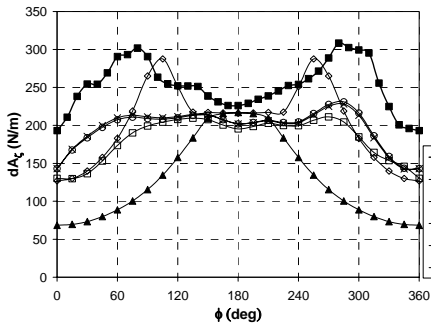


Fig. (a): $r/R=0.3$

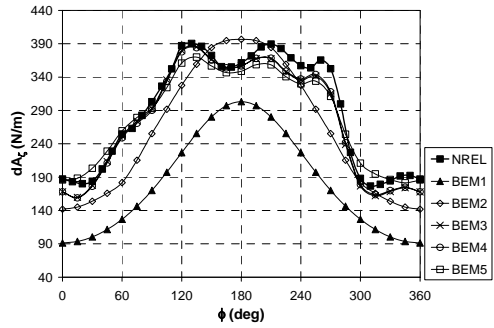


Fig. (b): $r/R=0.47$

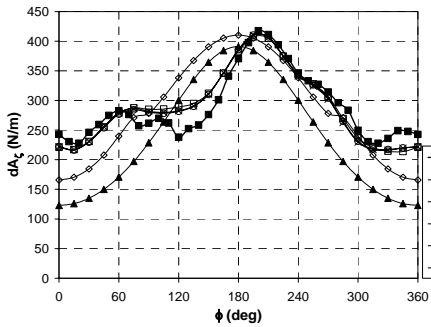


Fig. (c): $r/R=0.63$

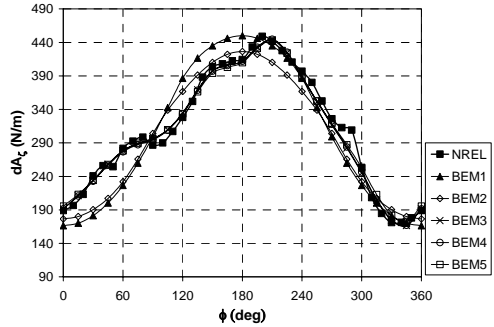


Fig. (d): $r/R=0.8$

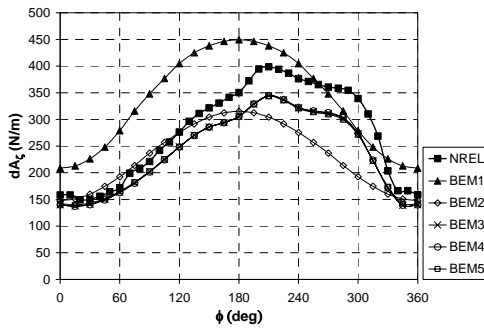


Fig. (e): $r/R=0.95$

Figure 6.66 – Variations of the normal loading at the blade lifting line with blade azimuth angle at $U = 15\text{m/s}$, $\Psi = 30^\circ$.

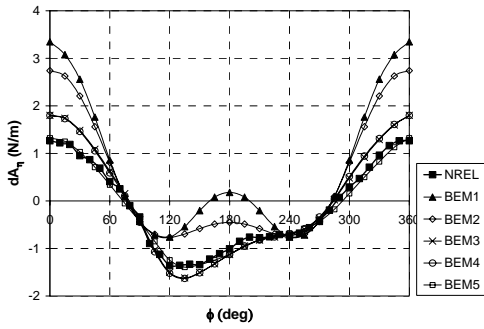


Fig. (a): $r/R=0.3$

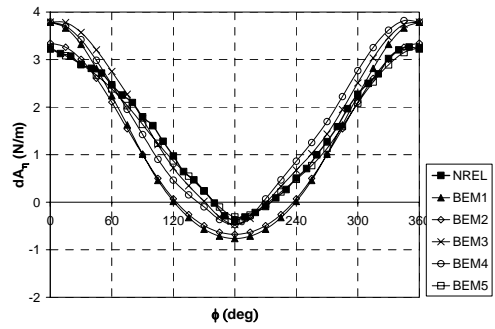


Fig. (b): $r/R=0.47$

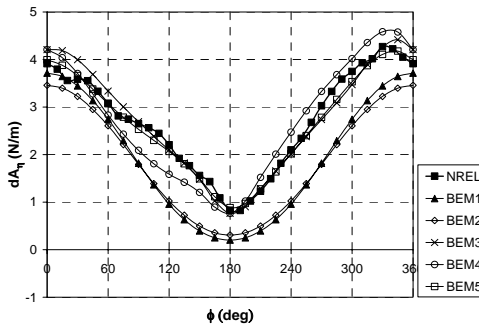


Fig. (c): $r/R=0.63$

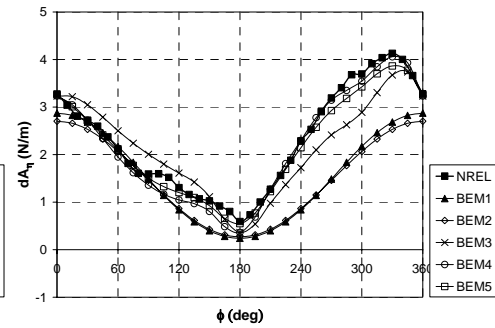


Fig. (d): $r/R=0.8$

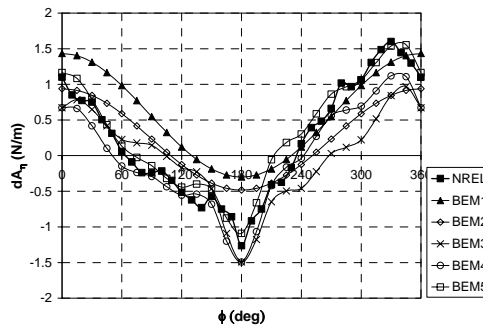


Fig. (e): $r/R=0.95$

Figure 6.67 – Variations of the tangential loading at the blade lifting line with blade azimuth angle at $U = 5\text{m/s}$, $\Psi = 30^\circ$.

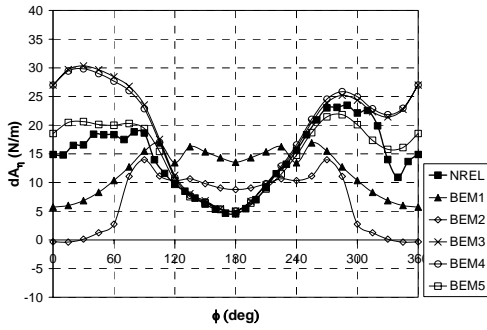


Fig. (a): $r/R=0.3$

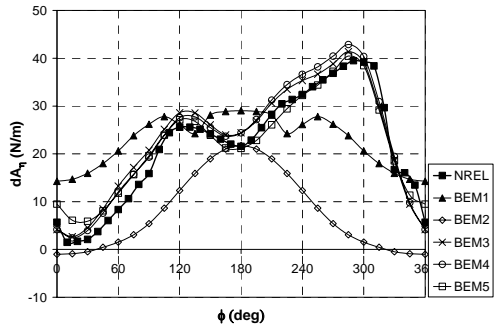


Fig. (b): $r/R=0.47$

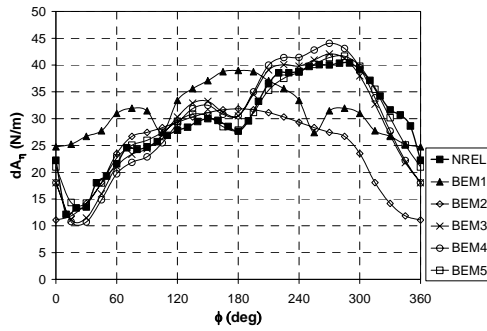


Fig. (c): $r/R=0.63$

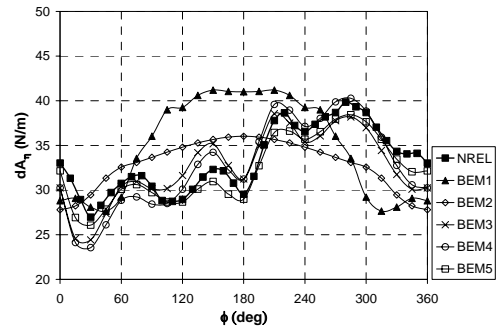


Fig. (d): $r/R=0.8$

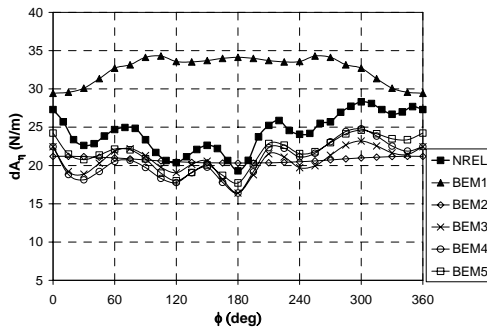


Fig. (e): $r/R=0.95$

Figure 6.68 – Variations of the tangential loading at the blade lifting line with blade azimuth angle at $U = 10\text{m/s}$, $\Psi = 30^\circ$.

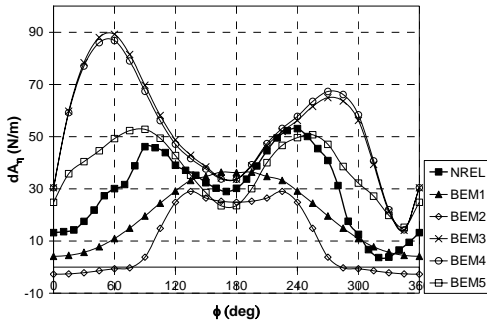


Fig. (a): $r/R=0.3$

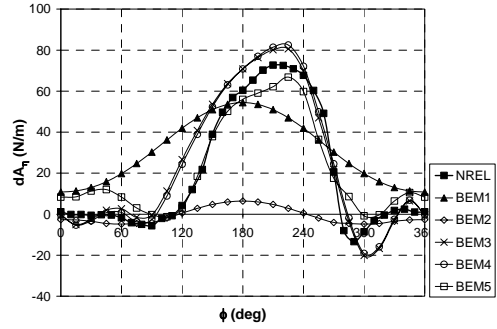


Fig. (b): $r/R=0.47$

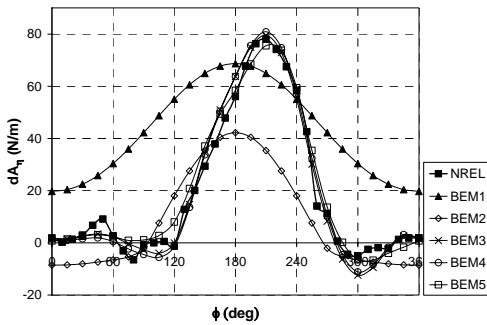


Fig. (c): $r/R=0.63$

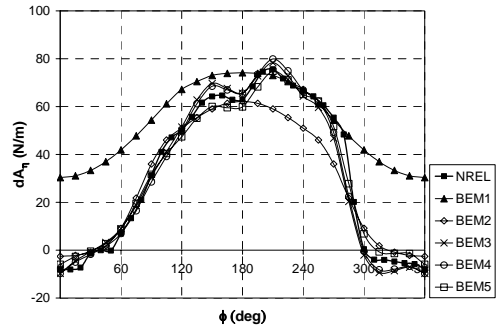


Fig. (d): $r/R=0.8$

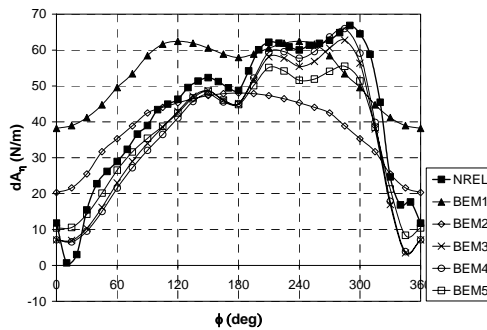


Fig. (e): $r/R=0.95$

Figure 6.69 – Variations of the tangential loading at the blade lifting line with blade azimuth angle at $U = 15\text{m/s}$, $\Psi = 30^\circ$.

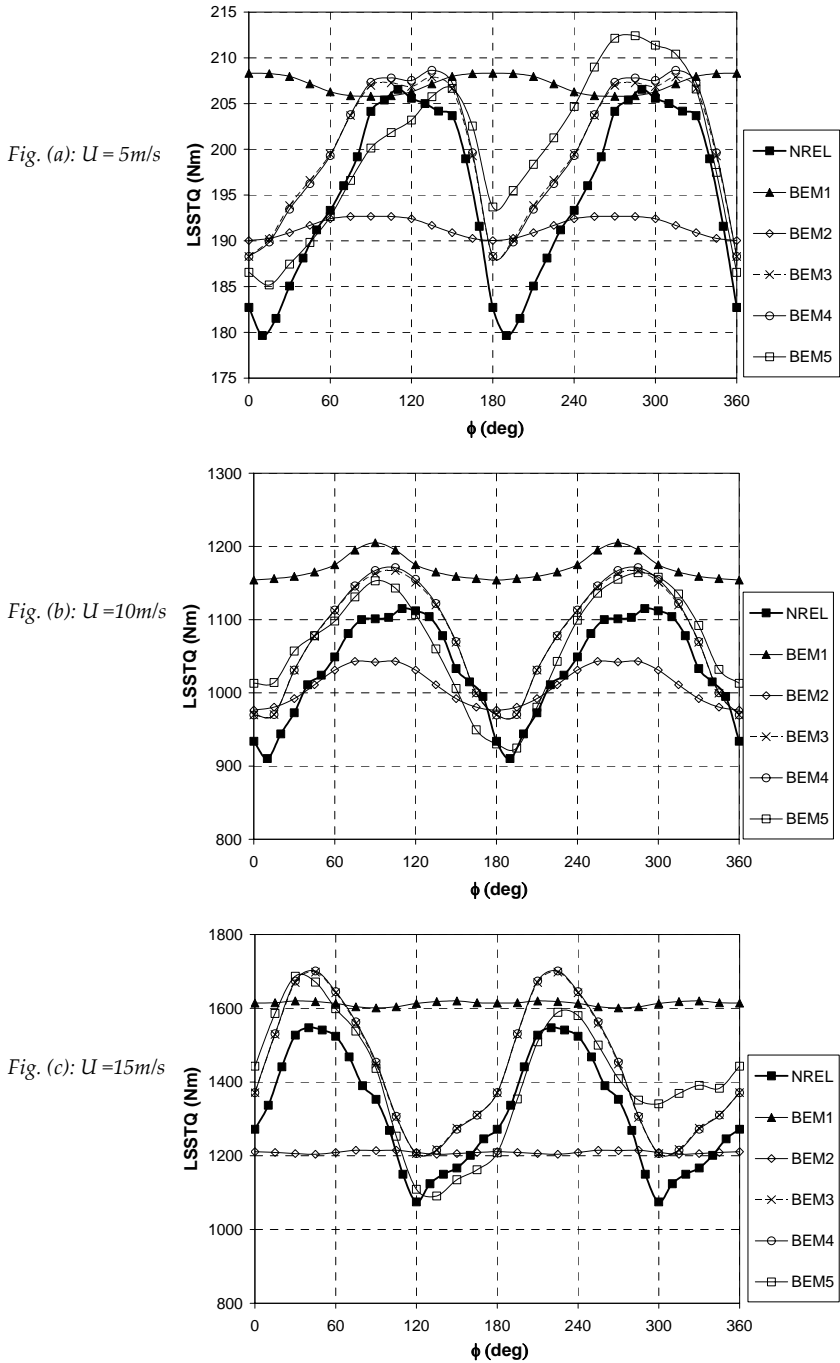


Figure 6.70 – Variation of the low-speed shaft torque with blade azimuth angle at $U = 5, 10, 15\text{m/s}$, $\Psi = 30^\circ$.

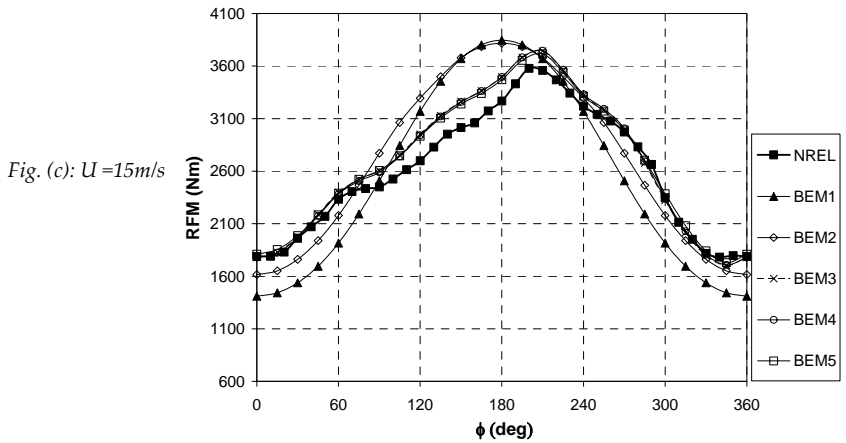
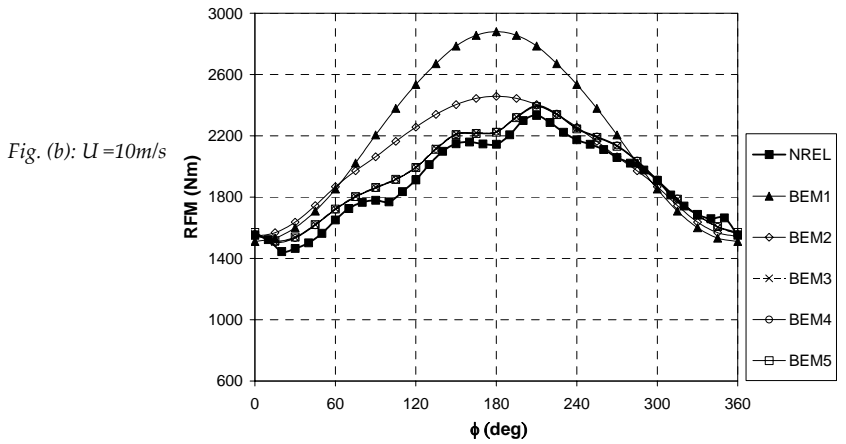
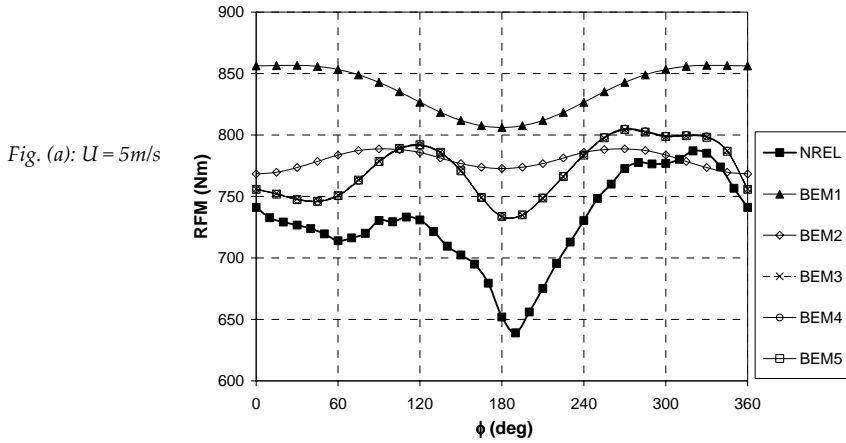


Figure 6.71 – Variation of the blade root flap moment with blade azimuth angle at $U = 5, 10, 15\text{m/s}$, $\psi = 30^\circ$.

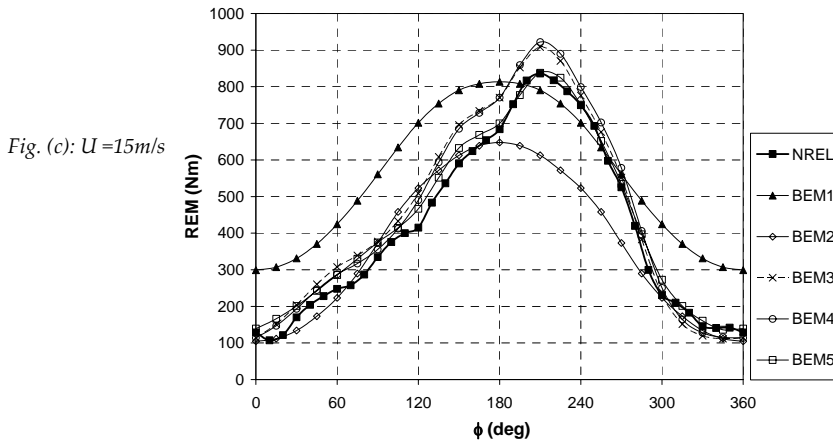
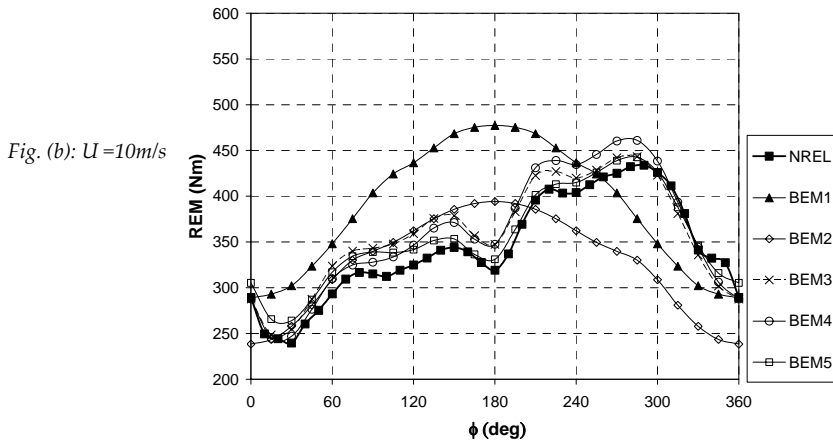
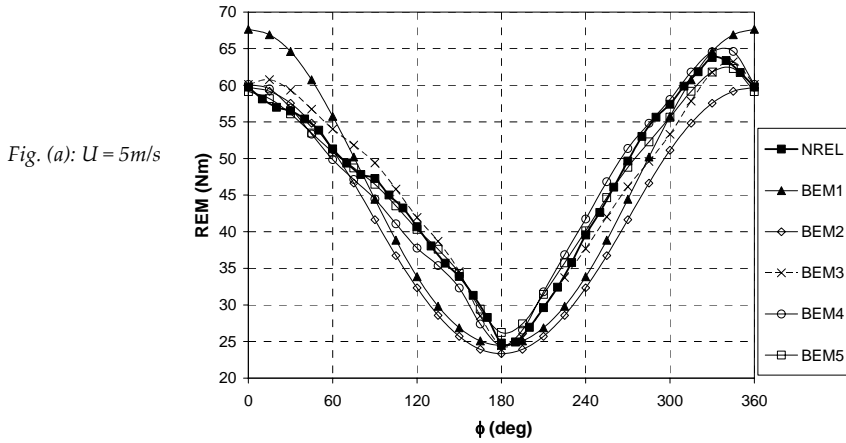


Figure 6.72 – Variation of the blade root edge with blade azimuth angle at $U = 5, 10, 15\text{m/s}$, $\Psi = 30^\circ$.

6.5 Conclusions

In this chapter, a novel approach was presented for using a free-wake vortex model for finding the angle of attack variations, inflow distribution at the rotorplane and wake geometry for the cases where the experimental data consists only of blade pressure measurements. This made it possible to carry out a deeper investigation of rotor aerodynamic phenomena and derive new aerofoil data and inflow corrections that would be very useful in developing better engineering models for BEM codes. The NREL Phase VI UAE experimental data was used for this case study and both axial and yawed conditions ($\psi=0^\circ$ and 30°) were studied. The wind tunnel measurements were readily available from NREL and no further measurements were required. New 3D aerofoil data were derived from the blade pressure measurements and the angle of attack distributions predicted by the free-wake vortex model. This data was compared with 2D static wind tunnel data for the S809 aerofoil. For axial conditions in which the local angle of attack is steady, two conclusions could be made:

- (1) for small angles of attack (less than the 2D static stalling angle), the new 3D aerofoil data is very close to the 2D aerofoil data except at the tip and root region. In the latter regions, the new 3D lift coefficient was found to be lower than the 2D aerofoil data.
- (2) for larger angles of attack, the new 3D aerofoil data was considerably different than the 2D data and the presence of stall-delay was evident, especially at the inboard sections of the blades. It was also observed that the increase in the lift coefficient due to stall delay is accompanied by a corresponding increase in the drag coefficient.

For yawed conditions, the local angle of attack was unsteady and a function of the blade azimuth angle. Therefore the new 3D derived aerofoil data for yaw was also unsteady. This data was compared with the 2D static wind tunnel aerofoil data as well as with the new steady 3D data obtained from axial conditions. Considerable hysteresis in both the lift and drag was found, especially at high angles of attack where dynamic stall takes place. It was found that the 3D unsteady coefficients could well exceed the corresponding steady values derived for axial conditions. It could also be concluded that the unsteady $C_l-\alpha$ and $C_{dp}-\alpha$ hysteresis loops were in general closer to the 3D steady values than to the corresponding 2D steady data. This was observed at both attached and stall conditions and it implies that 3D effects (in particular stall-delay) have a significant role in the unsteady flow behaviour of wind turbine blades.

The computed free-wake geometries were plotted together with the corresponding wake circulation distributions. These provided a pictorial explanation of how the bound circulation at the blades is diffused into the fluid stream under the action of complex 3D flows. In axial conditions, this bound circulation is diffused into the wake in the form of trailing circulation only, while in yawed conditions the bound circulation will transform

into wake circulation consisting of both trailing and shed circulation. It was noted that for the NREL rotor at low windspeeds, at which the angles of attack at the blades are small, the trailing circulation in the wake tends to be concentrated at the blade tip and root regions. For higher windspeeds, the trailing circulation is more dispersed radially, with the presence of horse-shoe vortices emerging from the middle blade sections. This behaviour was observed in both axial and yawed conditions. At $\psi=30^\circ$, the shed circulation levels in the wake were found to be generally small at all the windspeeds considered.

The induced velocity distributions predicted by the free-wake model for the given aerodynamic loading acquired from the blade surface pressure measurements were also investigated. These were found to vary considerably with windspeed and yaw. Both the distributions of the azimuthally averaged axial induction factor (a_1) and those of the axial induced factor at the lifting line of the blades ($a_{1,c}$) were plotted. For yawed conditions, a_1 was found to vary periodically with the rotor azimuth angle (ϕ) at frequency $2p$. At low windspeeds, this cyclic component was negligibly small, but it then became considerably larger at higher windspeeds. The variation of $a_{1,c}$ with the blade azimuth angle in yaw was also periodic. At low windspeeds, this periodic variation was found to be regular with a phase angle that changes with the radial location (r/R). At higher windspeeds however, the periodic variation does not remain regular and this results from the presence of horse-shoe vortices in the middle blade sections.

From the free-wake plots, it was possible to derive the approximate pitch of the helical vortex sheets in the wake. It was found that while the rotor speed was fixed, this pitch increases almost linearly with windspeed in both axial and yawed conditions. The wake expansion was found to be minimal and this is due to the fact that the turbine was generally operating at low thrust coefficients ($C_T < 0.6$, see table 6.1).

The angle of attack values derived by this novel approach were compared with the local flow angles (*LFA*) measured in the wind tunnel using the five-hole probes. Large differences were noted and this consolidates the fact that the *LFA* values cannot be assumed to be equal to the angle of attack when deriving new aerofoil data from rotor experiments. Since with a free-wake vortex model it is possible to determine the induced velocities at any point in the flow field, this novel approach provided the possibility to calculate the *LFA* values at the probe tip locations. These calculated *LFA* values were compared with the experimental results obtained with the five-hole probes. This comparison was a means for evaluating this approach for coupling the free-wake vortex model with the blade pressure measurements to find the angle of attack. It was found that in both axial and yawed conditions, the free-wake vortex model results for the *LFA* were in close agreement with the measured values at low windspeeds. At high windspeeds, the agreement was only good for radial locations $r/R > 0.67$. The agreement was not good for the inboard blade regions ($r/R < 0.67$), with the maximum discrepancy reaching 10° . It is likely that this disagreement is originating from the inherent limitations of the lifting line model embedded in the free-

wake vortex code. However, in the case of yawed conditions, the accuracy with which the five-hole probes measure the *LFA* is also being questioned because of the relatively large cyclic pitching rates created by the rotor yaw. Further work is required to evaluate the accuracy with which five-hole probes measure the *LFA* at large pitch rates.

Recommendations for future work

It is important to point out the fact that, although this study has successfully demonstrated the effectiveness of using a free-wake model in conjunction with blade pressure measurements to obtain further insight of wind turbine aerodynamics, the results obtained are subject to the following uncertainties:

- The accuracy of the results is dependent on the accuracy with which the free-wake vortex model models the blades and wake. In this study, a lifting line representation of the blades was used and further work is required to investigate the accuracy of lifting-line models in representing the blades. Lifting surface and panel methods are more accurate in capturing certain 3D flow effects around the blades. Further research is also required to validate the viscous modelling methodology adopted by the subject free-wake code.
- This study did not cater for the cycle-to-cycle variations observed in the measured values of C_n and C_t . These variations were considerably high in yawed conditions (refer to Fig. 6.5). In this study, only the mean values of C_n and C_t were used in the calculations. Future work will include a stochastic analysis to account for such cycle-to-cycle variations.

Investigating the improvement in BEM predictions with new 3D aerofoil data and inflow corrections

The new 3D aerofoil data derived from the blade pressure measurements in conjunction with the free-wake vortex model were used in a typical BEM code to model the NREL rotor in both axial/yawed and attached/stalled conditions. In this way it was possible to assess the improvement in BEM predictions were reliable 3D aerofoil data is used. For yawed conditions, new inflow corrections to account for skewed wake effects in BEM codes (F_{sa}) were also derived. It was possible to quantify the relative importance for such corrections. Various conclusions could be drawn from this study, and these provide more insight on how BEM models could be improved. Actually some of the findings consolidate what was found previously when analysing the TUDelft rotor. A detailed discussion on the limitations of BEM codes and the possibilities for improving such codes will be described in the next Chapter, (Chapter 7).

7. Guidelines for Improving the Reliability of BEM-based Design Codes

The research work on the TUDelft and NREL wind tunnel model turbines presented in this thesis introduced new methodologies for taking more benefit of limited experimental data to be able to obtain a deeper knowledge of HAWT aerodynamics. A major outcome was a deeper understanding of the limitations of BEM-based design codes in general and why these do not always predict accurate results in particular for the conditions of yaw and stall. This understanding provided further insight on how the accuracy of such codes can be improved through the development of better engineering models. In this chapter, the various limitations of typical BEM codes identified during the in-depth analysis of the TUDelft and NREL rotors in Chapters 4 and 6 respectively are summarised and discussed. Various guidelines on how these codes can be improved are also presented. These guidelines are applicable for modelling conditions in which the turbine is operating in a uniform and steady wind speed with the rotor yaw angle, tip speed ratio and blade pitch angle maintained constant with time.

7.1 Modelling of Aerofoil Data

It was evident through the analysis with the NREL rotor that the accuracy of BEM predictions for the blade load distributions is very much subject to what aerofoil data is used. The flow phenomena over a rotating wind turbine blade are far more complex than those observed in 2D static wind tunnel experiments and consequently the aerofoil data is also different. The differences are mainly noted in the blade tip/root region, at high angles of attack and in unsteady conditions (as for example in yawed rotors). With the novel approach presented in this thesis for finding the angle of attack using a free-wake vortex model, it was possible to derive new reliable aerofoil data for wind turbines from the blade pressure measurements taken during the NREL Phase VI experiments. A very interesting finding was that the BEM predictions improved considerably when this new aerofoil data was used. The improvement was noted even for situations that are known to be very difficult to predict accurately, mainly in highly stalled and yawed conditions. It can therefore be concluded that in many situations, BEM-based codes are deficient not necessarily because the BEM theory is in itself inadequate but because the aerofoil data used is not correct. More accurate engineering models that model aerofoil data need to be developed and made available to the wind turbine designer.

This study has also shown that the application of the standard Prandtl tip/root loss correction with the use of 2D static wind tunnel aerofoil data is inaccurate. It over-predicts

the loading at the blade tip in both the TUDelft and NREL rotors (see Fig. 4.109 and Figs 6.51(a)). This Prandtl correction works by artificially increasing the induction at the blade tip and root to reduce the angle of attack and hence the loading. This technique was found to over-predict the induction at the blade tip and root (see Fig. 4.103). A better way of applying the tip/root loss correction for the BEM theory should be based on modifying the 2D aerofoil data instead of the induction. However, from the newly derived 3D aerofoil data from the NREL blade measurements it was found that tip/root loss effects were already included and that the tip/root loss correction in the BEM calculations was not required. This suggests that if 3D aerofoil data is derived from blade pressure measurements or CFD, the tip/root loss correction is not required any longer in the BEM calculations.

From the new aerofoil data derived in this study for the NREL rotor in axial conditions (Figs. 6.19(a) and (b)), a new engineering model could be formulated. The model is still based on input from the 2D aerofoil data ($C_{l,2D}$ and $C_{d,2D}$) for both low and high angles of attack. The basic formulation is similar to that of present engineering models (e.g. those of Du and Selig [22] and Chaviaropoulos *et al.* [17] (Eqts. 3.31 and 3.33), but a tip/root loss correction factor is included. The 3D lift and drag coefficients are expressed as

$$C_{l,3D} = f * (C_{l,2D} + f_l (C_{l,lin} - C_{l,2D})) \quad (7.1)$$

$$C_{d,3D} = f * (C_{d,2D} + f_d (C_{d,2D} - C_{d,2D-MIN})) \quad (7.2)$$

f is a tip/root loss correction that corrects the aerofoil data and replaces the Prandtl correction. The tip/root loss correction is included because the 2D aerofoil data is still used as a basis for the model. From the analysis of the loading distributions on the NREL rotor in axial conditions, it was found that the following model for the factor f models the tip and root loss on this rotor adequately at all the tip speed ratios considered:

$$f = \left(\frac{2}{\pi}\right)^2 \cos^{-1} \left[\exp \left\{ -18 \frac{(1-r/R)}{r/R} \right\} \right] * \cos^{-1} \left[\exp \left\{ -3.8 \frac{(r/R - R_r/R)}{R_r/R} \right\} \right] \quad (7.3)$$

Parameters f_l and f_d are used to model the influences of blade rotation (stall-delay) on the lift and drag coefficients respectively. Values for these parameters were derived for the $C_{l,3D}$ and $C_{d,3D}$ values of Figs. 6.19(a) and (b). The results are plotted in Figs. 7.1(a) and (b). For $\alpha < \alpha_s$, the influences of blade rotation were found to be small and $C_{l,2D}$ and $C_{d,2D}$ are very close to $C_{l,lin}$ and $C_{d,2D-MIN}$, respectively. Therefore for $\alpha < \alpha_s$, f_l and f_d could be taken as zero in the modelling. For $\alpha > \alpha_s$, f_l and f_d were found to vary both with the radial location and angle of attack.

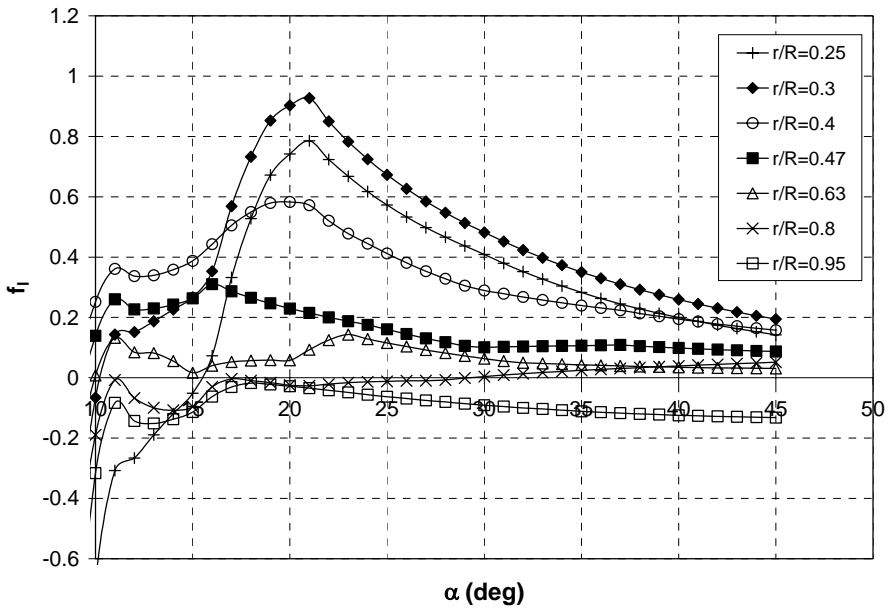


Figure 7.1(a) – Variation of f_i with angle of attack at different radial locations as derived from the results of Fig. 6.19(a) and using Eqs. 7.1 and 7.3.

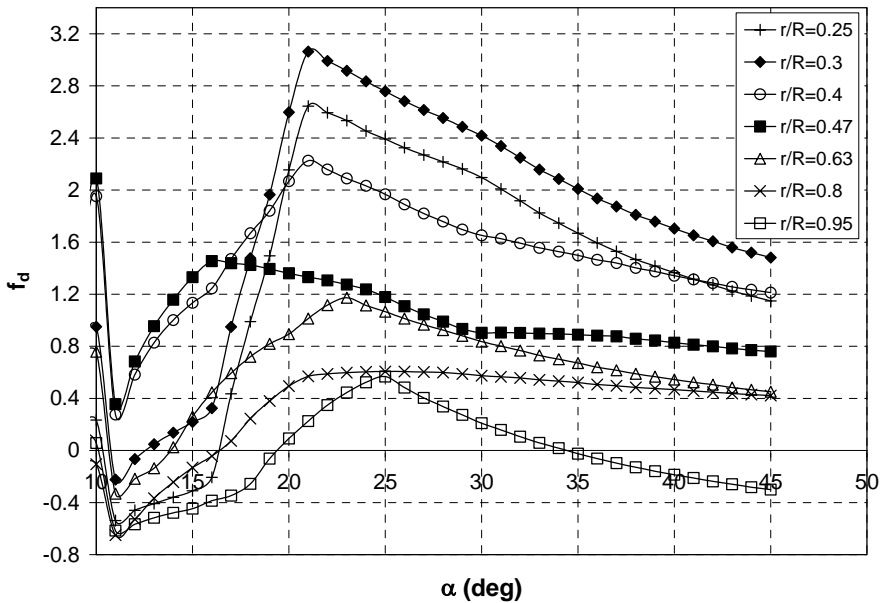


Figure 7.1(b) – Variation of f_d with angle of attack at different radial locations as derived from the results of Fig. 6.19(b) and using Eqs. 7.2 and 7.3.

In developing the new engineering model, the variations of f_l and f_d were modelled using the formulas:

$$\begin{aligned} f_l &= 0 & \text{if } \alpha \leq \alpha_s \\ f_l &= g(m_0 - m\alpha)e^{-a(\alpha - \alpha_s)} * \left(1 - e^{-0.003(\alpha - \alpha_s)^3}\right) & \text{if } \alpha > \alpha_s \end{aligned} \quad (7.4a)$$

$$\begin{aligned} f_d &= 0 & \text{if } \alpha \leq \alpha_s \\ f_d &= h(n_0 - n\alpha)e^{-b(\alpha - \alpha_s)} * \left(1 - e^{-0.003(\alpha - \alpha_s)^3}\right) & \text{if } \alpha > \alpha_s \end{aligned} \quad (7.4b)$$

where α_s was taken to be equal to 10^0 . The values of Figs. 7.1(a) and (b) were used to model parameters a, g, m_0, m, b, h, n_0 and n as function of the local solidity (c/r). When each of the latter seven parameters was plotted against c/r , it was found that it is impossible to model the variations with sufficient accuracy using a simple linear or quadratic fit. A third or fourth-order polynomial fit was required to model each of parameters a, g, m_0, m, b, h, n_0 and n as function of c/r , as follows:

$$a = -180.34\left(\frac{c}{r}\right)^4 + 236.02\left(\frac{c}{r}\right)^3 - 109.19\left(\frac{c}{r}\right)^2 + 20.01\left(\frac{c}{r}\right) - 0.927 \quad (7.5a)$$

$$g = 81.06\left(\frac{c}{r}\right)^3 - 70.19\left(\frac{c}{r}\right)^2 + 20.4\left(\frac{c}{r}\right) - 0.9 \quad (7.5b)$$

$$m_0 = -10.75\left(\frac{c}{r}\right)^3 + 0.99\left(\frac{c}{r}\right)^2 + 2.45\left(\frac{c}{r}\right) - 0.247 \quad (7.5c)$$

$$m = -0.2934\left(\frac{c}{r}\right)^3 + 0.1461\left(\frac{c}{r}\right)^2 - 0.005\left(\frac{c}{r}\right) + 0.0006 \quad (7.5d)$$

$$b = 2.26\left(\frac{c}{r}\right)^4 - 3.06\left(\frac{c}{r}\right)^3 + 1.346\left(\frac{c}{r}\right)^2 - 0.19\left(\frac{c}{r}\right) + 0.01 \quad (7.6a)$$

$$h = 0.17\left(\frac{c}{r}\right)^3 + 19.4\left(\frac{c}{r}\right)^2 - 5.49\left(\frac{c}{r}\right) + 1.84 \quad (7.6b)$$

$$n_0 = -88.85\left(\frac{c}{r}\right)^3 + 75.21\left(\frac{c}{r}\right)^2 - 15.1\left(\frac{c}{r}\right) + 0.72 \quad (7.6c)$$

$$n = -2.12\left(\frac{c}{r}\right)^3 + 2.29\left(\frac{c}{r}\right)^2 - 0.655\left(\frac{c}{r}\right) + 0.071 \quad (7.6d)$$

Although the above new model seems complex, it can still be handled very efficiently with personal computers. Figure 7.2 compares the 3D lift and drag coefficients ($C_{l,3D}$ and $C_{d,3D}$) predicted by this new engineering model (Eqts. 7.1–7.6) with those derived from the blade pressure measurements on the NREL rotor in conjunction with the free-wake vortex model (i.e. those plotted in Figs. 6.19(a) and (b)). It is shown that the new model can reproduce the results quite accurately. The 3D lift coefficient predicted by Snel’s model (Eqts. 3.30 with parameters a and b taken as 3 and 2, respectively) is also being included. It can be easily noted that the new engineering model provides much more accurate predictions than Snel’s model at the blade root where stall-delay is predominant. Another shortcoming of Snel’s model is that the drag coefficient remains uncorrected. From Figures 7.2, it is evident that the drag coefficient also needs to be corrected, as in fact is being carried out by the new model.

A limitation of the new engineering model (Eqts. 7.1–7.6) is that it has been developed based on a limited amount of data from a single rotor geometry, i.e. the NREL rotor with the S809 aerofoil shape for the blades. Further work is necessary to assess the validity of this model for other rotors and it is likely that further tuning would then be required. Also, this model is only valid when the rotor is operating in axial and steady conditions. The unsteady aerofoil data for yawed rotors may differ considerably from the corresponding steady data for axial conditions, especially at high angles of attack at which dynamic stall takes place. These differences were already discussed when deriving 3D unsteady aerofoil data from blade pressure measurements on the NREL rotor in yaw with the free-wake vortex model (*see* Figs. 6.33(a)-(j)). This derived data is quite unique since it includes the combined influences of unsteady effects (including dynamic stall) and 3D effects (stall-delay and tip/root loss). Developing a new improved engineering model for BEM-based codes to produce unsteady aerofoil data requires an elaborate analysis which is beyond the scope of this thesis. Yet the results of Figs. 6.33(a)-(j) should be very useful in developing such a model. A major finding from this study is that the unsteady 3D C_l - α and C_{dp} - α hysteresis loops are in general closer to the 3D steady aerofoil data than to the corresponding 2D steady data. This was observed at both attached and stall conditions and it implies that 3D effects (in particular stall-delay) have a significant role in unsteady flow behaviour of wind turbine blades.

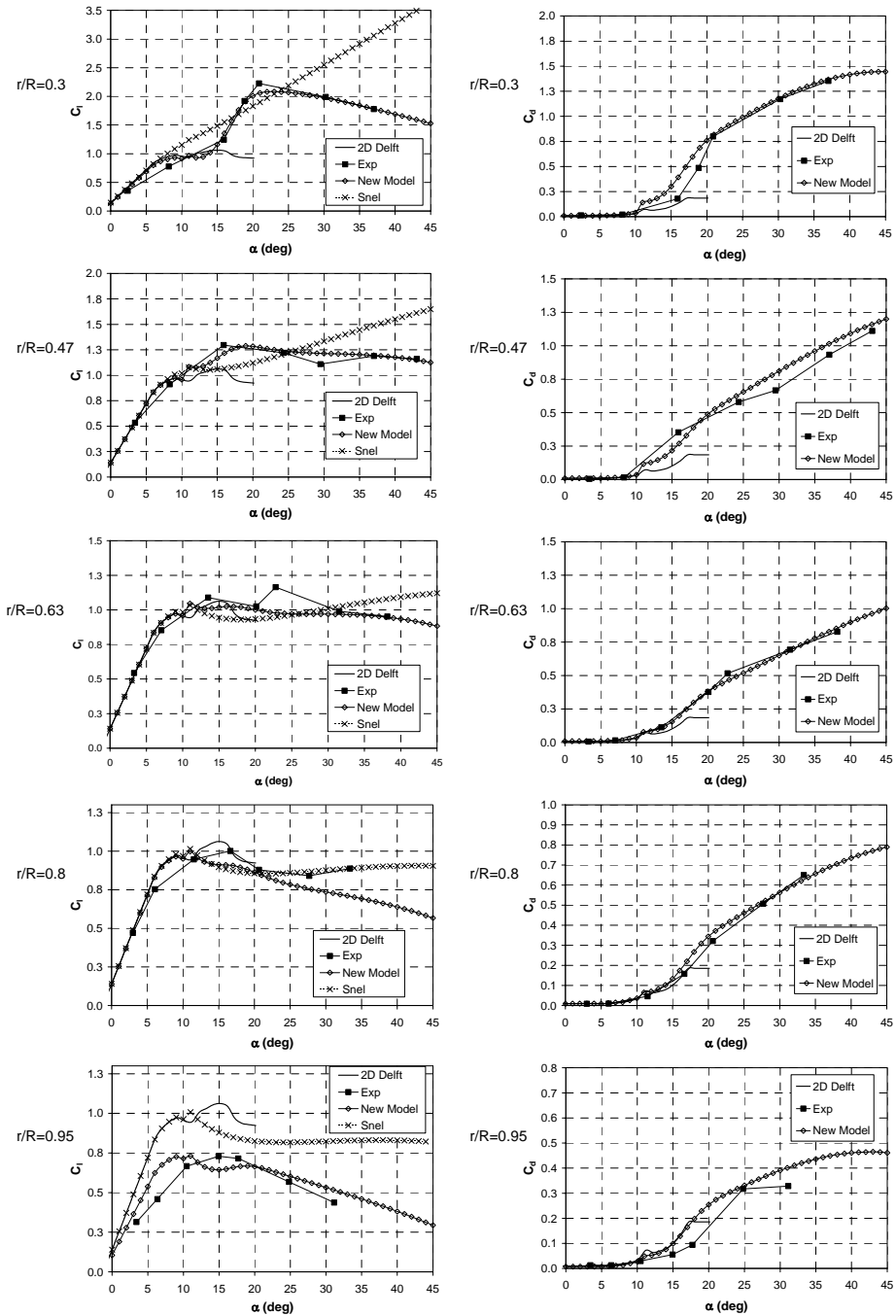


Figure 7.2 – Comparison of the lift and drag coefficients predictions by the new engineering model with those from Figs. 6.19(a) and (b). Snel's prediction of the lift coefficient is also included.

7.2 Correcting the induction for skewed wake effects in yaw

The BEM theory can produce quite accurate results for the aerodynamic load distributions in axial conditions provided reliable 3D aerofoil data is used. However this is not the case in yawed conditions since the availability of reliable 3D alone may still not be sufficient to provide accurate results. This is because the BEM theory lacks the physics to model the complex and skewed wake created by a yawed turbine. Consequently, apart from engineering models that provide reliable aerofoil data, other engineering models are additionally required to correct for skewed wake effects in yaw as already outlined briefly in Chapter 3, section 3.5.

In many state-of-the-art BEM-based design codes, the correction for skewed wake effects is carried out by introducing a correction factor F_{sa} as shown in Eq. 3.27. In effect, this correction factor corrects the ratio of the local induction factor at the blades ($a_{1,c}$) to the azimuthally averaged value (a_1) at different radial locations and azimuth angles of the blade. Various engineering models are used to model F_{sa} , some of which were presented in Chapter 3 (Eqts. 3.23-3.26). In this project, the induced velocity distributions for the TUDelft and NREL rotors in yaw were investigated in detail. In this way it was possible to study the variations of $a_{1,c}$ vs ϕ and thus be able to understand better the limitations of the engineering models currently available to model correction parameter F_{sa} in BEM-based design codes.

In the analysis of the TUDelft rotor, detailed hot-film measurements in the near wake were taken with the rotor operating at yaw angles $\psi=30^\circ$ and 45° with the tip speed ratio and blade tip pitch angle maintained fixed at 8 and 2° respectively. In the analysis of the NREL rotor, the novel approach for coupling the blade pressure measurements with the free-wake vortex model made it possible to estimate the unsteady induced velocity distributions at the rotorplane. These distributions were derived for different windspeeds with the yaw angle, rotor speed and blade pitch angle maintained fixed at 30° , 72rpm and 3° , respectively. Both the hot-film measurements on the TUDelft rotor and the free-wake calculations on the NREL rotor confirm that the periodic variation of $a_{1,c}$ vs ϕ on the blade lifting lines resulting from skewed wake effects in yawed rotors is far more different than the sinusoidal variation predicted by Glauert (Eq. 3.23). This is mainly due to root vorticity effects which tend to be predominant in wind turbines, as opposed to what is usually seen in helicopter rotors in forward flight. Actually this finding is not new as this was already discovered in the Joule projects [83, 84] and in the work of Schepers [69]. It was found in the present study that for high tip speed ratios ($\lambda=5.4-8$) at which the time-dependent angles of attack at the blades are small, the periodic variation of $a_{1,c}$ vs ϕ on both the TUDelft and NREL rotor was regular with a phase angle changing with radial location (see Figs. 4.89, 4.90 and Figs. 6.39(a), (b)). For such conditions, an engineering model of the form as that developed by the ECN (Eq. 3.26) tends to be suitable. However, it was discovered that for low tip speed ratios where the time-dependent angles of attack at the blades are large, the periodic variations of

$a_{1,c}$ vs ϕ on the NREL rotor as predicted by the free-wake code were found to be quite complex and irregular (see Figs. 6.39(c), (d) and (e)). These variations have a higher harmonic content than that catered for by Eq. 3.26. Yet it was found that a third order Fourier series of the following form would be sufficient:

$$F_{sa} = \frac{A_0}{2} + A_1 \cos(\phi + \varphi_1) + A_2 \cos(2\phi + \varphi_2) + A_3 \cos(3\phi + \varphi_3) \quad (7.7)$$

where A_0 , A_1 , A_2 and A_3 are the amplitudes of the respective harmonics and are a function of the yaw angle (Ψ), the radial location (r/R) and the tip speed ratio (λ). φ_1 , φ_2 and φ_3 are the phase angles of each harmonic in degrees and are also a function of Ψ , r/R and λ .

7.2.1 Development of engineering model using a heuristic approach based on Fourier series

In an attempt to derive a new improved engineering model for F_{sa} , the *HAWT_FWC* results of Figs. 6.38 and 6.39 were used to determine appropriate values for the amplitude and phase angle parameters of Eq. 7.7 to be able to model the NREL rotor at 30° yaw. To do so, Eq. 6.8 was applied to calculate F_{sa} at each blade azimuth angle (ϕ) and radial location (r/R) and at each windspeed ($U = 5, 7, 10, 13$ and 15m/s). Eq. 6.8 was applied with the Prandtl tip/root loss factor f set to unity (since this factor would not be required if the tip/root loss correction is applied to the aerofoil data instead to the induced velocities, as discussed earlier in section 7.1). Curve fitting numerical methods described in [27] were then applied to the third order Fourier series to derive the values of A_0 , A_1 , A_2 , A_3 , φ_1 , φ_2 and φ_3 . The resulting values are plotted in Figs. 7.3 and 7.4. It is observed from these plots that the required parameters are very sensitive to both the radial location (r/R) and the operating tip speed ratio (λ). The variations are quite irregular and this makes it difficult to derive an improved engineering model based on Eq. 7.7 that is valid for a wide range of operating conditions. One should also remember that the values shown in Figs. 7.3 and 7.4 are only valid for $\Psi=30^\circ$. For other yaw angles, new sets of values would be required. This makes matters even more complicated. Moreover, parameters A_0 , A_1 , A_2 , A_3 , φ_1 , φ_2 and φ_3 also depend on the geometry of the rotor and its blades. In fact when comparing the distribution for F_{sa} obtained from *HAWT_FWC* on the TUDelft rotor at $\Psi=30^\circ$ and $\lambda=8$ with those obtained for the NREL rotor at the same yaw angle and approximately same tip speed ($\lambda=7.54$), considerable differences were noted. Such difficulties indicate the complexity of the problem when dealing with yaw aerodynamics and that applying a heuristic approach for deriving a new improved engineering model for F_{sa} (i.e. deriving the model by only observing numerical results from measurements or advanced models without involving physical models) is quite restricted in providing more accurate predictions. A major limitation is that the derived engineering model will only be valid for the rotor and operating conditions for which it was originally derived.

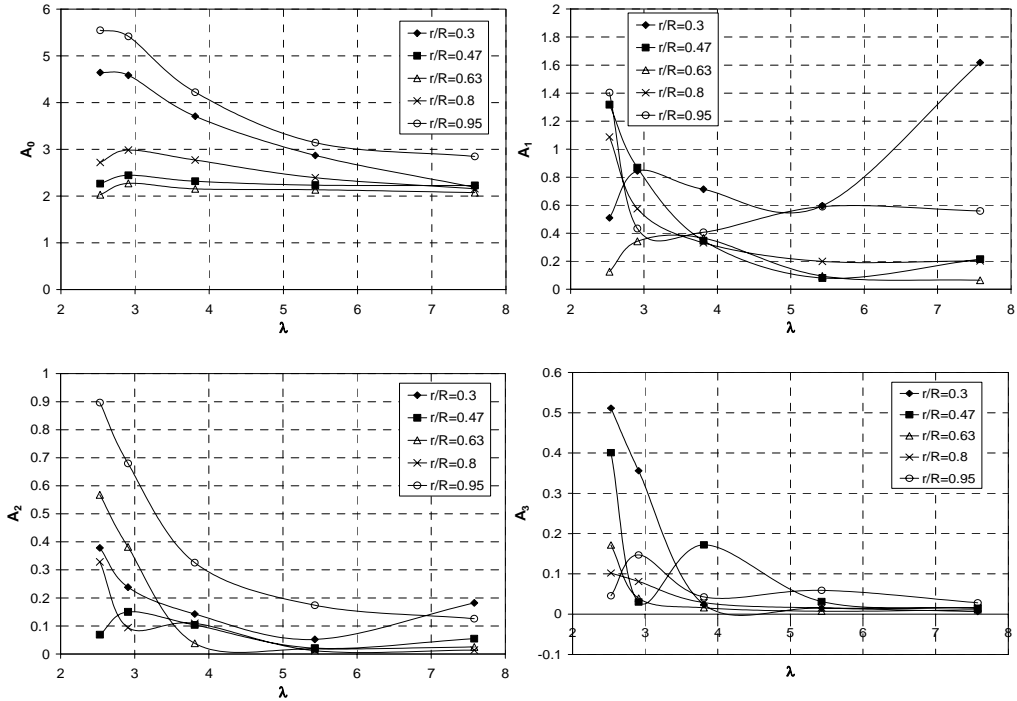


Figure 7.3 – Values of A_0 , A_1 , A_2 and A_3 that are required for improved engineering model for F_{sa} (Eq. 7.7) in order to yield an induced velocity distribution as predicted by HAWT_FWC for NREL rotor at $\Psi=30^\circ$.

7.2.2 Alternative approach using prescribed-wake vortex model

An important requirement for engineering models is that they should be valid for a wide range of rotor/blade geometries and operating conditions. Knowing the limited physical background of the BEM theory and keeping in mind the complexity of yawed rotor aerodynamics, it is vital for new improved engineering models for BEM-based design codes to implicitly make use of more comprehensive aerodynamic theory rather than simply be based on a heuristic approach. One possibility is to integrate a rigid or prescribed vortex model using the Biot-Savart law directly into the BEM code. This would not affect significantly the computational cost of the solution considering the fact that rigid and prescribed vortex models are by far much more computationally efficient than free-wake vortex models. But in doing so, it is necessary to check whether the vortex model adopted is sufficiently reliable to model the circulation in the wake. In this project, the computations with the free-wake vortex model HAWT_FWC on the NREL rotor have provided a better understanding of how the circulation is distributed in the rotor wake and how such a distribution influences the variation of $a_{1,c}$ vs ϕ (and hence also parameter F_{sa}). It was found

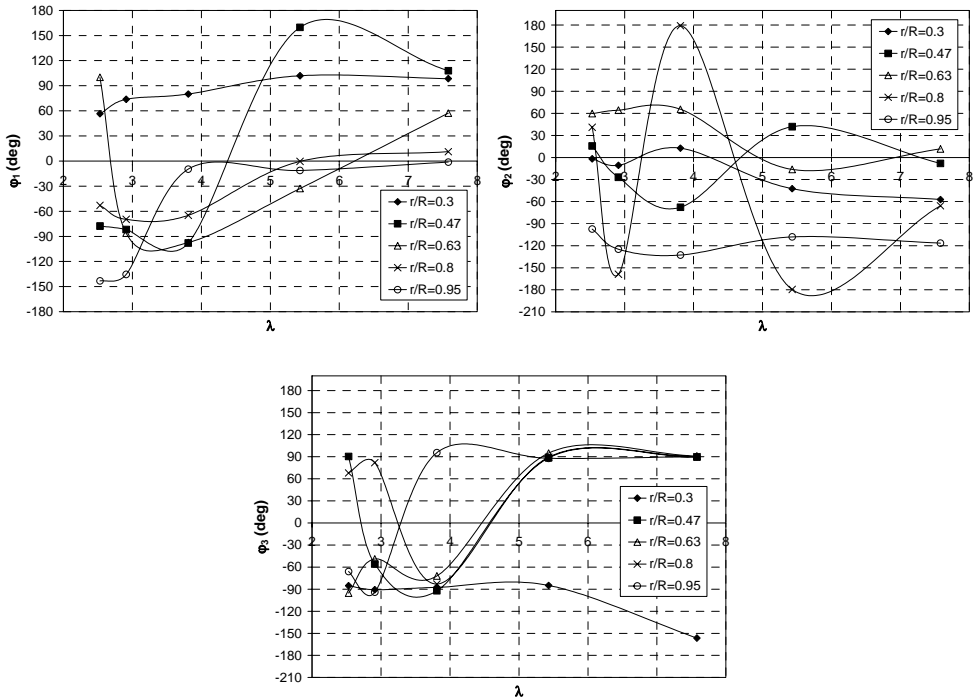


Figure 7.4 – Values of ϕ_1 , ϕ_2 and ϕ_3 that are required by improved engineering model for F_{sa} (Eq. 7.7) in order to an yield induced velocity distribution as predicted by HAWT_FWC for NREL rotor at $\Psi=30^\circ$.

that the regularity of the variation of $a_{1,c}$ vs ϕ at high tip speed ratios on both the TUDelft and NREL rotors results from the fact that the trailing circulation emanating from the blades is concentrated at the tip and root (see Figs. 5.46, 5.47 and Figs. 6.35(a), (c)). It could therefore be concluded that for such conditions, a rigid or prescribed vortex model consisting of only a single skewed tip vortex helix and a similar one at the root would likely be sufficiently accurate to model the wake provide that the pitch of each helix are prescribed correctly. However, at low tip speed ratios on the NREL rotor, the unsteady shedding of high trailing circulation at the middle blade sections caused the irregularity in variation of $a_{1,c}$ vs ϕ . For such conditions the rigid or prescribed vortex model should better consist of helical skewed vortex sheets in order to be able to include the effects of the high trailing circulation emanating from the middle sections of the blade.

In this project it was noted that the developed prescribed vortex model HAWT_PVC can produce induced velocity distributions that are reasonably close to those from the free-wake vortex model HAWT_FWC. For instance this could be observed on the TUDelft rotor predictions for $u_{a,c}$ at $\Psi=30^\circ$ and 45° (compare HAWT_PVC results of Figs. 4.91 and 4.92 with those of HAWT_FWC of Figs. 5.41 and 5.42). Re-call that in HAWT_PVC, the wake is

modelled as a vortex sheet and the Biot-Savart law is applied to calculate the unsteady induction in the flow field of the rotor with the bound circulation at the blades required as input. This vortex model is described in detail in section 4.3.3. The wake skew angle and pitch need also to be prescribed.

The reasonably good predictions from *HAWT_PVC* suggest that better predictions for yawed rotors can be achieved by BEM codes if this vortex model is integrated in the BEM solution. An approach for doing so is now proposed and is based on two simple models to interface a BEM code to *HAWT_PVC*:

1. the first model is used to determine an approximate pitch (p_w) for the helical vortex sheets modelled by *HAWT_PVC* from an azimuthally averaged axial induction factor computed by the BEM equation Eq. 3.21. This model is given by:

$$\frac{p_w}{R} = \frac{p \cos(\Psi)}{R} = \frac{2\pi}{\lambda} (\cos(\Psi) + a_1) \quad (7.8)$$

where a_1 is taken to be equal to the azimuthally averaged value at 70-80% R . The above equation was found to be reasonably accurate in estimating the helical pitch when comparing its predictions with those obtained on the TUDelft rotor using smoke visualisation experiments (see section 4.2.3) and those obtained on the NREL rotor using the free-wake calculations (see Figs. 6.18 and 6.36). The comparison is presented in Fig. 7.5. The values of a_1 at 70-80% R used in Eq. 7.8 for the TUDelft rotor were obtained from the hot-film measurements (Figs. 4.60, 4.89 and 4.90.) while those for the NREL rotor were obtained from *HAWT_FWC* (Figs. 6.21(d) and 6.38). The maximum percentage error p_w in this model was found to be less than 19%.

2. the second model is used to determine the wake skew angle (χ_s) required by *HAWT_PVC*. This is a new model that was derived from the smoke visualisation experiments on the TUDelft rotor (section 4.2.3) and is based on input of the axial thrust coefficient to find χ_s at a particular yaw angle. The quasi-linear relations between χ_s and C_T noted in these experiments (see Fig. 4.32) were used to develop this model. The model equations are given by:

$$\begin{aligned} |\chi_s| &= |\Psi| + \Delta_{\chi_s-\Psi} \\ C_{T0} &= 0.016|\Psi| - 1X10^{-4}\Psi^2 - 3X10^{-6}|\Psi|^3 \\ \Delta_{\chi_s-\Psi} &= a(C_T - C_{T0}) \\ a &= 0.4154|\Psi| - 0.002\Psi^2 \quad \text{if } C_{T0} > C_T \\ a &= 0 \quad \text{if } C_{T0} \leq C_T \end{aligned} \quad (7.9)$$

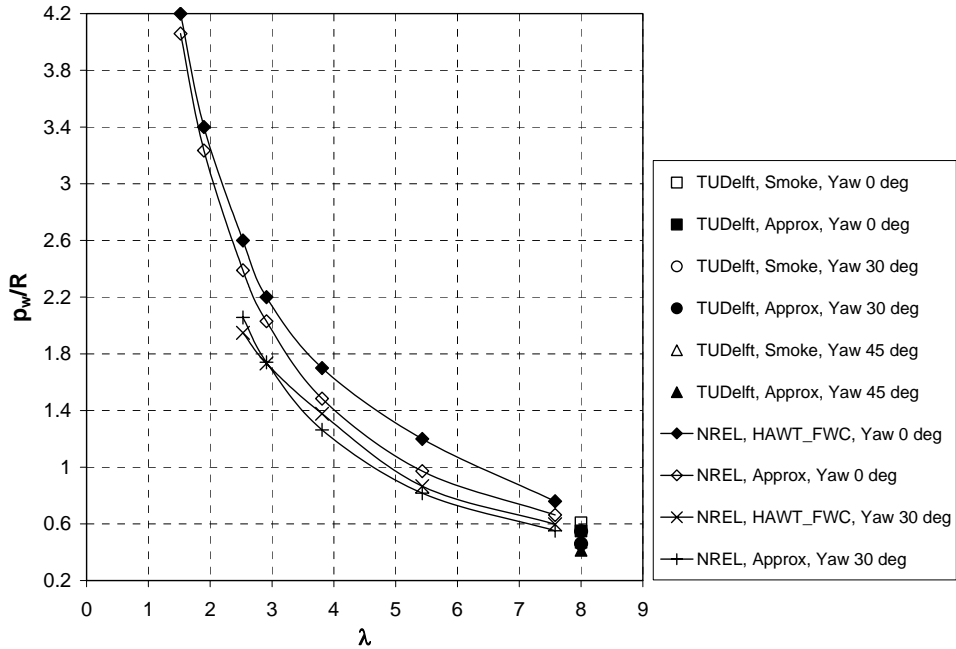


Figure 7.5 – Comparison of the helical wake pitch (p_w) predicted by Eq. 7.8 (Approx) with that obtained from smoke visualisation experiments (in the case of the TUDElft rotor) or from the free-wake vortex model HAWT_FWC (in the case of the NREL rotor).

where Ψ is the rotor yaw angle in degrees. C_T used here is the azimuthally averaged global value.

Figure 7.6 illustrates the proposed approach on how a typical BEM solution algorithm could be modified to be able to interface the prescribed vortex model HAWT_PVC to the BEM design-code. The approach consists of the following sequence of steps:

Step 1: initially the whole rotor revolution is sub-divided into a fixed amount of equally-spaced time steps as in Fig. 3.7.

Step 2: initial values for the local axial and tangential induction factors at the blades ($a_{1,c}$ and $a_{2,c}$) are assumed.

Step 3: the relative flow velocity component (V_m , V_ζ and V_r) and angles of attack (α) at the blades are found at each time step over the whole revolution.

Step 4: the 3D lift and drag coefficients ($C_{l,3D}$ and $C_{d,3D}$) are then computed using an engineering model similar to the one presented in Eqs. 7.1 – 7.6 in order to account for tip/root loss, stall-delay and unsteady effects (e.g. dynamic stall).

Chapter 7 – Guidelines for Improving the Reliability of BEM-based Design Codes

Step 5: the bound circulation distribution at the blades for each time step is then estimated using the Kutta-Joukowski equation:

$$\Gamma_{B,3D} = \frac{1}{2} cV_r C_{l,3D} \quad (7.10)$$

Step 6: The BEM Eq. 3.21 is solved iteratively to find a_1 .

Step 7: The axial thrust loading distribution at the blades is determined using Eq. 3.20a. Numerical integration is then applied to find the azimuthally averaged rotor global axial thrust coefficient C_T .

Step 8: Parameters p_w and χ_s are computed from Eqs. 7.8 and 7.9.

Step 9: The distribution for $\Gamma_{B,3D}$ from Step 5 is then prescribed to the prescribed vortex model *HAWT_PVC*, together with parameters p_w and χ_s from Step 8. *HAWT_PVC* then calculates a new distribution for $a_{1,c}$ and $a_{2,c}$ at the blades.

Step 10: The new values for $a_{1,c}$ and $a_{2,c}$ from Step 9 are compared with the previous values inputted to Step 3. Steps 3 to 9 are then repeated until convergence in $a_{1,c}$ and $a_{2,c}$ is achieved.

The interfacing of a prescribed vortex model into the BEM solution will obviously increase the computational cost. However, this is well accommodated by the increased efficiency of modern computers that are becoming available. Also the discretization of the vortex model in *HAWT_PVC* need not be set too fine to achieve very good numerical accuracy. The helical vortical wake need not extend too downstream from the rotorplane. In this project it was found that extending one rotor diameter downstream only is sufficient. The calculation of correcting parameter F_{sa} is not required since the distribution of $a_{1,c}$ is calculated directly by the vortex model.

In this approach, the influence of wake expansion is being ignored by taking parameters $R_{t,w1}$ and $R_{t,w2}$ in *HAWT_PVC* as zero. This influence is small when the rotor is operating at low thrust coefficients ($C_T < 0.6$) but may become important at higher thrust values.

The proposed approach of Fig. 7.6 for integrating prescribed vortex methods in BEM engineering codes is in fact very similar to prescribed-wake vortex methods as those used in references [19, 28, 90]. But instead of using empirical or semi-empirical models for prescribing the vortex wake pitch, the BEM equation (Eq. 3.21) and Eq. 7.8 are used instead. This makes the modelling less dependent on experimental input and simpler which in turn might turn out into reduced computational costs. Yet further work is still required to validate it over a wide range of rotor geometries and operating conditions. Further work is also necessary to examine any advantages over currently available prescribed-wake vortex methods as far as computational efficiency and reliability are concerned.

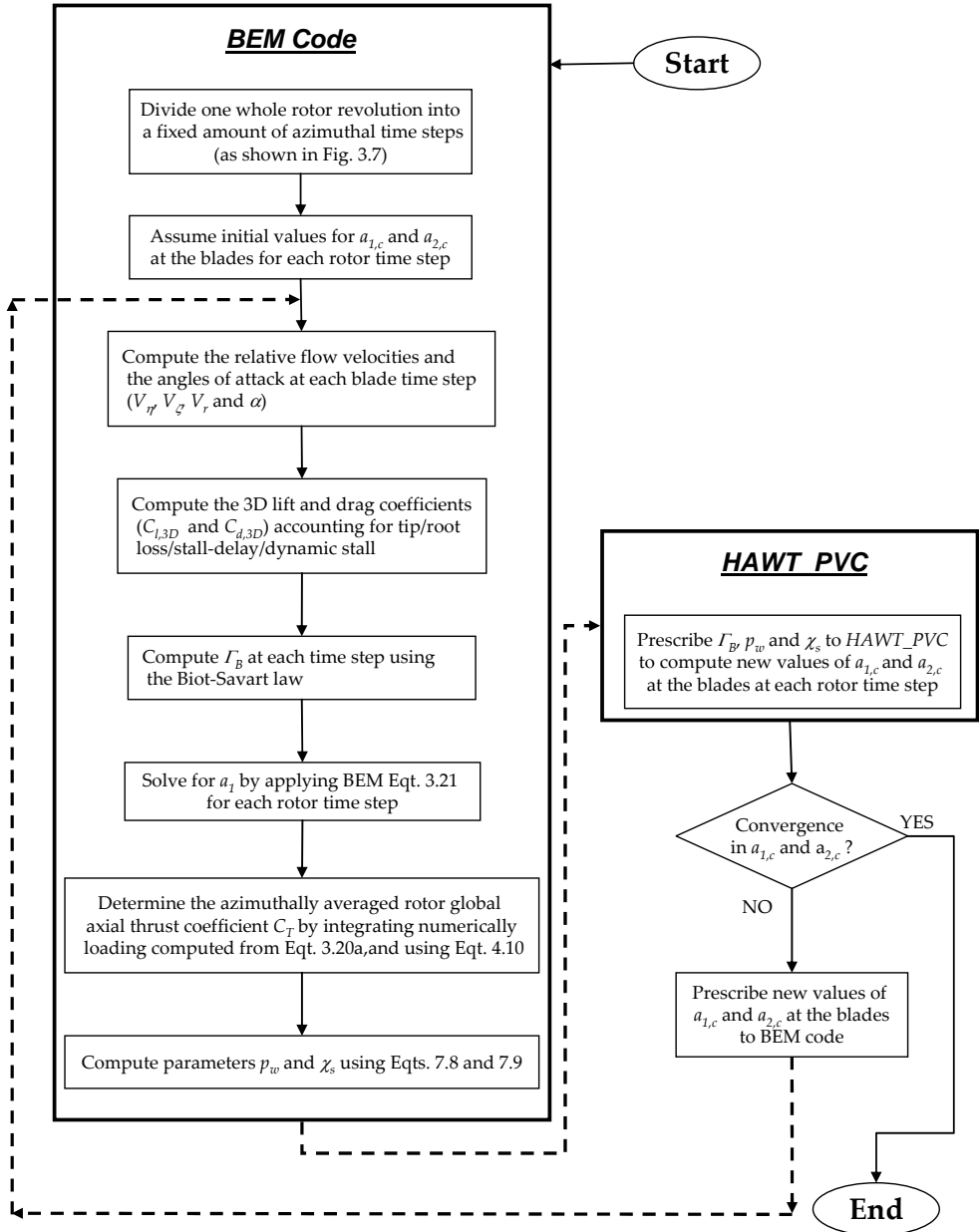


Figure 7.6 – Proposed approach for interfacing prescribed vortex code HAWT_PVC to a BEM code to improve BEM aerodynamic load predictions for wind turbines in yaw.

7.2.3 Correction to the axial momentum equation for yawed rotors

Although the alternative approach using a prescribed-wake vortex model described in section 7.2.2 above is a step forward to improve BEM predictions for yaw, there is still an important issue that still needs to be addressed if BEM models are to be improved for yawed wind turbines. It regards the deficiency of the momentum equation (Eq. 3.6) when treating yawed rotors. Bring in mind the work documented in section 4.4.1 in which the TUDelft rotor was used to assess the limitations of the BEM Eq. 3.6a. In this work, the hot-film near wake measurements on the TUDelft rotor were used to compute separately the right and left-hand parts of Eq. 3.21 (referred to F_{A1} and F_{A2} , respectively). The discrepancy between F_{A1} and F_{A2} was found to be very small at $\Psi=0^\circ$, but then became significant when considering $\Psi=30^\circ$ and 45° (see Figs. 4.100 and 4.101). The latter reflects the limitation and inadequacy of the momentum equation (Eq. 3.6a) for the axial thrust when modelling yawed rotors. As already discussed in section 4.4.1, this limitation yields an incorrect prediction for the azimuthally averaged axial induction factor (a_1). It can therefore be concluded that a correction for skewed wake effects in BEM codes should also correct the momentum equation by multiplying Eq. 3.21 by a correction factor k_a as given in Eq. 4.84.

Values for k_a for yawed rotors may be derived using experimental data and/or advanced models using Eq. 4.85. Note that a value of $k_a=1$ would imply that no correction to the momentum equation is required. In this project, values for k_a were derived for the TUDelft rotor using the inflow measurements in conjunction with unsteady aerofoil theory for $\Psi=30^\circ$ and 45° . It was found that k_a was less than unity and that the value decreases with yaw angle when maintaining λ and θ_{tip} constant (see Fig. 4.102). Values for k_a were also derived for the NREL rotor at $\Psi=0^\circ$ and 30° for different tip speed ratios using the blade pressure measurements and the free-wake vortex model *HAWT_FWC*. The values were found to be very close to unity at all tip speed ratios, even at $\Psi=30^\circ$.

The values of k_a derived from the aerodynamic analysis on the TUDelft and NREL rotors are plotted in Fig. 7.7. The results are plotted against the global axial thrust coefficient, C_T . The value of $k_a=1$ is included for the case in which $\Psi=0^\circ$ up to $C_T=1$. Beyond $C_T=1$, the momentum equation (Eq. 3.6a) is no longer valid and an equation such as Eq. 3.4b is used instead. It is apparent that k_a is dependent on both the yaw angle and the axial thrust coefficient. It appears that, for a given yaw angle, k_a will decrease with an increase in C_T . One can easily recognize the fact that the NREL rotor was operating at low values of C_T (refer to table 6.1) and this is the main reason why k_a was close to unity up to $\Psi=30^\circ$. On the other hand, the TUDelft rotor had large C_T values and consequently k_a was well below unity at both $\Psi=30^\circ$ and 45° .

Since only a limited set of operating conditions on both rotors were considered, it is difficult to develop an engineering model for k_a from the results in Fig. 7.7. The large uncertainties in

the k_a values of the TUDelft rotor at $\Psi=30^\circ$ and 45° resulting from the uncertainties in the inflow measurements from which they were originally derived, also make it difficult. However it is likely that it is possible that the variation of k_a with C_T at a given yaw angle varies as depicted in Fig. 7.7. In this case, the engineering model could be expressed mathematically as follows:

$$k_a(C_T, \Psi) = \frac{(1 - aC_T^3)}{2.718} e^{-C_T^b} \tag{7.11}$$

where parameters a and b are variables depending on the yaw angle. However, more analysis is requested to determine whether this is a typical variation for wind turbines by considering a wider range of rotors and operating conditions. Furthermore, experiments should be conducted to determine appropriate k_a values in yaw for large C_T values ($C_T > 0.6$).

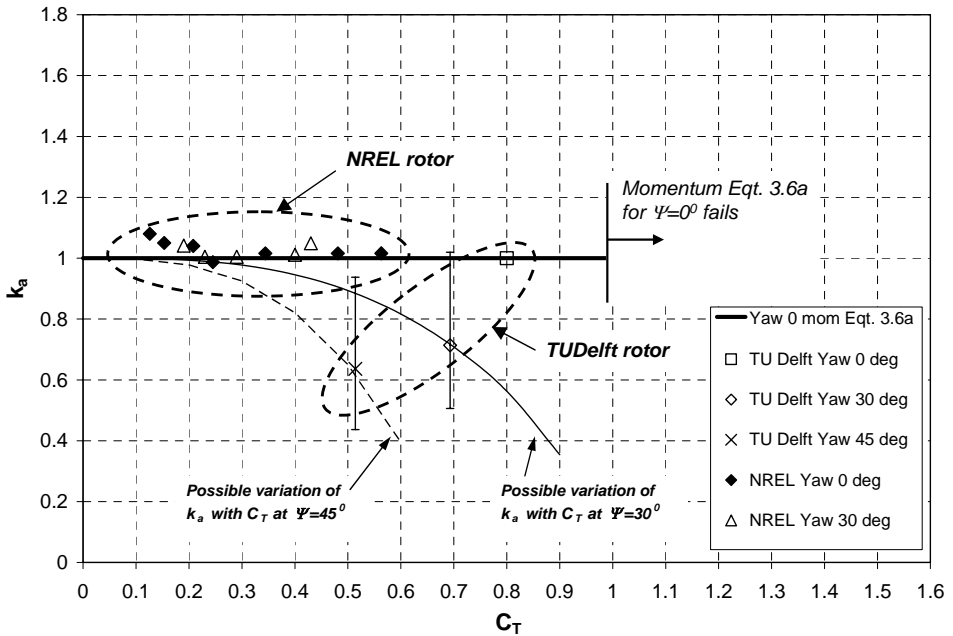


Figure 7.7 – Variation of k_a with C_T and yaw angle for the TUDelft and NREL rotors.

8. Project Outcome, Conclusions and Recommendations

8.1 Project Outcome

A thorough experimental investigation of a wind turbine's aerodynamic behaviour should include experimental data of the aerodynamic loading distributions along the blades, the inflow distributions at the rotorplane and in the near wake and measurements of the wake geometry. When the experimental data is limited because any of these three data sets is unavailable, it imposes restrictions to the detail to which aerodynamic analysis as well as BEM code validation can be done. This thesis focused on developing new methodologies for using limited experimental data available in conjunction with advanced aerodynamic models to derive the additionally required aerodynamic performance data for both axial and yawed wind turbines. Two particular methodologies were considered in this thesis and they were applied independently for two specific turbines:

1. In the first case, the TUDelft model turbine was tested in the open-jet wind tunnel facility at Delft University of Technology. Detailed hot-film measurements were performed in the near wake of the model turbine. Smoke visualisation experiments were also carried out to trace the tip vortex paths and hence obtain details of the rotor wake geometry. Due to limitations of the equipment it was impossible to measure the blade aerodynamic loads distributions. A methodology was developed to derive the time-dependent aerodynamic load distributions at the rotor blades from the hot-film measurements in conjunction with an advanced unsteady aerofoil model. Despite the fact that the analysis was only restricted to attached flow conditions at the blades (for which the unsteady aerofoil model is considerably accurate), this methodology was found to be quite challenging to apply due to the following two drawbacks: (a) First, the derived aerodynamic loads are very sensitive to the errors in the hot-film measurements. In other words, a small percentage error in the inflow measurements may result into a significantly larger error in the loading; (b) Second, it was found that the bound circulation derived using the employed unsteady aerofoil model was unrealistically high at the blade tip and root regions, even though the angle of attack was estimated directly from the inflow measurements. This was due to the fact that the unsteady aerofoil model used is a 2D model and thus does not cater for the highly 3D flow phenomena taking place at the blade tip and root. Therefore a correction had to be added.

The results derived from the inflow measurements on the TUDelft rotor were used to carry out a detailed investigation of a typical BEM code when modelling axial and yawed turbines. Despite that attached flow conditions were only being treated and also the fact that the results derived from the inflow measurements had a high level of uncertainty, it was still possible to have a better understanding of the limitations of BEM-based design codes and obtain further intuition of how these could be improved. The study demonstrated that the application of the standard Prandtl tip/root loss correction with the use of 2D aerofoil data is inaccurate as it over predicts the induced velocity at the blade tip and root regions. A better approach to correct for tip/root loss in the BEM theory is to correct the 2D aerofoil data rather than the local induction. When correcting for skewed wake effects in yaw, correcting the ratio of local blade element induced velocity to the annular average induced velocity alone may not always be sufficient. The annular averaged induced velocity itself may also need to be corrected.

2. In the second case, the NREL Phase VI wind turbine that was extensively tested in the NASA Ames wind tunnel in 2000 was analysed. In the experiments, time-accurate blade pressure measurements were taken with the rotor operating in both axial and yawed conditions together with strain gauge measurements for the output torque and the root flap/lead moments. However, detailed inflow measurements at the rotorplane were not carried out. In this project, a novel and comprehensive methodology was proposed for using the blade pressure measurements in conjunction with a free-wake vortex model to estimate the angle of attack distributions at the blades more accurately, together with the inflow distributions at the rotorplane and wake geometry. The study considered different operating tip speed ratios in both axial and yaw conditions that yielded both attached and separated flows over the blades. New 3D lift and drag aerofoil data were derived. It could be observed that this new data is considerably different from the corresponding 2D wind tunnel aerofoil data due to the presence of blade tip/root loss effects, stall-delay or else unsteady conditions resulting from rotor yaw (mainly dynamic stall). The derived free-wake geometry solutions for given blade loading conditions were plotted together with the corresponding wake trailing and shed circulation distributions. These plots helped comprehend how the unsteady bound circulation formed at the blades is eventually convected into the wake under the action of complex three-dimensional flows.

The new 3D lift and drag aerofoil data were then used to assess to improvement in BEM load predictions in axial and yawed conditions. The BEM predictions improved considerably even when dealing with highly stalled and yawed conditions. For yawed conditions, new inflow corrections to account for skewed wake effects in BEM codes were also derived. It was possible to quantify the relative importance for such corrections in improving BEM results.

From this project, guidelines on how BEM-based models can be improved are presented and discussed. These mainly fall under two classifications:

1. *Improvement of aerofoil data:* BEM predictions improve substantially when more accurate 3D aerofoil data is used. A new engineering model for the 3D lift and drag coefficients in steady axial conditions is proposed. The model is based on the results obtained from the NREL rotor. For yawed conditions, the newly derived aerofoil data is quite unique since it includes the combined effects of 3D effects (tip/root loss and stall-delay) and unsteady conditions (including dynamic stall). An important finding is that the derived aerofoil data from the NREL rotor in yawed conditions was in general closer to that derived for the same rotor in axial conditions than the 2D aerofoil data. This in fact reflects the considerable influence that 3D effects play on the unsteady local blade characteristics.
2. *Improvement of engineering models for skewed wake effects in yaw:* Improved engineering models to correct for skewed wake effects over a wide range of operating tip speeds are also necessary. An attempt was made to develop one such model from the unsteady induction distribution obtained for the NREL rotor using Fourier series. The model was intended to correct solely the ratio of the local induction at the blades to the corresponding annular averaged value. Although it was confirmed that a third order Fourier series is sufficient to represent the required corrections, it was found that the Fourier coefficients are highly dependent not only on the radial location and the yaw angle but also on the operating tip speed ratio. The dependency on the radial location and tip speed ratio was found to be quite irregular and therefore quite complex to model. Also comparison of the unsteady induction distributions of the TUDelft and NREL rotors suggest that there is also a considerable dependency on the rotor geometry. The analysis has shown that the use of this approach for developing an accurate engineering model applicable over a wide range of rotor geometries and operating conditions in yaw is difficult. This is a consequence of the fact that the physics behind the aerodynamics of yawed turbines is complex. An alternate approach is being proposed in which a BEM-code is interfaced to a prescribed vortex model to correct for skewed wake effects. This approach is more physically comprehensive and is therefore more reliable.

As already described earlier, correcting for skewed wake effects by only correcting the ratio of the local induction at the blades to the corresponding annular averaged value without correcting the ratio of annular averaged induced velocity itself may be insufficient. This is due to the inherent limitation of the axial momentum equation when treating yawed conditions. In some cases, another engineering model is required to correct the momentum equation. This correction is similar to that used to correct the same equation for high loading conditions. Whether this correction is required for yawed cases not only depends on the yaw angle but also on the axial thrust coefficient. From the analysis on the TUDelft and NREL rotor it was found that such a correction is not required up to a yaw angle of 30° as long as the axial thrust coefficient does not exceed 0.45. For higher axial thrust coefficients, an engineering model to correct the

momentum equation becomes a necessity. Such a model could be derived from wind tunnel experiments or advanced models such as free-wake vortex codes.

8.2 Conclusions

1. Using a free-wake vortex model it is possible to derive the angle of attack at the blades from blade pressure measurements in both axial and yawed conditions. From the derived angle of attack and from knowledge of the measured C_n and C_t values, new 3D steady and unsteady aerofoil data can be obtained.
2. With a free-wake vortex model it is also possible to derive from the blade pressure measurements the complex 3D induction at the rotorplane together with the wake geometry and circulation distribution. These are vital in order to have a better understanding of a wind turbine's aerodynamic behaviour in both steady and unsteady environments.
3. Given that reliable 3D aerofoil data is available, BEM predictions for wind turbines improve significantly, even for conditions of deep stall and rotor yaw. In many situations, BEM results for the blade aerodynamic loading distributions are unreliable not necessarily because the BEM theory is deficient but because incorrect aerofoil data is used.
4. The application of the standard Prandtl tip/root loss correction model with 2D aerofoil data in BEM codes is inaccurate since it over-predicts the induction at the blade tip/root. A more appropriate tip/root loss correction in the BEM theory is to correct the 2D aerofoil data rather than the induction.
5. When using 3D lift and drag aerofoil data derived directly from the blade pressure measurements, the tip/root loss correction model is no longer required in the BEM calculations. This is because the tip/root loss effects are already accounted for in the 3D aerofoil data.
6. To improve the BEM predictions in yawed wind turbines, the use of accurate 3D unsteady aerofoil data alone may not be sufficient. Two additional models need to be incorporated to correct the induction computed by BEM for skewed wake effects in yaw:

Model (a) – to correct the ratio of the local axial induction at the blades to the corresponding annular averaged value. Many models developed in the past years to correct this ratio in BEM codes are not accurate at all for many circumstances. Due to the complexity of yawed rotor aerodynamics, developing a new improved engineering model based on a heuristic approach is very difficult. This is because the ratio is not only dependent on the radial location (r/R) and yaw angle but also on the operating tip

speed ratio and rotor geometry. Therefore it is imperative to include more physical models as for example prescribed-wake vortex models using the Biot-Savart law.

Model (b) – to correct the axial momentum equation for its deficiency when treating yawed rotors. Yet, this correction is not required when considering small yaw angles ($\psi < 30^\circ$) and low axial thrust coefficients ($C_T < 0.45$).

8.3 Recommendations

This study has clearly demonstrated that, until the time will come when computer capacity becomes powerful enough to practically integrate the more advanced free-wake vortex methods and CFD techniques fully into wind turbine engineering design software, there is still considerable potential to improve the accuracy of BEM-based aerodynamic models. The following recommendations are being made for future work:

1. Emphasis is made on the urgent need for more reliable engineering models that predict 3D aerofoil data for wind turbine designers. Research efforts should focus on providing a better understanding of the flow physics locally around the rotating blades. More extensive blade pressure measurements are indispensably useful in reaching this aim and to further validate CFD models. Despite that Navier-Stokes solvers are still too computationally demanding to be fully encapsulated into wind turbine design software, they have a vital role in supporting the development of improved engineering models for aerofoil data to be used in BEM-based codes. Here it is important to point out the fact that the limited availability of accurate 3D aerofoil data for wind turbine applications is not only restricting BEM-based models from being more accurate, but also the more comprehensive models such as lifting-line free-wake vortex models and lifting-line/actuator disc CFD models.
2. The new engineering model for aerofoil data for axial conditions developed in this project using the NREL measurements needs to be validated for other rotor geometries. A similar engineering model for aerofoil data in unsteady conditions as in yawed turbines could be developed using the data being presented in this thesis.
3. As regards improving BEM predictions for the inflow distributions in yawed rotors, further work is required to validate the approach proposed for interfacing prescribed-wake vortex models to BEM codes. The work should investigate the improvement in predicting the unsteady induced velocity at the blades as well as the increased computational costs incurred by introducing the vortex model at different levels of wake discretization. As this proposed method still relies on the use of the axial momentum equation, further work is required to develop engineering models for parameter k_a in yaw. Experimental campaigns consisting of both blade pressure measurements and detailed near wake inflow measurements over a wide range of

Chapter 8 –Project Outcome, Conclusions and Recommendations

operating conditions (varying yaw angle and including both low and high operating thrust coefficients) are necessary in developing such models.

The new experimental data that will shortly become available from the EU-funded project MEXICO project (short for “Measurements and Experiments under Controlled Conditions”) should be of great benefit for the work being recommended here. In this project, a three-bladed model turbine with a geometry very similar to full-scale rotors will be extensively tested in the Dutch German DNW large wind tunnel. The turbine will have a diameter of about 4m and will be highly instrumented to be able to carry out both blade pressure measurements as well as detailed inflow measurements at the rotorplane and in the wake. Flow visualisation measurements will also be performed.

References

1. Afjeh A.A. and Keith T.G. Jr., "A Simplified Free Wake Method for Horizontal-Axis Wind Turbine Performance Prediction", *Journal of Fluids Engineering*, Vol. 108, pp. 400-406, 1986.
2. Ananthan S., Leishman J.G., Ramasamy M., "The Role of Filament Stretching In The Free-Vortex Modelling of Rotor Wakes, 58th Annual Forum and Technology Display of the American Helicopter Society International, Montreal, Canada, 2002.
3. Anderson J.D., "Fundamentals of Aerodynamics", McGraw-Hill, Third edition, USA, 2001, pp. 331-332.
4. Anderson M.B., Milborrow D.J., and Ross N.J., "Performance and Wake Measurements on a 3-m Diameter Horizontal Axis Wind Turbine", *DOE Contract Report No.E/5A/CON/1090/177/020*, University of Cambridge, England, 1982.
5. Bagai A. and Leishman J.G., "Rotor Free-Wake Modelling using a Pseudo-Implicit Technique Including Comparisons with Experimental Data", *Journal of the American Helicopter Society*, Vol. 40, No. 2, 1995.
6. Bareiß R. and Wagner S., "The Free-Wake/ Hybrid Wake Code ROLVM – A Tool for Aerodynamic Analysis of Wind Turbines," *European Wind Energy Conference, Lübeck-Travemünde, Germany, 1993.*
7. Barlow J.B., Rae W.H. and Pope A., *Low Speed Wind Tunnel Testing*, Wiley, New York, Third Edition 1999, Chapt. 17.
8. Beddoes T.S., "Practical Computation of Unsteady Lift," *Vertica*, 1984, 8 (1), pp. 55-71.
9. Benini E. and Toffolo A., "Optimal Design of Horizontal-Axis Wind Turbines Using Blade-Element Theory and Evolutionary Computation", *Journal of Solar Energy Engineering*, Nov. 2002, Vol. 124, pp. 357-363.
10. Bhagwat M.J. and Leishman J.G., "Generalized Viscous Vortex Model for Application to Free-Wake and Aeroacoustic Calculations," 58th Annual Forum and Technology Display of the American Helicopter Society International, Montreal, Canada, 2002.
11. Bierbooms W.A.A.M., "A Comparison between Unsteady Aerodynamic Models", *Proceedings from the European Wind Energy Conference, Amsterdam 1991.*

References

12. Björck A. and Thor S.E., "Dynamic Stall and 3D Effects", *Proceedings from The European Wind Energy Conference*, May 1996, Göteborg, Sweden.
13. Bruining A., van Bussel G.J.W., Corten C.P. and Timmer W.A., "Pressure Distributions from a Wind Turbines Blade: Field Measurements Compared to a 2-dimensional Wind Tunnel Data," *DUT-IVW-93065R*, Delft University of Technology, 1993.
14. Bruun H.H., *Hot-Wire Anemometry*, Oxford Science Publications, Oxford, England, 1995.
15. van Bussel G.J.W, "The Aerodynamics of Horizontal Axis Wind Turbine Rotors Explored with Asymptotic Expansion Methods", *Phd thesis, Delft University of Technology*, the Netherlands, 1995.
16. Chattot J.J., "Optimization of Wind Turbines Using a Helicoidal Vortex Model", *AIAA-2003-0522, Proceedings from 22nd ASME Wind Energy Symposium*, 2003, Reno, USA.
17. Chaviaropoulos P.K. and Hansen M.O.L., "Investigating Three-Dimensional and Rotational Effects on Wind Turbine Blades by means of a Quasi-3D Navier-Stokes Solver", *Journal of Fluids Engineering*, Vol. 122, June 2000, pp. 330-336.
18. Conlisk A.T., "Modern Helicopter Rotor Aerodynamics", *Progress in Aerospace Sciences*, Vol. 37, 2001, pp. 419-476.
19. Coton F.N., Wang T. and McD. Galraith R. A., "An Examination of Key Aerodynamic Modelling Issues Raised by The NREL Blind Comparison," *Wind Energy*, 2002; 5: pp. 199-212.
20. de Vries E., "Thinking Bigger – Are there limits to wind turbine size?", *Renewable Energy World*, May-June 2005.
21. Diveux T., Sebastian P., Bernard D. and Puiggali J.R., "Horizontal Axis Wind Turbine Systems: Optimisation Using Genetic Algorithms", *Wind Energy*, 2001; 4: pp. 151-171.
22. Du Z. and Selig M., "A 3D Stall-Delay Model for Horizontal Axis Wind Turbine Performance Predictions", *AIAA-98-0021, ASME Wind Energy Symposium*, Reno, 1998.
23. EWEA, "Wind Energy – The Facts", *European Wind Energy Association*, Brussels, 2004.

References

24. EWEA and Greenpeace, "Wind Force 12 – A Blueprint to Achieve 12% of the World's Electricity from Wind Power by 2020", *European Wind Energy Association*, Brussels, and Greenpeace, Hamburg, 2004.
25. EWEA, "Prioritising Wind Energy Research – Strategic Research Agenda of the Wind Energy Sector", *European Wind Energy Association*, Brussels, 2005.
26. van Garrel A., "Development of a Wind Turbine Aerodynamics Simulation Module", *National Energy Research Foundation, ECN-C-03-079*, 2003.
27. Gerald C.F. and Wheatley P.O., "Applied Numerical Analysis", Addison-Wesley Publishing Company, Fifth Edition, USA, 1994.
28. Gerber B.S, Tangler J.L, Duque E.P.N and Kocurek J.D, "Peak and Post Power Aerodynamics from Phase VI NASA Ames Wind Turbine Data", *Proceedings of the Special Topic Conference: the Science of Making Torque from Wind*, EWEA, Delft, The Netherlands, 2004.
29. Giguere P., Selig M.S., "Design of a Tapered and Twisted Blade for the NREL combined Experiment Rotor", *NREL/SR-500-26173*, NREL, Golden, CO, 1999.
30. Glauert H., "A General Theory for the Autogiro", *ARC R & M 786*, 1926.
31. Grant I., Mo M., Pan X., Parkin P., Powell J., Reinecke H., Shuang K., Coton F.N. and Lee D., "An Experimental and Numerical Study of the Vortex Filaments in the Wake of an Operational, Horizontal-axis, Wind Turbine," *Journal of Wind Engineering and Industrial Aerodynamics*, Vol. 85, 2000, pp. 177-189.
32. Grant I., Parkin P. and Wang X., "Optical Vortex Tracking Studies of a Horizontal Axis Wind Turbine in Yaw using Laser-Sheet, Flow Visualisation," *Experiments in Fluids*, Vol. 23, 1997, pp. 513-519.
33. Grant I. and Parkin P., "A DPIV Study of the Trailing Vortex Elements from the Blades of a Horizontal Axis Wind Turbine in Yaw," *Experiments in Fluids*, Vol. 28, 2000, pp. 368-376.
34. Gupta S. and Leishman J.G, "Accuracy of the Induced Velocity of Wind Turbine Wakes Using Vortex Segmentation", *AIAA-2004-0828, Proceedings from 23rd ASME Wind Energy Symposium*, Reno, 2004.
35. Hand M.M, Simms, Fingersh L.J., Jager D.W., Cortell J.R., Schreck S. and Larwood S.M., "Unsteady Aerodynamics Experiments Phase VI: Wind Tunnel Test Configurations and Available Data Campaigns", *NREL Technical Report NREL/TP-500-29955*, Golden, Colorado, Dec 2001.

References

36. Haans W., Sant T., van Kuik G.A.M. and van Bussel G.J.W., "Measurement of Tip Vortex Paths in the Wake of a HAWT under Yawed Flow Conditions", *Journal of Solar Energy Engineering, Special Issue on Wind Energy*, Vol. 127, No. 4, Nov. 2005, pp. 437-596.
37. Haans W., Sant T., van Kuik G.A.M. and van Bussel G.J.W., "Velocity Measurements in the Near Wake of a Horizontal Axis Wind Turbine", *Proceedings from the 31st European Rotorcraft Forum*, Florence, Italy, 2005.
38. Hendriks H.B. and Zaaijer M., "Dutch Offshore Wind Energy Converter – Executive summary of the public research activities", *Report by Energy Research Centre and Delft University of Technology*, the Netherlands, January 2004.
39. Himmelskamp H., "Profile Investigations on a Rotating Aircrew", *Dissertation Göttingen 1945, Reports and Translations No. 832*, Sept. 1947.
40. Johansen J. and Sørensen N.N., "Airfoil Characteristics from 3D CFD Rotor Computations", *Proceedings of the Special Topic Conference: the Science of Making Torque from Wind*, EWEA, Delft, The Netherlands, 2004.
41. Jones R.T., "Operational Treatment of the Non-Uniform Lift Theory in Airplane Dynamics," *NASA Technical Note 667*, 1938
42. Katz J. and Plotkin A., "Low Speed Aerodynamics", *Second Edition*, Cambridge University Press, 2001.
43. Kuhn M., "Dynamics and Design Optimisation of Offshore Wind Energy Conversion Systems", *Phd Thesis, Delft University Wind Energy Institute*, The Netherlands, 2001.
44. Laino D.J., Hansen A.C and Minnema J.E., "Validation of the Aerodyn Subroutines Using NREL Unsteady Aerodynamics Experiment Data", *Wind Energy*, Vol 5, 2002, pp. 227 – 244.
45. Liano D.J. and Hansen A.C, "Continued Validation of the Aerodyn Subroutines using NREL Unsteady Aerodynamics Experiment Data", *AIAA-2002-0518, Proceedings from 21st ASME Wind Energy Symposium*, Reno, 2002.
46. Lee D.J and Na S.U., "Numerical Simulations of Wake Structures Generated by Rotating Blades using a Time Marching Free Vortex Blob Method", *European Journal of Mechanics – B/Fluids*. Vol. 18(1), 1999.
47. Leishman J.G. and Beddoes T.S., "A Semi-Empirical Model for Dynamic Stall", *Journal of the American Helicopter Society*, Vol. 34, No. 3, pp. 3-17, 1989.

References

48. Leishman J.G., "Modelling Sweep Effects on Dynamic Stall", *Journal of the American Helicopter Society*, 34 (3), pp. 18-29, 1989.
49. Leishman J.G., "Principles of Helicopter Aerodynamics", *Cambridge University Press*, 2000.
50. Leishman J. G., "Challenges in Modelling the Unsteady Aerodynamics of Wind Turbines" *Wind Energy*, Vol. 5, No. 11, 2002, pp. 85-132.
51. Leishman J.G., Bhagwat M.J., and Bagai A., "Free-Vortex Filament Methods for the Analysis of Helicopter Rotor Wakes", *Journal of Aircraft*, Vol. 39, No. 5, pp 759-775, 2002.
52. Lindenburg C., "Investigation into Rotor Aerodynamics – Analysis of the stationary measurements on the UAE phase VI rotor in the NASA-Ames wind tunnel", *Netherlands Energy Research Foundation, ECN-C-03-025*, 2003.
53. Manwell J.F., McGowan J.G. and Rogers A.L., "Wind Energy Explained – Theory, Design and Application", *John Wiley & Sons Ltd.*, 2002.
54. Marshall J.S., "Inviscid Incompressible Flow", *John Wiley & Sons Ltd.*, 2001.
55. Mast E.H.M, Vermeer L.J., van Bussel G.J.W., "Estimation of the Circulation Distribution on a Rotor Blade from Detailed Wake Velocities", *Wind Energy* Vol. 7, 2004, pp. 189-209.
56. Medici D. and Alfredson P.H., "Measurements on a Wind Turbine Wake:3D Effects and Bluff-Body Vortex Shedding," *Proceedings of the Special Topic Conference: the Science of Making Torque from Wind*, EWEA, Delft, The Netherlands, 2004.
57. Michelsen J.A., "Basis3D – a Platform for Development of Multiblock PDE Solvers", *Technical Report AFM 92-05*, Technical University of Denmark, 1992.
58. Michelsen J.A., "Block Structured Multigrid Solution of 2D and 3D Elliptic PDE's", *Technical Report AFM 94-06*, Technical University of Denmark, 1994.
59. Oberkampf W.L. and Trucano T.G., "Verification and Validation in Computational Fluid Dynamics", *Progress in Aerospace Sciences*, Vol. 38, pp. 209-272, 2002.
60. Øye S., "Induced Velocities for Rotors in Yaw", *Proceedings of the Sixth IEA Symposium*, ECN, Petten, the Netherlands, 1992.
61. Rasmussen F., Hansen M.H., Thomsen K., Larsen T.J., Bertagnolio F., Johansen J. and Madsen H.A., Christian B. and Hansen A.M., "Present Status of Aerolasticity of Wind Turbines", *Wind Energy*, Vol. 6, 2003, pp. 213-228.

References

62. Ronsten G., "Static Pressure Measurements in a Rotating and non-Rotating 2.375m Wind Turbine Blade. Comparison with 2D Calculations", *Proceedings from the European Wind Energy Conference*, 1991, pp. 214-220.
63. van Rooij R.P.J.O.M., "Modification of the boundary layer calculation in RFOIL for improved airfoil stall prediction", Report *IW-96087R*, Delft University of Technology, 1996.
64. van Rooij R.P.J.O.M., "Description of the aerodynamic design process for a wind turbine rotor", Delft University of Technology, Section Wind Energy, Sept. 2003.
65. van Rooij R.P.J.O.M., Bruining A. and Schepers J.G., "Validation of Some Rotor Stall Models by Analyses of the IEA Annex XVIII field data", *Proceedings from the European Wind Energy Conference*, Madrid 2003.
66. van Rooij R.P.O.M., Timmer W.A. and Bruining A., "Determination of The Local Flow Angle on Rotating Blades", *Proceedings of the World Wind Energy Conference and Exhibition*, July 2002, Berlin, Germany.
67. Sant T., van Kuik G.A.M. and van Bussel G.J.W. , "Using Near Wake Measurements to Improve BEM Engineering Models for Yawed Wind Turbines", *Proceedings from the European Wind Energy Conference*, London 2004.
68. Sant T., van Kuik G.A.M. and van Bussel G.J.W., "Estimating the Angle of Attack from Blade Pressure Measurements on the NREL Phase VI Rotor using a Free-Wake Vortex Model: Axial Conditions", *Wind Energy*, DOI: 10.1002/we.210.
69. Schepers J.G., "An Engineering Model for Yawed Conditions, Developed on the Basis of Wind Tunnel Measurements", *AIAA-99-0039, ASME Conference*, 1999, Reno, USA.
70. Schepers J.G, Heidra J., Thomsen K., Larsen T.J., Foussekis D, Smith R.R., Kraan I., Visser B., Øye S., Ganander H., Carlen I., Belessis M., Voutsinas S., Drost L., "Verification of European Wind Turbine Design Codes", *Proceedings from the European Wind Energy Conference*, Copenhagen, 2001; pp. 581-586.
71. Scherer R., "Blade Design Aspects", *Renewable Energy*, 16 (1999) 1272-1277, Pergamon.
72. Schmitz S., Chattot J.J., "Application of a 'Parallelized Coupled Navier-Stokes/Vortex-Panel Solver' to the NREL Phase VI Rotor", *AIAA-2005-0593, Proceedings from 24th ASME Wind Energy Symposium*, Reno, 2005.
73. Schreck S., "The NREL Full-Scale Wind Tunnel Experiment – Introduction to the Special Issue", *Wind Energy*, Vol. 5, 2002, pp. 77-84.

References

74. Schreck S. and Robinson M., "Structures and Interactions Underlying Rotational Augmentation of Blade Aerodynamic Response", AIAA-2003-0520, *Proceedings from 22nd ASME Wind Energy Symposium*, Reno, 2002.
75. Schreck S. and Robinson M., "Competing Local and Global Influences on Rotationally Augmented HAWT Blade Aerodynamics", *Proceedings of the Special Topic Conference: The Science of Making Torque from Wind*, EWEA, Delft, The Netherlands, 2004.
76. Schreck S., Robinson M., Hand M. and Simms D., "Blade Dynamic Stall Vortex Kinematics for a Horizontal Axis Wind Turbine in Yawed Conditions", *ASME Journal of Solar Energy Engineering*, Vol. 123, pp. 272-281, Nov. 2001.
77. Sharpe D., Jenkins N., Bossanyi E. and Burton T., *Wind Energy Handbook*, John Wiley & Sons, New York, 2002.
78. Simms D., Schreck S., Hand M. and Fingersh L.J., "NREL Unsteady Aerodynamics Experiment in the NASA-Ames Wind Tunnel: A Comparison of Predictions to Measurements," *NREL Tech Report NREL/TP-500-29494*, Golden, Colorado, June 2001.
79. Snel H., "Heuristic Modelling of Dynamic Stall Characteristics", *Proceedings from the European Wind Energy Conference*, Dublin 1997.
80. Snel H., "Review of the Present Status of Rotor Aerodynamics", *Wind Energy*, Vol. 1, 1998, pp. 46-69.
81. Snel H., "Review of Aerodynamics for Wind Turbines", *Wind Energy*, Vol. 6, 2003, pp. 203-211.
82. Snel H., Houwink R., Bosschers J., Piers, W.J., van Bussel, G.J.W. and Bruining, A. "Sectional Prediction 3D Effects for Stalled Flow on Rotating Blades and Comparison with Measurements", *Proceedings from the European Wind Energy Conference*, 1991, pp. 395-399.
83. Snel H. and Schepers J.G. (ed), "Joint Investigation of Dynamic Inflow Effects and Implementation of an Engineering Method", *Netherlands Energy Research Foundation, ECN-C-94-107*, 1994.
84. Snel H. and Schepers J.G. (ed), "Dynamic Inflow: Yawed Conditions and Partial Span Pitch Control", *Netherlands Energy Research Foundation, ECN-C-95-056*, 1995.
85. Sørensen B., "Renewable Energy – Its physics, engineering, environmental impacts, economics & planning", *Elsevier Academic Press, Third Edition*, 2004.

References

86. Sørensen N.N., "A General Purpose Flow Solver Applied to Flow over Hills", Risø National Laboratory, Roskilde, Denmark, June 1995.
87. Sørensen N.N, Michelsen J.A., Schreck S., "Navier-Stokes Predictions of the NREL Phase VI Rotor in the NASA 80ft X 120ft Wind Tunnel", *Wind Energy*, Vol 5, 2002, pp. 151 – 169.
88. Spera D. A., "Wind Turbine Technology – Fundamental Concepts of Wind Turbine Engineering", ASME Press, New York, 1994.
89. Strelets M., "Detached Eddy Simulation of Massively Separated Flows", *AIAA 2001-0879*, 31st AIAA Aerospace Sciences Meeting and Exhibit, 2001.
90. Tangler, J.L., "The Nebulous Art of Using Wind Tunnel Aerofoil Data for Predicting Rotor Performance", *Wind Energy*, 2002, Vol. 5, pp. 245-257.
91. Tangler J.L., "Insight into Wind Turbine Stall and Post-stall Aerodynamics", *Wind Energy*, Vol 7, 2004, pp. 247-260.
92. van der Tempel J., "Design of Support Structures for Offshore Wind Turbines", *Phd Thesis*, Delft University of Technology, the Netherlands, 2006.
93. Theodorsen T., "General Theory of Aerodynamic Instability and the Mechanism of Flutter," *NACA Report 496*, 1935.
94. Thor S.E. and Taylor P.W., "Long-term Research Needs for Wind Energy for the Time Frame 2000-2020", *Wind Energy*, 2002; Vol. 5, pp. 73-75.
95. Tongchitpakdee C., Benjanirat S, Sankar L.N., "Numerical Simulation of the Aerodynamics of Horizontal Wind Turbines Under Yawed Flow Conditions", *AIAA-2005-0773, Proceedings from 24th ASME Wind Energy Symposium*, Reno, 2005.
96. Vermeer L.J., "Wind Tunnel Experiments on a Rotor Model in Yaw". *Proceedings of the 12th symposium on Aerodynamics of Wind Turbines*, Lyngby, 1998, pp. 11-20.
97. Vermeer N.J., "A New Rotor Model for Aerodynamic Measurements in the Improved Open Jet Wind Tunnel", *National Wind Energy Conference*, Lunteren, The Netherlands, 1990 (in Dutch).
98. Vermeer L.J., "A Review of Wind Turbine Wake Research at TUDelft", *AIAA-2001-0030*, Reno, 2002.
99. Vermeer L.J., Sørensen J.N. and Crespo A. "Wind Turbine Wake Aerodynamics", *Progress in Aerospace Sciences*, 2003, Vol 39, pp. 467-510.

References

100. Viterna L.A., and Corrigan R.D., "Fixed Pitch Rotor Performance of Large Horizontal Axis Wind Turbines," *Proceedings from the Workshop on Large Horizontal Axis Wind Turbines*, NASA CP-2230, DOE Publication CONF-810752, Cleveland, OH, NASA Lewis Research Centre, 1981.
101. Voutsinas S.G., Belessis M.A. and Huberson S., "Dynamic Inflow Effects and Vortex Particle Methods", *Proceedings from the European Wind Energy Conference*, Lübeck-Travemünde, Germany, 1993.
102. Wagner H., "Über die Entstehung des dynamischen Auftriebes von Tragflügeln", *Zeitschrift für Angewandte Mathematik und Mechanik*, 5 (1), 1925, pp 17.
103. Wood D.H., "A Three-Dimensional Analysis of Stall-Delay on a Horizontal-Axis Wind Turbine", *Journal of Wind Engineering and Industrial Aerodynamics*, Vol. 37, 1991, pp. 1-14.
104. Zhiquan Y., Xiog L., and Yan C., "Global Optimum Design Method and Software for Rotor Blades of Horizontal Axis Wind Turbines", *Wind Engineering*, Vol. 26, No. 4, 2002, pp. 257-267.

Appendix A - Maximum Power Coefficient for a Yawed Turbine Disc

The simple actuator disk theory of section 3.1 is used here to derive the maximum power coefficient for a yawed turbine. From simple energy considerations (neglecting energy losses due friction, a finite number of blades and other losses), the power extracted from the wind is equal to the rate of change of kinetic energy of the fluid flowing through the rotor. From Fig. 3.1, this is equal to

$$P = \frac{1}{2} \rho A U' \left[(U \cos(\Psi))^2 - (U \cos(\Psi) + u_{a1})^2 \right] \quad (\text{A.1})$$

Substituting Eq. 3.1 in the above equation and simplifying results in

$$P = 2 \rho A U^3 a_1 \left[1 + 2a_1 \cos(\Psi) + a_1^2 \right]^{\frac{1}{2}} \left[\cos(\Psi) + a_1 \right] \quad (\text{A.2})$$

Defining the power coefficient as $C_p = P / \left(\frac{1}{2} \rho A U^3 \right)$ and using Eq. A.2, the following expression results

$$C_p(a_1, \Psi) = 4a_1 \left[1 + 2a_1 \cos(\Psi) + a_1^2 \right]^{\frac{1}{2}} \left[\cos(\Psi) + a_1 \right] \quad (\text{A.3})$$

Eq. A.3 is plotted in Fig. A.1 for different yaw angles. It can be noted that as the yaw angle increases, the power coefficient at any induction factor decreases. The optimum value for a_1 occurs at lower values at higher yaw angles.

The maximum power coefficient, $C_{p,Max}$, at a particular yaw angle is found by partial differentiation, using $\frac{\partial C_p}{\partial a_1} = 0$. This yields the relation for the optimum axial induction

factor $a_{1,m}$, for a given yaw angle. This relation is

$$\frac{a_{1,m} \left[\cos(\Psi) + a_{1,m} \right]^2}{\left[\cos(\Psi) + 2a_{1,m} \right]} = - \left[1 + 2a_{1,m} \cos(\Psi) + a_{1,m}^2 \right] \quad (\text{A.4})$$

The above equation may be solved iteratively for $a_{1,m}$ to yield the variation of the optimum axial induction factor with yaw angle. This variation is plotted in Fig. A.2. For $\Psi=0^\circ$, term $a_{1,m}$ is equal to $-1/3$. As the yaw angle is increased, there is a slight increase in $a_{1,m}$ up to a yaw angle of about 30° . At larger yaw angles, $a_{1,m}$ starts to decrease rapidly until it reaches the value of zero at a yaw angle of 90° .

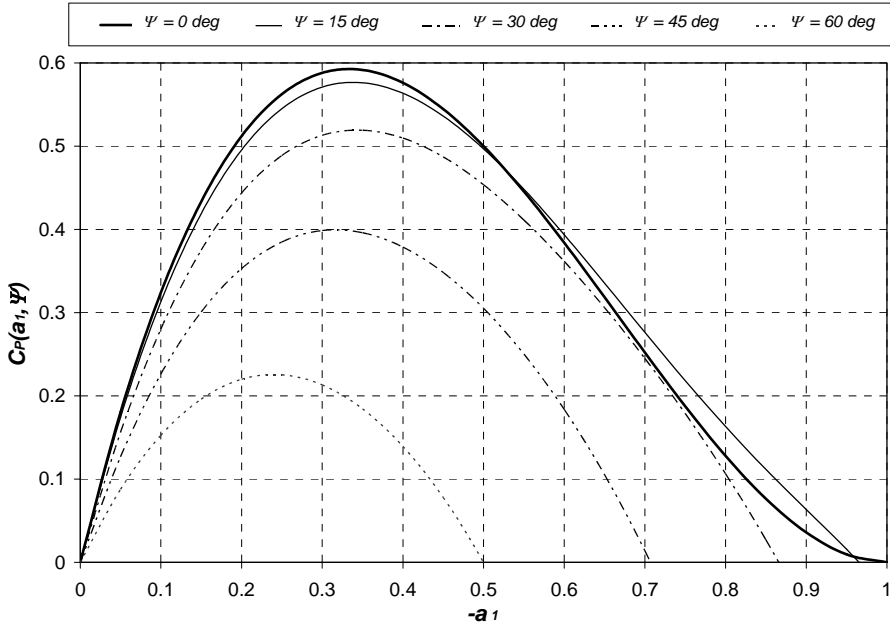


Figure A.1 – Variation of the power coefficient with the axial induction factor for different yaw angles as predicted by Eq. A.3.

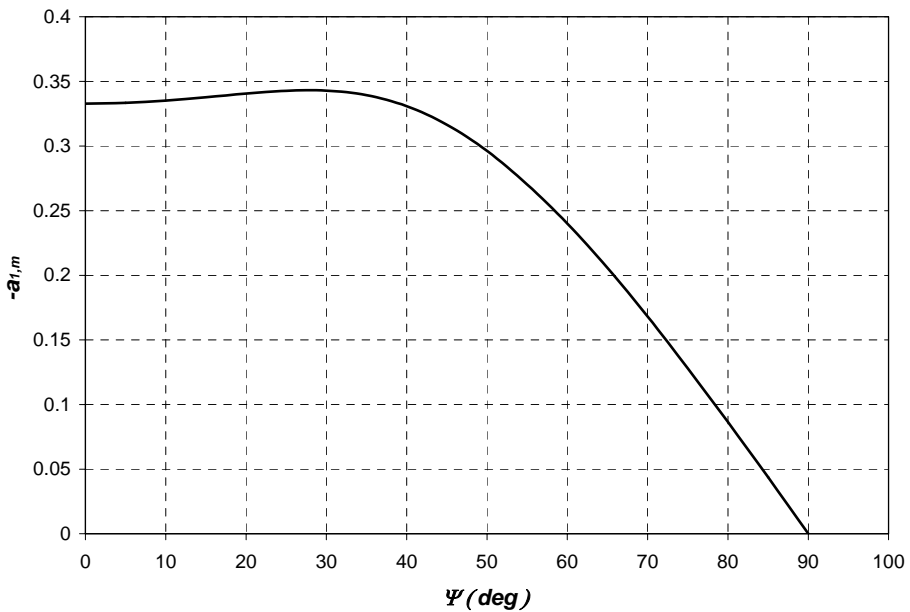


Figure A.2 – Variation of the optimum axial induction factor with yaw angle as predicted by Eq. A.4.

Substituting Eqt. A.4 in A.3 for the case in which $a_t=a_{1,m}$ results in the equation for $C_{P,max}$:

$$C_{P,Max}(a_{1,m}, \Psi) = \frac{4(-a_{1,m})^{3/2} [Cos(\Psi) + a_{1,m}]^2}{[Cos(\Psi) + 2a_{1,m}]^{1/2}} \quad (A.5)$$

Putting $a_{1,m}=-1/3$ in this equation for zero yaw results in $C_{P,Max}=16/27$ which is in fact the Betz efficiency. Eqt. A.5 gives the ideal wind turbine efficiency that can be reached at a given yaw angle.

Appendix B – Calculation of Aerodynamic Loads Induced at the Yaw Bearing

This appendix describes a numerical method to obtain the 3D forces and moments at the yaw bearing resulting from the aerodynamic forces at the blades. The loads are determined as a function of the rotor azimuth angle ϕ .

The known aerodynamic forces at the local η - ζ - ξ reference frame are first transformed to the X_a - Y_a - Z_a reference frame. These are then used to find the resultant (total) forces and moments at the yaw bearing O by numerical integration. In Fig. B.1, the blade element similar to that shown in Fig. 3.3 is illustrated in 3D space. The position of its centre with respect to O is defined by vector \vec{v}_o and is equal to

$$\vec{v}_{o(X_n-Y_n-Z_n)} = \begin{bmatrix} r \sin(\phi) \\ -d_a + \beta r \\ r \cos(\phi) \end{bmatrix} \quad (B.1)$$

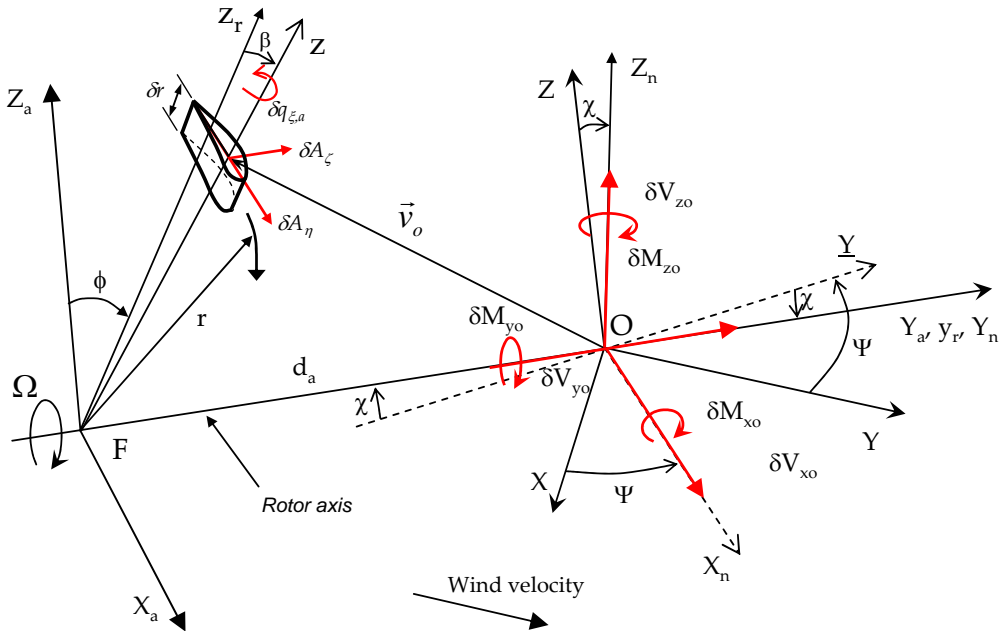


Figure B.1 – Aerodynamic forces and moments induced at yaw bearing O due to one blade element

The local aerodynamic forces at each blade element in the $X_a-Y_a-Z_a$ reference frame are denoted by δV_{xh} , δV_{yh} and δV_{zh} . The corresponding moments are δM_{xh} , δM_{yh} and δM_{zh} . These are obtained using the matrix transformation K such that

$$\begin{bmatrix} \delta V_{xh} \\ \delta V_{yh} \\ \delta V_{zh} \end{bmatrix} = K \begin{bmatrix} \delta A_\eta \\ \delta A_\zeta \\ 0 \end{bmatrix} \quad (\text{B.2})$$

and

$$\begin{bmatrix} \delta M_{xh} \\ \delta M_{yh} \\ \delta M_{zh} \end{bmatrix} = K \begin{bmatrix} 0 \\ 0 \\ \delta q_{\xi,a} \end{bmatrix} \quad (\text{B.3})$$

K is equal to the inverse of matrix S with Ψ and χ equal to zero (refer to Chapter 2, section 2.5). Now let δV_{xo} , δV_{yo} and δV_{zo} denote the aerodynamic forces at point O due to a single blade element and let the moments be δM_{xo} , δM_{yo} and δM_{zo} . These forces and moments are in the $X_n-Y_n-Z_n$ reference frame. From Fig. B.1 it can be shown that

$$\begin{bmatrix} \delta V_{xo} \\ \delta V_{yo} \\ \delta V_{zo} \end{bmatrix} = \begin{bmatrix} \delta V_{xh} \\ \delta V_{yh} \\ \delta V_{zh} \end{bmatrix} \quad (\text{B.4})$$

$$\begin{bmatrix} \delta M_{xo} \\ \delta M_{yo} \\ \delta M_{zo} \end{bmatrix} = \begin{bmatrix} \delta M_{xh} \\ \delta M_{yh} \\ \delta M_{zh} \end{bmatrix} + \vec{v}_{o(X_n-Y_n-Z_n)} \times \begin{bmatrix} \delta V_{xh} \\ \delta V_{yh} \\ \delta V_{zh} \end{bmatrix} \quad (\text{B.5})$$

Eqts. B.1..5 above are applied to each element of all the blades for different rotor azimuth angles. An index notation is adopted as for codes *HAWT_BEM* and *HAWT_LFIM* using parameters τ , b and i to denote the rotor time step, blade number and radial location of the blade respectively. The resultant forces and moments at the yaw bearing O due to a single blade are determined by numerical integration. Applying the trapezium rule and using the elemental values of each blade element, then the forces and moments at O due to a single blade n and at rotor azimuth angle τ may be expressed by

$$\begin{aligned}
 (V_{xo})_{\tau,b} &= \frac{1}{2} \left\{ (\delta V_{xo})_{\tau,b,0} + 2 \left[(\delta V_{xo})_{\tau,b,1} + \dots + (\delta V_{xo})_{\tau,b,i} + \dots + (\delta V_{xo})_{\tau,b,n-1} \right] + (\delta V_{xo})_{\tau,b,n-1} \right\} \\
 (V_{yo})_{\tau,b} &= \frac{1}{2} \left\{ (\delta V_{yo})_{\tau,b,0} + 2 \left[(\delta V_{yo})_{\tau,b,1} + \dots + (\delta V_{yo})_{\tau,b,i} + \dots + (\delta V_{yo})_{\tau,b,n-1} \right] + (\delta V_{yo})_{\tau,b,n-1} \right\} \\
 (V_{zo})_{\tau,b} &= \frac{1}{2} \left\{ (\delta V_{zo})_{\tau,b,0} + 2 \left[(\delta V_{zo})_{\tau,b,1} + \dots + (\delta V_{zo})_{\tau,b,i} + \dots + (\delta V_{zo})_{\tau,b,n-1} \right] + (\delta V_{zo})_{\tau,b,n-1} \right\} \\
 (M_{xo})_{\tau,b} &= \frac{1}{2} \left\{ (\delta M_{xo})_{\tau,b,0} + 2 \left[(\delta M_{xo})_{\tau,b,1} + \dots + (\delta M_{xo})_{\tau,b,i} + \dots + (\delta M_{xo})_{\tau,b,n-1} \right] + (\delta M_{xo})_{\tau,b,n-1} \right\} \\
 (M_{yo})_{\tau,b} &= \frac{1}{2} \left\{ (\delta M_{yo})_{\tau,b,0} + 2 \left[(\delta M_{yo})_{\tau,b,1} + \dots + (\delta M_{yo})_{\tau,b,i} + \dots + (\delta M_{yo})_{\tau,b,n-1} \right] + (\delta M_{yo})_{\tau,b,n-1} \right\} \\
 (M_{zo})_{\tau,b} &= \frac{1}{2} \left\{ (\delta M_{zo})_{\tau,b,0} + 2 \left[(\delta M_{zo})_{\tau,b,1} + \dots + (\delta M_{zo})_{\tau,b,i} + \dots + (\delta M_{zo})_{\tau,b,n-1} \right] + (\delta M_{zo})_{\tau,b,n-1} \right\}
 \end{aligned}
 \tag{B.6}$$

The resultant (total) forces and moments at O for a rotor with B blades are evaluated using equations B.6 above and summing up for each time step τ . This operation is expressed mathematically as

$$\begin{aligned}
 (S_{V_{xo}})_{\tau} &= \sum_{b=0}^{b=B-1} (V_{xo})_{\tau,b} & (S_{V_{yo}})_{\tau} &= \sum_{b=0}^{b=B-1} (V_{yo})_{\tau,b} & (S_{V_{zo}})_{\tau} &= \sum_{b=0}^{b=B-1} (V_{zo})_{\tau,b} \\
 (S_{M_{xo}})_{\tau} &= \sum_{b=0}^{b=B-1} (M_{xo})_{\tau,b} & (S_{M_{yo}})_{\tau} &= \sum_{b=0}^{b=B-1} (M_{yo})_{\tau,b} & (S_{M_{zo}})_{\tau} &= \sum_{b=0}^{b=B-1} (M_{zo})_{\tau,b}
 \end{aligned}
 \tag{B.7}$$

In fact $S_{V_{yo}}$ and $S_{M_{yo}}$ are equal to the rotor axial thrust and rotor output torque respectively (i.e. T and Q). The rotor output power is simply found from

$$P = S_{M_{yo}} \Omega = Q \Omega
 \tag{B.8}$$

Note that $S_{M_{zo}}$ is the moment about the Z_n axis and not about the Z axis. It is defined as the yawing moment about the Z_n axis. However when the rotor axis tilt angle χ is zero, then these would be the same. The loads of Eqts. B.7 may be expressed in non-dimensional form as shown in table B.1.

Table B.1: Dimensionless form for the resultant aerodynamic forces and moments at the yaw bearing O and the output power.

<i>Dimensionless Coefficient</i>	<i>Equation</i>
Side Thrust Coefficient	$C_{V_{xo}} = \frac{S_{V_{xo}}}{\frac{1}{2} \rho A U^2}$
Axial Thrust Coefficient	$C_{V_{yo}} = \frac{S_{V_{yo}}}{\frac{1}{2} \rho A U^2} = C_T$
Upward Thrust Coefficient	$C_{V_{zo}} = \frac{S_{V_{zo}}}{\frac{1}{2} \rho A U^2}$
Pitching Moment Coefficient	$C_{M_{xo}} = \frac{S_{M_{xo}}}{\frac{1}{2} \rho A U^2 R}$
Torque Coefficient	$C_{M_{yo}} = \frac{S_{M_{yo}}}{\frac{1}{2} \rho A U^2 R} = C_Q$
Yawing Moment Coefficient	$C_{M_{zo}} = \frac{S_{M_{zo}}}{\frac{1}{2} \rho A U^2 R}$
Power Output Coefficient	$C_P = \frac{P}{\frac{1}{2} \rho A U^3}$

Appendix C – Calculation of the Induced Velocity from a Vortex Filament using the Biot-Savart Law

Assuming that the region outside the vortex sheet and tip vortex is potential and the temperature is constant, the vortex systems in the rotor wake can be represented by the incompressible Biot-Savart law. For an incompressible fluid, the continuity equation which applies for the velocity field is given by

$$\nabla \cdot \vec{u} = 0 \quad (\text{C.1})$$

where \vec{u} is the velocity and ∇ is the gradient operator which in Cartesian coordinates is

$$\nabla = \hat{i} \frac{\partial}{\partial x} + \hat{j} \frac{\partial}{\partial y} + \hat{k} \frac{\partial}{\partial z} \quad (\text{C.2})$$

We may express the velocity field as the curl of a vector potential \vec{B} such that

$$\vec{u} = \nabla \times \vec{B} \quad (\text{C.3})$$

Since the curl of a gradient vector is zero, \vec{B} is indeterminate to within the gradient of a scalar function of position and time, and \vec{B} can be selected such that

$$\nabla \cdot \vec{B} = 0 \quad (\text{C.4})$$

The vorticity, ζ , is defined by

$$\zeta = \nabla \times \vec{u} \quad (\text{C.5})$$

Using Eqs. C.3 and C.5, the vorticity becomes equal to

$$\zeta = \nabla \times (\nabla \times \vec{B}) = \nabla (\nabla \cdot \vec{B}) - \nabla^2 \vec{B} \quad (\text{C.6})$$

Substituting Eq. C.4 in C.6 results in Poisson's equation for the vector potential \vec{B} given by

$$\zeta = -\nabla^2 \vec{B} \quad (\text{C.7})$$

The above equation may be solved for \vec{B} using Green's theorem. Substituting the resulting relation for \vec{B} in Eq. C.3 yields the following the Biot-Savart law:

$$d\vec{u} = \frac{\Gamma}{4\pi} \frac{d\vec{s} \times \vec{r}}{|\vec{r}|^3} \quad (\text{C.8})$$

This relation gives the induced velocity at a point A due to a single vortex line having a constant circulation Γ . $d\vec{s}$ is an elemental length of the vortex line and \vec{r} is the position vector from the node to the element $d\vec{s}$. The solution for Eqts. C.7 and C.8. may be found in various advanced aerodynamic textbooks such as Marshall [54, page 86] and Katz and Plotkin [42, page 173-174]. Note that the Biot-Savart law is only valid for incompressible flows.

Fig. C.1 shows a node A and a straight line vortex having endpoints B and C . The induced velocity at point A due to vortex BC is equal to u and is perpendicular to the plane $\vec{r} - d\vec{s}$. The induced velocity is obtained by integrating Eq. C.8 over the length of the vortex line.

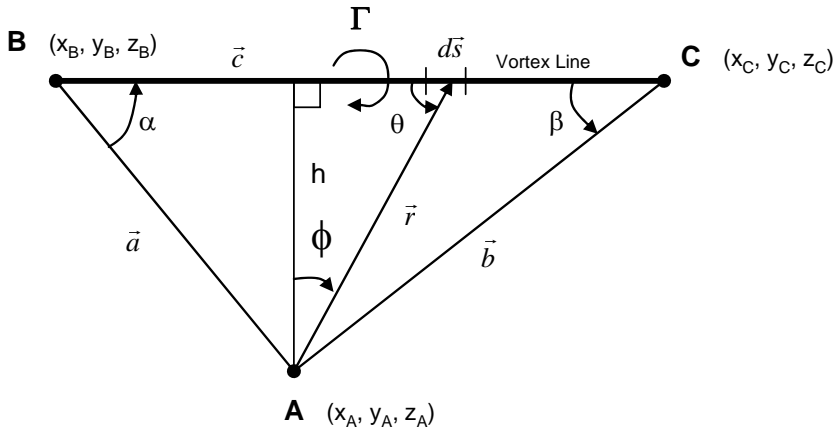


Figure C.1 - Vortex line geometry for calculation of the three-dimensional induced velocity at a point A

Define h as the perpendicular distance from node A to the vortex line and ϕ is the angle between h and \vec{r} . Then,

$$\sin \theta = \cos \phi = \frac{h}{r} \tag{C.9}$$

$$ds = d(h \tan \phi) = \left(\frac{h}{\cos^2 \phi} \right) d\phi \tag{C.10}$$

Now using relationship Eq. C.9, Eq. C.8 can be written in terms of h and ϕ .

$$du = \frac{\Gamma}{4\pi h} \cos \phi \, d\phi \tag{C.11}$$

Substituting in Eq. C.11 and integrating from $\phi = \alpha - \pi/2$ to $\pi/2 - \beta$

$$u = \frac{\Gamma}{4\pi h} \int_{\alpha - \frac{\pi}{2}}^{\frac{\pi}{2} - \beta} \cos\phi \, d\phi$$

or

$$u = \frac{\Gamma}{4\pi h} (\cos\alpha + \cos\beta) \quad (\text{C.12})$$

The velocity u is in a direction perpendicular to the $\vec{r} - d\vec{s}$ plane and hence perpendicular to the plane of the vectors \vec{a} and \vec{b} . Now define positive circulation Γ such that \vec{u} points into the paper as shown in Fig. C.1. Now \vec{u} can be written as

$$\vec{u} = u \frac{\vec{a} \times \vec{b}}{|\vec{a} \times \vec{b}|} \quad (\text{C.13})$$

To derive the three-dimensional induced velocity \vec{u} in terms of \vec{a} and \vec{b} , define \vec{c} as

$$\vec{c} = \vec{b} - \vec{a} \quad (\text{C.14})$$

Using the dot and cross-product relations and Fig. C.1,

$$-\vec{a} \cdot \vec{c} = |\vec{a}| |\vec{c}| \cos\alpha \quad (\text{C.15})$$

$$\vec{b} \cdot \vec{c} = |\vec{b}| |\vec{c}| \cos\beta \quad (\text{C.16})$$

$$h = |\vec{a}| \sin\alpha = \frac{|\vec{a} \times \vec{c}|}{\vec{c}} \quad (\text{C.17})$$

and from the definition of \vec{c} we have

$$|\vec{a} \times \vec{c}| = |\vec{a} \times (\vec{b} - \vec{a})| = |\vec{a} \times \vec{b}| \quad (\text{C.18})$$

$$|\vec{b} \times \vec{c}| = |\vec{b} \times (\vec{b} - \vec{a})| = |\vec{a} \times \vec{b}| \quad (\text{C.19})$$

The vector identities in Eqts. C.15-C.19 can be employed to prove that

$$\left(\frac{\cos\alpha + \cos\beta}{h} \right) = \frac{(|\vec{a}| + |\vec{b}|)(|\vec{a}\vec{b}| - \vec{b} \cdot \vec{a})}{|\vec{a} \times \vec{b}| |\vec{b}| |\vec{a}|} \quad (\text{C.20})$$

Substituting Eq. C.20 in C.12 and C.13 we get

$$\vec{u} = \frac{\Gamma}{4\pi} \left(\frac{(|\vec{a}| + |\vec{b}|)(|\vec{a}||\vec{b}| - \vec{b} \cdot \vec{a})}{|\vec{a}||\vec{b}||\vec{a} \times \vec{b}|^2} \right) (\vec{a} \times \vec{b}) \quad (\text{C.21})$$

To express the three dimensional components of the induced velocity in Cartesian co-ordinate form, we proceed as follows:

The positions of points A, B and C shown in Fig. C.1 have co-ordinates (x_A, y_A, z_A) , (x_B, y_B, z_B) and (x_C, y_C, z_C) respectively. Vectors \vec{a} and \vec{b} may be written in vector form as

$$\vec{a} = (x_B - x_A)\underline{i} + (y_B - y_A)\underline{j} + (z_B - z_A)\underline{k} \quad (\text{C.22})$$

$$\vec{b} = (x_C - x_A)\underline{i} + (y_C - y_A)\underline{j} + (z_C - z_A)\underline{k} \quad (\text{C.23})$$

Eqs. C.22 and C.23 are substituted in Eq. C.21 to get

$$u_x = \Gamma * G_X \quad (\text{C.24})$$

$$u_y = \Gamma * G_Y \quad (\text{C.25})$$

$$u_z = \Gamma * G_Z \quad (\text{C.26})$$

G_x , G_y and G_z are the geometric influence coefficients given by

$$G_x = \frac{(r_1 + r_2)}{2\pi r_1 r_2 [(r_1 + r_2)^2 - L^2]} [(z_A - z_C)(y_C - y_B) - (y_A - y_C)(z_C - z_B)] \quad (\text{C.27})$$

$$G_y = \frac{(r_1 + r_2)}{2\pi r_1 r_2 [(r_1 + r_2)^2 - L^2]} [(x_A - x_C)(z_C - z_B) - (z_A - z_C)(x_C - x_B)] \quad (\text{C.28})$$

$$G_z = \frac{\Gamma(r_1 + r_2)}{2\pi r_1 r_2 [(r_1 + r_2)^2 - L^2]} [(y_A - y_C)(x_C - x_B) - (x_A - x_C)(y_C - y_B)] \quad (\text{C.29})$$

where

$$r_1 = [(x_A - x_B)^2 + (y_A - y_B)^2 + (z_A - z_B)^2]^{1/2} \quad (\text{C.30})$$

$$r_2 = \left[(x_A - x_C)^2 + (y_A - y_C)^2 + (z_A - z_C)^2 \right]^{1/2} \quad (\text{C.31})$$

$$L = \left[(x_C - x_B)^2 + (y_C - y_B)^2 + (z_C - z_B)^2 \right]^{1/2} \quad (\text{C.32})$$

Eqts. C.24...C.32 are the discretization equations for the Biot-Savart law to determine the 3D velocities (u_x , u_y and u_z) at any point A in the flow field induced by a straight-line vortex filament having a circulation Γ . However a problem exists in calculating the induced velocities close to the vortex filaments. For points on the vortex filaments the self-induced velocity is zero, but for points moving close to a vortex filament the induced velocity will tend to infinity, according to Biot-Savart's law. So for calculating induced velocities in such points some form of de-singularisation is required. One way of dealing with this problem is to apply a cut-off method: when the perpendicular distance h is less or equal to a cut-off distance δ , the induced velocities are set to zero. Another approach is to apply a vortex core model as explained in section 5.2.2.

The distance h may be found from the vector relation

$$h = \frac{|r_1 \times r_2|}{|r_2 - r_1|} \quad (\text{C.33})$$

From Eqts. C.30-C.32,

$$h = \frac{\sqrt{\Delta_1^2 + \Delta_2^2 + \Delta_3^2}}{L} \quad (\text{C.34})$$

where

$$\Delta_1 = (y_B - y_A)(z_C - z_A) - (y_C - y_A)(z_B - z_A) \quad (\text{C.35})$$

$$\Delta_2 = (x_B - x_A)(z_C - z_A) - (x_C - x_A)(z_B - z_A) \quad (\text{C.36})$$

$$\Delta_3 = (x_B - x_A)(y_C - y_A) - (x_C - x_A)(y_B - y_A) \quad (\text{C.37})$$

Appendix D – Linear and Spline Numerical Interpolation

Interpolation is a method of constructing new data points from a discrete set of known data points. Given a sequence of $n+1$ distinct data points $[x_i, y_i]$ that may not be evenly spaced such that

$$x_0 < x_1 < \dots < x_{n-1} < x_n$$

we can fit in a piecewise function between each of two successive data points to form an interpolating function $G(x)$ where

$$G(x) = \begin{cases} g_0(x) & x \in [x_0, x_1] \\ g_1(x) & x \in [x_1, x_2] \\ g_i(x) & x \in [x_i, x_{i+1}] \\ \vdots & \vdots \\ g_{n-1}(x) & x \in [x_{n-1}, x_n] \end{cases} \quad (D.1)$$

where $g_i(x)$ is the fitted function between the two successive data points (see Fig. D1). One or more constraints are applied to the fitted functions such that $G(x)$ is continuous in the range $x_0 \dots x_n$.

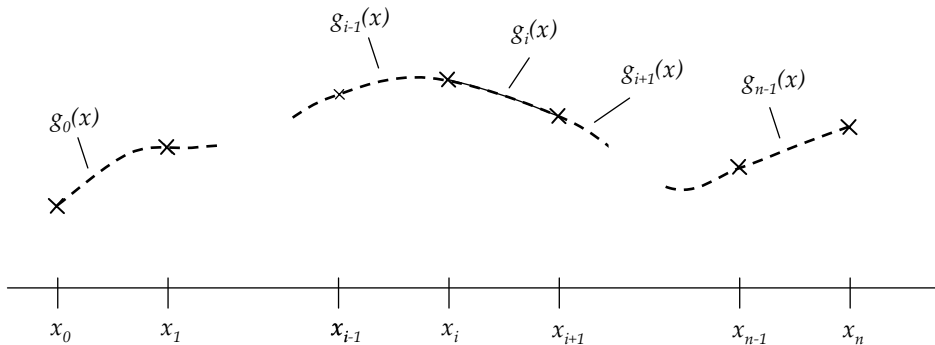


Figure D.1 - Interpolation by fitting piecewise functions between data points

Linear Interpolation

The most simple form of interpolation is linear interpolation where the data points are graphically connected by straight lines. The resulting function $G(x)$ is a polygon.

Algebraically, each $g_i(x)$ is a linear function constructed as

$$g_i(x) = y_i + \frac{y_{i+1} - y_i}{x_{i+1} - x_i} (x - x_i) \quad (D.2)$$

Since $G(x)$ must be continuous at each data point, then

$$g_i(x_i) = g_{i+1}(x_i) \quad i = 0, 1, \dots, n-2 \quad (D.3)$$

This is the case for which

$$g_{i-1}(x_i) = y_{i-1} + \frac{y_i - y_{i-1}}{x_i - x_{i-1}} (x_i - x_{i-1}) = y_i$$

$$g_i(x_i) = y_i + \frac{y_{i+1} - y_i}{x_{i+1} - x_i} (x_i - x_i) = y_i$$

Cubic Spline Interpolation

Cubic spline interpolation refers to interpolation in which the fitted functions consist of cubic polynomial functions having the form

$$g_i(x) = a_i(x - x_i)^3 + b_i(x - x_i)^2 + c_i(x - x_i) + d_i \quad (D.4)$$

The following constraints are applied:

$$g_i(x_i) = y_i, \quad i = 0, 1, \dots, n-1 \quad \text{and} \quad g_{n-1}(x_n) = y_n \quad (D.5a)$$

$$g_i(x_{i+1}) = g_{i+1}(x_{i+1}) \quad i = 0, 1, \dots, n-2 \quad (D.5b)$$

$$g'_i(x_{i+1}) = g'_{i+1}(x_{i+1}) \quad i = 0, 1, \dots, n-2$$

(D.5c)

$$g''_i(x_{i+1}) = g''_{i+1}(x_{i+1}) \quad i = 0, 1, \dots, n-2 \quad (D.5d)$$

Eqts. D.5 say that the cubic spline fits to each of the points (D.5a), is continuous (D.5b), and is continuous in slope and curvature (D.5c and D.5d) throughout the region spanned by the points.

If there are $n+1$ points, the number of intervals and the number of $g_i(x)$'s are n . There are thus four times n unknowns, which are the $\{a_i, b_i, c_i, d_i\}$ for $i = 0, 1, \dots, n-1$. Eqt. (D.5a) immediately yields

$$d_i = y_i, \quad i = 0, 1, \dots, n-1 \quad (D.6)$$

Eq. D.5b gives

$$\begin{aligned} y_{i+1} &= a_i (x - x_i)^3 + b_i (x - x_i)^2 + c_i (x - x_i) + y_i \\ &= a_i h_i^3 + b_i h_i^2 + c_i h_i + y_i, \quad i = 0, 1, \dots, n-1 \end{aligned} \tag{D.7}$$

where $h_i = x_{i+1} - x_i$, the width of the i th interval.

To relate the slopes and curvatures of the joining splines, we differentiate Eq. D.4 with respect to x :

$$g'_i(x) = 3a_i h_i^2 + 2b_i h_i + c_i \tag{D.8}$$

$$g''_i(x) = 6a_i h_i + 2b_i, \quad \text{for } i = 0, 1, \dots, n-1 \tag{D.9}$$

Denoting the second derivative by S such that $S_i = g''_i(x_i)$ for $i = 0, 1, \dots, n-1$ and $S_i = g''_i(x_i)$, apply Eq. D.9

$$\begin{aligned} S_i &= 6a_i (x_i - x_i) + 2b_i \\ &= 2b_i \\ S_{i+1} &= 6a_i (x_{i+1} - x_i) + 2b_i \\ &= 6a_i h_i + 2b_i \end{aligned}$$

Thus we can write

$$b_i = \frac{S_i}{2} \tag{D.10}$$

$$a_i = \frac{S_{i+1} - S_i}{6h_i} \tag{D.11}$$

Substitute the relations for a_i , b_i and d_i given by Eqs. D.6, D.10 and D.11 into Eq. D.4 and then solve for c_i :

$$\begin{aligned} y_{i+1} &= \left(\frac{S_{i+1} - S_i}{6h_i} \right) h_i^3 + \frac{S_i}{2} h_i^2 + c_i h_i + y_i \\ c_i &= \frac{y_{i+1} - y_i}{h_i} - \frac{2h_i S_i + h_i S_{i+1}}{6} \end{aligned}$$

We now apply the constraints that the slopes of the two cubics that join at $[x_i, y_i]$ are the same. For the equation in the i th interval, Eq. D.5c becomes with $x=x_i$,

$$y'_i = 3a_i (x_i - x_i)^2 + 2b_i (x_i - x_i) + c_i = c_i \tag{D.12}$$

In the previous interval, from x_{i-1} to x_i , the slope at its right end will be

$$\left[\begin{array}{ccccccc} \frac{(h_0 + h_1)(h_0 + 2h_1)}{h_1} & \frac{h_1^2 - h_0^2}{h} & & & & & \\ & h_1 & & & & & \\ & & 2(h_1 + h_2) & & & & \\ & & h_2 & & 2(h_2 + h_3) & & \\ & & & & h_3 & & \\ & & & & \ddots & & \\ & & & & & \frac{h_{n-2}^2 - h_{n-1}^2}{h_{n-2}} & \frac{(h_{n-1} + h_{n-2})(h_{n-1} + 2h_{n-2})}{h_{n-2}} \\ & & & & & & \end{array} \right] \quad (D.18)$$

After solving for $S_1, S_2, S_3, \dots, S_{n-1}$ using the coefficient matrix above, S_0 and S_n are computed using Eqts. D.15 and D.16. Then coefficients a_i, b_i, c_i and d_i for the cubics in each interval are determined from

$$\begin{aligned} a_i &= \frac{S_{i+1} - S_i}{6h_i} \\ b_i &= \frac{S_i}{2} \\ c_i &= \frac{y_{i+1} - y_i}{h_i} - \frac{2h_i S_i + h_i S_{i+1}}{6} \\ d_i &= y_i \end{aligned}$$

From these, various points on the interpolating curve may be computed.

Appendix E – Vortex Filament Stretching

Because in a free-wake solution the points in the fluid flow field are allowed to convect freely, the vortex filaments will be strained as the adjacent nodes will move relative to each other. This causes a change in vorticity of the individual filaments which in turn results in changes of the induced velocity field around the vortex core. This effect is illustrated pictorially in Fig. E.1.

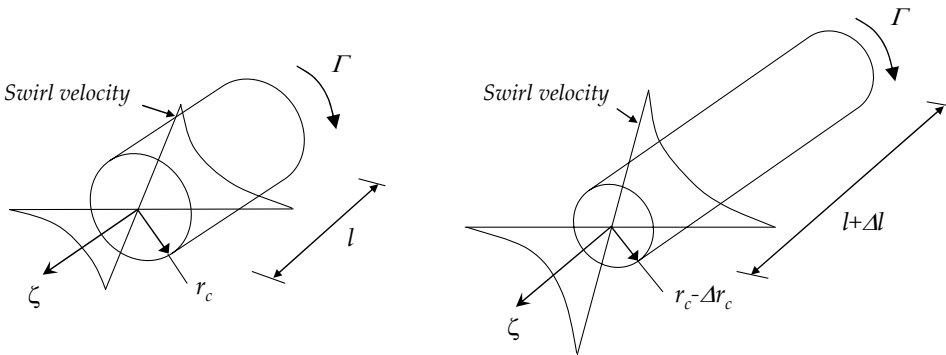


Figure E.1 – Schematic showing the effect of vortex filament stretching: The vorticity increases resulting in a higher swirl velocity.

Ananthan *et al.* [2] present the following correction for filaments stretching effects:

Consider a vortex filament with its location in space defined in time step τ by two adjacent nodes having position vectors \vec{r}_a and \vec{r}_{a-1} as shown in Fig. E.2.

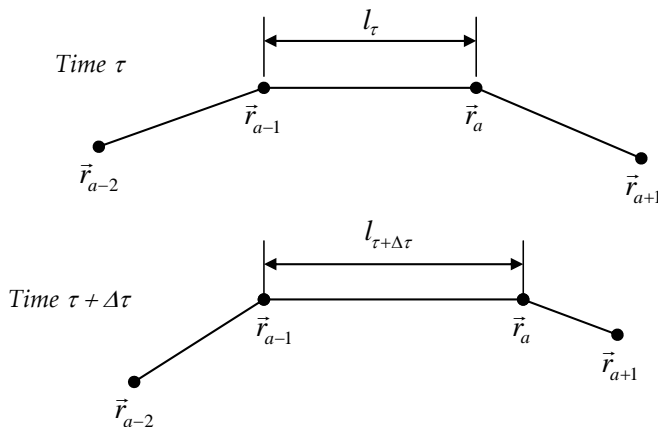


Figure E.2 – Schematic representation of straining in a vortex filament

Because the filament is a straight line segment, its length is given by

$$l_\tau = \left| \vec{r}_a - \vec{r}_{a-1} \right| \quad (\text{E.1})$$

The rate of change of the length of the filament as it convects through the velocity field is given by

$$\frac{dl}{d\tau} = \frac{d(\vec{r}_a - \vec{r}_{a-1})}{d\tau} = \vec{V}_a - \vec{V}_{a-1}$$

The new length of the vortex filament at the next time step ($\tau + \Delta\tau$) is then given by

$$l_{\tau+\Delta\tau} = \left| \vec{V}_a - \vec{V}_{a-1} \right| * \Delta\tau \quad (\text{E.2})$$

The filament strain experienced by the vortex filament over time interval $\Delta\tau$ can then be evaluated from

$$\mathcal{E} = \frac{(l_{\tau+\Delta\tau} - l_\tau)}{l_\tau} \quad (\text{E.3})$$

Because Helmholtz's third law requires that the net strength of any vortex filament should remain constant, the product of the vorticity and its cross-sectional area should also remain constant. To find the effect of strain on vorticity, the vorticity in the filament can be assumed to be concentrated inside a cylinder of length l , with an effective core radius r_c . Since the flow field considered has a constant density, the principle conservation of mass can be used to determine the effective change in the core radius as a result of the change in filament length, Δl . The principle of momentum conserved is also implicitly obeyed. Thus,

$$\begin{aligned} \pi r_c^2 l &= \pi (r_c - \Delta r_c)^2 (l + \Delta l) \\ \left(\frac{r_c - \Delta r_c}{r_c} \right)^2 &= \frac{l}{l + \Delta l} \\ \therefore \Delta r_c &= r_c \left[1 - \frac{1}{\sqrt{1 + \mathcal{E}}} \right] \end{aligned} \quad (\text{E.4})$$

To include the effect of filament straining into the wake solution, an initial core radius must be calculated based on viscous diffusion behaviour. Then the change in core radius due to straining effects is computed using

$$r_{c_{eff}} = r_c \left(\frac{1}{\sqrt{1 + \mathcal{E}}} \right) \quad (\text{E.5})$$

Curriculum Vitae

Tonio Sant was born in Malta on 13th January in 1977. He completed his primary education at Stella Maris School, Balzan and his secondary education at St. Aloysius College, B'Kara. He started his studies in Engineering at the University of Malta in 1995 and graduated in Mechanical Engineering in 1999 with first class honours (*summa cum laude*). His thesis was titled "*Investigating the Aerodynamic Behaviour of Yawed Horizontal-Axis Wind Turbines*" and was awarded as the best mechanical engineering project for that year.

In July 1999, Tonio was employed with STMicroelectronics (Malta) Ltd. as a process engineer in one of the production lines manufacturing integrated electronic chips. In March 2000, he joined Air Malta as an aircraft maintenance engineer. On employment, he followed courses and hands-on training on aircraft maintenance at Air Malta's engineering base, at Lufthansa Technik in Frankfurt and at the Boeing Training Centre, in Seattle. On completing the training, his work focused on the inspection and maintenance of airplanes' structures of Air Malta's Boeing B737 and Airbus A320 fleet. Furthermore, Tonio was also responsible for organising courses for airplane mechanics related to airplane structural inspection and repair.

In 2002, Tonio was engaged temporarily in the newly formed company Lufthansa Technik Malta where he provided technical support in airplane maintenance planning and in training new technical staff.

In January 2003, he joined the Faculty of Engineering at the University of Malta as an assistant lecturer in Mechanical Engineering. At the same time he joined the Delft University Wind Energy Institute (DUWIND) as a Phd student within the Faculty of Aerospace Engineering. His research work focused on the aerodynamics of wind turbines and was supervised by Prof. dr. ir. Gijs van Kuik and Dr.ir. Gerard van Bussel. The research was supported by the University of Malta and Delft University of Technology.

During his Phd studies, Tonio also had a number of duties within the Faculty of Engineering at the University of Malta. He was responsible for teaching *heat transfer*, *fluid mechanics* and *turbo-machinery* (including *wind energy*) to students following the B.Eng. (Hons.) course. He also supervised four final year projects related to wind turbine aerodynamics. He was involved in the installation and performance testing of a small-scale grid-connected wind turbine at the University of Malta.

Tonio's main interests are wind energy, aerospace engineering, theology and nature. He is married to Maris and they live in Malta.

E-mail: tonio.sant@um.edu.mt

Author Publications

1. Sant T., "Investigating the Aerodynamic Behaviour of Yawed Horizontal-Axis Wind Turbines", *B. Eng. (Hons.) thesis*, University of Malta, Malta 1999.
2. Sant T., van Kuik G.A.M. and van Bussel G.J.W., "Using Near Wake Measurements to Improve BEM Engineering Models for Yawed Wind Turbines", *Proceedings from the European Wind Energy Conference*, London 2004.
3. Sant T., "Exploiting the Maltese Waters for Offshore Wind Energy", feature article in the Sunday Times of Malta, 6th March, 2005.
4. Sant T., Haans W., van Kuik G.A.M. and van Bussel G.J.W., "An Approach for the Verification and Validation of Rotor Aerodynamics Codes Based on Free-wake Vortex Methods", *Proceedings from the 31st European Rotorcraft Forum*, Florence, Italy, 2005.
5. Haans W., Sant T., van Kuik G.A.M. and van Bussel G.J.W., "Velocity Measurements in the Near Wake of a Horizontal Axis Wind Turbine ", *Proceedings from the 31st European Rotorcraft Forum*, Florence, Italy, 2005.
6. Caruana C. Sant T., Agius A. and Spiteri Staines C., "Measurement and Analysis of The Performance of a Small-Scale Grid-Connected Wind Turbine Operated in the Maltese Islands," Conference *Renewable Energies on Malta and Beyond*, organized by the Institute of Energy Technology, University of Malta, Sept., 2005.
7. Haans W., Sant T., van Kuik G. and van Bussel G.J.W., "Measurement of Tip Vortex Paths in the Wake of a HAWT under Yawed Flow Conditions", *Journal of Solar Energy Engineering, Special Issue on Wind Energy*, Vol. 127, No. 4, Nov. 2005, pp. 437-596.
8. Sant T., van Kuik G.A.M. and van Bussel G.J.W., "Estimating the Angle of Attack from Blade Pressure Measurements on the NREL Phase VI Rotor using a Free-Wake Vortex Model: Axial Conditions", *Wind Energy*, Vol. 9, No. 6, 2006, pp. 549-577.
9. Sant T., van Kuik G.A.M. and van Bussel G.J.W., "Estimating the Angle of Attack from Blade Pressure Measurements on the NREL Phase VI Rotor in Yaw using a Free-Wake Vortex Model", *Proceedings from the 25th Wind Energy Symposium and the 44th AIAA Aerospace Meeting*, Reno, NV, USA, Jan. 2006.
10. Haans W., Sant T., van Kuik G.A.M. and van Bussel G.J.W., "Stall in Yawed Flow Conditions – a correlation of Blade Element Momentum Predictions to

Experiments”, *Proceedings from the 25th Wind Energy Symposium and the 44th AIAA Aerospace Meeting*, Reno, NV, USA, Jan. 2006.

11. Haans W., Sant T., van Kuik G.A.M. and van Bussel G.J.W, “Stall in Yawed Flow Conditions – a correlation of Blade Element Momentum Predictions to Experiments”, *Journal of Solar Energy Engineering*, Vol. 128, No. 4, Nov. 2006, pp. 472-480.